

Western Australian School of Mines

Seismic Response of Large-scale Structures

Ellen C Morton

**This thesis is presented for the Degree of
Doctor of Philosophy
of
Curtin University**

January 2019

Declaration

To the best of my knowledge and belief this thesis contains no material previously published by any other person except where due acknowledgment has been made.

This thesis contains no material which has been accepted for the award of any other degree or diploma in any university.

Signature:

Date:

Acknowledgements

I would like to sincerely thank Professor Ernesto Villaescusa for all his support encouragement, and guidance throughout the project. Without it this thesis would not have been completed.

I would also like to thank Chris Ho for the little ditty macros that have simplified my life and meant this research was as comprehensive as it was.

Thank you also to Dr Alan Thompson for reading my thesis and providing the grammatical corrections. I will eventually get the hang of it.

Finally, to the following sites for providing the data that has enabled this research to take place.

- Goldfields St Ives Argo (Sarah Webster and others)
- Northern Star Kanowna Bell Operations (Richard Varden)
- Codelco PTY LTD El Teniente Esmeralda Operations (Cesar Pardo)
- Kalgoorlie Consolidated Gold Mines Mt Charlotte Operations (Anthony Gleeson)
- Poseidon Australia Black Swan Nickel
- Big Bell (John Player)
- Copper Mines of Tasmania Mt Lyell Operations (David Cuello)

Table of Contents

DECLARATION	2
ACKNOWLEDGEMENTS	3
TABLE OF CONTENTS	I
LIST OF FIGURES	VII
LIST OF TABLES	XV
ABSTRACT	XVI
1. INTRODUCTION	1
1.1 MINING INDUCED SEISMICITY	2
1.2 ACOUSTIC EMISSION RESEARCH	3
1.3 THESIS SCOPE	4
1.4 THESIS STRUCTURE	5
1.5 ASSUMPTIONS	6
2. MINING SEISMIC DATA BACKGROUND	9
2.1 SEISMIC MONITORING IN MINING	9
2.2 MINE SITE DATA COLLECTION	11
2.2.1 DATA COLLECTION	12
2.2.2 SEISMIC NETWORK REVIEW	13
2.2.3 SEISMIC DATA VALIDATION	13
2.2.4 STRUCTURE SELECTION	16
2.2.5 DOMAIN DEFINITION	16
2.2.6 DATA EXTRACTION	19
2.2.7 DATA ANALYSIS	19
3. MINE SITE DATA REVIEW	20
3.1 ST IVES - ARGO	20
3.1.1 LOCATION AND GEOLOGICAL SETTING	20
3.1.2 MINING METHOD.....	21
3.1.3 LITERATURE REVIEW.....	22
3.1.4 DATA AVAILABILITY.....	22
3.1.5 DISCUSSION ON SEISMICITY AT ARGO.....	22
3.1.6 STRUCTURES FOR ANALYSIS.....	26

3.2	KANOWNA BELLE	35
3.2.1	LOCATION AND GEOLOGICAL SETTING	35
3.2.2	MINING METHOD.....	38
3.2.3	LITERATURE REVIEW.....	39
3.2.4	DATA AVAILABILITY	40
3.2.5	DISCUSSION ON SEISMICITY AT KANOWNA BELLE	41
3.2.6	STRUCTURES FOR ANALYSIS.....	47
3.3	ESMERALDA	55
3.3.1	LOCATION AND GEOLOGICAL SETTING	55
3.3.2	MINING METHOD.....	57
3.3.3	LITERATURE REVIEW.....	58
3.3.4	DATA AVAILABILITY.....	58
3.3.5	DISCUSSION ON SEISMICITY AT ESMERALDA	63
3.3.6	STRUCTURES FOR ANALYSIS.....	70
3.4	MT CHARLOTTE	80
3.4.1	LOCATION AND GEOLOGICAL SETTING	80
3.4.2	MINING METHOD.....	82
3.4.3	LITERATURE REVIEW.....	82
3.4.4	DATA AVAILABILITY.....	83
3.4.5	DISCUSSION ON SEISMICITY AT MT CHARLOTTE	83
3.4.6	STRUCTURES FOR ANALYSIS.....	89
3.5	BLACK SWAN	97
3.5.1	LOCATION AND GEOLOGICAL SETTING	97
3.5.2	MINING METHOD.....	99
3.5.3	LITERATURE REVIEW.....	99
3.5.4	DATA AVAILABILITY.....	100
3.5.5	DISCUSSION ON SEISMICITY AT BLACK SWAN.....	100
3.5.6	STRUCTURES FOR ANALYSIS.....	104
3.6	BIG BELL	107
3.7	MT LYELL	110
3.7.1	LOCATION AND GEOLOGICAL SETTING	110
3.7.2	MINING METHOD.....	110
3.7.3	LITERATURE REVIEW.....	111
3.7.4	DATA AVAILABILITY.....	111
3.7.5	DISCUSSION ON SEISMICITY AT MT LYELL.....	112

3.7.6	GREAT LYELL FAULT	115
3.8	DISCUSSION.....	117
4.	<u>MINING SEISMOLOGY RESEARCH</u>	<u>119</u>
4.1	INTRODUCTION	119
4.2	SOUTH AFRICA	119
4.3	CANADA	124
4.4	AUSTRALIA	127
4.5	DISCUSSION.....	137
5.	<u>CURRENT MINING SEISMIC DATA ANALYSIS</u>	<u>139</u>
5.1	LOCATION	140
5.1.1	BACKGROUND.....	140
5.1.2	APPLICATION AND DISCUSSION	143
5.2	DAILY HISTOGRAM ANALYSIS.....	149
5.2.1	APPLICATION AND DISCUSSION	149
5.3	EVENT MAGNITUDE.....	152
5.3.1	MAGNITUDE - TIME HISTORY ANALYSIS.....	153
5.3.2	APPLICATION AND DISCUSSION	155
5.4	FREQUENCY - MAGNITUDE ANALYSIS.....	158
5.4.1	APPLICATION AND DISCUSSION	160
5.5	DIURNAL ANALYSIS AND OMORI RE-ENTRY ANALYSIS.....	161
5.5.1	APPLICATION AND DISCUSSION	163
5.6	S:P-WAVE ENERGY ANALYSIS	165
5.6.1	APPLICATION AND DISCUSSION	167
5.7	ENERGY INDEX (EI).....	168
5.7.1	APPLICATION AND DISCUSSION	170
5.8	CUMULATIVE APPARENT VOLUME (CAV)	171
5.8.1	APPLICATION AND DISCUSSION	173
5.9	DISCUSSION.....	176
6.	<u>EARTHQUAKE SEISMOLOGY RESEARCH</u>	<u>178</u>
6.1	COMPARING SEISMIC SCALES.....	179
6.2	STAGES OF FAILURE	180
6.3	PRECURSORS TO FAILURE	186
7.	<u>ASSOCIATING MINING AND EARTHQUAKE SEISMOLOGY</u>	<u>190</u>

7.1	INTRODUCTION	190
7.2	STRUCTURAL BEHAVIOUR IN THE MINING ENVIRONMENT	191
7.3	BARRIERS AND ASPERITIES	192
7.4	FAILURE DEFINITIONS	194
7.5	CONDITIONAL ANALYSIS.....	195
8.	<u>EVENT RATE.....</u>	<u>197</u>
8.1	THEORY OF STRUCTURAL BEHAVIOUR IN ACOUSTIC EMISSIONS.....	197
8.2	CUMULATIVE NUMBER OF EVENTS	200
8.3	TIME DIFFERENCE ANALYSIS	204
8.3.1	ANALYSIS METHOD	204
8.3.2	TIME DIFFERENCE FIXED EVENT RESULTS	205
8.3.3	TIME DIFFERENCE RESULTS BY STEPPING DATA	207
8.3.4	ROLLING AVERAGES USING FIXED DATA NUMBERS	209
8.3.5	DISCUSSION OF TIME DIFFERENCE RESULTS.....	213
8.4	ACCUMULATED EVENTS ANALYSIS.....	214
8.4.1	TIME FRAMES FOR ASSESSMENT	214
8.4.2	DAILY EVENT RATE ANALYSIS.....	215
8.4.3	ROLLING AVERAGE DAILY EVENT RATES	221
8.5	DISCUSSION.....	227
9.	<u>SPATIO-TEMPORAL CLUSTERING</u>	<u>228</u>
9.1	EVENT LOCATION GENERAL PRINCIPLES	228
9.2	METHODS OF CLUSTERING	231
9.2.1	FRACTAL DIMENSION.....	231
9.2.2	SPATIAL CORRELATION LENGTH	232
9.3	ANALYSIS METHOD.....	234
9.4	DAILY SCL RATE.....	234
9.5	7 DAY SCL RESULTS.....	237
9.6	7 DAY GROUP 20 RESULTS	241
9.7	DISCUSSION.....	242
10.	<u>MAGNITUDE AND B-VALUE</u>	<u>243</u>
10.1	INTRODUCTION.....	243
10.2	MAGNITUDE AND B-VALUE CONCEPT	243
10.3	TEMPORAL CHANGES IN B-VALUE	245

10.4	B-VALUE CALCULATION	248
10.4.1	CUT-OFF VALUE (M_c)	249
10.4.2	DATA STEPS	251
10.5	MAGNITUDE VARIABILITY (B-VALUE ESTIMATION) EVALUATIONS.....	251
10.5.1	AVERAGE DAILY MAGNITUDE VARIATIONS.	251
10.5.2	7 AND 14 DAY ROLLING AVERAGES	255
10.6	MAGNITUDE ANALYSIS	258
10.7	DISCUSSION.....	262
<u>11.</u>	<u>ENERGY RELEASE RATE</u>	<u>263</u>
11.1	INTRODUCTION.....	263
11.2	ANALYSIS METHOD	266
11.3	RESULTS	266
11.3.1	ENERGY PER DAY	266
11.3.2	7 DAY AVERAGE ENERGY	271
11.4	DISCUSSION.....	271
<u>12.</u>	<u>COMPARISON OF PRECURSORS.....</u>	<u>274</u>
12.1	PRECURSORS CALCULATED USING THE DAILY AVERAGES	274
12.2	PRECURSORS CALCULATED USING THE 7 DAY AVERAGES	276
12.3	FORWARD ANALYSIS	278
12.4	DISCUSSION.....	279
<u>13.</u>	<u>DISCUSSION.....</u>	<u>280</u>
13.1	INCORPORATION OF GEOLOGY INTO ANALYSIS	281
13.2	SENSITIVITY OF SEISMIC SYSTEMS	282
13.3	TIMING OF SEISMIC SYSTEM INSTALLATION	283
13.4	DATA PROCESSING TIME FRAMES	283
<u>14.</u>	<u>CONCLUSION.....</u>	<u>284</u>
14.1	RECOMMENDED FURTHER WORK	285
<u>15.</u>	<u>REFERENCES</u>	<u>286</u>
	<u>APPENDIX 1 – CALCULATION OF SEISMIC PARAMETERS.....</u>	<u>292</u>
	<u>APPENDIX 2 – CUMULATIVE EVENT RATE CHARTS</u>	<u>293</u>
	<u>APPENDIX 3 – TIME DIFFERENCE CHARTS.....</u>	<u>294</u>

<u>APPENDIX 4 – DAILY EVENT RATES.....</u>	<u>295</u>
<u>APPENDIX 5 – DAILY AND 7 DAY EVENT RATE CHARTS.....</u>	<u>296</u>
<u>APPENDIX 6 – SCL 7 DAY GROUP 5 CHARTS</u>	<u>297</u>
<u>APPENDIX 7 – MVM DAILY AND 7 DAY CHARTS.....</u>	<u>298</u>
<u>APPENDIX 8 – ENERGY DAILY CHARTS</u>	<u>299</u>
<u>APPENDIX 9 – PRECURSOR COMPARISON CHARTS - DAILY AVERAGES, INSTANTANEOUS FAILURES RESULTS</u>	<u>300</u>
<u>APPENDIX 10 – PRECURSOR COMPARISON CHARTS - DAILY AVERAGES, ACCELERATING SLIP FAILURES RESULTS</u>	<u>301</u>
<u>APPENDIX 11 – PRECURSOR COMPARISON CHARTS - 7 DAY AVERAGES, INSTANTANEOUS FAILURES RESULTS</u>	<u>302</u>
<u>APPENDIX 12 – PRECURSOR COMPARISON CHARTS - 7 DAY AVERAGES, ACCELERATING SLIP FAILURE RESULTS</u>	<u>303</u>

List of Figures

Figure 2.1: Typical magnitude distribution of a seismic data set.....	15
Figure 2.2: Poor magnitude distribution suggesting further investigation of the magnitude calculations.	15
Figure 2.3: Strong correlation of events to the structure.....	17
Figure 2.4: Poor correlation of events to structure.....	18
Figure 2.5: Domains boundary creation using a single surface.	18
Figure 2.6: Domain boundary creation using two surfaces.....	19
Figure 3.1: “Schematic west east cross section highlighting the numerous ore surfaces of the Argo deposit” Andrews, 2006, modified after Dusci et al., 2003.....	21
Figure 3.2: Argo seismic sensor locations looking north with ore bodies indicated. The lower 4 sensors (circled) were inoperable for much of the monitoring period.	23
Figure 3.3: Argo seismic event locations.....	24
Figure 3.4: Magnitude distributions for the Argo mine site.....	25
Figure 3.5: Argo structures for analysis (looking west)	26
Figure 3.6: Distances of events from the A1 Shear.	27
Figure 3.7: Event locations for the A1 Shear.....	28
Figure 3.8: Separation of dataset into FW and HW domains.....	30
Figure 3.9: Distances of events from the North Dyke hangingwall and footwall.....	31
Figure 3.10: Seismic event locations for the North Dyke looking north.....	32
Figure 3.11: Distances of events to the FW contact of the Mini Dyke.....	33
Figure 3.12: Locations of events associated with the Mini Dyke.....	34
Figure 3.13: Schematic cross section of the Kanowna Belle deposit (Ross et al. 2004)	36
Figure 3.14: WASM structural model of Kanowna Belle.	37
Figure 3.15: Layout of the Kanowna Belle mining blocks (after Varden and Esterhuizen, 2012).....	39
Figure 3.16: Kanowna Belle seismic sensor locations looking north.....	41
Figure 3.17: Kanowna Belle seismic sensor locations looking west.	42
Figure 3.18: Total cumulative event rate for Kanowna Belle.	43
Figure 3.19: Cumulative event rate between Dec 2009 and Feb 2010 indicating no events between the 31 st Dec 2009 and the 18 th Feb 2010.....	43
Figure 3.20: Kanowna Belle seismic event locations looking north.	45
Figure 3.21: Magnitude distribution of Kanowna Belle seismic events.	46
Figure 3.22: Kanowna Belle structures for analysis.....	47

Figure 3.23: Distances of seismic events to the Fitzroy Fault.....	48
Figure 3.24: Location of events for the Fitzroy Fault.	49
Figure 3.25: Layout of the NE structures and their domain definitions.....	51
Figure 3.26: Distances of events to the NE faults.....	52
Figure 3.27: Distances of events located in the HW of S169 and distance of events located in the FW of S121.....	52
Figure 3.28: Locations of seismic events for the NE fault Group 1.	53
Figure 3.29: Locations of seismic events for the NE fault Group 2.	54
Figure 3.30: The El Teniente geological setting Stern et al., 2011.	56
Figure 3.31: Plan of El Teniente Mine site with various mining districts.....	57
Figure 3.32: Esmeralda structural model prior to reinterpretation.	60
Figure 3.33: Revised fault model for Esmeralda mine site (plan view).	61
Figure 3.34: Dyke models for Esmeralda site.....	62
Figure 3.35: Location of El Teniente seismic sensors (plan view).	64
Figure 3.36: Sensor locations with reference to the Esmeralda extraction level (looking west).	64
Figure 3.37: Plan of the locations of the events in the Esmeralda seismic database.	65
Figure 3.38: Curve distributions of magnitudes for 1999 – 2000, 2001 – Oct 2002 and Oct 2002 – 2004.	67
Figure 3.39: The differences between the original magnitudes and the newly calculated magnitudes clearly indicate an anomaly in the data in 2001 and 2002. ...	68
Figure 3.40: Distribution of the newly calculated magnitudes between Jan 2001 and Oct 2002.	68
Figure 3.41: Large events (over 1M _L) at Esmeralda concentrate around the diorite dykes (plan view).	69
Figure 3.42: Esmeralda structures for analysis.	70
Figure 3.43: FaultP_1 with seismic sensors.	71
Figure 3.44: Distances of seismic events from FaultP_1.....	72
Figure 3.45: Locations of events on FaultP_1.....	72
Figure 3.46: Fault B old models	73
Figure 3.47: Fault B new models. Part C is indicated in red.	74
Figure 3.48: Seismic event distance distribution away from Fault B_C.	75
Figure 3.49: Locations of events on FaultB_C.	76
Figure 3.50: Events removed from inside the dyke model to prevent distance anomalies.	78
Figure 3.51: Seismic event distance distribution away from FW Dyke.....	78

Figure 3.52: Locations of seismic events within the FW Dyke.....	79
Figure 3.53: Mt Charlotte geological units and faults in (L) Plan and (R) section Ridley and Mengler, 2000.....	81
Figure 3.54: Seismic sensor locations at Mt Charlotte (looking north).....	84
Figure 3.55: Seismic event locations from the MSRAP dataset looking west.	87
Figure 3.56: Magnitude distribution for Mt Charlotte MSRAP dataset.....	88
Figure 3.57: Mt Charlotte faults for analysis.	89
Figure 3.58: Distances of seismic events from Maritana Fault.	90
Figure 3.59: Locations of events for the Maritana Fault.....	91
Figure 3.60: Distances of events from the Reward Fault.....	92
Figure 3.61: Locations of events on the Reward Fault.	93
Figure 3.62: Flanagan fault offsets.....	94
Figure 3.63: Distances of events from Flanagan_1 Fault.	95
Figure 3.64: Locations of events on Flanagan1 Fault (looking east).....	96
Figure 3.65: Long section of the Silver Swan Underground mine (looking west). ...	98
Figure 3.66: Seismic sensor locations at Black Swan.	101
Figure 3.67: Locations of events at Black Swan.....	102
Figure 3.68: Magnitude distribution for Black Swan.	103
Figure 3.69: Feral Fault projection with descriptions at intersection points.....	105
Figure 3.70: Distances of events from the Feral Fault.....	105
Figure 3.71: Locations of seismic events for the Feral Fault.	106
Figure 3.72: Projection of the survey pickups at each of the incept points.....	109
Figure 3.73: Mt Lyell layout (Sharrock and Cuello, 2016).....	110
Figure 3.74: Mt Lyell seismic sensor locations.	112
Figure 3.75: Mt Lyell seismic event locations.	113
Figure 3.76: Magnitude distribution for the Mt Lyell mine site.....	114
Figure 3.77: Comparison of the distribution of magnitudes using the old and new formulas.....	114
Figure 3.78: Great Lyell structure.....	115
Figure 3.79: Distances of events from the Great Lyell Shear.	116
Figure 3.80: Event locations for the Great Lyell Shear.	116
Figure 4.1: Six models of induced seismicity proposed by Hasegawa et al., 1989.	124
Figure 4.2: Determination of the probability of R4 or R5 damage on the RDS using EVP and PPV_{max} (after Heal, 2010).....	133
Figure 4.3: Idealised failure progression of faults at Kundana Gold Mine later shown to be too simplistic (Slade, 2004).	134

Figure 4.4: Comparison of AE rates with loading and observations in small scale tunnel simulations (Kusui and Villaescusa, 2016).	136
Figure 5.1: Clustered seismic data (Hudyma and Potvin, 2009).....	142
Figure 5.2: Events related to the Feral Fault. The locations of the events alone do not provide adequate information for detailed analysis.	144
Figure 5.3: Feral Fault “groups” using the MS RAP method.....	144
Figure 5.4: Events for the Flanagan Fault demonstrating clustering around stope abutments.....	145
Figure 5.5: Clustering of events on Esmeralda FaultB_C structure shows a strong correlation with intersecting geological features.....	146
Figure 5.6: Esmeralda Fault B-C failure progression with time (looking perpendicular to the fault).....	148
Figure 5.7: Daily events for the Argo Mini Dyke.	150
Figure 5.8: Significant increase in event rate on Mt Charlotte’s Maritana Fault. ...	151
Figure 5.9: Magnitude time history chart (Mikula et al., 2008)	154
Figure 5.10: Cumulative event chart for North East Faults Group 1.	155
Figure 5.11: Cumulative event chart for the Flanagan Fault.....	156
Figure 5.12: Rolling maximum magnitude (100 events) for TBSD (grey), FFG (red) and FFSD (Black).	157
Figure 5.13: b-value theory. The red line suggests a fault slip mechanism whereas the blue line suggests “stress change”.....	159
Figure 5.14: Example of Omori analysis (ACG, 2005).....	162
Figure 5.15: Example of diurnal analysis (Mikula et al., 2008).....	163
Figure 5.16: Diurnal analysis for Kanowna Belle NE faults group 2.....	164
Figure 5.17: Diurnal analysis for Flanagan_1 fault.	165
Figure 5.18: Concept of Energy Index as provided by Mendecki, 1997.....	169
Figure 5.19: Log Energy / Log Moment chart for Feral fault.	170
Figure 5.20: Example of CAV and EI analysis from Mendecki et al., 2010.	172
Figure 5.21: Cumulative apparent volume for Flanagan Fault.....	174
Figure 5.22: CAV results for Esmeralda FaultP_1 between Jan 2000 and Dec 2003	175
Figure 6.1: Stages of failure according to Main and Meredith, 1989 (not to scale)	183
Figure 6.2: Stages of failure adapted from Lei et al., 1992.....	184
Figure 6.3: Progression of failure identified by AE results through a testing of a heterogeneous sample (Lei et al., 2003).....	185
Figure 6.4: Repetition of increases in event rate indicates failure of multiple asperities (Lei et al., 2003).....	185

Figure 6.5: Types of waveforms identified by Lei et al 2003(a).....	188
Figure 7.1: Barrier model (after Aki, 1984).	193
Figure 7.2: Asperity model after (Aki, 1984).	193
Figure 7.3: Example of spreadsheet macro layout.	196
Figure 7.4: Example of conditional analysis on a decreasing trend.	196
Figure 8.1: Exponential increase in event rate with increasing stress (Main and Meredith, 1989).	198
Figure 8.2: Repetition of increases in event rate indicates failure of multiple asperities (Lei et al., 2003).....	199
Figure 8.3: Example of the cumulative event rate for a large-scale structure (Fault P1).....	201
Figure 8.4: Closer examination of the Example 2 failure.	202
Figure 8.5: Closer examination of the apparently non-conformist event shows further embedded nucleation.	202
Figure 8.6: Calculation of the gradient of the cumulative event rate.	203
Figure 8.7: Concept of increasing event rate and decreasing time difference.	204
Figure 8.8: Example of erratic nature of time difference (NE G2).	206
Figure 8.9: Summary of time-difference decreasing trends for each fault.....	207
Figure 8.10: Data point stepping.	208
Figure 8.11: Summary results from data smoothing using the stepped method. ...	208
Figure 8.12: Method for determining rolling average for a fixed number of events.	209
Figure 8.13: Smoothing of results using average time difference data calculations (NE G2).	211
Figure 8.14: Summary of time difference results.	212
Figure 8.15: Example of events per day chart indicating failures (Feral Fault).	216
Figure 8.16: General increasing trend in daily event rate (Feral Fault).	217
Figure 8.17: Percentage of instantaneous failures indicating increasing trends in the days prior to the event.	218
Figure 8.18: Percentage of accelerating slip failures indicating increasing trends in the days prior to the event.	219
Figure 8.19: Example of fluctuating daily event rate (FW Dyke).	220
Figure 8.20: Example of data smoothing (Fault B_C).....	222
Figure 8.21: Instantaneous failures rolling average summary.	223
Figure 8.22: Example of improved results due to data smoothing of instantaneous failures (FW Dyke).....	224

Figure 8.23: Results on the conditional analysis for daily event rate data smoothed over 7 days (instantaneous failures).	224
Figure 8.24: Summary of rolling average results for accelerating slip failures.	225
Figure 8.25: Example of improved results as a consequence of smoothing (Fault B_C).	226
Figure 9.1: Coalescence of AE events demonstrated after Lockner et al., 1991...	229
Figure 9.2: Failure progression of multiple asperities (Lei et al., 2003a).....	230
Figure 9.3: Spatial correlation length (SCL) is calculated by linking events into pairs and then calculating the distance between each pair.	233
Figure 9.4: Trends in SCL and fractal dimension during failure.	233
Figure 9.5: Example of SCL results highlighting increase in event rate with decrease in SCL (Feral Fault).	235
Figure 9.6: Results of conditional analysis of the daily SCL for instantaneous failures.	236
Figure 9.7: Results of conditional analysis of the daily SCL analysis for accelerating slip failures.....	236
Figure 9.8: Explanation of the determination of number of events for the calculation of the SCL over 7 days with a group size of 5.	237
Figure 9.9: Example of phases of failure evident in the 7 day group 5 SCL results (Flanagan Fault).	238
Figure 9.10: Results of 7 day group 5 conditional analyses for instantaneous failures.	240
Figure 9.11: Results of 7 day group 5 conditional analyses for accelerating slip failures.....	240
Figure 9.12: Comparison of average results of the conditional assessment of the instantaneous failures from the 7 day group 20 data with the results from the 7 day group 5 and daily group 5 data.	241
Figure 9.13: Comparison of average results of the conditional assessment of the instantaneous failures from the 7 day group 20 data with the results from the 7 day group 5 and daily group 5 data.	242
Figure 10.1: b-value is determined by the slope of the Magnitude – Frequency chart.	244
Figure 10.2: Typical change in b-value during testing of a sample (after Main and Meredith, 1989).	246
Figure 10.3: Limits of sensitivity for the seismic data records.....	249
Figure 10.4: Example of cut-off value determination (FW Dyke).	250
Figure 10.5: Example of the daily MVM (NE Faults G2).....	253

Figure 10.6: Results of daily MVM conditional analysis on instantaneous failures.	254
Figure 10.7: Results of daily MVM conditional analysis on accelerating slip failures.	254
Figure 10.8: Example of 7 day average MVM (NE Faults G2).	256
Figure 10.9: Average results of data smoothing for instantaneous failures.	257
Figure 10.10: Average results of data smoothing for accelerating slip failures.	257
Figure 10.11: Example of the average daily magnitude with the phases of failure characterised (Feral Fault).	259
Figure 10.12: Qualitative assessment of the increasing trend prior to rupture (Feral Fault).	260
Figure 10.13: Results of average daily magnitude conditional analysis on instantaneous failures.	260
Figure 10.14: Average magnitude trends indicting phases of failure (Feral Fault).	261
Figure 10.15: Results of data smoothing of average magnitude for instantaneous failures.	262
Figure 11.1: Contouring of the energy of the AE events in the latter stages of sample failure clearly indicate strength heterogeneity (Lockner et al., 1991)	264
Figure 11.2: Comparative behaviour of cumulative energy over time with b-value and the phases of failure (after Lei, 2006).	265
Figure 11.3: Example of average daily energy with the cumulative event rate. Time periods A and C highlight where that the energy is low during periods of low seismic activity. Time period B indicates where high energy confers with failure (FW Dyke).	267
Figure 11.4: Examination of the trend in 2007 that highlights increasing event rate with low values of energy (FW Dyke).	268
Figure 11.5: Results of conditional analyses of daily energy release for instantaneous failures.	270
Figure 11.6: Results of conditional analyses of daily energy for accelerating slip failures.	270
Figure 11.7: Average 7 day energy for FW Dyke.	272
Figure 11.8: Comparison of results of conditional analysis for energy release for instantaneous failures.	273
Figure 11.9: Comparison of results of conditional analysis for energy release for accelerating slip failures.	273

Figure 12.1: Average results of the conditional analysis of instantaneous failures for each precursor.....	275
Figure 12.2: Average results of the conditional analysis of accelerating slip failures for each precursor.....	275
Figure 12.3: Average results of the conditional analysis of instantaneous failures for each precursor.....	277
Figure 12.4: Average results of the conditional analysis of instantaneous failures for each precursor.....	277
Figure 12.5: Average results for the number of days that show an increasing trend in the overall dataset.	278

List of Tables

Table 3.1: Data availability for St Ives Argo.....	22
Table 3.2: Log of inoperability of components of the seismic monitoring system at Argo.....	23
Table 3.3: Kanowna Belle model names compared with WASM model names.	38
Table 3.4: Data availability for Kanowna Belle.	40
Table 3.5: WASM model with corresponding model names at depth.....	50
Table 3.6: Data availability for Esmeralda site	58
Table 3.7: Summary of faults within the Mt Charlotte mining area.....	80
Table 3.8: Data availability for Mt Charlotte.....	83
Table 3.9: Filtering criteria and number of events removed from data set.	86
Table 3.10: Data availability for Black Swan.	100
Table 3.11: Average orientations of survey pickups (taken from models at individual locations).	109
Table 3.12: Data availability for Mt Lyell.....	111
Table 4.1: Rock damage prediction model due to seismic events used by Albrecht, 2005.	128
Table 4.2: Ground support energy capacity rating system (after Heal, 2010).	131
Table 4.3: Geological factor description (after Heal, 2010).....	131
Table 4.4: Rockburst Damage Scale (after Heal, 2010).	133
Table 4.5: Seismic hazard matrix proposed by Heal, 2010.	133
Table 5.1: Static b-values for large-scale structures.....	160
Table 5.2: S:P ratios for large-scale structures.	168
Table 6.1: Summary of the behaviour of rock samples during the phases of failure.	181
Table 8.1: Summary of the effects from AE testing of the failure phase and rock mass properties on the event rate (Lei et al. 2004).....	198
Table 8.2: Values used to aid in smoothing the time difference data.....	210
Table 8.3: Average number of events on the day of and days prior to the instantaneous failure.....	220
Table 10.1: Cut-off values for each structure.	250

Abstract

Most rock masses exhibit non-linear failure properties due to inherent strength variations and pre-existing discontinuities. As stresses and strains are altered due to mining, strain accumulation occurs within the rock mass. The stronger the rock mass, the more strain that can be accumulated. When the accumulated strain reaches the maximum rock mass strain at a particular location, fracturing occurs. The associated release of energy that occurs during the fracturing process is measured by accelerometers and defined as a seismic event. The larger the strain accumulation, the more energy that may be released at failure and, correspondingly, the larger the seismic event. All seismic events represent failure of varying scales.

Seismicity is a vast area of research that encompasses multiple scales of failure and multiple areas of discipline. This thesis examines both the fields of mining-induced seismicity and earthquake science. The effect of mining-induced seismicity on the stability of many deep mining operations and the safety of the workforce is well-documented. These effects include on-going instability of excavations that significantly increase ground support costs, decrease productivity and have led to serious injuries and fatalities.

Earthquake scientists have been conducting research into precursors to large earthquakes for almost 50 years. The premise of the research is that changes in seismic data trends (precursors) occur prior to the failure of the rock mass. Due to the scale of the earthquake sized failures scientist have undertaken research on small scale core samples within the laboratory. The assumption is that failures are self-similar and scale independent. This means that the same mechanisms of failure occur on all scales. Through analysis of data from the testing of small-scale samples precursory behaviour was identified. Precursory behaviour suggests that prior to failure the rock mass exhibits recognisable patterns that suggest the impending failure. The patterns described as stages. The stages of failure are typically referred to as the primary, secondary and nucleation phases (Mogi, 1962a, Lei et al., 2003a, etc.). During the primary stage of failure, the rock mass exhibits elastic behaviour with a low seismic rate. In the secondary stage, failure begins to coalesce, and seismicity increases gradually. In the final stage of failure a rapid increase in seismicity is observed just prior to final failure. Throughout the literature the most common parameters that demonstrate precursory behaviour are event rate, location, magnitude and energy.

Mine site data represents the intermediate scale of failure between the earthquake scale failure and the laboratory testing. A methodology was developed to enable the analysis of seismic data specific large-scale structures that have been modelled by the mine sites. Seven mine sites provided data for a range of analysis to be undertaken.

The analysis was twofold. Using the mine site data, evaluations were undertaken to determine if incorporating local geological features improved the current analysis techniques. This analysis demonstrated that whilst some improvements were noted in general the current analysis techniques were too static and did not effectively consider the variations in the data over time.

The seismic data from the large-scale structures were also assessed to determine if precursory trends could be identified prior to failure. The parameters evaluated were event rate, spatial correlation length, b-value and energy release. The analysis included the evaluation of changes in each parameter with time. Failures were described as seismic events with magnitudes greater than a specified magnitude threshold and days where over 20 events occurred. These were called instantaneous failures and accelerating slip failures respectively. Over 300 failures on 15 structures were back analysed to quantify the success of the trends.

Conditional analysis, determining whether a parameter was changing prior to failure, was undertaken. This analysis involved a simple yes / no test. If, in the day prior to failure (rupture), positive correlations with the expected trend occurred then the previous day is analysed until a negative result is achieved. Analysis of the daily changes in the parameters could not determine conclusive results. However, changes in the 7-day rolling average of each parameter provided meaningful results. The results demonstrated that it is difficult to determine impending failure further than 5 days prior to the occurrence. However, the change between the primary and secondary stages of failure can be identified in seismic data 2 – 3 days prior to failure. Nucleation typically occurs minutes or hours prior to failure and was not easily identified in all parameters. As it is possible that the stages can be identified it suggests that dynamic failures with the rock mass are self-similar and that similar patterns can be observed at all scales.

Forward analysis undertaken to determine how frequently changes in each parameter were observed to determine if the parameter could be practically applied in the mining environment. The results demonstrated that most parameters occurred infrequently enough (<10 times per year) that analysis of the parameters is practical and useful.

1. Introduction

The term seismicity implies a large range of concepts and analytical methods over a broad range of scientific disciplines. Despite sometimes overly complex descriptions, seismicity is the measured response of rock mass failure. Seismology is the study of that failure. The field of seismology can generally be divided into 3 distinct topics based on scale; earthquake seismology, induced seismology and simulated seismology. Earthquake seismology is the most well-known of the three topics. Earthquake events occur over a scale of several hundreds of kilometres and generally lead to significant destruction of infrastructure and loss of life. Research into earthquakes is extensive with entire research units dedicated to data collection and analysis. Data from earthquakes is collected on national and international seismic networks.

Induced seismology incorporates mining-induced seismicity and fluid-induced seismicity. Failure generally occurs on scales between centimetres and metres. Fluid induced seismicity occurs during the filling of reservoirs or the pumping of gas wells and is caused by pore pressure changes within the rock mass. Increasing pore pressure causes strain to accumulate in weaknesses in the rock mass resulting in failure. Similarly, decreases in pore pressure cause relaxation of the rock mass also resulting in failure.

Mining-induced seismicity is more common than the general public realise. Mining depths throughout the world are ever increasing as demand for natural resources increase and resources become less accessible. At depth, stresses and strains are closer to equilibrium with the rock mass strength. By creating voids within the rock mass these stresses are modified and occasionally concentrated resulting in rock mass failure. Seismicity is typically the direct output of this rock mass failure. The resultant damage to excavations can be significant and impact on the safety of the mining environment. Typically, this data is collected using specialised monitoring equipment (seismic systems) installed within the mining environment. Failure and seismicity in the mining environment is the focus of this thesis and is described in more detail in the following chapter.

Simulated seismology, also referred to as acoustic emission studies, is the study of small-scale laboratory replications of rock fracturing. Seismicity is believed to be scale invariant. The theory suggests that trends and patterns observed in small scale simulations can be used to examine larger scale events. Laboratory experiments involving the testing of rock samples to assess their failure mechanisms have been undertaken in an attempt to understand the behaviour of larger scale structures. These laboratory studies have typically been applied to earthquake research; however very few of these studies have been applied to mining seismicity.

1.1 Mining induced seismicity

Mining induced seismicity has been a risk factor world-wide since at least the early 1900s. As mines have increased in depth and a greater understanding of rock strengths and stresses has developed, more awareness of mine seismicity has increased.

Detailed studies of seismicity in hard rock mining have been increasing since the 1980s. Mining-specific monitoring began in the 1980s with several seismic monitoring trials conducted in Canada and South Africa. These trials identified the need for more robust mining – specific solutions. These solutions were developed separately in South Africa and Canada in the 1990s.

At the time of writing the Institute of Mine Seismology (IMS) who supply and install mining seismic monitoring systems, supported 232 customers in 31 countries with 62 of these systems currently active within Australia (Institute of Mine Seismology, 2013).

The analysis of the data from these monitoring systems was developed to complement the development of the monitoring systems. The analyses typically consider event rate, location energy and magnitude. These are discussed in later Chapters.

Aside from IMS, there are numerous research organisations throughout the world undertaking research on mining induced seismicity. The analysis techniques have changed very little since the 1990s. Much of the research is focused on data analysis without consideration of the geological environment in which the seismicity is occurring. The analyses contained within this thesis are twofold: Firstly, traditional cluster methods will not be used. Instead a domain approach will be used to create data subsets specific to known large-scale structures. The current analysis techniques will be applied to the structure data to determine if the analysis methods have been improved using the domaining method. The latter half of the thesis will focus on the analysis of the data subsets using theories developed in acoustic emission research.

1.2 Acoustic emission research

Earthquakes have affected intercontinental regions of the world arguably since the beginning of time. Recent large earthquakes in Iran (2003), Indonesia (2004), Pakistan (2005), China (2008), Haiti (2010), Japan (2011) and Italy (2016) have led to large losses of life and substantial damage to infrastructure.

Earthquake seismology is the study of large-scale energy releases usually related to rock structure movements caused by plate tectonics and volcanic activity. Earthquake seismology is a large field of science and it is outside the scope of this thesis to provide a comprehensive background into this area. The monitoring of earthquakes presents several challenges. Monitoring over hundreds of kilometres both across the earth's surface and into the earth surface presents many challenges. Attempting to do this with an incomplete geological understanding of the rock mass complexities and with enough accuracy to ensure all events are recorded is near on impossible. Additionally, large-scale faults do not fail at regular intervals. Dense seismic networks were setup in Japan (the Tokai experiment) and the USA (the Parkfield experiment) in the mid-1990s around areas of expected seismic release (Kagan, 1997). Both these experiments have only had limited success in the last 20 years – primarily due to the lack of large seismic events.

In the 1960s it was recognised that earthquakes were the manifestation of fracturing (Mogi, 1962). It was further assumed that earthquakes are scale invariant i.e. that the fundamental concepts apply over all scales. This theory has become generally accepted and acoustic emission studies have been used to overcome the limitations of earthquake scale studies.

Simulation of the behaviour of large-scale rock fracturing is conducted predominantly by testing small-scale core samples and analysing the acoustic response of the sample during failure. This field of research began in the 1950s and 60s and has been on-going since the 1970s. From these studies a series of precursory trends in the seismic data have been identified that have potential to indicate impending failure. These results have been used to investigate trends in earthquake seismicity with varying success. Very few studies have been undertaken on applying these theories to mining seismic data.

The purpose of this research is to examine rock failure precursors discovered in simulated seismology and apply the same analysis techniques to mining induced seismic data from mine sites to determine if the same patterns can be determined.

1.3 Thesis scope

The general purpose of this thesis is twofold. Firstly, a methodology will be developed to enable the analysis of seismic data on specific large-scale structures. This methodology will be systematic using software typically available to mining practitioners and can be repeated on multiple structures. The data from these structures will be analysed using current analysis techniques to determine if any improvements are achieved by analysing specific structures.

The second and more significant purpose of the thesis is to determine if patterns of failure on specific large-scale structures within the mining environment can be identified. These patterns of failure have been observed in laboratory tests and in some earthquake data sets. In terms of scale, structures within the mining environment are on the intermediate scale between the earthquake and laboratory scales. If failure patterns can be observed, it suggests that rock fracturing patterns are scale-independent. Unique methods of analysis will be developed to enable the execution of this analysis.

1.4 Thesis structure

This thesis discusses a broad range of topics including the individual mines, the structural geology of each of the mines, mining seismic data, mining seismic research and analysis and earthquake research and analysis. The approach to earthquake analysis is then applied to the mining seismic data. Each of these areas are not necessarily directly related to each other. Research within the mining environment has many concepts that are distinctly different from those within the field of earthquake analysis.

The following introduction will provide a broad overview to the scope of this research. To provide a clear structure for the remainder of the thesis it has been separated into three distinct sections; Mine site seismic data, Mining seismology research and data analysis and Earthquake seismology research and data analysis. Each section comprises several chapters.

To unite the different areas of seismology, the thesis will be structured around data collected from seven mine sites. The Mine Site Seismic Data section provides an overview of each mine site and presents the seismic data and faults for analysis. This section contains Chapters 2 and 3. The purpose of these chapters is to provide a background to the data sets and give an insight into the quality of the data as they are used for analysis in the later chapters and to provide a new methodology for creating data subsets for analysis.

The Mining Seismology Research and Data Analysis section is comprised of Chapters 4 and 5. The aim of the section is to review the current research and analysis practices in the mining industry. The current seismic analysis techniques will be applied to the new datasets created in the Mine Site data section to determine if the practices can be improved upon.

Chapters 6 to 11 form the basis of the original research component and are contained within the Earthquake Seismology Research and Data Analysis section. The concepts and analysis presented here are unrelated to the current mining practices of the previous section. The chapters review current analysis techniques in earthquake applications. The chapters present theories regarding self-similarity in rock failure and precursory behaviour prior to rock failure. These theories have been developed from acoustic emission research and outline several parameters that once analysed may demonstrate impending failure. Methods to analyse these concepts were developed and applied to the mine site data. The purpose of these chapters is to determine if trends in approaching failure determined from laboratory testing can be identified in the mining seismic data. Chapter 12 highlights the best parameters for using in mining seismic hazard identification.

The final 2 chapters (Chapters 13 and 14) provide the discussion and conclusions of the results and Chapter 15 presents the references for the entire thesis.

1.5 Assumptions

There were many assumptions made throughout the thesis. These often concerned the following areas:

- Quality of the instrumentation
- Quality of the seismic data
- Accuracy of the fault models

These assumptions have been discussed throughout the thesis in the relevant sections. However, there are several primary assumptions that have been made that must be outlined to give context to the following discussions.

Firstly, seismic events equate to failure of the rock mass. For energy to be released, sufficient energy must be stored. This cannot occur in weak or broken material. Any discussions regarding seismic events being related to intact rock failure or structural failure are superfluous. Structures are inherently heterogeneous and for fault movement to occur some level of intact rock failure must occur. Chapter 7.3 discusses the concept of barriers and asperities that explains this assumption of structural failure occurring because of failure through intact rock.

The second primary assumption concerns the behaviour of large-scale structures. The current analysis methods for seismic data assume that events located spatially near to each other are related and those remote to each other are not. In this thesis a domaining method is used to select data along the length of a large-scale structure. It is assumed that these events are related to each other regardless of the distance apart. It can be likened to the butterfly affect; the failure of a small asperity at one end of a large-scale structure may influence the stress distribution across the entire structure and cause a large asperity to fail at the other end of the structure.

Mine Site Seismic Data

2. Mining seismic data background

Despite a large volume of intensive research concerning mining induced seismicity, much of it ignores the geological setting. The premise of the current research is that the geological setting is crucial to understanding the seismic behaviour of the rock mass and that the major cause of mining induced seismicity is failure of pre-existing structures. At mining scales, large-scale structures typically represent the weakest point in the rock mass. Furthermore, research into the behaviour of large-scale structures and failure mechanisms within the mining environment are limited. Understanding the behaviour of these structures is critical to reducing rock instability and improving safety within the mining environment.

2.1 Seismic monitoring in mining

There are two principal companies that provide seismic monitoring systems for the mining industry. These are the Canadian based Engineering Seismology Group (ESG) and the South African based Institute of Mine Seismology (IMS).

The Canadian seismic monitoring system began as a Queens University research project in the 1980s (Engineering Seismology Group Inc, 2013). The project was developed in response to safety concerns in the North Ontario mining district. The commercial company Engineering Seismology Group (ESG) was setup in the early 1990s once the research project concluded. This company developed the ESG seismic monitoring system.

The South African seismic monitoring system was developed by the Institute of Mine Seismology (IMS) – formerly ISS International in the 1990s (Institute of Mine Seismology, 2013). The initial research for applying seismic monitoring in mines was conducted under a Safety in Mining Research Advisory Committee (SIMRAC) research project (Mendecki et al., 1996).

Monitoring is undertaken through accelerometers or geophones installed within the rock mass. The monitoring instruments transmit the ground vibrations to a central control box which then transfers the signals and the time to a central computer.

Both companies sell proprietary software for the processing and analysis of the seismic signals. IMS provides a program called “TRACE” whilst ESG provides a software suite called Hyperion Seismic Software (HSS) for processing seismic events.

Processing is first conducted by the software, converting the signal into a seismic waveform. P and S wave initiation points are first selected automatically by the

software (based on signal processing theories) and the software then calculates location, energy, moment and a range of other seismic source parameters. These are discussed later in this chapter. The automatic selection of P and S wave initiation points is often inaccurate due to high noise-to-signal ratios created by the mining environment. This causes errors in the location and seismic source parameters. Consequently, it is necessary to manually process each seismic event. Manual processing involves the operator selecting the P and S wave initiation points on the seismic wave related to the event for each sensor. Where the initiation points are not clear due to signal interference the wave for that sensor will be rejected from the calculations. Where there is not enough information to undertake parameter calculations the overall event is rejected. This review is also required to remove blasts and other mining related sound waves from the dataset to ensure reliable data for analysis. Manual processing is often undertaken by the on-site Geotechnical Engineer or a trained Geotechnical Assistant. In recent years it has become more common to outsource manual processing to specialist service companies.

All data used within this study was collected using IMS monitoring systems and processing software. No further mention will be made of the ESG system. The IMS system calculates a large assortment of seismic source parameters for each individual seismic event. The following parameters are typically used in analysis:

- Location
- Energy
- Moment
- Potency
- Magnitude
- Corner frequency
- Radius
- Apparent Stress
- Apparent Volume

Descriptions and equations for each of these parameters are included in Appendix 1.

2.2 Mine site data collection

Seven sites provided data for analysis as part of this project:

- St Ives Argo (now closed - Goldfields)
- Kanowna Bell Operations (Northern Star)
- El Teniente Esmeralda (Codelco)
- Mt Charlotte Operations (Kalgoorlie Consolidated Gold Mines)
- Black Swan Nickel (now closed - currently owned by Poseidon Australia)
- Big Bell (now closed – formerly owned by Harmony)
- Mt Lyell (now closed - Copper Mines of Tasmania)

The objective of the following investigations is to conduct seismic analyses specific to geological features of each mine site. To achieve this, the seismic databases were divided into subsets based on the proximity of seismic events to large-scale structures. The process of data validation and partitioning was undertaken in the following sequence:

1. Data collection
2. Seismic network review
3. Structural model validation
4. Seismic data validation
5. Domain definition
6. Distance analysis
7. Data extraction
8. Data analysis

Some of these steps were iterative as in a number of cases errors were identified during the analyses that led to re-validation and re-analysis of the data. Once validation was complete only 6 sites were used in the analysis. This is discussed in Chapter 3.

2.2.1 Data collection

The following data were requested from each mine site:

- Seismic data
- Seismic system sensor locations
- Seismic system history
- Geological models
- Excavation layout – including decline, levels and mined stopes.

2.2.1.1 Seismic data

Seismic data was used for improving the traditional analysis and developing and testing new analysis techniques proposed.

2.2.1.2 Seismic system sensor locations

Seismic sensor locations were used to determine the adequacy of the coverage of the seismic monitoring system. In particular, the locations were used to examine the coverage for specific large-scale structures being analysed.

2.2.1.3 Seismic system history

The seismic monitoring system history was used to identify periods where changes to the monitoring system may affect the analysis results e.g. system upgrades or outages that create artificial changes in the seismic event rate. Where this data is missing system inoperability may be inferred from the seismic data.

2.2.1.4 Geological models

The geological models form the basis of all the analysis in later chapters. They were used to create seismic data subsets specific to the structures. This process is described in Chapter 2.2.5. The accuracy of the geological models can have a significant influence on the results of this analysis. The structure was not analysed in cases where the accuracy cannot be verified.

2.2.1.5 Excavation layout – including decline, levels and mine stopes.

The excavation layouts were requested to provide context to the seismic data.

2.2.2 Seismic network review

The design of any monitoring system can have a significant effect on the quality of the data. Often the design of mine seismic systems is limited by the geometry of the mining development. Typically, sensors are installed in short (<20m) boreholes drilled off a mining access drive. This frequently leads to planar or semi-planar arrays that limit the ability of the systems to accurately locate seismic events and to accurately calculate source parameters.

The aim of this review was to ensure there were adequate sensors within a reasonable distance of each structure with coverage including both the hangingwall and footwall contacts.

The accuracy of a seismic system is difficult to determine given the number of variables that cannot be quantified. It is also difficult to determine the number and spatial distribution of sensors that are required for adequate monitoring.

To provide a gauge of the accuracy of the seismic data structure subsets, the number of sensors within 200m of the structure was determined along with the location of the sensors.

2.2.3 Seismic data validation

Each dataset was reviewed by examining the following:

- Scatter within the data set
- Seismic source parameters
- Magnitude trends

The scatter within the data can indicate problems with processing and / or the presence of unprocessed data in the dataset; however, this scatter may be natural and therefore should be also taken in context with the seismic source parameters. Erroneous (e.g. Infinite S:P ratios) or missing seismic source parameters also indicate similar issues.

Magnitude is calculated using the moment and / or energy values. Magnitude was reviewed in several ways. Theoretically, the magnitude distribution should be logarithmic due to the formula's logarithmic base. However, the lower end of the magnitude scale is heavily influenced by the seismic monitoring system sensitivity. Smaller events below the threshold value (indicated by the statistical mode of the seismic data) may or may not be detected depending on the distance from the seismic sensors. The smaller the event and the further these events occur from the seismic sensors the less likely they are to be detected. Accordingly, the distribution of the magnitudes is smooth and similar to a normal distribution (Figure 2.1). Where poorly distributed magnitude data was identified (Figure 2.2) further investigations were undertaken.

The magnitude / energy ratio and the magnitude / moment ratios were also analysed through graphical methods. Discrepancies in these ratios suggest anomalies in the calculation of the seismic parameters. Often this is the result of poor processing techniques e.g. blasts not being removed from the data set or poor allocation of P or S wave arrival times.

Data that were found to have a poor distributions or poor ratios were either re-calculated or removed from the dataset. Each site section contains a discussion on this process.

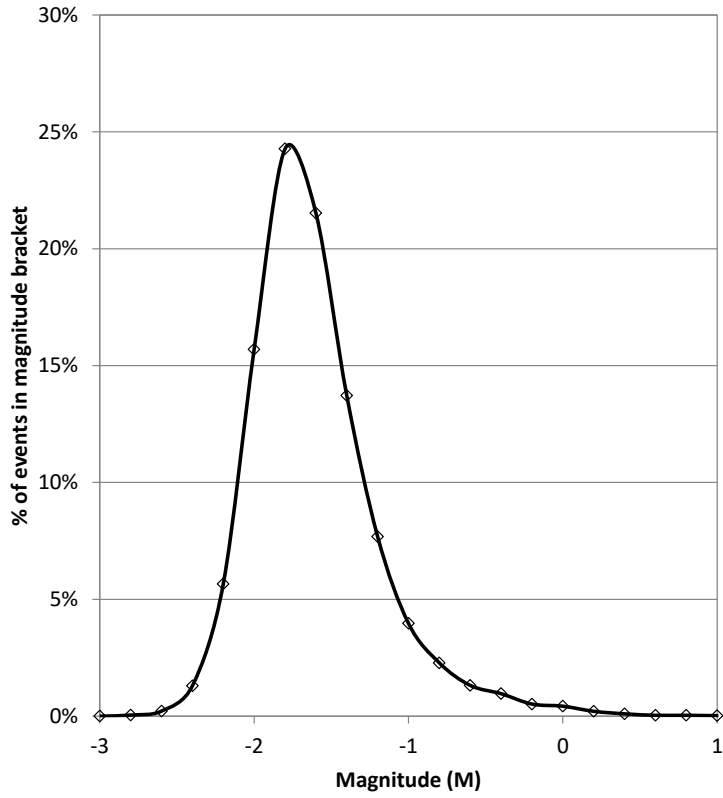


Figure 2.1: Typical magnitude distribution of a seismic data set.

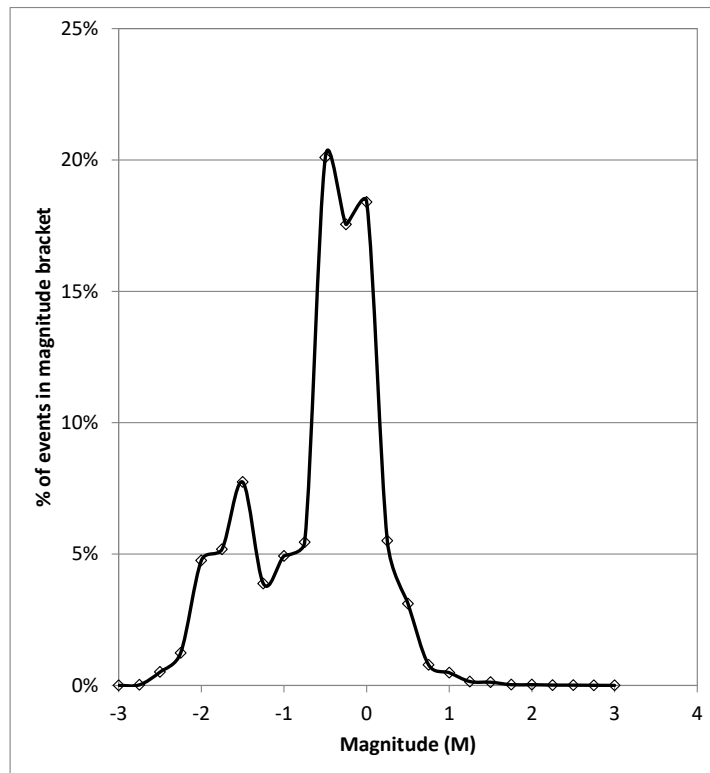


Figure 2.2: Poor magnitude distribution suggesting further investigation of the magnitude calculations.

2.2.4 Structure selection

A structure was selected for analysis for a number of reasons. Typically, the structure was identified through mine site back analysis as being related to a large seismic event. This association is often anecdotal rather than scientific. The basis of the relationship between the events and the structure is often spatial, related to the proximity of the large event or damage to the projected location of the structure.

Structures were also selected for their orientation or location with respect to the ore body.

2.2.4.1 Structural model validation

The structural models were provided by each mine site. The models typically consisted of planes derived from drill hole intercepts and mapping data. The amalgamation of the discrete intercepts into a large-scale structure was conducted by the geologist and was open to some interpretation.

The location and orientation of the intercept points were validated against the structural model to ensure accuracy. If discrepancies existed, it was possible in some cases to re-interpret the structure based on the number of points available or the drill hole database (where available). If the structural model could not be validated, analysis was not undertaken.

2.2.5 Domain definition

Rock mass characteristics determine the seismic behaviour of large-scale structures. Consequently, the data from each individual large-scale structure must be extracted from the overall dataset and analysed separately.

As discussed previously, the association between large seismic events and structures is often subjective. It was necessary to remove any prejudice in assigning events to a specific large-scale structure. To achieve this, seismic data were selected in a specified band or domain each side and parallel to the large-scale structure.

The thickness of the domain away from the large-scale structure (measured in metres perpendicular to the large-scale structure) was based on the density of the data around the large-scale structure. To calculate the density and to determine the domain distance the perpendicular distance of each point to the structure surface was calculated and then analysed.

In a simple geological environment, where the structural models and seismic data are both accurate, structures are narrow (<5m), individual faults are separated by some distance and seismicity is strongly controlled by structures. In these environments many events will occur within 5m of the surface (Figure 2.4). As the distance from the structure contact increases, the influence of the fault decreases resulting in a decrease in the number of seismic events. At some distance away from the structure, other structures begin to be incorporated into the data set resulting in a rise in seismic data density. The point at which the number of events is lowest is selected as the appropriate thickness of the domain.

In some cases, the distance analysis does not show a strong relationship to the large-scale structure (Figure 2.4). This may be due to a complex geological environment or the location inaccuracy inherent in the data. In such cases the domain distance is selected on other criteria. These criteria are explained in the structure sections in the following chapter.

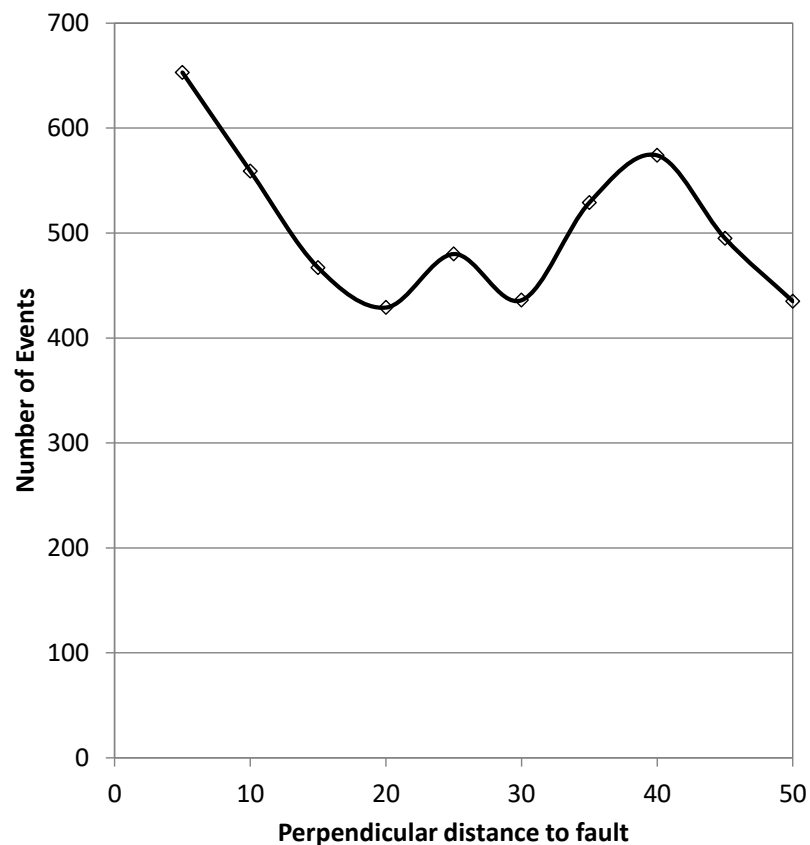


Figure 2.3: Strong correlation of events to the structure

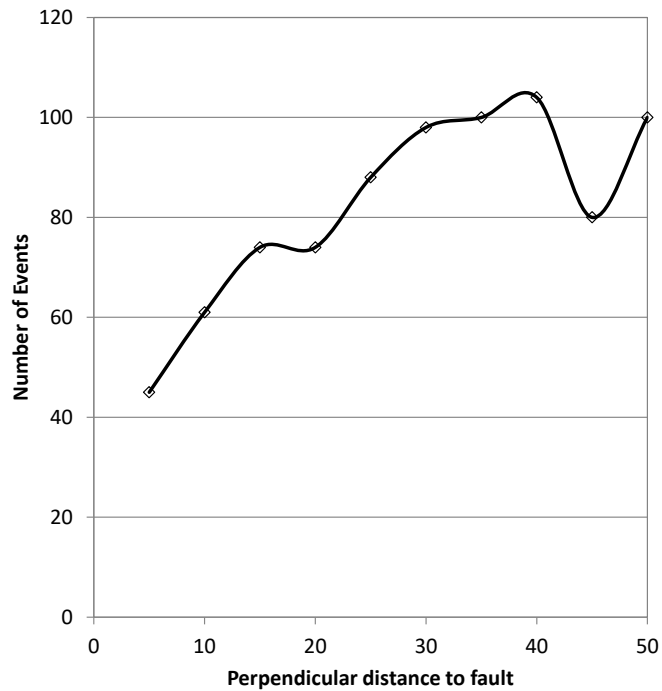


Figure 2.4: Poor correlation of events to structure

2.2.5.1 Domain boundary development

Based on the domain distance analysis, domain boundaries were created. The boundaries were created within the Leapfrog™ software by offsetting the large-scale structure surface by the domain distance (Figure 2.5). Where a structure was represented by two surfaces (i.e. a footwall and a hangingwall surface) each surface was offset separately away from the structure (Figure 2.6).

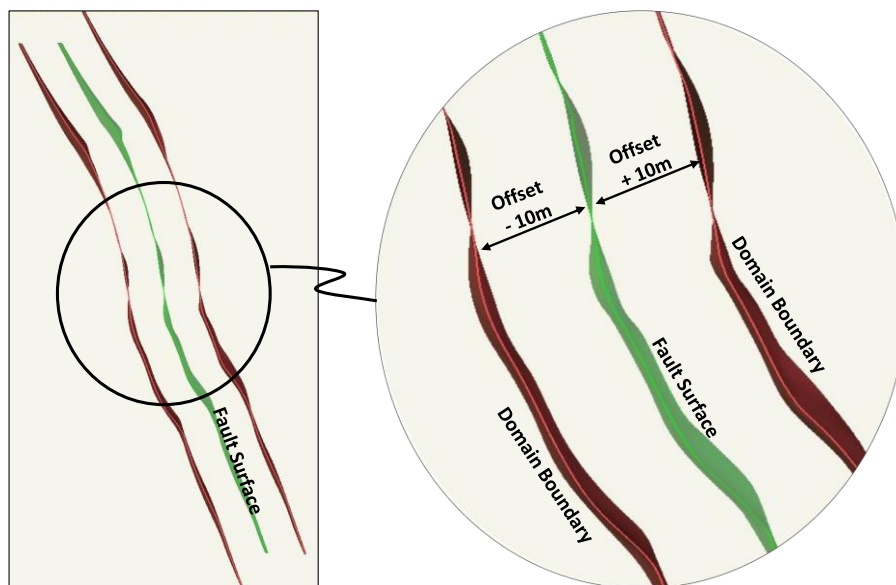


Figure 2.5: Domains boundary creation using a single surface.

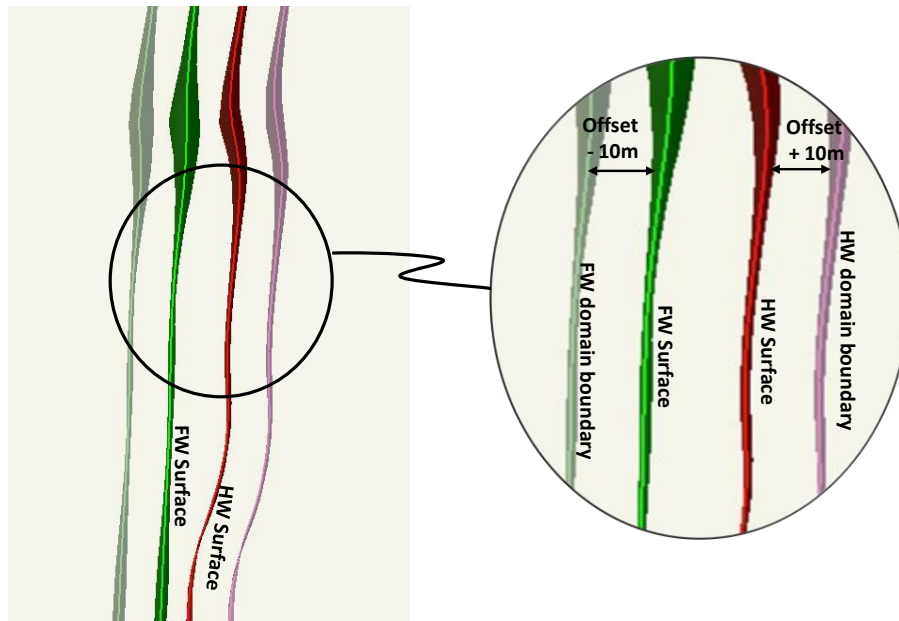


Figure 2.6: Domain boundary creation using two surfaces.

2.2.6 Data extraction

Seismic data points within the domain boundaries were extracted using the Leapfrog™ software. This created a data subset, for which the analysis of the large-scale structure was undertaken.

It is assumed that all data occurring within the domain is associated with the failure of the structure.

2.2.7 Data analysis

Two stages of data analysis were undertaken. Firstly, common mining analysis techniques were applied to the new data subsets to determine if some of the flaws in the current techniques could be improved. The results of these analyses are provided in Chapter 5.

Additionally, data analysis principles utilised in earthquake research will be explored. These techniques will be applied to the mine site structural data sets. Further discussions on the analysis and techniques are provided in later chapters.

3. Mine site data review

3.1 St Ives - Argo

3.1.1 Location and Geological setting

The Argo mine site is located within the St Ives gold complex, 25km south-west of Kambalda, Western Australia. Argo is located on the western limb of the Kambalda-St Ives Anticline and is hosted within the Condenser Dolerite unit (Andrews, 2006). The Condenser Dolerite is intruded between the Paringa Basalt and the Black Flag group units and is up to 500m thick.

Ore bodies within Argo are hosted within shear zones of several orientations. The main mineralised shear zones are the A1, B1, B2 and H1; however, the models and mining records suggest several other splays and sub parallel structures also exist.

Andrews, 2006, states that the A1 shear zone “*is a north-south-striking 50° west-dipping structure*”. The B1 and B2 parallel shear zones dip between 25 and 35 degrees to the west; however localised variations exist. The H1 shear zone is “moderately dipping” also to the west and has several sub-parallel shears (H2 and H4 shear zones). Figure 3.1 (Andrews, 2006) shows a section of the ore body with the relevant shear zones indicated.

According to the models provided, there are 3 main dykes intersecting the deposit: North Dyke, South Dyke and Mini Dyke. All three are sub-vertical mafic dykes trending east-west. The contacts are typically sheared. Additional to these main dykes, Andrews, 2006 also notes “*several swarms of NW-trending, moderate to steeply-dipping felsic and intermediate porphyritic intrusives*”. These intrusives are less extensive than the main mafic dykes and are consequently not modelled.

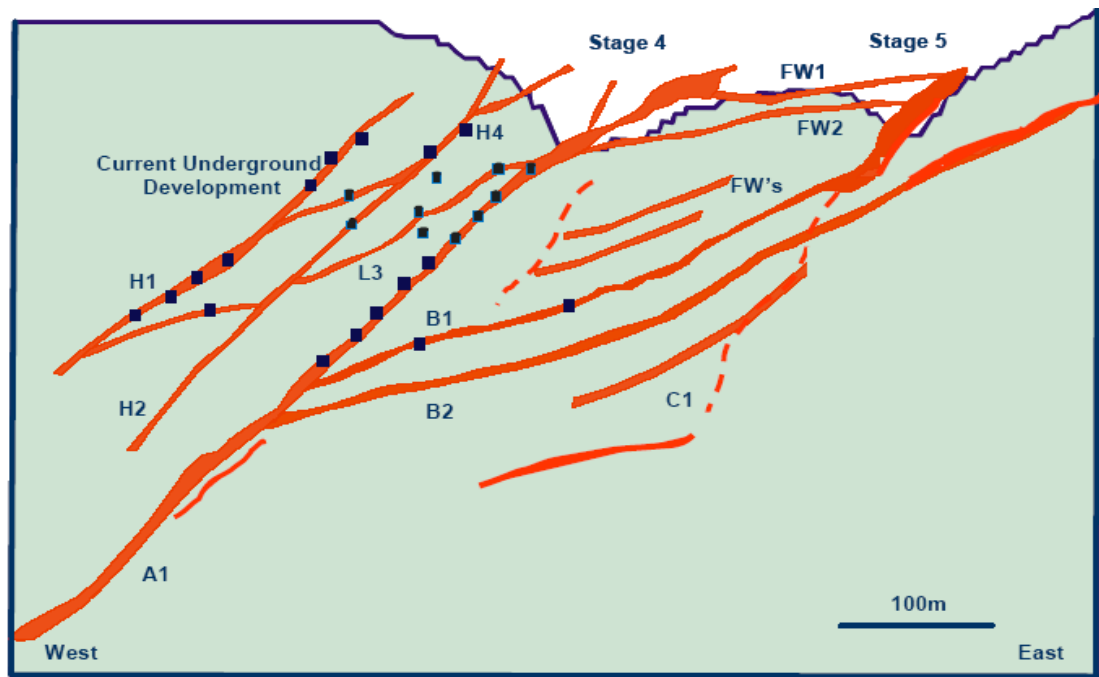


Figure 3.1: “Schematic west east cross section highlighting the numerous ore surfaces of the Argo deposit” Andrews, 2006, modified after Dusci et al., 2003.

3.1.2 Mining Method

Underground mining began in 2002 utilising the modified Avoca method. The method involved establishing ore drives within the ore body and working from the base of defined panels upwards. Stopes are continuously mined with fill being placed as extraction occurs. The upper ore body was broken in 4 mining panels whilst the lower ore body was broken into 2 mining panels.

Andrews, 2006 states that the modified Avoca method became inefficient due to a combination of geotechnical reasons and poor implementation (blasting and backfill lag). In 2004 a new method involving strategic placement of pillars was evolved. The method enabled multiple production levels to be extracted. Andrews claims that the new method was financially more viable and stoping was more stable.

The principal of the new method was to place pillars in areas where a poorer rockmass was expected. Instability of the stoping was generally associated with structures and hence pillars were typically placed where large scale structures were present. There is no further published information on the success or otherwise of the mining method. The Argo seismic hazard management plan (Webber, 2010) suggests that stoping sequence and pillar placement continued to require modelling management throughout the mine life.

The site was closed in 2014 at the completion of mine life.

3.1.3 Literature review

Whilst much has been published on the analysis of seismicity at the St Ives site of Junction, very little has been published on seismicity at the Argo mine site. Published papers specific to Argo seismicity could not be found.

3.1.4 Data Availability

Table 3.1 lists the data that have been provided by St Ives Gold Fields staff members for the purpose of this analysis. The mining extraction sequence for the A1 ore body has been provided by Site Engineers; however, the information for the other ore bodies is only partially available.

Table 3.1: Data availability for St Ives Argo.

	Data Type	Argo
Seismic Data	Data Available	✓
	Data processed	✓
Seismic System	Sensor location	✓
	Significant hardware upgrades	✓
	Significant outages	x
Geology	Major structure well defined	✓
	Minor structure defined	x
Mining Information	Decline files	✓
	Level files	✓
	Stope Voids	✓
	Vertical development	✓
	Level development history	x
	Stoping history	#
# data only partially available		

3.1.5 Discussion on Seismicity at Argo

The seismic monitoring system, consisting of eight sensors, was commissioned in August 2007. On the 1st of July 2008 an additional four sensors were connected to the system. The sensor locations (Figure 3.2) indicate reasonable coverage in the upper areas of the mine but sparse coverage in the lower levels.

The inoperability of components of the system (or the system itself) can influence the number of events being collected or influence the seismic source parameters, leading to incorrect interpretation of results. Geotechnical Engineers on site have kept logs of the seismic system and seismic sensor functionality (Table 3.2). The entire system was inoperable between the 23rd of Dec 2009 and the 27th of January 2010. Large seismic events occurred on the 12th and 14th of January during a period of inoperability and consequently are not present within the database.

The lower 4 sensors were inoperable for significant portions of the monitoring period. These sensors provided the primary coverage for the deeper extents of the mine. Any outages have the potential to greatly affect the location of the events and the calculation of the seismic source parameters of events at depth.

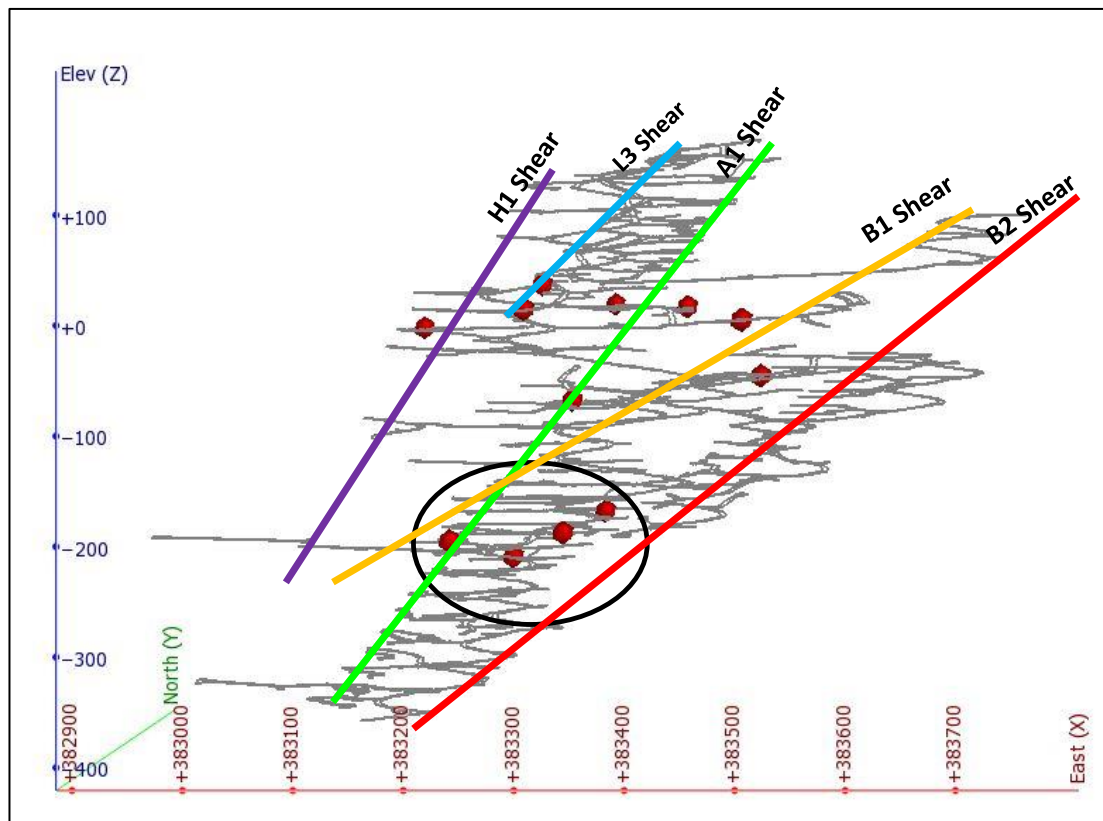


Figure 3.2: Argo seismic sensor locations looking north with ore bodies indicated. The lower 4 sensors (circled) were inoperable for much of the monitoring period.

Table 3.2: Log of inoperability of components of the seismic monitoring system at Argo.

Date From	Date To	Component inoperable
5/05/2009	24/10/2009	Lower system (4 sensors)
21/11/2009	2/12/2009	Lower system (4 sensors)
23/12/2009	27/01/2010	Entire system
17/03/2010	20/04/2010	Lower system (4 sensors)
29/09/2010	9/10/2010	Lower system (4 sensors)

Seismic data from Argo mine site were collected in October 2010. The data set has a start date of 17/08/2007 and ends at the time of extraction from the database (10/10/2010). In total the data set comprises of 11000 data points (Figure 3.3). The data had been recently re-processed by trained seismologists and consequently it can be assumed that the quality of processing is high.

The locations of the seismic events (Figure 3.3) are typically concentrated around the major ore bodies namely the A1, B1, B2 and H1. Very little scatter of data outside the mining area was observed further confirming reasonable accuracy.

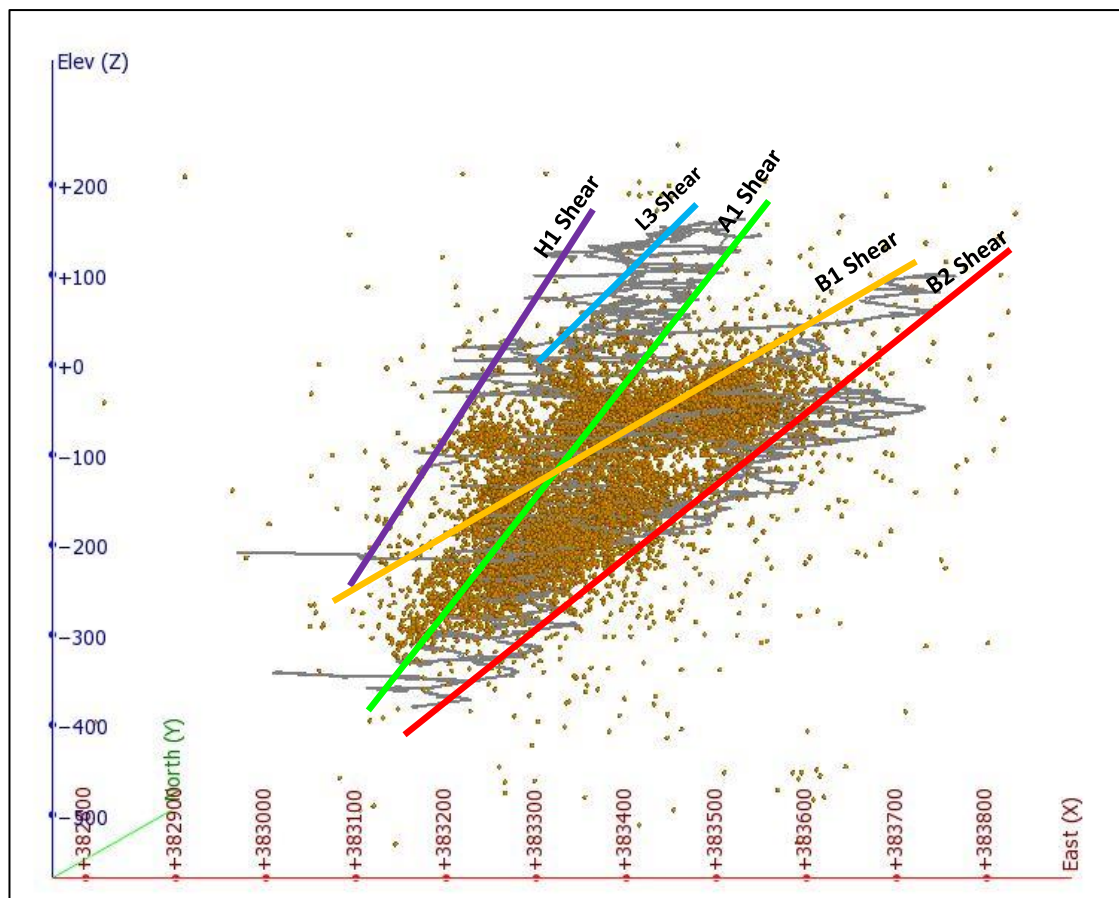


Figure 3.3: Argo seismic event locations.

The magnitudes were calculated using the standard IMS local magnitude equation (Equation 3.1). The magnitude variations (Figure 3.4) for the site were between $-2.9M_L$ and $1.9M_L$ with the median being $-1.7M_L$. The Site Geotechnical Engineers suggested that events over $0M_L$ resulted in damage to the rock mass and events over magnitude $0.5M_L$ typically result in damage to ground support systems. In total there were 45 events over $0M_L$ and 8 events over $0.5M_L$.

$$M_L = 0.272 \log_{10} E + 0.392 \log_{10} M_o - 4.62$$

Equation 3.1

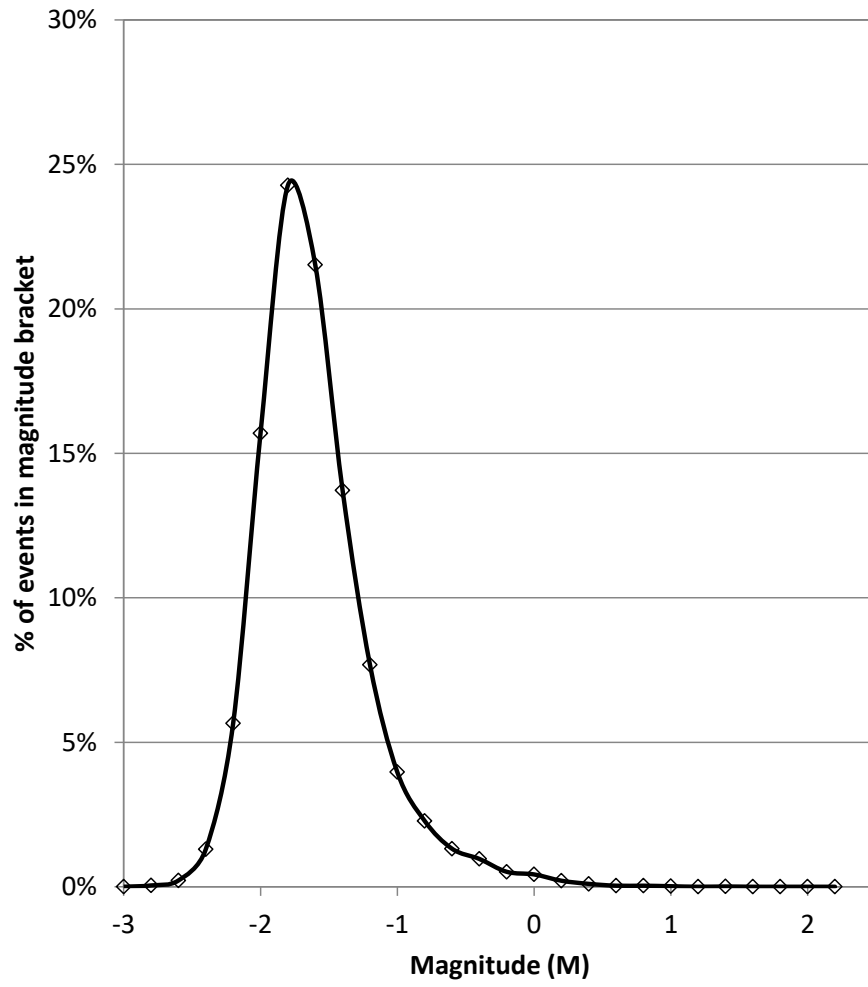


Figure 3.4: Magnitude distributions for the Argo mine site.

3.1.6 Structures for Analysis

The A1 Shear and two cross-cutting structures (the North Dyke and Mini Dyke) will be analysed (Figure 3.5).

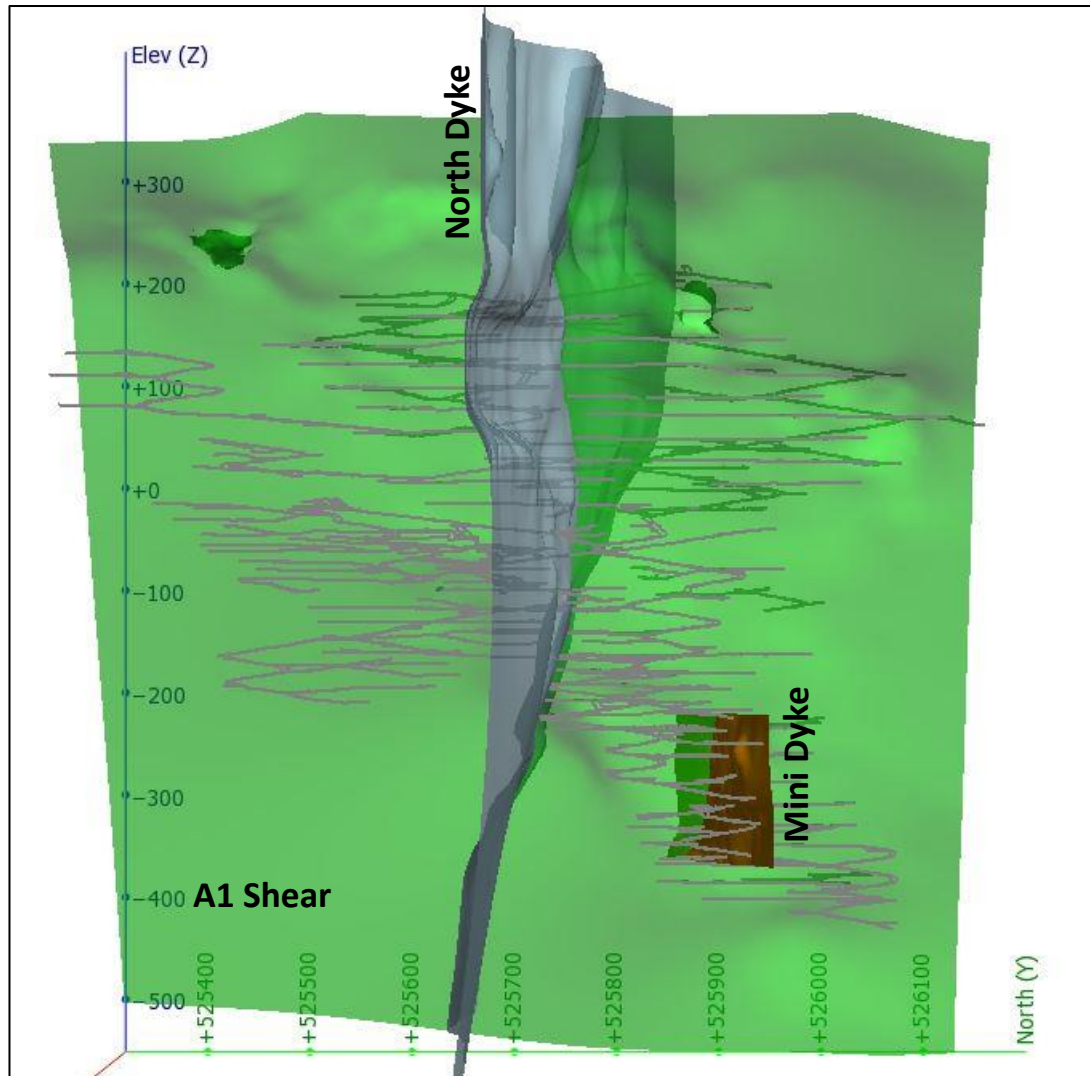


Figure 3.5: Argo structures for analysis (looking west)

3.1.6.1 A1 Shear

The A1 Shear is one of the main ore-bearing hosts with a significant amount of extraction taking place on the shear. The shear strikes north-south and dips at approximately 55 degrees towards the west. Infill on the shear is typically “*quartz-chlorite-biotite-albite-sulphide mylonite*” with some areas of localised brecciation Gressier and Kolkert, 2002.

As this is one of the ore-bearing structures, all 12 sensors are within 150m of the A1 Shear with 9 of the sensors within 100m. Four sensors are located in the hangingwall of the structure, but these are all in the upper areas of the mine. The lowest sensor is located at -230mRL although the decline extends 200m below this. The lack of sensors and poor distribution in the lower areas of the mine may affect the accuracy of the data at depth.

The domain offset distance was determined to be $\pm 20\text{m}$ based on the event distribution perpendicular to the shear (Figure 3.6). Overall the domain width is 42m. The A1 data subset comprises of 2120 events (Figure 3.7). The magnitude for the A1 Shear ranges from $-2.8M_L$ to $1.4M_L$ with a median of $-1.8M_L$ – slightly lower than the overall median of $-1.7M_L$.

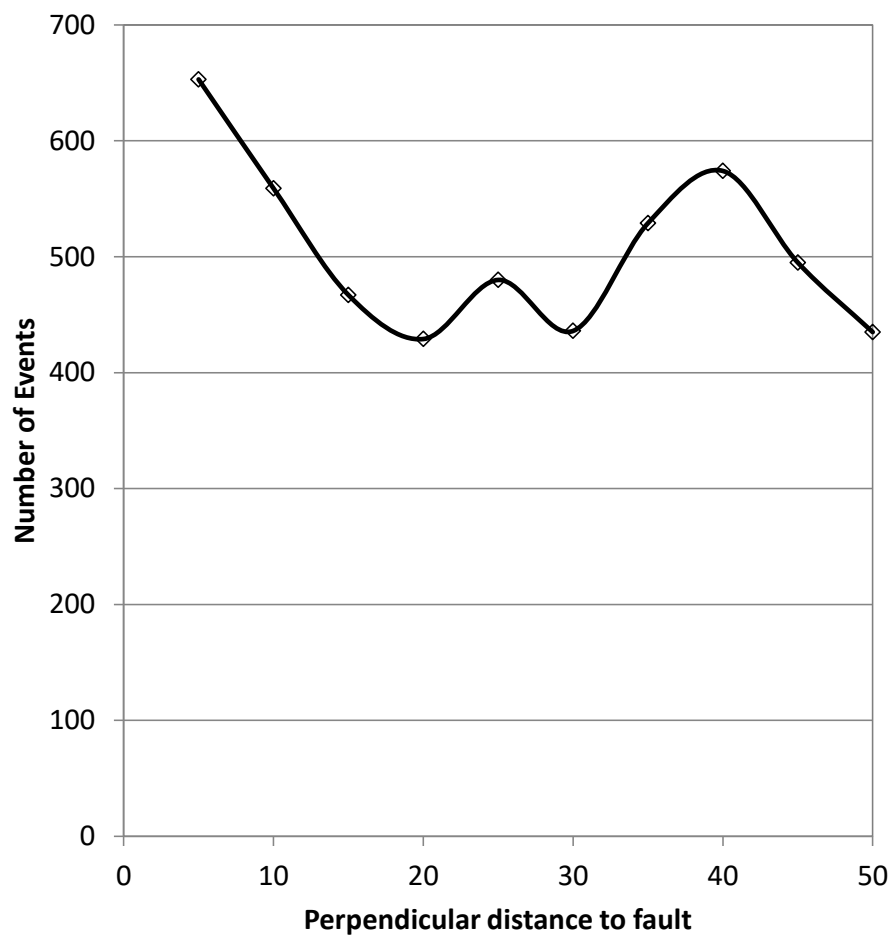


Figure 3.6: Distances of events from the A1 Shear.

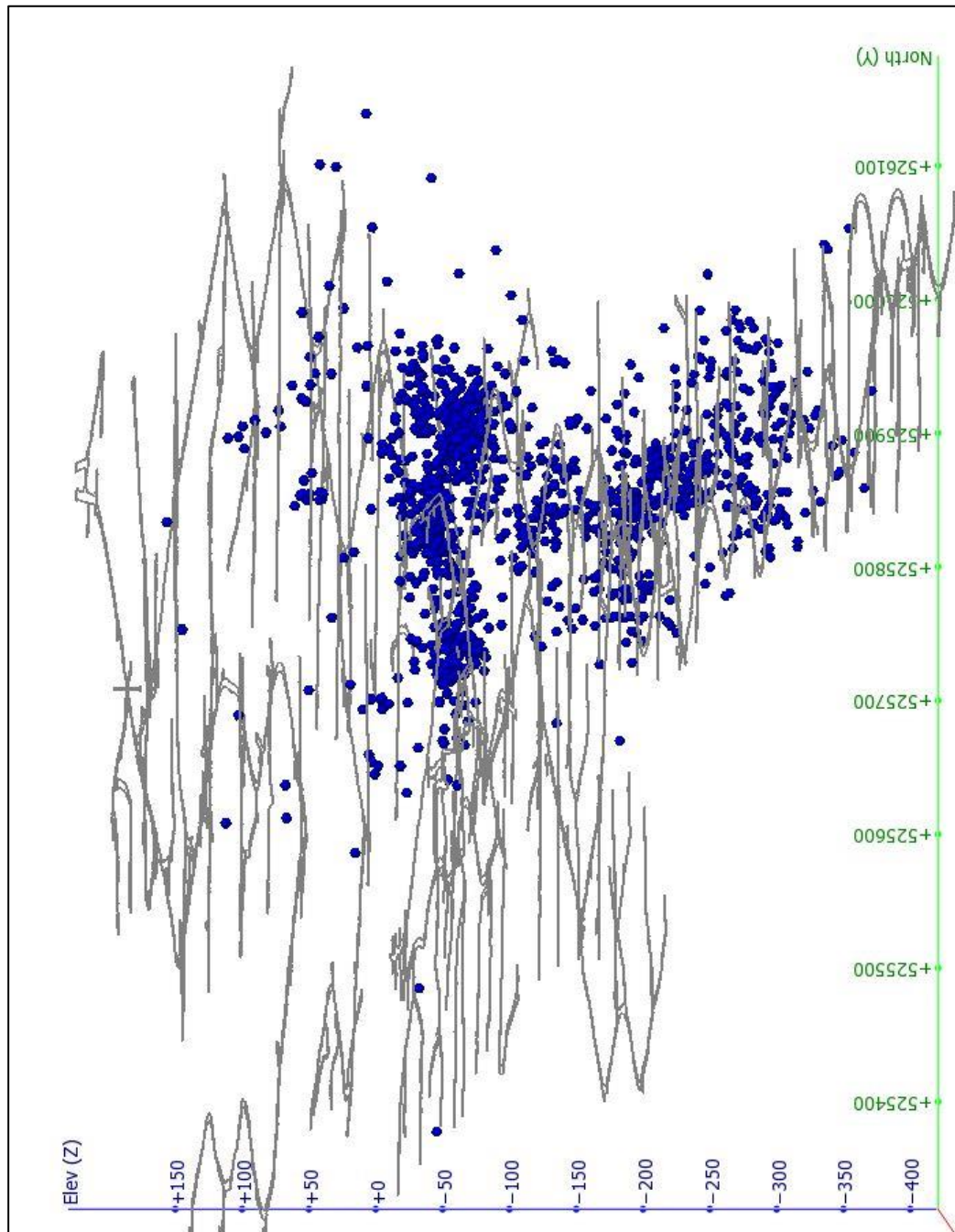


Figure 3.7: Event locations for the A1 Shear.

3.1.6.2 North Dyke

The North Dyke is the largest of the three mafic dykes intersecting the Argo deposit. The vertical to sub-vertical dyke strikes east-west and intersects all the mining areas and was selected for this reason.

As the North Dyke is central to the mine, all seismic sensors are located within 200m. Despite the proximity of the sensors, there is only 1 sensor located in the hangingwall of the dyke. As with the A1 Shear there are no sensors below -238mRL and consequently data accuracy at lower depths may be compromised.

This dyke is approximately 20m wide with both the hangingwall and footwall contact models provided by the site. To account for the width, the entire dataset was separated into footwall and hangingwall subsets (Figure 3.8). Distances were calculated separately for each subset. The results of the distance analysis for the footwall and hangingwall are provided in Figure 3.9. They indicate that events 15m outside dyke contacts were likely to be associated with the dyke. The overall domain width is 50m. The total number of events in the North Dyke data subset is 635 (Figure 3.10). The magnitudes range from $-2.8M_L$ to $0.9M_L$ with a median of $-1.7M_L$.

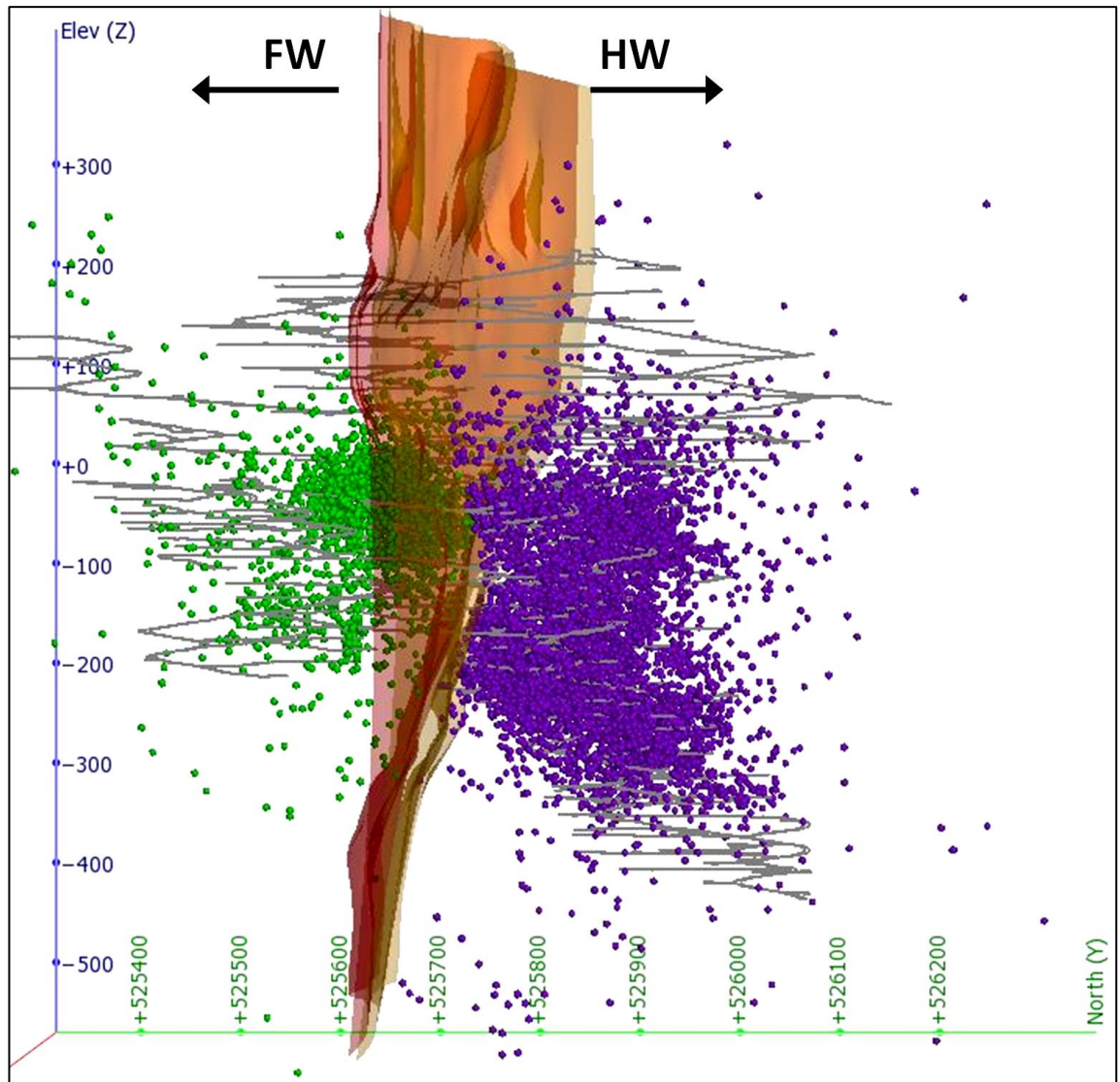


Figure 3.8: Separation of dataset into FW and HW domains.

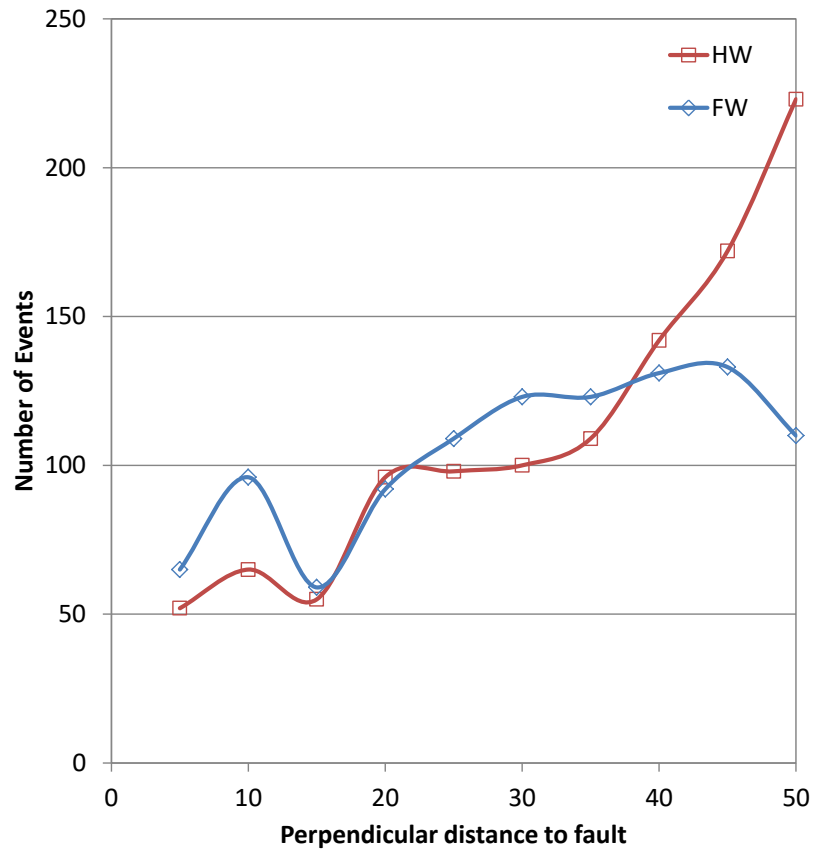


Figure 3.9: Distances of events from the North Dyke hangingwall and footwall.

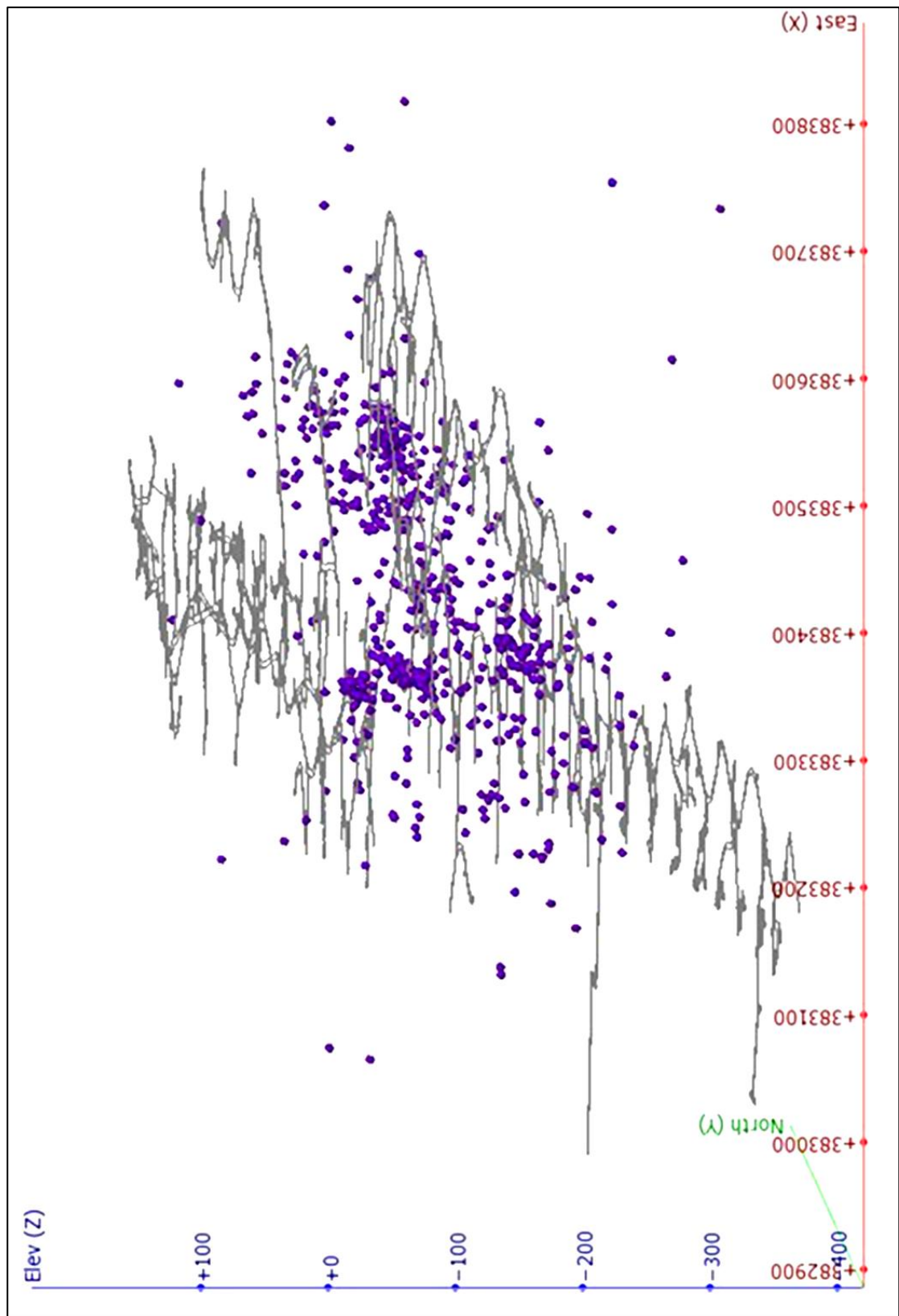


Figure 3.10: Seismic event locations for the North Dyke looking north.

3.1.6.3 Mini Dyke

Mini Dyke is the least defined of the 3 main mafic dykes at Argo. It was first identified in the lower levels of the mine below the N16 level (-100mRL) due to associated strong seismic activity. The model is well defined below the N16 level; however, the Site Geotechnical Engineers have suggested it is more pervasive than the model suggests and extends higher up in the mine.

No sensors were located below the -238mRL which may influence data accuracy.

The dyke is 2m wide and the FW model was used to establish the domains. The domain distance is set at the distance of $\pm 15\text{m}$ (Figure 3.11). The overall domain width is 32m. The Mini Dyke data subset comprises of 790 events (Figure 3.12). The magnitudes range from $-2.5M_L$ to $0.8M_L$ with a median of $-1.6M_L$. This median value is slightly higher than the median of the total dataset ($-1.7M_L$).

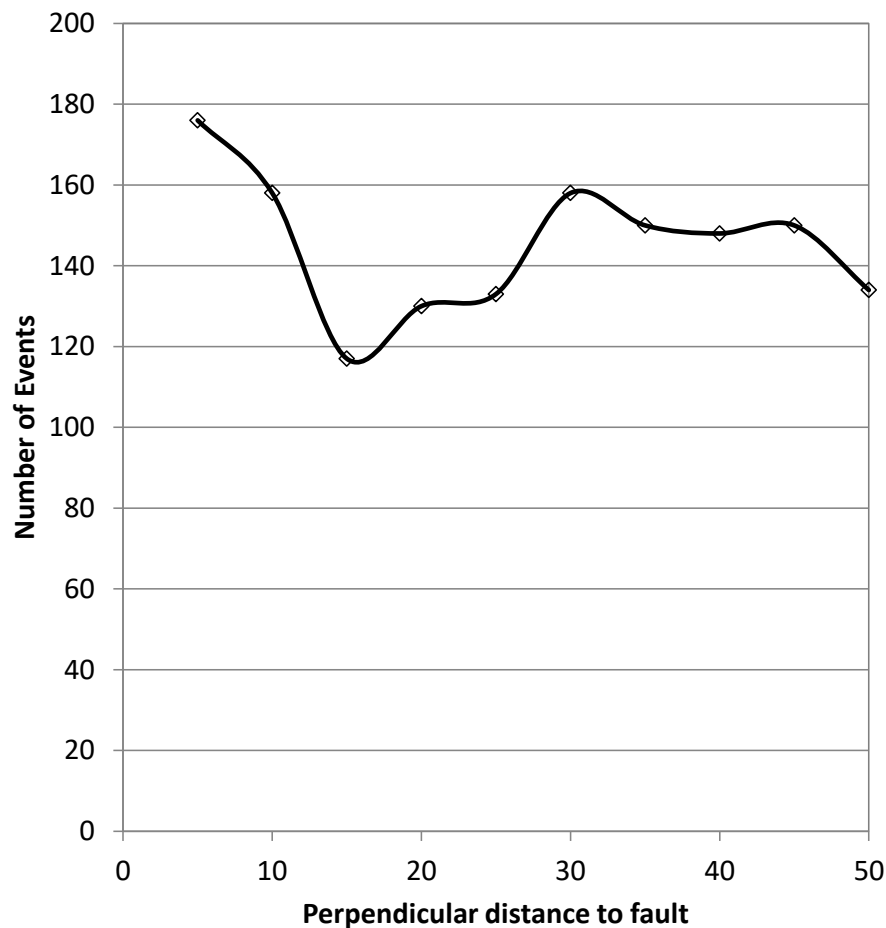


Figure 3.11: Distances of events to the FW contact of the Mini Dyke.

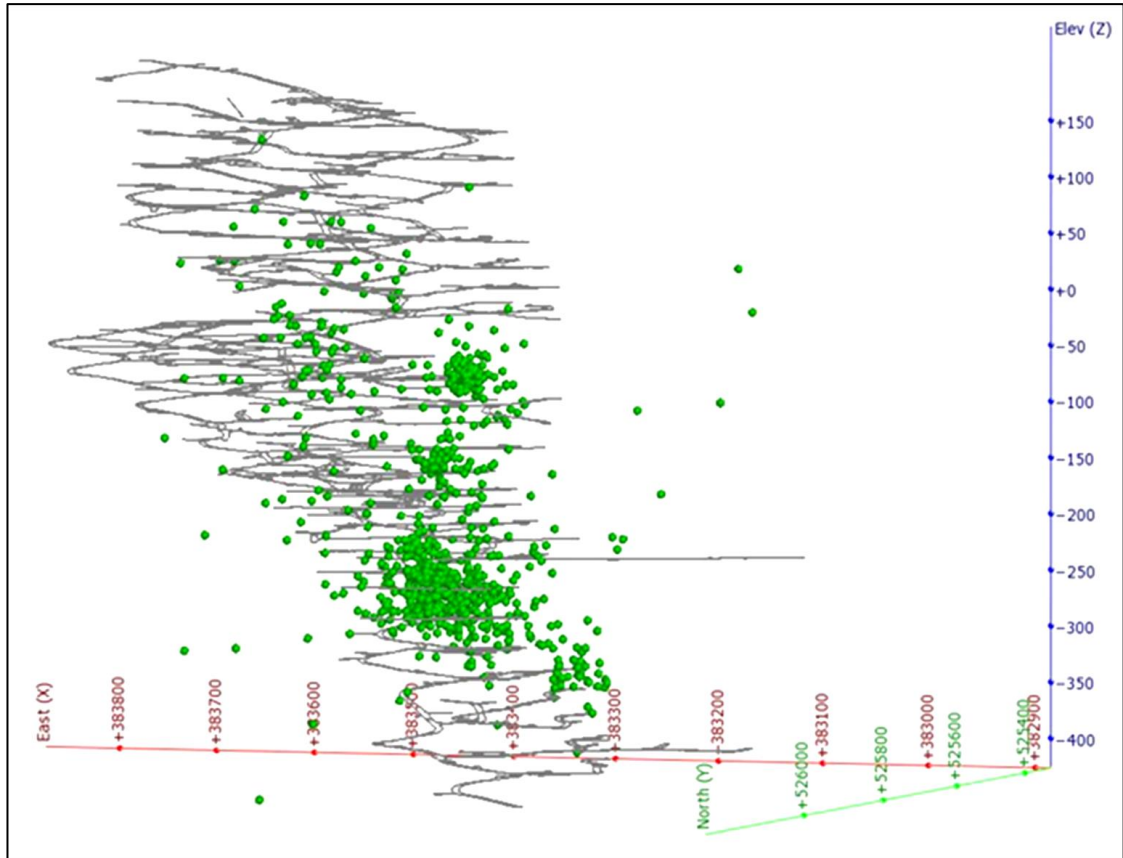


Figure 3.12: Locations of events associated with the Mini Dyke

3.2 Kanowna Belle

3.2.1 Location and Geological setting

The Kanowna Belle deposit is located 20km north east of Kalgoorlie. The ore body is hosted in the Fitzroy structural zone which separates the hangingwall and footwall sequences (Figure 3.13).

The hangingwall sequence consists of felsic, volcanoclastic siltstones and pebble conglomerates intruded by basaltic, andesitic and porphyritic dykes (Ross et al., 2004). The footwall sequence consists of “*volcanogenic conglomerates separated by thin lenses of arkosic grit and sandstone... The grain size ranges from sand sized particles to boulders up to 1m in diameter*” (Ross et al., 2004).

The Fitzroy structural zone hosts the ore body and consists of the Fitzroy Mylonite, the Fitzroy shear zone and the Fitzroy fault. It is interspersed by gold hosting porphyritic intrusions.

The Fitzroy shear zone is structurally complex with evidence of several generations of the deformation events. The zone strikes NE - SW and dips moderately to the south east. The Fitzroy fault forms the footwall of the Fitzroy structural zone. Further discussion of this fault is found further on in this chapter.

Smaller scale structures are extensive and highly complex. A detailed structural model (Figure 3.14) was developed for a stoping performance study conducted at the Western Australian School of Mines (WASM) (Cepuritis, 2011). An updated version of this model was provided by site for use within this project. The two models have differing naming conventions with some structures represented in both models. The WASM naming convention will be used. Table 3.3 correlates the site structure names with the WASM model.

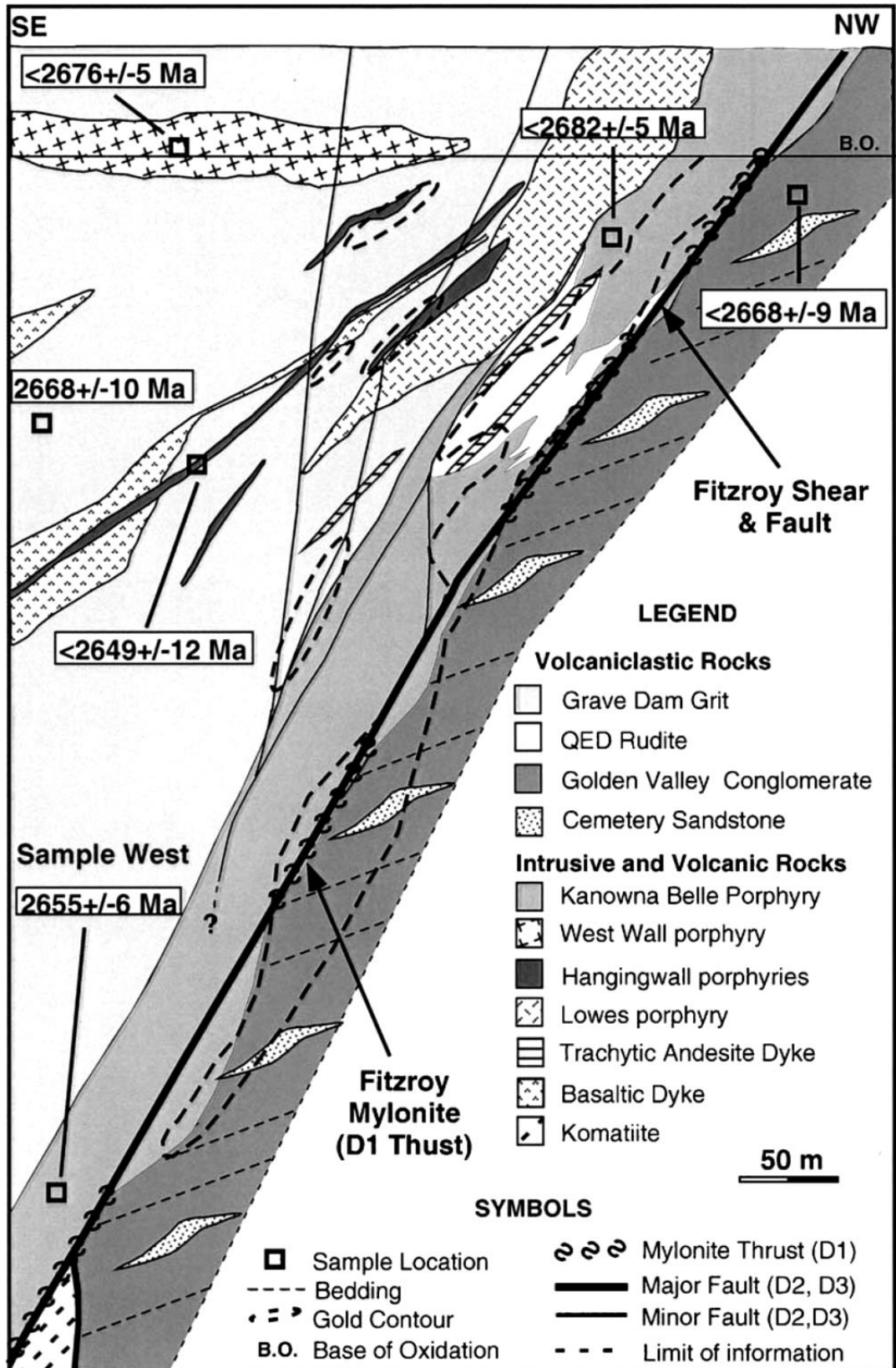


Figure 3.13: Schematic cross section of the Kanowna Belle deposit (Ross et al. 2004)

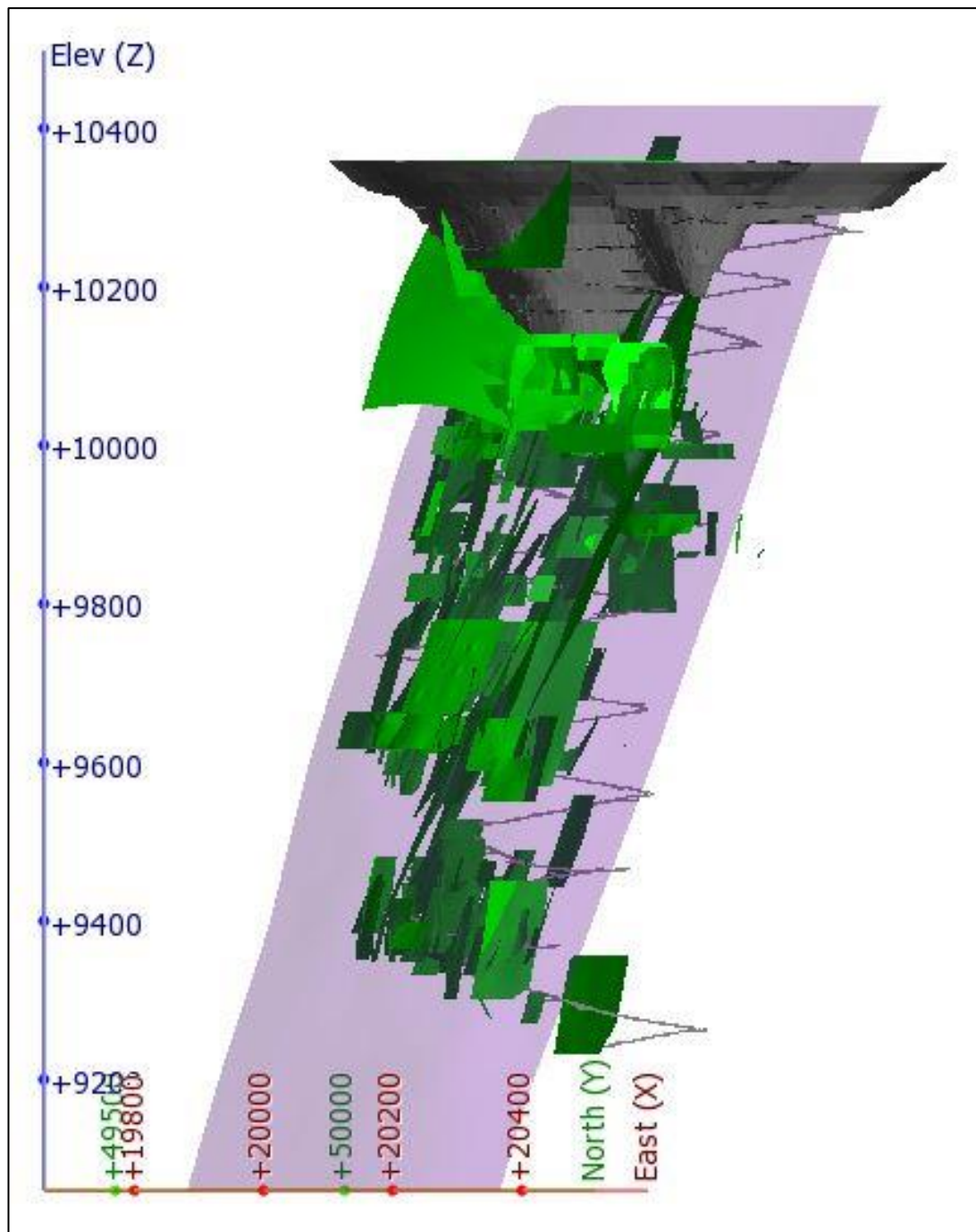


Figure 3.14: WASM structural model of Kanowna Belle.

Table 3.3: Kanowna Belle model names compared with WASM model names.

Kb model name	WASM model name	Comments
Alida	S315	
Beatrix	S307	
Claire	S364	
Denise	S323	
Elanor	S323	Same data points as Denise
Frieda	S329	
Gertrude	S389	
Harriet	S333	
Irene	S355	
Jane	S354	
Kate	S355	Same data points as Irene
Lynn	S353	
Maisey	S374	
Nancy	S393	
Olivia		No matching file
Penny	S391	
Queeny	S357	
Rose	S360	(without curve at end)
Sophia		Aligned with sections of several structures including S380, S360, and S391
Tina	S407	
Ursula	S395	(planar rather than curved surface)
Violet		No matching file
Wendy	S368	
Xena		No matching file – new orientation
Felsic contact Isa E	S118	

3.2.2 Mining Method

The transition from Open Pit mining to Underground mining began in 1996 (Varden and Esterhuizen, 2012). By 2000 the decline was 950m below surface. The mine has been divided into stoping blocks lettered from A to E and based on depth and position of the Fitzroy Fault in relation to the ore body. The primary mining method is open stoping with sublevel spacing and stope dimensions depending on the prevailing geotechnical conditions for each block. Stope sequencing is typically undertaken from the centre out towards the peripheries and bottom up using back fill.

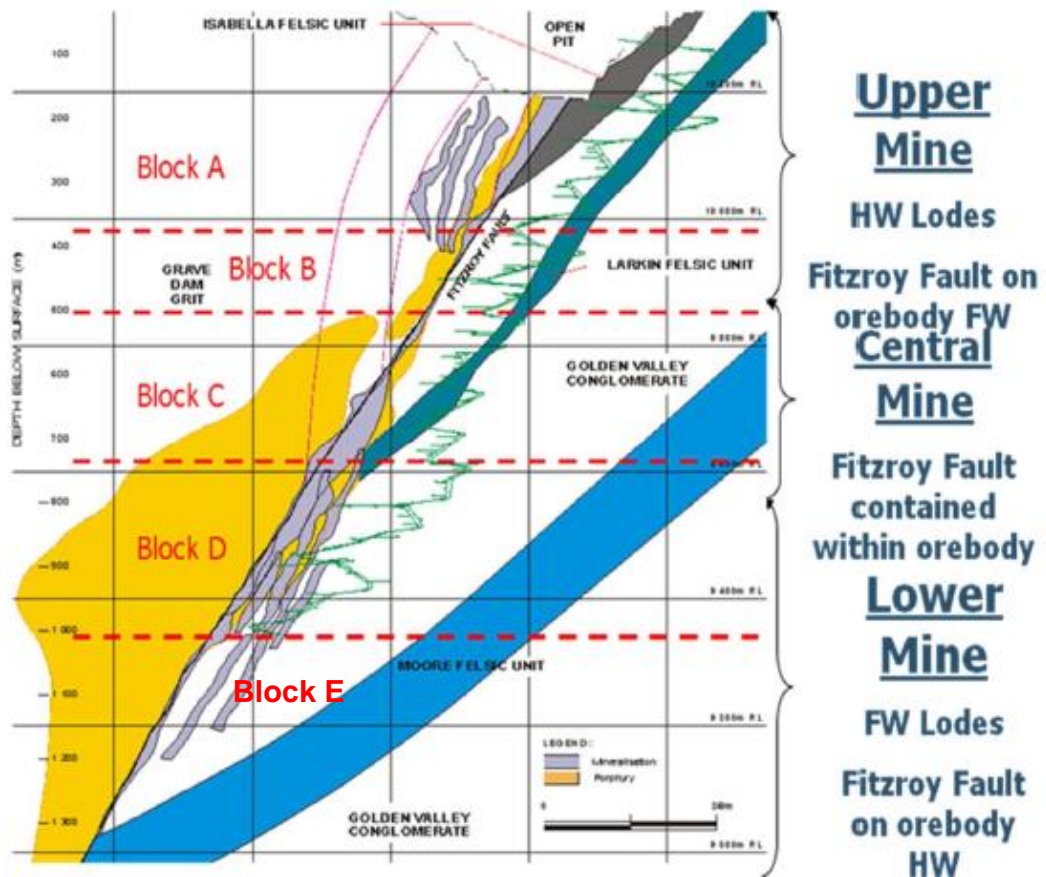


Figure 3.15: Layout of the Kanowna Bell mining blocks (after Varden and Esterhuizen, 2012)

3.2.3 Literature review

As with Argo, very little has been published on seismicity at Kanowna Belle. Most papers regarding to seismicity relate to dynamic ground control at Kanowna Belle to prevent damage (Varden et al., 2008).

Varden and Esterhuizen, 2012 outline the history of seismicity at Kanowna Belle. The authors state that seismicity is structurally controlled and has increased with increasing depth. Seismicity in block D (740m to 1010m below surface) accounts for almost 60% of all events with a significant number causing damage. In the lower levels (1010 – 1270m below surface) changes to the mine design and sequencing have reduced the level of seismicity.

Heal, 2010 reviewed 5 damaging events (resulting in 34 damage locations) at Kanowna Belle. All events occurred in the vicinity of a structure or geological contact.

3.2.4 Data availability

Three data sets were acquired from site over 4 years (2008, 2010 and 2012). The 2012 dataset is the most comprehensive and has been used in this analysis. Table 3.4 lists all data provided by site for analysis.

Table 3.4: Data availability for Kanowna Belle.

	Data Type	Kanowna Belle
Seismic Data	Data Available	✓
	Data processed	✓
Seismic System	Sensor location	✓
	Significant hardware upgrades	x
	Significant outages	x
Geology	Major structure well defined	✓
	Minor structure defined	✓
Mining Information	Decline files	✓
	Level files	✓
	Stope Voids	✓
	Vertical development	✓
	Level development history	x
	Stoping history	✓
# data only partially available		

WASM recently completed a research project involving the non-linear modelling of the extraction sequence using geological structures at Kanowna Belle mine site (Cepuritis, 2011). Consequently, the mining data and the geological information was cleaned and validated.

3.2.5 Discussion on Seismicity at Kanowna Belle

The Kanowna Belle seismic monitoring system consists of 32 sensors. Two sensors are replacements for malfunctioning sensors and are installed in approximately the same location as the previous sensor. The locations of the seismic sensors are provided in Figure 3.16 and Figure 3.17. The sensors closely follow the dip of the ore body with most of the sensors located in the footwall and only a few sensors in the hangingwall. This may affect accuracy of events deep in the footwall or the hangingwall.

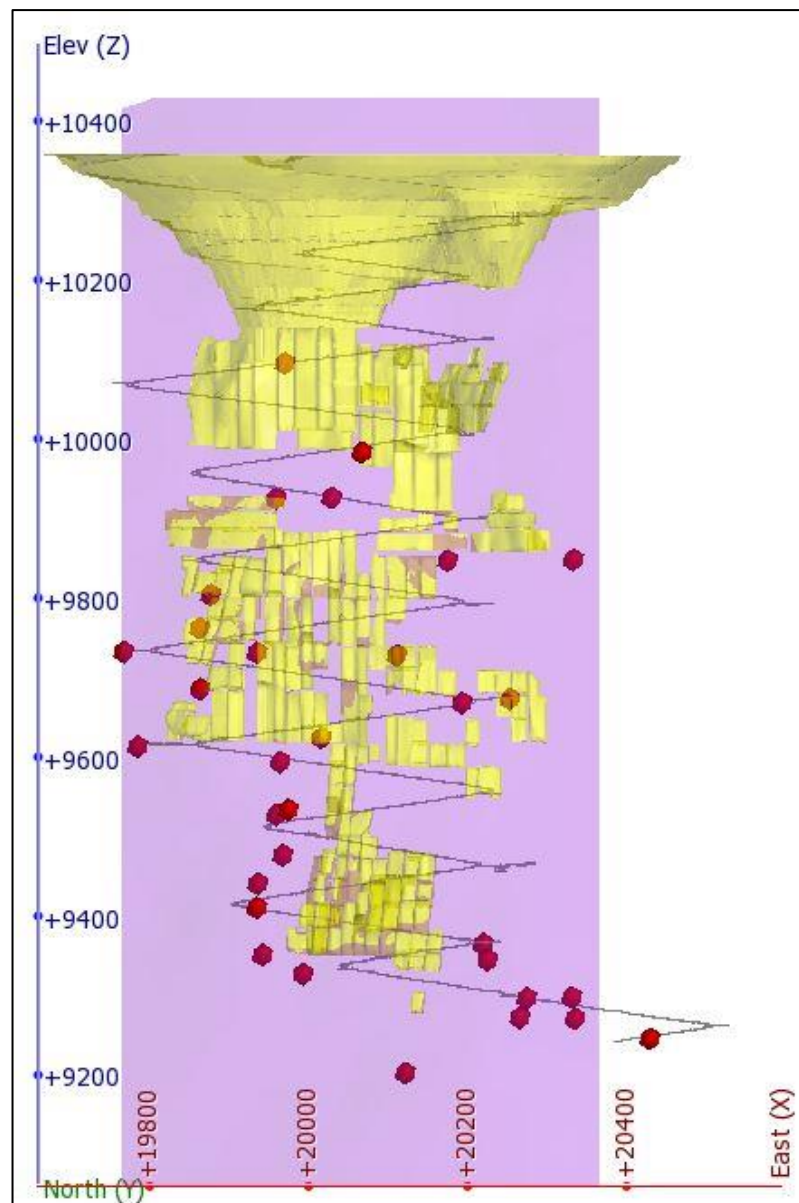


Figure 3.16: Kanowna Belle seismic sensor locations looking north.

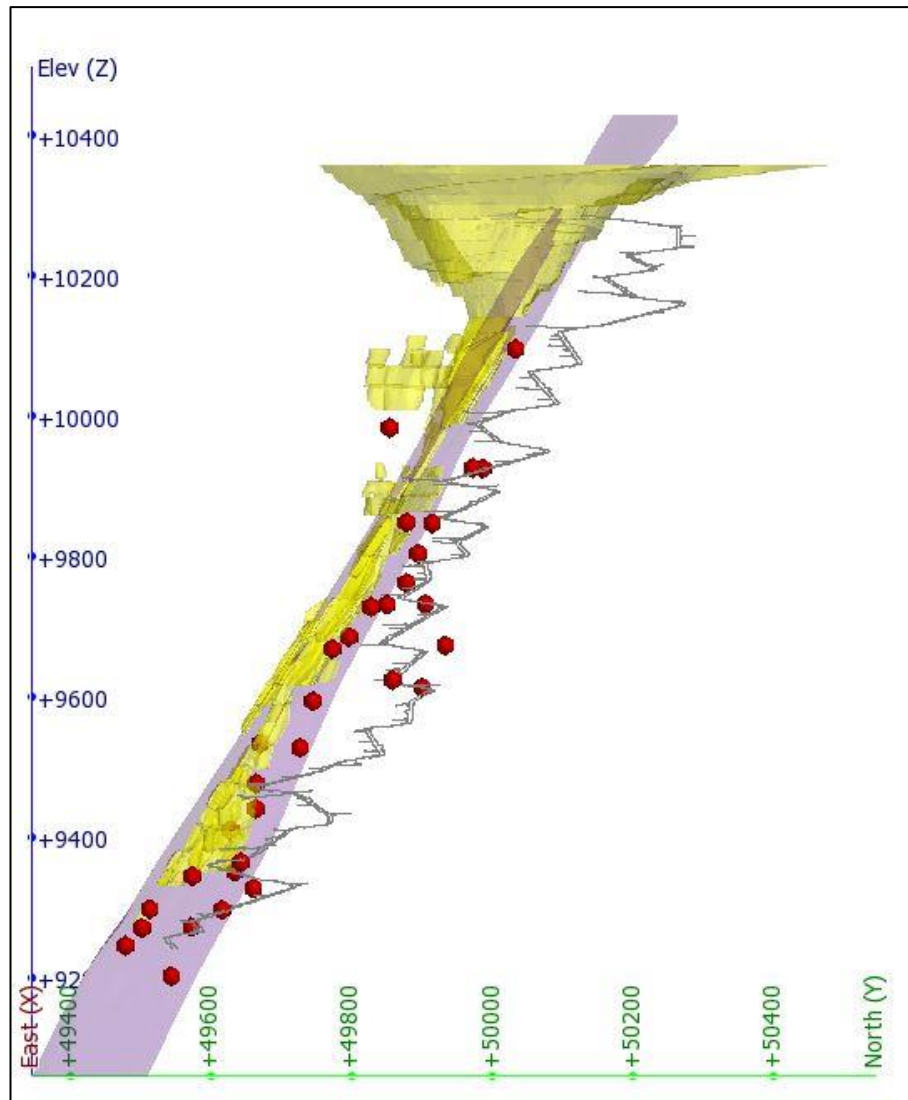


Figure 3.17: Kanowna Belle seismic sensor locations looking west.

As indicated in Table 3.4, no seismic system functionality data were available at the time of data collection. These data are not routinely recorded and cannot be provided. A review of the cumulative number of events was undertaken. The cumulative event rate is provided in Figure 3.18. There appears to be a full system outage between December 2009 and February 2010 indicated by an unusually low event rate accumulation (Figure 3.19).

Significant increases in event rate can indicate a change in the monitoring system sensitivity. Large increases in the event rate occur in July 2002, December 2006 and February 2010. Some of these variations are likely to be associated with the commissioning of extra sensors; however, without confirmation of the commissioning dates, it will be assumed that these changes are associated with normal seismicity rates.

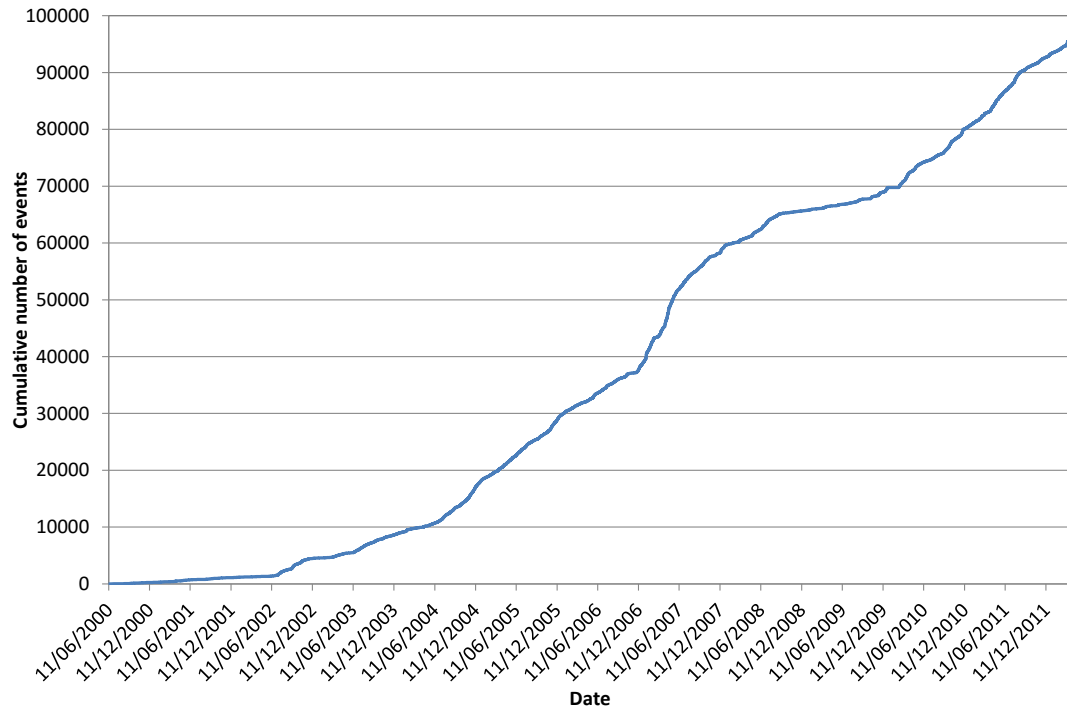


Figure 3.18: Total cumulative event rate for Kanowna Belle.

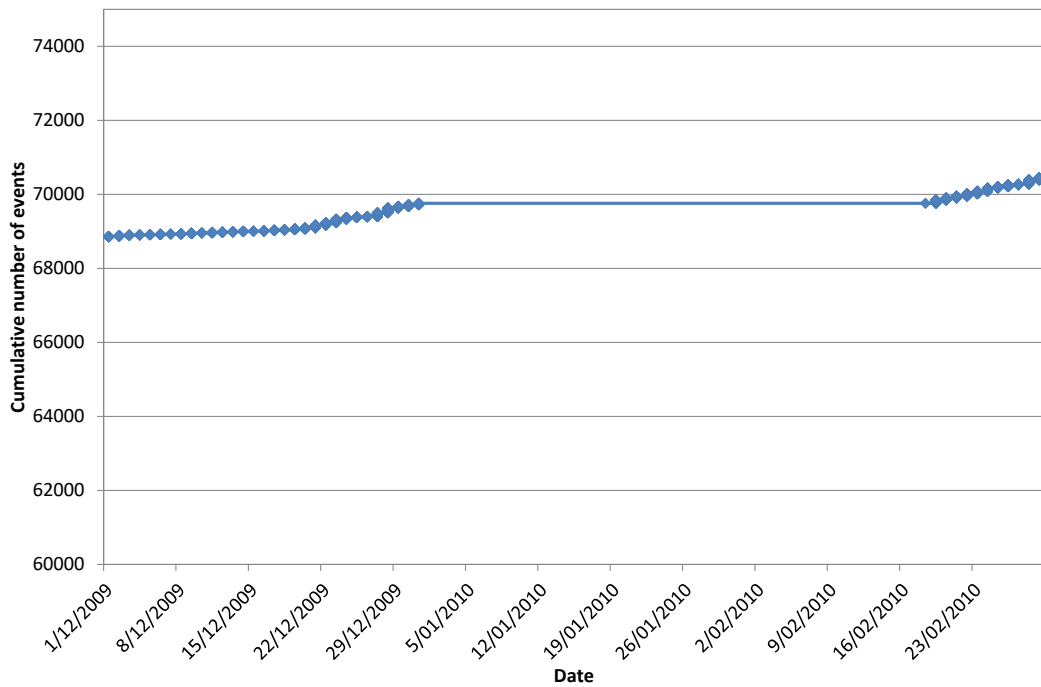


Figure 3.19: Cumulative event rate between Dec 2009 and Feb 2010 indicating no events between the 31st Dec 2009 and the 18th Feb 2010.

The Kanowna Belle seismic dataset exported from the IMS system consists of almost 96000 records starting from 10th of June 2000 ending on the 3rd of April 2012. The locations of events are provided in Figure 3.20.

At the time of collection, the seismic data were processed by mine site engineers. Four events are located above the surface RL of approximately 10350m. These events have been removed from the dataset. A further 600 events are missing the XYZ values or seismic source parameters and have also been removed from the dataset. As with the seismic sensor locations, the seismic event locations correlate with the ore body and follow the dip closely. It is difficult to determine if the events are located primarily on the ore body or whether the seismic sensor locations play a role in restricting the monitoring range.

The exported data do not contain the magnitude values. Magnitudes were calculated using the site magnitude formula given by Equation 3.2.

$$M_L = 0.272 \log_{10} E + 0.392 \log_{10} M_o - 4.62$$

Equation 3.2

E and M_o represent total Energy and total Moment. The constants represent site specific values. The magnitude values range between $-5.7M_L$ and $2.3M_L$ (Figure 3.21). The median value is $-2.8M_L$. Site evaluations suggest that seismic events over magnitude $0M_L$ cause obvious damage to excavations. There are 310 events over this threshold.

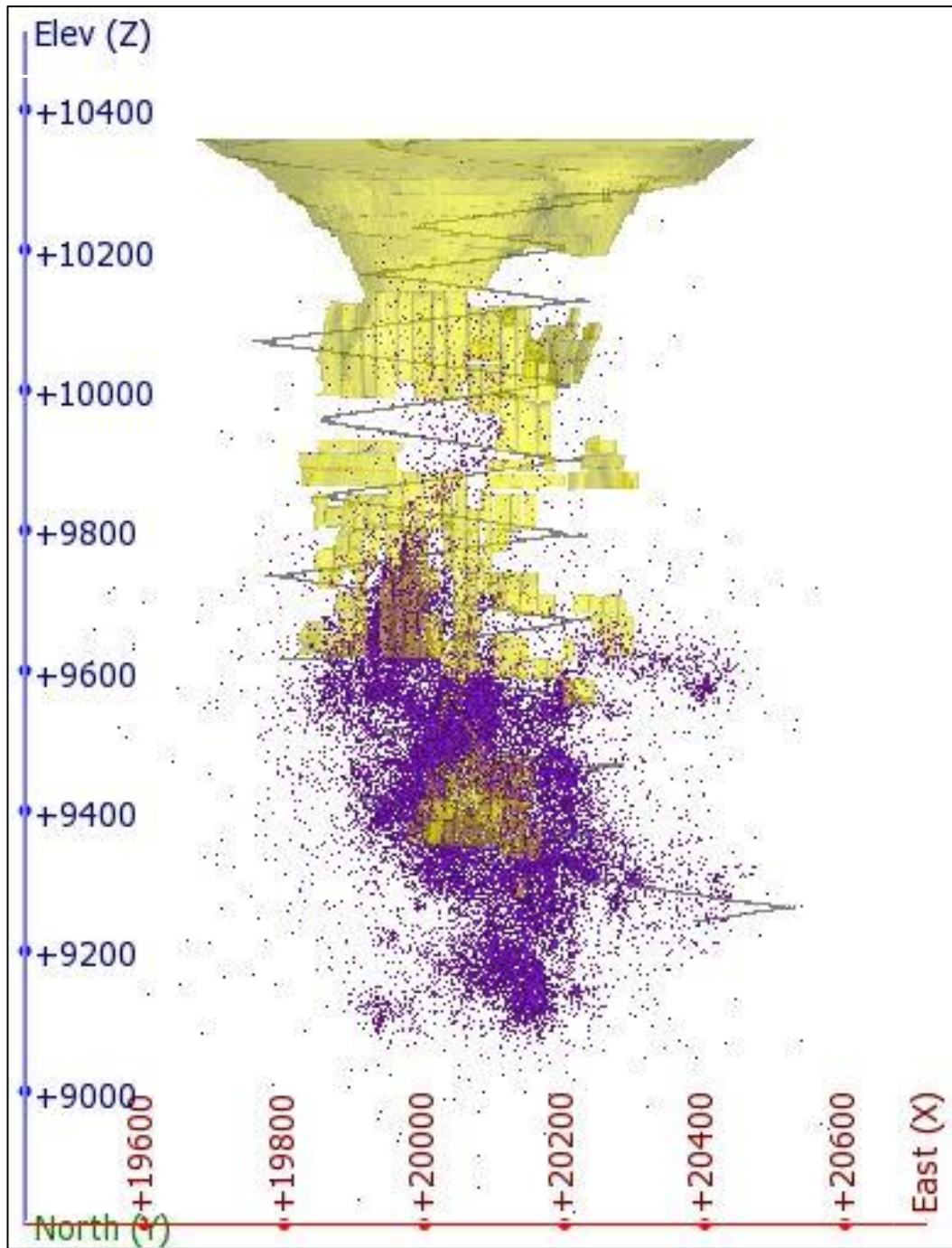


Figure 3.20: Kanowna Belle seismic event locations looking north.

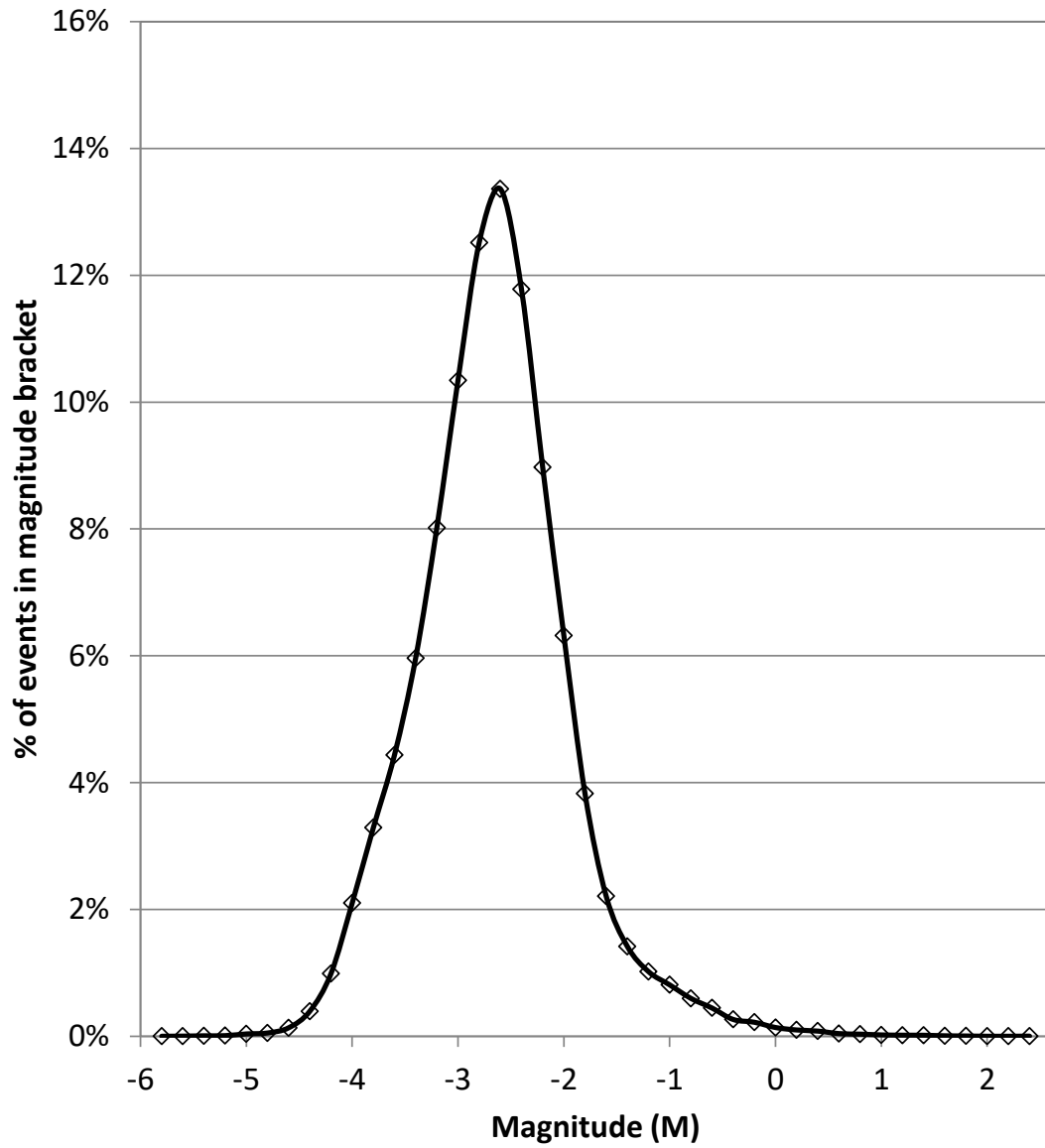


Figure 3.21: Magnitude distribution of Kanowna Belle seismic events.

3.2.6 Structures for Analysis

The following structures have been selected for analysis: Fitzroy Fault and the NE fault set (Figure 3.22). Due to the size of the North East Fault set it was broken into 2 groups.

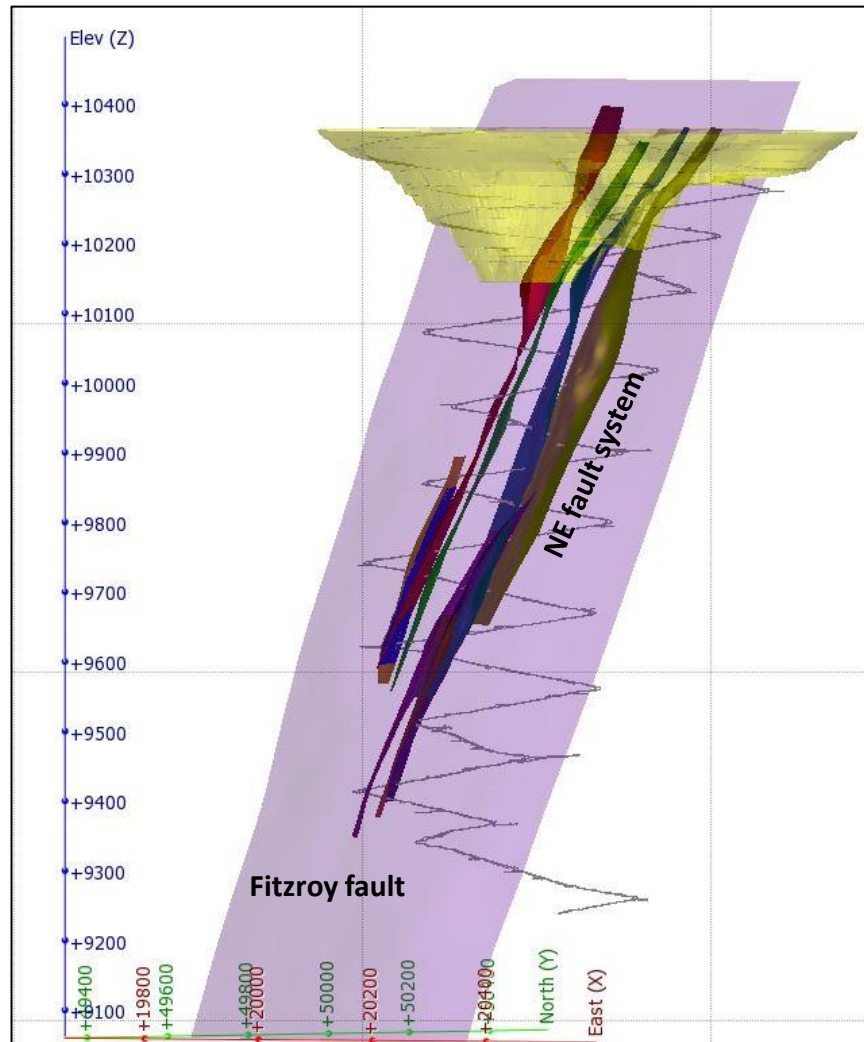


Figure 3.22: Kanowna Belle structures for analysis.

3.2.6.1 Fitzroy fault

The Fitzroy Fault forms the footwall of the Fitzroy structural zone. The fault is sub-parallel to the ore body strike but is oblique to the ore body dip. The *“position of this structure relative to the mining hangingwall and footwall change(s) with depth”* (Cepuritis, 2011). The fault dips moderately to the south east. The fault is characterised by *“a planar clay pug zone, 1–10 cm in width”* (Ross et al., 2004).

The Fitzroy Fault was selected for analysis due to its large scale in relation to the mining infrastructure. As this structure is closely linked to the ore body the seismic sensor coverage is similar to that of the entire mine (Figure 3.16 and Figure 3.17). All seismic monitoring sensors are within 200m of the fault although only 2 sensors are located in the HW.

The results of the distance to fault analysis (Figure 3.23) indicate the optimum domain distance is $\pm 20\text{m}$. The overall domain thickness is 40m. The data subset contains over 14,500 seismic events (Figure 3.24). The magnitudes range from $2.3M_L$ to $-5.5M_L$ with a median of $-2.9M_L$. The median for Fitzroy Fault is slightly lower than that of the overall dataset ($-2.8M_L$).

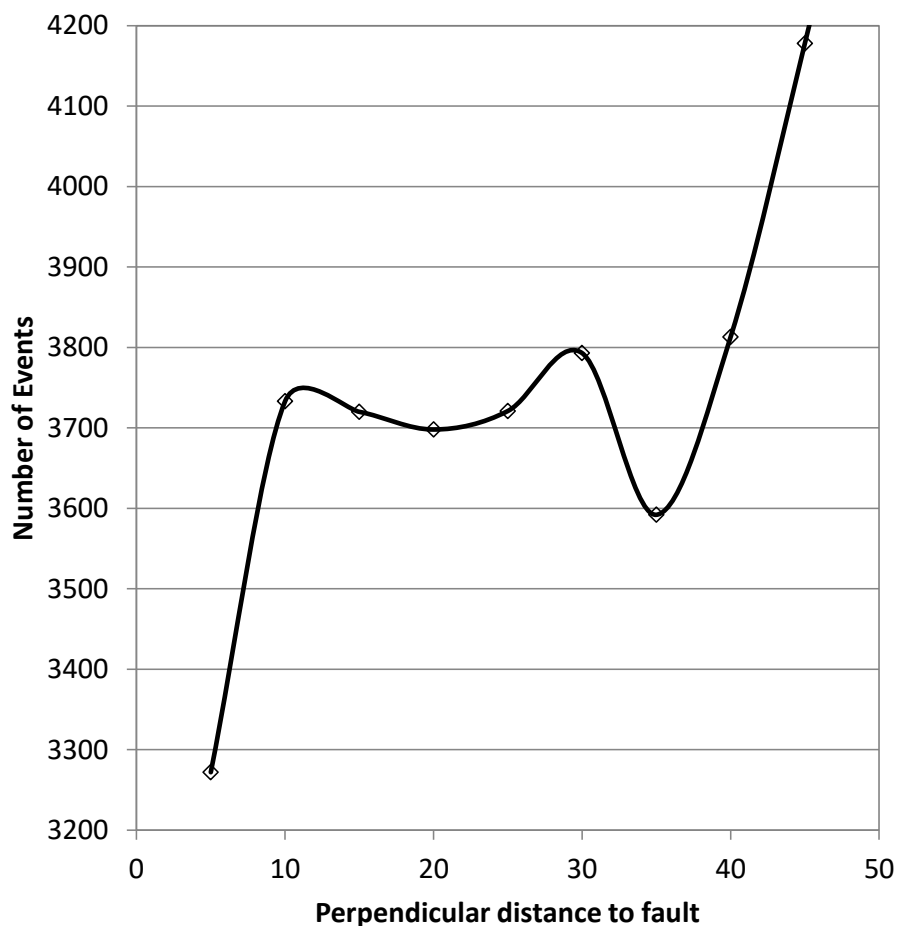


Figure 3.23: Distances of seismic events to the Fitzroy Fault.

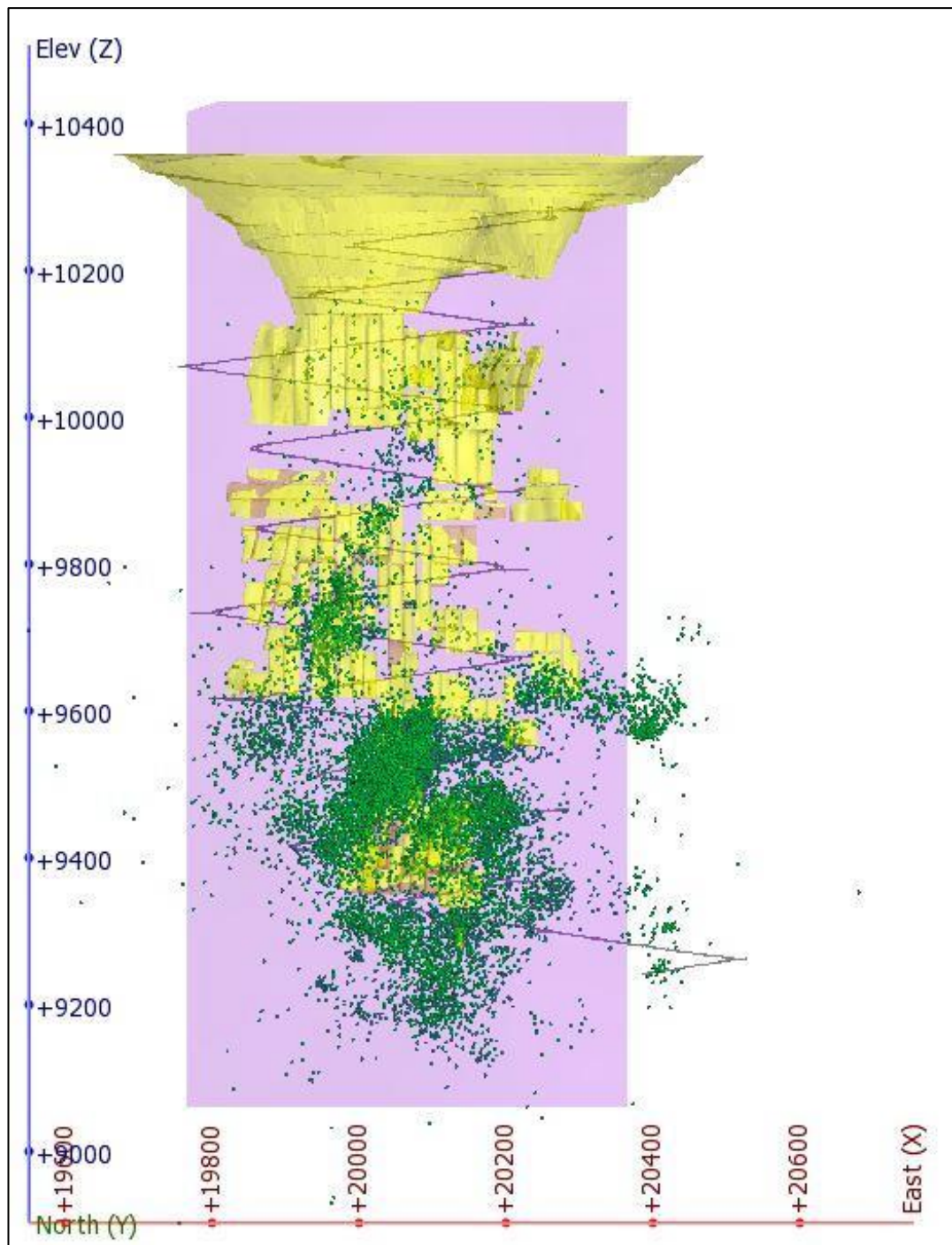


Figure 3.24: Location of events for the Fitzroy Fault.

3.2.6.2 NE Fault system

The North East fault system (NE Faults) comprises of four moderately dipping (65°) structures, striking NE. These structures (Figure 3.25) are named (left to right) S169, S118, S150 and S121. The WASM model does not extend below 9600mRL. Below this level, Kanowna Belle staff developed a new model using their own naming convention. Table 3.5 provides the additional models that appear to correspond, in location, dip and orientation, with the main faults.

The NE faults were selected for analysis due to their large scale and oblique orientation to the main ore body. The seismic monitoring system provides good coverage in the mid-levels of the mine (9900mRL – 9700mRL) with at least 5 sensors within 200m in both the HW and the FW. As the depth increases the faults diverge from the central mine area and sensors are mostly located between the structures and progressively further into the footwall beyond the 200m threshold.

Table 3.5: WASM model with corresponding model names at depth.

WASM Model	WASM below 9750mRL	Site Model
S121	No further models.	
S150	S333	Harriet
	S330	
	S329	
S118	S323	Denise / Elanor*
S169	S315	Alida
* Denise and Elanor correspond to the same model.		

In the upper areas of the mine the structural regime is relatively simple with the NE faults being the dominant large-scale structures with a consistent spacing. The structural model becomes more complex below 9750mRL with the formation of several new large-scale structures with similar orientation to the NE faults. The main NE faults converge into 2 distinct groups separated by approximately 70 – 80m.

To enable analysis, structures S169 and S118 were analysed together (Group 1) and S150 and S121 were analysed together (Group 2). The distance charts (Figure 3.26) clearly showed the influence of adjacent structures. The S118 structure indicates a peak at 15m away from the structure. This corresponds with S169. The S150 structure indicates a peak at 40m. This distance corresponds approximately with the distance to both S118 and S121 depending on depth. The FW boundary of Group 1 (S169_S118) and the HW boundary of Group 2 (S150_S121) were set at 15m to avoid overlaps between the 2 groups. The HW boundary of S169 and the FW boundary of S121 were determined using the standard method (Figure 3.25).

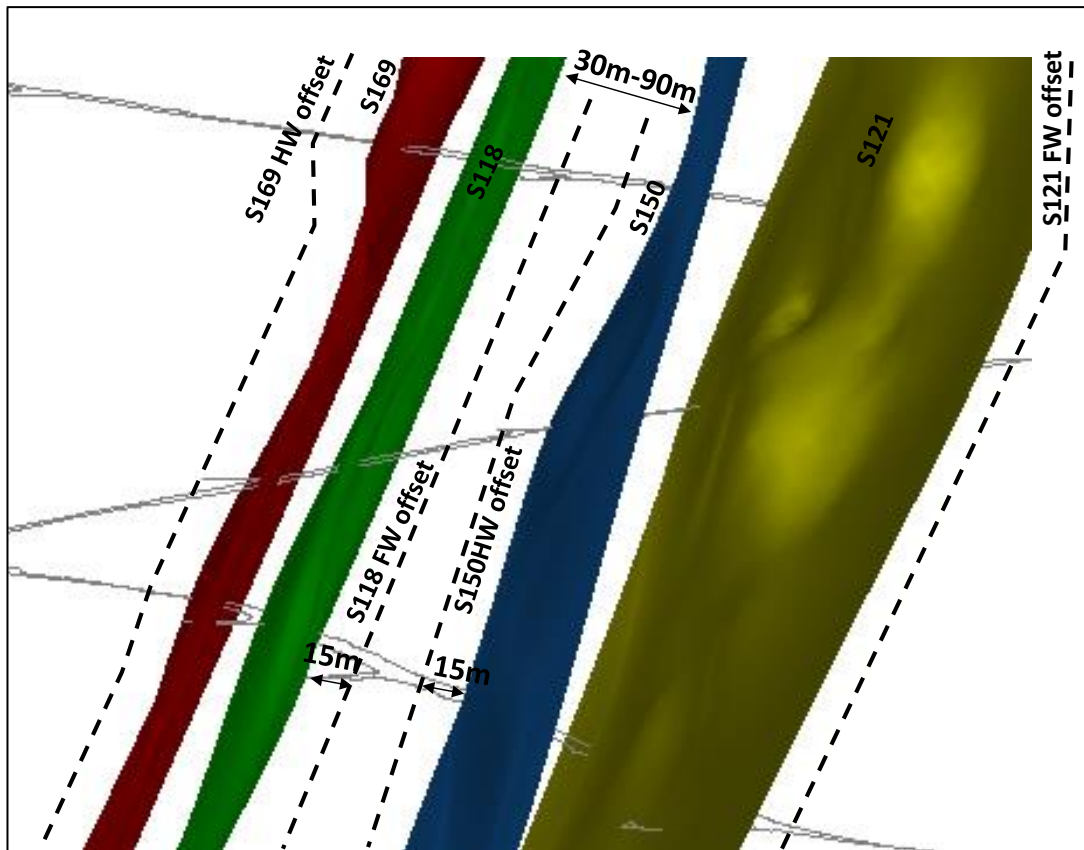


Figure 3.25: Layout of the NE structures and their domain definitions.

3.2.6.2.1 North East Group 1 - S169_S118

The FW domain distance for the S169_S118 group was set at 15m to prevent overlaps with Group 2. The HW domain distance was determined as 25m using the standard method (Figure 3.27). The total domain width was 55m. The seismic dataset subgroup contains over 18,000 events (Figure 3.28). The magnitudes range from $-5.1M_L$ to $0.8M_L$ with a median of $-2.6M_L$. The median is slightly higher than the overall site median of $-2.8M_L$.

3.2.6.2.2 North East Group 2 - S150_S121

The HW domain distance for the S150_S121 group was set at 15m. The FW domain distance was determined to be 15m using the standard method (Figure 3.27). The overall domain width is 70m. The seismic data subset contains 20,000 events (Figure 3.29). The magnitudes range from $-5.5M_L$ to $2.3M_L$. The median is $-2.9M_L$ slightly lower than the overall site average.

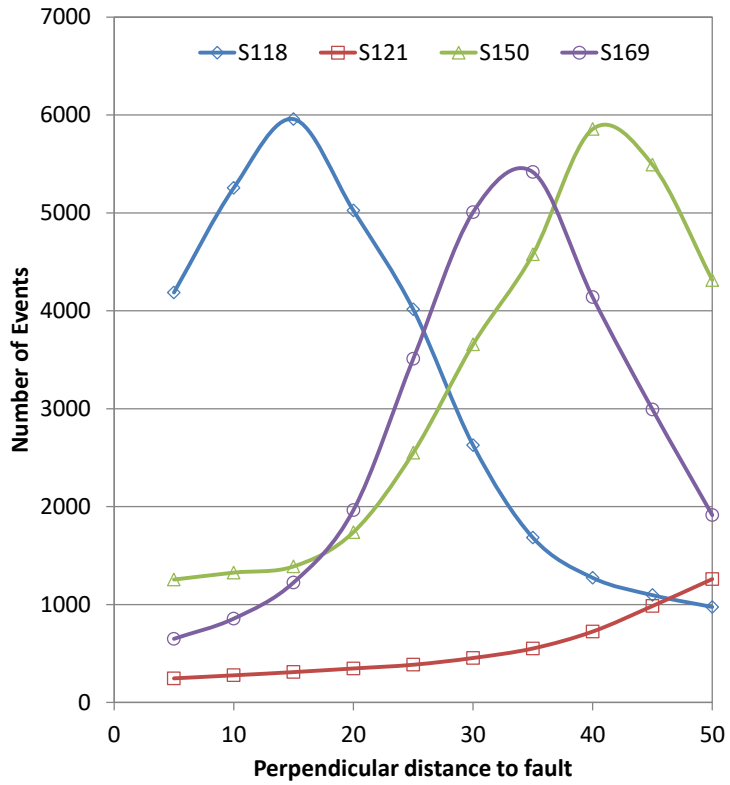


Figure 3.26: Distances of events to the NE faults.

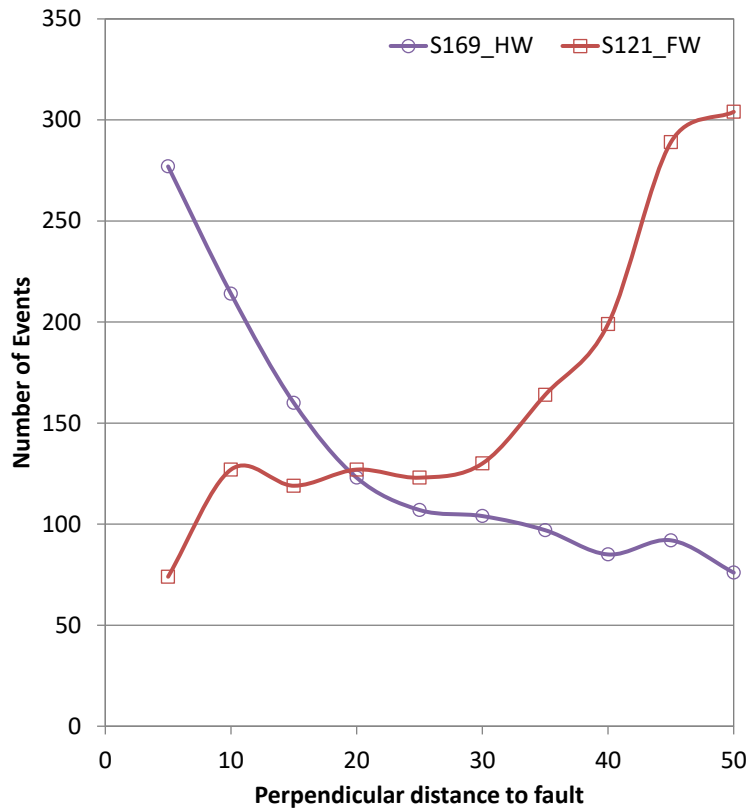


Figure 3.27: Distances of events located in the HW of S169 and distance of events located in the FW of S121.

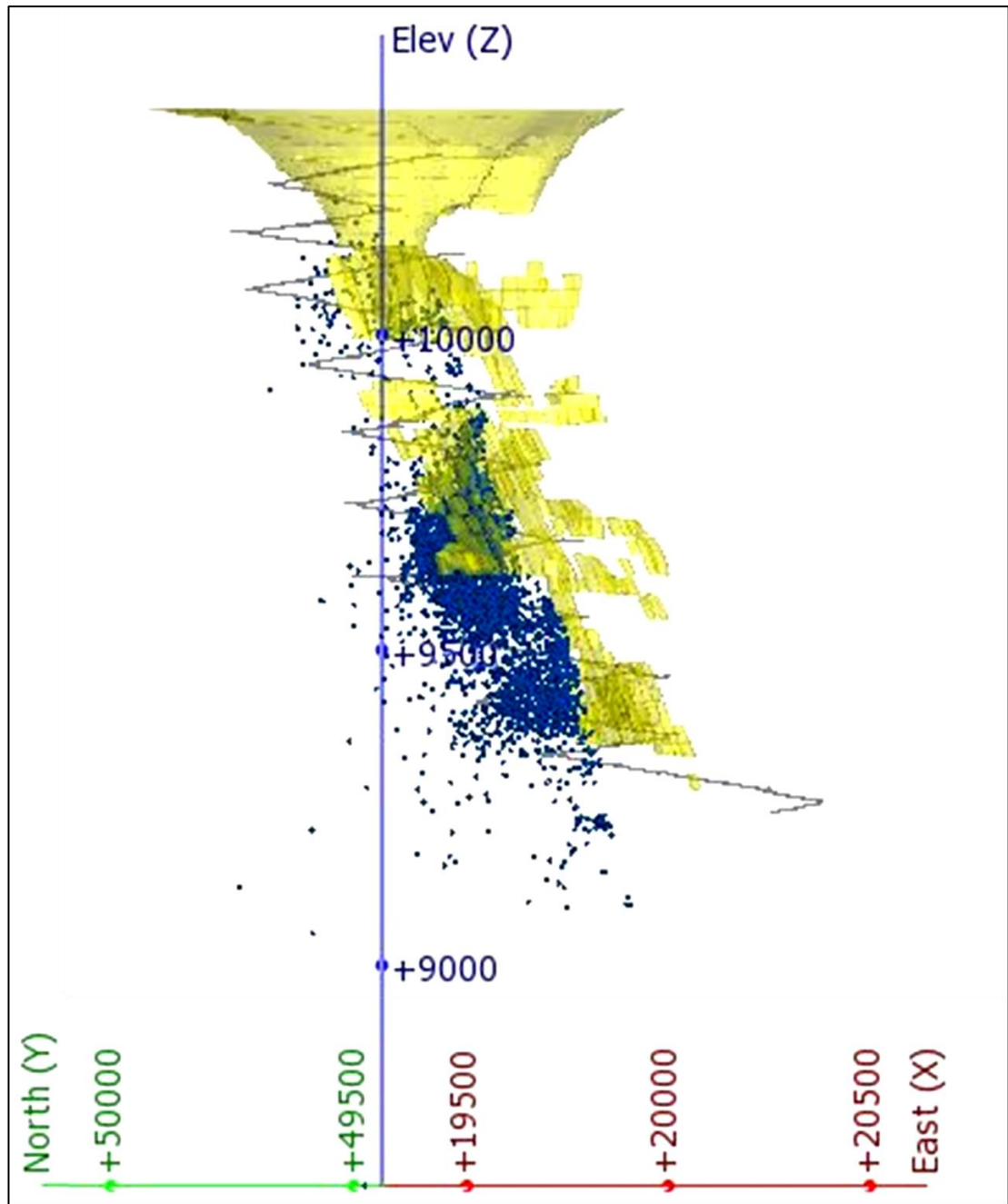


Figure 3.28: Locations of seismic events for the NE fault Group 1.

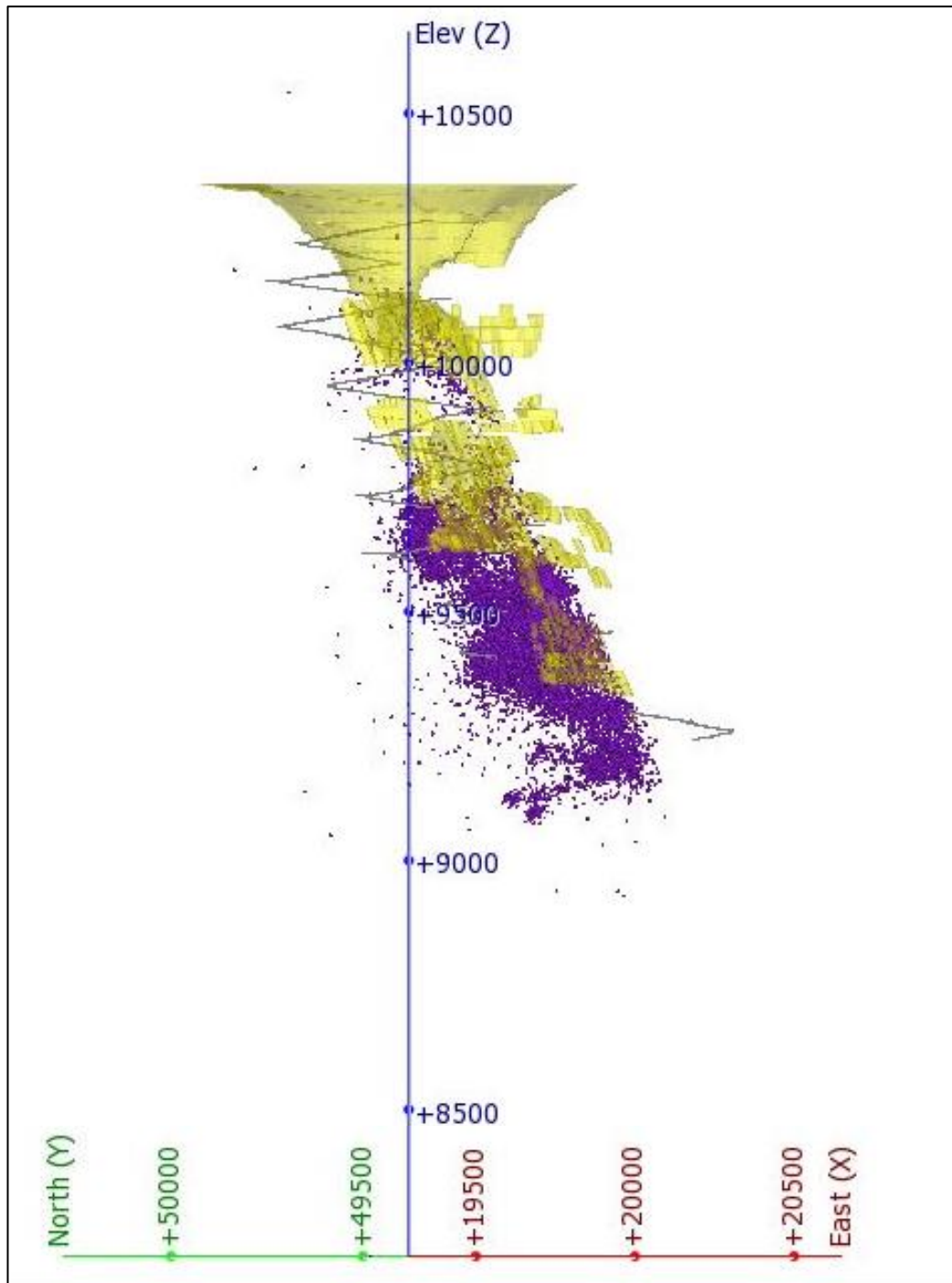


Figure 3.29: Locations of seismic events for the NE fault Group 2.

3.3 Esmeralda

3.3.1 Location and Geological setting

Esmeralda mine site is part of the El Teniente mine complex, operated by Codelco Mining Company. El Teniente, one of the world's largest copper mines, is located in the Andes mountain range near Sewell, Chile, 75 km south of the capital Santiago.

The El Teniente ore body is hosted by the mineralised Teniente mafic complex consisting of "*gabbros, diabases, basaltic and basaltic andesite porphyries*" (Brzovic, 2010). This complex is contained within the north-south striking Dorsal Mioliminar structural belt 140 – 150km wide and stretching the full length of Chile (Camus, 1975).

The geology of the El Teniente mining area is dominated by the Braden caldera. The caldera is a barren brecciated volcanic pipe which has intruded through the mafic complex. This pipe forms the centre of the mine site. The surrounding rock mass is characterised by "*volcanic flows and pyroclastics sheets with interbedded continental sediments cut by intermediate to felsic intrusives*" (Camus, 1975). The mafic complex is intersected by felsic intrusives and breccias most notably the locally named diorite porphyry (also called the Sewell Tonalite) and dacite porphyry. A plan of the El Teniente geological setting is provided in Figure 3.30 (Stern et al., 2011).

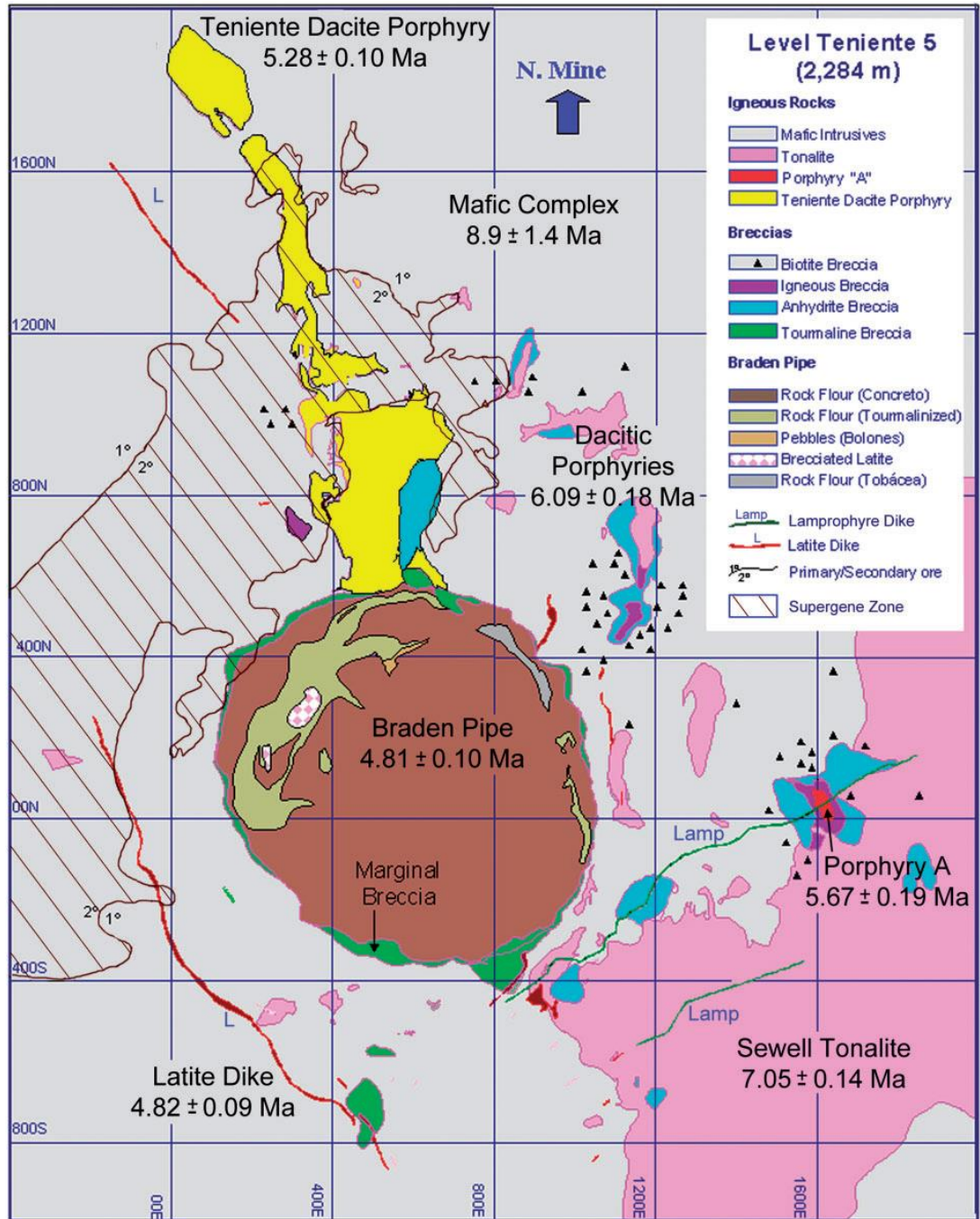


Figure 3.30: The El Teniente geological setting Stern et al., 2011.

3.3.2 Mining Method

The current El Teniente mine site comprises of 6 mining districts. These are shown in Figure 3.31. The Esmeralda Block Cave is located on the eastern side of the caldera. Undercutting began in 1996. The caving front was designed to progress from North to South. Instability in the pre-undercut occurred in between 2000 and 2005 and again between 2008 and 2010 causing significant delays to production.

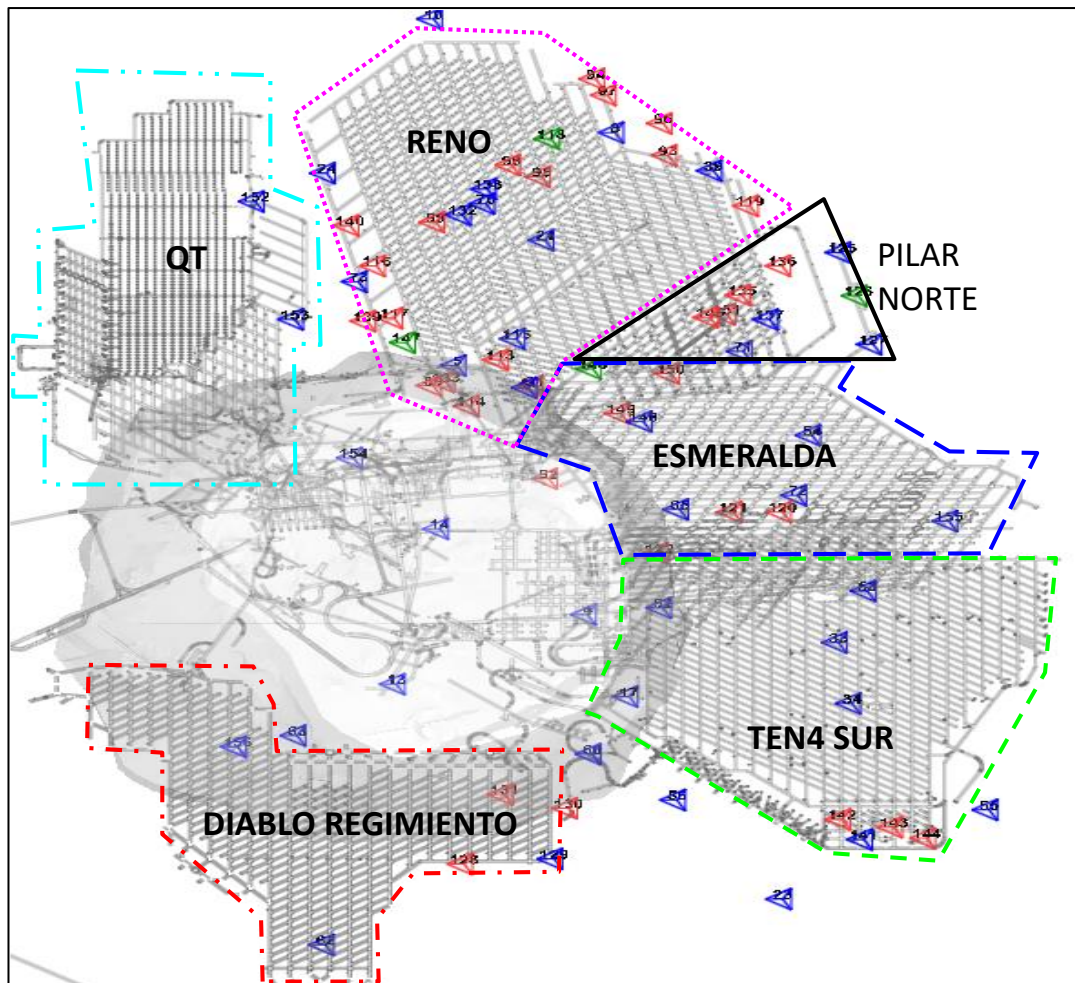


Figure 3.31: Plan of El Teniente Mine site with various mining districts.

3.3.3 Literature review

Several reviews of seismicity have been undertaken at El Teniente (Rojas et al., 2000, Potvin et al., 2010). Brzovic, 2010 states that several mining sectors (Ten Four, Reno) have suffered complete or temporary closures due to seismicity related rock mass damage.

Brzovic, 2010 studied the focal mechanism of seismic events at both Reno and Esmeralda. He found that the majority of seismic events at Esmeralda were related to failure along large-scale structures or re-fracturing of veins. Very little intact rock failure was observed.

No further papers have been published specifically concerning the Esmeralda sector.

3.3.4 Data Availability

The data in Table 3.6 have been provided by Codelco Mining Company for the Esmeralda mine site.

Table 3.6: Data availability for Esmeralda site

	Data Type	Esmeralda
Seismic Data	Data Available	✓
	Data processed	✓
Seismic System	Sensor location	✓
	Significant hardware upgrades	x
	Significant outages	x
Geology	Major structure well defined	✓
	Minor structure defined	✓
Mining Information	Decline files	#
	Level files	#
	Caving history	#
# data only partially available		

The data for the analysis contained within this thesis relate solely to Esmeralda mine. It is recognised that interactions with other mining sectors may create seismic events within the Esmeralda sector. It is also possible that structures extend beyond the Esmeralda mining district and associated seismicity is not within this dataset.

The data were initially provided for a concurrent research project at WASM (Pardo and Villaescusa, 2012, Pardo Mella, 2015). The geological model contains a large complex of faults, as well as several intrusive diorites. The original fault model (Figure 3.32) was developed from interpreted sections. The model contained over 170 structures, many of similar orientations. Some structure sets (particularly the B faults) were inconsistent in orientation down dip. To improve the models for this analysis the fault section data were reinterpreted creating more consistent models and orientations.

The new model (Figure 3.33) contains approximately 60 structures. Four pervasive fault orientations are identified and indicated by colour. The first, known as the P system faults, are displayed in green. These faults are approximately vertical, striking WSW. The Fault B structures (indicated in orange) are vertical and loosely strike SE/NW; however, the profile of these faults is curved and the orientation changes slightly with strike. The J system faults, shown in magenta, are moderately dipping NNE striking. Another minor fault system is also apparent. This system, indicated in dark blue, is vertical, striking NE/SW but is anecdotally inconsistent and open to interpretation.

The dyke model is provided in Figure 3.34. The dolerite dykes are indicated in red. These models have also been slightly modified to simplify the geometry and smooth the models.

Block caving is the primary method of extraction at El Teniente including the Esmeralda site. Only plans of the current extraction level were provided. Footprints of the cave between 1999 and 2009 were also provided.

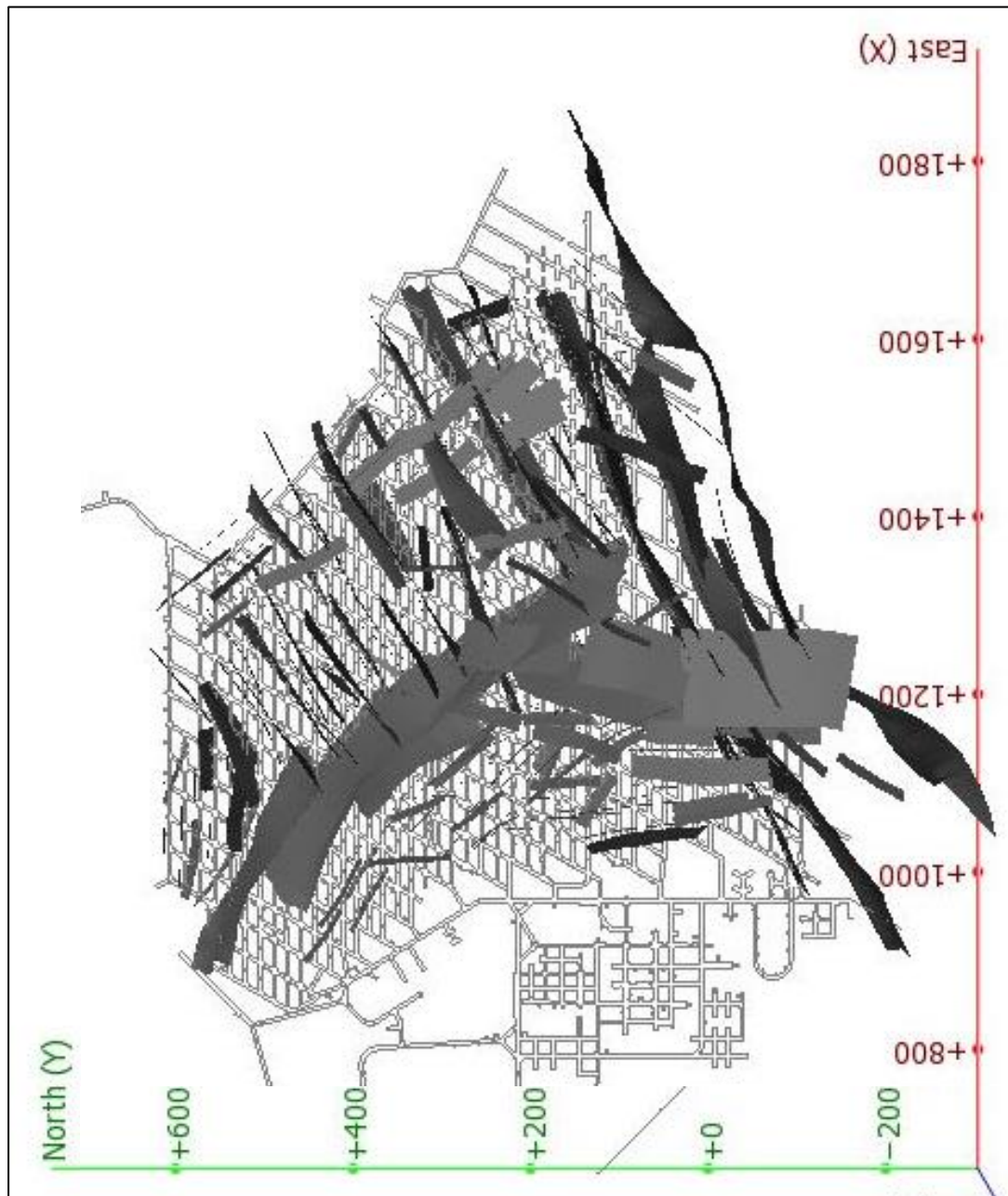


Figure 3.32: Esmeralda structural model prior to reinterpretation.

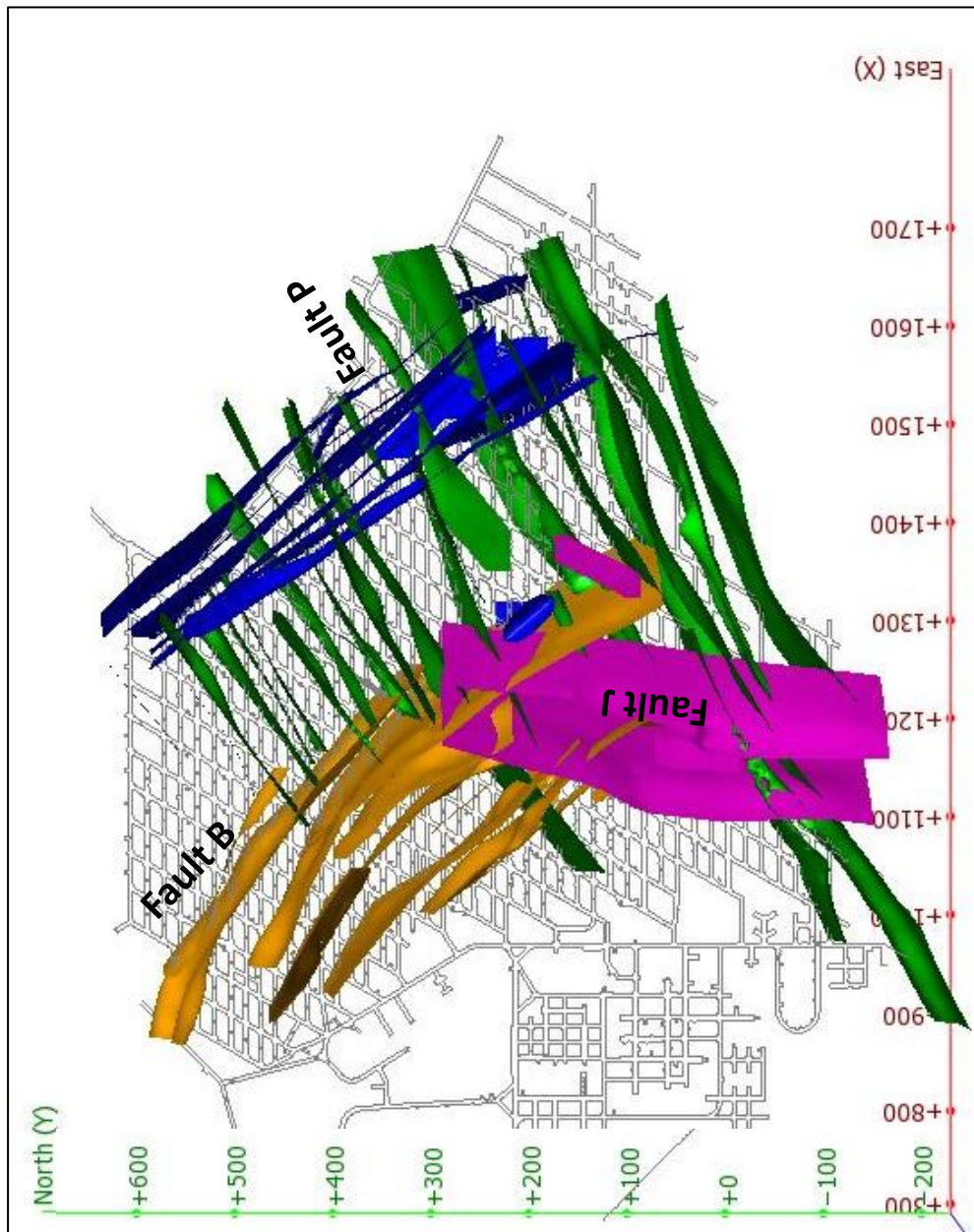


Figure 3.33: Revised fault model for Esmeralda mine site (plan view).

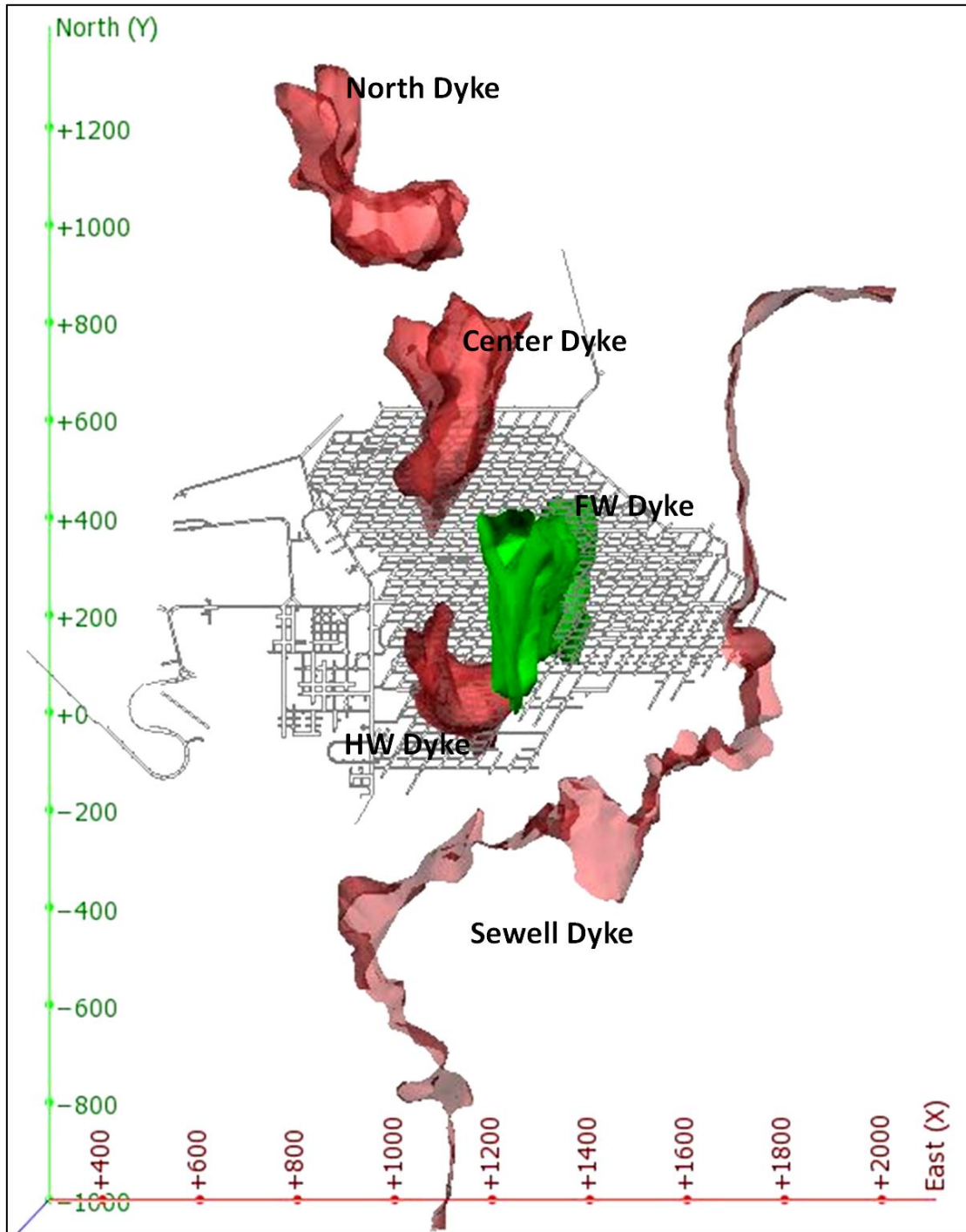


Figure 3.34: Dyke models for Esmeralda site.

3.3.5 Discussion on Seismicity at Esmeralda

The entire El Teniente mine complex is monitored by a single seismic system with sensors installed in all districts. The locations of the sensors are provided in Figure 3.35. There are 14 sensors within the Esmeralda district and another 15 in the adjacent Pillar Norte district. Most of the sensors are located below the extraction level of the mine (Figure 3.36). Any sensor may be used in the processing of a single event in any of the mining districts.

Information on monitoring system changes and the on-going functionality of the system was not provided. Due to this lack of data, it will be assumed that changes in the seismic source parameters and event rates are the result of changes in the seismicity trends and not changes in the seismic system.

The seismic database provided was filtered by location to only include events in the Esmeralda mining district. The filtered database contains almost 380,000 events spanning from January 1992 to February 2010. The event locations are provided in Figure 3.37.

At other sites, the dispersion of the locations of the events outside the mining area can provide some guide as to the quality of the dataset. In the case of this dataset, the events were extracted from a larger database and consequently outliers are inherently removed.

Despite the filtering, some scatter in the locations of the events is apparent. This is potentially a function of the mechanics of the rock mass behaviour. Caving is a large-scale mining method and stress redistribution can cause rock mass failure far in advance of the cave front. At Esmeralda, this is further complicated by the adjacent caving operations. It will be assumed that the large event location scatter is caused by natural mechanisms (i.e. rock mass failure) rather than artificial causes (i.e. poor data).

The number of events is highest to the north. This is due to cave progression which starts in the north and migrates to the south but may also relate to the influence of adjoining operations.

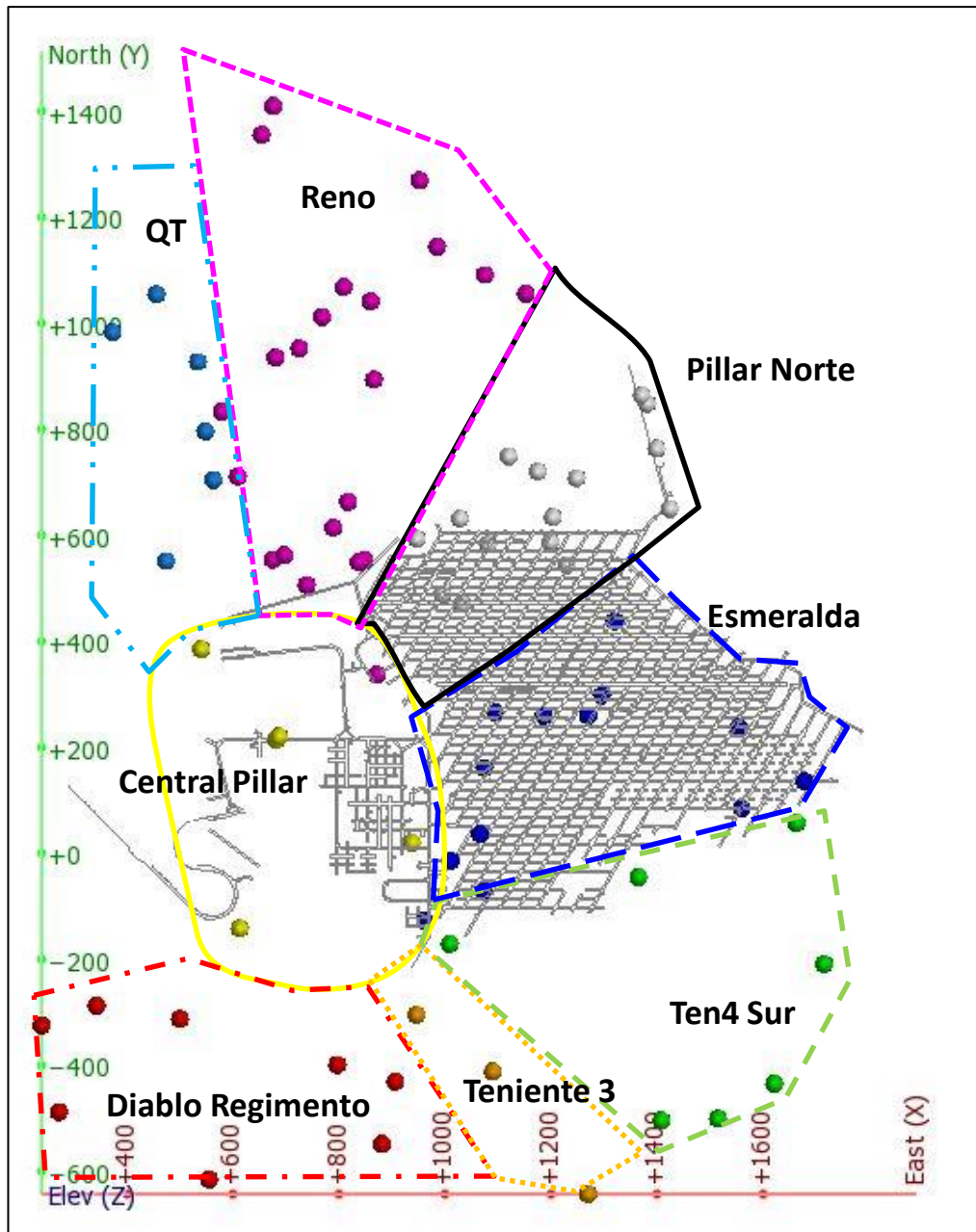


Figure 3.35: Location of El Teniente seismic sensors (plan view).

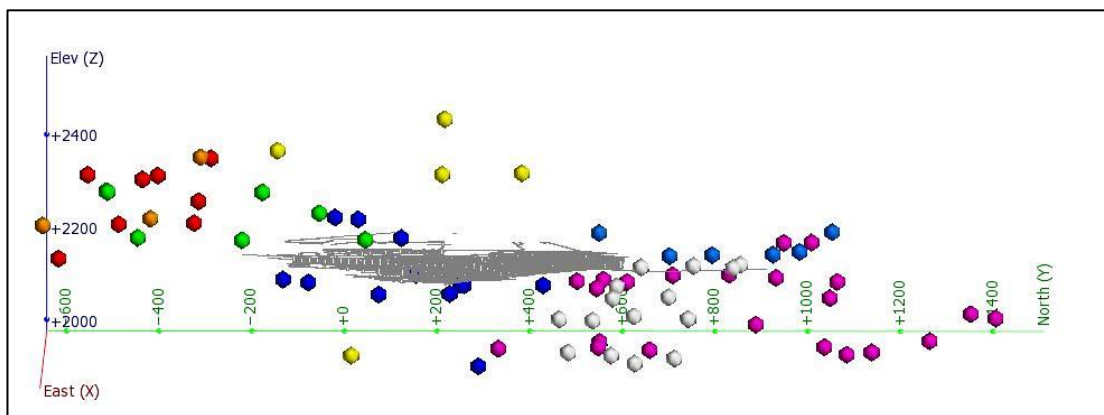


Figure 3.36: Sensor locations with reference to the Esmeralda extraction level (looking west).

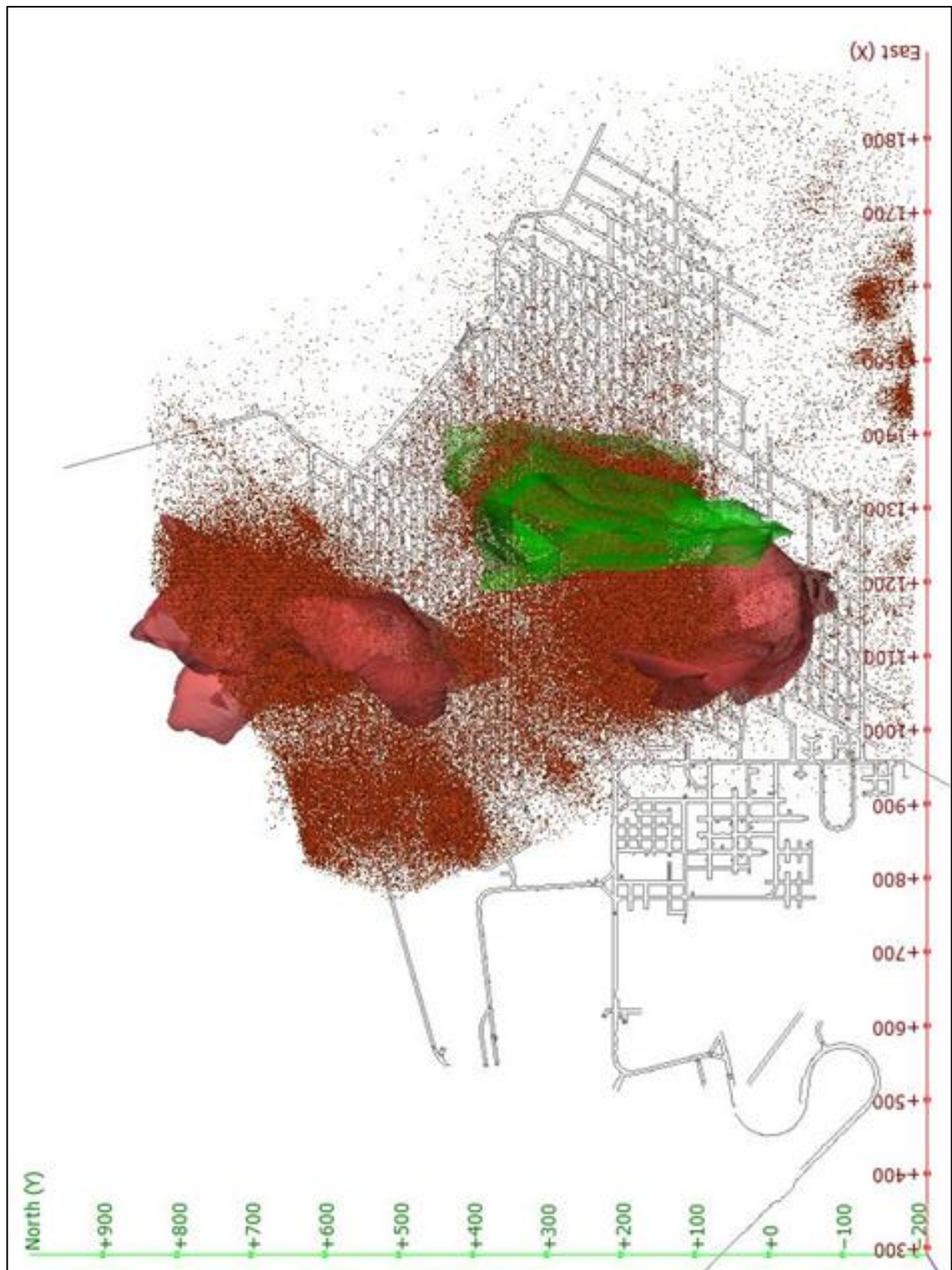


Figure 3.37: Plan of the locations of the events in the Esmeralda seismic database.

Seismic parameters also provide an insight into data quality. A review of the seismic parameters for each event identified subtle variations in the seismic magnitudes between January 2001 and October 2002. Figure 3.38 shows the magnitude distributions from Jan 1999 to Dec 2000, Jan 2001 to Oct 2002 and Oct 2001 to Dec 2002. The magnitude distribution before 2001 and after 2002 typically exhibits a normal distribution with the mode occurring between -0.5 and $0M_L$. The magnitude distribution between Jan 2001 and Oct 2002 is anomalous.

Further investigations were conducted to ensure the quality of the dataset. No anomalies could be readily identified in the trend of the energy or moment data. The site magnitude (m) was calculated using the moment magnitude scale given by Equation 3.3 where M represents moment.

$$m = \frac{2}{3} \text{Log}M - 6.01$$

Equation 3.3

The magnitudes were re-calculated using this formula. If the magnitude calculations were correct, the differences between the provided magnitudes and the re-calculated magnitudes should be consistent (allowing for decimal place rounding). Figure 3.39 shows the differences between the provided and re-calculated magnitudes between 1999 and 2002.

The data clearly indicate an anomaly in the calculation between Jan 2001 and Oct 2002. No anomalies were apparent in the base data (moment), consequently the re-calculated magnitudes were used for all further analysis. The corrected magnitude distribution for the 2001 to Oct 2002 period is provided in Figure 3.40. The magnitudes range from $-3.0M_L$ to $2.7M_L$ with the median being $-0.4M_L$.

Events over magnitude $1M_L$ were considered damaging events. Almost 2000 events occur over magnitude $1M_L$ (Figure 3.41). Most of the high magnitude events are associated with the diorite dykes. Some high magnitude activity also occurs in alignment with Fault B. Several clusters (blue circles) are not associated with known structures or dykes.

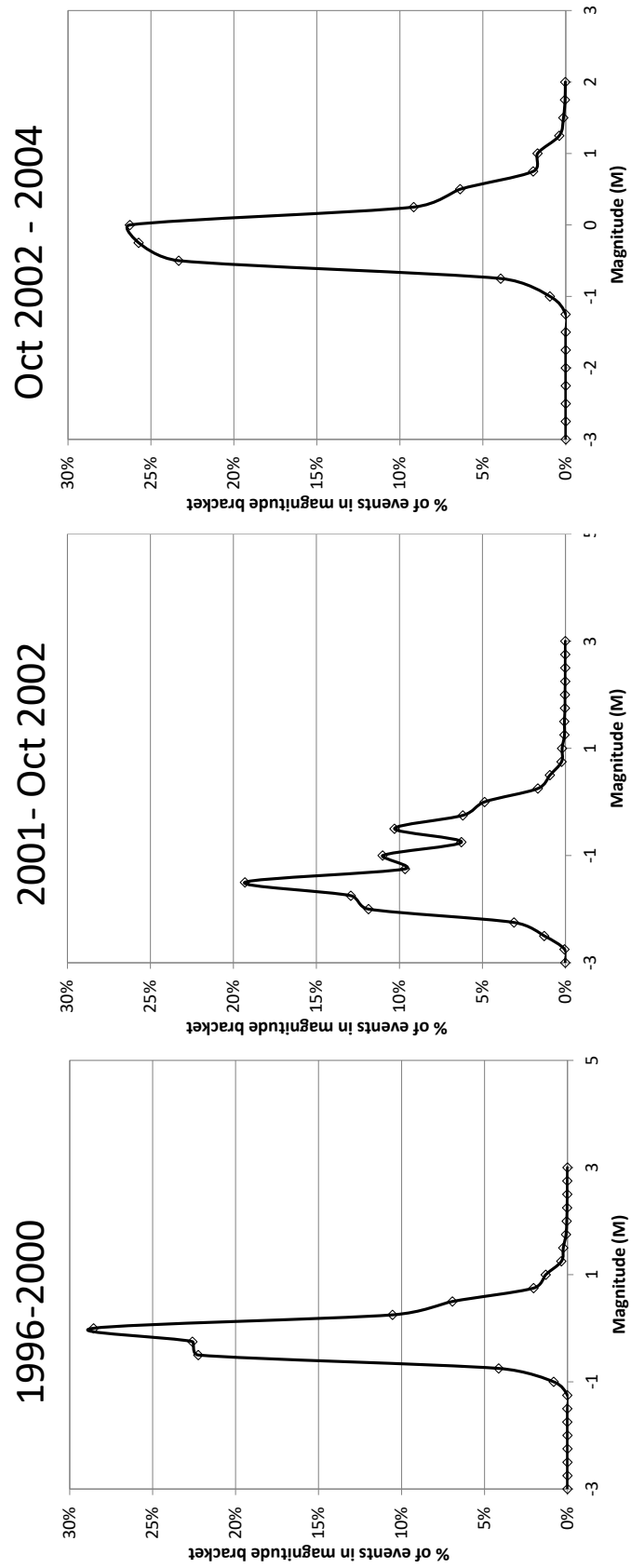


Figure 3.38: Curve distributions of magnitudes for 1999 – 2000, 2001 – Oct 2002 and Oct 2002 – 2004.

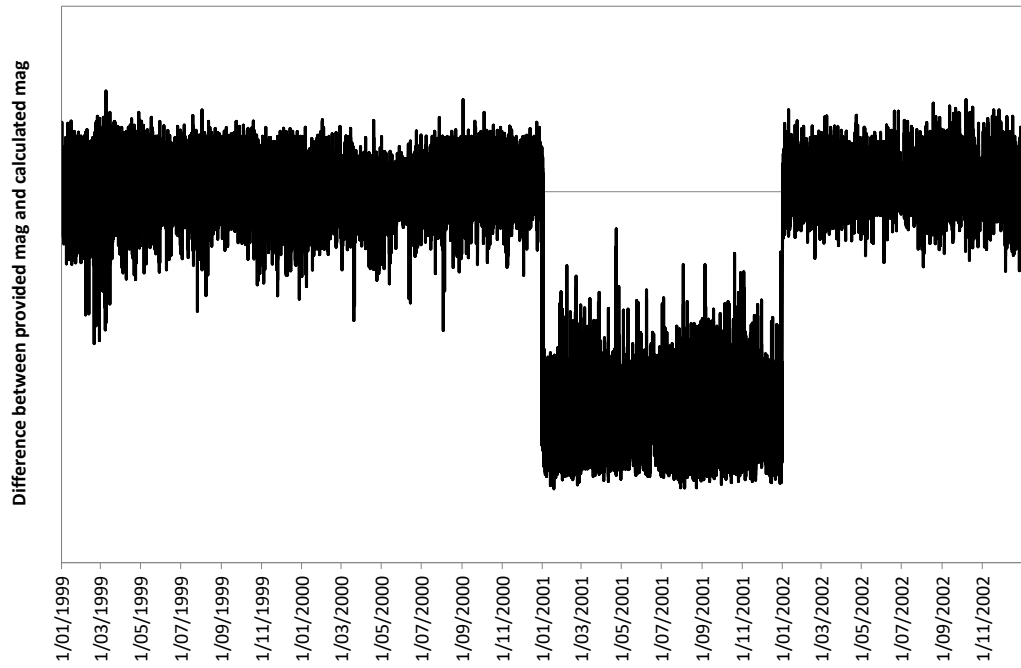


Figure 3.39: The differences between the original magnitudes and the newly calculated magnitudes clearly indicate an anomaly in the data in 2001 and 2002.

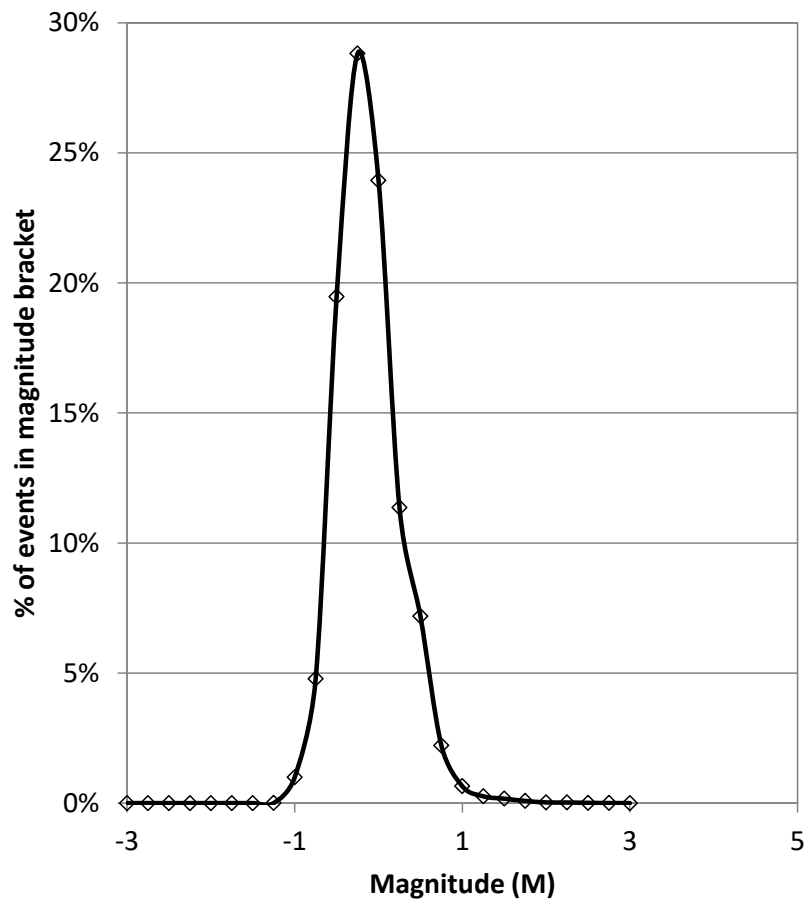


Figure 3.40: Distribution of the newly calculated magnitudes between Jan 2001 and Oct 2002.

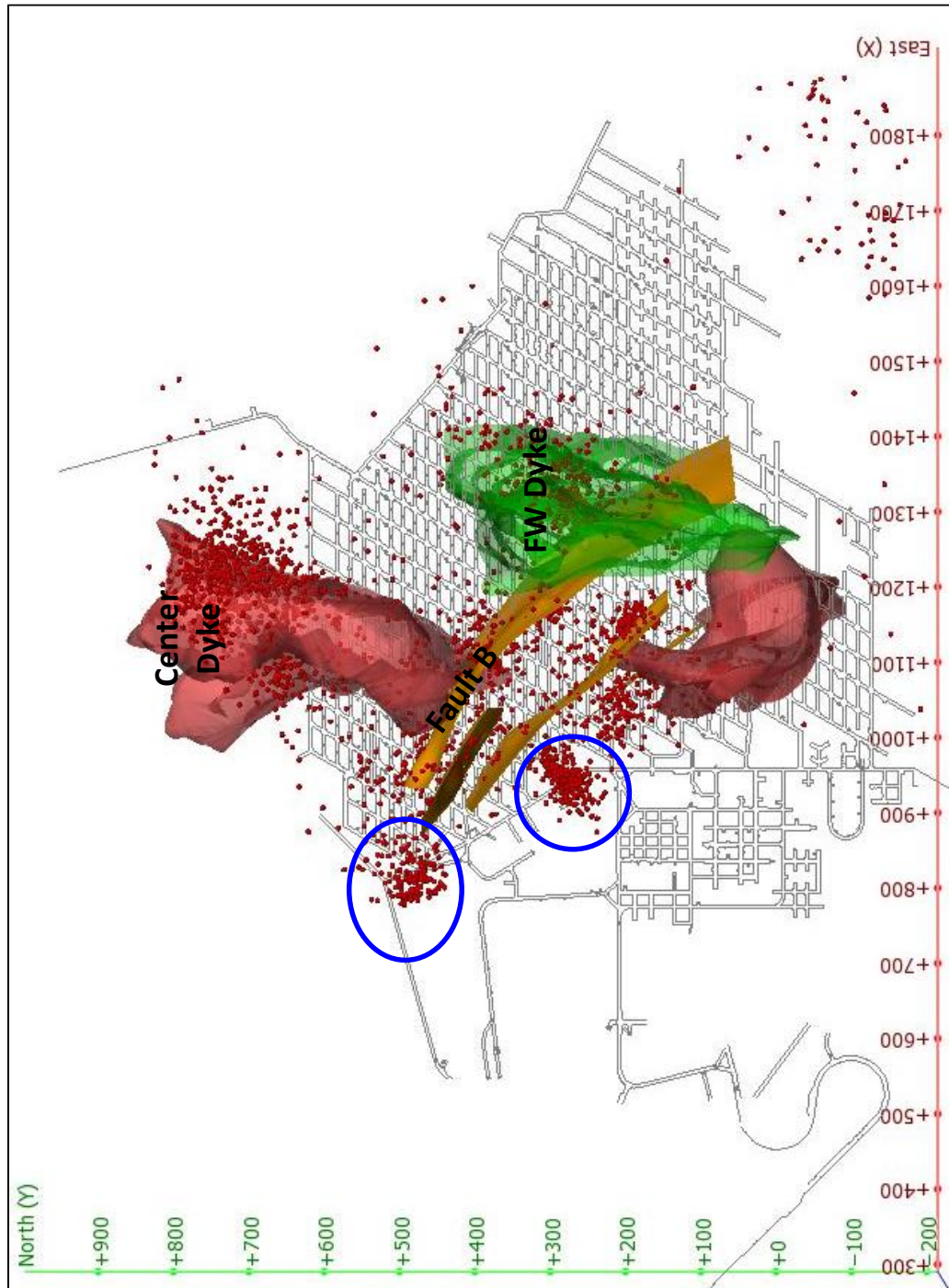


Figure 3.41: Large events (over 1ML) at Esmeralda concentrate around the diorite dykes (plan view).

3.3.6 Structures for Analysis

The following structures have been selected for analysis: FaultP_1, FaultB_C and the Footwall (FW) Dyke (Figure 3.42)

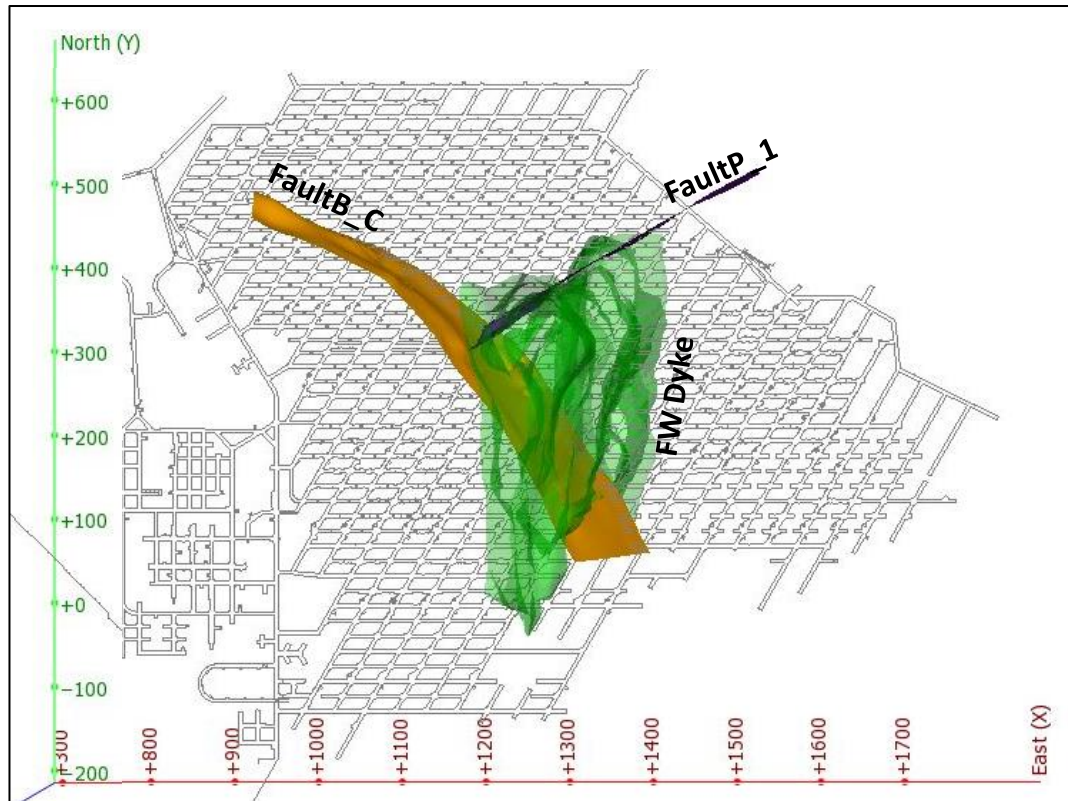


Figure 3.42: Esmeralda structures for analysis.

3.3.6.1 Fault P Stage 1

P system faults are a pervasive large-scale structure set located in the hangingwall of the Fault B fault system. These faults are approximately vertical, striking WSW / ENE. The re-interpretation of structures has not significantly changed the Fault P models.

Back analysis of drive failures at Esmeralda identified the P system faults as having a major influence on instability in the mine. The P system fault located in the centre of the instability (referred to as FaultP_1) was chosen for analysis.

FaultP_1 has 7 sensors located within 200m of the fault; 5 located within the Esmeralda mining district and 2 located in the Pillar Norte mining district (Figure 3.43). All sensors are located below the extraction level. This is likely to affect the accuracy of the data around the caving area.

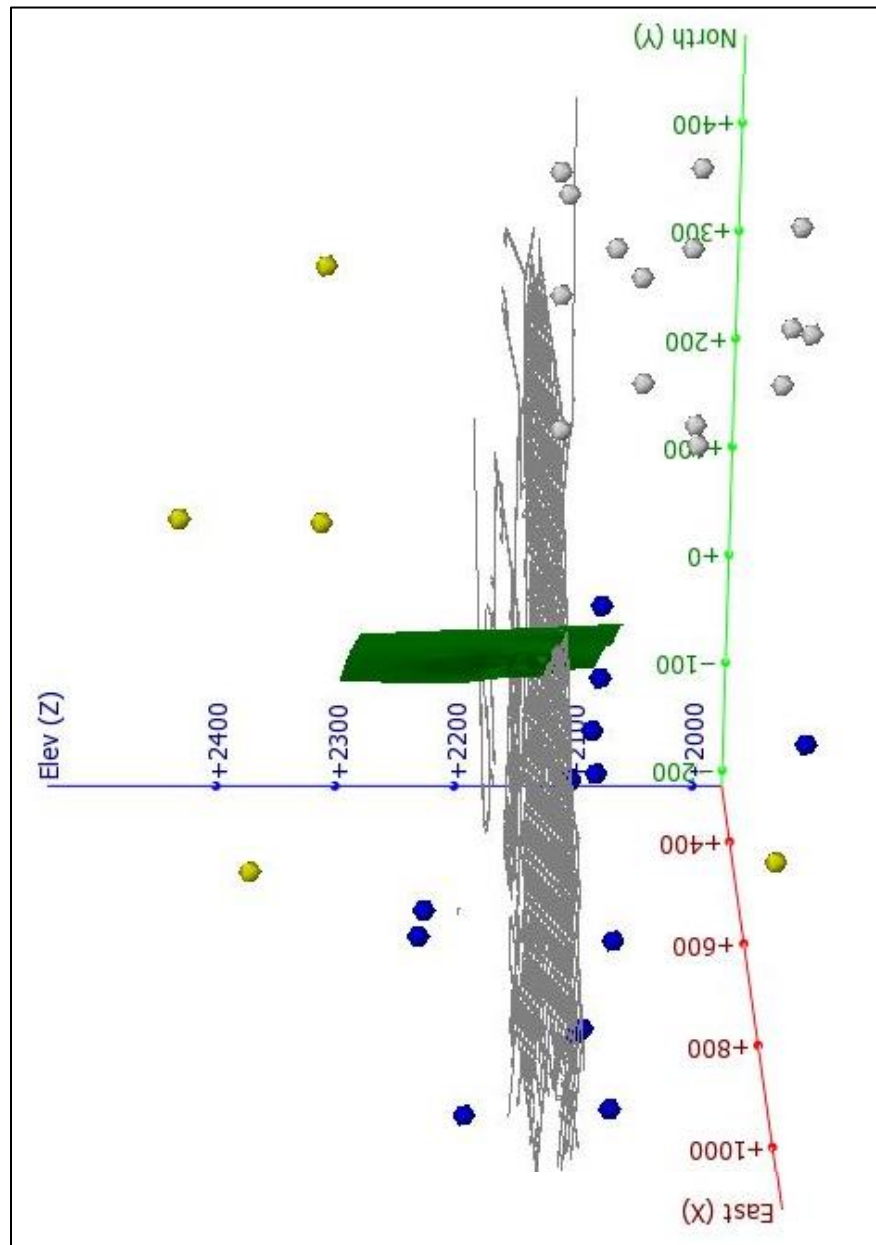


Figure 3.43: FaultP_1 with seismic sensors.

The domain distance was created at $\pm 15\text{m}$ (Figure 3.44). The overall domain width is 30m. The FaultP_1 data subset using this value comprises of approximately 3500 events (Figure 3.45). The magnitudes for FaultP_1 range from $-1.5M_L$ to $1.5M_L$ with a median of $-0.3M_L$. The median is slightly higher than that of the overall dataset.

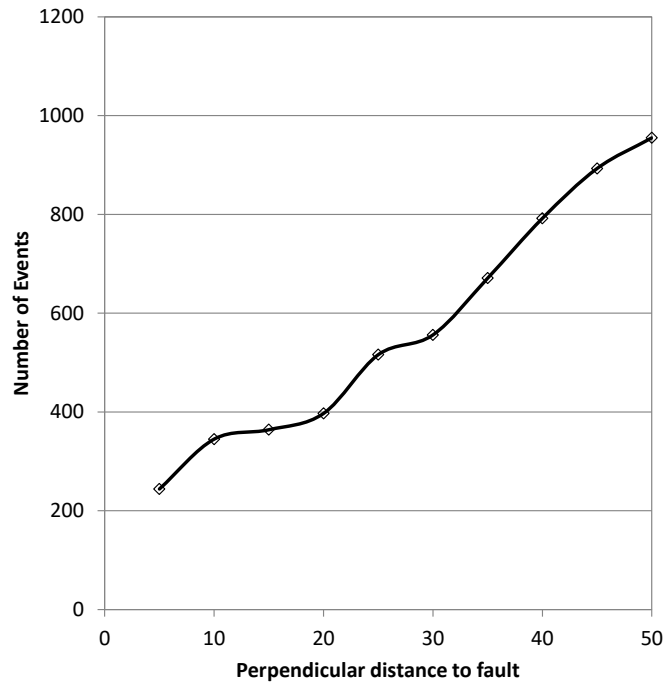


Figure 3.44: Distances of seismic events from FaultP_1.

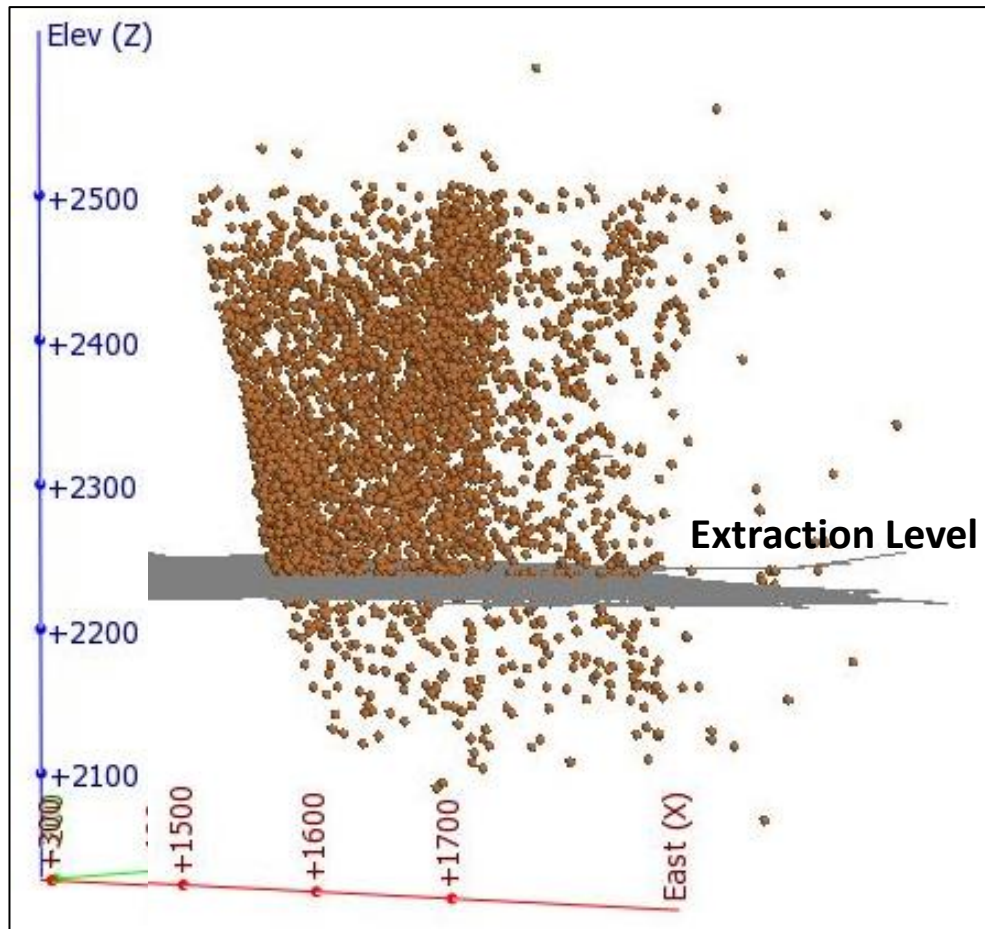


Figure 3.45: Locations of events on FaultP_1.

3.3.6.2 Fault B

The Fault B structures are vertical and loosely strike SE/NW; however, the profile of these structures is curved and the azimuth changes slightly with strike.

The original Fault B models indicated that the dip of the sub-parallel structures vary and converge at depth. Re-interpretation of the intercepts within the model was undertaken. The new Fault B models are more vertical and indicate the structure spacing is approximately 20m. Several of the smaller area planes have been merged to form larger structures. A comparison of the old and new models is provided in Figure 3.46 and Figure 3.47. The largest Fault B structure (called part C) is selected for analysis. This fault is indicated in red in Figure 3.47.

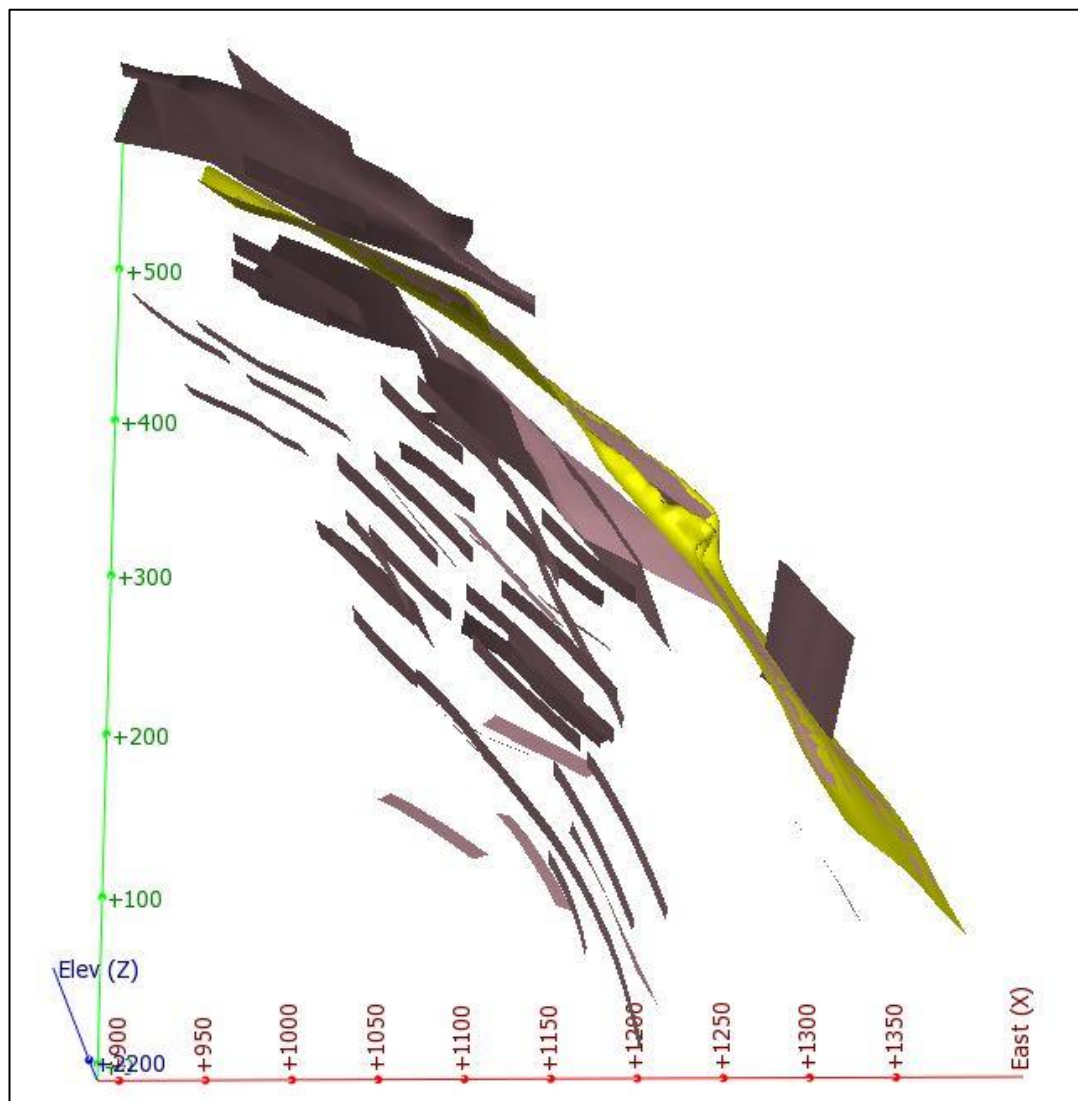


Figure 3.46: Fault B old models

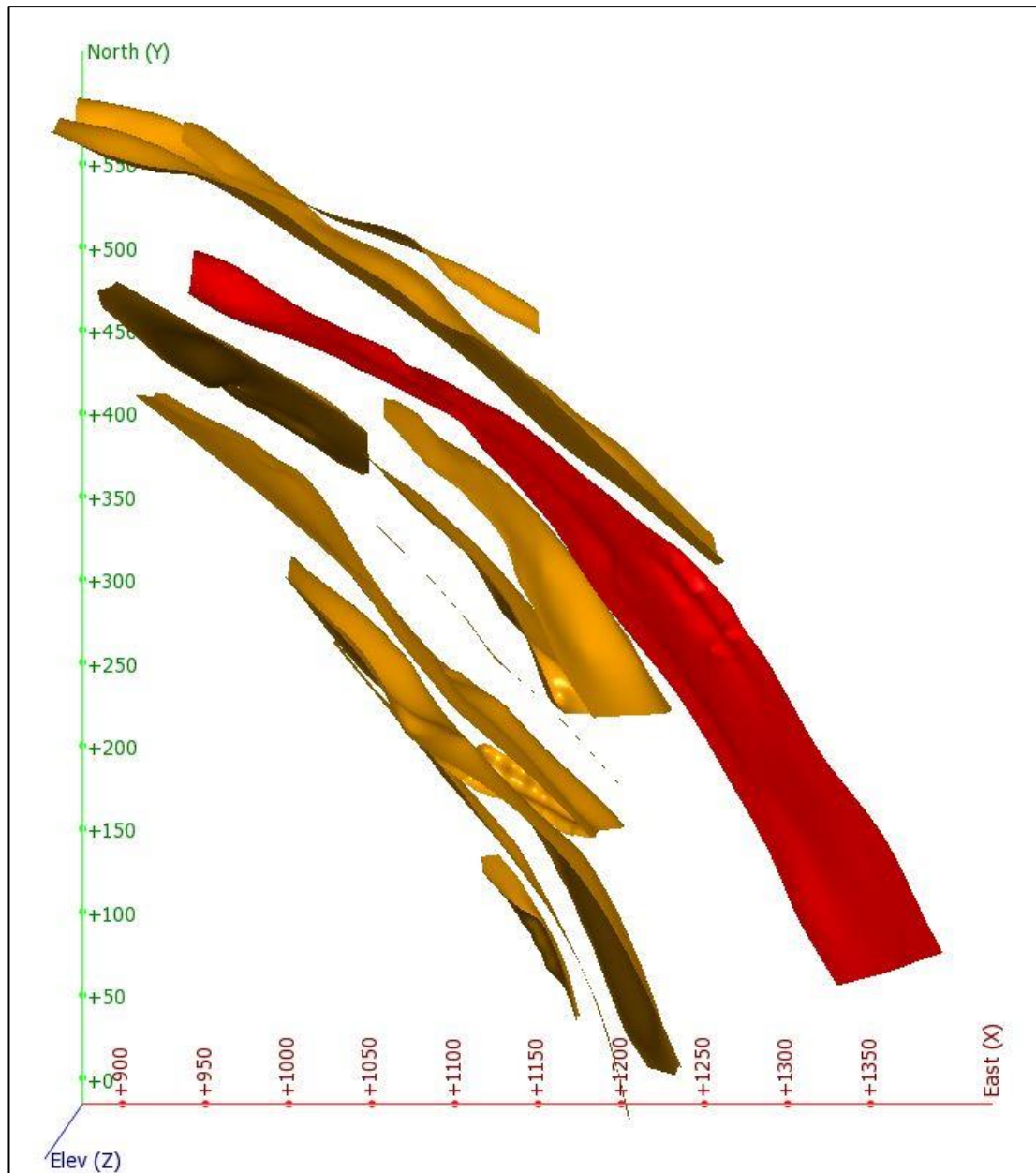


Figure 3.47: Fault B new models. Part C is indicated in red.

There are 13 sensors located within 200m of FaultB_C. Six sensors are located in each of the Esmeralda and Pillar Notre mining districts with one sensor located in the Ten4 Sur district. The Ten4 Sur sensor is the only sensor located above the extraction level depth. This may affect the location accuracy of events around the cave.

The distances of events from the fault analysis are provided in Figure 3.48. The results indicate the optimum domain distance is $\pm 25\text{m}$; however, a review of the spacing between the structures suggests that this will cause overlaps with sub-parallel faults. To prevent overlapping a domain distance of $\pm 15\text{m}$ was chosen for an overall domain width of 30m . The data subset contains over 30,000 seismic events (Figure 3.49). The magnitudes for FaultB_C range from $-1.6M_L$ to $2.3M_L$ with a median of $-0.5M_L$. The median value is slightly lower than the site median ($-0.4M_L$).

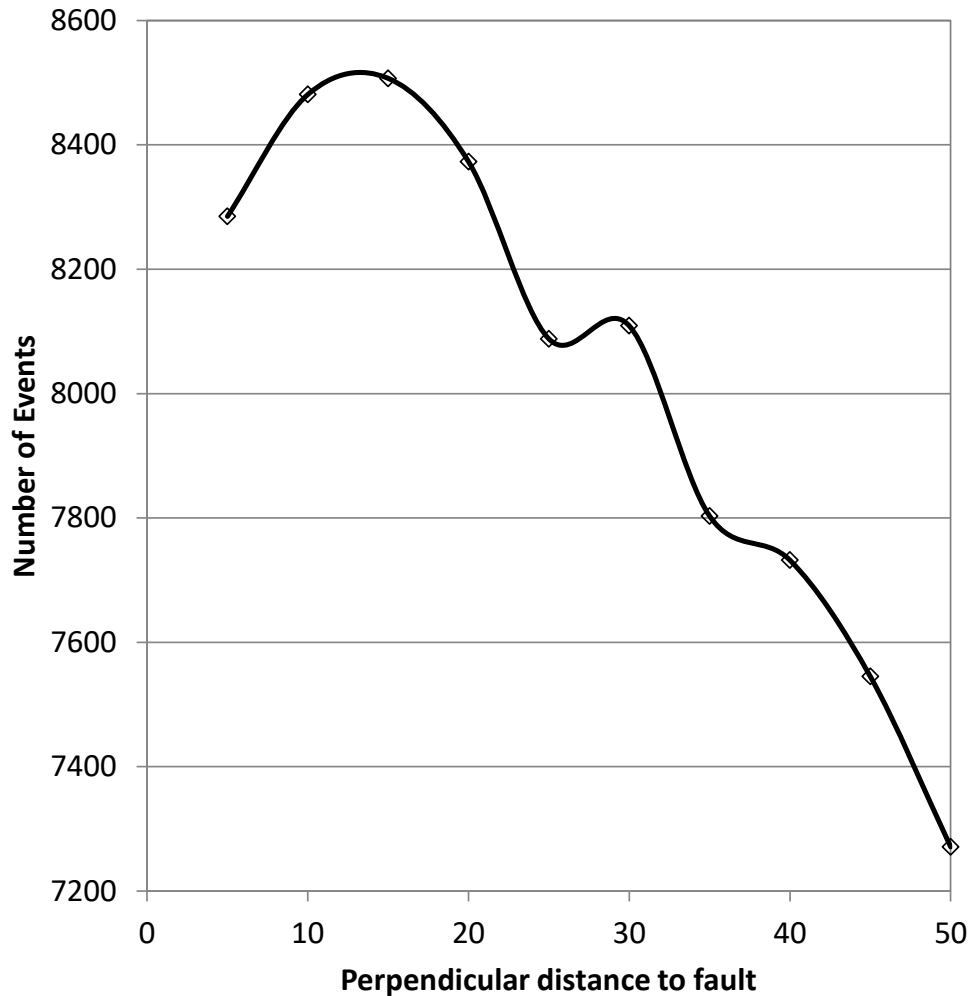


Figure 3.48: Seismic event distance distribution away from Fault B_C.

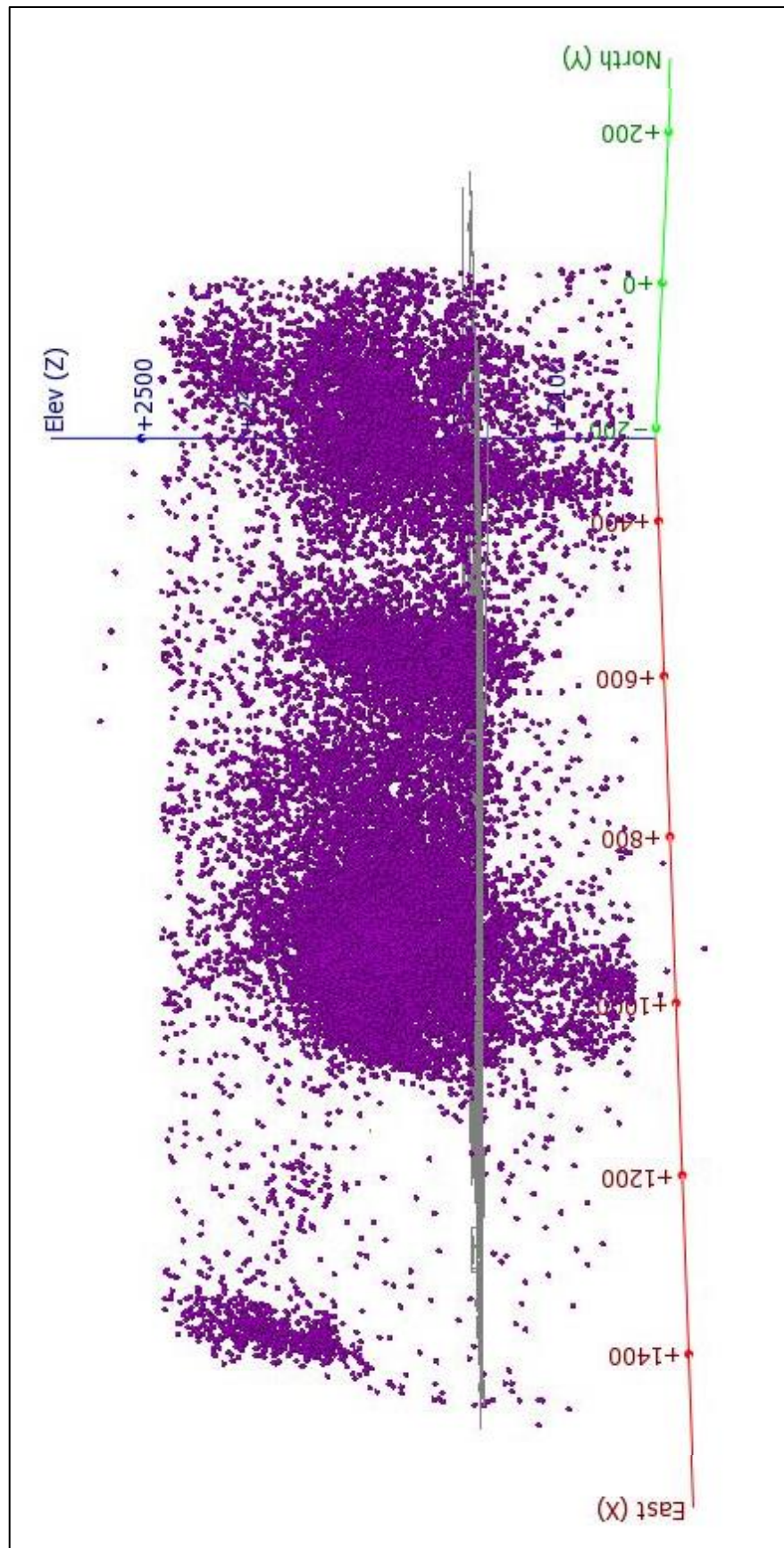


Figure 3.49: Locations of events on FaultB_C.

3.3.6.3 FW Dyke

The Footwall Dyke (FW Dyke) is one of the main diorite dykes associated with the Esmeralda ore body (Figure 3.34). The vertical dyke is oval in shape and approximately 250 - 300m long and 80m wide. Its long axis is oriented North-South. A large number of high magnitude events occur in close proximity to all the dyke contacts. The FW Dyke was selected to determine if any of these large events are preceded by precursors using the analysis techniques developed for this thesis.

The original model was slightly modified to provide a more consistent, regular model. This did not change the overall shape of the dyke.

There are 8 seismic sensors within 200m of the FW Dyke. Six of these occur in the Esmeralda mining district with one located in each of the Ten4 Sur and Pillar Norte districts. Only the Ten4 Sur sensor is located above the extraction level. This is likely to affect the seismic event location accuracy in the upper levels of the mine.

The FW Dyke is a closed structure meaning seismic events can occur in all directions from the model boundary. To account for this, the domain creation process must be modified. To create the domain boundary, all events from inside the boundary were removed from the dataset. The distance to the boundary was calculated for the events on the outside of the dyke (Figure 3.50). The results are provided in Figure 3.51. The analysis shows a domain boundary of $\pm 30\text{m}$ is appropriate. As the dyke is closed all events inside the dyke will also be associated with the dyke. The number of points in the FW Dyke dataset is almost 66,000 points (Figure 3.52). The magnitudes range from $-1.8M_L$ to $2.3M_L$ with a median of $-0.5M_L$. The median for the FW Dyke is slightly lower than that of the overall dataset.

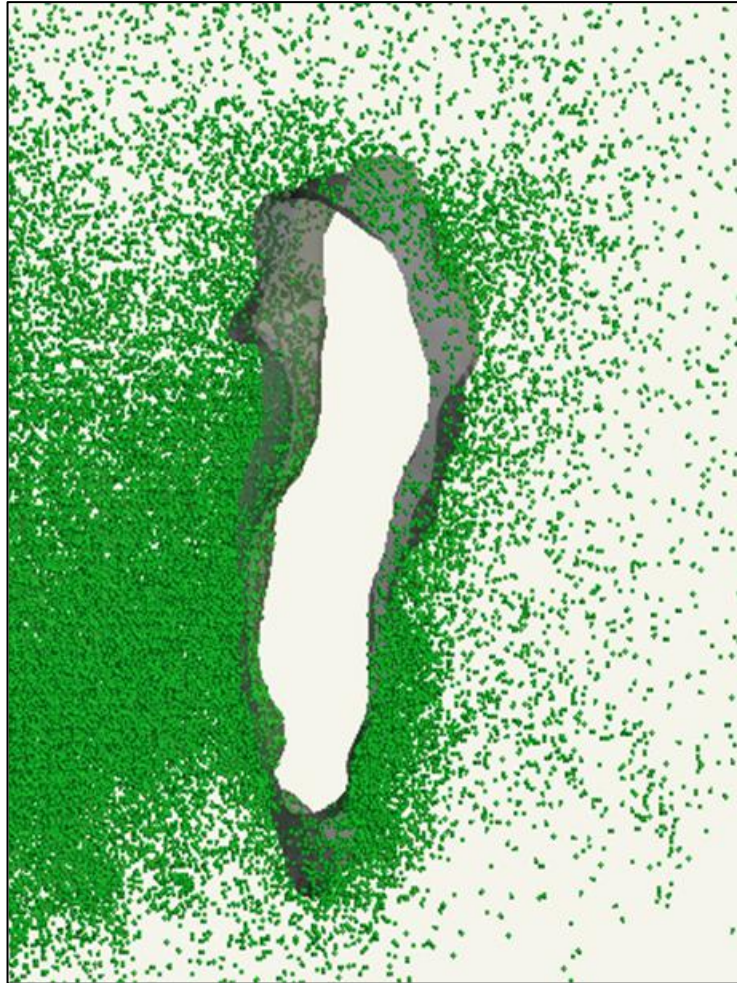


Figure 3.50: Events removed from inside the dyke model to prevent distance anomalies.

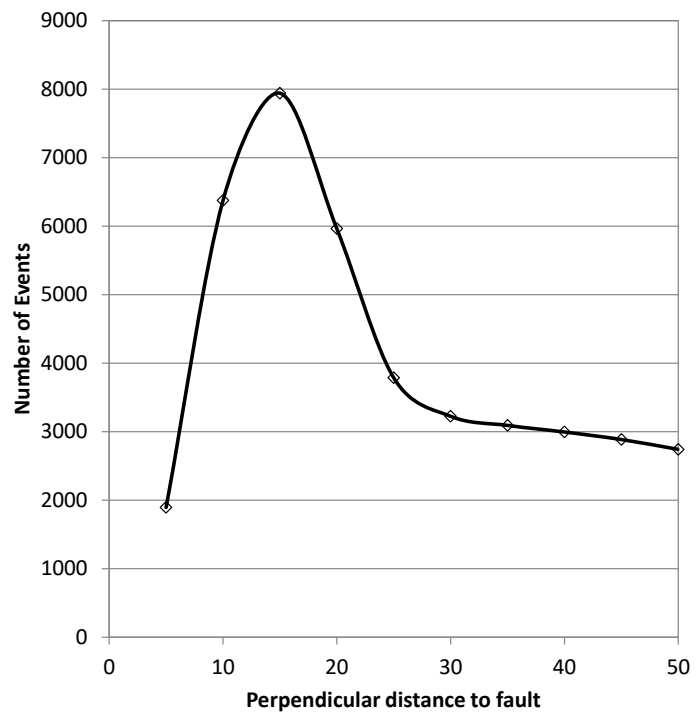


Figure 3.51: Seismic event distance distribution away from FW Dyke.

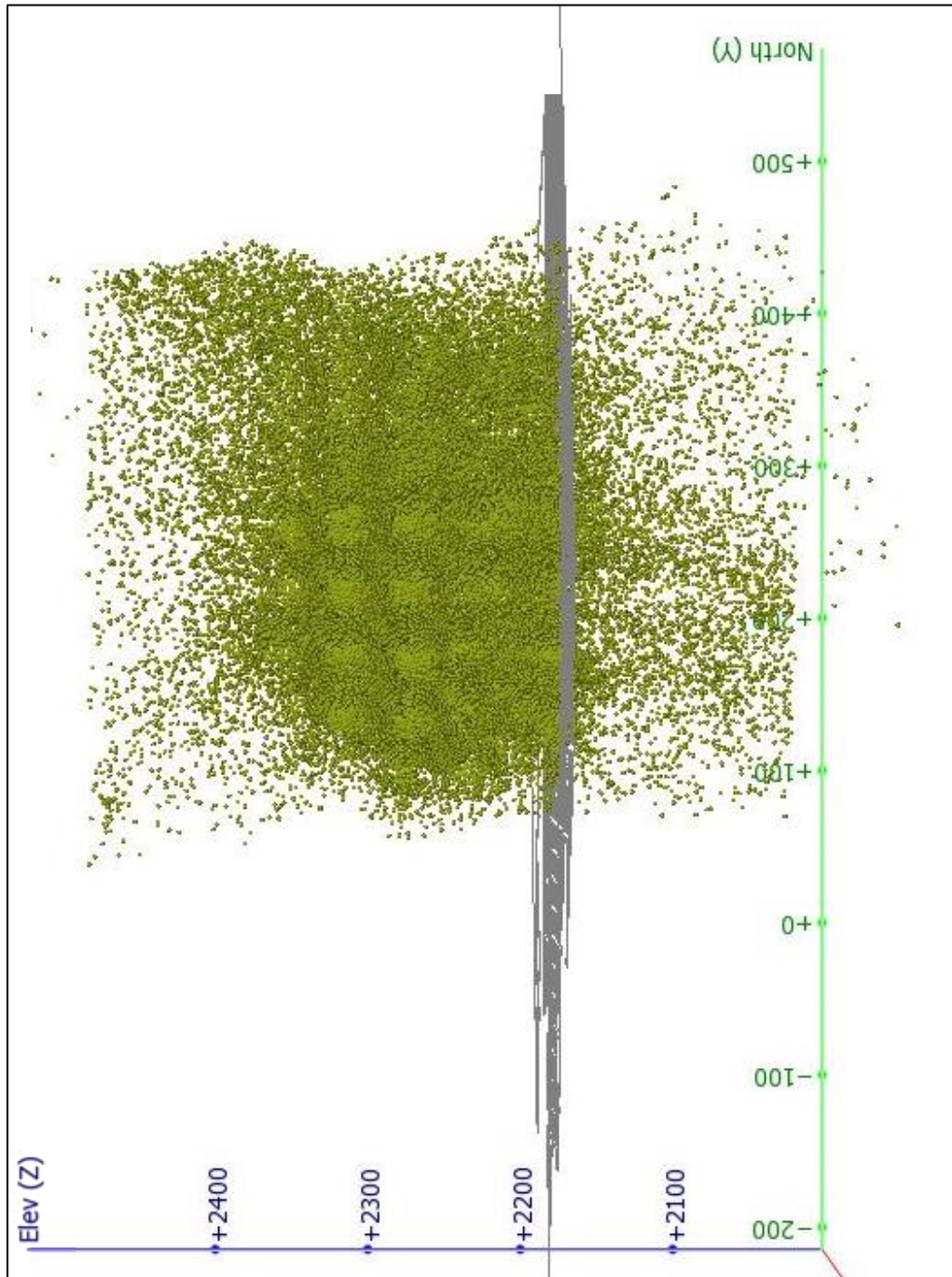


Figure 3.52: Locations of seismic events within the FW Dyke.

3.4 Mt Charlotte

3.4.1 Location and Geological setting

Mt Charlotte underground mine is owned and operated by Kalgoorlie Consolidated Gold Mines (KCGM). The mine site is located alongside the Kalgoorlie township and within the KCGM Superpit mining enclosure.

The geology of the Kalgoorlie terrain has been extremely well researched with many papers published on the topic (e.g. Phillips, 1986, Clout et al., 1990, etc.). The Mt Charlotte ore body is hosted entirely within the Golden Mile Dolerite (GMD) which is zoned into 10 sub-units of varying grain size (Ridley and Mengler, 2000).

The Kalgoorlie terrain has undergone at least 7 deformation events. These events are called events D1 – D7 and represent specific geological events and result in structures of specific orientations.

The ore body is intersected by several significant regional faults. In chronological order these faults are: Golden Mile fault, Flanagan Fault, Neptune fault, Maritana fault, Shea fault, Reward fault(s), and the Charlotte fault(s) (Figure 3.53). A summary of the strikes and plunges of each of these faults is provided in Table 3.7.

Table 3.7: Summary of faults within the Mt Charlotte mining area.

Fault Name	Deformation Event	Strike / Trend	Plunge
Golden Mile	D1	N – S Strike	
Flanagan	D2	NW Strike	Mod West
Neptune	D2	NW Strike	Mod West
Shea	D2	NW Strike	Mod West
Maritana	D4	N Strike	Vert / steep W
Reward	D4	N Strike	Vert / steep W
Charlotte	D4	N Strike	Vert / steep W

The Golden Mile fault is the oldest of the faults and is offset by all other faults. It is between 0.1 and 1.5m wide and is filled with fine grained gouge.

The Flanagan fault set includes the Flanagan Fault, The Neptune Fault and the Shea fault. These faults were formed either late in the D1 or during the D2 deformation event and are reverse thrust faults that strike NW and dip moderately to the west. The infill of these faults “*ranges from micro-breccia to cataclasite and foliated cataclasite*”, with overprinted “*by quartz veining, associated alteration and mineralisation*” (Clout et al., 1990).

The Charlotte fault set comprises of the Maritana, Reward and Charlotte faults. The faults are typically moderately to steeply dipping, north south striking oblique faults that cut all other faults. The vertical Maritana fault is between 0.5m and 1m wide with strong foliation.

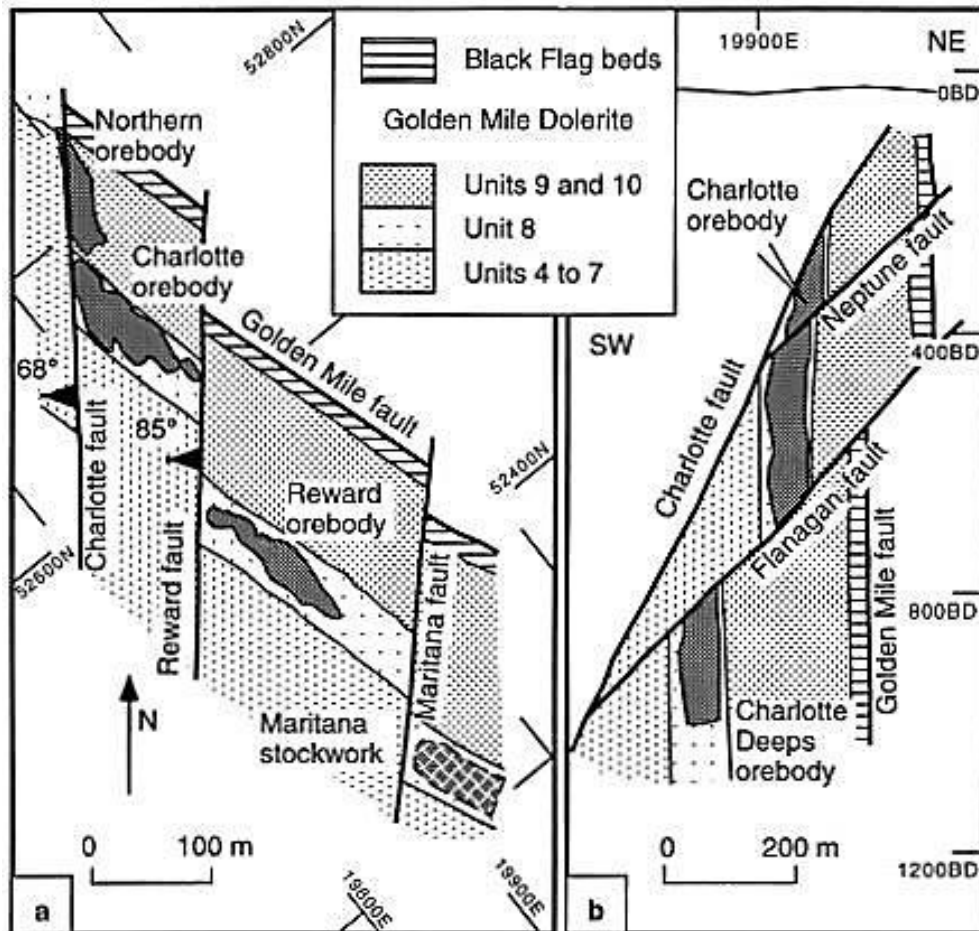


Figure 3.53: Mt Charlotte geological units and faults in (L) Plan and (R) section Ridley and Mengler, 2000.

The Reward fault is variable over its extent. In the upper parts of the mine the vertical fault is between 2m and 30m wide and filled with fine grained strongly foliated fault rock. Evidence from a site visit suggests that at depth this fault separates into several discrete faults. The fault model provided by site contains one main Reward Fault projected to upper parts of the mine and 11 smaller parallel faults in the lower part of the mine spaced over a horizontal distance of 235m.

The Charlotte fault is the latest of the faults being formed during the D4 deformation event. It is moderately dipping and between 1 and 3m wide filled with strongly foliated cataclasite. All the faults in the Charlotte set are overprinted with quartz stock work veining and alternation.

3.4.2 Mining Method

The Mt Charlotte ore body is associated with (though not part of) the infamous Kalgoorlie Golden Mile. Small scale intermittent mining has been undertaken on the site since the late 1800s. Large scale mining commenced in 1963 (KCGM, 2018).

Over the years a variety of mining methods have been utilised. These include cut and fill, long hole open stoping and sub-level caving (Mikula and Lee, 2000). Recently long hole open stoping has been used to extract remnant pillars left from previous mining methods.

In 2015 the Mt Charlotte underground mine was used to access to the Hidden Secret Ore Body (KCGM, 2018). This ore body is not part of this research.

3.4.3 Literature review

Mt Charlotte was one of the first mines in Australia to recognise seismicity as an operational risk and to install a seismic monitoring system. There are 2 separate seismic databases. The first was recorded on a portable seismic system developed by CSIR in South Africa and was operational between 1994 and 2005. Analysis of this seismic dataset has been extensively published. References include Mikula and Poplawski, 1995, Poplawski, 1997, Hudyma and Mikula, 2001, Heal, 2010. This dataset was not provided for analysis and is not considered. The consensus of the analysis is that seismicity at Mt Charlotte is strongly controlled by the fault movements. These movements are often triggered by stress redistributions created by blasting.

A second permanent seismic monitoring system was installed in 2005 and utilises the IMS seismic monitoring system. Corskie, 2013 suggests that discrepancies occur in the calculation of the seismic source parameters between the two data sets and states that the data “*cannot be compared (between the two sets) with absolute confidence*”. The analysis in this thesis relates exclusively to the IMS dataset. Very little has been published in relation to these data. Corskie, 2013 suggests that errors occur within the dataset with data not completely processed and blasts often tagged as seismic events.

3.4.4 Data Availability

The data in Table 3.8 was provided by KCGM staff members for preliminary analysis.

Table 3.8: Data availability for Mt Charlotte.

	Data Type	Mt Charlotte
Seismic Data	Data Available	✓
	Data processed	#
Seismic System	Sensor location	✓
	Significant hardware upgrades	#
	Significant outages	x
Geology	Major structure well defined	✓
	Minor structure defined	x
Mining Information	Decline files	#
	Level files	#
	Stope Voids	✓
	Vertical development	✓
	Level development history	x
	Stoping history	#
# data only partially available		

The level files provided are complete to Level 25 (790m below surface). No files exist between Level 25 and Level 39 suggesting the mining layout provided is incomplete.

Two sets of seismic data were provided by the site. Both data sets have the same date range extending from August 2005 until October 2010. The first set of data was provided during a preliminary scoping visit in October 2010. These data were exported from the seismic analysis software MSRAP in mid-October 2010 and comprises of almost 14000 events. The second set of data was exported directly from the IMS seismic event database. The dataset contains almost 35000 events and was exported in late October 2010.

3.4.5 Discussion on Seismicity at Mt Charlotte

Eighteen monitoring sensors have been installed since 2005. Seismic sensor locations are provided in Figure 3.54. Several sensors have become inactive since that time. No further information is provided on the monitoring system functionality. A review of the cumulative event rate and events per day indicate no obvious extended periods of inactivity.

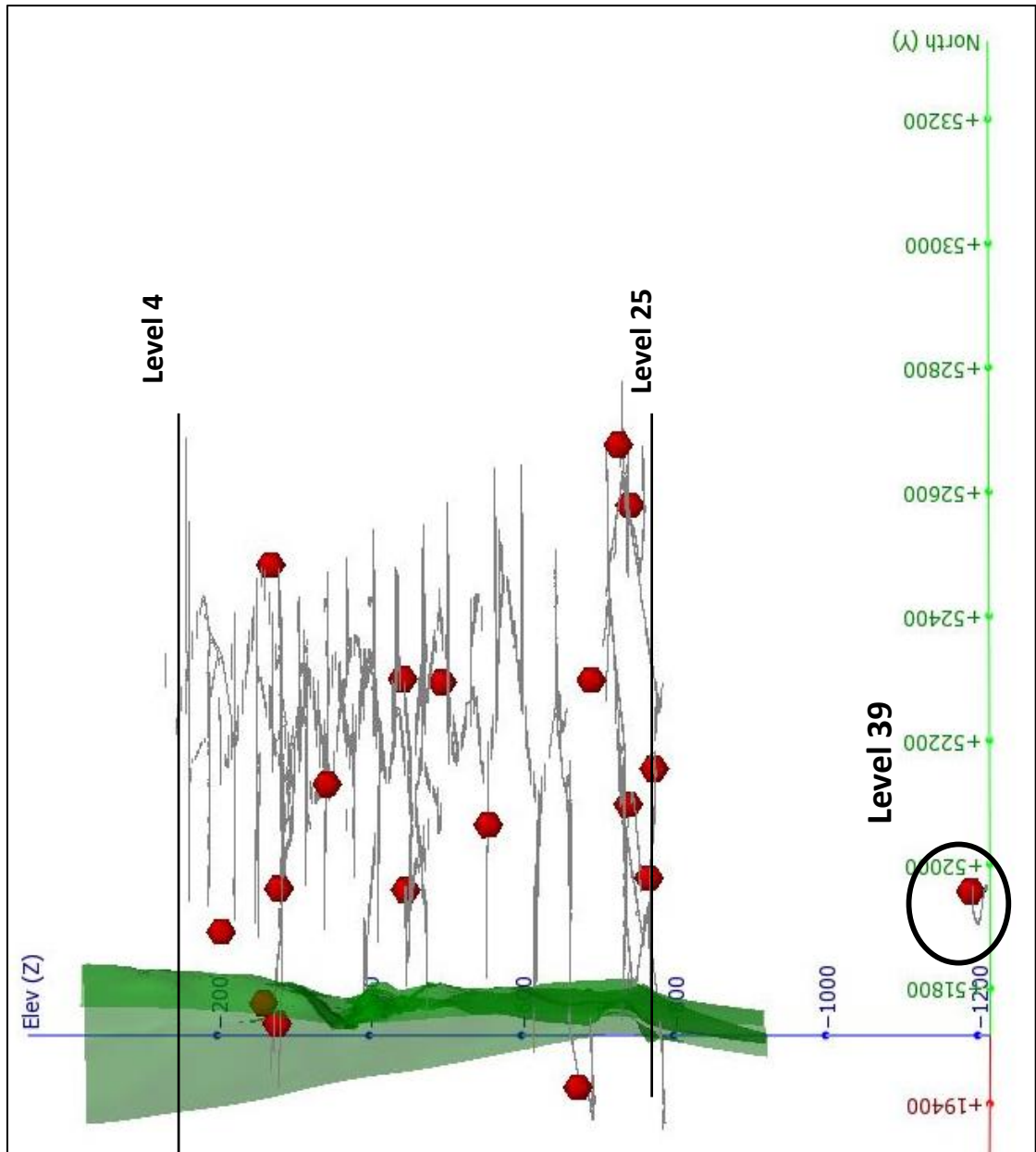


Figure 3.54: Seismic sensor locations at Mt Charlotte (looking north).

As mentioned, two data sets were provided by the site. A review of the second data set found the following inconsistencies in the data:

- The depths of the data range from 32km above the surface to 32km below the surface. The events above the surface are clearly incorrect and have been removed from the dataset. The lowest sensor is located 1200m below surface. Events deeper than approximately 2500m are likely to be outside the detection capabilities of a standard mining seismic monitoring system and are also likely to be invalid.
- The magnitude values range from -99.9M_L to 2147M_L. This range is implausible. Events of -99.9M_L typically did not have any values for other seismic parameters attached to the event.
- Events over 5M_L were typically located outside the mining boundary.

These data errors can be a result of several individual or combined factors

- Errors in exporting the data from the monitoring system resulting in blasts and rejected events being imported with properly processed events.
- Blasts have not been tagged in the database.
- Not all events have been manually processed.
- Poor processing techniques being applied.

A verbal discussion with out-going Geotechnical Engineer John Corskie suggests that some events have been processed poorly in the past and have not been rectified within the database. He states in his thesis on stoping at Mt Charlotte, that the “*ISS system data set has a lot of scatter with blasts often included as seismic events and large errors in locations of outlying events*” (Corskie, 2013). Despite this, the most likely explanation is poor exporting of parameters resulting in a compromised dataset.

In an attempt to improve the quality of the dataset, the anomalous events were removed from the dataset. Table 3.9 provides the criteria for filtering and the number of events removed as a result of those criteria.

Table 3.9: Filtering criteria and number of events removed from data set.

Filter Category	No of events removed
Seismic events above surface RL 0	3204
Events over 2.5km below surface	267
Events of magnitude >9.9	282
Events over magnitude 5	46

In total, approximately 3800 events (10%) were removed from the ISS dataset prior to analysis. A further review of the dataset concluded that the dataset was untrustworthy and could not be used in this analysis.

The MSRAP dataset contains fewer events (13800 events) than the IMS dataset and appears to have fewer errors. The locations of all events are provided in Figure 3.55. Some scatter is present outside the mining area; however, this is consistent with the other mine site datasets provided for this analysis.

The MSRAP dataset still contains 47 events located above the surface and 2 events located below 2000m. These events have been removed from the dataset. A large cluster of events occurs above 300mRL. These could be considered anomalous; however, the events are located in close proximity to stoping and are assumed to be accurate.

The moment magnitude scale is used as the local magnitude scale M_L , given by Equation 3.4.

$$M_L = \frac{2}{3} \log_{10} M_o - 6.03$$

Equation 3.4

The magnitude range is much more credible varying from $-2.6M_L$ to $2.2M_L$ with a median of $-1.5M_L$. The magnitude distribution (Figure 3.56) appears typical of other sites. Site engineers believe events over $0M_L$ cause obvious damage to the excavation. In total there are almost 340 events above this threshold.

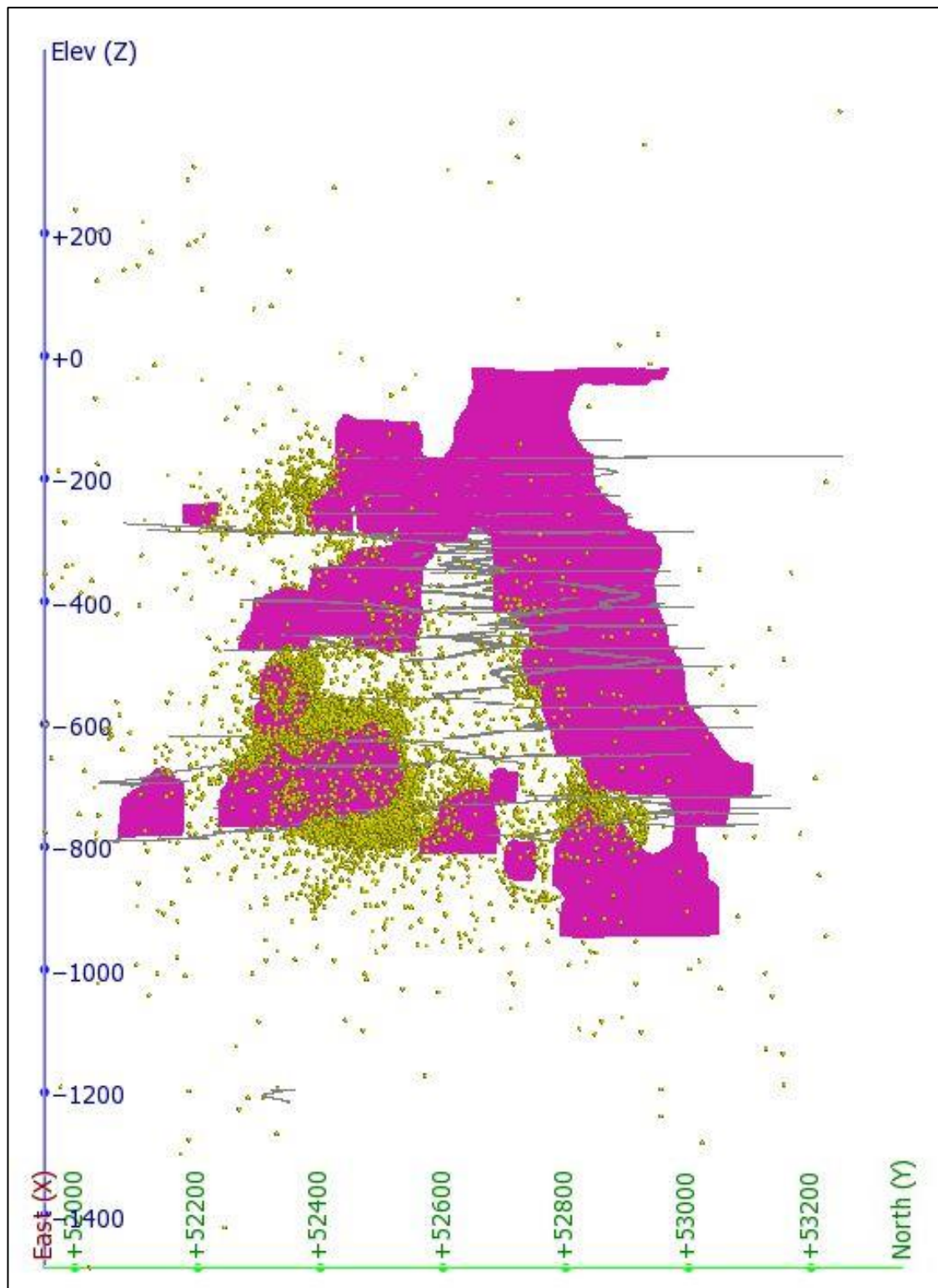


Figure 3.55: Seismic event locations from the MSRAP dataset looking west.

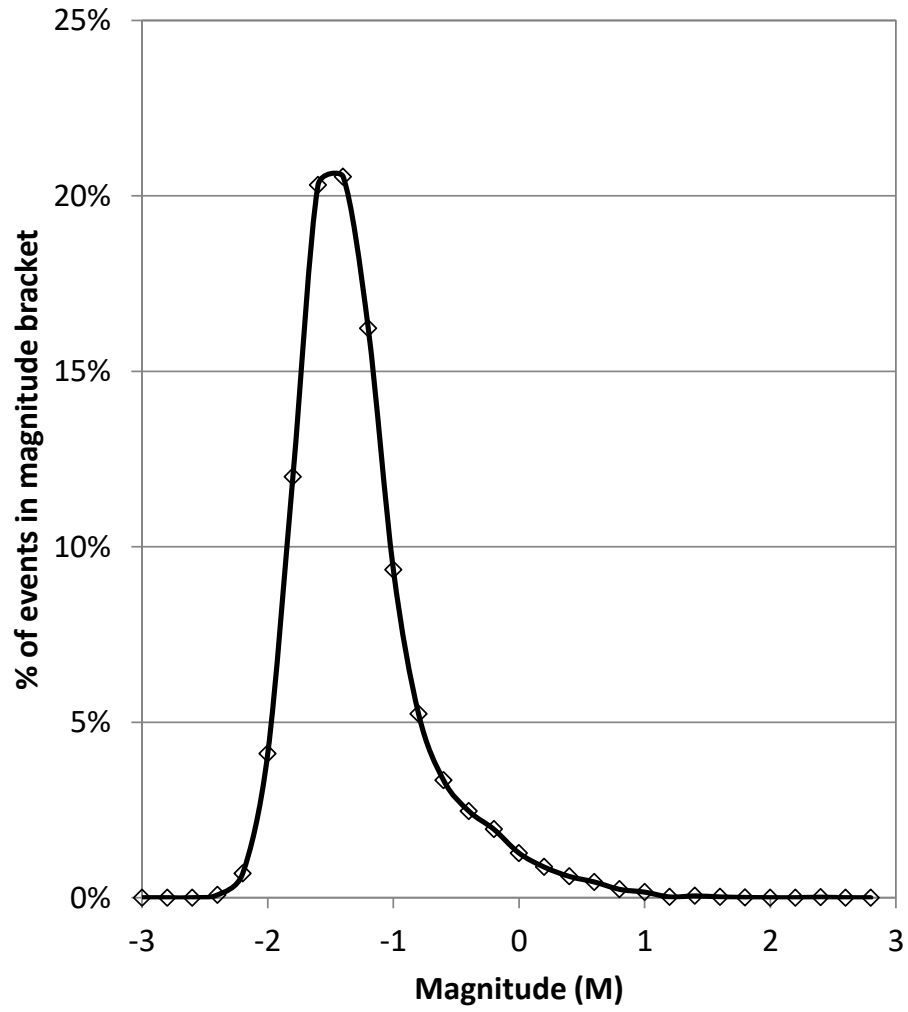


Figure 3.56: Magnitude distribution for Mt Charlotte MSRAP dataset.

3.4.6 Structures for Analysis

Three faults were selected for analysis; these were the Maritana, Reward and Flanagan faults (Figure 3.57).

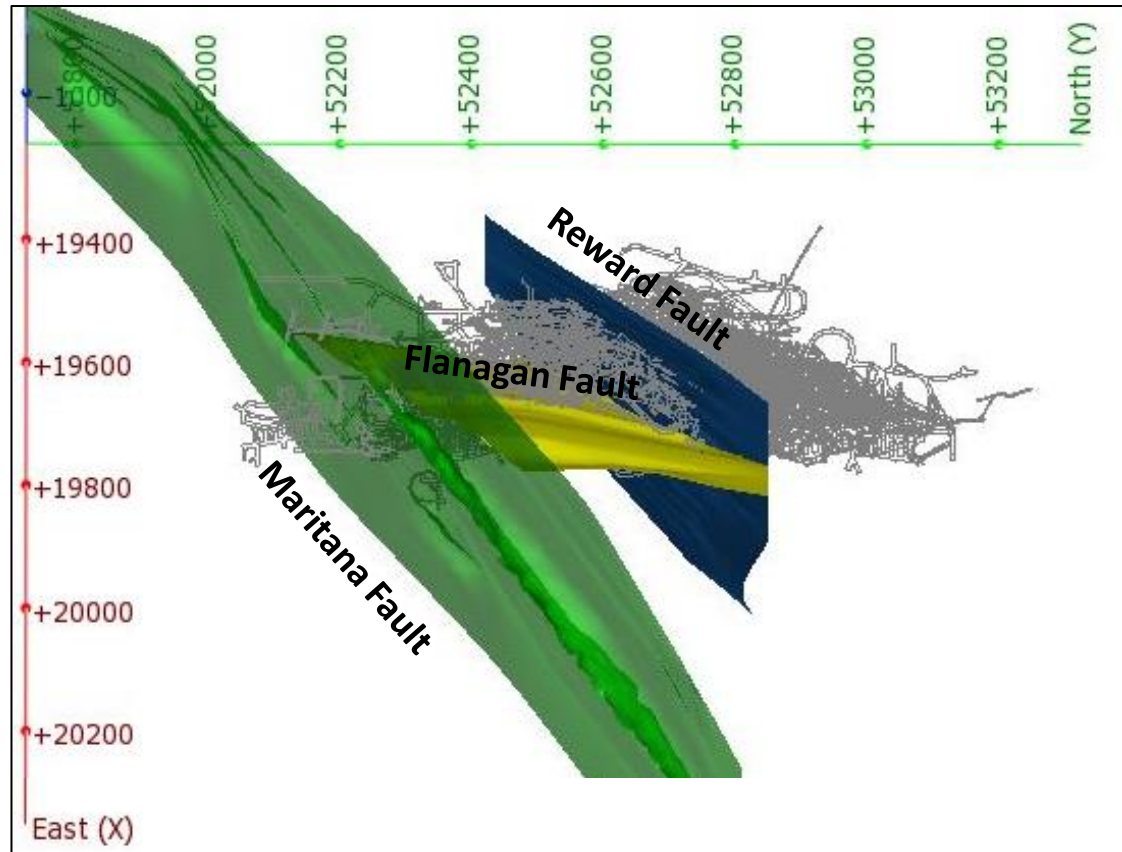


Figure 3.57: Mt Charlotte faults for analysis.

3.4.6.1 Maritana Fault

The Maritana Fault is a vertical NE - SW trending structure that terminates the Mt Charlotte ore bodies at the southern end. Stoping in close proximity to the fault is minimal with the majority occurring on the northern side of the fault. Several areas of development pass through the fault including the main decline at 280m below surface.

This structure is selected for its regional significance and due to its terminations of the ore bodies. There are 4 sensors within 200m of the fault in the upper levels. However below 285mRL there are only 3 sensors within 200m of the fault to a depth of -770mRL. This is likely to affect the density of the data at the lower end of the magnitude scale and the accuracy of the location data for events on the fault below 300mRL.

The perpendicular distance from the fault to all seismic events was calculated. A domain of $\pm 20\text{m}$ was selected based on analysis of the data. The Maritana Fault data subset consists of 250 data points (Figure 3.59). The magnitudes for the Maritana Fault range from $-2.0M_L$ to $1.1M_L$ with a median of $-1.3M_L$. The median value for the Maritana Fault is higher than the median for the overall dataset ($-1.5M_L$) suggesting larger events occur on this fault. This is likely to be influenced by the low number of events associated with this fault.

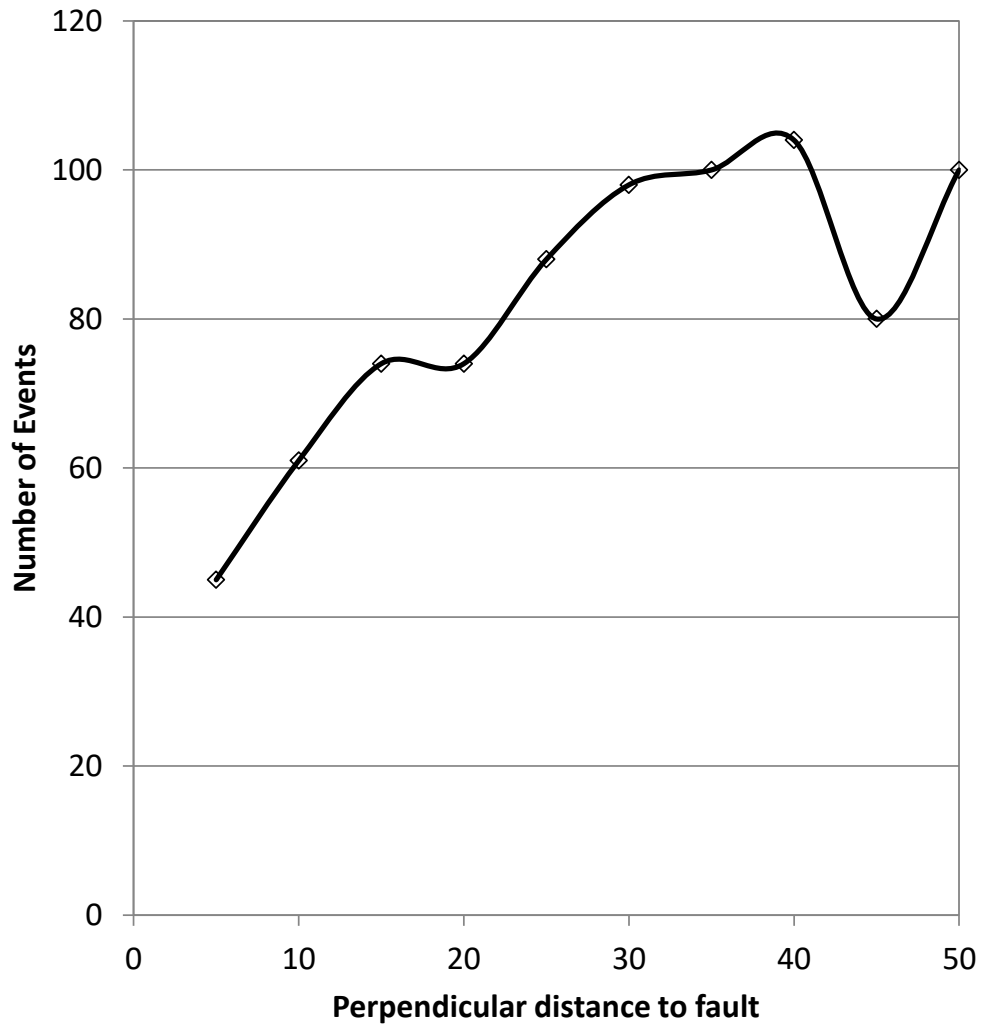


Figure 3.58: Distances of seismic events from Maritana Fault.

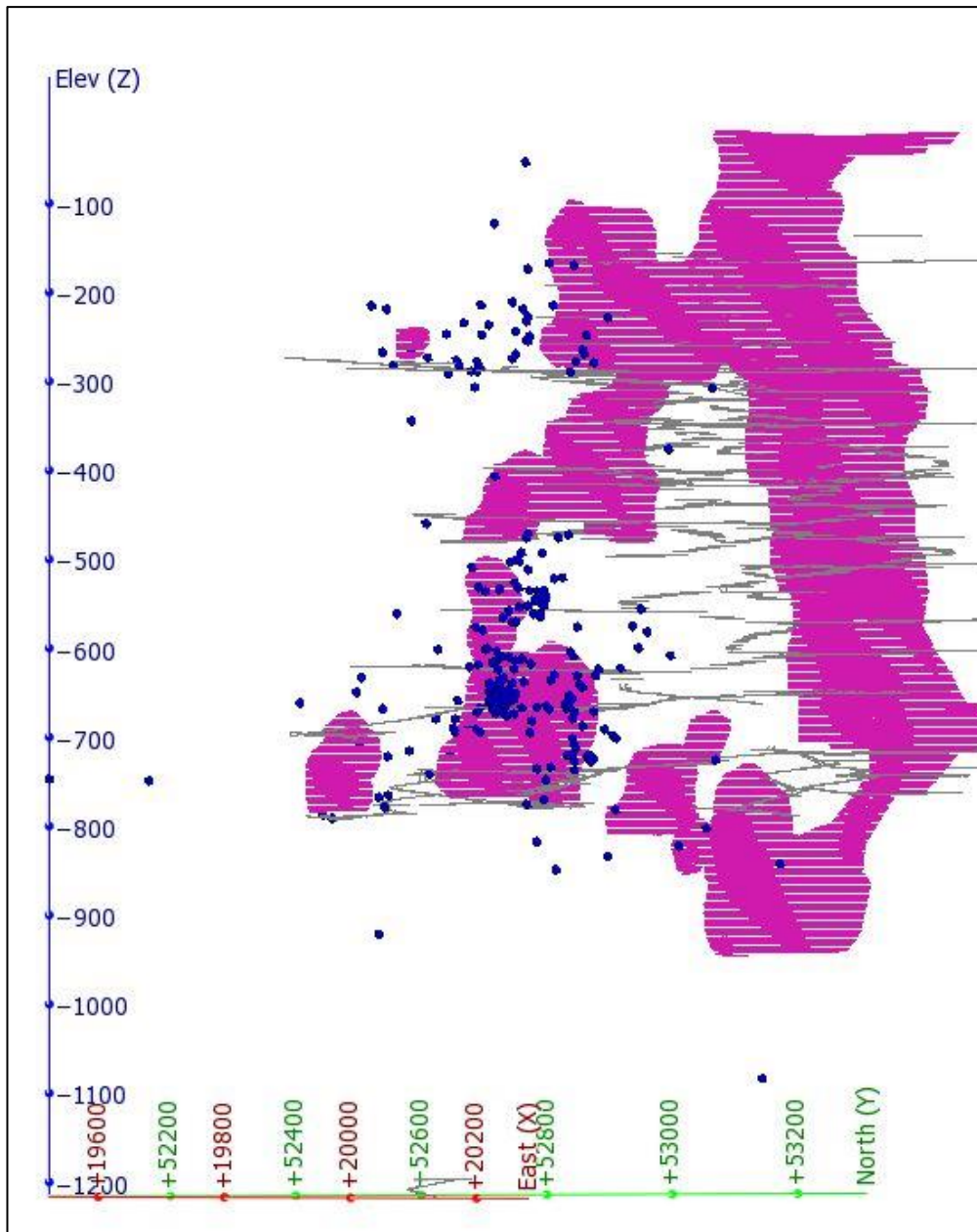


Figure 3.59: Locations of events for the Maritana Fault.

3.4.6.2 Reward Fault

The Reward Fault is a vertical to sub-vertical structure parallel to the Maritana and Charlotte faults and oblique to the main ore bodies. The Reward Fault offsets the ore bodies creating two distinct sections; the Maritana to Reward section and the Reward to Charlotte section. Stopping occurs on both sides of the fault. This fault is reported by site engineers to react seismically to mining activity and to affect the stability of the mining environment.

As the Reward Fault is located in the centre of the mining area, 11 seismic sensors are located within 200m of the fault at varying depths.

The perpendicular distances from the fault to all seismic events were calculated (Figure 3.60). A domain distance of $\pm 15\text{m}$ was selected for the Reward Fault based on analysis of the data. The number of points comprising this data subset is 1500 events (Figure 3.61). The magnitudes for the Reward Fault range from $-2.3M_L$ to $0.8M_L$ with a median of $-1.5M_L$. The median was the same as for the overall dataset.

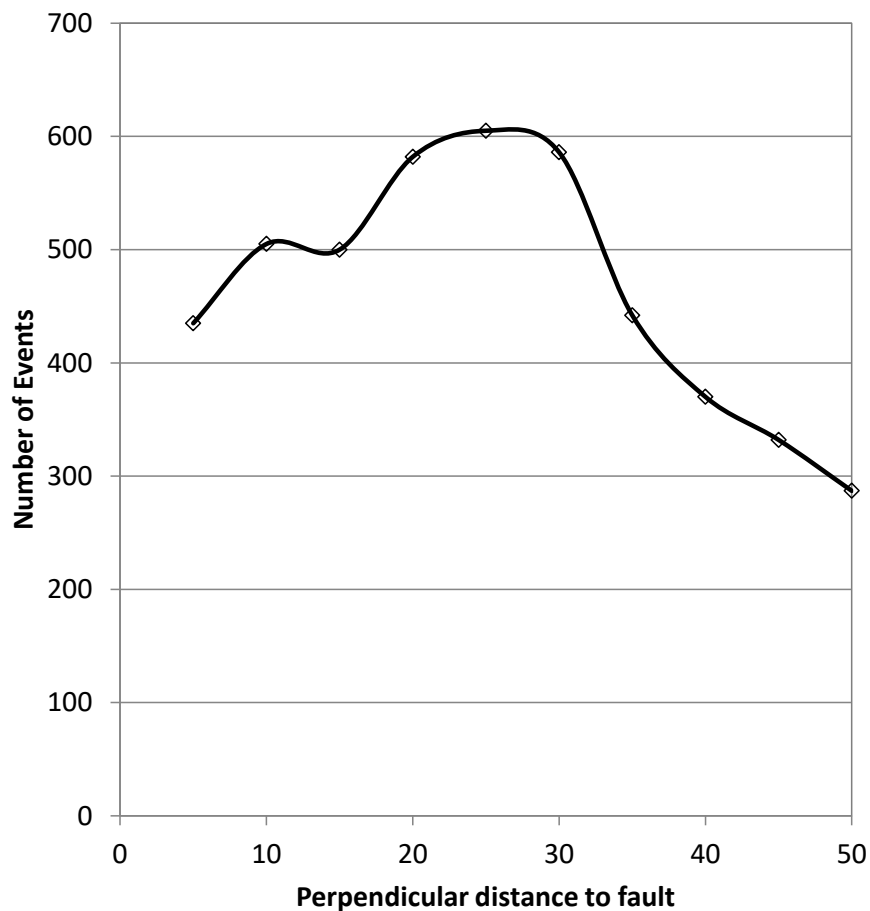


Figure 3.60: Distances of events from the Reward Fault.

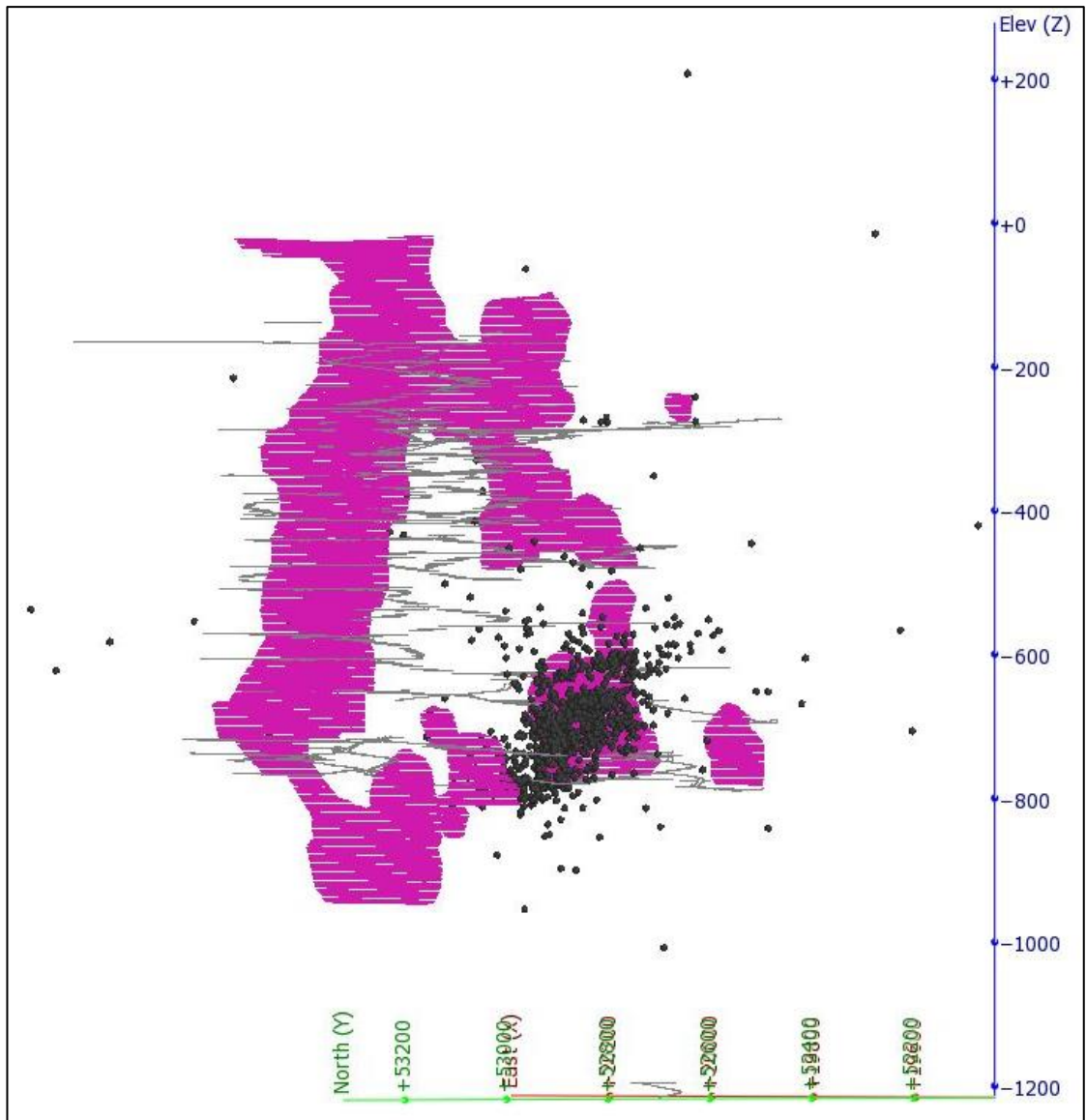


Figure 3.61: Locations of events on the Reward Fault.

3.4.6.3 Flanagan Fault

The Flanagan Fault strikes NW / SE and dips moderately to the west. It is an early stage fault and is consequently offset by later stage faults. The models provided by site extend between the Charlotte and Maritana faults with a 90m offset along the NE – SW trending Reward Fault.

For analysis this fault was separated into two discrete structures. Flanagan_1 extends from the Maritana Fault to the Reward Fault and Flanagan_2 extends from the Reward Fault to the Charlotte Fault (Figure 3.62). As the majority of the seismicity on Flanagan fault occurs between the Mariana and Rewards faults, only Flanagan_1 Fault will be analysed. To facilitate this, all the data outside the boundary between the Maritana and Reward faults were removed prior to the distance analysis being undertaken.

Like the Reward Fault, Flanagan_1 Fault is located in the central mining area and has a large part of the seismic sensor network located within 200m.

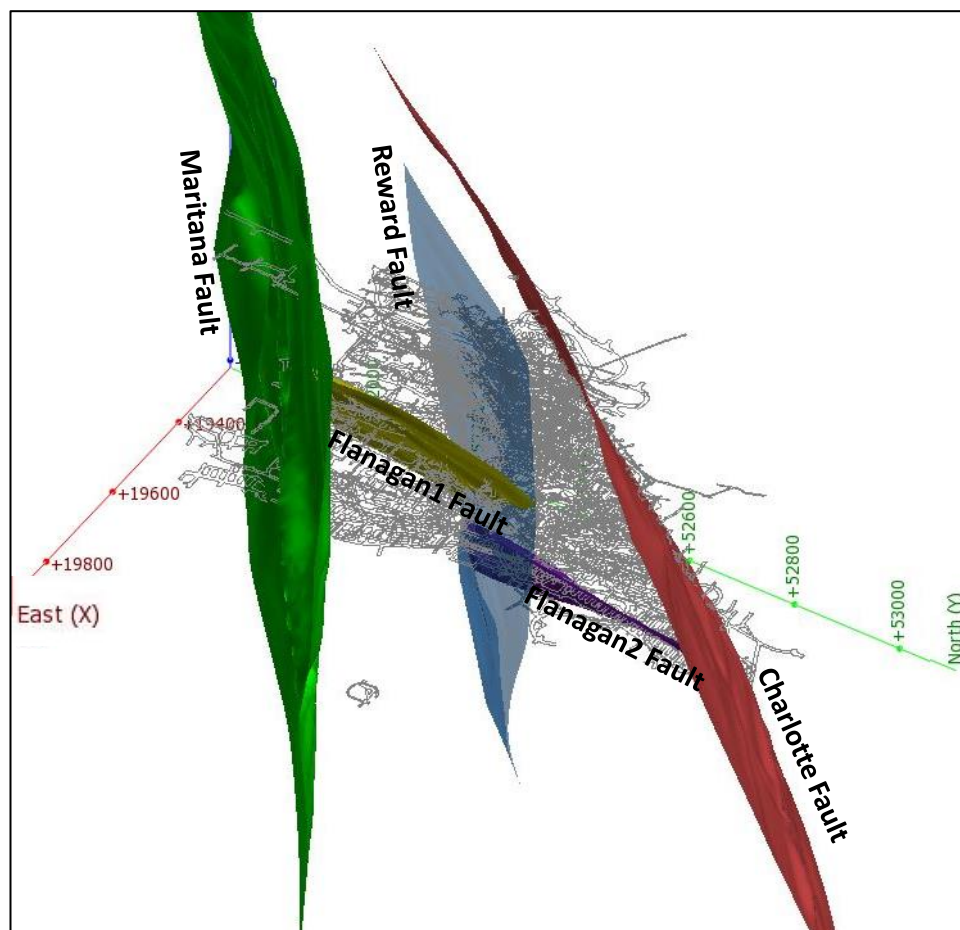


Figure 3.62: Flanagan fault offsets.

The distances of events from Flanagan 1 Fault are provided in Figure 3.63. The distance chart does not provide a clear indication of the influence of the fault. There are a significant number of events up to 30m away from the structure. This may be a result of the structure being a zone rather than a single plane or may be the result of other structural influences. It will be assumed that these events are associated with the fault. A distance of $\pm 30\text{m}$ will be used to create the Flanagan Fault data subset. The total domain width is 60m. The number of points comprising this data subset is 4987 (Figure 3.64). The magnitudes for the Flanagan Fault range from $-2.3M_L$ to $2.2M_L$ with a median of $-1.6M_L$. The median value is slightly lower than the overall dataset ($-1.5M_L$).

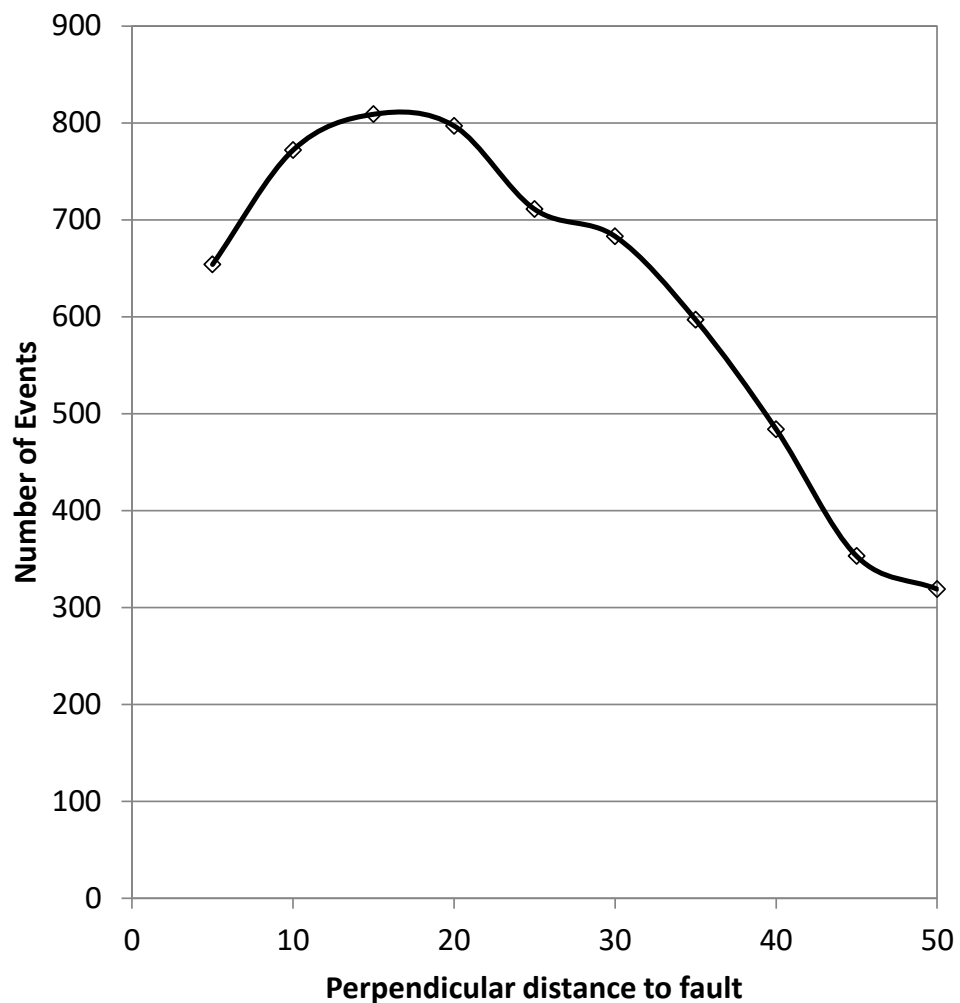


Figure 3.63: Distances of events from Flanagan_1 Fault.

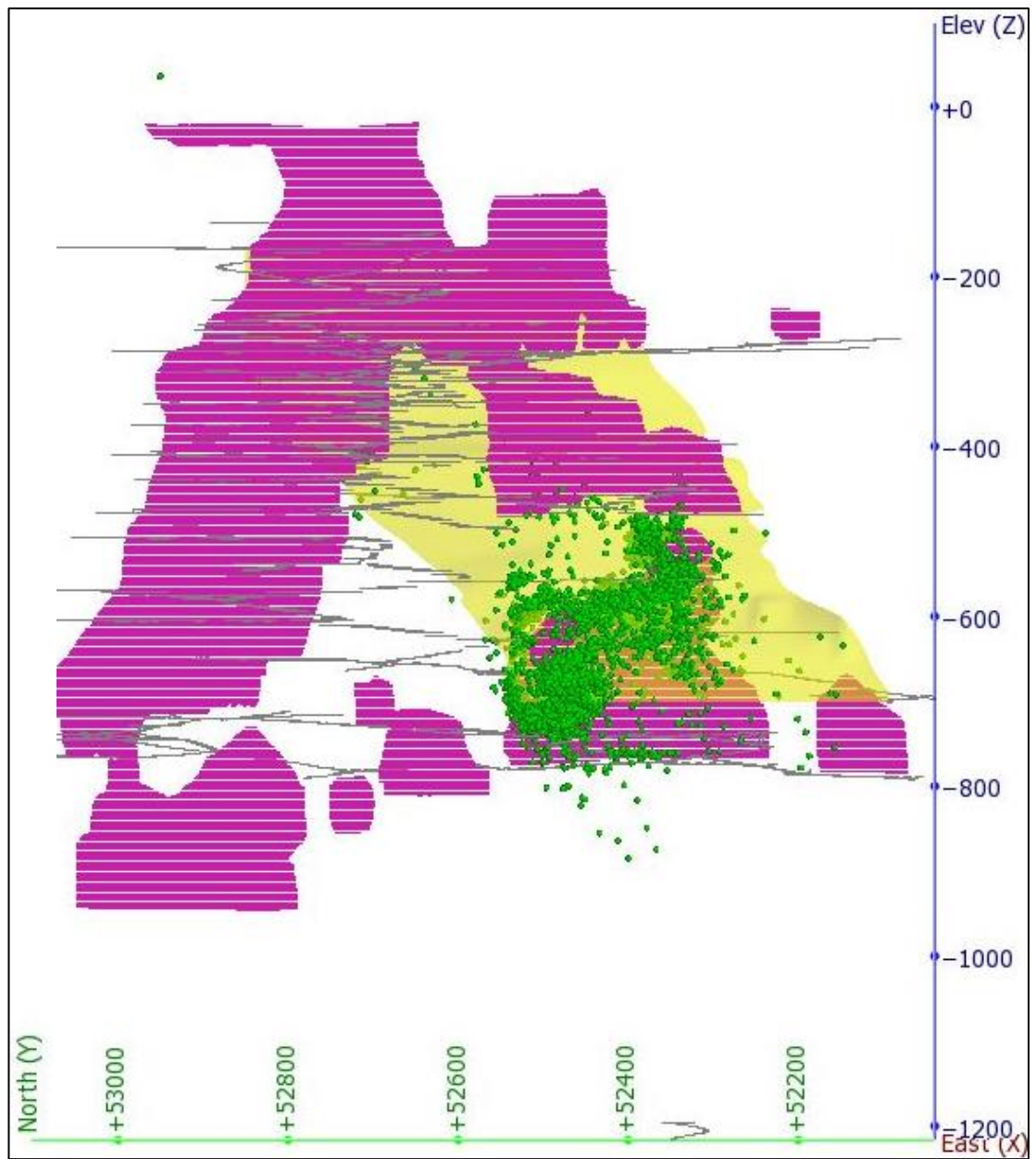


Figure 3.64: Locations of events on Flanagan1 Fault (looking east).

3.5 Black Swan

3.5.1 Location and Geological setting

The former Black Swan Nickel Mine is located 53 kilometres north-north east of Kalgoorlie-Boulder, Western Australia. The site comprises of the Silver Swan Underground mine and the Black Swan Disseminated Pit. The site was closed in early 2009 due to low commodity prices and challenging mining conditions. This study focuses on seismicity in the Silver Swan Underground mine between 2003 and 2005.

Mineralisation was discovered in the 1960s with the discovery of the Cygnet ore body. Mine development began in March 1996 targeting the high-grade Silver Swan ore body. Further drilling identified several other deposits including the Gosling, White Swan, Odette and Trumpeter ore bodies. A cross section of the mine is provided in Figure 3.65.

Morton and Sweby, 2005 provide the following geological description:

“Nickel Sulphide mineralisation at Black Swan is hosted by the Black Swan Komatiite Complex, 3.5 km long by 0.6km thick arcuate lens of Archaean olivine cumulates and Spinifex textured komatiite flows. The complex, as well as a broad sequence of intermediate felsic lavas and volcanic sediments enclosing it, are situated on the northeast dipping, northeast facing limb on the Kanowna-Scotia anticline.

Subsequent to mineralisation, serpentinite alteration and later talc carbonate alteration occurred during low-grade metamorphism.

Nickel sulphide mineralisation occurs on, or adjacent to, the steeply east dipping ultramafic footwall contact.

The rock types at Black Swan Nickel generally include footwall felsic volcanics, sulphide ore bodies (massive and disseminated) and hangingwall talc-carbonated ultramafics”.

Three dyke swarms are present, identified solely by rock type rather than orientation. The rock types are felsic intrusive, dolerite and porphyry. The dykes are highly sporadic. Representative models are not produced due to changeable orientations and geology and high levels of alteration.

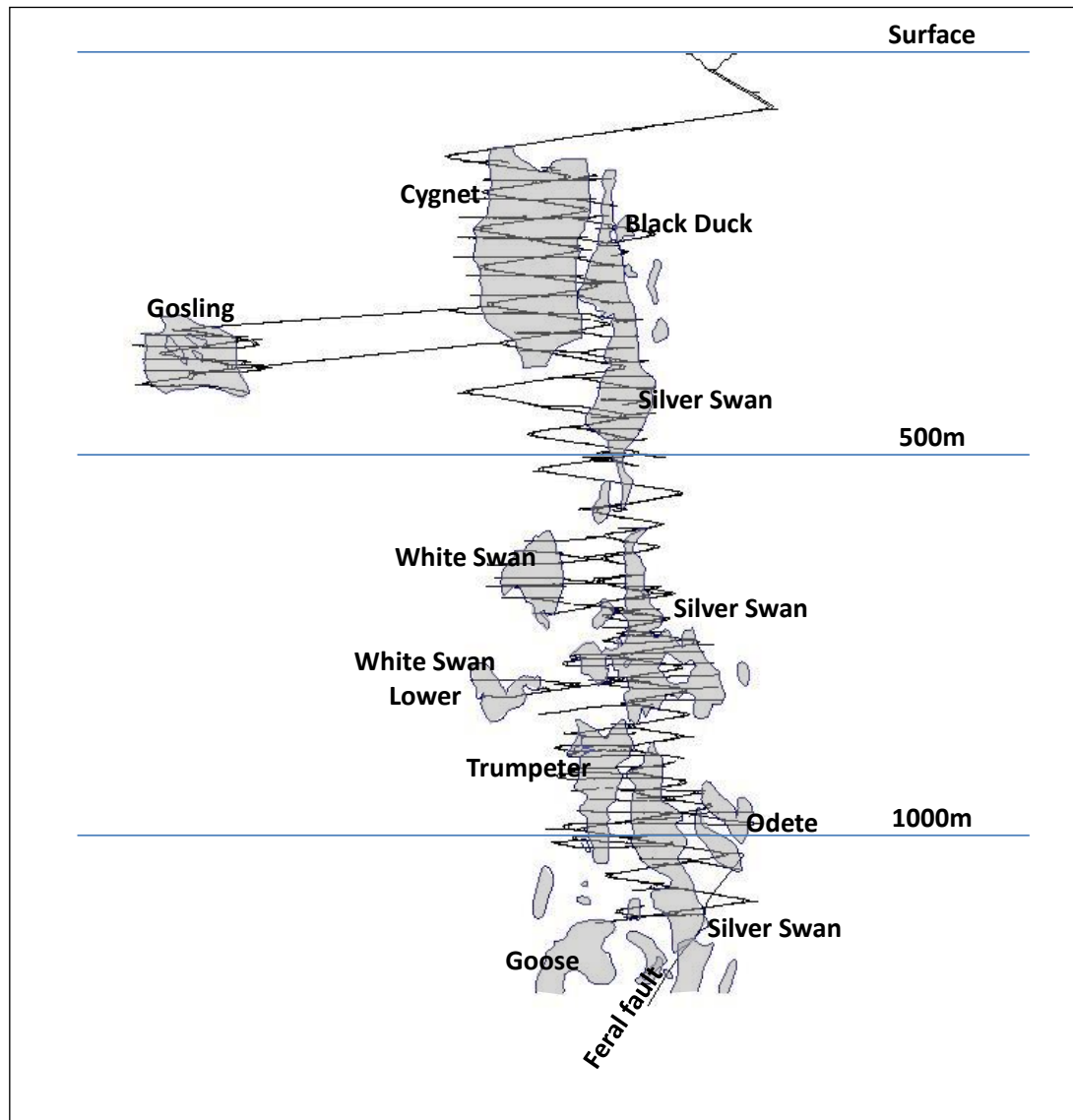


Figure 3.65: Long section of the Silver Swan Underground mine (looking west).

Large-scale structures within the mine are also not well delineated. No models exist for large-scale structures above 800m below surface. Several small faults are identified within the White Swan Lower ore body and a large fault (Feral Fault) terminates the Odete ore body below 1000m.

Seismicity, noted as rock noise by the underground operators, was first detected in 2001. A temporary monitoring system was used to undertake precautionary monitoring in 2002. These data were collected by a consultant and are not included in this study. A permanent monitoring system was first installed in May 2003. The data from this system have been included in this study.

3.5.2 Mining Method

Mining began in 1996. The primary mining method was open stoping with rock fill and CRF. The main Silver Swan shoot was mined in panels consisting of 3 levels. Stopes were mined bottom up from the north to the south. The inter-level spacing was between 15m and 20m. In some areas some cut and fill was utilised however this was not the primary method of extraction.

Due to poor management development was undertaken a long time ahead of the stoping sequence – in some cases up to 4 years ahead. Significant deformation was experienced within the 500 series levels (between 500mRL and 600mRL) as a result of poor rock mass conditions and the significant time lag. Significant deformation was also experienced in a 15m zone through the centre of the 300 series levels (between 300mRL and 400mRL). This was thought to be controlled by a structural feature although no specific feature was ever formally modelled.

3.5.3 Literature review

Seismic data were provided to the Australian Centre of Geomechanics (ACG) for analysis as part of the Mine Seismicity and Rockburst Risk Management project. The only published analysis was conducted as part of this project.

Owen, 2006 conducted the most extensive review of seismicity at Black Swan. The analysis follows the typical mine site analysis described in Chapter 5. Most of the analysis was conducted on groups of data generated by a clustering algorithm. Owen, 2006 found that “16 cluster groups had a fresh fracture related source mechanism, 35 had a shear related source mechanism and 36 had a mixed mechanism”. Feral Fault analysis was represented by more than one seismic “group”. Groups in the footwall were noted to have the following characteristics:

- *“S:P ratio plots indicating a mixed mechanism;*
- *Ongoing seismic activity outside stoping periods, rather than flurries of events, and no obvious diurnal correlation with stope blasting times;*
- *bi-modal b-value plots, usually with one large event distinct from the steeper trend of smaller events”.*

Further studies at Black Swan (e.g. Heal, 2010) all refer to this work by Owen . No further publications on seismicity at Black Swan are available.

3.5.4 Data Availability

The data in Table 3.10 were acquired from Black Swan in 2005.

Table 3.10: Data availability for Black Swan.

	Data Type	Black Swan
Seismic Data	Data Available	✓
	Data processed	✓
Seismic System	Sensor location	✓
	Significant hardware upgrades	✓
	Significant outages	x
Geology	Major structure well defined	✓
	Minor structure defined	x
Mining Information	Decline files	✓
	Level files	✓
	Stope Voids	#
	Vertical development	#
	Level development history	x
	Stoping history	#
# data only partially available		

Much of the information that is available is from first-hand knowledge.

The first seismic monitoring system was installed in May 2003 and upgraded in early 2004. Specific seismic system functionality is not available; however, it is known that frequent short-term outages were experienced. A long-term, whole system outage was experienced for two days in November 2004 after a large seismic event caused significant damage in the main access of the mine. In 2004, processing of the seismic data was contracted to IMS (formerly ISS). All data in the dataset were re-processed by IMS indicating software upgrades are not likely to impact on the results.

The stoping information is available on a monthly basis; however, the boundaries to the stopes are only approximate.

3.5.5 Discussion on Seismicity at Black Swan

The seismic system was installed in May 2003 and initially consisted of 6 sensors. An extension of the seismic was undertaken in January 2004 when another 5 sensors were installed in the lower levels of the mine. During this installation one of the upper sensors was moved to the lower part of the mine. The locations of the sensors are provided in Figure 3.66. The seismic data were collected from May 2003 to August 2005 and contains 16000 events. The locations of the events are provided in Figure 3.67.

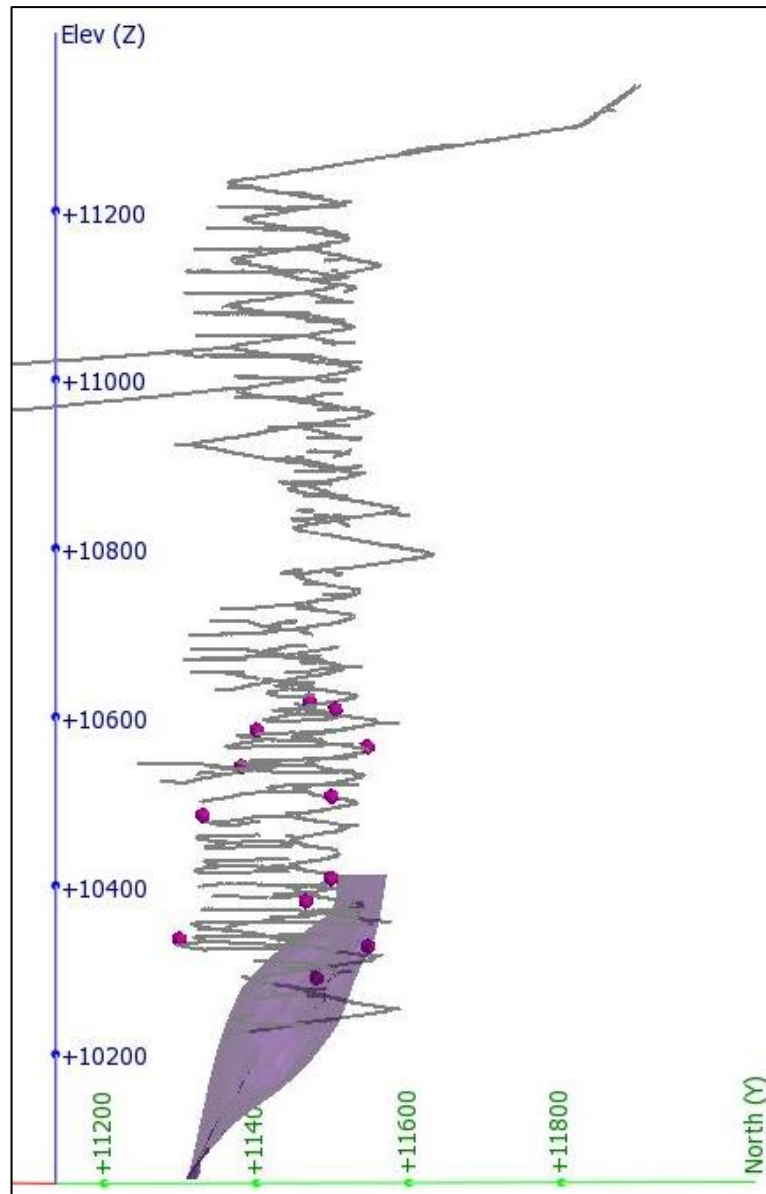


Figure 3.66: Seismic sensor locations at Black Swan.

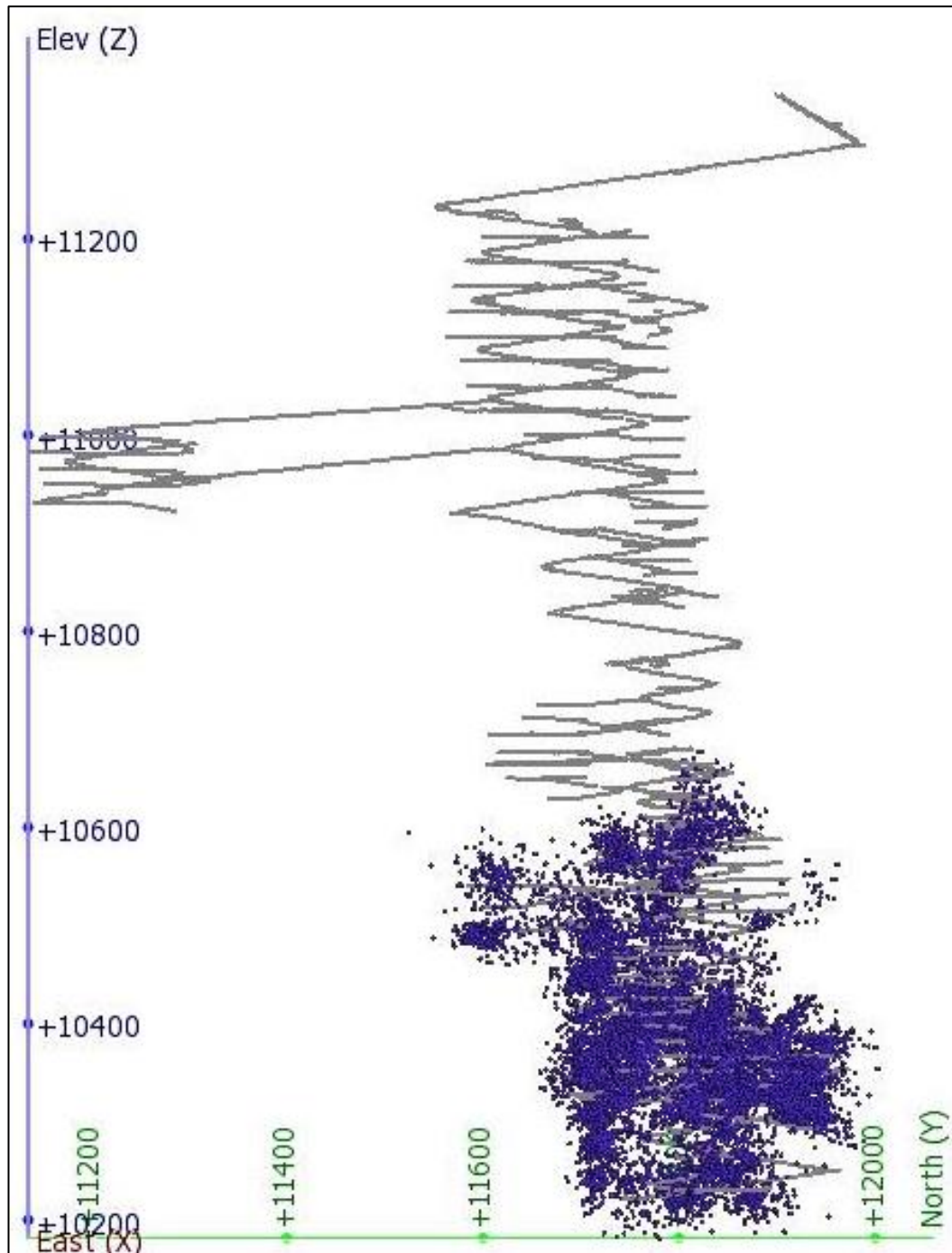


Figure 3.67: Locations of events at Black Swan.

The magnitudes have been calculated using Equation 3.5. The magnitude distribution of seismic events is provided in Figure 3.68 and is similar to those at other sites with a normal distribution. The magnitudes range from $-8.5M_L$ to $2.1M_L$. The minimum magnitude is much lower than other sites but corresponds with observations on site. The threshold for damaging events is $0M_L$. There are 130 events over this threshold.

$$M_L = 0.272 \log_{10} E + 0.392 \log_{10} M_o - 4.62$$

Equation 3.5

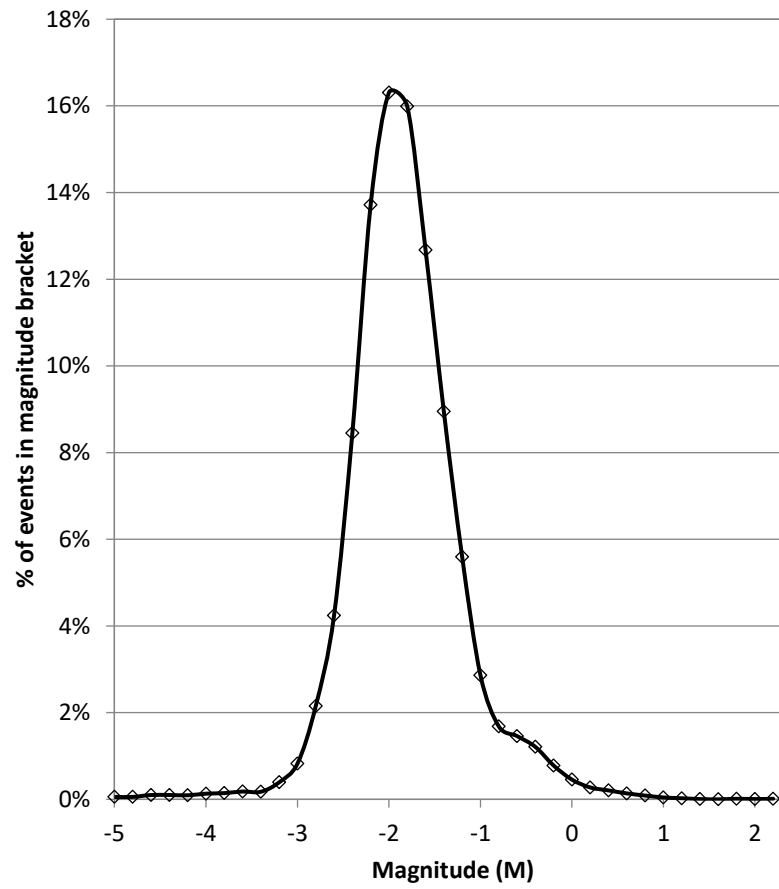


Figure 3.68: Magnitude distribution for Black Swan.

3.5.6 Structures for Analysis

The Feral Fault is the only well-modelled fault at Black Swan. This fault model will be used in this analysis.

3.5.6.1 Feral Fault

The Feral Fault was the only major structure identified at Black Swan Nickel prior to 2005. The fault dips at approximate 60 degrees towards the south east. It intersected the ore body at approximately 1000m below surface and terminates the Odete ore body. The Feral Fault can be traced to at least 1500m below surface, intersecting mining excavations at several intervals.

All seismic sensors are within 200m of the fault; however only 4 sensors are within 100m with no sensors deeper than 1300m below surface. This is likely to affect the accuracy and sensitivity of the seismic source parameters of events at depth.

The fault's characteristics, determined from mapping a drill core intercepts, are highly changeable with its width varying from 0.2 to 15 metres. Infill varies between dyke material (intermediate dolerite) and clay, with the contacts varying between healed and open. Figure 3.69 provides the description of the fault at both drill hole and mining intersections. Several large seismic events causing damage to excavations were attributed to movement on the fault. This structure was selected for analysis due to its significance to the Black Swan operations.

The distance to fault chart (Figure 3.70) indicates a strong seismic influence approximately 20m from the fault. The drilling data suggest that the fault is at times more of a shear zone and can be up to 20m wide. To ensure all events are captured, the domain distance is set as $\pm 30\text{m}$. The number of points comprising this data subset is 4950 (Figure 3.71). The magnitudes for the Feral Fault range from $-6.8M_L$ to $1.7M_L$ with a median of $-2.0M_L$. The median for the Feral Fault is similar to that of the overall dataset.

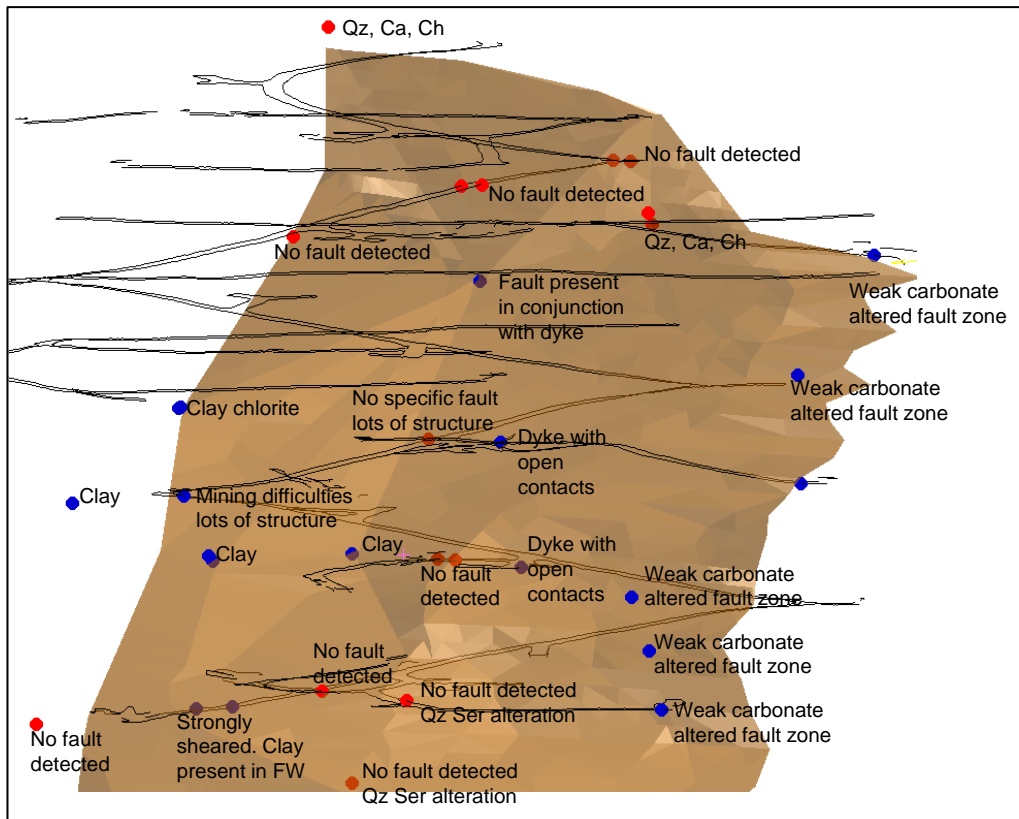


Figure 3.69: Feral Fault projection with descriptions at intersection points.

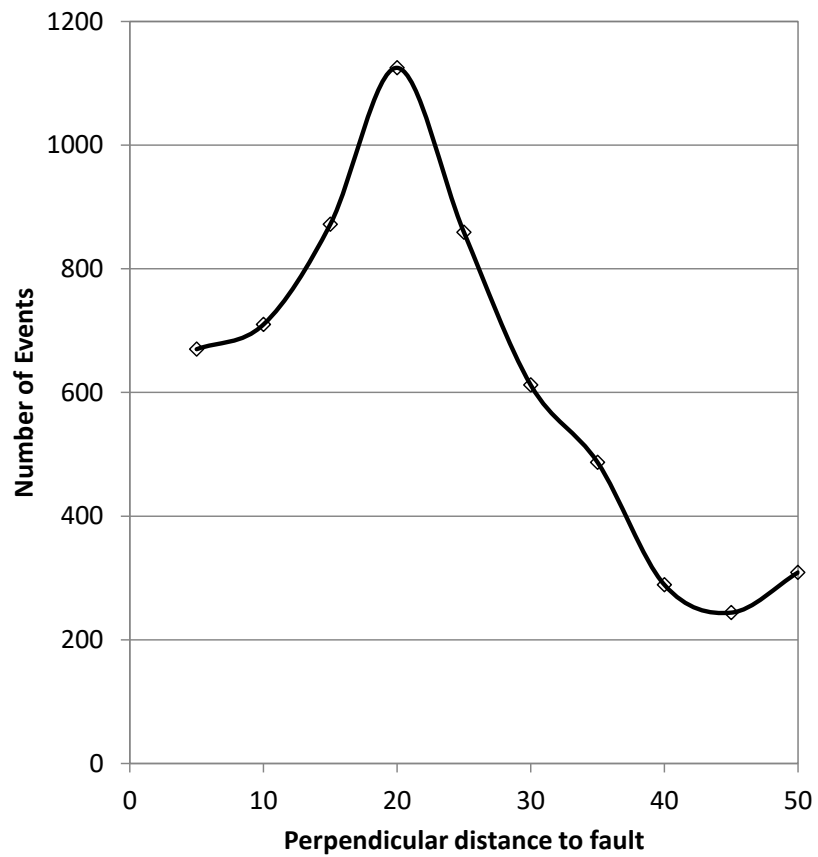


Figure 3.70: Distances of events from the Feral Fault.

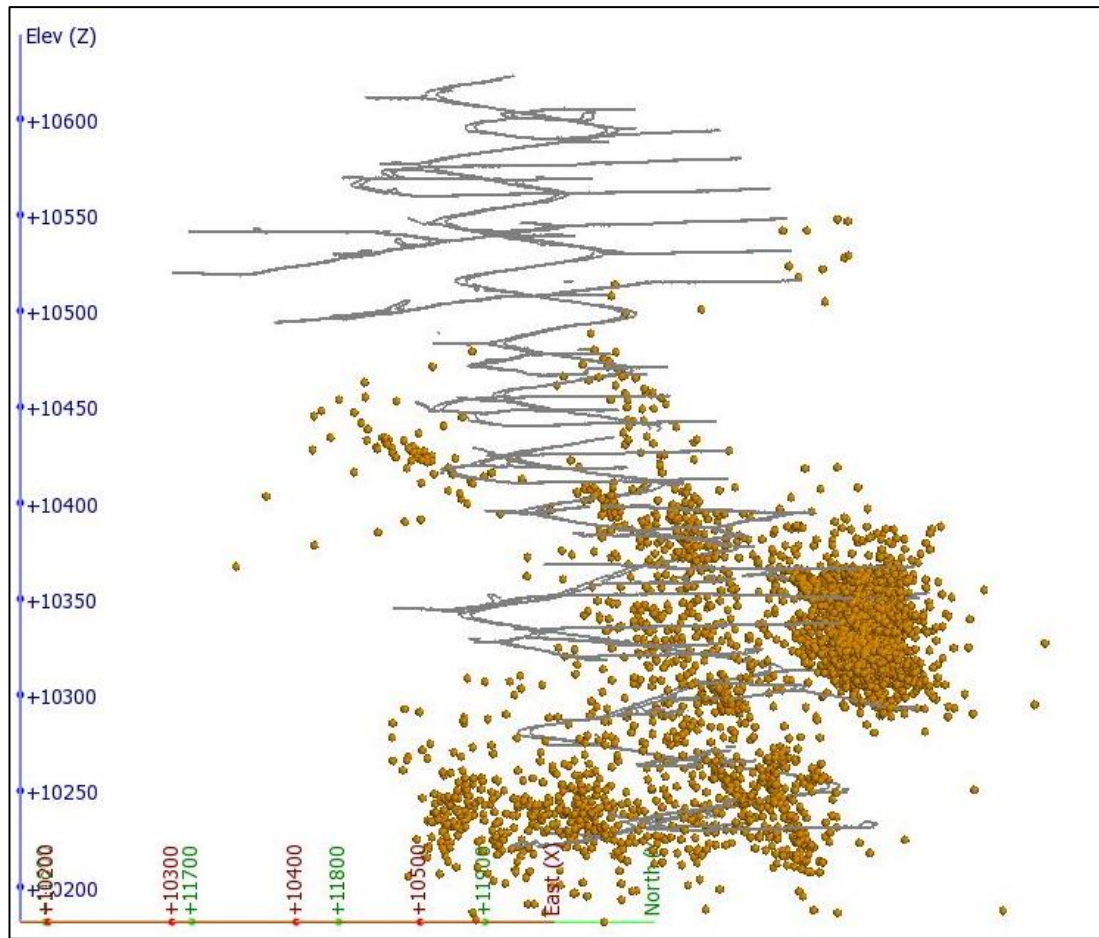


Figure 3.71: Locations of seismic events for the Feral Fault.

3.6 Big Bell

The former Big Bell Gold Mine is located 30km WNW of Cue in the Murchison district of central Western Australia. Mining of the Big Bell deposit began in the early 1900s and continued intermittently until July 2003 when the site was closed. At the time of closure, the main mining method was sub level caving.

The Big Bell gold deposit is hosted in a narrow greenstone belt comprising of mafic and felsic volcanics interbedded with metasediments bounded by granite Phillips and Nooy, 1988.

Many papers have been published on seismicity and dynamic ground support at Big Bell. The majority of the papers were presented by the site based Engineer and the Consultant responsible for the development of the seismic monitoring system and the seismic analysis (Turner and Player, 2000, Player, 2004a, Player, 2004b). The Big Bell seismic data were also provided to the ACG for the Mine Seismicity and Rockburst Risk Management project. This has resulted in extensive analyses in the ACG reports and publications (Grincer, 2002, Reimnitz, 2004, Hudyma, 2005, Heal, 2010).

The seismic data and structural features at Big Bell were analysed in much the same way as the other sites. The second graphitic shear was identified as a major contributor to seismic related instability in the mine. Grincer, 2002 and Reimnitz, 2004 both conducted detailed analysis of the Big Bell data set. Both researchers found inconsistencies in the geological model. Grincer, 2002, suggested that the models may be inaccurate or incomplete. Reimnitz, 2004 conducted a review of the seismicity on the second graphitic shear located in the footwall of the Big Bell Gold Mine. He stated that the second graphitic shear was modelled as a planar structure although some exposure details were discarded due to discrepancies with the model.

The graphitic shear model is based on pickups at the following locations within the mine; the 320 stockpile, two locations on the decline between the 410 and 435 levels and two locations between the 510 and 535 levels. A review of the survey pickups of the structure at intercepts in the mining development shows varying orientations (Figure 3.72). The orientations indicated by the points in the pickups are provided in Table 3.11. Whilst the general orientation is approximately easterly, the variations in the dip, particularly at the 410 / 435 upper and 510 / 535 lower locations, suggest the structure is unlikely to be linear and cannot be modelled as such. Further validation of the model is not possible due to the lack of additional information (such as drill hole intercepts). The accuracy of the geological model significantly impacts on the method of analysis in later chapters. Due to the inaccuracy of the information provided this site cannot be confidently assessed. The site has been included in this review as the inaccuracy of this model raises an important argument. Without understanding the geological setting of a mine site, detailed analysis of the seismic data and the failure mechanisms associated with seismicity can be highly misleading. Furthermore, such a lack of understanding renders most analysis futile and open to conjecture.

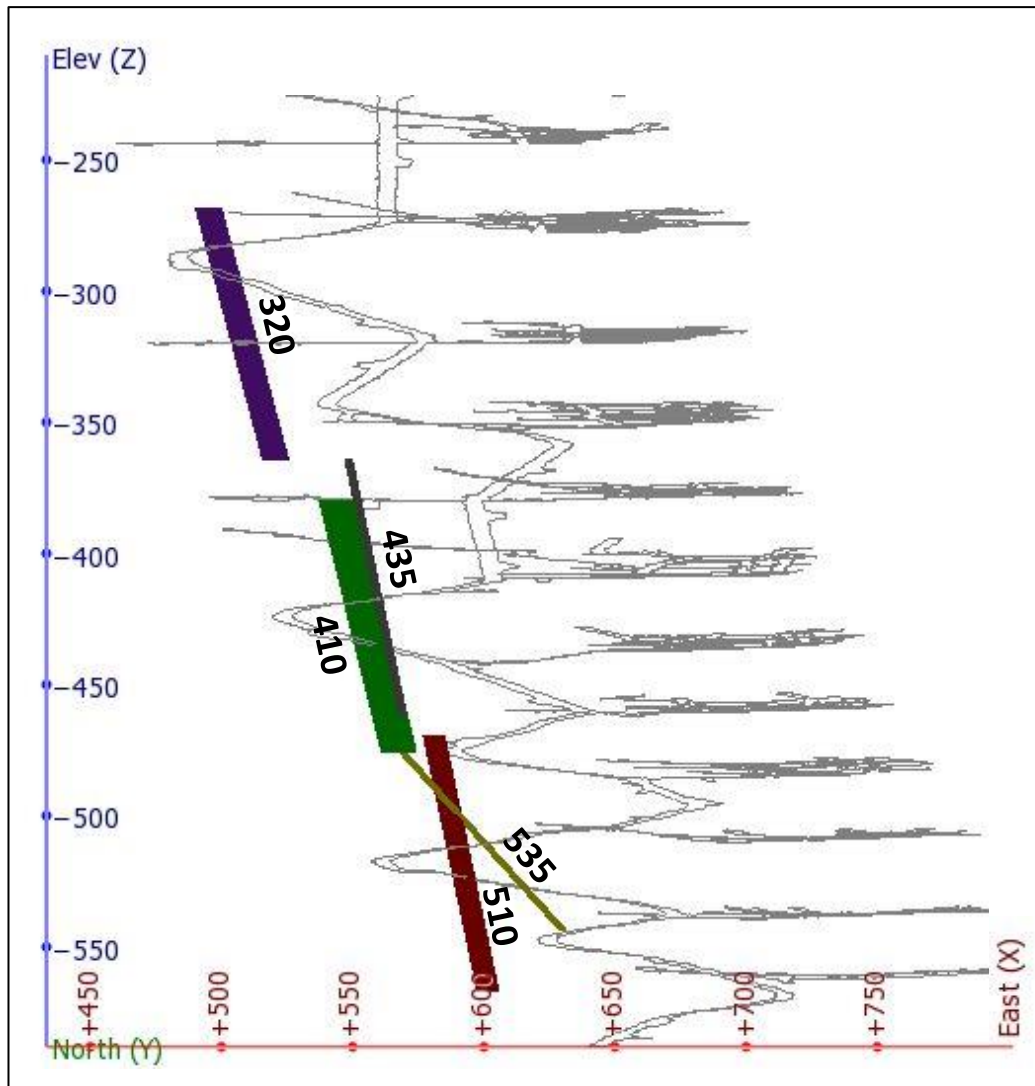


Figure 3.72: Projection of the survey pickups at each of the inception points.

Table 3.11: Average orientations of survey pickups (taken from models at individual locations).

Location	Average dip	Spread of dips at location	Average dip direction	Spread of dip directions at location
320 Level SP	75	5	84	7
Decline 410 / 435 upper	70	31	83	20
Decline 410 / 435 lower	79	9	89	7
Decline 510 / 535 upper	78	6	82	14
Decline 510 / 535 lower	38	23	94	20

3.7 Mt Lyell

3.7.1 Location and Geological setting

Mt Lyell Copper Mine is located on the west coast of Tasmania near Queenstown. It is owned by Copper Mines of Tasmania (CMT) – a subsidiary of the Vedanta resources group.

The Prince Lyell deposit is located in the Mt Read Volcanics and is bounded by the Owen Conglomerate. The Great Lyell fault forms the contact between the two rock units.

3.7.2 Mining Method

Mining has been undertaken at Mt Lyell for over 100 years. Raymond, 1995 states that “early mining was centred on the high grade copper deposits in the North Lyell area and on The Blow deposit. Subsequently, the majority of ore from the Mount Lyell field was extracted from the West Lyell area, comprising the Prince Lyell, "A" Lens and Royal Tharsis copper orebodies”.

Mining began from the Prince Lyell deposit in 1972 (Sharrock and Cuello, 2016). The primary method was open stoping. In 1995 sub-level caving was adopted to recover remnant pillars from the open stoping areas. Sub-level caving continued until the mines closure in 2014.

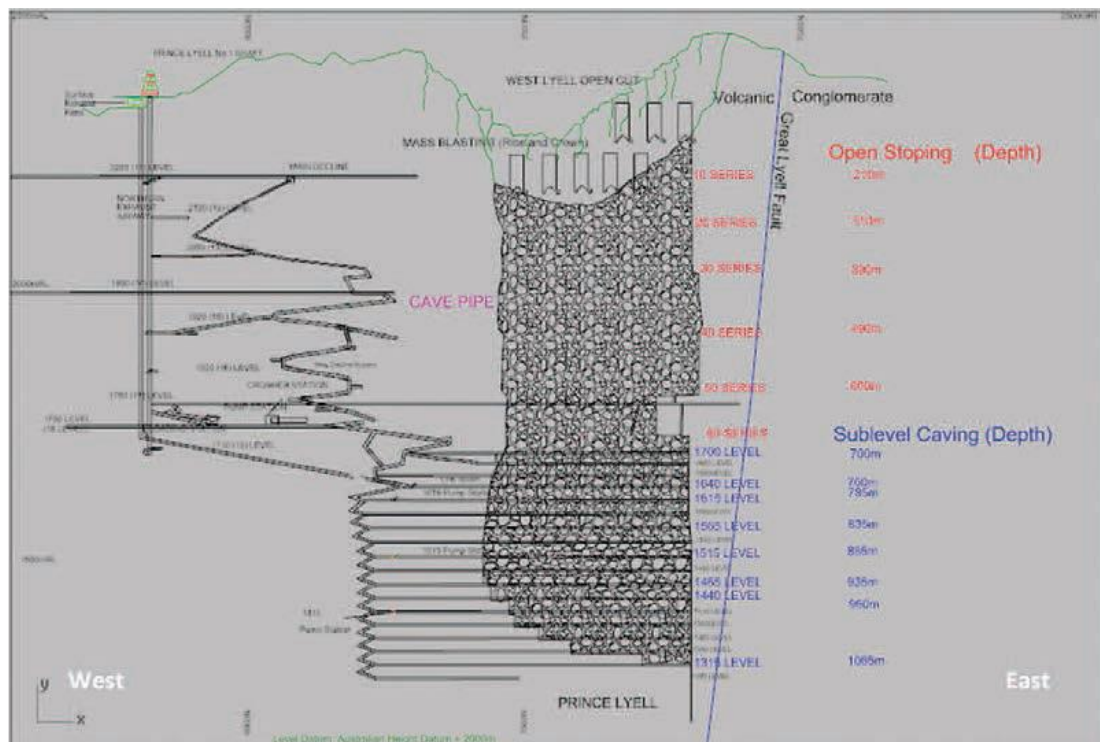


Figure 3.73: Mt Lyell layout (Sharrock and Cuello, 2016)

3.7.3 Literature review

Despite its history very little has been published regarding the Mt Lyell deposit. No published papers can be found discussing seismicity within the ore body.

3.7.4 Data Availability

Table 3.1 outlines the data that was provided by the site in 2013.

Table 3.12: Data availability for Mt Lyell.

	Data Type	Mt Lyell
Seismic Data	Data Available	✓
	Data processed	✓
Seismic System	Sensor location	✓
	Significant hardware upgrades	x
	Significant outages	#
Geology	Major structure well defined	✓
	Minor structure defined	x
Mining Information	Decline files	✓
	Level files	✓
	Stope Voids	✓
	Vertical development	x
	Level development history	x
	Stoping history	#
# data only partially available		

The seismic system comprises of 8 sensors. Three sensors were disconnected in November 2012 and replaced. One sensor became inoperative in Feb 2013 and was replaced in April 2013. No system functionality records are kept; however, there is an obvious system outage between July and October 2012.

Seismic data was collected between 11/05/2012 and 05/09/2013. In total the dataset comprises of 4243 events. The magnitudes were calculated using Equation 3.6. No explanation was provided regarding the selection of the constants.

The mining layouts were provided however, the extraction sequence was not provided.

$$M_L = 0.516 \log_{10} E + 0.344 \log_{10} M_o - 6.572$$

Equation 3.6

3.7.5 Discussion on Seismicity at Mt Lyell

As discussed, the seismic system layout consists of 10 sensors (Figure 3.74). The sensors are concentrated around the sublevel caving areas with sensors also installed around the capital development areas. As the sensors are limited by access to development areas the array is very planar. Seismicity in the caving area and in the FW of the caving area will have inherent inaccuracies.

Figure 3.75 provides the seismic event locations. The cluster to the upper right of the figure is approximately 400m from the main development area. It is likely to be associated with a regional fault or a previous mining district; however, this information has not been provided. A review of the seismic event locations also highlighted 12 events over 1.5km from the mining boundary. The Mine Site Engineers suggest that these were regional events and recommended they be removed from the dataset. This brings the total number of events in the database to 4231.

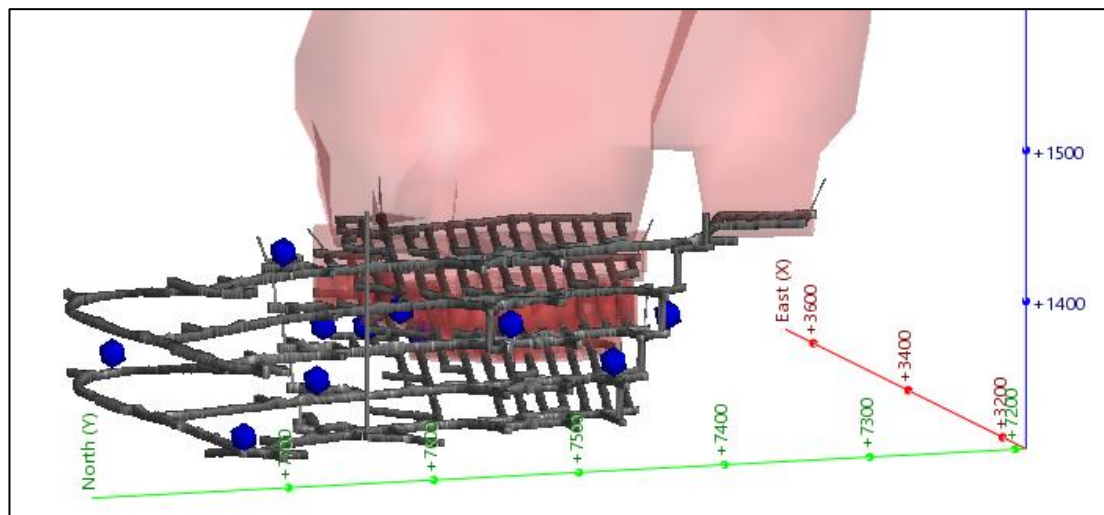


Figure 3.74: Mt Lyell seismic sensor locations.

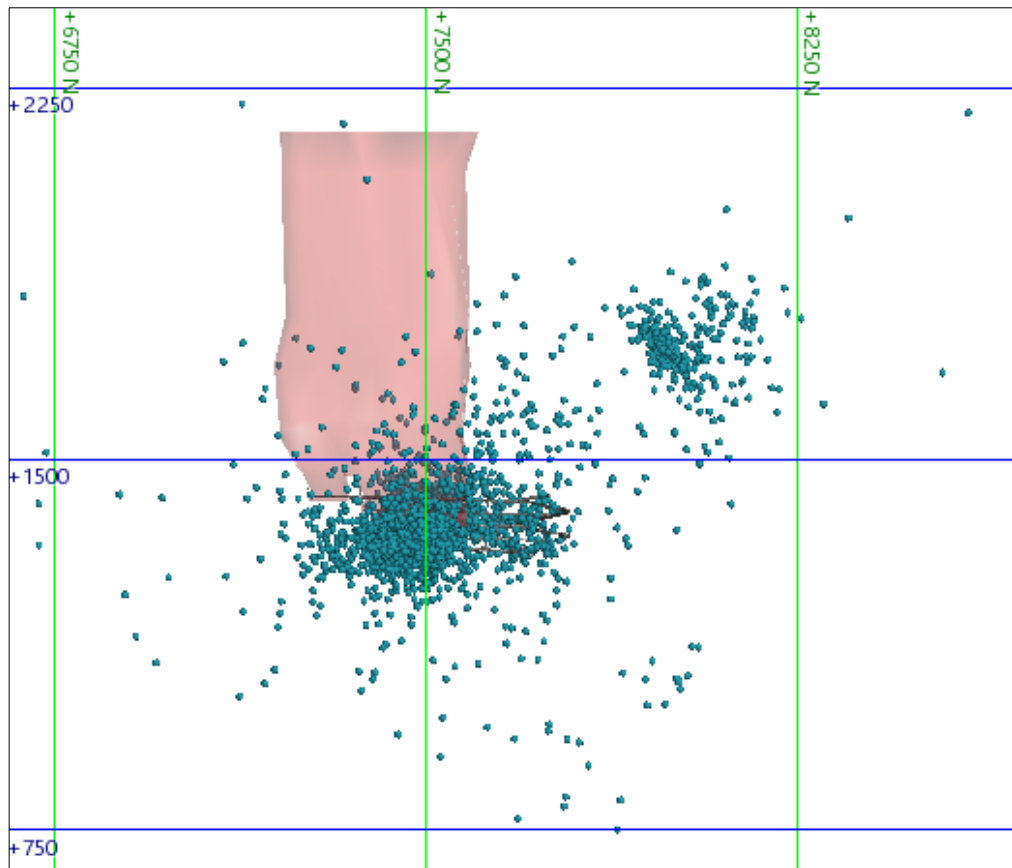


Figure 3.75: Mt Lyell seismic event locations.

The magnitude distribution is provided in Figure 3.76. For the seismic catalogue to be accurate the seismic data should be evenly distributed across the magnitude bands. This is clearly not the case with a spike in the data at $-2.5M_L$. There does not appear to be a discrepancy in the Log Energy / Log Moment ratio that would explain this spike. There appears to be a change in the calculation of the Energy and Moment values around October 2012; however, removing data from prior to November 2012 does not remove the spike. Given there is no explanation for the constants used in the magnitude calculation, magnitude was re-calculated using the standard ISS formula (Equation 3.7). The results (Figure 3.77) show that the magnitude distribution is slightly higher than the previous calculations and that the spike has been removed. All analysis moving forward will use the new formula.

$$M_L = 0.272 \text{Log}_{10} E + 0.392 \text{Log}_{10} M_o - 4.62$$

Equation 3.7

Using the new formula, the maximum magnitude is $2.1M_L$ and the minimum is $-3.0M_L$. There is a total of 131 events over the $0M_L$ threshold.

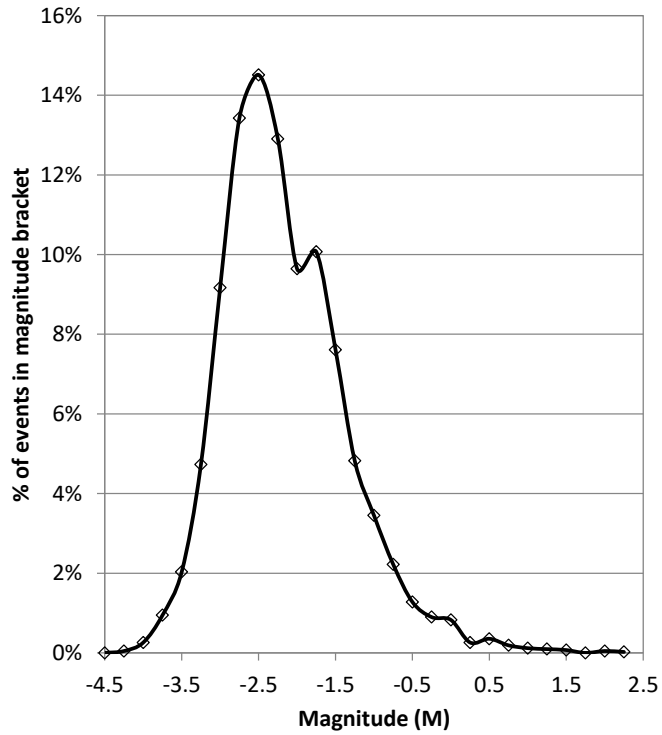


Figure 3.76: Magnitude distribution for the Mt Lyell mine site.

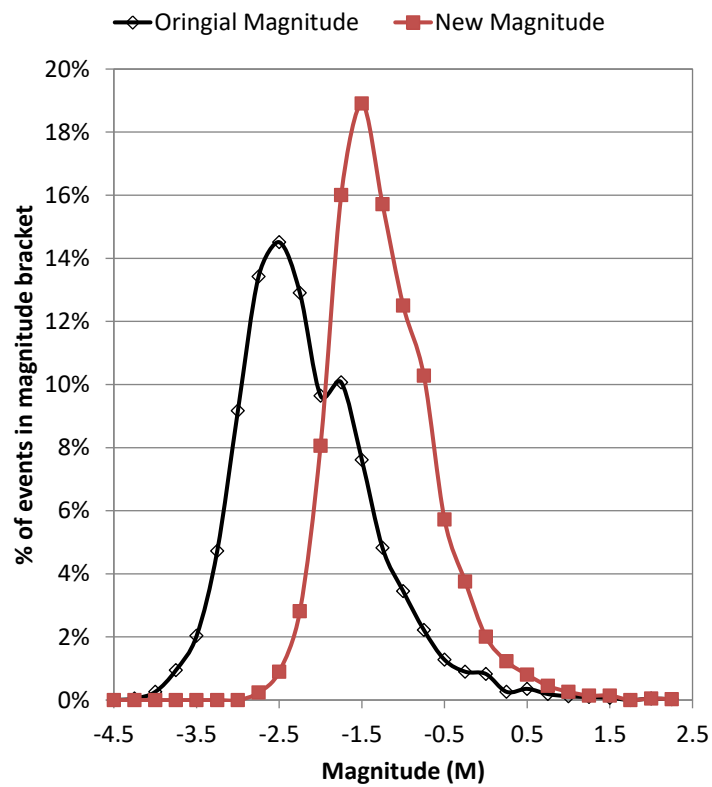


Figure 3.77: Comparison of the distribution of magnitudes using the old and new formulas.

3.7.6 Great Lyell Fault

Several areas were examined for analysis including the area of the sub-level cave. The Great Lyell fault was selected for analysis due to its location alongside the sublevel cave. This fault forms the boundary between the Mt Read Volcanics and the Owen Conglomerates (Figure 3.78). All infrastructure and mining are located in the HW of the fault (in the Mt Read Volcanics).

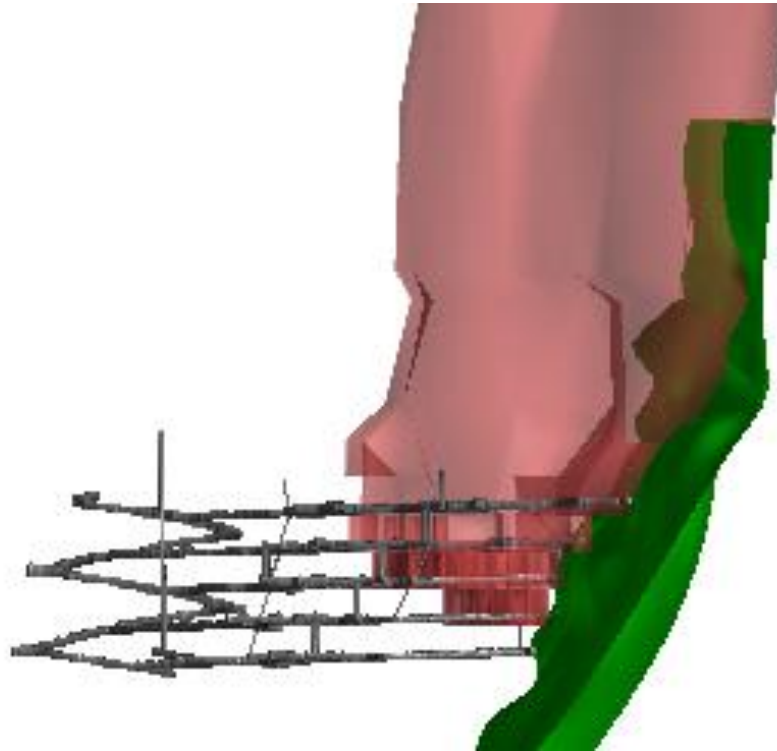


Figure 3.78: Great Lyell structure.

Seismic sensor coverage is primarily in the hangingwall of the structure with no sensors in the footwall. As discussed in the previous section all sensors are located surrounding the development area. This may affect the accuracy of the results.

The domain distance analysis is provided in Figure 3.79. A domain distance of 15m was selected creating a total domain width of 30m. The event locations for the Great Lyell fault are provided in Figure 3.80. The events are primarily clustered around the development areas coinciding with the locations of the sensors. The total number of events is 247. The maximum magnitude is $1.4M_L$ and the minimum is $-2.3M_L$. The median value is $-1.2M_L$ which is slightly higher than the overall site median of $1.5M_L$. There are 14 events over the damage threshold of $0M_L$. This number is relatively high in comparison with other structures selected for analysis. This may be due to recalculation of the magnitudes.

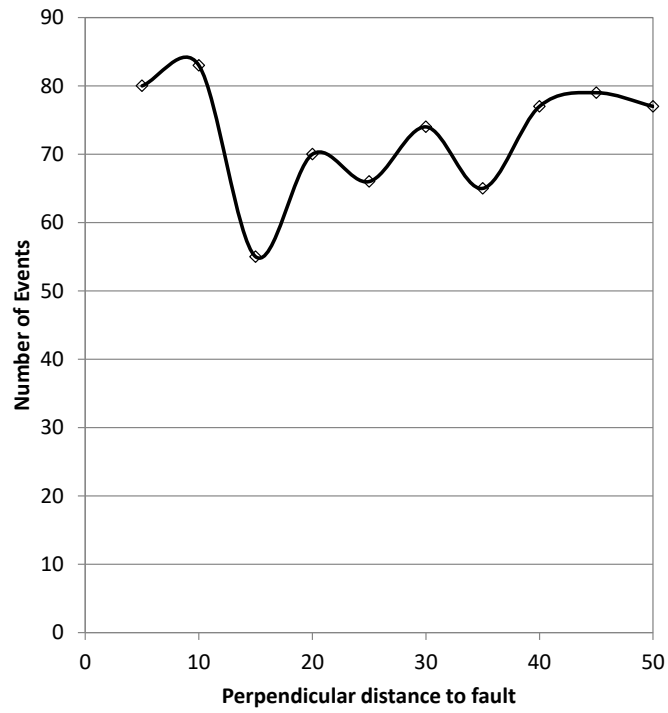


Figure 3.79: Distances of events from the Great Lyell Shear.

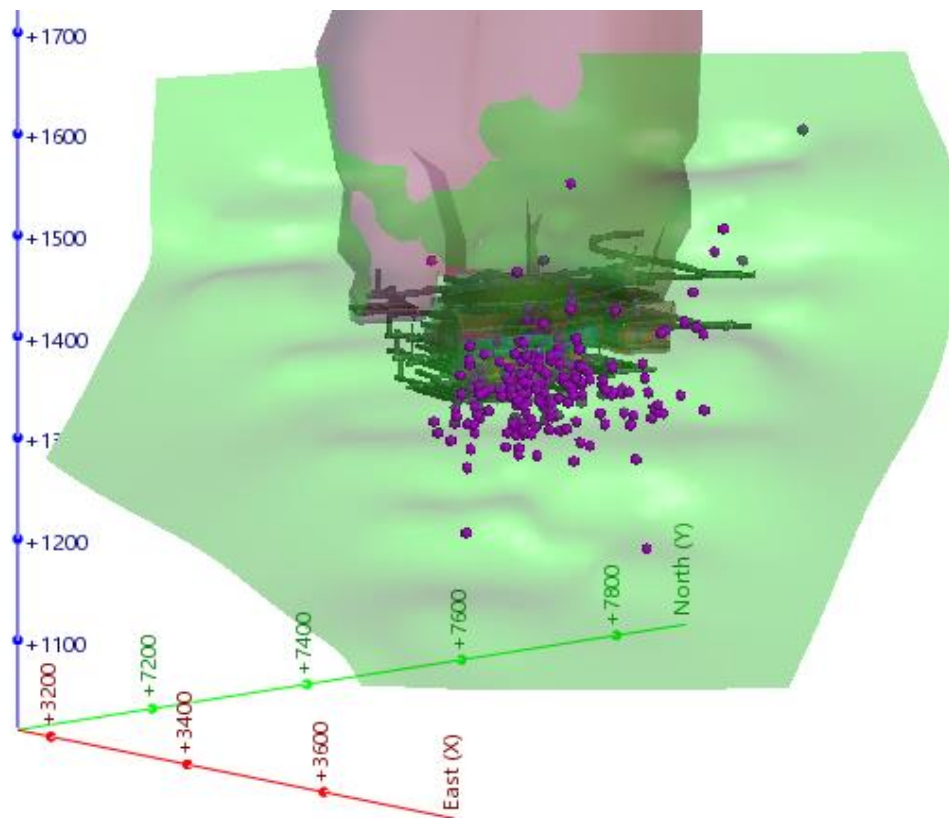


Figure 3.80: Event locations for the Great Lyell Shear.

3.8 Discussion

As with any analysis, the quality of the data is a significant limitation. As the previous sections have indicated, any analyses require careful consideration of the data and a review of the quality of the data. Sites where there has been a high turnover in staff and / or poor staff training can be seen to have a lower quality of data resulting in misleading analyses.

Whilst every attempt has been made to remove errors within the datasets, it is accepted that imperfections will still exist. This does not make the following analyses invalid. In the end the datasets are representative of data analysed by Mine Site Engineers every day in managing seismic risk. Any improvement in the analysis methodology is going to contribute to the knowledge and understanding of the mining environment and improve workplace safety standards.

It is acknowledged that the mining method and mining rates can have a significant influence on the seismic behaviour of large-scale structures. However, the aim of the thesis is to improve current analysis techniques and to determine whether patterns of failure can be discerned within the mining seismic data. By analysing data from a number of structures within a variety of mining environments that utilise different mining methods the effect of these variables can be indirectly determined.

Mining seismology research and data analysis

4. Mining seismology research

The following two chapters summarise the most recent research being undertaken and their application in mining seismology. This chapter will provide an overview of the current research programs in Canada, South Africa and Australia. Chapter 5 will give a detailed review of the each of the parameters currently being applied in analyses on Australian mines. The most common of these parameters will then be assessed in the mine site datasets. The analysis will compare the results of the overall dataset and the fault datasets to determine if focussing the dataset to specific structures alters the outcomes of the analysis.

4.1 Introduction

Research into mining induced seismicity is extensive with highly diverse areas of interest. These areas include fracture mechanisms, seismic monitoring, hazard management, stress modelling and dynamic ground support to name but a few.

The largest and most concise research programs have been undertaken in South Africa, Canada and Australia. With such a large body of literature it is necessary to limit the fields of research to areas relevant to this thesis. The focus of the following section will be specifically on seismic data analysis techniques in these three countries.

4.2 South Africa

South Africa has a long history of mining induced seismicity and consequently also a long history of seismic research. Durrheim and Riemer, 2010 outline 100 years of seismic research in South Africa. With such a vast history of research the number of publications on the topic is extensive. Since 1991 the principal body for overseeing this research is the Safety in Mining Research Advisory Committee (SIMRAC). According to Wright et al., 2003, SIMRAC have 4 research areas focused on mine seismicity:

- *“Understanding rock behaviour and assessment of the seismic risk*
- *Prevention of seismicity*
- *Controlling rock burst damage*
- *Technology transfer”.*

Over 85 papers have been published on the topic of seismicity and rock bursts between 1993 and 2012. The majority of the reports (over 70%) were published prior to 2003. Only a few reports have been published since 2012. With such an extensive body of research it is impractical to review every research paper. Therefore, only the main reports relevant to this thesis will be reviewed.

Esterhuizen (Esterhuizen, 1994, Esterhuizen, 2000) conducted a series of studies on the excess shear stress and loading system stiffness using two-dimensional and three-dimensional modelling. The concept of excess shear stress and loading system stress was well developed in South Africa by the early 1990s. Modelling will not be discussed.

Mendecki et al., 1996 (also Mendecki, 1997) aimed to “*develop methodologies for long-, intermediate- and short-term rockburst prediction based on quantitative data provided by modern seismic networks*”. The report discusses a large gamut of seismic monitoring and analysis. The monitoring aspect discusses the types of transducers, seismic sensor density, network configuration and velocity models that enable adequate data collection. The seismic analysis contains chapters on seismic probability and predictability based on fractal calculations as well as discussion on various seismic source parameters.

The limits of predictability were examined for the following parameters:

- Location (X, Y, X)
- Distance between events
- Distance between events with consideration of source size
- Time between events
- Log energy
- Log moment

The study found that seismic events can be theoretically predicted using limits of probability. The time frame for prediction ranges between a few hours and 3 weeks. The most successful predictions could be made based on the location of events, specifically, through analysis of the X or Y positions. The Z position was less predictable. This is likely to be a function of the shallow dipping nature of the South African ore bodies and may not apply to other mining districts. The parameters which showed the least possibility of event prediction were the log energy and log moment.

Mendecki et al., 1996 also recommended several seismic parameters for use in seismic analysis. These included: seismic moment, seismic energy, apparent stress, energy index, source volume and clustering.

The United States Geological Survey describes seismic moment as “*a measure of the size of an earthquake based on the area of fault rupture, the average amount of slip, and the force that was required to overcome the friction sticking the rocks together that were offset by faulting*” (USGS, 2016). Seismic energy is the area under the seismic wave and is the theoretical energy produced by the failure. Apparent volume is said to represent the volume of rock undergoing inelastic straining during a seismic event. Further discussion of this parameter is provided in Chapter 5.8. Seismic stress, strain and viscosity are all parameters related to changes within the rock mass as a result of the event whilst diffusion and Schmidt number relate to the volume of rock mass being affected by seismicity. Descriptions of all the parameters mentioned are provided in Appendix 1. These parameters now form the basis of current analysis techniques applied in mining and are discussed in the following section. Several small case studies were provided to demonstrate the application of the analysis of the seismic parameters.

Prediction of rockbursts was also researched by de Beer, 2000. He aimed to bridge “*the gap between quantitative monitoring and automated interpretation for prediction*”. The project developed an algorithm for testing a concept called time to failure. This concept uses a seismic event as the “*critical point*” and suggests the behaviour of precursors prior to the critical point conform to a power law (Equation 4.1).

$$\frac{d\Omega}{dt} = k(t_f - t)^m$$

Equation 4.1

Where Ω is the predictor, t_f is the failure time or critical point, t is the current time and k and m are constants.

De Beer uses 9 measures of seismic release in the algorithm. They are:

- Cumulative square root of the scalar seismic moment
- Cumulative square root of the radiated seismic energy
- Cumulative apparent volume
- Apparent volume scaled by the inverse median energy index
- Cumulative inverse seismic Schmidt number
- Cumulative inverse of the seismic stress
- Cumulative seismic strain
- Cumulative seismic diffusion
- Cumulative inverse seismic viscosity

Only a years' worth of data was analysed using the algorithm. No geology was used to limit the spatial extent of the data. The algorithm detected significant changes in the "*deformation variable apparent volume and seismic moment*" that were consistent with changes in the mining rate. "*The stress variable, seismic energy, does not show this pattern clearly*". Overall "*of the 371 predictions made, 23.45% were successful and 76.55 were false positive*". Whilst the predictors succeeded in some cases (24%), it was 3 times more likely that the prediction of a large event was incorrect.

Kgarume, 2010 studied the hazard posed by aftershocks of large seismic events. He investigated the aftershock sequence of main shocks using the Gutenberg - Richter relationship, Bath's law and the Modified Omori law. The results indicate that the Gutenberg - Richter relationship and the Modified Omori law both applied to aftershock sequences in mining; however, Bath's law was not applicable. The "*dependency of mine tremor aftershocks on mining conditions (stresses, strain rates and geological features)*" was also assessed. The results indicated that the aftershock event rate was not influenced by any of these features.

Reimer and Durrheim, 2011 highlight that research in mining seismicity in South Africa is dwindling with "*no current fundamental seismic research being conducted*" by major mining research organisations. One project recently completed is a collaborative effort between Japanese Earthquake researchers and South African Mine Seismicity researchers. This project was established under the banner SATREPS (Science and Technology Research Partnership for Sustainable Development). Ogasawara et al., 2009 stated that the 5 year project entitled "*Studies of seismic hazard mitigation in deep level South African mines*" had the following aims:

- *“To learn more about earthquake generation mechanisms through monitoring in close proximity to the seismic source in South African gold mines. This knowledge will contribute to efforts to upgrade schemes of seismic hazard assessment and to limit and mitigate the seismic risks in deep and highly stressed mine and in areas vulnerable to natural earthquakes.*
- *To develop human and technical capacity in South Africa.*
- *To upgrade the South African national seismic network”.*

The project involved concentrated seismic monitoring of mining fronts and well-defined geological structures. Mapping and testing of the geological properties of the structures were undertaken to adequately define the structures and allow for detailed analysis. Monitoring was undertaken using strain and tilt meters, closure monitoring as well as an acoustic emission monitoring system installed ahead of the mining front. The analysis aimed to attempt to better explain seismic deformation and fracture mechanisms. This project was completed in August 2015 and not all results are currently publicly available. The final report for the project will be released in late 2016. However, several papers regarding the report have been released.

The results from monitoring of a mining front at Cooke4 Gold Mine are provided in Moriya et al., 2015. Six accelerometers and 24 acoustic emission sensors were installed in a rock volume of 95x50x30m ahead of the stoping front. The results demonstrated that the majority of seismicity occurred only approximately 20m forward of the mining front. Seismicity migration was consistent with advancement of the mining front. Clustering analysis showed that activity formed distinct linear trends. Two of the trends concurred with existing geological features however the majority of features were limited to 10-30m in length and were parallel to the stoping front.

Naoi et al., 2015 examined the same data specifically on the two pre-existing structural features. Illogically, events at intersections between structures were removed *“to avoid contamination from other clusters”*. Focal mechanism analysis showed that the larger events exhibited normal slip in line with the fault plane. Temporal studies show that b-values decreased as both the seismic event rate and magnitude increased. The b-value is discussed in detail in Chapter 10. As no large events occurred during the 3 month monitoring period definite associations with failure could not be determined.

4.3 Canada

Canada's history of mining induced seismicity is not quite as long as South Africa. Blake and Hedley, 2003 state that mining induced seismicity has been present in Canada since at least the 1930s.

Hasegawa et al., 1989 reviewed seismicity trends in coal, potash and hard rock mines in Canada prior to the implementation of seismic monitoring. They proposed six failure mechanisms (Figure 4.1): (a) roof collapse due to dynamic or static failure due to seismic loading, (b) pillar bursting "due to convergent forces...and... time dependent after effects" (c) tensile failure of the competent cap rock due to excessive spans. The final three mechanisms (d-f) relate to structural failure. The mechanisms depend on the slip directions of the structural feature and the angle of repose relative to the excavations. These failure mechanisms are derived from observations of damage related to seismic events. They state that the most common type of failure is structural failure.

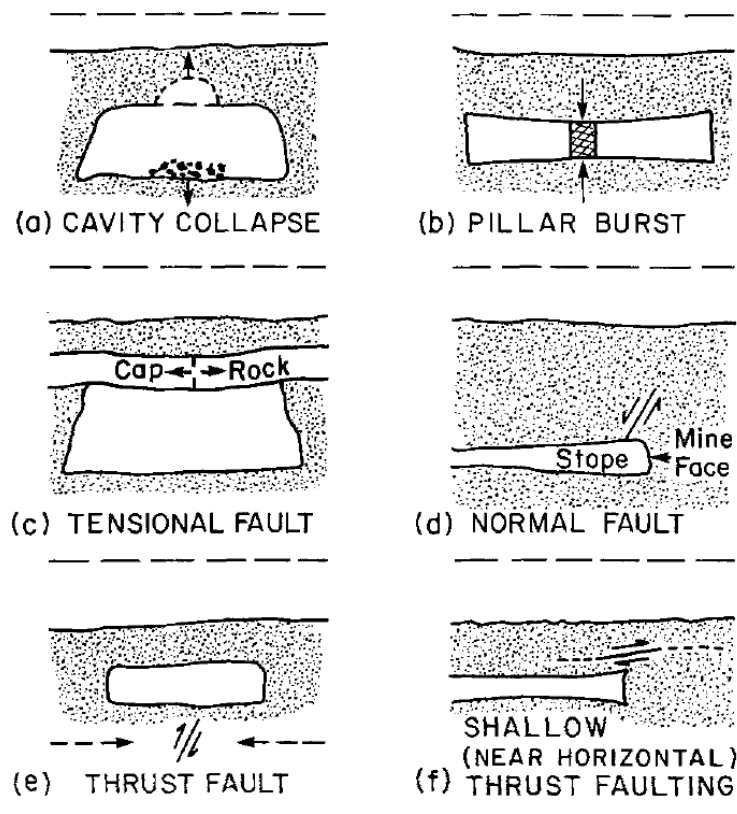


Figure 4.1: Six models of induced seismicity proposed by Hasegawa et al., 1989.

Hedley and Udd, 1989 outline the development of the Ontario rockburst project. The project “*was initiated in September 1985 in response to a growing problem in Northern Ontario hard rock mines, which has resulted in fatalities, mine closures, lay-offs and abandonment of ore reserves*”. The project mainly consisted of the installation of a seismic monitoring network in the Ontario region. The project highlighted the lack of understanding of seismic theory and consequently the Canadian Rockburst Research Project was established by the Mining Research Directorate (later incorporated into Canadian Mining Industry Research Organization – CAMIRO). The major deliverable of the project was the Rockburst Research Handbook (CAMIRO, 1996) which consists of 6 volumes of seismic theory including seismic principles, numerical modelling and dynamic ground support. It also contains case studies of mine sites throughout Canada. Many of the results provided in the handbook are now outdated or are not relevant to this thesis.

Falmagne, 2002, investigated brittle fracture and crack propagation theories. She used the results of mining seismic monitoring to determine a damage scale called the degradation index. This index was determined by dividing the cumulative apparent volume by the cumulative cluster index. The cumulative apparent volume “*represents the volume of rock that is undergoing inelastic straining during a seismic event*” whilst the cluster index is a measure of the coalescence of fracturing based on the size of individual events and distance between consecutive events. The results show that an increase in the degradation index suggests fracturing is occurring randomly throughout the rock mass whilst a decrease in the index suggests that damage is concentrating in a particular area. Falmagne then used modelling to determine the localised stress paths around 3 mine openings from the Lac Shortt mine. The modelling results were compared with the location of clustering and were shown to be able to indicate locations of rock mass damage.

Coulson, 2009 aimed to determine “*at what point regional rock mass failure occurs and whether mine induced seismicity can be used to define the stages of failure*”. The basis of the analysis was principal component analysis (PCA). The PCA analysis “*involves positioning a spherical volume of dimension D on an event in the cluster and then determining the mean hypocentral location of all the events inside this volume*”. The distribution of the data (mainly the orientation of the clusters) was then analysed. He used this analysis as “*a statistical technique for the determination of spatial trends in a cluster of seismic events*”. The first step in the analysis was to define a cluster of events. This was completed using “*a combination of visual extent and seismic event density to determine regions where coalescence may be taking place*”. Temporal distribution was also considered in the selection of clusters.

Coulson used two mining case studies; the Williams Mine and the Golden Giant Mine both located in the Hemlo area of Northern Ontario. The Williams study showed that the PCA was able to determine the yield front ahead of mine development. The orientation of the PCA clusters was consistent until instability was initiated, after which the trend in the clusters change orientation. Once the rock mass had yielded the cluster volume became “*aseismic*”. This yield front correlated with results from deformation monitoring conducted using SMART cables. The results could also be replicated using 3D linear elastic modelling. The Golden Giant study showed similar results with the failure mechanism described as dilation with strain softening.

Coulson then undertook a focal mechanism study on 243 seismic events in a specific cluster from the Golden Giant Mine. All these events were determined to be fault – slip failure with most of these events (82%) represented by reverse faulting. The orientation of the fracturing concurred with geological trends and the stable PCA trends.

The majority of recent Canadian seismic research appears to be focused on the development of dynamic ground support with few papers published on the analysis of seismicity and its relationship to discontinuities in the rock mass.

4.4 Australia

The majority of mine seismicity research has been conducted by the Australian Centre of Geomechanics (ACG, 2009). The Mine Seismicity and Rockburst Risk Management project was established in 1999 and is currently in its third phase of funding. According to the 10 year project summary 5 PhD theses and 1 Master's thesis and over 100 papers have been completed over the course of the project.

The project started with the objective to “*advance the responsible application of seismic monitoring systems in WA mines and deliver strategies to quantify and mitigate the risk of mine seismicity and rockbursting*” (ACG, 2009).

The key achievement of the project has been the development of the Mine Seismicity and Rockburst Analysis Program (MSRAP). This program was initially designed as an analysis package to complement the IMS monitoring system which at the time lacked a straightforward comprehensive visualisation and analysis package.

The basis of the program lies in clustering of seismic events based on spatial characteristics and seismic source mechanisms. Individual clusters are then combined into groups (called seismic sources) and the groups are analysed to determine a seismic hazard rating.

Reimnitz, 2004, introduced the concept of incremental work density (IWD) which “*can be used to evaluate the relative likelihood of seismic activity during mechanical shearing on pre-existing planes of weakness*”. Incremental work density is a function of the “*level of driving shear stress and the change in the inelastic shear deformation during mechanical shearing*”. The analysis used Map3D™ linear-elastic modelling to calculate the incremental work density. He applied this concept to two shears located in the footwall of the Big Bell Gold Mine. The results of the research indicated that linear-elastic modelling is able to replicate the spatial distribution of the seismic events. However, it could not replicate the energy and moment distributions. As discussed in Chapter 3.6 and by the authors own admission the structural models are inaccurate. Consequently, the validity of any outcomes is questionable.

Albrecht, 2005 aimed to “develop site specific empirical models to predict locations of rockburst damage at mines”. Damage as a result of seismic events was investigated at three mines; namely Big Bell gold mine, St Ives Junction mine site and Mt Charlotte. He suggested that the risk of damage at a particular location is determined by the dynamic load at the excavation boundary and the excavation condition. The derivation of these parameters is complicated. Table 4.1 is provided as an attempt to clarify these parameters.

Table 4.1: Rock damage prediction model due to seismic events used by Albrecht, 2005.

General model	Specific component	Description	Formula
Dynamic load	Amplitude of the ground motion	Measured using Peak particle velocity (PPV)	$PPV = \frac{PPA}{2\pi f_c}$ PPA – Peak particle acceleration f_c – corner frequency
	Wavelength or frequency (λ) of the seismic wave relative to the excavation span (D)	Calculated by dividing the wavelength of the seismic wave by the span of the excavation	$\frac{\lambda}{D} = \frac{B_0}{f_c D}$ B_0 – P or S wave velocity
Excavation condition	Boundary stress state	σ_1, σ_3, τ and σ_n calculated at boundary nodes of the excavation	Calculated using Map3D modelling package
	Yield state of the rockmass at the excavation boundary	Ratio of static stress to the strength of the rock mass	Back analysis parameter calculated using the major principle stresses, shear stresses and / or the UCS.
	Excavation geometry	Effective radius parameter calculated using average distance to points	$ERF = \frac{0.5}{\frac{1}{n} \sum_{\theta=1}^n \frac{1}{r_\theta}}$ n – number of rays r_θ - distance from the centroid to the excavation boundary θ - angular increment
	Orientation of excavation relative to geological features	Minimum angle between the orientation of the drive and the critical angle	The dip and strike of the drive are subtracted from the dip and strike of the critical feature (geological feature or major principal stress).
	Rock mass type and characteristics of geological features	Calculated using Q^*	$Q^* = \frac{RQD}{J_n}$ RQD – rock quality designation J_n – joint set number
	Rock mass fatigue at excavation surface	Cumulative sum of seismic energy release.	$RF = \sum_1^n E_o$ n – number of events whose radii intersect the excavation E_o – seismic source energy of an event intersection the excavation
	Excavation stiffness	Specified using Local energy release density (LERD)	Calculated from Map3D modelling software.
	Support capacity	Capacity of the installed support based on energy and displacement capabilities.	Table provided in paper for support calculations

Needless to say, each of these parameters carries many assumptions and a heavy reliance on Map3D modelling. The use of Map3D to determine stress states at excavation boundaries is highly presumptuous. Albrecht stated that “*the model assumes linear elastic continuum rock mass behaviour, and is therefore best suited to linear and homogenous materials*”. Rock mass behaviour by its very nature is well known to be non-linear and heterogeneous. The models lack the specific details to definitively replicate the complexities of the stress paths around excavation. Furthermore, the PPV of a seismic event and how it relates to seismic waves has not been proven by quantitative measures and remains conceptual. Several attempts have been made to measure wave velocities at the surface of excavations but to-date no data have been verified. Additional to the mechanics of failure the support capacity is also subjective. Energy and displacement capacities are based on best case scenarios with no regard for installation quality or prior loading effects.

Hudyma, 2008 evaluated several parameters as measures of seismicity. These were S:P ratio, magnitude time history, apparent stress time history and diurnal analysis. These concepts have been described in detail in Chapter 5. He found that each parameter was able to provide an insight into the seismic behaviour of the rock mass. He also discussed the clustering theory that forms the basis of the MSRAP program. He provided several clustering methodologies including single link and complete link clustering. Further discussion on clustering can be found in Chapter 9.

Mikula et al., 2008 developed a generic seismic risk management plan (SRMP) as part of the MERIWA project M386 (Mine seismicity and rockburst risk management project-Phase III). It is suggested as industry best practice that mine sites with mine seismicity risks should have a plan that outlines how the site manages the seismic risk. The generic plan provides a layout for the document as well as a recommendation on the parameters that should be analysed. These parameters form the basis of analysis in the following section and will not be discussed further here.

Heal, 2010 aimed to develop a correlation between seismic source parameters and rock mass damage as the result of a seismic event. He compared observations of seismic event damage from 13 Australian underground mines with the damage from field testing conducted as part of the research. Through his research Heal determined that a combination of factors “*contributes to the occurrence or otherwise of rockburst damage*”. These factors are:

- Stress conditions
- Energy absorption capacity of the installed ground support
- Excavation span
- Proximity of event to large-scale structures
- Peak particle velocity at the location of the damage

He developed a series of empirical factors that are combined to determine a seismic hazard rating for excavations. The process in calculating the seismic risk begins with determining a damage initiation factor (DI) and a depth of failure factor (DF).

The DI is calculated by dividing the stress conditions factor by the energy capacity factor (Equation 4.2). The stress conditions are defined as the percentage of static loading (σ_{IT}) to the intact rock strength (Equation 4.3). The static load is defined as the “*total maximum principal stress (pre-mining plus mining induced) in the vicinity of the workplace being evaluated*”. Heal suggests that it is “*best evaluated using numerical modelling*”.

$$\text{Damage initiation factor} = \frac{\text{stress conditions factor}}{\text{energy capacity factor}} \quad \text{Equation 4.2}$$

$$\text{Stress conditions factor} = \frac{\sigma_{IT}}{UCS} \times 100 \quad \text{Equation 4.3}$$

The energy capacity of the ground support is not a numerical calculation but rather determined using an empirical approach based on testing conducted during the research. Table 4.2 provides the rating system. This rating approach disregards installation quality or previous damage.

The DF parameter is calculated by dividing the excavation span factor by the geological factor (Equation 4.4). The excavation span is “*simply the largest circle than can be drawn internal to the excavation*”. A multiplication factor is added where “*the excavation surface has more than one free face, such as a stope brow*”.

$$\text{Depth of failure factor} = \frac{\text{excavation span factor}}{\text{geological factor}}$$

Equation 4.4

The geological factor (Table 4.3) is an empirical factor based on the proximity of the excavation to major structures within the mine. This factor is overly simplistic and fails to fully account for all local geological conditions.

Table 4.2: Ground support energy capacity rating system (after Heal, 2010).

Classification	Surface support	Reinforcement	Energy Capacity rating	Example
Low	None	Spot bolting	2	Spot bolting with split sets or solid bar bolts, minimal surface support
Moderate	Mesh or fibrecrete	Pattern bolting	5	Pattern bolting with split sets or solid bar reinforcement, with mesh or 50mm fibrecrete
Extra bolting	Mesh or fibrecrete	Pattern bolting with second pass of pattern bolting	8	Pattern bolting with split sets or solid bar reinforcement, with mesh or 50mm fibrecrete. Plus, an additional pass of pattern reinforcement such as solid bar bolts.
High static strength	Mesh or fibrecrete	Pattern bolting and pattern cable bolts	10	Pattern bolting with split sets or solid bar reinforcement, with mesh or 50mm fibrecrete. Plus, pattern cable bolting
Very high dynamic capacity	Dynamic surface support	Pattern dynamic support	25	Pattern bolting with dynamic ground reinforcement such as cone bolts, with a dynamic resistant surface support system.

Table 4.3: Geological factor description (after Heal, 2010).

Geological factor	Description
0.5	<p>Seismically active major structure:</p> <p>Major structural features such as faults, shears or discrete contacts intersect the location and act as a potential failure surface promoting rock mass failure.</p> <p><i>Example: the rock mass fails back or along a major fault, increasing the depth of failure considerably more than would otherwise occur in rock mass.</i></p>
1	<p>Unfavourable rock mass / No major structure:</p> <p>The orientation of the rock mass discontinuity fabric may promote or enhance the rock mass failure. Generally, this factor is applied when there are local cases in which the rock mass discontinuities promoted falls of ground much larger than would be expected.</p> <p><i>Example: a heavily jointed, blocky rock mass with kinematically unstable rock mass blocks. The rock mass is prone to deeper than normal gravity driven failure mechanisms.</i></p>
1.5	<p>Massive rock mass / No major structure:</p> <p>The rock mass is essentially massive or non-persistent rock mass discontinuities may exist, including possible blast damage related fracturing. There are no major structures such as faults or shears, which may promote or enhance rock mass failure.</p>

The damage initiation factor (DI) and the depth of failure factor (DF) are used to calculate the excavation vulnerability potential (EVP) (Equation 4.5). The EVP is then multiplied by the maximum peak particle velocity expected (PPV_{max}) to calculate the rockburst damage potential (RDP) (Equation 4.6). This value is determined from maximum peak-to-peak velocity of the largest seismic event and the magnitude of the event.

$$EVP = DI \times DF = \frac{\text{Stress initiation factor}}{\text{Energy Capacity factor}} \times \frac{\text{Excavation span factor}}{\text{Geological factor}} \quad \text{Equation 4.5}$$

$$RDP = EVP \times PPV_{max} \quad \text{Equation 4.6}$$

Many of these parameters rely on empirical observations and are highly subjective. Furthermore, the classifications represent limited circumstances and lack the flexibility for the range of situations encountered in mining applications. Heal readily admits that the PPV at the damage site cannot be determined and has never been measured. Consequently, estimates of this value are derived from the far-field PPV.

Heal also investigated the damage caused by seismic events. He created a rockburst damage scale (RDS) consisting of 5 categories (Table 4.4). Notably, the non-damage locations and events where damage was categorised as R1 were removed from the analysis as *“their inclusion would greatly bias the final analysis of the case history data towards the lower end of the scale and potentially affect any criteria developed for forecasting potential rockburst damage”* (Heal, 2010).

A chart plotting the PPV_{max} versus the EVP combined with the RDS is used to determine the probability of *“severe rockburst damage”* (Figure 4.2). Severe rockburst damage is defined as the ejection of >10t of material. This corresponds to categories R4 and R5 on the RDS. Typically, this parameter must be tailored to local mine site conditions.

The seismic risk is determined using a risk matrix (Table 4.5). The RDP and the probability rating form the top of the matrix and a third parameter called Exposure forms the vertical component. Owen, 2004 provided the framework for the *“exposure”* rating. It is based on the level of access personnel have to an excavation and values range from 100 to 1000.

Table 4.4: Rockburst Damage Scale (after Heal, 2010).

Rockburst damage scale	Rock Mass damage	Support damage
R1	No damage, minor loose	No damage
R2	Minor damage <1t displaced	Support system is loaded, loose in mesh, plates deformed
R3	1 – 10t displaced	Some broken bolts
R4	10 – 100t displaced	Major damage to support system
R5	>100t displaced	Complete failure of support system

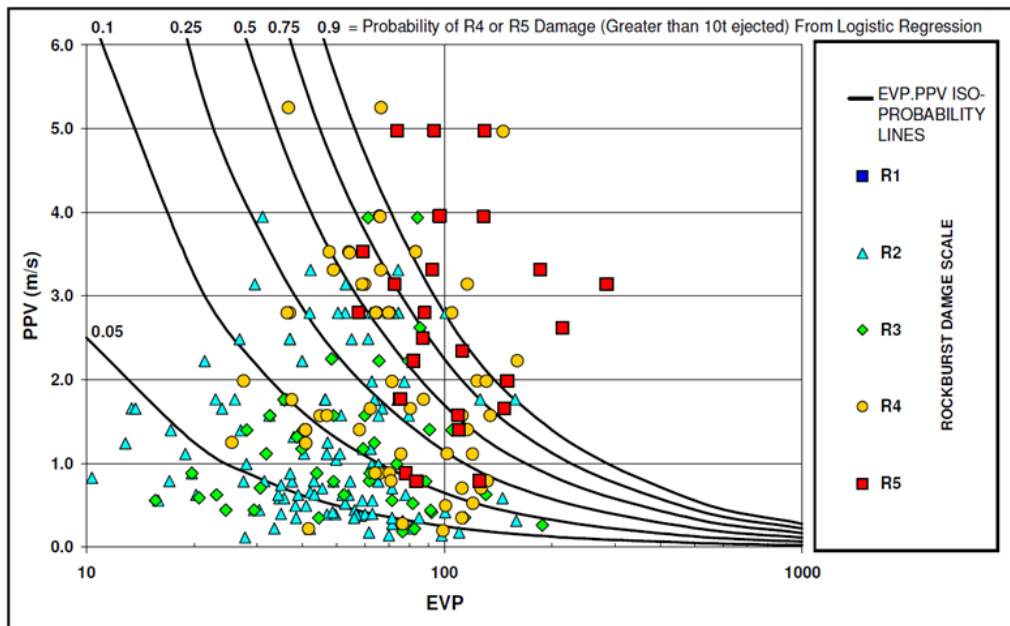


Figure 4.2: Determination of the probability of R4 or R5 damage on the RDS using EVP and PPV_{max} (after Heal, 2010).

Table 4.5: Seismic hazard matrix proposed by Heal, 2010.

	RDP	<25	25-65	65-115	115-170	170-225	225-280	>280
	Criteria: P (R4, R5)	<0.05	0.05-0.1	0.1-0.25	0.25-0.5	0.5-0.75	0.75-0.9	<0.9
Excavation type / activity	Exposure rating							
Restrictive access (no entry)	100	VL	VL	L	M	M	H	H
Decline	1000	VL	L	M	M	H	VH	VH
Travelway – no active mining	1000	VL	L	M	M	H	VH	VH
Travelway – mining on the level	2000	VL	L	M	M	H	VH	VH
Production mucking area	3000	VL	L	M	M	H	VH	VH
Busy level / travelway drive / access	4000	VL	L	M	M	H	VH	VH
Development mining	7000	L	M	M	H	VH	VH	E
Production drilling	10000	M	H	H	H	VH	E	E
Production charge-up	10000	M	H	H	H	VH	E	E
Infrastructure areas / workshops	14000	M	H	VH	VH	E	E	E

Where VL=very low, L = low, M = Moderate, H = high, VH = very high and E = extreme

In Australia, there is limited major research conducted on seismicity outside the ACG. Slade, 2004 discussed the seismic characteristics of faults at the Kundana Gold Mine located in the Eastern Goldfields of Western Australia. The aim of the research was to quantify the strength characteristics of the large-scale faults at Kundana Gold Mine using numerical modelling as a back-analysis tool. These characteristics were then used for forward modelling and seismic hazard management.

He used the modelling software program MAP3D™ *“to determine the normal, shear, principal and minor stress values at the site of seismic events... for an individual structure of a specific orientation”*.

Popular theory suggests that the relationship between σ_1 and σ_3 and between the shear stress and normal stress at the location of a seismic event is linear. Slade found that the fault data did not display linear characteristics but instead indicated multiple populations. He suggested that this may be the result of classic progressive failure (Figure 4.3). Further analysis shows that this failure mechanism is too idealised and *“various modes of failure existed at any time period”*.

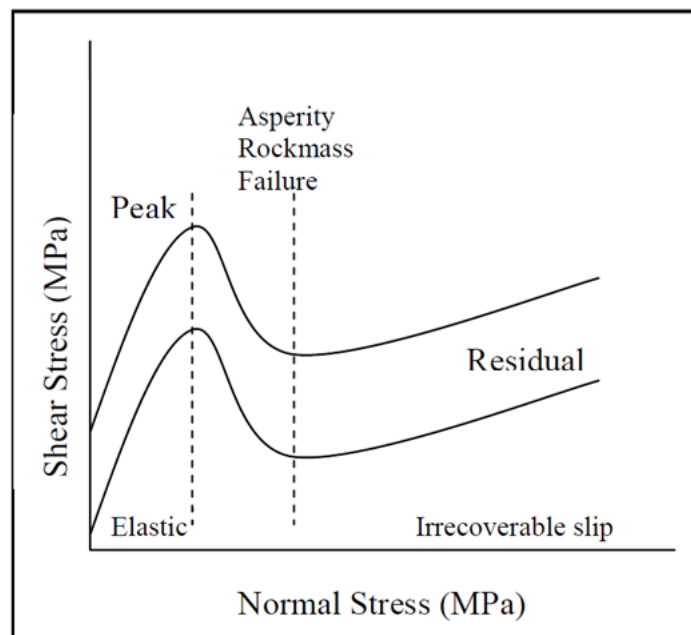


Figure 4.3: Idealised failure progression of faults at Kundana Gold Mine later shown to be too simplistic (Slade, 2004).

Overall Slade found that *“the simple process of calculating normal and shear stress at a seismic location utilising an elastic numerical model, has resulted in similar failure envelopes for each fault”*. He suggests that the results provide extremely low residual friction angles and were unlikely to be realistic.

The research enabled a better understanding of the faults at the Kundana operations. Some correlation was found in the Mohr-Coulomb seismic strength criterion and a calibrated strain strength criterion based on closure monitoring in the ore drives. Whilst this enabled more accuracy within the models Slade still didn't describe them as completely accurate stating that *“seismicity did not always follow regular and understandable / predictable patterns. This is particularly descriptive of seismic activity associated with fault slip movement”*.

Technological advances have enabled more back analysis of seismicity using stress modelling to determine stress states in the rock mass prior to large seismic failures. Parameters assessed included local energy release density (LERD) and the loading system stiffness (LSS) which have gained popularity as measures for instability (Wiles, 2002, Wiles, 2005). These are determined using linear elastic modelling. More recently non-linear modelling has become popular with detailed back analysis said to be able to predict rock mass deformation (Beck et al., 2010). As the analysis will not be undertaken in this thesis no further reviews in this area will be discussed.

In recent years the Western Australian School of Mines (WASM) has conducted a series of experiments simulating the dynamic failure of rock masses surrounding tunnels (Kusui and Villaescusa, 2016). Their research involves drilling 200mm tunnels into 400mm sandstone blocks and installing ground support. The tunnels are subsequently loaded using an Instron testing machine with monitoring undertaken using 2 acoustic emission sensors and a high-speed camera. The experiments were able to induce dynamic failure of the rock mass as well as characterise the failure sequence. Figure 4.4 shows the acoustic emission activity in comparison with observations of the failure progression and loading during an experiment. Most significantly the experiments have found an overall increase in seismicity rates prior to failure with a drop in activity rates immediately prior to failure. This is in contrast with commonly held beliefs regarding seismic event rates. Further discussion of this will be undertaken in later sections.

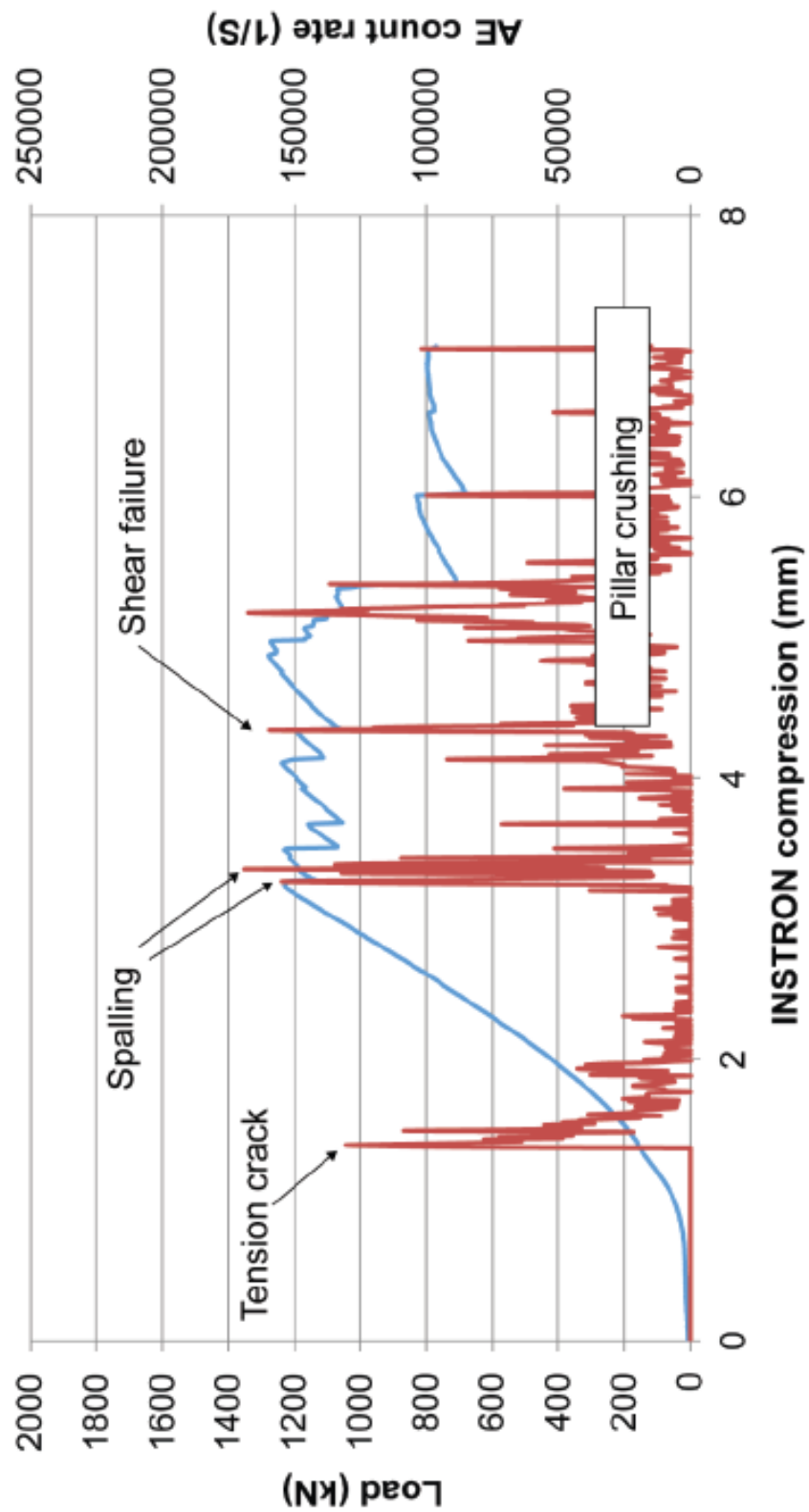


Figure 4.4: Comparison of AE rates with loading and observations in small scale tunnel simulations (Kusui and Villaescusa, 2016).

4.5 Discussion

Whilst it is obvious that there has been extensive research undertaken in the field of mining seismology, most of the research has been undertaken with the exclusion of geological models and without incorporation of large-scale structures.

Heal, 2010 states that *“There has been substantial research undertaken in the field of quantitative seismology and there is a good understanding of the seismic source mechanisms and seismic data analysis techniques”*.

Whilst there has been substantial research undertaken, it is debatable that there is a good understanding of the seismic source mechanisms and the data analysis techniques. These concepts have often been developed independently of any knowledge of the rock mass and do not take into consideration the rock mass characteristics and its inherent heterogeneity.

The following excerpt from Hudyma, 2008 indicates this lack of understanding:

“...if a fault is slipping, not all of the events recorded near the fault will be fault-slip events. Some of the events will be secondary rockmass re-adjustments to the fault-slip on nearby geological discontinuities (such as joints, dykes and other conjugate features). The seismic characteristics of these secondary events will be strongly related to the local rockmass and stress conditions at the point of the secondary re-adjustment, and may be dissimilar to the predominant fault-slip failure mechanism. Often secondary seismic events occur in close proximity to the primary fault slip failure. It may not be practical or possible to try to separate or clearly distinguish the secondary event mechanism from the primary event mechanism. Ultimately, any seismic analysis technique will have to be able to tolerate the occurrence of extraneous secondary seismic events”.

More recent research suggests that large-scale structures play a much larger role in the cause of mining induced seismicity than previously assumed. Heal, 2010 found a strong correlation between structures and rock mass damage. From 254 cases of excavation damage as a result of seismic events he found that approximately 59% of cases coincided with the existence of structures close to the excavation.

Large-scale structures are normally inhomogeneous in nature. Cross-cutting structures contribute to this heterogeneity. Furthermore, strain can only accumulate in unbroken rock. All seismic events represent a release of accumulated strain and failure. Whether that failure results in a large regional adjustment along a large-scale structure, or a small localised adjustment is a function of the rock mass and the inherent loading conditions.

Several authors have attempted to include fault models in the analysis of clusters (e.g. Hudyma, 2008). However, the clusters are not generated based on the structural models but rather are compared with the models after clustering has been undertaken. This results in the analyses being highly subjective and based on the interpretation of the person undertaking the investigation.

The current analysis techniques proposed in the ACG generic seismic risk management plan (SRMP) (Mikula et al., 2008) are somewhat circular in their argument. Clusters are generated based on the spatial distribution of seismic events and then groups are created for clusters with like characteristics (such as S:P ratio and Energy Index). These characteristics are then analysed to determine the failure mechanism for the group.

Linear elastic modelling (both 2D and 3D) has been referred to extensively throughout the seismic literature. Whilst many of the results suggest a good correlation with the conclusions of the reports, the determination of the input parameters for the rock mass is still somewhat vague and empirical.

Conclusions based on damage observations such as those by Heal, 2010, can be misleading as they are based on the response of the excavation surface. Frequently there is not a detailed understanding of the conditions of the excavation boundary prior to the event or a proper assessment of the conditions. The suitability of the ground support systems is also often not questioned. Further discussion on this point is outside the scope of this thesis.

5. Current mining seismic data analysis

Data analysis is undertaken after the seismic data have been processed. This often involves importing the base seismic data into an analysis package from the processing software. In Australia the predominant analysis packages are MSRAP developed by the Australian Centre for Geomechanics (ACG) as part of the MERIWA project M386 and VANTAGE™ developed by IMS to complement the processing software TRACE™.

Vantage™ *“is used to visualise and study micro-seismicity both spatially and temporally”* (Institute of Mine Seismology, 2013).

The basis of MSRAP lies in clustering of seismic events based on spatial and temporal characteristics (Hudyma and Potvin, 2009). The analysis method (included in this chapter) is applied to either the entire dataset or individual clusters. Further discussion on the validity of this method is included in the following sections.

The generic seismic risk management plan (SRMP) (Mikula et al., 2008) provided to sponsors of MERIWA project M386 (Mine seismicity and rockburst risk management project-Phase III) suggests the following parameters should be included in the analysis of mining seismic data:

- Event Magnitude,
- Event location,
- Frequency magnitude analysis,
- S:P-wave energy analysis,
- Magnitude time history analysis,
- Instability analysis,
- Diurnal Analysis,
- Daily histogram analysis,
- Omori re-entry analysis.

A review of several confidential mine site seismic hazard management plans suggests that mines sites typically analyse subsets of this list depending on local conditions. These parameters all fit within the bounds of where, when and how much – generally this is the order in which they are analysed. The exclusion of geology is the biggest limitation of the analysis process recommended in the SRMP. These parameters are reviewed in the following chapters. The theory and research regarding each parameter are provided. Each parameter is analysed using examples from the mine site data. A comparison of the results of analysis using the typical seismic data and the analysis of the data specific to the large-scale structures was undertaken to determine if improved results can be achieved.

Note that instability analysis consists of the interpretation of the energy index (EI) and cumulative apparent volume (CAV). These parameters are reviewed separately.

5.1 Location

The location of each event is derived from data recorded by the seismic monitoring system. It is usually the first parameter to be analysed. Locations are used to determine zones of seismic activity by assessing short term convergence of events (clustering) and in the assessment of larger events. Safety of underground personnel and excavation damage are the primary focus of both assessments.

5.1.1 Background

A description of the calculation of location and other basic seismic parameters can be found in Appendix 1. The accuracy of the location of a seismic event is highly dependent on many factors. Mendecki, 1997, states that *“the location error depends on the following factors:*

- *Errors in the arrival time determination.*
- *Inadequate knowledge of the velocity model.*
- *Inaccuracy in the station co-ordinates.*
- *The method of solution.*
- *The spatial distribution of stations with respect to the event.”*

Furthermore, the quality of the waveform (amplitude variation with time) and processing can also have a large impact on the accuracy. Whilst some of these factors can be quantified, most cannot. The compound error is near on impossible to quantify and hence is generally ignored during analysis.

Single link (SLINK) and complete link (CLINK) clustering used to group events together spatially. This method is purely based on the proximity of one seismic event to another and does not consider local geological features or rock mass characteristics. Whilst it is possible for the operator to assign clusters to relevant features manually, this task is arduous and often not undertaken. Consequently, detailed analysis of individual clusters may not relate to the rock mass behaviour.

Hudyma and Potvin, 2009 state that MSRAP uses “*spatial, temporal and seismic source parameter data*” characteristics to automatically create clusters. An example of spatial clusters is provided in Figure 5.1. The cluster names in the example suggest they are associated with geological features. However, this association is purely subjective based on visual proximity to features. There are two circled clusters labelled “Stiff dyke” (1 and 2). These clusters are seemingly associated with an intrusive feature; however, both clusters are spherical in shape and ill defined.

The “soft dyke” that is indicated in the example (shown by the dashed line) has four individual clusters located along its extent. Analysis of indicators, such as those in the following sections, is likely to be misrepresentative of the actual mechanisms of failure for the entire structure. This has the potential to lead to inaccurate interpretation of the seismic hazard of the feature.

Hudyma and Potvin suggest that the following parameters are used for temporal clustering:

- “*Median S-wave to P-wave energy.*”
- *The b value from the Gutenberg–Richter frequency – magnitude relationship.*
- *The x axis intercept (a/b) from the Gutenberg–Richter frequency–magnitude relationship.*
- *The temporal increases in apparent stress.*
- *Diurnal and phasor analysis.*
- *Trends from daily event histograms.*
- *The presence of large seismic events in a cluster.*
- *Patterns in event magnitude from a magnitude–time history analysis”.*

The exact methodology for temporal clustering is not detailed and it is unclear how it is undertaken. Furthermore, Wesseloo and Potvin, 2012 state that “*spatial clustering has formed the basis of MS-RAP analysis methods in the past and continues to be an important part of the seismic management and analysis system*”. They suggest that the clusters are combined to form groups based on similar seismic characteristics and analysis is then undertaken on the seismic group (called the seismic source).

They clearly state that no method exists for automating the grouping of the seismic clusters. Hence, the process of defining seismic clusters for analysis is subjective, based on the experience of the operator and the knowledge of the site conditions.

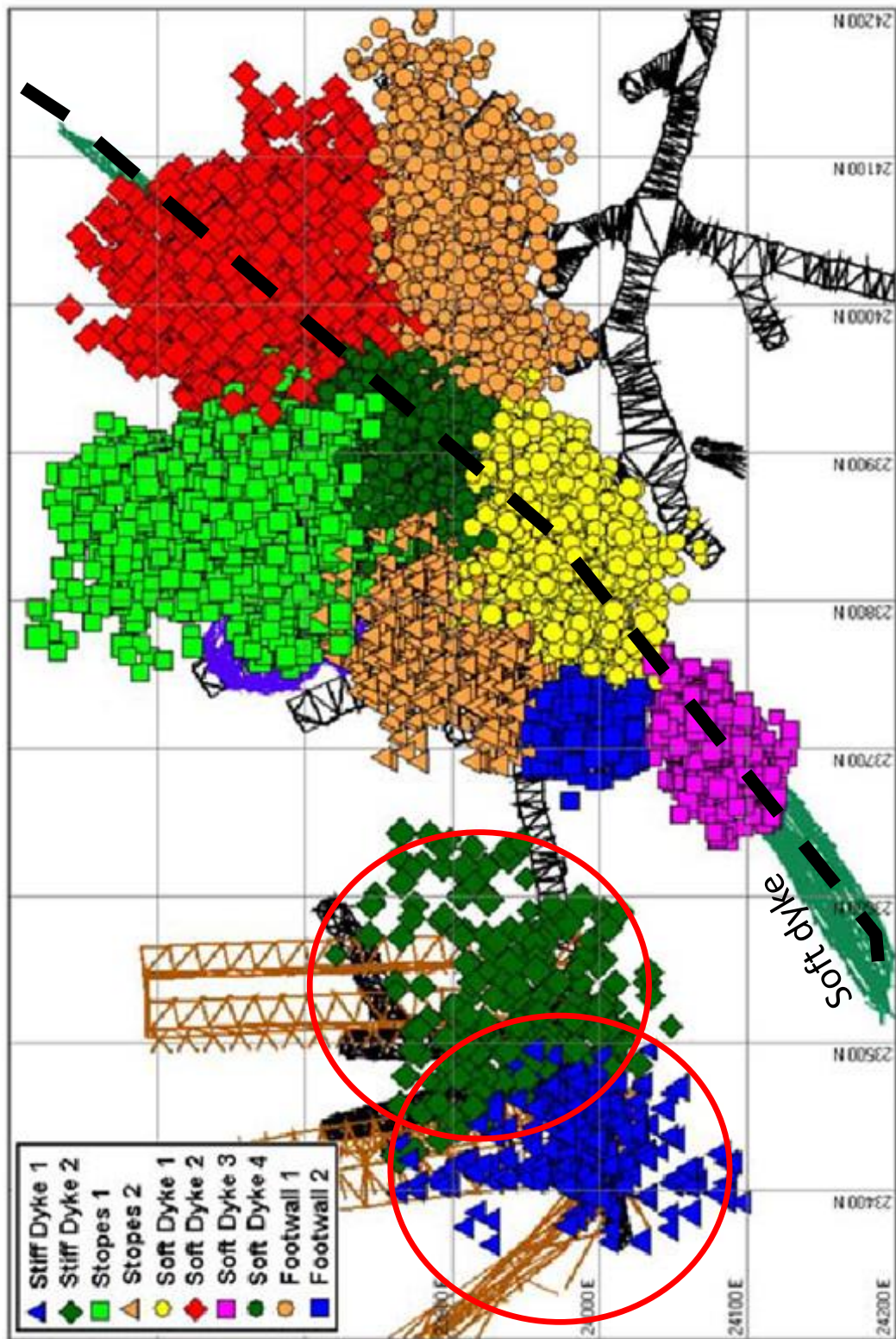


Figure 5.1: Clustered seismic data (Hudyma and Potvin, 2009)

5.1.2 Application and Discussion

As discussed, clustering data using spatial and seismic source characteristics without relation to geology introduces bias into the interpretation of the data and consequently limits the applicability of the analysis. Chapter 2.2.5 describes the method of creation of the structural data subsets used in this thesis. This methodology removes the location subjectivity surrounding geological features. All events analysed in the following chapters are assumed to be related to large-scale structural failure. Figure 5.2 is an example of the seismic event locations associated with the Black Swan Feral Fault. Figure 5.3 provides the locations of events that were associated with the Feral Fault using the ACG “group” approach. The number of events using the ACG approach was 679 whereas using the domain method the total number of events was 4950.

Regardless of the method of seismic event grouping, distributions alone provide little-to-no information regarding the seismic behaviour of the structures. Comparison with mining extraction areas such as stoping locations or other geological features can provide more information regarding the failure processes. Clustering around stope abutments (Figure 5.4) suggests seismicity may be controlled by mining activity. This was particularly observed in the faults associated with the Mt Charlotte mine. Care must be taken in this assumption where barren regions are controlled by structures (i.e. intercepting dyke or fault offsetting the ore body) as is the case at Mt Charlotte. Clustering is also often associated with cross structures. This is particularly the case for the Esmeralda FaultB_C structures (Figure 5.5) where the majority of events were clustered around intersecting dykes.

Seismicity distributed evenly across an entire structure with little to no clustering can indicate larger regional instability. Additional care must be taken in analysing large datasets with extended time frames as progressive failure cannot be identified.

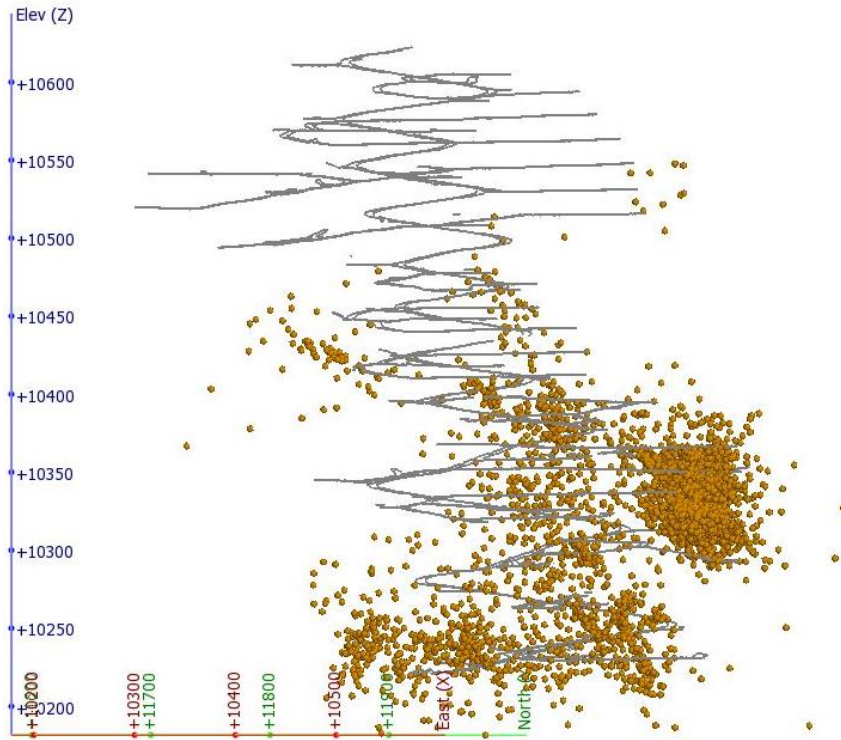


Figure 5.2: Events related to the Feral Fault. The locations of the events alone do not provide adequate information for detailed analysis.

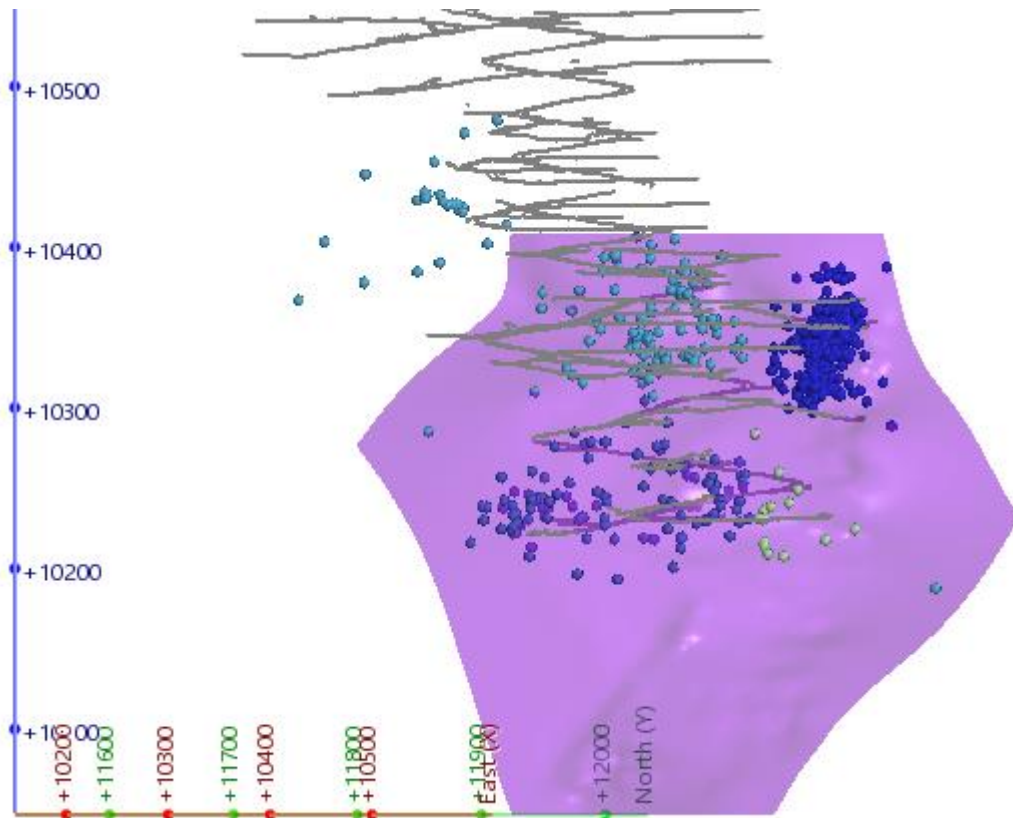


Figure 5.3: Feral Fault “groups” using the MS RAP method.

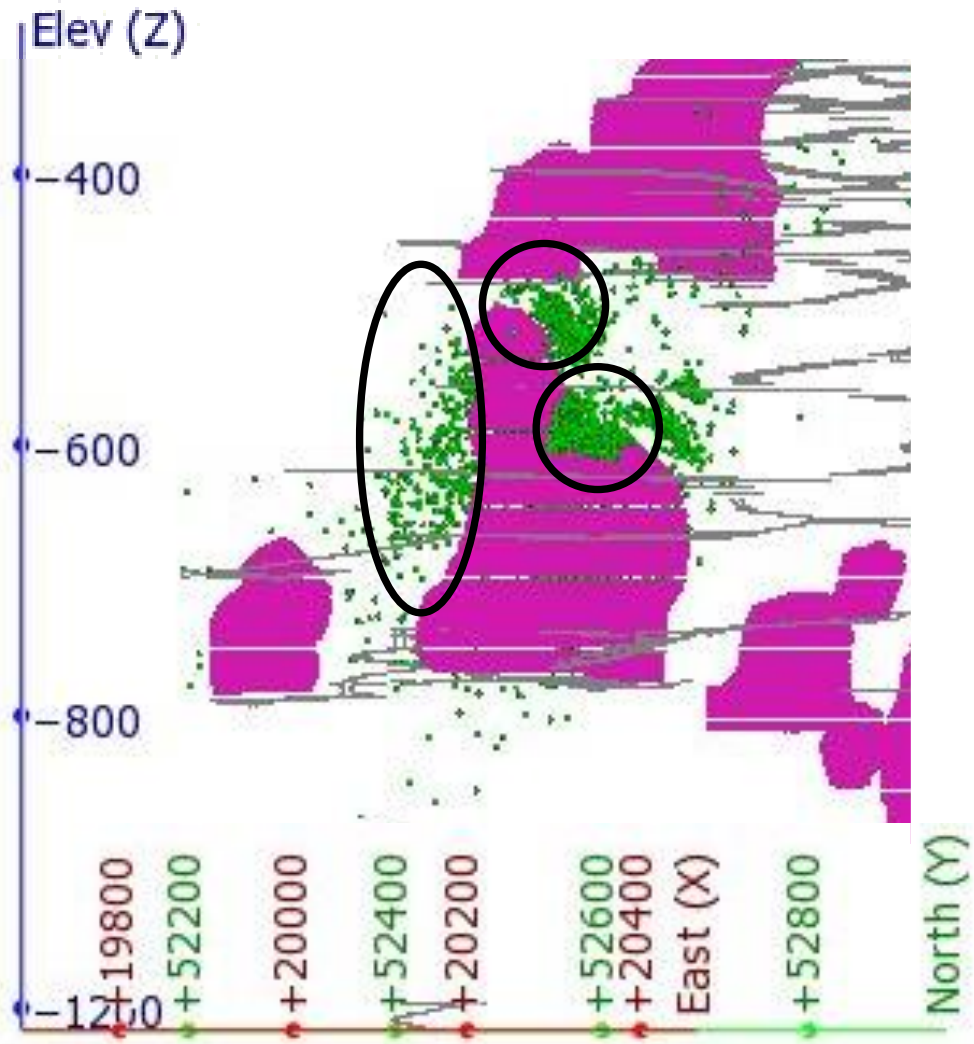


Figure 5.4: Events for the Flanagan Fault demonstrating clustering around stope abutments.

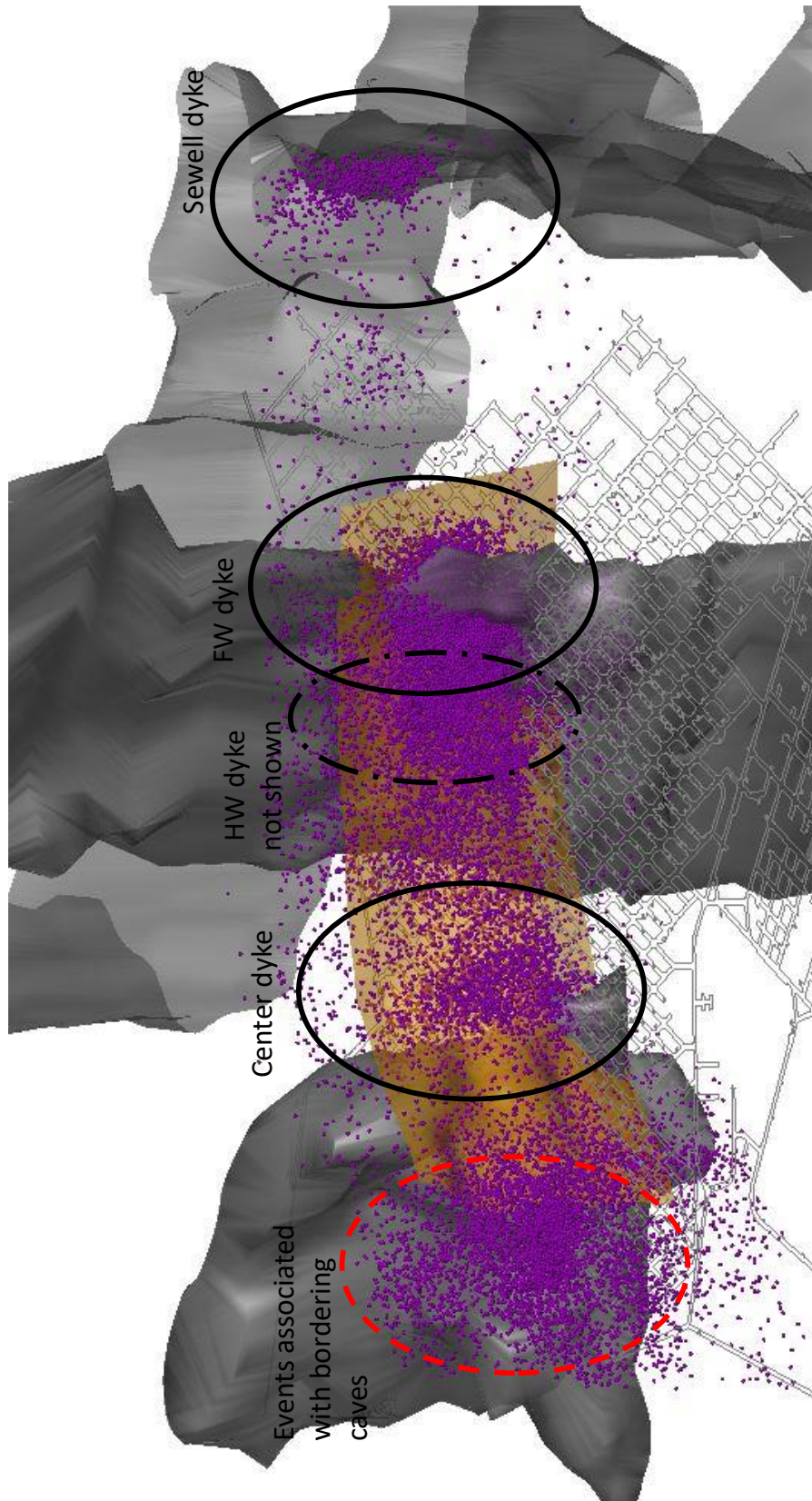


Figure 5.5: Clustering of events on Esmeralda FaultB_C structure shows a strong correlation with intersecting geological features.

Whilst seismic location is the most important seismic parameter, analysis in isolation from other parameters is of limited benefit. Some of the following analysis incorporates parameters such as magnitude with location. This can assist in identifying areas of higher seismic risk but is still limited in its value.

Arguably the second most important seismic parameter is time. Without temporal analysis it is difficult to determine the progression of the formation of these clusters and how they relate to each other in time. This is particularly relevant when comparing with mining extraction. Figure 5.6 is an example of how temporal analysis can be used to track failure progression. Esmeralda Fault B_C is parallel to the direction of caving at Esmeralda. The figure indicates seismicity every 3 years from 1998. Comparison with the cave front position can provide information on the progression of failure along the fault ahead of the front. Unfortunately, this information was not available as part of this study. Furthermore, the data from 2004 to 2007 indicates a change in failure progression with the fault being active in 3 locations rather than following the typical progressive behaviour. The two sections that do not conform to the typical progression are circled. These areas correspond to intersections with dykes. This will be discussed further in Chapter 9 where fractal dimension and spatial correlation length will be used to quantify the extent of clustering on the large-scale structures. The values are calculated using a rolling dataset method enabling temporal analysis of the data.

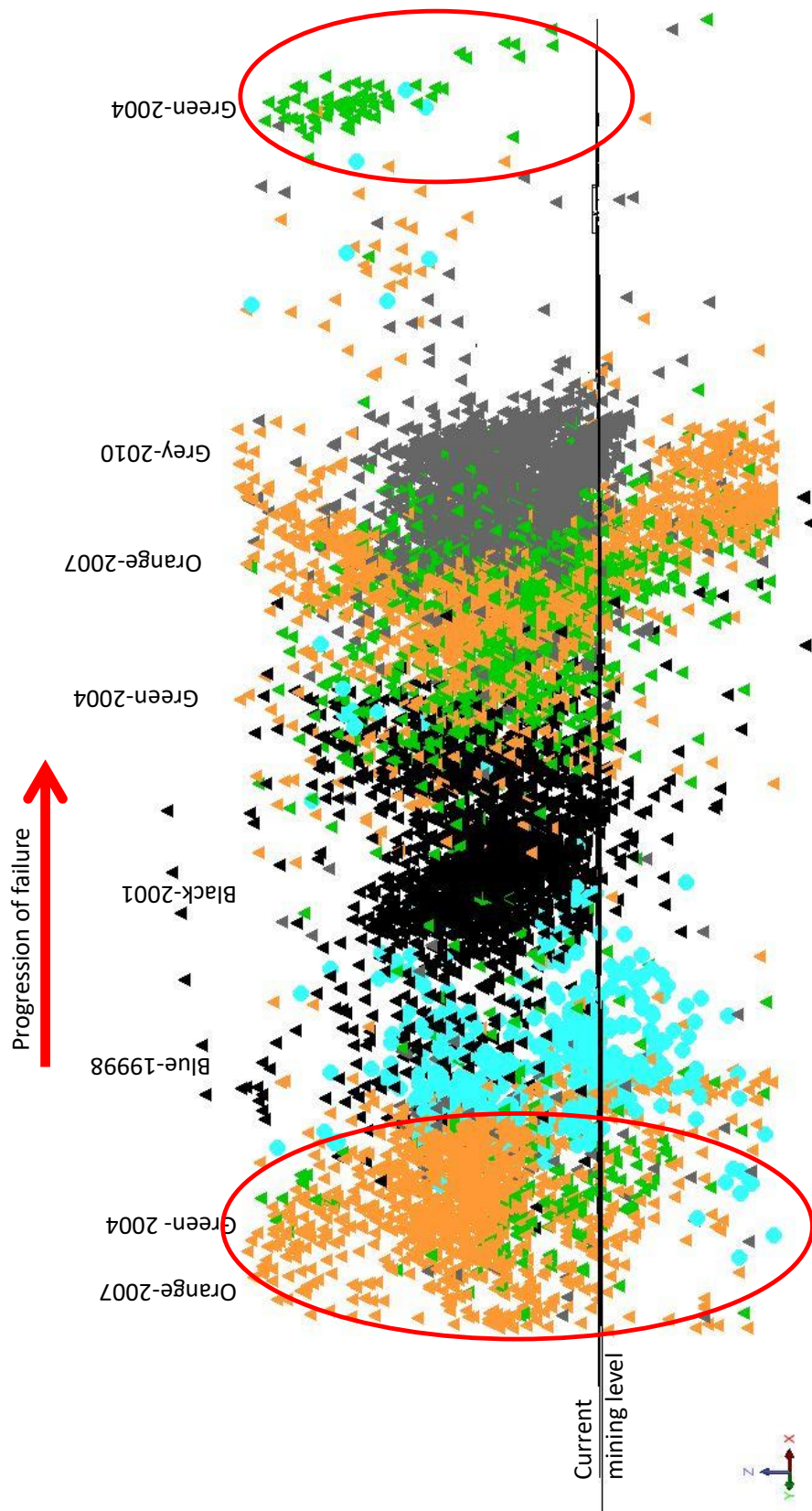


Figure 5.6: Esmeralda Fault B-C failure progression with time (looking perpendicular to the fault).

5.2 Daily histogram analysis

This analysis aims to identify large increases in seismicity rates. Large increases concentrated within limited areas indicate damage to the rock mass and hence increases in loading of ground support systems. Generally, with the occurrence of concentrated increases in seismic events, sites will investigate the specific location of the “cluster”, the cause of the increase and whether there is risk to personnel.

Overall this analysis is highly subjective and site specific. To remove some of the prejudice, sites must understand the failure mechanisms and define what constitutes a large increase and how it is relevant to the site.

5.2.1 Application and discussion

Generally, with the occurrence of concentrated increases in seismic events, Mine Site Engineers will investigate the cause of the increase and evaluate whether there is risk to personnel. Figure 5.8 and Figure 5.7 show the daily histogram for Argo Mini Dyke and the Mt Charlotte’s Maritana Fault.

The Mini Dyke data trend is erratic with increases and decreases occurring on a daily basis. This is typical of most mining seismic data. Analysis solely based on the current daily trends is likely to be ineffective due to the sporadic nature of the data. To overcome this, it is necessary to examine the trend of the data rather than the individual daily values. For this purpose, a 14-day moving average has been added to these charts. Increases and decreases in the seismic behaviour of the structure are much more apparent and the base level of seismicity is easily identifiable.

The Maritana Fault data suggest a large increase in the seismic event rate on the 2nd of July 2008. However, this chart alone does provide information for analysis. To assess large increases in events effectively it is necessary to assess where these events are occurring and the relationship of these events to mining activity.

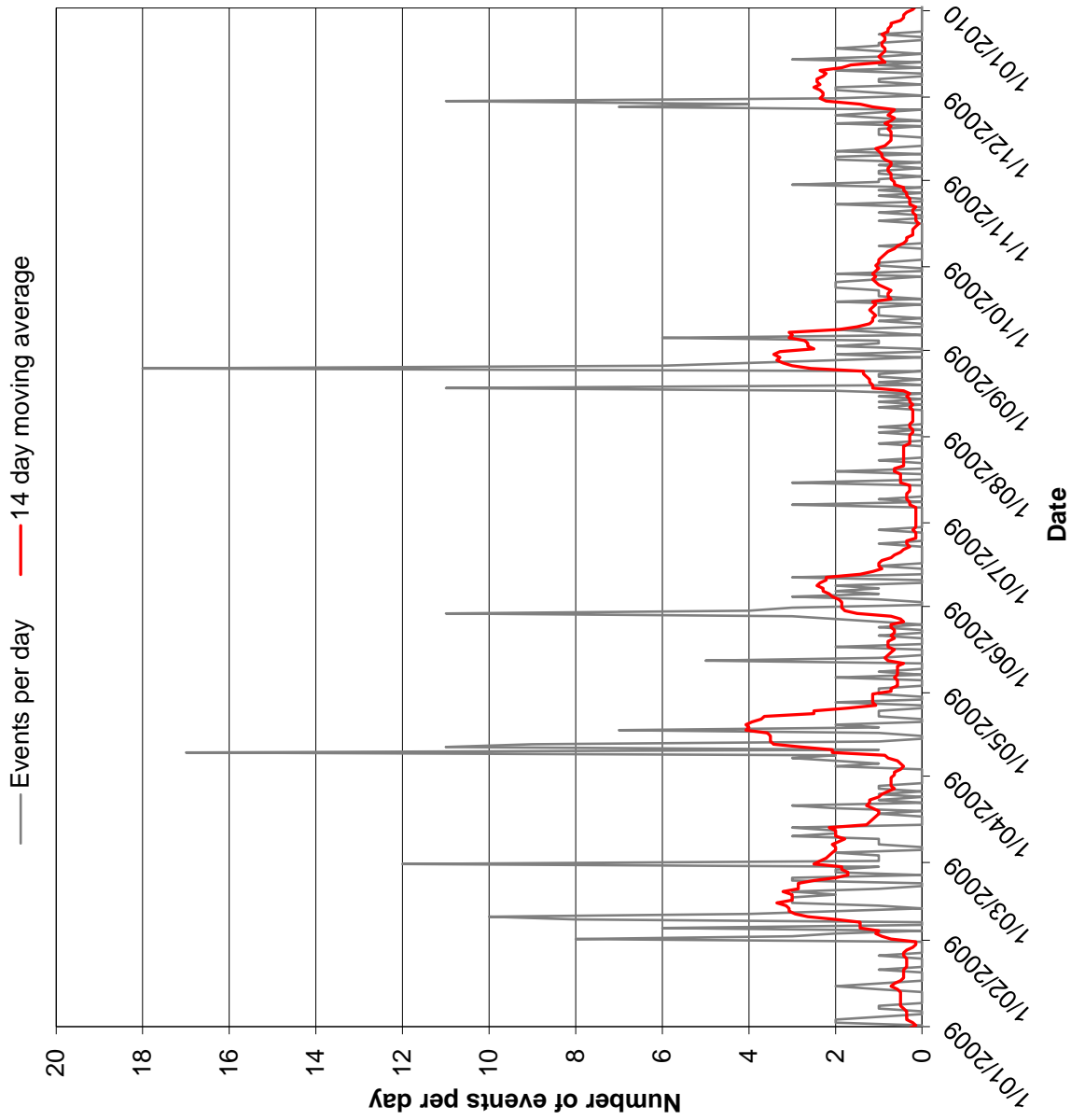


Figure 5.7: Daily events for the Argo Mini Dyke.

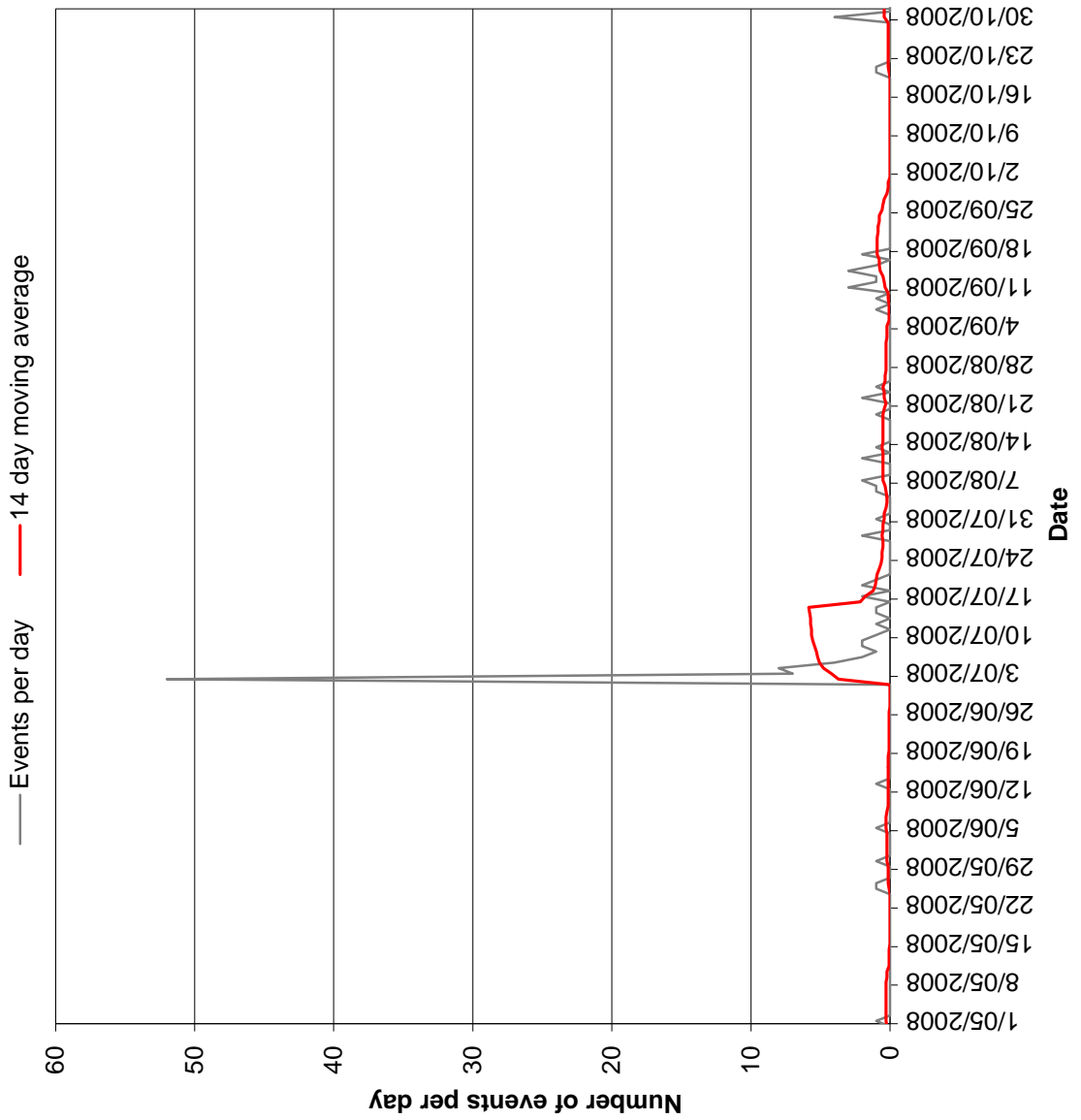


Figure 5.8: Significant increase in event rate on Mt Charlotte's Maritana Fault.

5.3 Event Magnitude

Magnitude is a generic term used to describe the size of an event based on specific seismic source parameters. The most common scales in Earthquake seismology are the Richter Scale and the Moment Magnitude Scale. However, mining seismic analysis tends to utilise different scales better suited to smaller events. Several of the more commonly referred to scales are discussed in Appendix 1. All magnitude scales have logarithmic bases (base 10).

The IMS monitoring system calculates a range of magnitudes. Most sites use the local magnitude (M_L). The default local magnitude formula is:

$$M_L = \alpha \log E + \beta \log M + \gamma$$

Equation 5.1

Energy (E) and Moment (M) are calculated by the monitoring system software and α , β and γ are constants. These constants are typically set at the default system values of 0.272, 0.392 and -4.62 respectively. Whilst some sites use the default constants, other sites have modified the constants or use an alternative magnitude scale (typically the Moment Magnitude Scale). The formula used at each site is detailed in previous chapters.

Magnitude is typically analysed in several ways. Within the local magnitude scale, mine sites will have an empirical magnitude threshold that defines a “significant” event. This threshold is usually developed as a result of observation of damage related to single seismic events. Usually, events over this threshold are analysed individually, with detailed back analysis undertaken. These investigations generally comprise of a site inspection and a back analysis of the cause of the event and may be combined with a risk assessment. The threshold values for each site were discussed in Chapter 3.

Magnitude is also analysed temporally. This analysis is called the magnitude-time history analysis and is discussed in the following chapter.

5.3.1 Magnitude - time history analysis

This analysis involves the qualitative study of the magnitude - time history chart for consistencies in the data. The time-history chart consists of a magnitude vs time chart and a cumulative number of events chart (Figure 5.9). Mikula et al., 2008 suggest this analysis "*may be the most insightful technique for analysing mine seismicity data*". They suggest the following points can indicate the seismic hazard:

- The behaviour of the cumulative number of events suggests behaviour of the rock mass. It is advised that a stepped behaviour suggests a strong correlation between rock mass response and blasting and that a constant rate of change is more likely to represent fault-slip type movements.
- The largest event can indicate the seismic hazard.
- The "*number of large events gives an indication of the rockmass damage potential*".
- An increasing trend in the magnitude suggests rock mass failure is increasing.

The largest event concept suggests that the largest event indicates that another larger event is possible. It also implies that an increasing trend in magnitude indicates that rock mass damage presents a higher seismic risk.

It is illogical to assume that magnitude is ever increasing. A seismic event represents failure of the rock mass. Once failure has occurred in a portion of the rock mass it is no longer capable of storing energy that can be released as a seismic event. Consequently, the seismic risk is reduced rather than increased.

Despite the above points the following section applies this analysis to the structural domain data subsets described in Chapter 3. The aim of this analysis is to determine if there is any improvement in the analysis by using the domain method.

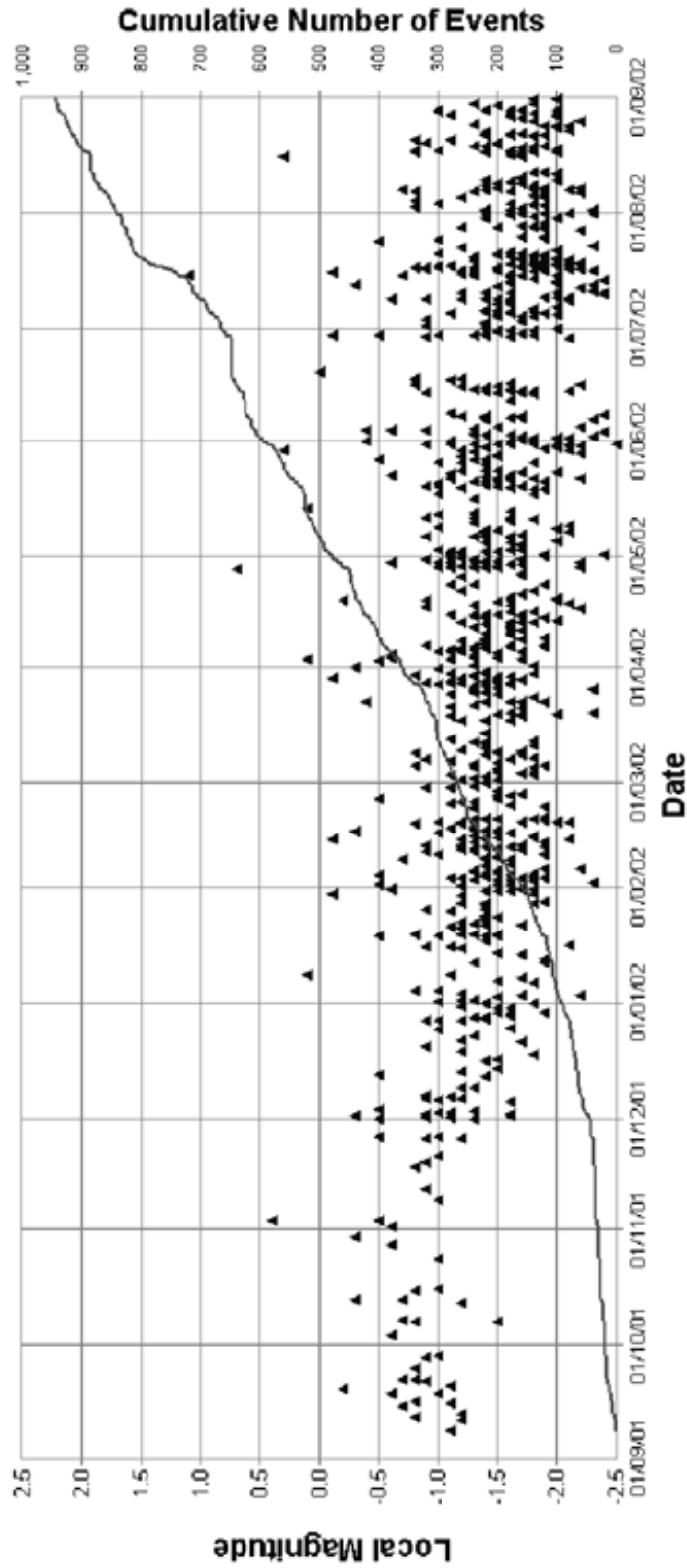


Figure 5.9: Magnitude time history chart (Mikula et al., 2008)

5.3.2 Application and Discussion

The magnitude - time history is assessed by assessing the following charts:

- cumulative number of events chart.
- magnitude vs time chart.

5.3.2.1 Cumulative number of events

The cumulative number of events over 3 years for the NE Group 1 faults and the Flanagan Fault are provided in Figure 5.10 and Figure 5.11, respectively. The NE G1 faults typically show consistent seismic patterns with steady increases in the cumulative event rate. Theoretically this does not indicate stick-slip style movement. In contrast the Flanagan Fault cumulative event rate is stepped which according to the theory suggests a strong correlation with mining activity. This analysis is purely qualitative and is open to subjectivity. It is possible for large-scale structures to display irregular failure patterns and yet still be representative of a fault-slip mechanism. This is particularly likely in undulating structures or structures with strong asperities. Chapter 8 further discusses these concepts and presents a more quantitative methodology for analysing the cumulative event chart.

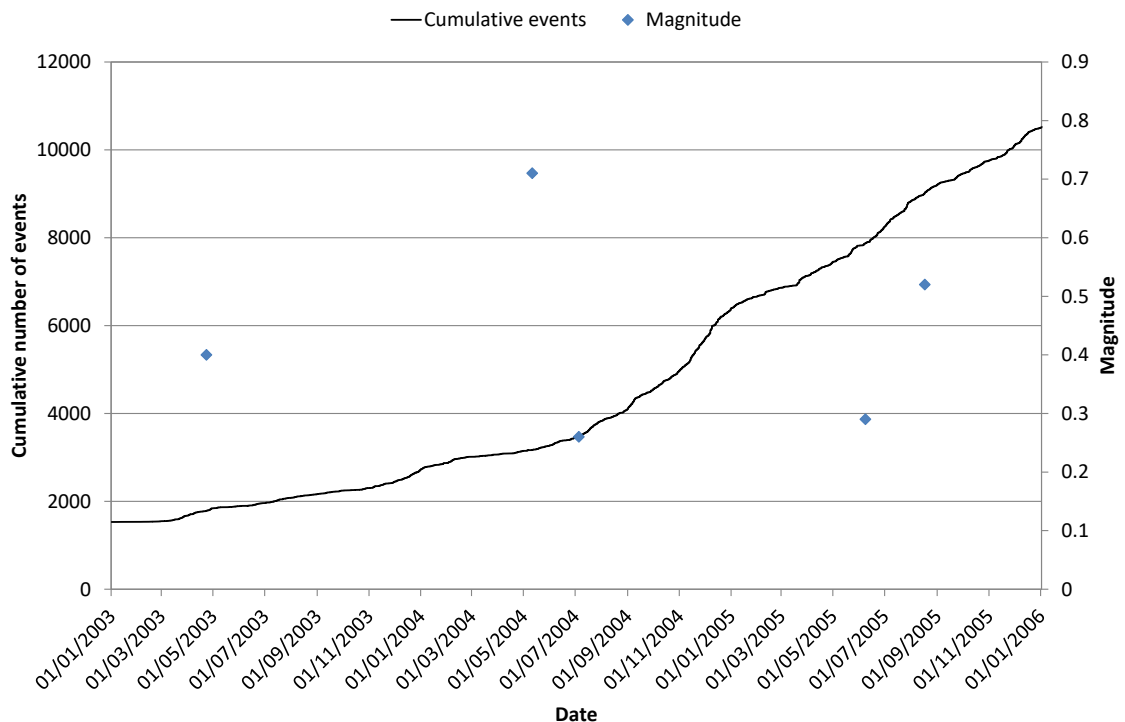


Figure 5.10: Cumulative event chart for North East Faults Group 1.

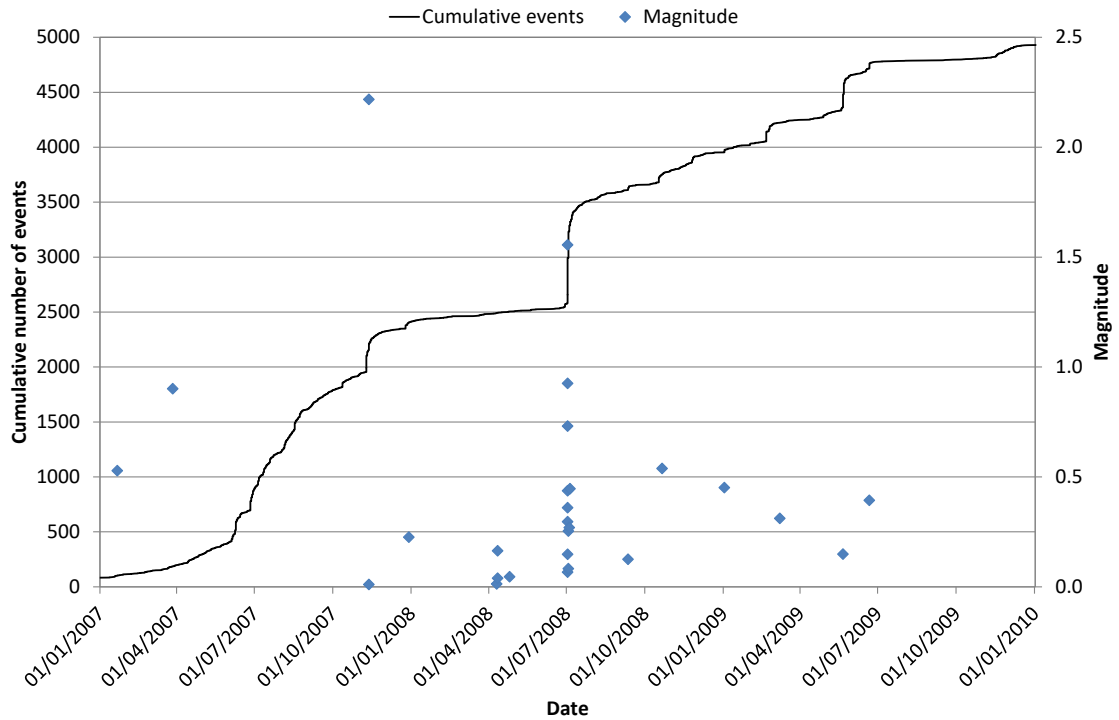


Figure 5.11: Cumulative event chart for the Flanagan Fault.

5.3.2.2 Largest event and magnitude trend

The quantification of the magnitude - time history is not provided in the SRMP. A rolling maximum magnitude was used to determine if the largest event concept could be proven. The maximum magnitude for a set number of events was determined. In this case 100 events have been used. An example is provided in Figure 5.12. The example shows the magnitude time history for the “Total Black Swan Database” (TBSD), the “Feral Fault Groups” (FFG) allocated in MSRAP and the “Feral Fault Structural Domain” (FFSD). The maximum magnitude on the Feral Fault occurred in November 2004. Due to the minimal numbers in the FFG the trend line for this data has the least accuracy – there is no change in the maximum magnitude prior to the event. The TBSD data is generally erratic and patterns cannot be ascertained from the data. The FFSD data does show an increasing trend prior to an event. In this case it appears that taking out the subjectivity of selecting data on structures has led to an improvement in the analysis. Further analysis of trends in magnitude will be undertaken and discussed in Chapter 10.

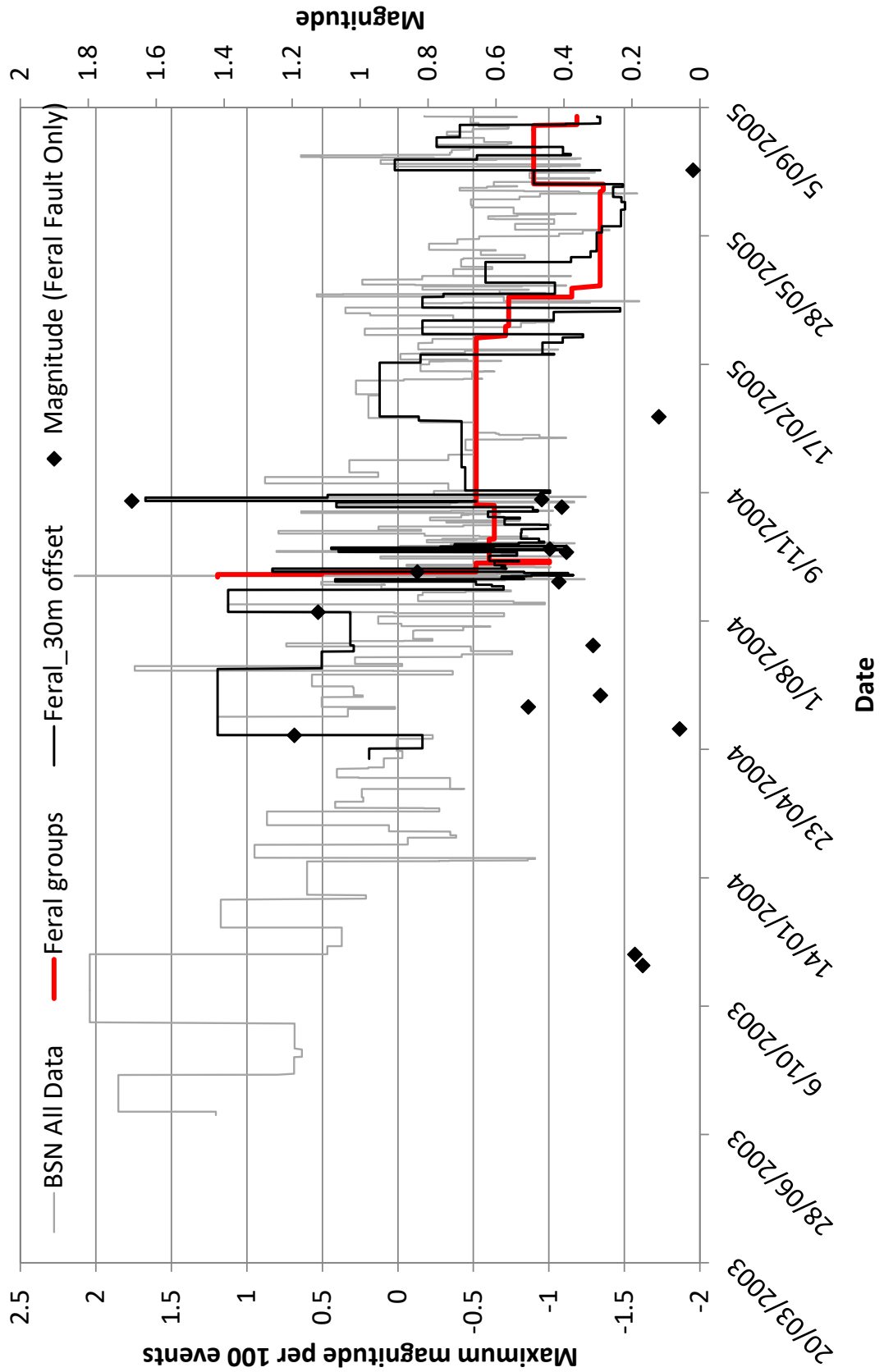


Figure 5.12: Rolling maximum magnitude (100 events) for TBSD (grey), FFG (red) and FFSD (Black).

5.4 Frequency - magnitude analysis

A frequency - magnitude analysis examines the relationship between the number of events occurring within a magnitude bracket ($N(M)$) and the magnitude (M). This relationship is known as the Gutenberg – Richter relationship and is expressed using Equation 5.2:

$$\log N(M) = a - bM$$

Equation 5.2

Essentially, the log relationship base is 10, thus for each magnitude bracket (whole increment) with N number of events, the next magnitude bracket down will have N^{10} events. For example, when b -value equals 1 then for every event of $2M_R$ there will be 10 events of $1M_R$ and 100 events of $0M_R$. The primary assumption is that the relationship between magnitude and the number of events exhibits a log-linear relationship. Whilst most authors conclude that this assumption is correct and “*the magnitude-frequency relation holds for virtually all magnitude ranges, in all locations, and at all times*” (Rundle, 1989), some authors suggest that the behaviour is non-linear at the upper and / or the lower ends of the scale (e.g. Aki, 1987). Figure 5.13 indicates an example of the log - linear curve. It indicates a non-linear portion of the curve at the lower end of the magnitude scale; however, this is likely to be a function of the limits of the sensitivity of the monitoring system rather than a function of the natural data. Consequently, this portion is ignored in the following analyses.

The constants a and b are determined by the line of the graph (Figure 5.13). The constant “ a ” is the intercept of the line represented by Equation 5.2 with the y axis (i.e. when $M = 0$). This value indicates the rate of seismicity; the higher the value, the higher the seismic event rate. This value is not commonly analysed using this chart. The constant “ b ” is known as the b -value and represents the slope of the line. A higher b -value suggests a steeper gradient and consequently a lower risk whereas a shallow angle suggests a greater number of large events and consequently a higher risk. The intercept of the linear trend with the x axis is said to indicate the largest likely event.

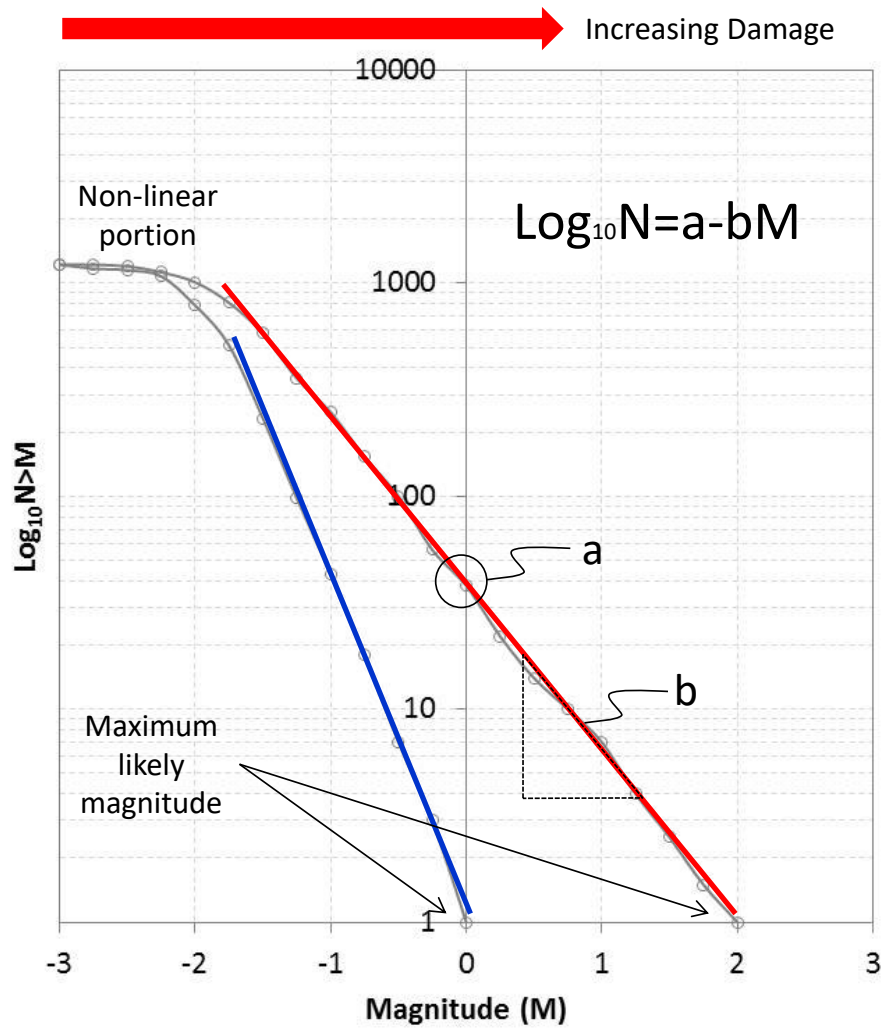


Figure 5.13: b-value theory. The red line suggests a fault slip mechanism whereas the blue line suggests “stress change”.

The SRMP suggests b-values less than 0.8 (shallow slopes as shown in red) indicate that the failure mechanism of the seismicity in the dataset is predominately fault-slip. Higher values in the range of 1.2 – 1.5 (steeper slopes as shown in blue) suggest the predominant failure mechanism in the dataset is related to “stress change” (associated directly with stress change due to mine blasting and void creation). This is not substantiated by basic failure mechanism principles. “Stress change” is likely to be the cause of all seismic events – without a change in stress the rock mass remains in equilibrium and hence no failure should occur. Furthermore, fault movements are not necessarily independent of intact rock mass failure. Most faults are not homogeneous and for failure to occur the rock mass must have the ability to accumulate strain or deform. Further discussion on this is included at the end of this chapter.

5.4.1 Application and discussion

The analysis of the b-value on mine sites is usually conducted on the entire dataset or clusters of data with a fixed time scale. Theoretically the static b-value should be close to 1. Mikula et al., 2008 state that b-value can be assessed in the following way:

“Fault-slip related seismicity frequently has a very low b-value (often less than 0.8). Seismicity as a result of stress change (associated directly with stress change due to mine blasting) frequently has a b-value in the range of 1.2 to 1.5”.

Table 5.1 provides the static b-value for each structure domain dataset described in Chapter 3. For comparison the total site b-values are provided as well as MSRAP fault “group” b-values where the group data was available. The combined b-values have been determined using all group data associated with a fault. Traditionally each group would be analysed separately.

Table 5.1: Static b-values for large-scale structures.

Site	Structure	Domain data b-value	Total Site b-value	MSRAP combined groups b-value
Argo	A1 Shear	1.1	1.3	1.1
Argo	North Dyke	1.1		1.4
Argo	Mini Dyke	1.1		0.9
Esmeralda	Fault B_C	1.5	1.6	
Esmeralda	Fault P	1.5		
Esmeralda	FW Diorite	1.7		
Kanowna Belle	Fitzroy Fault	0.8	0.9	
Kanowna Belle	NE Fault Group 1	1.0		
Kanowna Belle	NE Fault Group 2	0.8		
Mt Charlotte	Flanagan	1.0	1.0	
Mt Charlotte	Maritana	0.9		
Mt Charlotte	Reward	1.1		0.7
Black Swan	Feral	1.0	0.9	1.0
Mt Lyell	Great Lyell	0.7	0.7	0.7

The values suggested by Mikula et al., 2008 are not supported by these results. The results show all the large-scale structures, aside from the Esmeralda and Mt Lyell structures, have a b-value close to 1 supporting observations from earthquakes. The results from Esmeralda structures are typically higher than the other sites whilst the Mt Lyell results are lower. The overall site b-values are also at the extreme ends of the scale for both sites. The Esmeralda results are not related to the number of events in the catalogue as the Kanowna Belle structures have low b-values but a similar number of events to the Esmeralda structures. The difference in the b-values may be mechanistic given that Esmeralda employs a cave mining method whereas the other sites utilise different forms of stoping, however, Mt Lyell is a sublevel caving operation which should theoretically also present a similar failure mechanism.

There is a large body of research that suggests that the b-value varies with time. Scholz, 1968 determines that b-values can indicate temporal variations that indicate changes in the micro-fracturing process.

Some studies have examined the temporal changes of b-values for mining induced seismicity. These studies have been conducted on limited datasets and have proven inconclusive. Temporal analysis of the b-value is not commonly used in mining applications. This aspect of the frequency magnitude analysis will be examined as part this thesis and is discussed in Chapter 10.

5.5 Diurnal Analysis and Omori re-entry analysis

The Omori law is based on the principle that *“a strong earthquake is followed by weaker ones and when it is violent and destructive the number of minor shocks following it may amount to hundreds or even thousands”* Omori, 1894.

The theory suggests that for a period after a seismic event the rock mass is excited producing an increase in the seismic event rate which then decreases exponentially with time (Figure 5.14). The increase in seismicity is proportional to the magnitude of the event. The larger the event the greater the increase in seismic activity. Additionally, the magnitude of the subsequent events will not be greater than the magnitude of the original event.

Excitation of the rock mass can also be caused by stress redistribution around newly created voids. In hard rock underground mining excavations are created or extended by blasting using explosives. Blasting typically occurs at set times during the day. Most sites experience increases in seismicity following blasting times. Diurnal analysis is simply the analysis of the time of day of seismic events and specifically the decay of the event rate after blasting (Figure 5.15). The diurnal analysis is used to determine when the seismic rate falls below an empirical safety threshold. This empirical threshold is used as safety guideline for personnel entering underground excavations after firing. In the case of Figure 5.15, an increase in seismic rate can be clearly identified in the 5am time bracket. By 7am seismic rates have returned to typical levels.

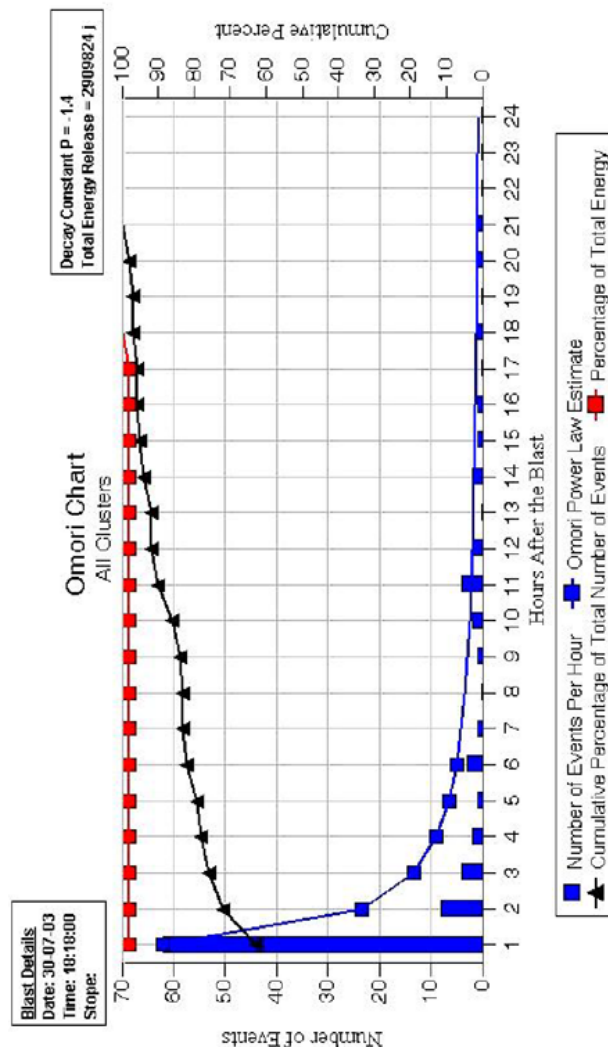


Figure 5.14: Example of Omori analysis (ACG, 2005).

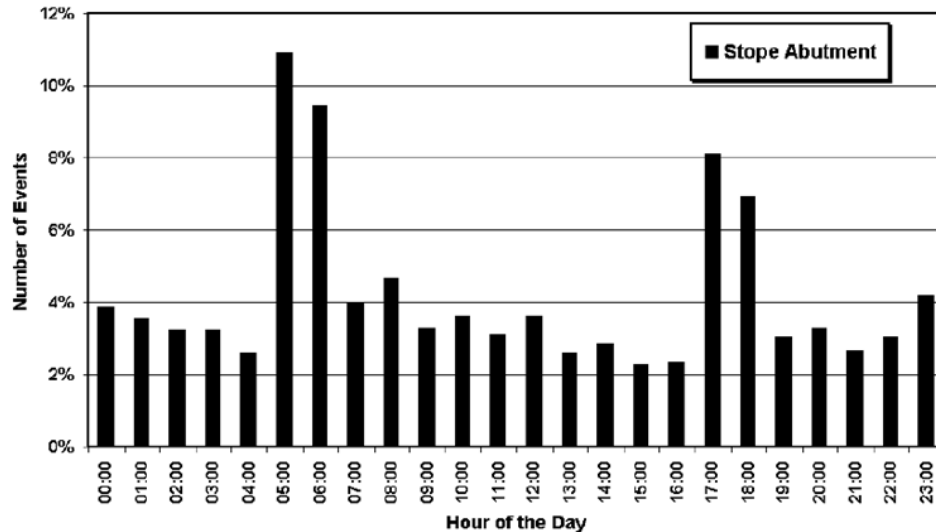


Figure 5.15: Example of diurnal analysis (Mikula et al., 2008).

It is widely reported that many sites experience large events outside of blasting times, the time of which cannot be predicted. Gibowicz and Kijko, 1994 state that events close to mining excavations are typically controlled by the rate of mining; however, events on geological discontinuities (which tend to have higher magnitudes and hence be of higher risk) have an erratic time distribution.

Hudyma, 2008 states that “*the seismic response varies according to the local rockmass failure mechanism and the distance to mining influences*”. Events associated with blasting are “*small and in close proximity to the blast*”. Events “*more distant from mining*” exhibit a random time distribution.

Events outside blasting related exclusion times pose the greatest risk to underground personnel; however current analysis techniques cannot adequately identify or reduce this risk.

5.5.1 Application and Discussion

Diurnal and Omori analyses are used for determining re-entry periods for excavations after blasting. Analysis of the large-scale structure data indicates that only the Kanowna Belle structures have a strong correlation to blasting (e.g. NE faults group 2 - Figure 5.16). Investigation of the NE Faults G2 seismicity trends shows that overall seismic activity correlates with blasting. However, 63% of events over magnitude $0M_L$ occur outside blasting times. All other structures show little or no clear blasting trends with a significant number of events (large and small) occurring outside blasting times.

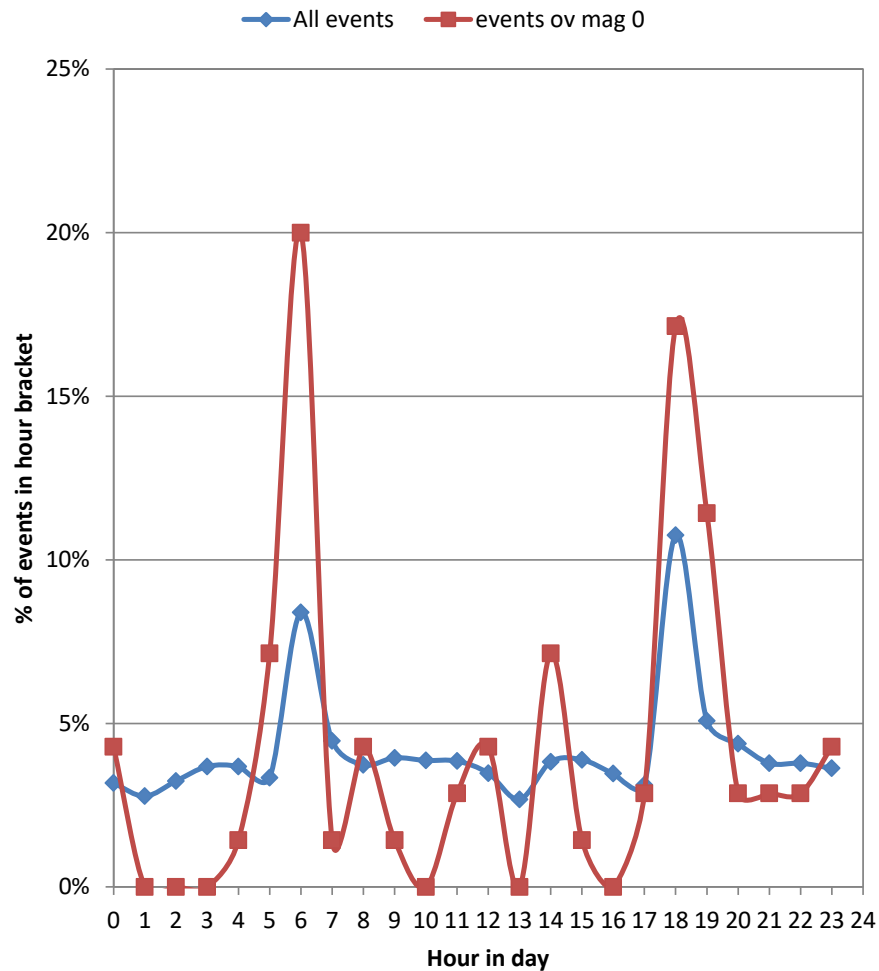


Figure 5.16: Diurnal analysis for Kanowna Belle NE faults group 2.

The Argo A1 Shear has 36% of events occurring in the 6am and 6pm time windows suggesting a weak correlation with blasting. A further 36% occur between 7am and 9am. The additional 28% occur at random times throughout the day. The North Dyke and Mini Dyke show even less correlation with blasting times. This is likely to be due to the orientation of the dykes perpendicular to the ore body.

Mt Charlotte uses re-entry analysis extensively in its seismic hazard management; however diurnal analysis indicates little correlation to blasting (Figure 5.17).

Diurnal analysis may be used for specific individual blasts to determine if the seismic rate has returned to background levels prior to allowing re-entry into working areas. However, as a generic analysis technique it cannot eliminate the risk of exposure of operators to large seismic events.

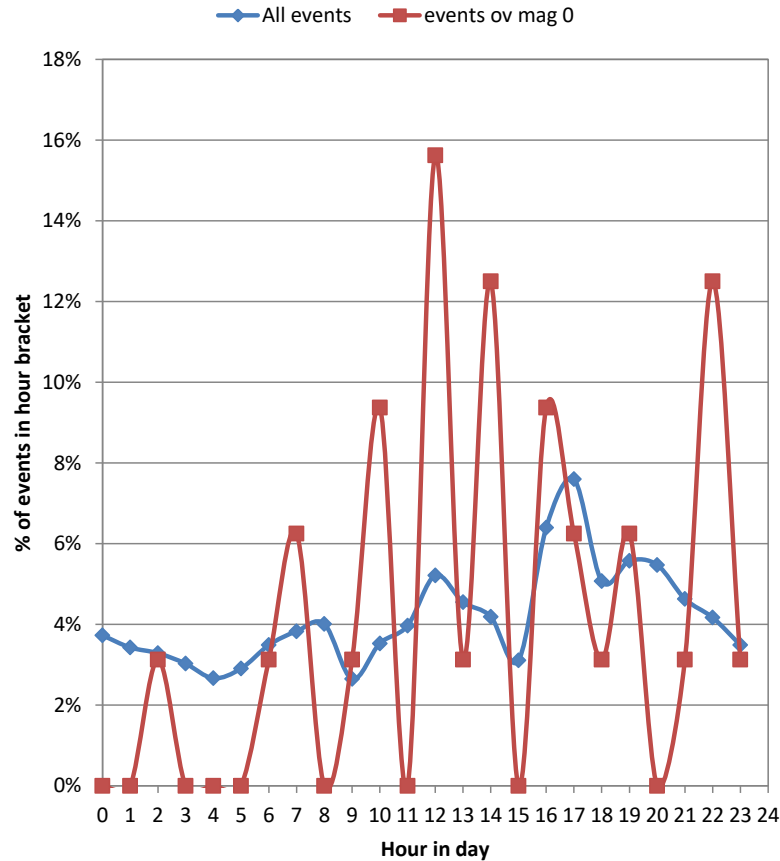


Figure 5.17: Diurnal analysis for Flanagan_1 fault.

5.6 S:P-wave energy analysis

Seismic wave forms consist of a compression wave (P wave) and a transverse wave (S wave). Energy is determined from the waveform by calculating the area under the wave velocity - time curve. The ratio of the S wave energy to the P wave energy is suggested to represent the failure mechanism occurring during the seismic event. The SRMP states that “*for fault-slip type events, there is considerably more energy in the s-wave than in the p-wave (Boatwright and Fletcher, 1984), with the ratio of the s-wave energy to the p-wave energy frequently greater than 10*”. Boatwright and Fletcher, 1984 conducted a study on 9 small seismic events (<1.7M). They allude to discrepancies in the S:P wave. The results of the study suggest that there is bias in energy estimates due to either “*a predominantly nodal source / receiver geometry for the P waves or a set of site specific effects which systematically amplify the S wave motion*”. A specific numerical value for the S:P wave is not suggested by the authors.

Gibowicz et al., 1991 studied over 100 seismic events from the Atomic Energy of Canada Limited's underground research laboratory in Manitoba. They found that the S:P ratio ranged from 1 to 90 with 40% of the events being less than 10. In explaining the low S:P wave energies they state the following:

“The observed energy depletion in S waves could be explained by a nondouble-couple focal mechanism of some events, enriching the energy radiated in P waves, implying that, although in most cases shear failure is the dominant mode of failure around the shaft excavation at the Underground Research Laboratory, tensile failures or most probably shear failures with tensile components can also occur. Increasing evidence shows that this is especially true for small events induced by mining, although nonshearing components are usually found to be rather small (e.g., Rudajev and Sileny, 1985; Sileny, 1989). In the case of the granite at URL, the fractures may be first initiated by a mechanism rich in tensile components prior to shear failure becoming dominant along the same fractures”.

In general it has been found that many mining events typically have low S:P ratios and there are some indications from focal mechanism studies that this is the result of a complex failure mechanisms (Gibowicz and Kijko, 1994). Beck, 2004 suggests that this analysis is qualitative rather than quantitative. He states that “*extreme values would be required for strong confidence*” and that his experience indicated that the measure is not absolute and is frequently “*ambiguous*” and “*misleading*”.

Despite the recommendations, it is typical practice to use an S:P ratio of 10 as a determinant value for failure mode. Values less than 10 indicate “*strain, bursting, volumetric stress change events and caving related events*” (Hudyma et al., 2003). The SRMP suggests that rather than volumetric changes the failure mechanism is tensile failure. In contrast the SRMP suggests values over 10 indicate a fault-slip mechanism. To define such a precise number for one case or another is incorrect - and not supported by the research. Very little is understood about the mechanics of failure at the source of a seismic event. It may be possible to distinguish between the failure modes of events that have a very low S:P ratio and events that have a very high S:P ratio. However, all seismic events are complex failures that cannot be characterised so succinctly.

5.6.1 Application and Discussion

The theory presented in the SRMP states that fault slip failures should exhibit S:P ratios over 10. Accordingly, the data in the structure subsets defined earlier should indicate a fault slip mechanism. Table 5.2 provides the S:P ratio results for the Mine Site structures. The analyses indicate that the Esmeralda and Mt Charlotte structures exhibit strong fault-slip characteristics whilst the Kanowna Belle faults display volumetric failure characteristics. The Argo and Black Swan faults indicate both fault-slip and volumetric failure characteristics. These results mirror the overall site datasets. The complete Esmeralda and Mt Charlotte datasets indicate strong fault-slip mechanisms (12% and 20% <10 respectively). The overall Argo and Black Swan datasets are more evenly distributed with 42% and 49% of events having S:P ratios of less than 10. The S:P ratio for the Kanowna Belle dataset was not provided in the data from the mine site. It was calculated by dividing the S energy by the P energy. Using this methodology, 95% of events have an S:P ratio less than 5. This suggests that either the calculations or the data may be incorrect. An analysis of the S and P energies provided suggest that the individual energies do not match the total energy provided by the site. This indicates errors in the data.

Aside from the Kanowna Belle data, the results appear to support the conclusion that fault-slip events can be characterised by the S:P ratio. However, given that the structure results mirror the overall site data, the apparent correlation between S:P ratios and failure mechanisms become less conclusive. Either the failure mechanisms at all the sites in these analyses are predominantly fault-slip or the energy changes are the result of external influences. The distance of an event from the seismic sensor and interruptions (such as voids) in the ray path can cause energy diffusion prior to the wave being monitored by the seismic sensor. Furthermore, the selection of the P and S wave positions during processing can also affect the ratio.

Further work is required to more conclusively determine if the S:P ratio can indicate failure or if changes in the S:P ratio are affected by seismic monitoring and processing limitations.

For the sites where a combination of volumetric and fault-slip failure was determined (Black Swan and Argo), temporal analysis is recommended to determine if changing mechanisms can be identified. Asperities on faults can be assumed to behave like intact rock and hence exhibit volumetric failure. Fault slip failure occurs after the volumetric failure. Once an asperity has been completely fractured, fault-slip failure is more likely.

Table 5.2: S:P ratios for large-scale structures.

Site	Structure	Median S:P ratio	% S:P <5	% S:P 5-10	% S:P >10
Argo	A1 Shear	13.0	17.6%	22.4%	60.1%
Esmeralda	Fault B_C	18.0	0.4%	15.8%	83.8%
Esmeralda	Fault P	26.4	0.3%	1.2%	98.4%
Black Swan	Feral	8.8	39.6%	12.5%	47.9%
Kanowna Belle	Fitzroy Fault	0.4	93.5%	2.3%	4.2%
Mt Charlotte	Flanagan	26.9	2.6%	10.6%	86.9%
Esmeralda	FW Diorite	18.6	0.2%	13.7%	86.0%
Mt Charlotte	Maritana	20.1	8.3%	17.0%	74.8%
Argo	Mini Dyke	9.7	18.8%	32.4%	48.8%
Kanowna Belle	NE Faults Group 1	0.4	99.2%	0.5%	0.4%
Kanowna Belle	NE Faults Group 2	0.3	97.5%	1.2%	1.3%
Argo	North Dyke	15.2	17.4%	20.6%	62.0%
Mt Charlotte	Reward	27.6	3.7%	8.6%	87.7%

5.7 Energy Index (EI)

The generic SRMP (ACG, 2008) suggests that instability analysis “involves comparing two seismic source parameters, Energy Index (EI) and Cumulative Apparent Volume” (CAV). The energy index is said to be a measure of “the concentration and accumulation of stress in the rockmass”. Instability is said to occur when the EI decreases and the CAV increases.

Energy Index forms the basis for many analysis techniques. Mendecki, 1997 states that energy index is the “ratio of the observed radiated seismic energy of that event to the average energy radiated by events of the seismic moment taken from the logE versus logM relation”.

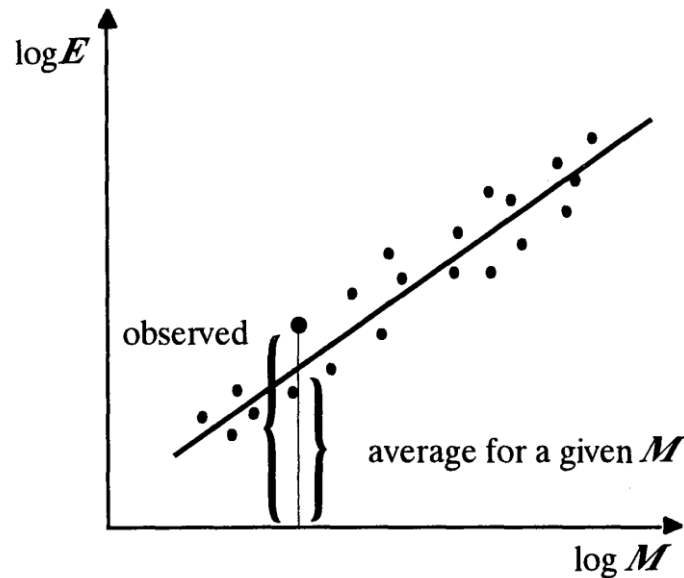


Figure 5.18: Concept of Energy Index as provided by Mendecki, 1997.

Essentially, the log energy vs log moment chart is used to determine a linear relationship between the two parameters (Figure 5.18). This relationship forms the average calculation. The ratio of each event is then divided by the average to achieve the Energy Index. More simply it can be described using the following formula:

$$EI = \frac{\text{measured Energy}}{\text{Average energy for given Moment}}$$

Equation 5.3

The SRMP suggests that “when an area... is accumulating stress the EI for related seismic events is greater than one”. Comparatively when EI is less than 1 less energy is being expended than expected and hence the “structure starts to fail” (ACG, 2008).

5.7.1 Application and Discussion

Fundamentally, the flaw in the Energy Index concept lies with the log energy / log moment chart. Figure 5.19 represents the Feral Fault data and is representative of most mine site data. The distribution of the log Energy value for any given Moment is significant. As these axes are logarithmic, the actual spread of values is more pronounced. Defining a linear relationship with such large variations is misleading. The r^2 value of the linear regression of the log Energy / log Moment charts for each Mine Site structure is typically less than 0.5. The exceptions are the Esmeralda structures which have r^2 values of approximately 0.65. Statistically, these values do not represent a strong trend. Furthermore, as indicated in Figure 5.19 the linear trend does not match the data at the upper end of the moment scale. This is partially due to the logarithmic distribution of events. The significant number of small events compared with large events heavily biases the linear equation resulting in a poor match at the upper end of the scale. Most large events will occur above the linear regression line and hence the EI will be greater than one. This supposedly relates to stress accumulation rather than failure. However, significant releases in energy are related to failure. The theory of this analysis is non-intuitive.

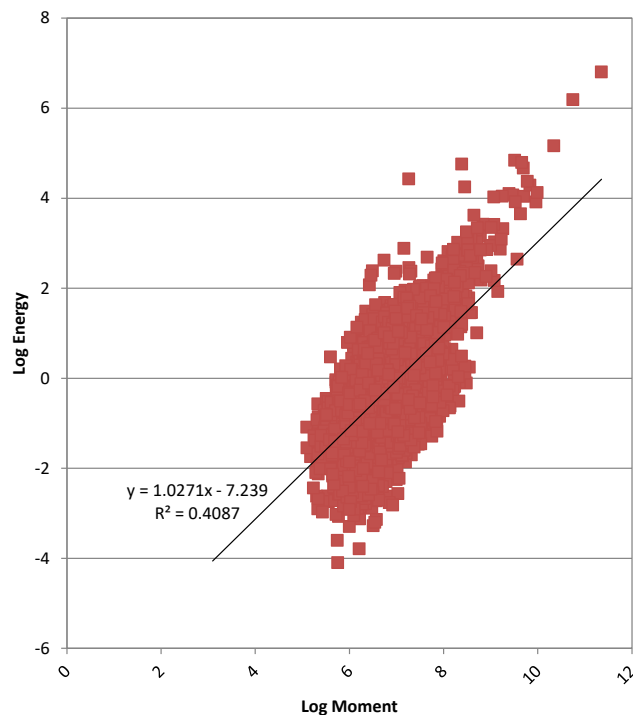


Figure 5.19: Log Energy / Log Moment chart for Feral fault.

5.8 Cumulative Apparent Volume (CAV)

The cumulative apparent volume (CAV) is suggested to be a measure of the rock mass deformation. It represents the volume of rock undergoing inelastic straining during a seismic event. It is determined by relating apparent stress, moment and energy (Equation 5.4). Apparent stress is described by Boatwright and Fletcher, 1984 as the “*ratio of the radiated energy to the moment multiplied by the rigidity (shear modulus)*”. They suggest the apparent stress is an estimate of stress release at the seismic source. Further information on apparent stress is provided in Appendix 1.

$$V_A = \frac{M_o}{2\sigma_A} = \frac{M_o^2}{2\mu E}$$

Equation 5.4

This is one of the few analyses in the current techniques that use temporal analysis. Instability is said to be indicated by an increasing CAV and a decreasing EI (Figure 5.20).

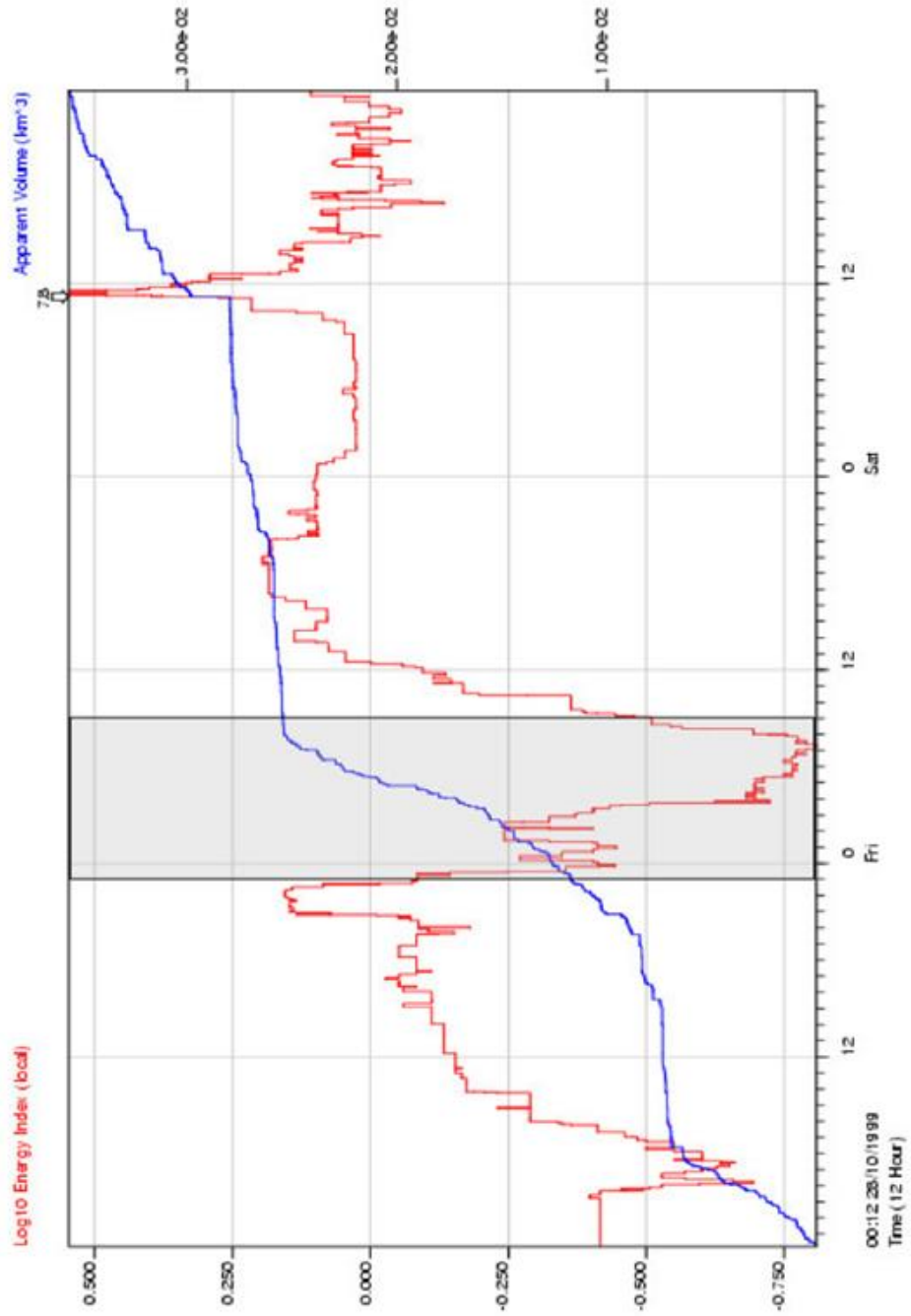


Figure 5.20: Example of CAV and EI analysis from Mendecki et al., 2010.

5.8.1 Application and Discussion

Figure 5.21 shows the results for the Flanagan Fault between January 2007 and December 2008. Whilst the CAV can be seen to increase significantly as a result of a significant number of events in a short period of time (days), moderate to large events appear to have a varying effect on changes in the CAV. Theoretically, a large event should initiate large stress changes which should represent large volumetric changes.

In 2001 Esmeralda experienced on-going instability that resulted in loss of production and necessitated rehabilitation of large areas of the undercut level. Back-analysis suggested the instability was caused by movement along the P system faults. FaultP_1 is central to the area of instability. If CAV is an indicator of instability, sharp increases in CAV should be evident between late 2000 and 2002. The CAV results for this period are provided in Figure 5.22. Two periods of instability are recognisable between 2001 and 2003. The first is between August 2001 and March 2002 and the second is between November 2002 and April 2003. Site reports suggest that damage was being observed by mid 1999. Throughout 2000 and early 2001 rock falls and large seismic events caused significant damage. These events are not indicated in the results. Furthermore, changes in CAV closely mirror the cumulative event rate. These results show that in application the theory is inconclusive. The cumulative event rate is a simpler measure to calculate and accordingly the value of a CAV analysis must be questioned.

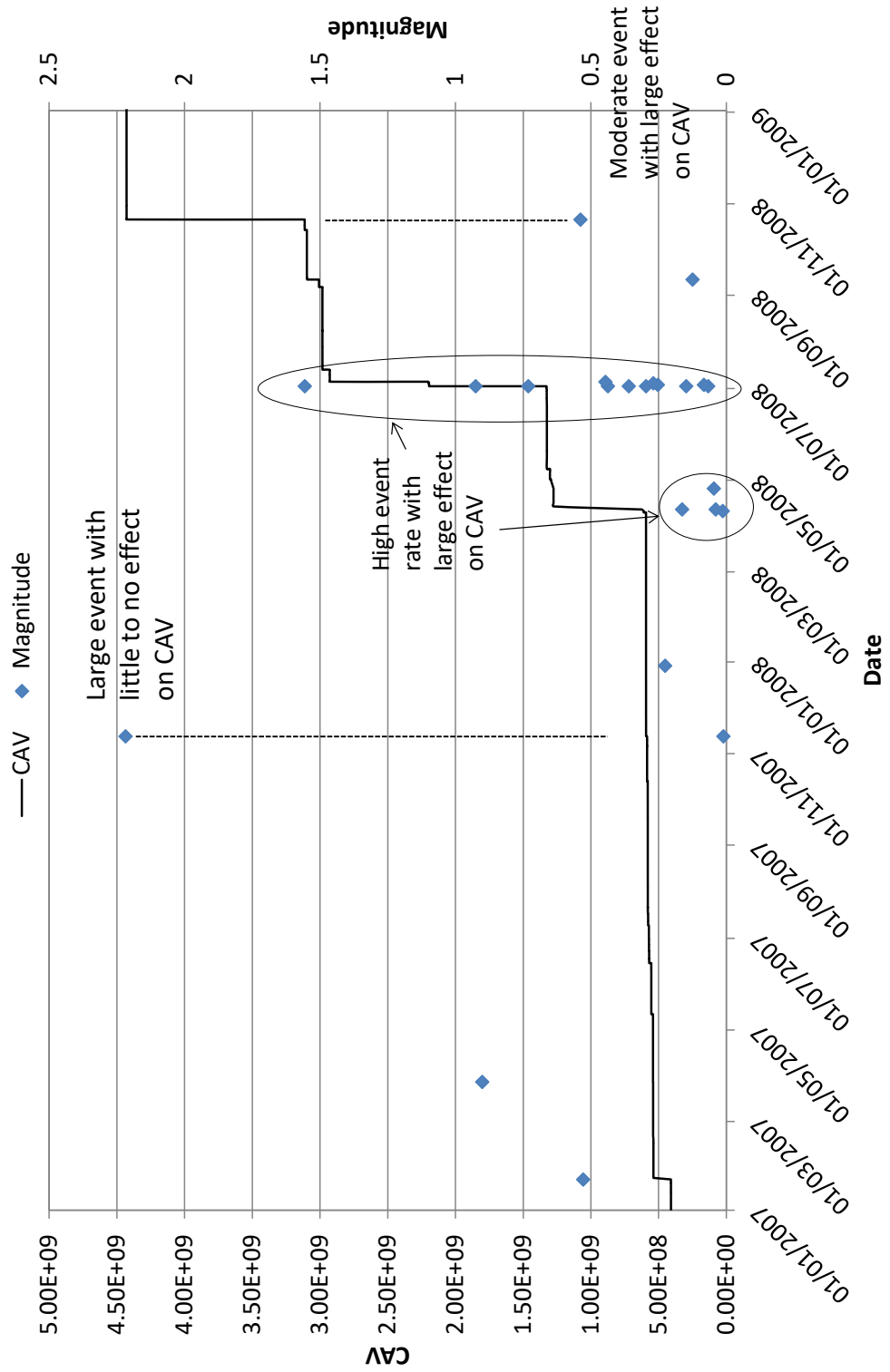


Figure 5.21: Cumulative apparent volume for Flanagan Fault.

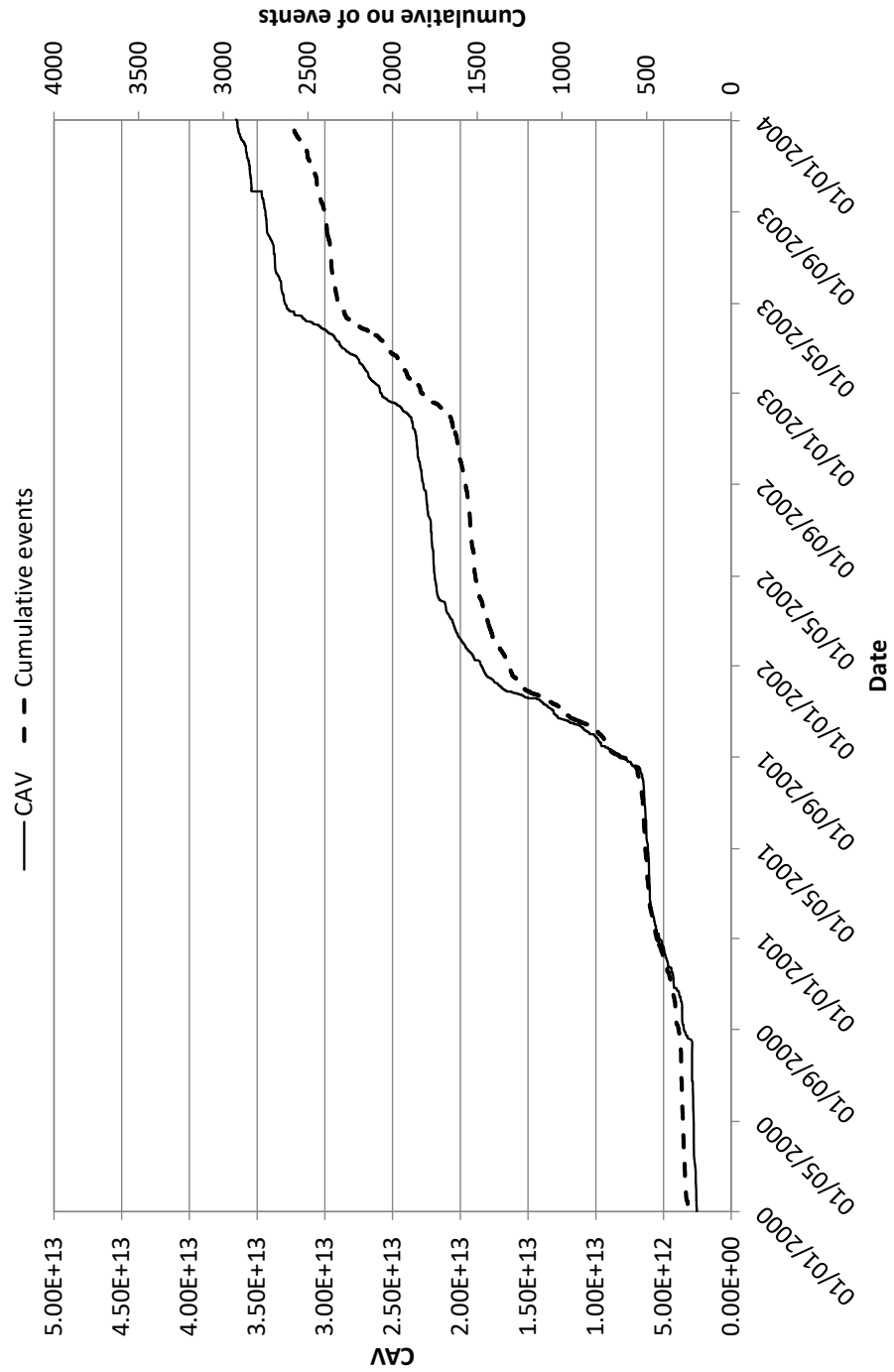


Figure 5.22: CAV results for Esmeralda FaultP_1 between Jan 2000 and Dec 2003

5.9 Discussion

The incorporation of structural domaining into the analysis techniques proposed in the SRMP (Mikula et al., 2008) assists in removing some of the bias in the current clustering methodologies. Both the location and the cumulative event rate can provide reasonable insight into the seismic behaviour of the rock mass. Some of the results of the analysis (such as the S:P ratio and the Energy Index) were predetermined by the analysis technique and the validity should be seriously questioned. The other parameters when used in combination with a detailed knowledge of the rock mass and the mining environment can assist in determining the seismic behaviour of a structure. The circumstances in which this benefit may be achieved appears to be very site specific. What may apply at one site may not apply at another.

Despite the limited apparent success of these techniques, fundamentally, static analysis of data without consideration of time – even clustered spatially or constrained by geology - does not indicate the changing nature of the mining environment. The creation of voids in the rock mass induces stress changes that are transient. Localised areas may initially experience an increase in stress and yet with increasing extraction undergo complete stress reduction. The methodology for the current analysis techniques do not take this into account. This may result in the seismic hazard for a particular area being drastically overestimated. Furthermore, the current analysis techniques do not consider natural geological variations. As discussed in Chapter 4.5, geological structures are inherently inhomogeneous. Attempting to characterise their failure mechanisms as solely fault-slip or stress-induced failure is ignoring this heterogeneity.

Temporal analysis can overcome these limitations. By examining parameters over time, changes in the behaviour of the fault can be determined and thus the seismic hazard associated with these faults can be better determined. The following chapters examine research into Earthquake seismology specific to identifying and analysing rock mass failure. Some of these concepts will be used to analyse the Mine Site structural data sets. The aim of the analyses will be to determine if impending failure can be defined for mining scale structures.

Earthquake seismology research and data analysis

6. Earthquake seismology research

Due to the significant impact of earthquakes, seismology is highly researched with many government research organisations and several journals dedicated to the field. Topics include velocity models, seismic wave attenuation, back analysis of significant events, fault failure mechanisms, to name but a few. Many of the theories presented by researchers and scientists in the field of seismology are highly contentious and rigorously debated. For every concept confirmed in case studies, there are usually case studies that refute its validity. Given this, any research in the field of seismology will have proponents and opponents. To remain concise this section will provide an overview of research related to seismic indicators of the fracturing of structures specifically called precursors. It will encompass literature in both earthquake seismology and acoustic emission testing. The main theories will be tested in the subsequent chapters to determine their applicability to mining and their validity will be argued in the discussion of the results at the end of each section.

Research into precursory indications of structural failure in earthquake data has been on-going worldwide since the 1960s. Scholz et al., 1973 suggests that “*anomalous behaviour*” can be observed in parameters such as fluid pressure, electrical and magnetic fields and radon emissions. These parameters are mostly external to the mechanics of failure. The following chapters will investigate research that focuses on changes in seismic source parameters prior to a large event (failure).

6.1 Comparing seismic scales

As discussed in Chapter 1 researchers in the 1960s recognised that earthquake seismic records were incomplete. They determined that the monitoring of the testing of rock samples could simulate a complete seismic record. This led to the theory that earthquake behaviour is the same at all scales. This is referred to as self-similar or scale invariant behaviour (Mogi, 1962, Mogi, 1968, Hardy, 1972, Scholz et al., 1973).

Acoustic emission testing has been conducted since the 1960s with the aim of measuring the response of the rock mass to various loading conditions. It developed from the crack propagation and fracturing studies developed in the 1950s. Mogi, 1962a was the first to relate acoustic emission studies in rock samples to earthquake studies. He conducted a series of compression and bending tests and measured the acoustic response of the rock samples.

Modern acoustic emission testing involves monitoring micro-cracking of rock samples tested in the laboratory, typically under triaxial test conditions. Monitoring is undertaken using piezoelectric transducers attached to the sample. The sample sizes vary between 5cm x 1.6cm \varnothing (Scholz, 1968a) and 190mm x 76mm (Lockner et al., 1992). The number of sensors varies between 2 (Meredith et al., 1990) and 32 sensors (Lei et al., 2000a).

Acoustic emission testing over the last 30 years has led to two critical concepts. Firstly, that rock failure occurs in three hierarchical stages. Secondly, that each of these stages has characteristic indicators that together define precursory behaviour. These concepts form the basis of the results of this thesis and are discussed in the following sections.

6.2 Stages of failure

The concept of stages of failure was first developed in the 1970s. The stages are based on temporal changes in the nature and behaviour of the acoustic emission events. Mogi, 1962a was the first to note changes in the acoustic emission rate during testing. The results suggest four stages of failure.

“Stage (1) In this stage, elastic shocks seldom occur and the stress-strain relation is linear (elastic deformation only take place (sic)).

Stage (2) The frequency of elastic shocks is small and they take place sporadically.

Stage (3) The occurrence of elastic shocks is remarkable and their frequency increases in proportion to the applied stress. On the other hand, the stress-strain relation deviates from the linearity, that is, the non-elastic deformation is more predominant in this stage.

Stage (4) in the last stage, just before the rupture of the specimen, the frequency of elastic shocks increases more rapidly and they occur in succession. Microscopically, the main rupture is considered to begin in this stage”.

Scholz, 1968a also observed similar behaviours stating that *“At low stress, a flurry of activity occurs; this activity soon dies down to a very low level. At stresses near approximately half the fracture strength, microfracturing activity begins to build up once more and steadily increases until just before fracture, when a very rapid acceleration of activity occurs”.* This behaviour is further confirmed by Main et al., 1989, Meredith et al., 1990, Lei et al., 2000 amongst others. The observations for each of these authors are provided below; however, for clarity and simplicity Table 6.1 provides a summary of the behaviour at each stage.

Table 6.1: Summary of the behaviour of rock samples during the phases of failure.

Phase	Pre Nucleation		Nucleation (III)		Rupture
Author	Primary (I)	Secondary (II)	Quasi Static (a)	Quasi Dynamic (b)	Dynamic Failure (c)
Mogi, 1962a	<ul style="list-style-type: none"> Elastic deformation Stress strain curve linear Few AE events 	<ul style="list-style-type: none"> Sporadic AE 	<ul style="list-style-type: none"> Stress strain curve becomes non-linear Large increase in AE proportional to increase in stress 		<ul style="list-style-type: none"> Significant increase in AE just prior to rupture with multiple successive events
Scholz et al., 1973	<ul style="list-style-type: none"> Accumulation of tectonic strain Slow steady increase in effective stress 	<ul style="list-style-type: none"> Dilatancy occurs at a faster rate allowing pore water to mobilise. Mobilisation causes a drop in pore water pressure. Change in pore water pressure causes a change in compressional (P wave) velocity reducing the compressional to shear wave velocity ratio Dilatancy restricted however the effective stress continues to rise 	<ul style="list-style-type: none"> Effective stress continues to rise Saturation regained but pore pressure remains low. Compressional to shear wave velocity ratio increases. 		<ul style="list-style-type: none"> Failure cause by rising in effective stress and a rise in pore pressure.
Main and Meredith, 1989b	<ul style="list-style-type: none"> Elastic build-up of strain energy. 	<ul style="list-style-type: none"> Inelastic strain hardening due to dilatancy. 	<ul style="list-style-type: none"> Precursory stress drop Coalescence of micro-fractures. b-value maximum 	<ul style="list-style-type: none"> Pore fluid diffusion “Quasi static slip between asperities” b-value minimum 	<ul style="list-style-type: none"> “Dynamic slip of the fault behind the crack tip”
Lei et al., 1992, Lei et al., 2000a, Lei et al., 2003a	<ul style="list-style-type: none"> Mobilisation of pre-existing cracks – in coarse grained samples this may be along grain boundaries AE level increase with increasing stress levels. Most pre-cursors erratic or non-conclusive Fractal dimension increases. 	<ul style="list-style-type: none"> Begins between 65 and 90% of the final fracture strength Interaction of micro-cracks with some migrating clustering. Most common failure mode tensile failure. Fractal dimension decreases. b-value fluctuates but maximum 	<ul style="list-style-type: none"> Asymptotic increase in AE rate. Merging of clusters to form failure planes. All failure modes represented. Increase in magnitude resulting in decrease in b-value. 	<ul style="list-style-type: none"> Asymptotic increase in AE rate. 	

Scholz et al., 1973 described 3 stages of failure. He states that “*Stage I consists of the accumulation of tectonic strain, which produces a slow, steady increase of effective stress. At point b, the stress has become large enough to begin producing dilatancy at a rate faster than the rate at which pore water can flow into the newly created pore volume*”. The resultant drop in saturation and pore pressure produces a decrease in the ratio between the compressional velocity and the shear velocity. As water flows from the surrounding rock mass dilatancy is restricted causing the effective stress to rise. This is referred to as dilatancy hardening and is characteristic of Stage II.

At point “c” (beginning of Stage III) saturation is regained and the velocity ratio increases while the pore pressure remains low. Failure occurs at point d and is directly related to the continued rise of the effective stress and an increase in pore pressure as saturation increases. The basis of this model (referred to as the dilatancy model) comes from measured changes in the velocity model and from laboratory experiments.

Main and Meredith, 1989 note that the same stress decreases observed by Scholz et al. described above were also observed in dried rock samples suggesting that pore pressure is not the only governing failure mechanism. They base the stages of failure on stress accumulation over time. Figure 6.1 provides a schematic representation of the stages with time and loading – it is not to scale. Stage 1 is characterised by an “*elastic build-up of strain energy*”, Stage 2 comprises of “*inelastic strain hardening due to dilatancy*”. Stage 3 is “*a precursory stress drop or strain softening*”. Stage 3 is broken into three sub-stages. The first (a) is identified by coalescence of micro-cracking, the second (b) by pore fluid diffusion and (c) “*quasi static slip between asperities*”. Stage 4 is rapid failure – specifically “*dynamic slip of the fault behind the crack tip*”. Stage 5 accounts for the aftershock sequence and accompanying “stress drop”.

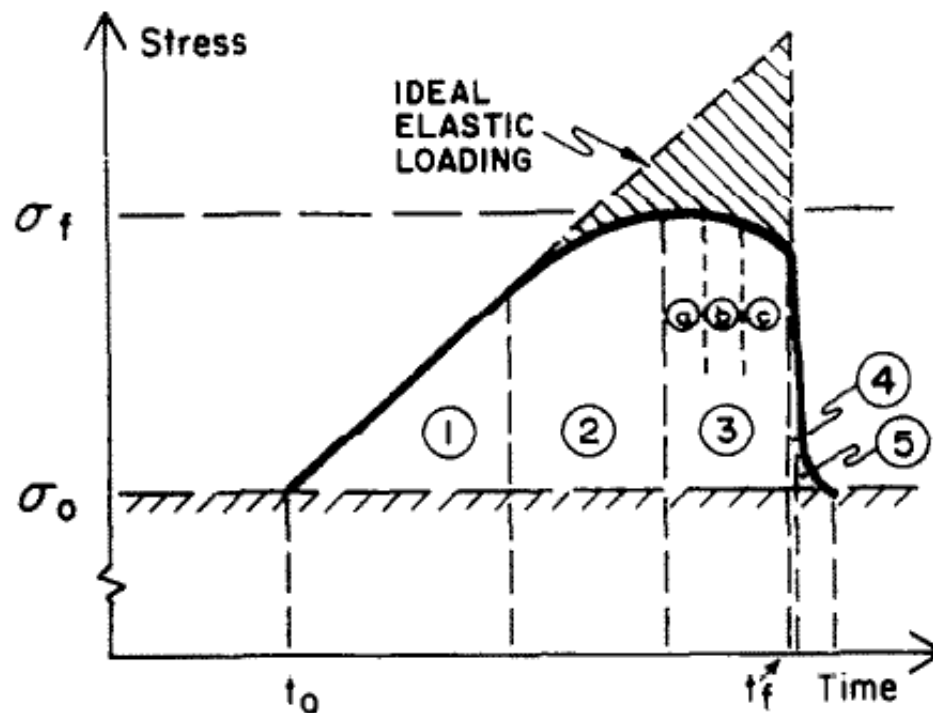


Figure 6.1: Stages of failure according to Main and Meredith, 1989 (not to scale)

Lei et al., 2003a defines the three stages as the primary, secondary and nucleation phases (Figure 6.2). The nucleation phase is further broken into sub-stages. The primary phase is also referred to as the initiation process and is the start of the failure of the sample. As stress levels are increased in the sample, acoustic emission levels begin to increase. The increase is associated with the mobilisation of pre-existing cracks although at this stage the distribution is random. When the sample has achieved between 65 and 90% of the final fracture strength the event rate increases from background levels to a steady occurrence rate.

As the stress level increases the acoustic emission rate, and hence the density of micro-cracking, increase. This is called the secondary phase and is characterised by the interaction of cracking resulting in the formation of strong clusters. This phase is also referred to as the clustering phase. Clusters tend to migrate in space although grain boundaries may affect the path (Lei et al., 1992). The primary and secondary phases are often combined to be called the pre-nucleation phase (Lei, 2003b).

The final stage is only a small proportion of the test and is called the nucleation phase. This phase is broken into at least 3 components with an initial quasi-static fault growth phase, a quasi-dynamic phase followed by dynamic rupture. The quasi-static phase is characterised by an increase in the acoustic emission rate and a merging of clusters to form clear failure planes. During this stage clear indicators of failure emerge. These indicators are called pre-cursors and form the basis of the investigations and analyses in the following chapters. The quasi-dynamic phase and dynamic rupture comprise of the rupture and failure of the sample. The dynamic phase includes the aftershocks associated with failure.

Most early acoustic emission test work was undertaken on homogeneous rock samples. Lei et al., 2003a tested the theory of self-similarity by testing a sample containing a pre-existing heterogeneous discontinuity. The outcome of the testing was able to identify the failure of individual asperities (Figure 6.3). The test also showed that each stage of failure was evident in the failure of individual asperities (Figure 6.4). The test work supported the theory of scale invariance.

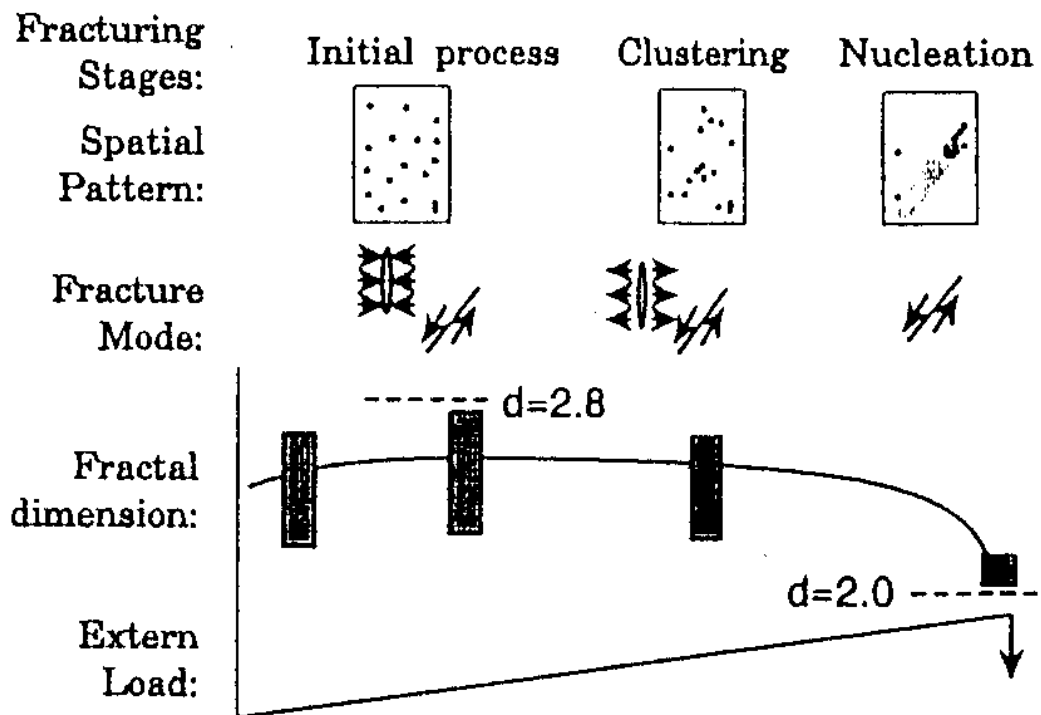


Figure 6.2: Stages of failure adapted from Lei et al., 1992.

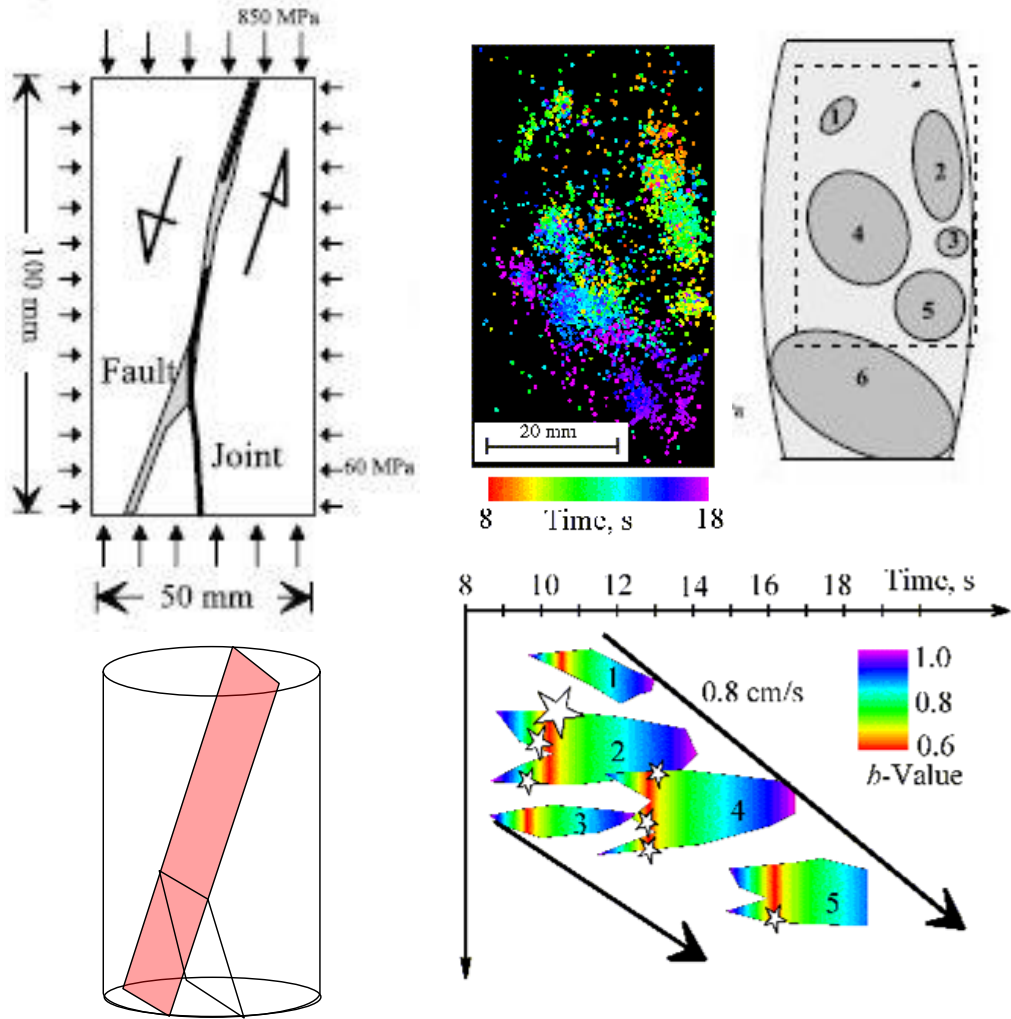


Figure 6.3: Progression of failure identified by AE results through a testing of a heterogeneous sample (Lei et al., 2003).

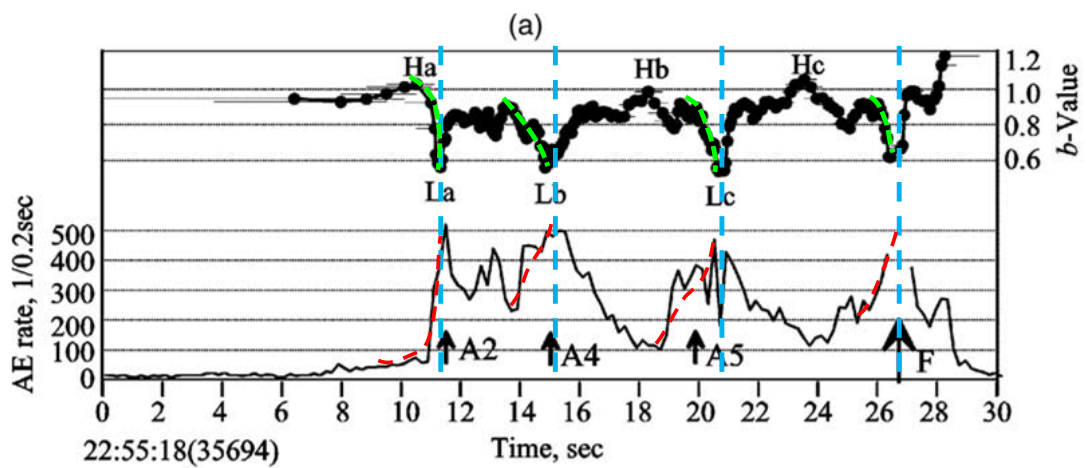


Figure 6.4: Repetition of increases in event rate indicates failure of multiple asperities (Lei et al., 2003).

Whilst there has been some success in applying principles developed by acoustic emission techniques to earthquakes, there are a large number of cases where laboratory testing has not fully translated to earthquake behaviour. Wyss, 2001 provides some reasoning for this. Firstly, he states that “*the information in our earthquake catalogs (sic) and records falls far short of what is needed*”. Secondly, Wyss states that “*the problem of earthquake physics is difficult, because the source, deep in the earth, is not directly accessible for experiments*”. He elaborates stating that due to these depths, the knowledge of the rock mass is not complete and whilst analysis is often conducted on known faults, large earthquakes frequently occur on unknown structures. Despite this, it is commonly accepted that behaviour of rock failure is generic across all scales. The principles obtained in acoustic emission studies will be applied to mining seismic records to ultimately assess the validity of self-similarity theories.

6.3 Precursors to failure

The previous section has provided a brief summary of the phases of intact failure. As stated the final nucleation phase is broken into 3 components – the quasi-static propagation phase, quasi-dynamic phase and dynamic rupture. The “holy grail” of seismic analysis is to identify the quasi-static phase which in-turn provides an indication of likely failure. This particular phase is delineated by temporal changes in seismic parameters. These parameters are called precursors. In the last 30 years, temporal changes in some precursors have been identified as indicating impending rock failure. Geller, 1997 provides a summary of the attempts at prediction up until 1997. Further authors include Mogi, 1962b, Scholz, 1968c, Main and Meredith, 1989, Lei et al., 1992, Lei et al., 2003a. The following list provides a summary of the precursors most commonly referred in the literature:

- Velocity changes
- Waveform
- Failure mode
- Event rate
- b-value
- Event location
- Energy release rate

Velocity changes were first noticed by Russian researchers in 1969 (Scholz et al., 1973). They noticed disparities in the ratio between the velocity of the P wave and the S wave just prior to failure. This gave rise to the dilatancy model discussed by Scholz.

Lei et al. 2003(a) observed variations in the P wave arrivals of acoustic emission wave forms. Further examination suggests that there are four main types of P wave arrival as indicated in Figure 6.5.

“Type I events have an abrupt P wave onset. There are no clear initial phase observed and the waveform reaches maximum amplitude within a few cycles of the first P arrival”. Typically Type I events have a lower maximum amplitude. The significance of this type of event is not discussed.

“Type II events have slow rising P-amplitudes similar to those observed in earthquake records”. Seismologists studying earthquake records suggest that this “may represent the transition from quasi-dynamic failure to dynamic failure”.

“Type III events have a high frequency, small amplitude initial phase that increases slowly in amplitude with time”. It is speculated that this is in fact two events with the initial small amplitude belonging to the start of one event and the slow increase indicating two events merging.

“Type IV events exhibit initial waveforms of progressively increasing amplitude”. These events are typically higher magnitude events and are assumed to be “associated with the fracture of an asperity containing many sub-asperities”.

Seismic event waveforms will not be analysed as part of this thesis, but it is recommended for future research to provide a greater understanding of the rock mass behaviour in the mining environment.

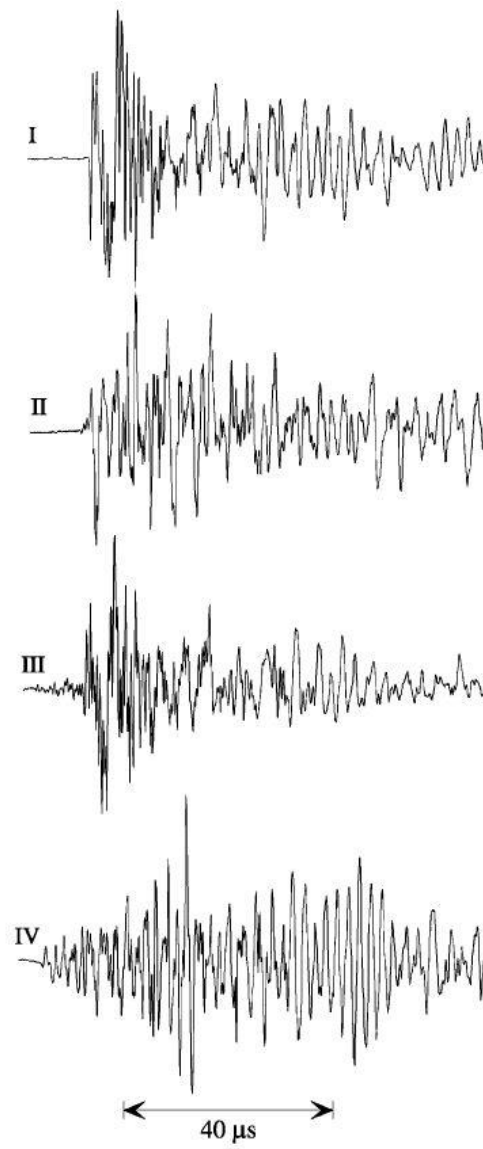


Figure 6.5: Types of waveforms identified by Lei et al 2003(a).

Lei et al., 1992 analysed the focal mechanism solution of some acoustic emission events to determine the mode of failure. Four types of fracturing were identified:

- Type T: tensile cracking
- Type S: shear cracking
- Type TS: Slip along the crack with tensile cracking at the tip
- Type TTS: Slip along the crack with two tensile cracks of different orientations at the crack tips.

In general, type T was the predominant failure mechanism observed prior to and during the initiation of the fault. However, during nucleation, all failure mechanisms were represented with no particular type being predominant. Type T failure was the least predominant.

The failure modes of mining seismic events will also not be discussed in this thesis. Again, future research should examine this aspect of seismicity and its applicability to mining. Understanding the fracture mechanisms will greatly improve the understanding of the failure mechanisms in mining excavations and has the potential to greatly improve safety standards.

The event rate, b-value, location and energy release rate will be discussed in detail in the following sections. Analysis methods for the mining data were developed and a discussion of the results presented.

7. Associating mining and earthquake seismology

7.1 Introduction

Research is limited into the behaviour of large-scale structures and failure mechanisms within the mining environment. Understanding the behaviour of these structures is critical to reducing rock falls and improving safety within the mining environment.

Mining-induced seismicity occurs on a scale between laboratory scale simulations and earthquakes. A large volume of research concerning mining induced seismicity, ignores the geological setting. This is despite delineation of large-scale structures being possible due to information provided by diamond drilling programs and direct observations of exposures in excavations.

The premise of this research is that the geological setting is critical to understanding the seismic behaviour of the rock mass and that the major cause of mining induced seismicity is failure associated with pre-existing structures. Large-scale structures typically represent the weakest point in the rock mass at a mining scale.

It was demonstrated in Chapter 5 that the analysis techniques currently used in mining are flawed. Earthquake seismic investigations typically utilise considerably more temporal analysis. The following research aims at developing and applying the techniques common in earthquake science to mining seismic data to determine if similar patterns of failure can be determined. Principally, the focus will be on the analysis of the following parameters:

- Event rate – cumulative event rate.
- Event location – Fractal dimension and spatial correlation length.
- b-value.
- Energy release rate.

Each parameter will be assessed on its own merits before a comparison of the parameters is undertaken. It is not within the scope of this thesis to analyse all parameters together.

Some authors have attempted to apply these techniques to mining applications (e.g. Urbancic et al., 1992, Kijko and Funk, 1996, Mendecki et al., 1996, Lachenicht, 2001 Spottiswoode et al., 2000 etc.). These attempts have typically been applied sparingly with only a few case studies undertaken. Most of these attempts at analysis have concentrated on spherical clusters of seismic activity that have been derived from density calculations or single link clustering with no relation to local geological features. The outcomes of their research will be reviewed in more detail in the following chapters.

The objective of this research is to use statistical analysis techniques to confirm whether the behaviour of large-scale structures is similar to rock samples and earthquakes. Attempts will be made to determine if the precursory stages of failure can be identified and how far in advance these stages occur. If similar behaviour can be confirmed, it is likely to lead to a better understanding of mining-induced seismicity and the impact of large-scale structures on the mining environment.

7.2 Structural behaviour in the mining environment

Most rock masses exhibit non-linear failure properties due to inherent strength variations and pre-existing discontinuities. As stresses and strains are altered due to mining, strain accumulation occurs within the rock mass. The stronger the rock mass, the more strain that can be accumulated. When the accumulated strain reaches the maximum rock mass strain at a particular location, fracturing occurs. The associated release of energy that occurs during the fracturing process is measured by accelerometers and defined as a seismic event. The larger the strain accumulation, the more energy that may be released at failure and correspondingly the larger the seismic event.

All seismic events represent failure of varying scales. Large-scale instability is the primary concern in the mining environment. These failures affect the stability of the excavations with adverse effects on the stability of the mining operation and safety for personnel.

Many researchers (Mogi, 1962, Scholz, 1968a, Main and Meredith, 1989b, Lei et al., 1992, etc) have observed that ultimate failure of a rock sample is controlled by the formation of micro-fractures at relatively low confining pressures and temperatures. This formation of micro-fractures and the overall behaviour of the rock samples is thought to represent the formation and movement of fault within the rock mass. Measurement of acoustic emissions has been used to study the formation of micro-fractures in rock samples to enable a better understanding of earthquake occurrences.

7.3 Barriers and Asperities

As discussed throughout this thesis large-scale structures are not homogeneous. A single structure may consist of the sections of healed, unhealed and fractured infill. Additionally the infill material may exhibit varying strength characteristics. Aki, 1984 presents a theory that attempts to represent the heterogeneity of structures. He uses the terms “asperity” and “barrier” to describe zones of heterogeneity along fault planes. The theory presents two models of failure. The first is the Barrier model (Figure 7.1). In this model, the structure, prior to failure is uniformly “stressed”. When structural failure occurs, the displacement along the discontinuity is non-uniform. Weaker sections fail, and stronger sections remain intact. Barriers are defined as the sections of fault remaining intact and specifically arrest movement of the fault. The second model is the Asperity model (Figure 7.2). In this model the initial stress distribution is non-uniform. Asperities are defined as intact sections of an essentially failed fault zone. These sections allow for the accumulation of strain. Structural failure is the fracturing of the asperity and release of the accumulated strain creating a completely fractured structure. These two models are not independent, and both models may occur at different locations along a large-scale structure.

Multiple deformation phases within the geological environment often lead to healing and remobilisation of structures. The Western Australian Goldfields region, where 5 of the 7 mine sites are located, is renowned for its multiple deformation phases. These phases are associated with different fracturing orientations and intrusion events. These create significant intersections and interactions of structures. All structures analysed within this thesis display significant heterogeneity. Unlike other authors, it will be assumed that failure at the intersection of two geological features is associated with, and a function of, the properties of both structures. Hence, if an event occurs at the intersection of two structures, the domaining method will have the event within both datasets. Furthermore, it is assumed that large-scale structures contain inherent strength variations along their extent. The asperity model has been adopted for this thesis. This implies that slip on large-scale structures is often initiated when stronger zones (asperities) fail.

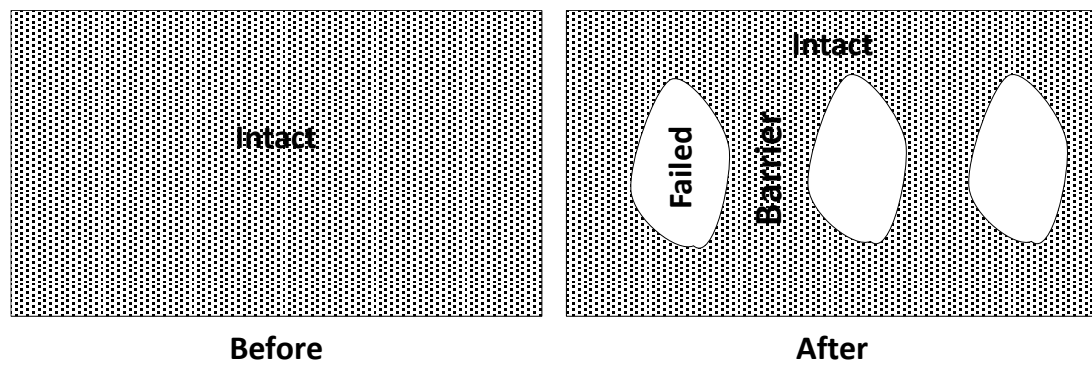


Figure 7.1: Barrier model (after Aki, 1984).

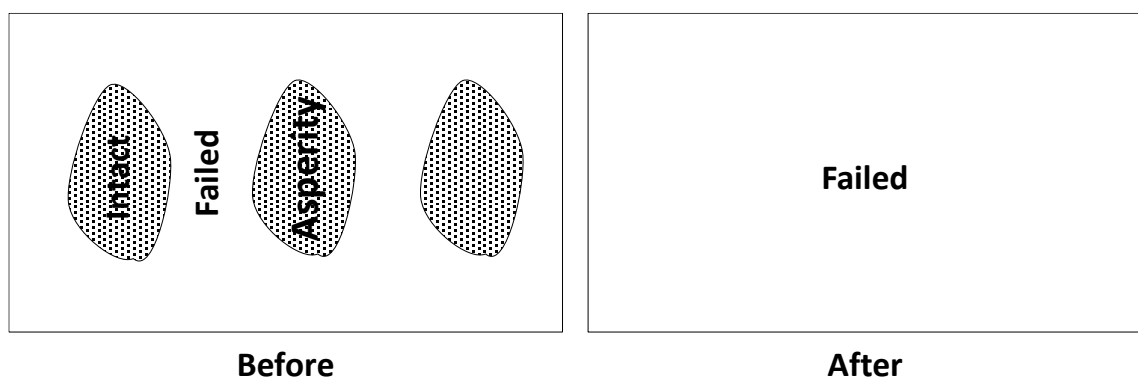


Figure 7.2: Asperity model after (Aki, 1984).

7.4 Failure definitions

Generally, there are three basic mechanisms of large-scale structural instability:

- Instantaneous failure
- Creep
- Stick-slip movement.

Instantaneous failures are the most obvious and easily defined as these are represented by large seismic events. Each mine site will have a differing definition of “large” based on the scale of the operation, the acceptable risk profile and the design capacity of the ground support. Large events are usually defined by correlating the extent of damage to excavations attributed to an individual event and the local magnitude of the event. Typically, sites using the ISS seismic scale use a local magnitude of $0M_L$ as the threshold for seismic hazard mitigation and analysis. Esmeralda uses the moment-magnitude scale and applies a threshold of $1M_L$.

Creep failure is defined by consistent events of similar (typically small) magnitudes along the extent of a structure. These cause rock mass degradation over time. In underground environments this instability is observed as deformation and rock mass yielding. It is typically managed by changing or upgrading ground support systems to match localised conditions. Creep behaviour is difficult to confidently identify and hence will not be directly analysed.

Stick-slip movements are more difficult to define. They are represented by repeated stop / start occurrences whereby a rapid increase in seismic activity occurs followed by a period of relative inactivity. Within this thesis, stick–slip movements are defined as large increases in seismicity over short periods of time. Due to the nature of the stick-slip movements each failure will be referred to as accelerating slip. This definition presents two challenges; what constitutes a large increase in seismic activity and what is a short period of time. No research could be found that quantifies progressive failures associated with mining-induced seismicity. Consequently, for this thesis episodes of over 20 events per day will be used to define this failure pattern.

7.5 Conditional analysis

The aim of this thesis was to determine if failure patterns observed in acoustic emission tests could be observed in mining seismic data. To evaluate this, failure as defined in the previous section, was used as the 0 event (in terms of event reference number and time). Analysis was conducted to determine if results of the calculations of the various analysis parameters are changing in the period before Event 0. The premise of the analysis is a simple yes / no test: Is the value increasing (or decreasing) compared to the previous value? If the value is positive the following value is assessed until all values report no. The number of positive confirmations is then counted at relevant intervals. This has been called conditional analysis.

To undertake this analysis, the seismic dataset for each large-scale structure was compiled in a MS Excel spreadsheet. Dates of failure were entered into a separate spreadsheet. A formula determined the row number of the event. A macro then retrieved the values in the rows prior to the specified row number. The number of values retrieved was specified. An example of the spreadsheet is provided in Figure 7.3. In all assessments 10 values was used. This could apply to events or days. Ten was selected as it was deemed far enough removed (in terms of time) from the original value to establish trends. If the trend appeared to extend beyond 10 values this number could be increased however it was not found to be necessary.

Once the data for the failures were collated, further calculations were used to determine if the value of each data point is greater or lower than the previous value. An assessment was then applied whereby each data point was assessed to determine if the result of the data point was greater or smaller than the previous data point. If the result of the assessment is positive (i.e. the data point is greater or smaller than the previous data point and hence confirming an increasing or decreasing trend) then the next point is assessed. This assessment is continued until a negative result is achieved or the limit of the data has been reached (in most cases 10 data points prior to failure). Whether the positive criterion is decreasing or increasing depends on the parameter being assessed. A decreasing example is provided in Figure 7.4.

Large event date	4/03/2008 18:33	28/07/2008 7:15	← Date and time of event entered
Row number	85	329	← Row number retrieved by formula
T-1	2.00	0.54	
T-2	1.80	0.59	
T-3	2.04	0.58	
T-4	1.85	0.24	
T-5	1.08	0.22	← Values prior to event retrieved by macro.
T-6	1.08	0.22	
T-7	0.85	0.27	
T-8	0.79	0.20	
T-9	0.83	0.28	
T-10	0.83	0.28	

Figure 7.3: Example of spreadsheet macro layout.

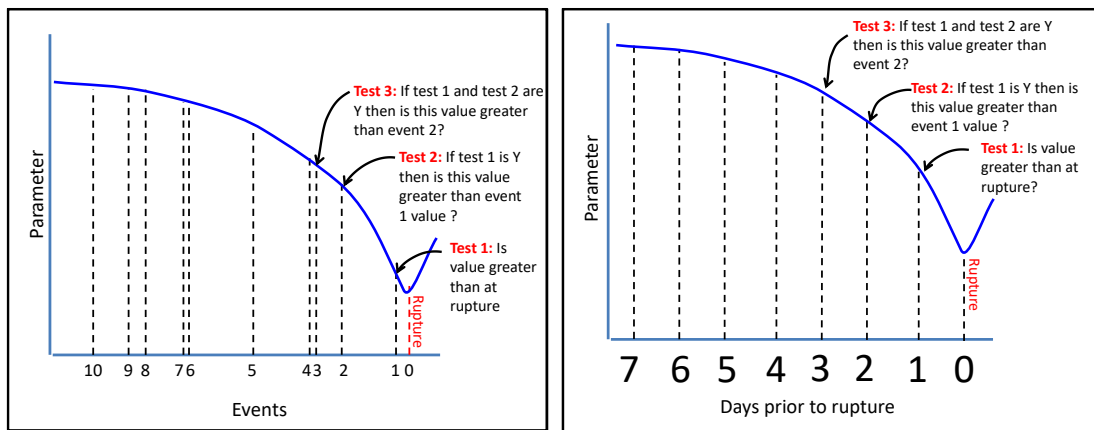


Figure 7.4: Example of conditional analysis on a decreasing trend.

The following Chapters outline each of the parameters described in the introduction to this Chapter. Each chapter discusses the theory and research that outlines the precursory behaviour related to the data. Analysis methods for parameters are described and then applied to the mine site data sets. The results of the analysis are then presented.

8. Event rate

8.1 Theory of structural behaviour in acoustic emissions

As implied in the previous sections, event rate is one of the most deterministic features of the phases of failure. This chapter will review the theory behind event rate changes prior to failure and undertake analysis on the mining seismic data to determine if similar patterns of failure can be determined.

Event rate increases are steady during the early phases of failure but increase asymptotically as the sample nears failure (Figure 8.1). Table 8.1 provides a summary of the changes in event rate prior to failure of samples of varying characteristics (Lei et al., 2004). During sample loading the event rate increased. Weak rock samples exhibited little AE and hence the various phases of failure could not be readily identified. The mudstone sample with strong asperities only exhibited seismic behaviour towards the end of the test, indicated by the rapid onset and immediate increase in AE events. The primary and secondary phases could not be identified however this may be due to a resolution issue whereby smaller events could not be detected by the recording system.

The hard rock samples all displayed high AE levels in comparison with the weaker samples. The behaviours of the hard rock samples were similar in the primary phase, slightly different in the secondary phase and significantly different in the nucleation phase.

The fine grained homogeneous samples typically fractured rapidly with several large pre-cursory events. The rapid nature of the failure resulted in only slight fluctuations of the AE rate.

The coarse-grained heterogeneous samples exhibited a more complex failure mechanism and consequently fluctuations in the AE rate were apparent. The coarse-grained samples typically have a slightly higher AE rate during the primary and secondary phases than the fine grained samples. This is attributed to a higher number of pre-existing fractures. Typically, the event rate in the nucleation phase is similar with a rapid increase in events.

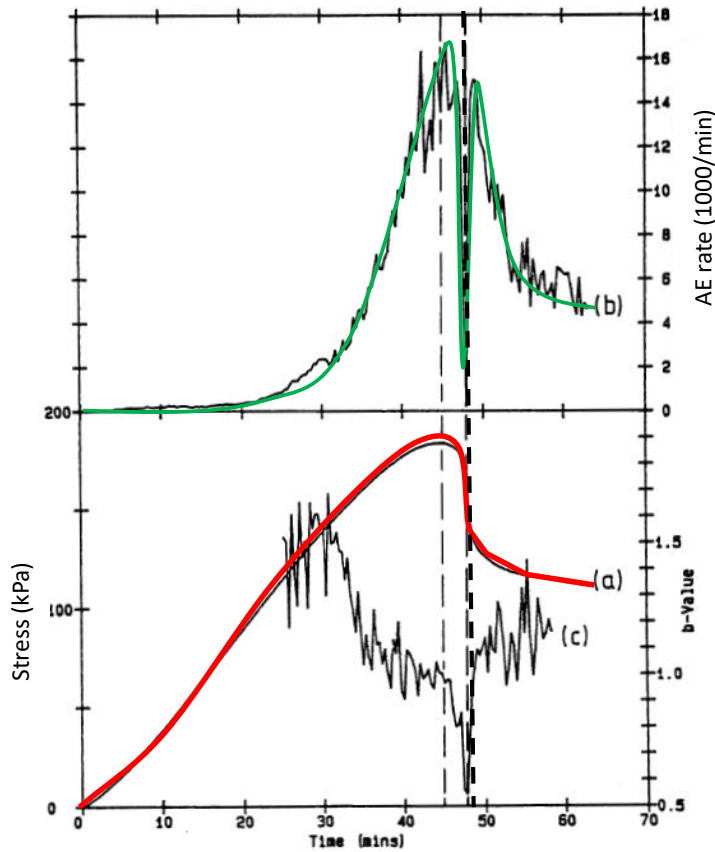


Figure 8.1: Exponential increase in event rate with increasing stress (Main and Meredith, 1989).

Table 8.1: Summary of the effects from AE testing of the failure phase and rock mass properties on the event rate (Lei et al. 2004).

Phase	Sample rock characteristics			
	Coarse grained homogeneous Granitic Porphyry with single pre-existing strongly healed joint (SF)	Coarse grained heterogeneous Granite with single pre-existing strongly healed joint (HF)	Mudstone with single pre-existing joint with strong asperities and weaker sections (AF)	Mudstone with single pre-existing weak homogeneous joint (WF)
Primary	<ul style="list-style-type: none"> Initiation of AE at 60% of final strength Slow increase in AE rate with stress 	<ul style="list-style-type: none"> Initiation of AE at 65% of the peak strength Gradual increase in AE rate with time and stress 	<ul style="list-style-type: none"> Cannot be identified due to no significant AE 	<ul style="list-style-type: none"> Cannot be identified due to no significant AE
Secondary	<ul style="list-style-type: none"> Gradual increase in AE rate 	<ul style="list-style-type: none"> Further increase in the AE rate with time and stress 	<ul style="list-style-type: none"> Cannot be identified due to no significant AE 	<ul style="list-style-type: none"> Cannot be identified due to no significant AE
Nucleation	<ul style="list-style-type: none"> Foreshock, main shock, aftershock sequence present but slight 	<ul style="list-style-type: none"> Initial fluctuation in AE rate followed by a sharp increasing in the number of events. In the fluctuation phase the number of events per second ranges from 40 to 400. Before failure AE rate is approx. 5000 events per second 	<ul style="list-style-type: none"> Sudden initiation with rapid increase of AE events 	<ul style="list-style-type: none"> Cannot be identified due to no significant AE

Lei et al., 2003 tested a sample with multiple asperities along the crack length. Clear patterns were observed during the nucleation phase. The sample exhibited a repetition of the typical event rate pattern within the nucleation phase (Figure 8.2). Each rapid increase in the AE rate was followed by a large main shock.

The cyclic nature of the event rate is important to mining applications and it is presumed similar patterns will be observed in mining seismic data. The following section attempts to determine if asymptotic increases are identifiable prior to failure. Failure definitions described in Chapter 7.4 will be used (i.e. instantaneous failures over the magnitude threshold set by the site and accelerating slip failures defined by days where more than 20 events occur). Conditional analysis (Chapter 7.5) will be used to statistically determine how frequently these trends occur and how far prior to the failure they are determinable.

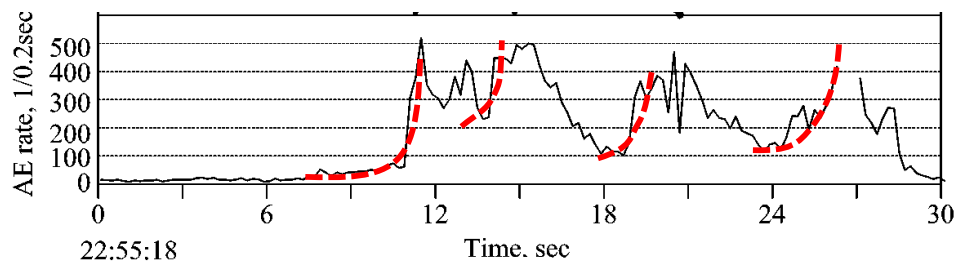


Figure 8.2: Repetition of increases in event rate indicates failure of multiple asperities (Lei et al., 2003).

8.2 Cumulative number of events

The cumulative number of events is simply the rolling count of the number of events occurring. As each event occurs it is added to the tally. The cumulative event chart displays the cumulative event count with time. The cumulative event rate summarises the number of events occurring over time. Low seismic event rates will have a flat gradient where as high seismic event rates will have a steep gradient. An example of the cumulative event rate chart is provided in Figure 8.3. The cumulative event rate charts for each mine site large-scale structure are provided in Appendix 2. In Figure 8.3 it is obvious that there are periods of high event rates and low event rates. The phases are apparent on a global scale with at least 2 long-term nucleation phases. Visually analysing the charts on a macro scale can provide some insight into failures at a macro setting however the charts are highly sensitive to the time scale at which they are being viewed. A closer examination of the highlighted Example 2 is provided in Figure 8.4. Multiple phases of failure can be seen within the macro failure. Two of the instantaneous failures appear to concur with smaller nucleation phases. However, one event appears to occur outside the nucleation phase. Further examination of this event on a shorter time scale shows that there is further embedded nucleation occurring (Figure 8.5). This highlights the failings of qualitative assessments. More measurable methods of assessment are required.

To quantify the acceleration of seismic activity, changes in the gradient of the cumulative event rate chart are used. The gradient is calculated by dividing the change in number of events (in the case of the cumulative chart, this equals 1) by the timeframe over which the events occur (Equation 8.1). This is demonstrated in Figure 8.6.

$$\Delta ER = \frac{1}{(t_2 - t_1)}$$

Equation 8.1

Where t_1 and t_2 are the times of consecutive events.

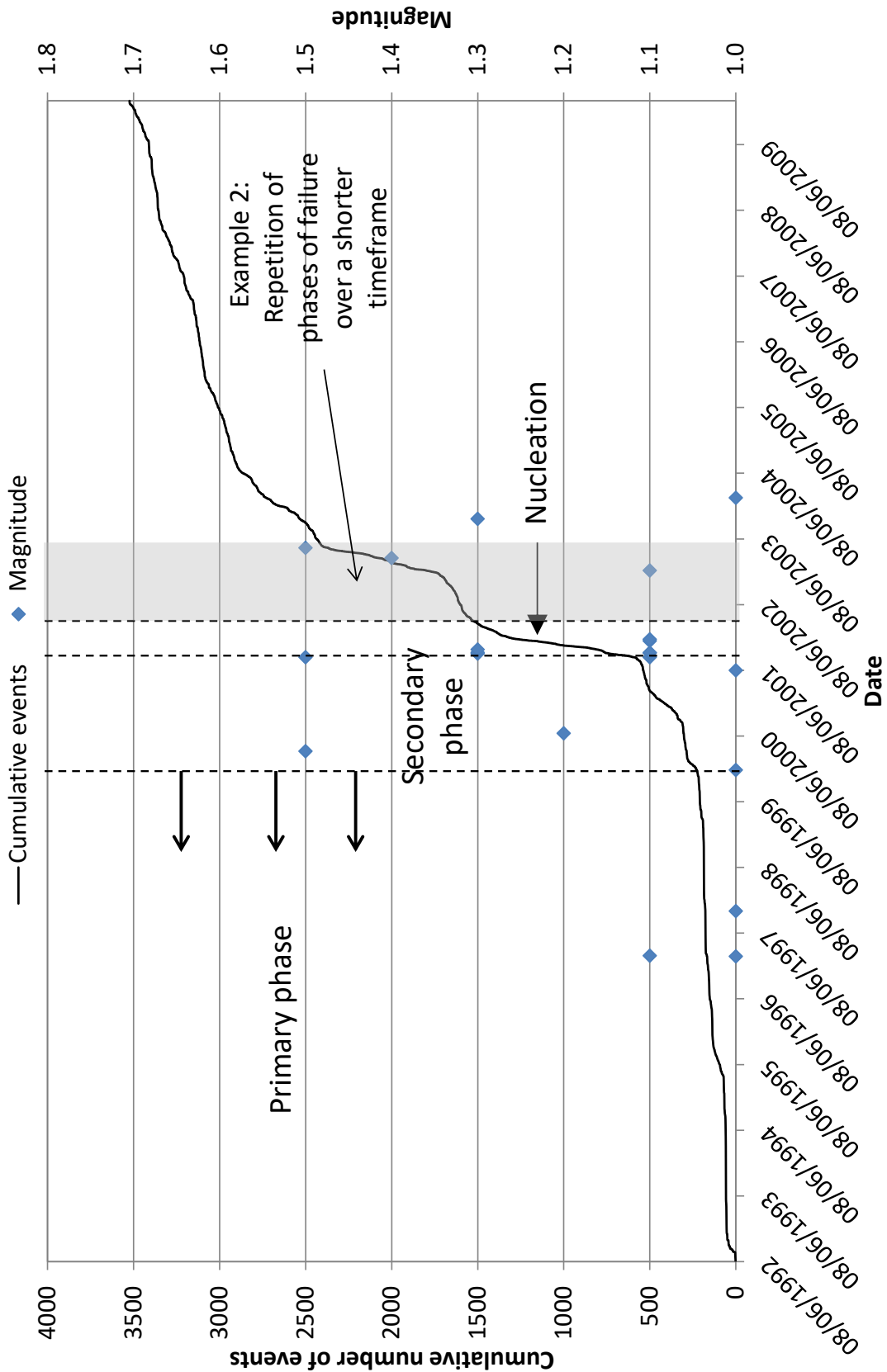


Figure 8.3: Example of the cumulative event rate for a large-scale structure (Fault P1).

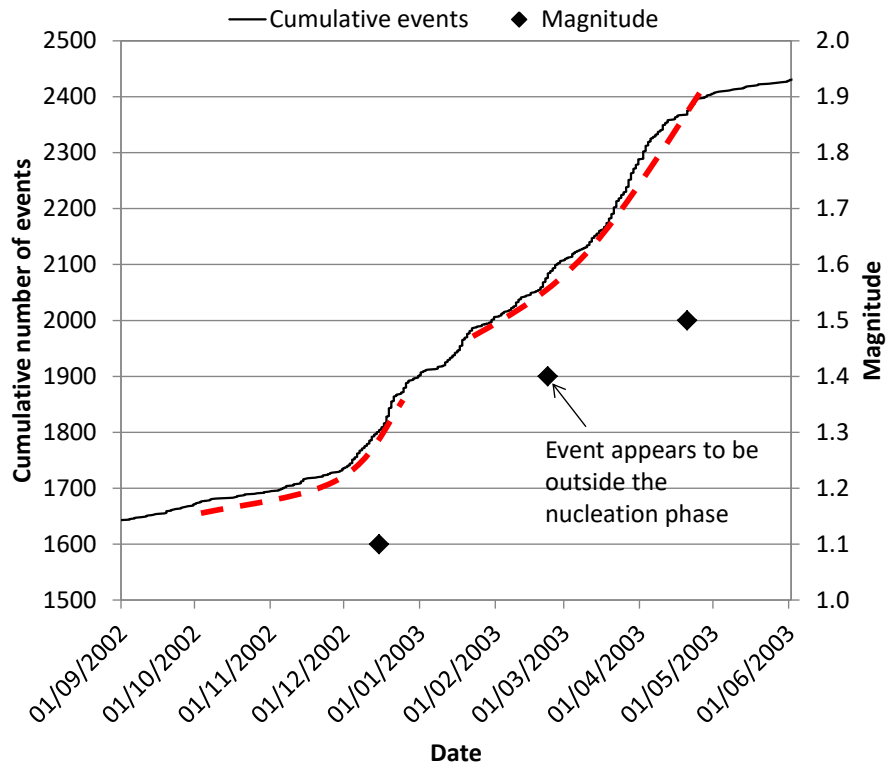


Figure 8.4: Closer examination of the Example 2 failure.

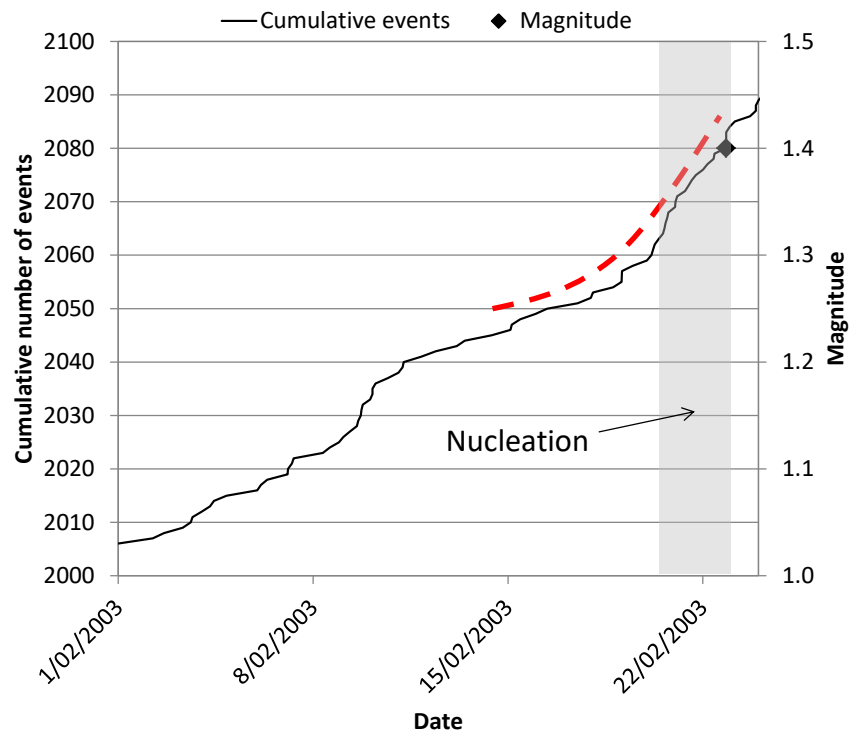


Figure 8.5: Closer examination of the apparently non-conformist event shows further embedded nucleation.

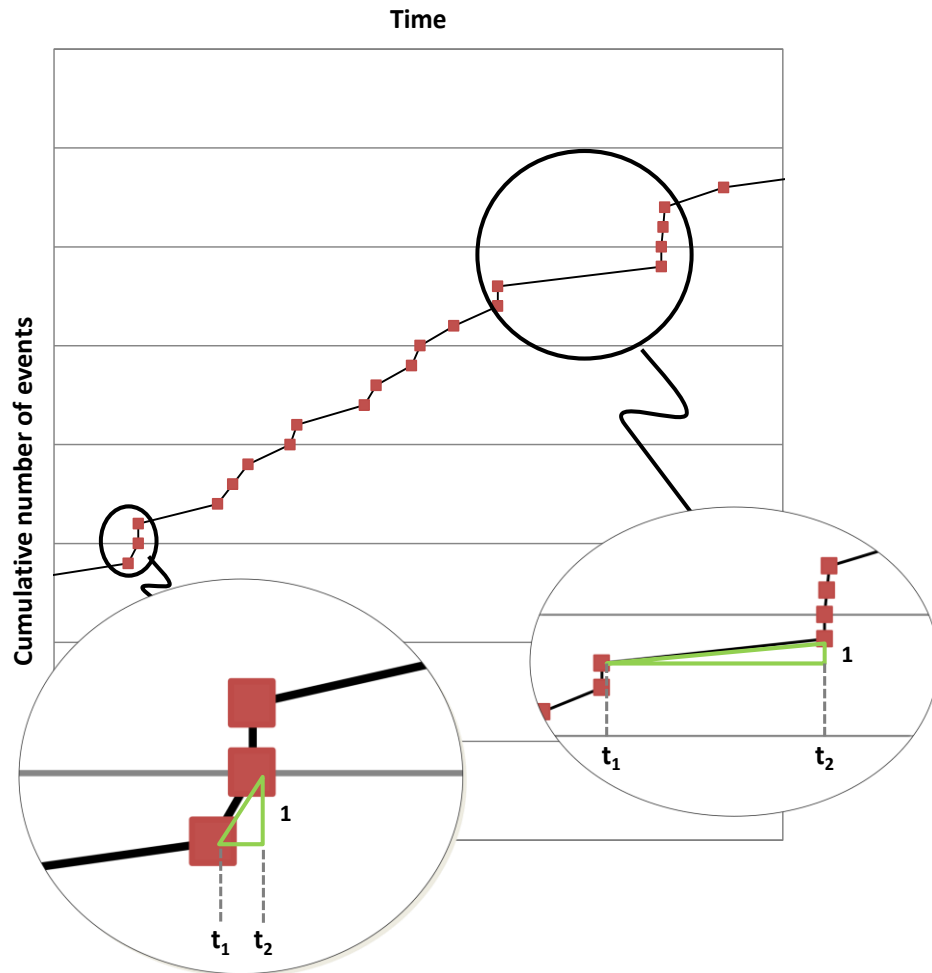


Figure 8.6: Calculation of the gradient of the cumulative event rate.

The aforementioned equation is problematic when applied to mining seismic datasets as frequent simultaneous events cause divisions by zero. Furthermore, many sites also exhibit frequent lapses in seismic activity. Consequently, analysis of the gradient of the cumulative event chart between individual events is not practical. In order to avert some of these issues the time difference (t_2-t_1) was assessed in its own right. The results are presented in the following section.

8.3 Time difference analysis

8.3.1 Analysis method

An increasing cumulative event rate suggests that events are occurring more frequently with less time between individual events. This suggests that the time difference (t_2-t_1) will decrease prior to failure (Figure 8.7).

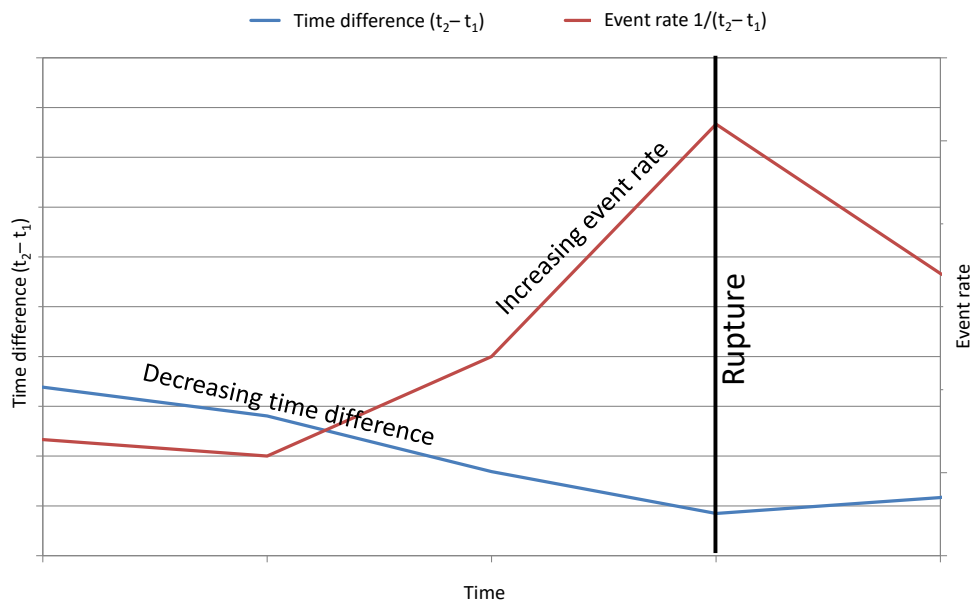


Figure 8.7: Concept of increasing event rate and decreasing time difference.

In order to evaluate this theory, individual failures on each structure were analysed. As described previously, failure is categorised as either instantaneous failure or accelerating slip. Only instantaneous failure was analysed using this method. Accelerating slip is not associated with a single point in time and hence is difficult to assess using this specific method.

Conditional analysis (Chapter 7.5) is used to quantify the results. The analysis involves assessing the time difference between events immediately prior to the failure. Each event is analysed to determine if the time difference is increasing or decreasing. Where structures have significant number of failures only 50 were analysed. The data is then collated to determine the percentage of events that show a decreasing trend as well as how far prior to the event the trend continues.

8.3.2 Time difference fixed event results

The event time-difference vs time charts for each large-scale structure are provided in Appendix 3. An example from the results is provided in Figure 8.8. The example shows a clear indication of the phases of failure with the primary phase characterised by erratic occurrence of events. The events become slightly less erratic in the secondary phase and during nucleation the time difference reduces significantly. The decrease in time difference is associated with a very short but significant increase in the event rate. Rupture occurred on the 15th of February during the nucleation process with a 1.1M_L event. These phases are evident in many of the datasets however rupture as per the definitions in this thesis is not always associated with the nucleation phase.

Results of the conditional analyses are provided in Figure 8.9. These results show that time difference generally only decreases 2 – 3 events prior to the rupture. Furthermore, only approximately 20% of ruptures display this trend. On average 50% of ruptures indicate a decreasing trend on the events prior to the rupture. These results suggest that the time difference between consecutive events is erratic. Two events can occur almost simultaneously but may or may not be followed by further successive events in the following hours. Despite this, trends such as those presented in Figure 8.8 are apparent. Smoothing the time difference data may improve the identification and quantification of these results.

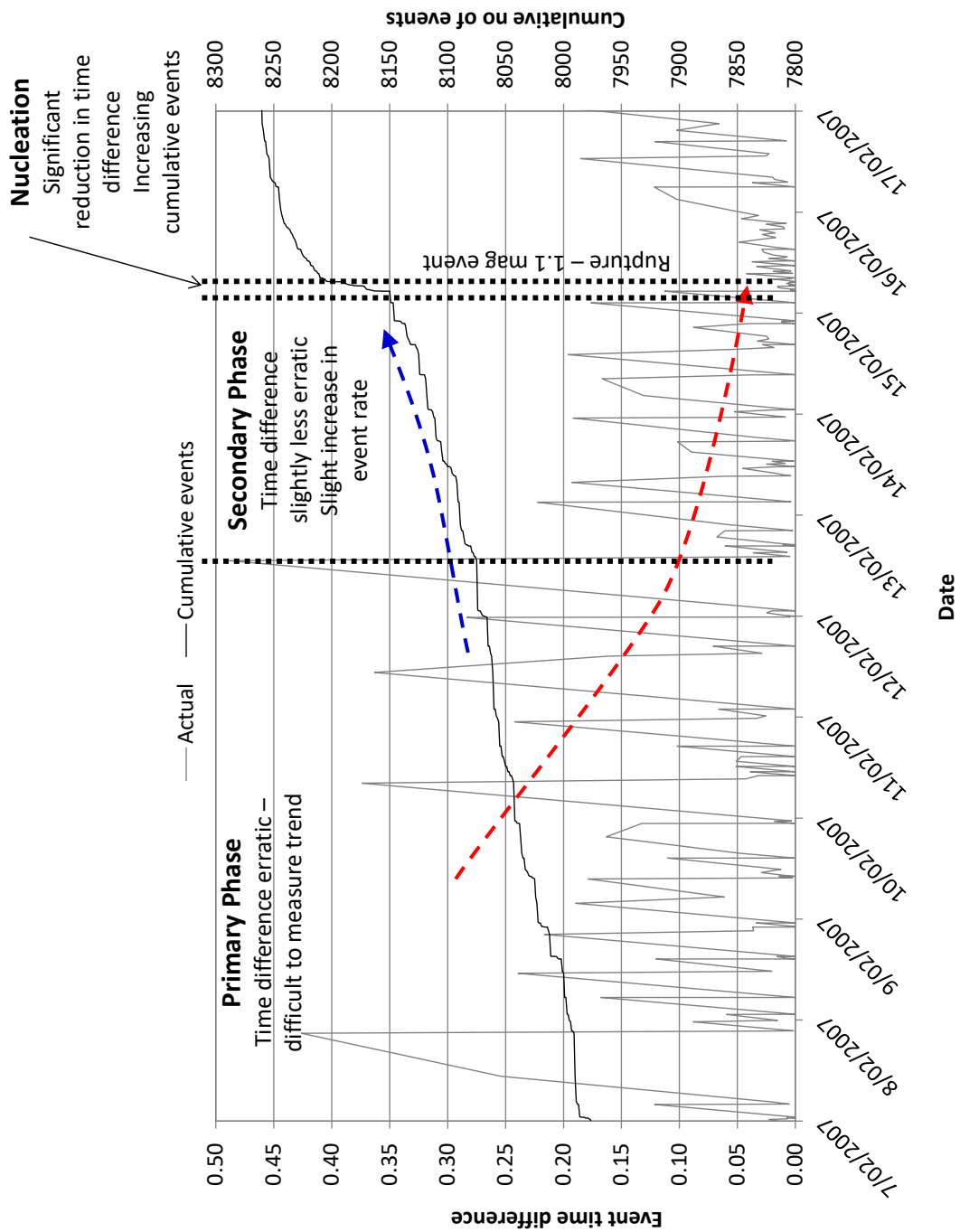


Figure 8.8: Example of erratic nature of time difference (NE G2).

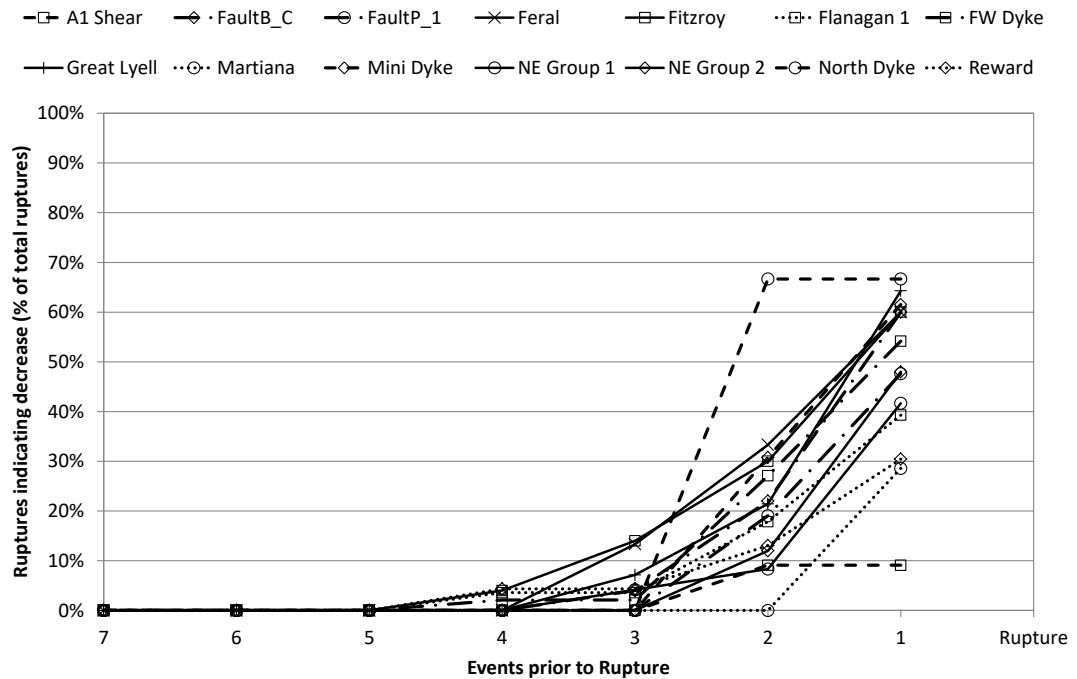


Figure 8.9: Summary of time-difference decreasing trends for each fault.

8.3.3 Time difference results by stepping data

In order to improve the results a method of determining the overall trend of the dataset was required. Initially, the data was smoothed using a step approach utilised by Lei et al., 2000b and others. This technique involves conducting the same calculation ($t_x - t_1$) but skipping or stepping over data points (Figure 8.10). The following data steps were used to attempt to smooth the results:

- 2 events ($t_2 - t_1$)
- 5 events ($t_5 - t_1$)
- 10 events ($t_{10} - t_1$)
- 50 events ($t_{50} - t_1$)

A comparison of the conditional analysis average results for each method is provided in Figure 8.11. The results show smoothing the data increases the success of identifying the decreasing trend further away from the rupture. However, a 50% success rate for identifying the rupture was not considered statistically reliable. In order to attempt to improve the ability to identify the decreasing trend several other methods were developed.

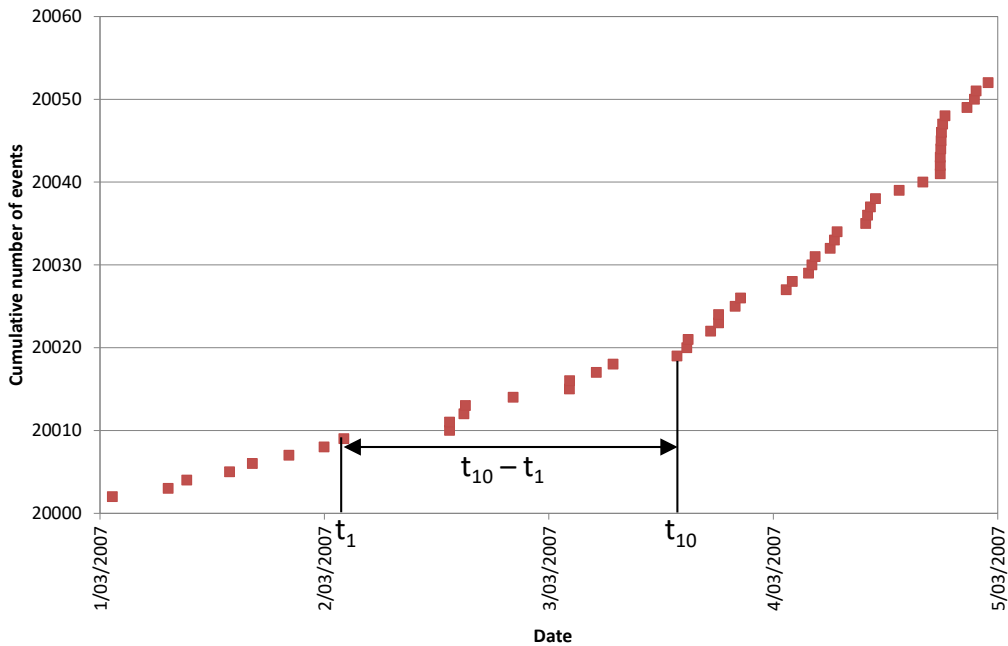


Figure 8.10: Data point stepping.

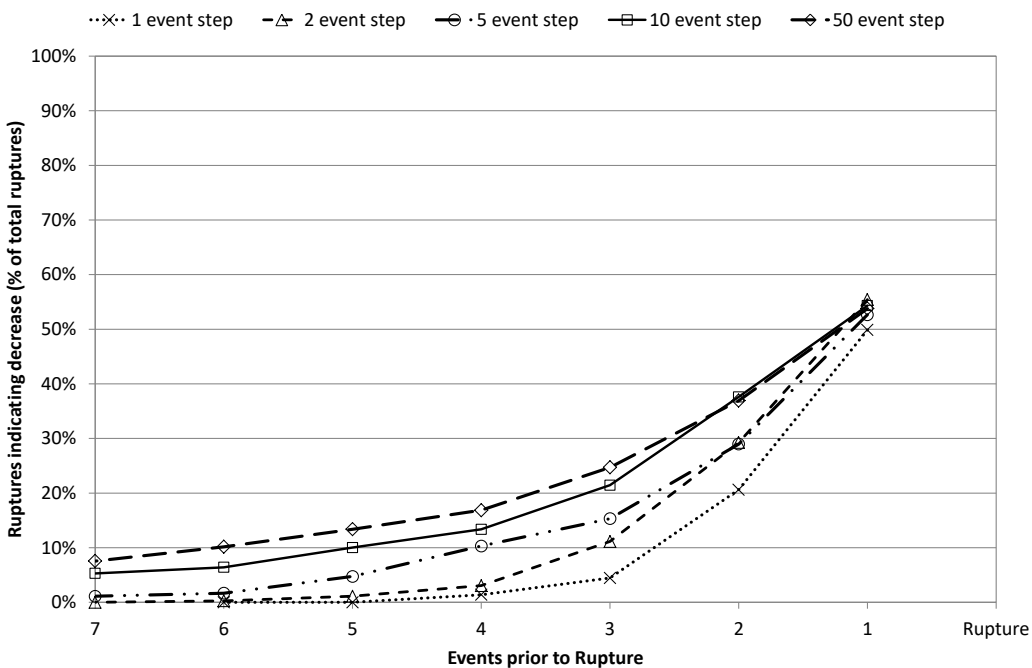


Figure 8.11: Summary results from data smoothing using the stepped method.

8.3.4 Rolling averages using fixed data numbers

Instead of stepping the data as in the previous method, data smoothing was attempted using a rolling average method. Rolling averages are calculated by averaging the time difference between single events over a number of events (N) (Figure 8.12). The following fixed numbers of events were considered:

- 10 events (N=10)
- 20 events (N=20)
- 50 events (N=50)

Due to the variability in the number of data points in each dataset, some curves were successfully smoothed whilst others remained unaffected. In order to apply a more balanced approach the number of events included in the averaging was determined by the number of data points in the dataset. Time differences were assessed over the following number of events:

- 5% of the dataset ($N_{5\%}$)
- 10% of the dataset ($N_{10\%}$)
- Average number of events per week (N_{avwk})
- Average number of events per month (N_{avmth})

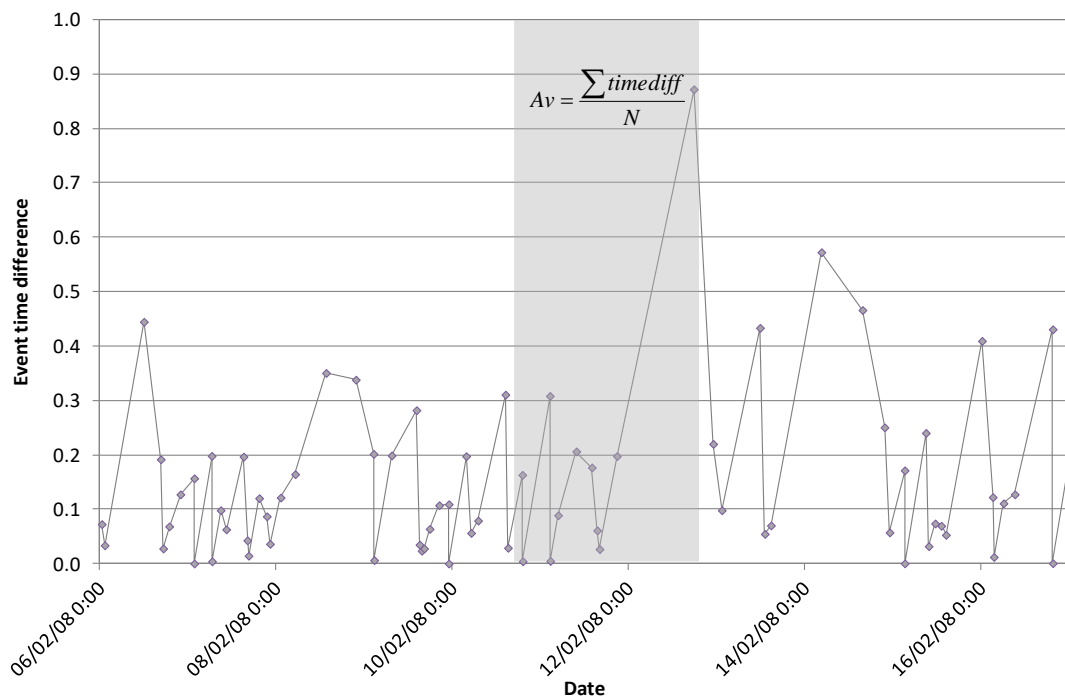


Figure 8.12: Method for determining rolling average for a fixed number of events.

For example, the Esmeralda FW dyke dataset contains almost 66000 events. Five percent of the dataset equates to 3300 events and hence the smoothed time difference calculation would be $t_{3300}-t_1$. Table 8.2 contains the time step values for each structure. The calculated values were rounded for efficiency in the calculations. The time step values once calculated were then presented in charts as time vs time difference. Figure 8.13 provides an example of the smoothed results.

Using the example in Figure 8.8, Figure 8.13 shows a comparison of the various results for the Kanowna Belle NE group 2 structures. The phases of failure are clearly identifiable in the averaged results for 10, 20 and 50 data points. However, the smoothing effect is too great where a large number of data points have been used (over 100 points). Rupture is still obvious; however, the change between the primary and secondary phases is not. In this case 50 data points is the most applicable number. The chart shows a gradual increasing time difference trend during the primary phase. Just into the secondary phase the maximum value is reached after which there is a slow general decline. Late in the secondary phase there appears to be a fluctuation in the time difference which is followed by rapid nucleation and rupture. To determine if these trends can be quantified, conditional analyses were again undertaken.

Table 8.2: Values used to aid in smoothing the time difference data.

Structure	Events	Av weekly		Av Monthly		5%		10%	
		Calced	Input	Calced	Input	Calced	Input	Calced	Input
A1 Shear	2120	12	10	54	50	106	100	212	200
FaultB_C (1998 - 2010)	30741	47	50	209	200	1537	1500	3074	3000
FaultP_1 (1999 - 2010)	3524	6	5	25	25	176	175	352	350
Feral	4950	41	40	177	175	248	250	495	500
Fitzroy	14475	23	25	101	100	724	725	1448	1450
Flanagan 1	4987	19	20	83	80	249	250	499	500
FW Dyke (2000 - 2010)	66046	122	120	537	540	3302	3300	6605	6600
Great Lyell	247	3	5	15	15	12	10	25	25
Maritana	250	1	1	5	5	13	15	25	30
Mini Dyke	791	5	5	20	20	40	40	79	80
NE Group 1	18070	29	30	127	130	904	900	1807	1800
NE Group 2	20038	32	30	140	140	1002	1000	2004	2000
North Dyke	635	4	5	17	20	32	30	64	60
Reward	1496	6	5	24	25	75	75	150	150

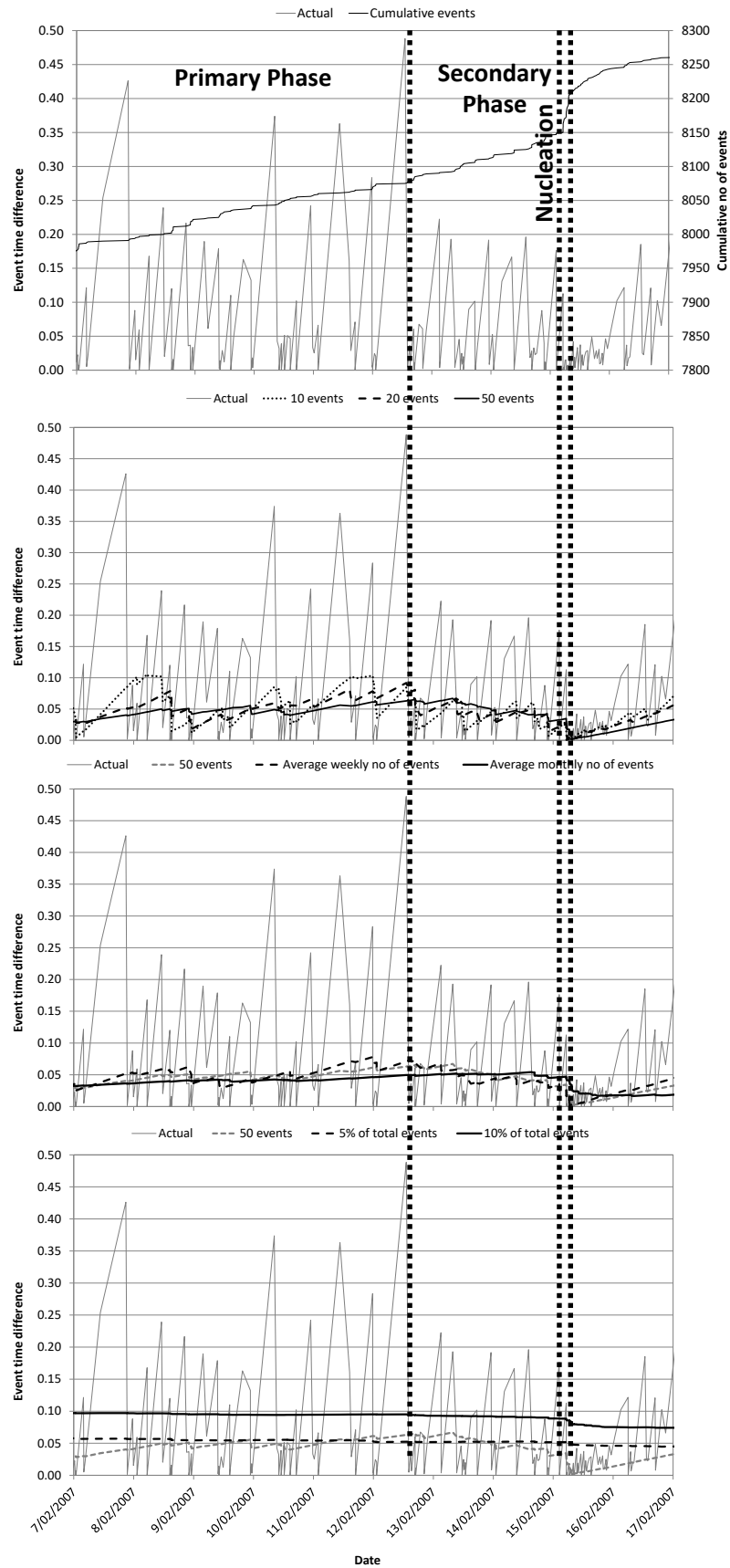


Figure 8.13: Smoothing of results using average time difference data calculations (NE G2).

Figure 8.14 shows the average results of the conditional analyses for each smoothed dataset. The smoothing methodology has improved the overall results 2 and 3 events away from the failure with decreasing trends in 30% and 20% of cases respectively (up from 20% and 5% respectively). The numeric value of the data step that is used to smooth the results has a negligible effect. Larger data steps provide slightly better results; however, these are not considered to be consequential. Despite this, there was no improvement in the results just before final rupture as only 50% of the failures have a decreasing time difference prior to the rupture.

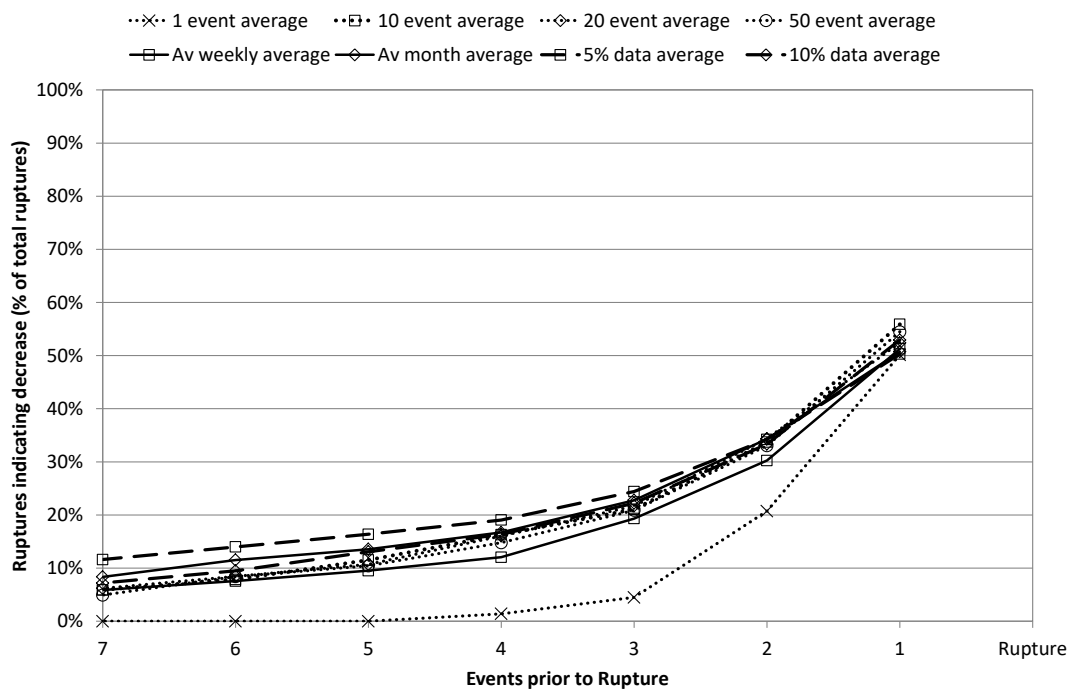


Figure 8.14: Summary of time difference results.

8.3.5 Discussion of time difference results

The limited success of this process may be explained by 2 factors; the nucleation process and the analysis method. The fluctuations observed at the end of the secondary phase may indicate that the decreasing trend cannot be readily quantified using a specific numerical method. Furthermore, the nucleation process is so rapid that it is difficult to identify.

The analysis method using individual events as the basis is problematic due to the completeness of the dataset and the sporadic nature of mining seismicity. The completeness of the dataset depends on the density of the seismic sensors around the structure. Smaller seismic events that indicate the background trend in seismic patterns are often missing. This results in higher fluctuations in events than might otherwise actually be occurring hence the sporadic appearance of mining seismicity. This leads to the second limitation of this analysis.

These analyses show that only 20% of ruptures have a decreasing trend that can be identified 4 events away from the final rupture. Even if the results were more definitive, from a practical perspective a 4 event trend is difficult to recognise prior to a failure. The time over which 4 events occur can range from weeks to minutes depending on the dataset and the structural behaviour. Furthermore, there are a significant number of occurrences where the time between 4 consecutive events is decreasing. For example, analysis of the data from the A1 shear for the time difference averaged over 10 events shows that there are 132 occurrences of 4 consecutive events indicating a decreasing trend. This equates to on average 4 occurrences per month.

An alternative method of assessing the data is required to improve the analysis technique. The method must utilise practical time frames that are appropriate to methods of analysis on mine sites as well consider other methods of failure such as accelerating slip.

8.4 Accumulated events analysis

8.4.1 Time frames for assessment

As discussed previously the gradient of the cumulative event rate cannot be reliably used to determine specific failures on structures. The analysis of trends between individual events has proven to be erratic and inconclusive. Rather than assessing changes in data across individual events, a broader scale approach is proposed.

This method evaluates the cumulative event rate using time as a fixed variable; that is the number events per hour, day, week or month. These periods can be quantified as short term (hours), medium term (days, weeks) and long term (months, years).

Short-term time frames would attempt to identify increasing trends in the cumulative event rate on an hourly basis. This level of analysis – though potentially successful in identifying trends - is generally difficult to apply in the mining environment. The processing of seismic data (picking of P and S waves) is often conducted in batches at the start or end of the day. Processing and analysis also require significant man-hours. To identify changes in the seismic behaviour of the rock mass in the hours prior to an event requires constant surveillance of the monitoring system. This is rarely achievable and, consequently, rapid changes in seismic behaviour of the rock mass are not identified until after the occurrence.

Long-term increases in the cumulative event rate are also difficult to identify whilst in progress. Monthly changes in the seismic event rate may be subtle (20-50 events per month) or highly fluctuating but cumulatively significant. It is often not until rock mass damage is discernible that trends are identified as significant.

Medium term analysis involves assessing the seismic data for changes over periods of days or weeks. This level of analysis can be managed on a practical level by mines sites. Evaluation of daily trends forms the basis for the following analysis.

8.4.2 Daily event rate analysis

The number of events per day was calculated in order to analyse the seismic data trends over a medium timeframe. Theoretically the daily event rate should exponentially increase in the days prior to failure. An example of the daily event rate is provided in Figure 8.15. The daily events charts for each structure are provided in Appendix 4. The example provided highlights the clear presence of ruptures. Figure 8.16 provides a detailed examination of the rupture in August 2004. This example uses the case of accelerating slip rate rather than instantaneous failure. The daily event rate decreases slightly in the primary phase from approximately 8 events per day to a minimum of 3 events per day. A steady increase is then observed during the secondary phase. The change from the secondary phase to the nucleation phase can be argued as can the rupture definition; however, the overall acceleration in the event rate is clear. Conditional analysis techniques (Chapter 7.5) were used to substantiate and quantify this trend.

This methodology enables the assessment of both instantaneous failures and accelerating slip failures. As described previously, accelerating slip is defined as 20 events occurring in a day.

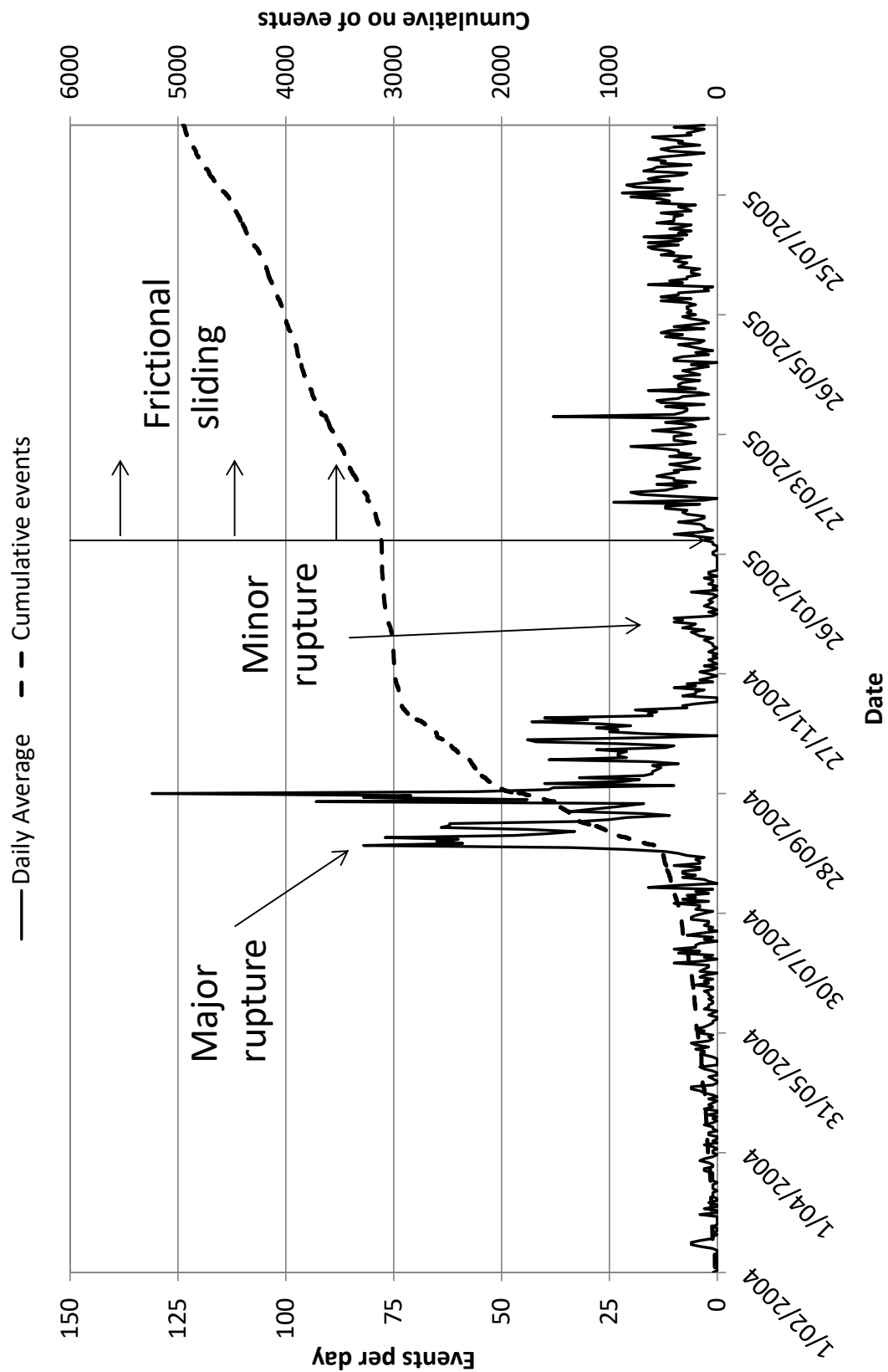


Figure 8.15: Example of events per day chart indicating failures (Feral Fault).

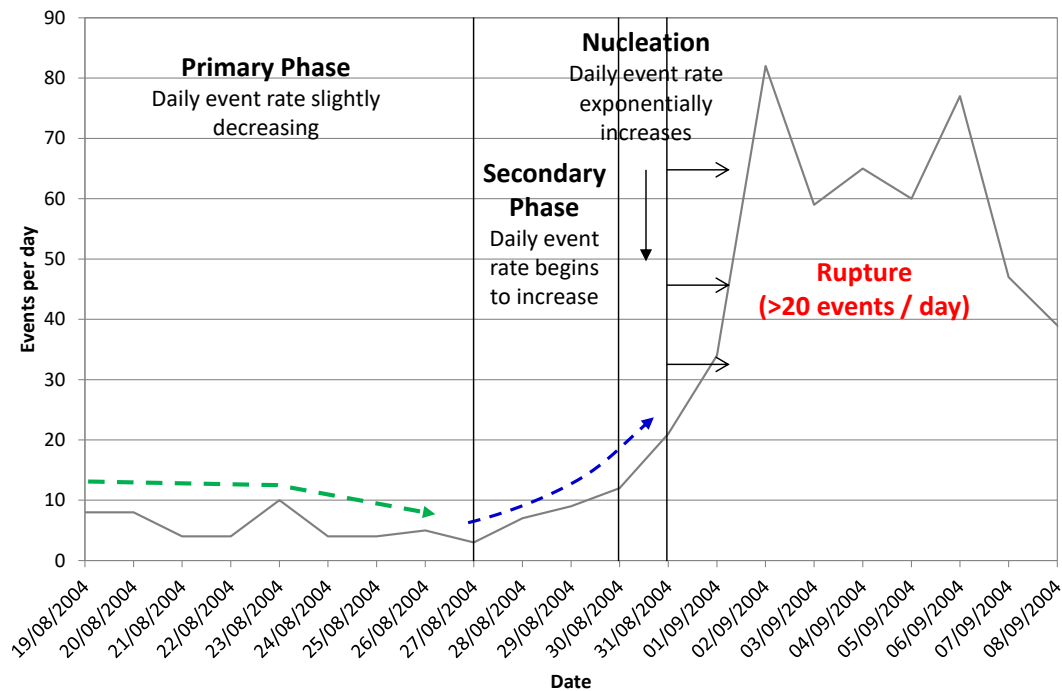


Figure 8.16: General increasing trend in daily event rate (Feral Fault).

A summary of the results of the conditional analysis of all faults investigated is provided in Figure 8.17. The results indicate that, on average, 73% of instantaneous failures have a higher event rate on the day of the event compared with the day prior to the event. Argo structures (A1 shear, Mini Dyke and North Dyke) all indicated above an 80% success rate for increasing trends the day prior to failure. The North Dyke and the Maritana Fault showed all failures with an increasing trend prior to rupture. These structures are the only ones with less than 10 failures recorded which may be biasing the results. The FW dyke at Esmerelda provided the least positive outcome with only 50% of events indicating an increasing trend the day before rupture.

On average 5% of events indicate a consistently increasing trend from 3 days prior to the failure. Although this is a low percentage of events it indicates that the transition from the primary phase to the secondary phase occurs between 2 and 3 days prior to failure. No evidence of instability could be observed further than 5 days from the rupture.

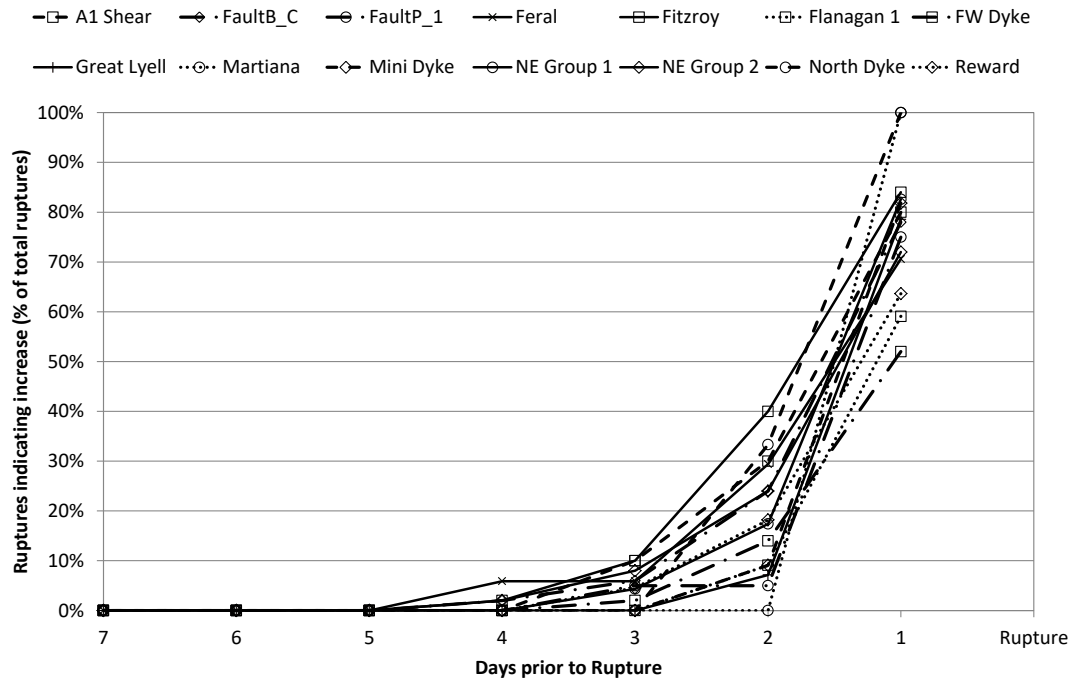


Figure 8.17: Percentage of instantaneous failures indicating increasing trends in the days prior to the event.

Accelerating slip failures were evaluated in the same way as the instantaneous failures. The summary results for all structures investigated are provided in Figure 8.18. The Day 1 results are marginally lower than the results of the instantaneous failures with only 70% of failures indicating an increasing trend the day before the accelerating slip failure. Despite this, these failures are more easily identified further from the event with 10% of failures indicating increasing trends 3 days prior to the event and 5% providing positive results 4 days prior to the failure. This supports the change from primary to secondary phases occurring at approximately 2 - 3 days prior to failure. As with the instantaneous failures no failures showed indications of instability 5 days prior to rupture.

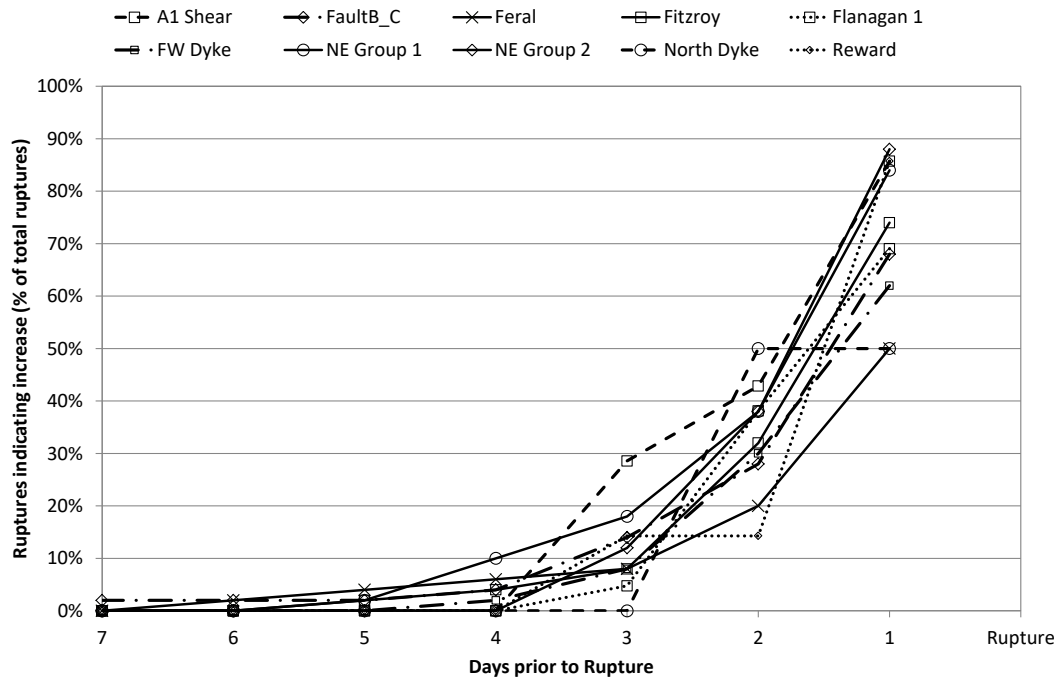


Figure 8.18: Percentage of accelerating slip failures indicating increasing trends in the days prior to the event.

Whilst there are clear examples of consistent daily event rate increase prior to failure (as presented in Figure 8.16) in most cases there are fluctuations in the rate prior to rupture (Figure 8.19). The fluctuations become obvious when examining the number of events on the day of the failure compared with the number of events in the days prior (Table 8.3). The number of events on the day prior to the failure is significantly lower than that on the day of the failure. Frequently, the main failure event may be the only event on that given day or the failure is one of several that occur on the same day. It is also frequent to not have events in the days leading up to a failure. The overall trend in the data though still appears to be either stable or increasing. This is consistent with observations of the secondary and nucleation phases. Decreasing trends are associated with the primary phase.

In order for trends to be recognised in a practical environment they need to be clearly identified much earlier from failure. In an attempt to achieve this, the data were smoothed using a rolling average analysis technique similar to that used in the fixed event analysis described earlier in this chapter. The concept and results are provided in the following sections.

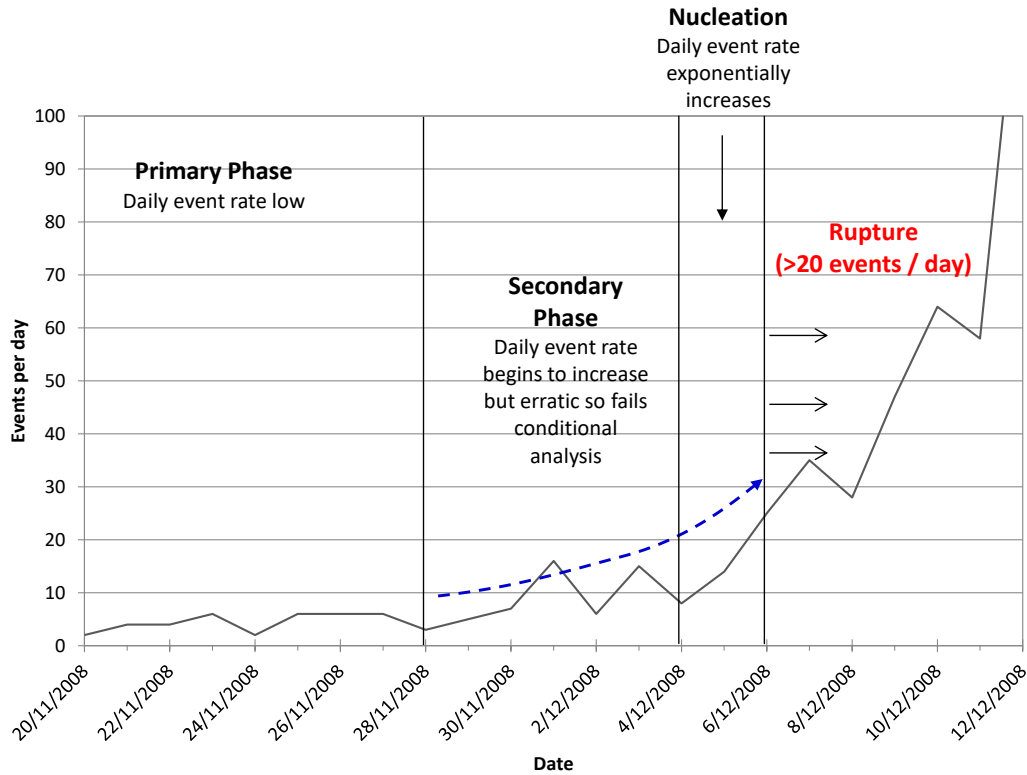


Figure 8.19: Example of fluctuating daily event rate (FW Dyke).

Table 8.3: Average number of events on the day of and days prior to the instantaneous failure.

Results for SUCCESSFUL trends ONLY												
Structure	No. events on day of failure			No. events on day before failure			No. events 2 days before failure			No. events 3 days before failure		
	Av.	Max	Min	Av.	Max	Min	Av.	Max	Min	Av.	Max	Min
A1 Shear	13	42	1	4	18	0	6	14	1	3	5	1
Fault B_C	9	23	1	2	10	0	2	7	0	3	5	0
FaultP_1	5	18	1	2	13	0		4			3	
Feral	18	82	1	10	44	0	6	20	0		7	
Fitzroy	32	203	1	3	19	0	2	7	0	1	2	0
Flanagan 1	167	413	1	4	13	0	1	1	0			
FW Dyke	12	78	1	8	56	0	4	14	0		13	
Great Lyell	5	12	2	1	3	0	0	1	0			
Maritana	24	52	1	23	52	1						
Mini Dyke	7	17	1	1	2	0	0	0	0			
NE Group 1	11	30	1	4	18	0	8	16	1		4	
NE Group 2	26	176	1	5	34	0	5	23	0	7	20	0
North Dyke	8	14	2	1	2	1		0				
Reward	8	26	1	1	10	0	1	4	0		3	

8.4.3 Rolling average daily event rates.

As with the time-difference analysis it was necessary to smooth the daily event rate data to remove the high levels of fluctuation. In order to achieve this, rolling averages of the events per day (d_x) were calculated. This calculation is undertaken by counting the events over the specified time period (d) and dividing by the number of days (n) (Equation 8.2)

$$d_x = \frac{\sum_n^1 d}{n}$$

Equation 8.2

The following periods of time were considered:

- 2 days
- 3 days
- 7 days
- 14 days

An example from the results is provided in Figure 8.20. The following sections provide the results of the analysis for each of the smoothed data.

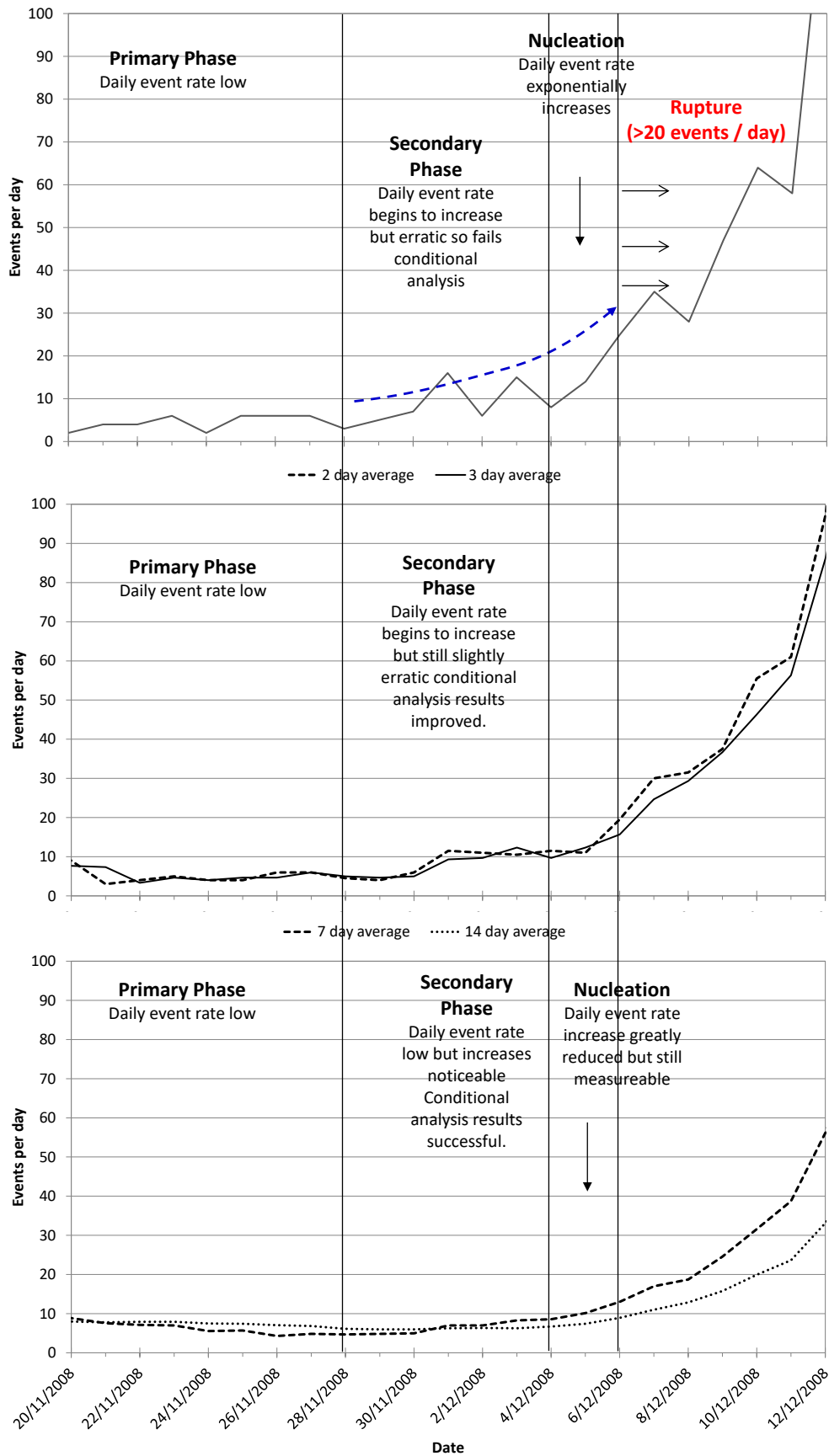


Figure 8.20: Example of data smoothing (Fault B_C).

8.4.3.1 Instantaneous failures

The average results of the conditional analysis are provided in Figure 8.21. The results of the 7 day rolling time interval analysis for each structure are provided in Appendix 5. Smoothing the data has not greatly improved the predictability of events close to rupture (1 day prior). This is as expected due to the low number of events during the nucleation process. The aim of this analysis is to determine the change from the primary to secondary phase which would indicate impending instability. On average, the smoothing process has improved the identification of this stage. Using 7 day smoothing, on average, 25% of events can be identified 3 days prior to rupture. Almost 10% of events can be distinguished at 6 days prior to rupture. Four structures indicate a definite improvement in the determination of failure: FW Dyke (30% improvement), Reward (15 % improvement) and NE group 1 (10% improvement). The FW dyke summary is provided as an example in Figure 8.22. Other individual faults indicate varying degrees of improvement. Figure 8.23 shows the 7 day smoothed results for each large-scale structure. The results show a high degree of variability between the various structures. Each structure would need to be assessed on its own merits to implement this analysis in a practical environment. However, any consecutive increase in the daily event rate should be analysed.

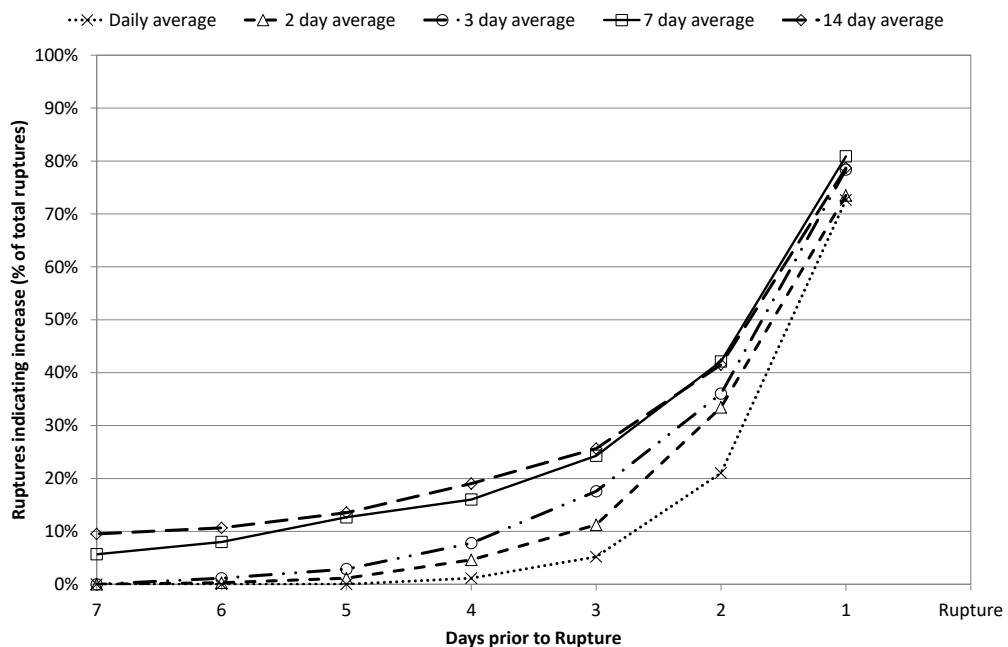


Figure 8.21: Instantaneous failures rolling average summary.

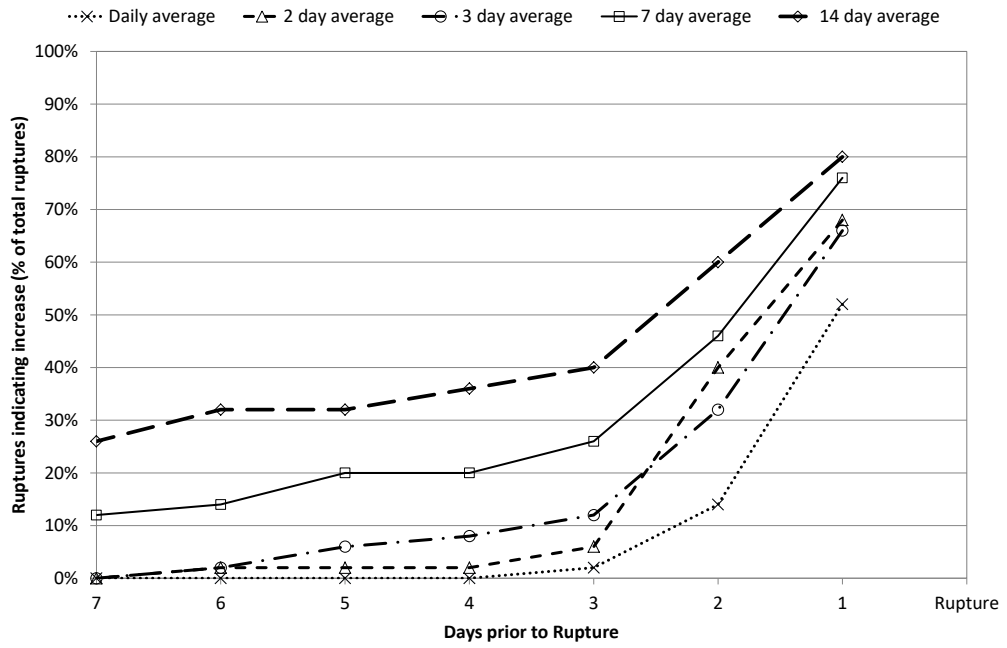


Figure 8.22: Example of improved results due to data smoothing of instantaneous failures (FW Dyke).

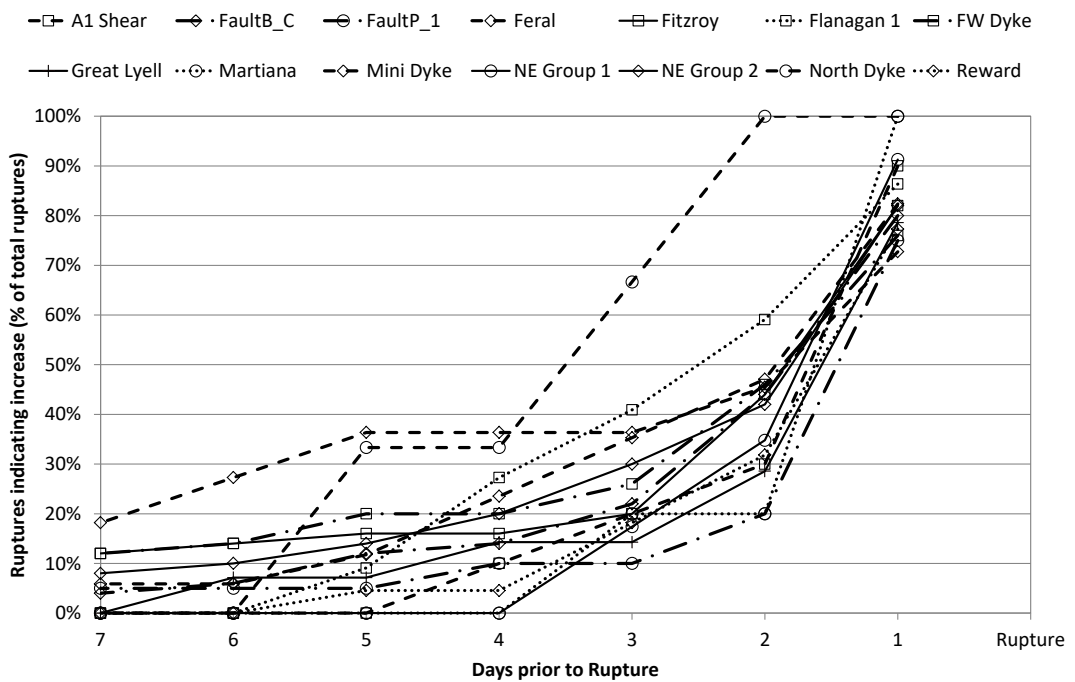


Figure 8.23: Results on the conditional analysis for daily event rate data smoothed over 7 days (instantaneous failures).

8.4.3.2 Accelerating slip

The average results for the conditional analyses of the accelerating slip events are provided in Figure 8.24. This method is much more conclusive for this type of failure (compared with the instantaneous failures). In general, all faults exhibited an improvement in the determination of failure. Marginal increases (10 – 20%) in successful prediction were observed 1 – 2 days prior to the failure. At earlier times prior to failure (3 and 4 days prior) almost all faults showed a 30 – 40% increase in the determination of failure. Fault B_C is provided in Figure 8.25 as an example. The 14 day smoothed results show that 25% of the accelerating slip failures can be identified 7 days prior to failure. The results show that these types of failure are much more predictable than instantaneous failures. These results are logical given that accelerating failure is defined by the number of events in a day.

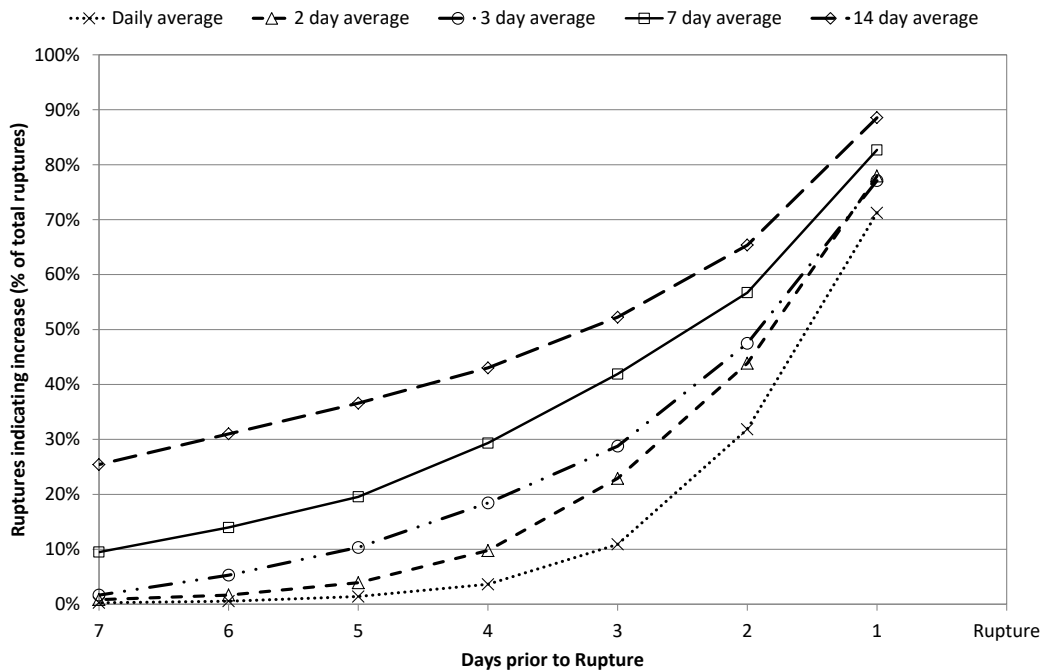


Figure 8.24: Summary of rolling average results for accelerating slip failures.

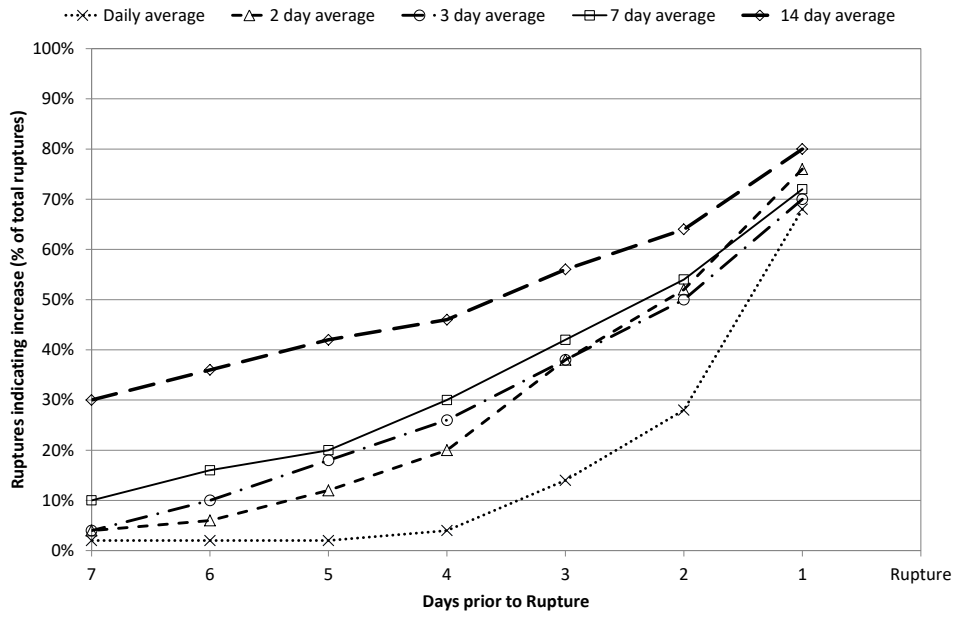


Figure 8.25: Example of improved results as a consequence of smoothing (Fault B_C).

8.5 Discussion

The results demonstrate that the mining induced seismicity is sporadic. Whilst 2 events can occur in close succession, it may be days or weeks between seismic episodes. This often results in what Mikula et al., 2008 describe as stepped behaviours in structures. The sporadic stress releases that result in inconsistent seismic episodes may be as a consequence of intermittent mining extraction rates causing increases and decreases in seismic rates or it may be the result of a stick-slip mechanism of structural failure. Additionally, the above mechanisms are exaggerated due to limitations of the monitoring systems in both location extents and magnitude. Denser seismic arrays with more sensitive accelerometers and geophones may smooth out some of the fluctuations in results. Smoothing out fluctuations through data manipulation improves the results over longer time periods. However, the improvements are often marginal given the time periods analysed.

Despite the limitations of the data, failure patterns observed within acoustic emission results can be observed both qualitatively and quantitatively. The results have clearly shown that the transition from the primary stage of failure to the final nucleation can be determined.

The best parameter for quantitative analysis was the 7 day rolling average event rate. Using this parameter, it can be determined that the transition from the primary to secondary stage of failure occurs approximately 4 days prior to instantaneous failures and 6 -7 days prior to accelerating slip failures.

9. Spatio-temporal clustering

9.1 Event location general principles

Event location is undoubtedly the most important individual parameter of a mining induced seismic event. Without knowing where the event has occurred most other analysis is futile. Despite its importance as a parameter it appears to be less thoroughly investigated than the event rate and the b-value. Chapter 5.1 discussed methods of clustering currently used in the mining industry. These methods are primarily used to group seismic data together using spatial proximity to enable further analysis (Hudyma, 2008). In those analyses time is treated as a separate variable. For this analysis grouping of seismic data has already been undertaken by applying structural domains (Chapter 2.2.5). The following sections examine the location of the event on the structure in relation to surrounding events as a variable with time.

Observations of earthquake locations and locations within rock samples indicate that as rupture approaches the events coalesce from a random distribution to a defined failure plane with increasing stress. Scholz, 1968a analysed 22 events from an acoustic emission test and concluded that *“events that occur below the point of rapid acceleration of activity could be considered independent, whereas events above it could not”*. He goes on to state that *“as stress approaches the fracture strength they (the events) begin to coalesce in some way to form a fault”*. An example of the coalescence prior to failure is provided in Figure 9.1.

Mogi, 1968 conducted similar experiments using a greater number of source locations which confirmed this behaviour. He also identified similar trends prior to several large earthquakes, although acknowledged that it was not present prior to every earthquake. This theory has been further demonstrated by numerous authors including Lockner et al., 1991, Lei et al., 1992, Kijko and Funk, 1996, Enescu and Kiyoshi, 2001 amongst others.

Lockner et al., 1992 observed that homogeneous materials showed very little signs of clustering prior to the fault nucleation stage whereas heterogeneous samples indicated clear signs of clustering during the secondary stage of failure.

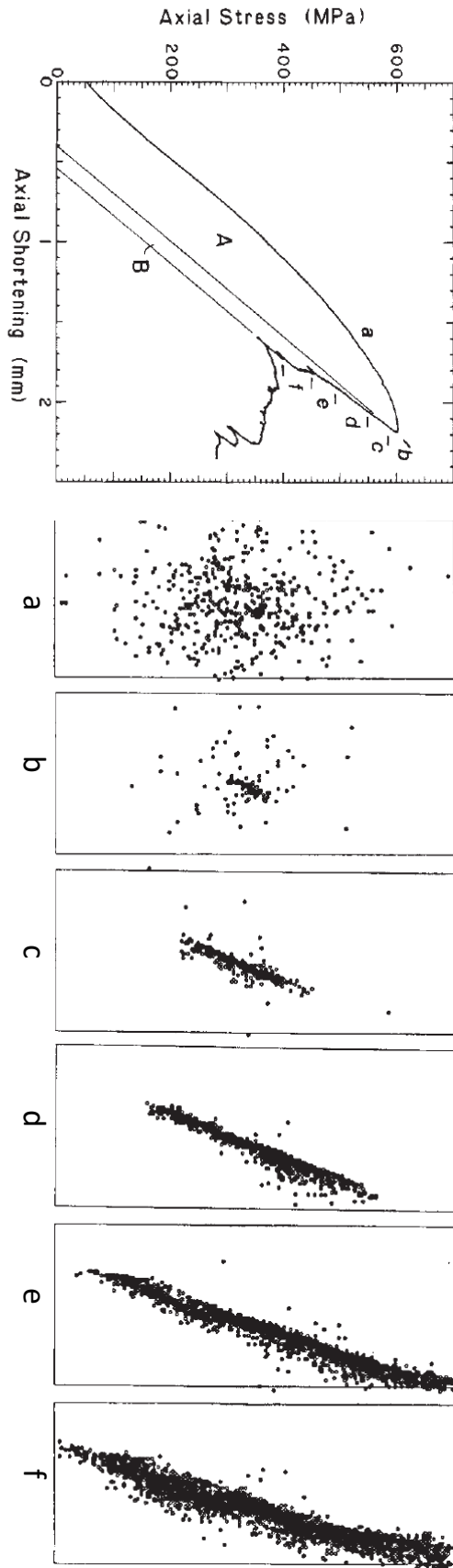


Figure 9.1: Coalescence of AE events demonstrated after Lockner et al., 1991.

Lei et al., 2003 tested a sample with multiple asperities along a pre-existing asperity. Clear patterns were observed during the nucleation phase. The sample exhibited a repetition of the typical event rate pattern within the nucleation phase. Each rapid increase in the AE rate was followed by a large main shock. Analysis of the location of the events during each of these rises indicated that progressive failure of the asperities occurred (Figure 9.2). The asperities located towards the top of the sample failed first and a failure front (called the process zone) was created as each proceeding asperity became active. The damage zone occurs behind the failure front. Events continue in the damage zone after the failure front has passed until final failure of the sample is achieved. A rapid increase in AE rate occurred just prior to overall failure of the sample.

There are many methods used to quantify the extent of clustering. The next section provides an overview of the methods used to determine changes in clustering with time.

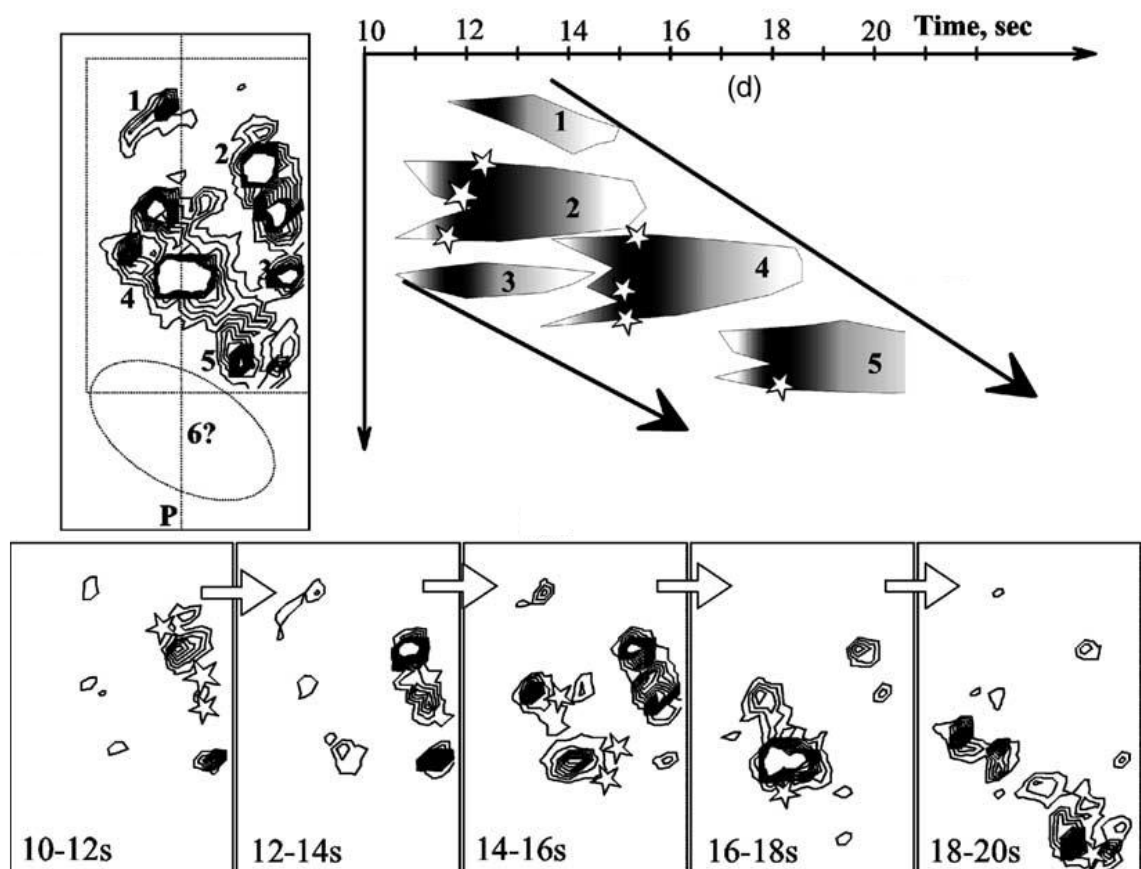


Figure 9.2: Failure progression of multiple asperities (Lei et al., 2003a).

9.2 Methods of Clustering

Whilst there are several methods of comparing seismic event locations in time (e.g. Principal component analysis (CAMIRO, 1996), Epidemic type aftershock sequencing (Lei et al., 2008)) the main methods utilise fractals or spatial correlation length. Both these parameters assess the distance relations between events and will be discussed in the following sections.

9.2.1 Fractal dimension

“Fractals” is a branch of statistics oriented to analysing self-similarity and scale invariance within the natural environment. Fractal relationships within earthquake data have been observed by many researchers.

The aim of using fractal analysis in assessing the spatio-temporal behaviour of seismic data was to determine if acoustic emission data could be compared with earthquake data (Hirata et al., 1987) This is undertaken using the fractal dimension. Fractal dimension is calculated in 2 stages. Firstly, the correlation integral determines the distance between pairs of events and groups them (Equation 9.1).

$$C(r) = \frac{2N_r(R < r)}{N(N - 1)}$$

Equation 9.1

where $N_r(R < r)$ is the number of pairs with distance smaller than r and N is the total number of events analysed. If the distribution of the pair distances is fractal then $C(r)$ is proportional to the power of the r distance (Equation 9.2).

$$C(r) \propto r^D$$

Equation 9.2

The power function D is the fractal dimension. During the analysis Hirata et al., 1987 noted that “*the fractal dimension decreases with the evolution of rock fracturing*”. They also state that if the events are located randomly in three dimensions, the fractal dimension D is 3 or greater. If the fractal dimension is less than 3 it indicates that events are coalescing and that they are self-similar in scale i.e. that they are comparable at all scales. The results indicate that some clustering of acoustic emission hypocentres indeed exist indicating the fractal nature of seismicity.

Lei et al., 1992 also found that “*the fractal dimension changes during fracturing, suggesting that the heterogeneity of micro-crack distribution changes during the fracturing process*”. The study also found that samples with larger grain sizes typically have lower fractal dimensions indicating closer spatial locations compared with the AE locations in fine grained homogeneous rock masses. Typically the fractal dimension for each sample is between 1.8 and 2.2 (Lei et al., 2004, Lei, 2006).

Despite these observations Hirata, 1989 states there are limitations to the application of fractal theory. The fundamental principle lies in theoretical self-similarity and the assumption that the data is fractal in nature. Since it cannot be confirmed that the data used in this thesis is in fact fractal to begin with, this analysis will not be undertaken.

9.2.2 Spatial correlation length

Lei and Satoh, 2007, proposed to use the spatial correlation length rather fractal dimension for quantifying clustering of seismic data. Frohlich and Davis, 1986 were the first to apply this method to seismic data. SCL is estimated using single link cluster analysis (Figure 9.3) whereby a hypocentre is grouped with its nearest neighbour. This pair is then grouped again to form a cluster of hypocentres with the number of hypocentres within the set being specified (N). For each pair, the distance between it and the next closest pair is calculated. The spatial correlation length (SCL) is the average distance within the cluster.

Frohlich and Davis, 1986 suggest that given the tendency for this method to form linear chains it is well suited to the assessment of seismic data associated with faulting.

Lei and Satoh, 2007, used this method alongside fractal dimension and b-value and noted similar patterns of behaviour (Figure 9.4). Overall the SCL stays relatively stable during the primary stage of failure. During the secondary stage of failure, the SCL drops to a global minimum before increasing during the nucleation phase. The following analysis will assess this parameter to determine if these patterns can be identified.

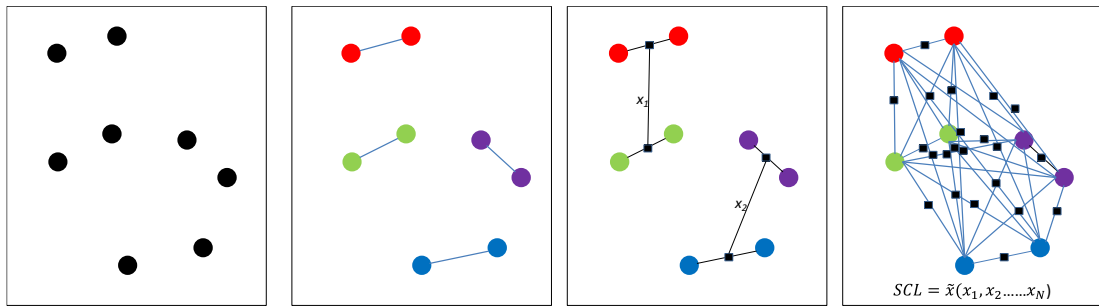


Figure 9.3: Spatial correlation length (SCL) is calculated by linking events into pairs and then calculating the distance between each pair.

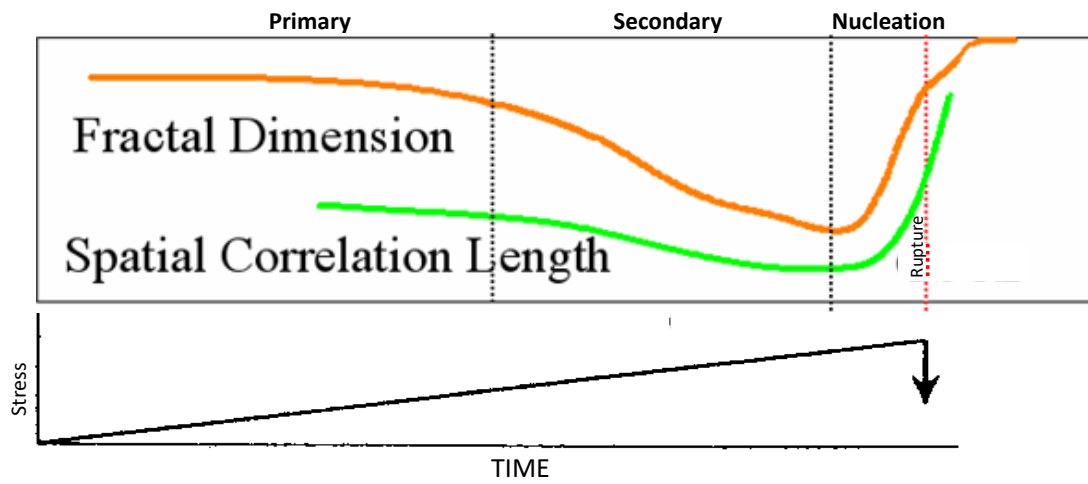


Figure 9.4: Trends in SCL and fractal dimension during failure.

9.3 Analysis method

As previously discussed, single link clustering is used extensively to group seismic data together prior to analysis. When using it for grouping data together the maximum tolerable distance is specified. In this case the data has already been clustered and the SCL is calculated over time periods. The distance relationship between all events within a specific time period is calculated without limitations on the distance.

The calculation of the SCL parameter was undertaken using a program written in python script. The input parameters were X, Y, Z coordinates and date. In order to undertake the calculation a minimum number of points are required. The program was written to enable this parameter to be defined by the user. Due to the low number of points within most datasets a “group size” of 5 was selected. This means that SCL will only be calculated on days where 5 or more events occur. All events occurring on the day are still used in the calculation.

The program calculates the distances between each set of events on the day and then takes the average. Whilst 5 events were used for all faults, a review of changing this parameter was undertaken. The results are included in the sections below.

9.4 Daily SCL rate

An example of the Daily SCL rate is provided in Figure 9.5. A qualitative evaluation of the results indicates that instantaneous failures are not necessarily associated with low SCL values. However, accelerations in the seismic event rate do concur with decreases in SCL. Conditional analysis was undertaken on each event to determine if the decreasing trend could be quantified. The results for instantaneous failures and accelerating slip failures are provided in Figure 9.6 and Figure 9.7 respectively. The results indicate poor correlations between instantaneous failures and the SCL trend with less than 30% of failures indicating a decreasing trend a prior to rupture. Accelerating slip failures have a much higher rate of success with approximately 50% (on average) of all failures showing a decreasing trend the day prior to rupture. Despite this only 20% of events have a decreasing trend 2 days prior to rupture.

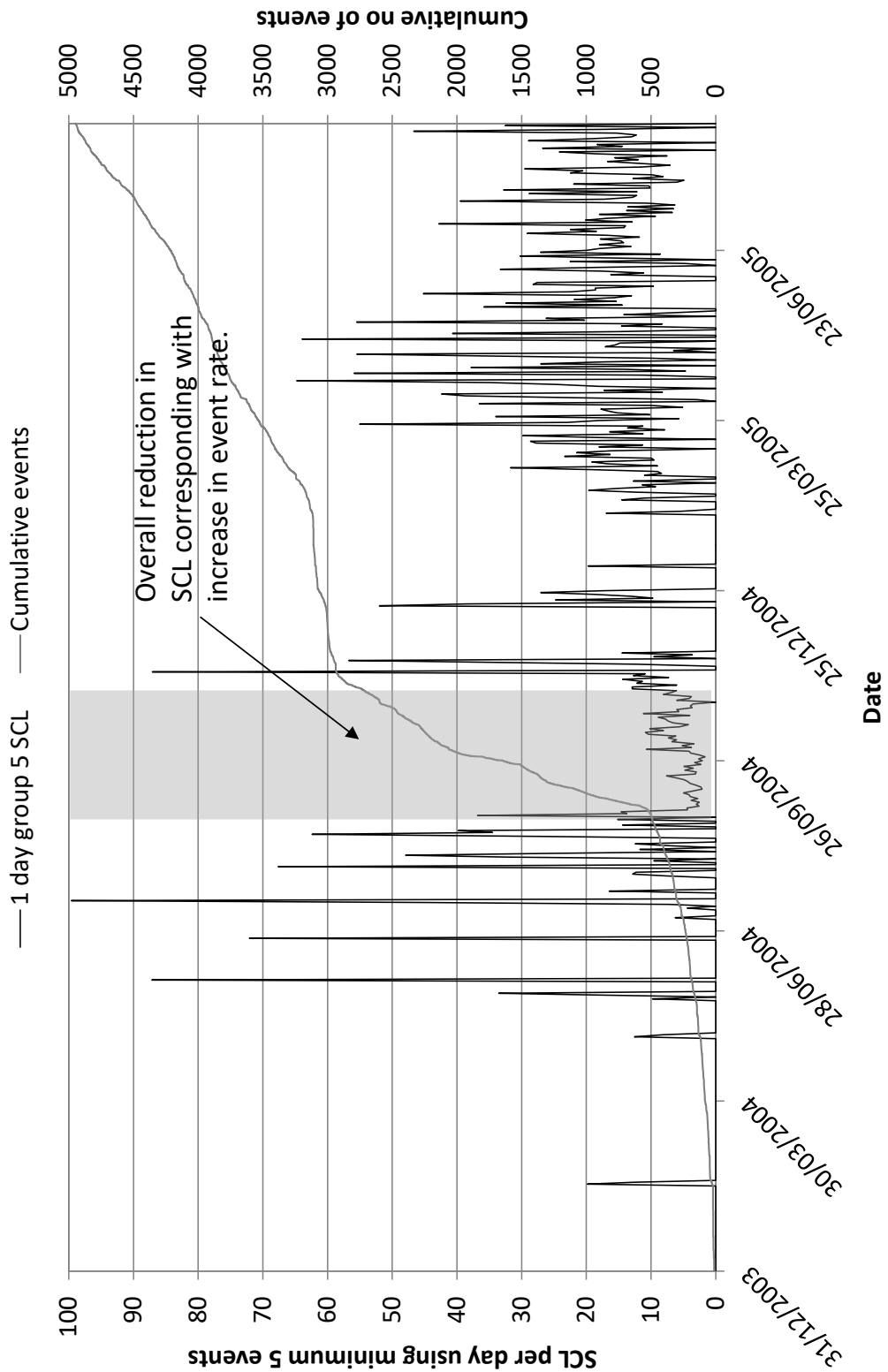


Figure 9.5: Example of SCL results highlighting increase in event rate with decrease in SCL (Feral Fault).

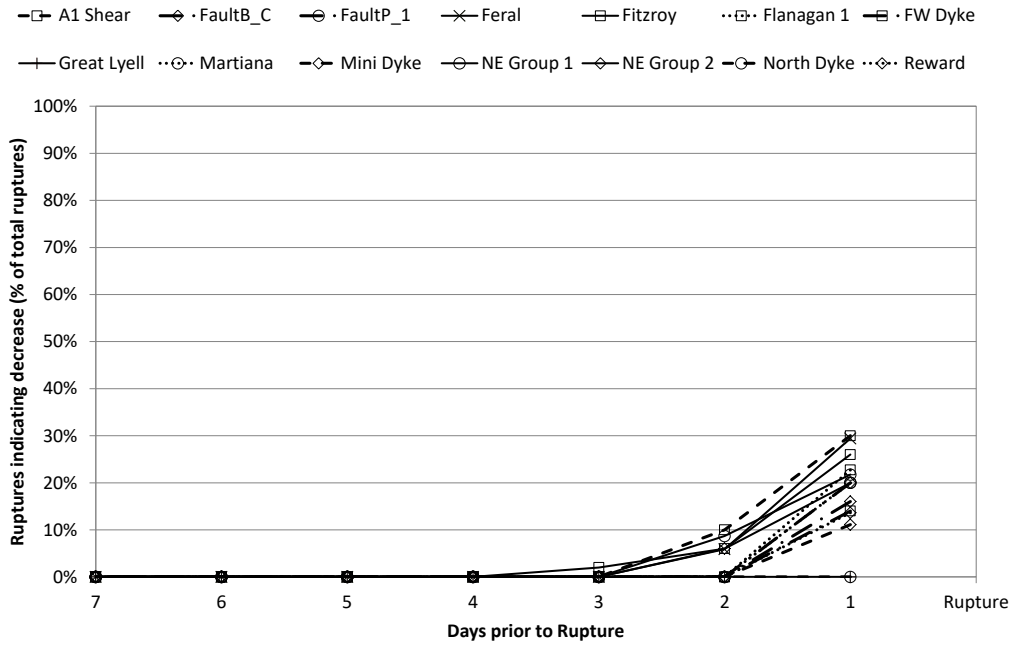


Figure 9.6: Results of conditional analysis of the daily SCL for instantaneous failures.

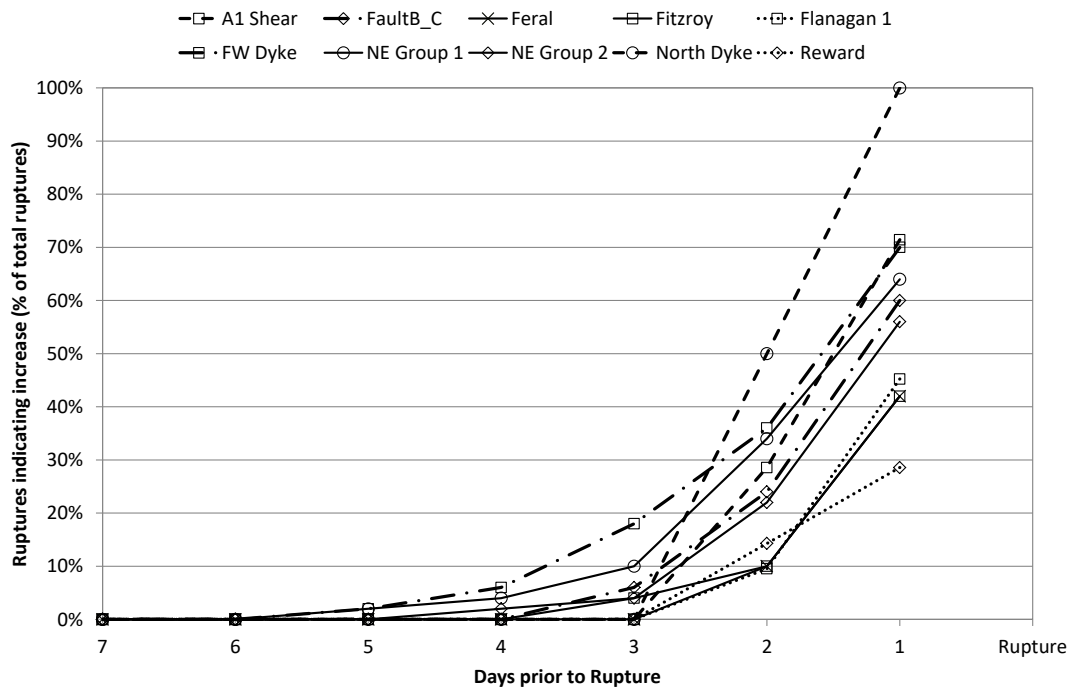


Figure 9.7: Results of conditional analysis of the daily SCL analysis for accelerating slip failures.

9.5 7 Day SCL results

The program was modified to calculate the SCL for days where 5 events have occurred in the previous week. An example of the determination of the number of events is provided in Figure 9.8.

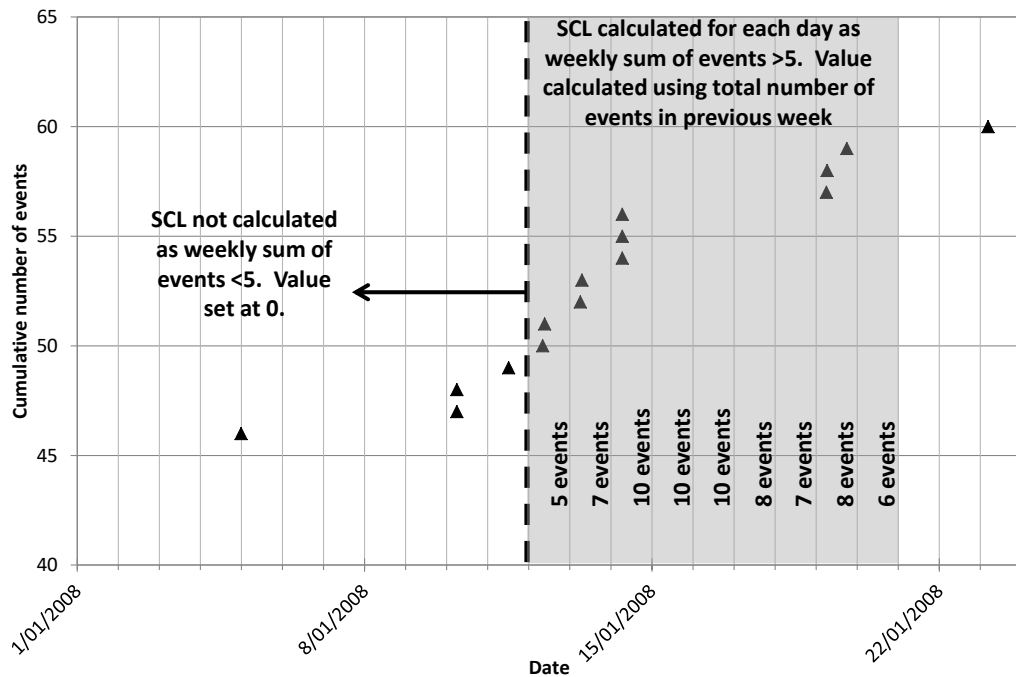


Figure 9.8: Explanation of the determination of number of events for the calculation of the SCL over 7 days with a group size of 5.

The number of monitoring days with greater than 5 events in the previous week increased from 20% for the daily SCL to over 50% using this method. Generally, the faults with high activity rates had values calculated for over 70 of monitoring days whereas structures with low activity rates had values calculated for 25-30% of monitoring days.

Individual results for each structure are provided in Appendix 6. An example of the 7 day SCL results is provided in Figure 9.9. Qualitatively, almost all faults have a large increase in the seismic event rate when the SCL drops below 10. This can be used as a deterministic risk assessment. Whilst the drop cannot determine where the failure is occurring if the SCL is less than 10 then failure is likely to be occurring and further assessment is required.

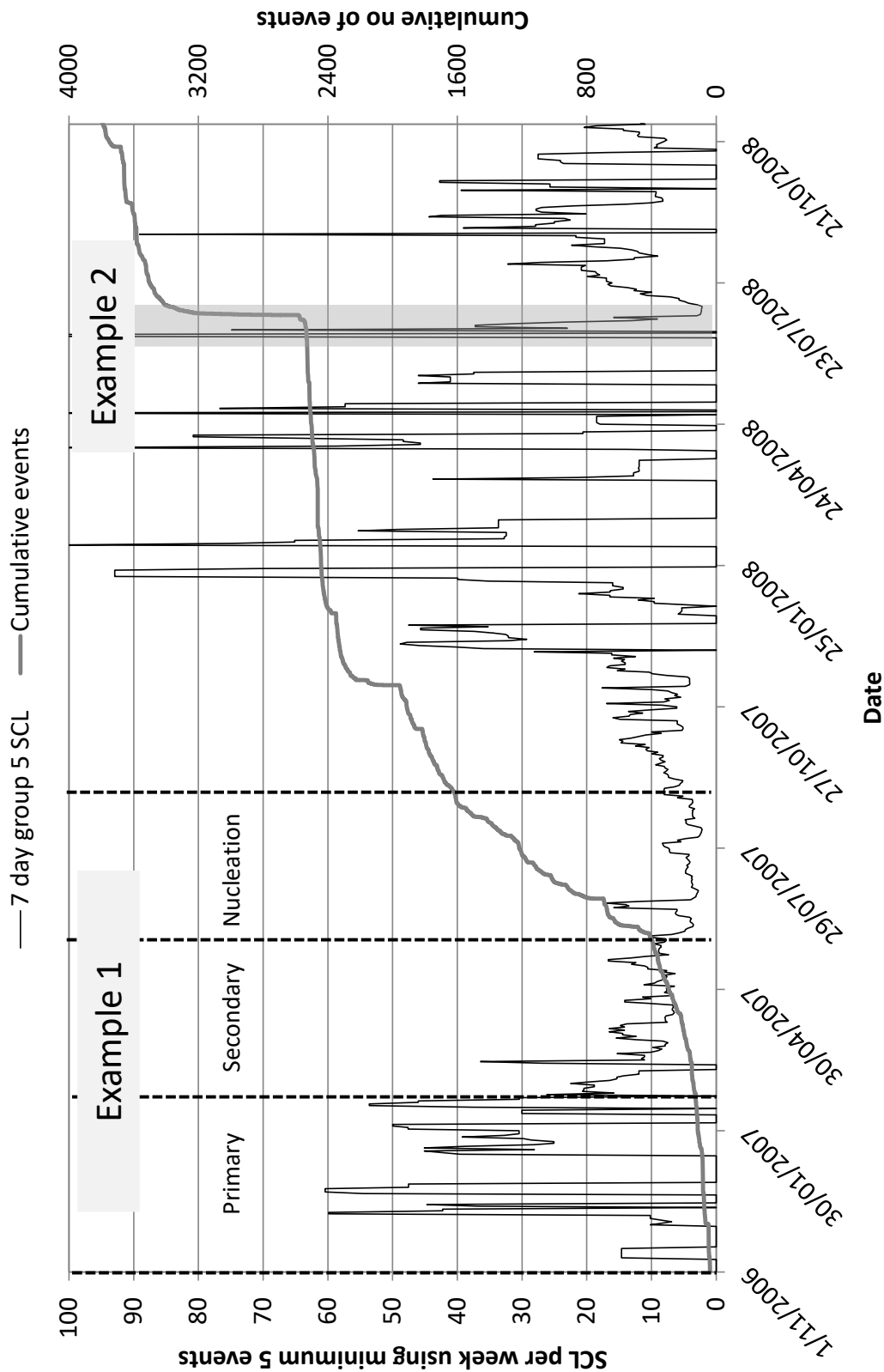


Figure 9.9: Example of phases of failure evident in the 7 day group 5 SCL results (Flanagan Fault).

The results of the conditional analysis are provided in Figure 9.10 and Figure 9.11 (instantaneous failures and accelerating slip failures respectively). The results indicate a much higher degree of success compared with the daily results. On average 50% of instantaneous failures and 70% of accelerating slip failures indicate a decreasing trend the day prior to rupture. For instantaneous failures the transition between the primary and secondary stage of failure is identifiable only 1 -2 days prior to rupture however the confidence limit is still very low. Only 20% of instantaneous failures indicate a decreasing trend 2 days prior to rupture.

Accelerating slip failures however have a much clearer transition between the primary and secondary stages of failure. Decreasing trends in the SCL can be identified as far out as 4 days prior to rupture with 20% of failures indicating a decreasing trend this far out.

Overall the results indicate that clustering is strong prior to accelerating slip failures but not prior to instantaneous failures. This result is logical given that accelerating slip failures generally suggest progressive failure at a crack tip. This causes a concentration of many events in a small area and hence the event rate increases and the SCL decreases. Instantaneous failures, however, cannot occur without an accumulation of stress in a particular location. For stress to accumulate fracturing must be minimal and hence very little clustering of events would be observed.

Although these results appear conclusive the effect of the group size must be assessed. The following section assesses the results of using 20 events within a week in the calculations.

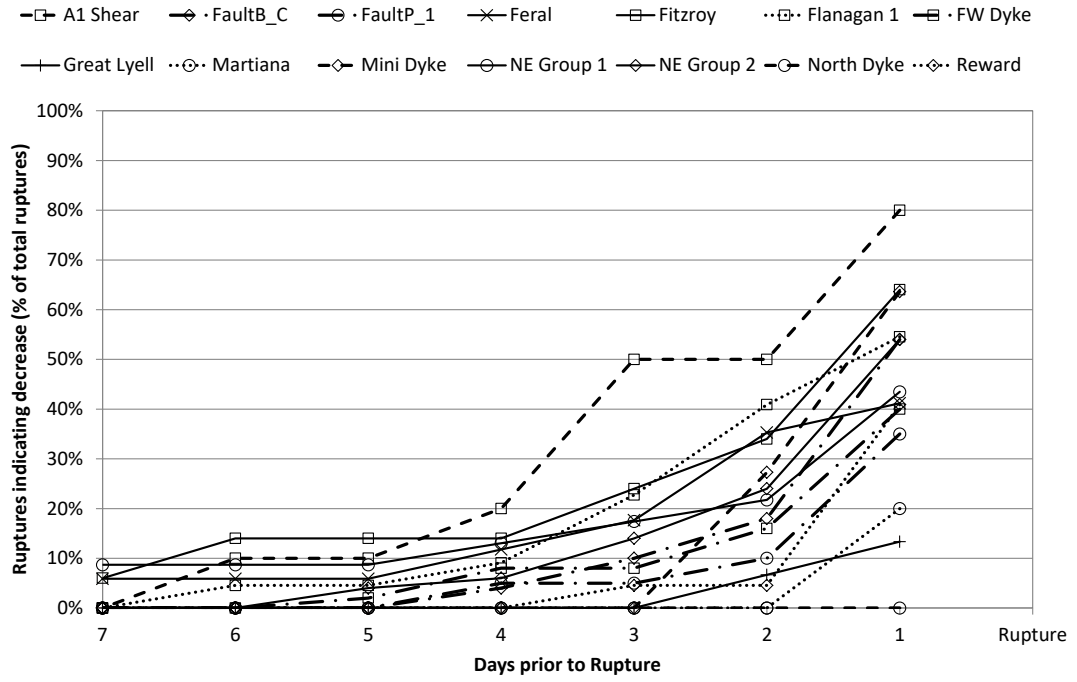


Figure 9.10: Results of 7 day group 5 conditional analyses for instantaneous failures.

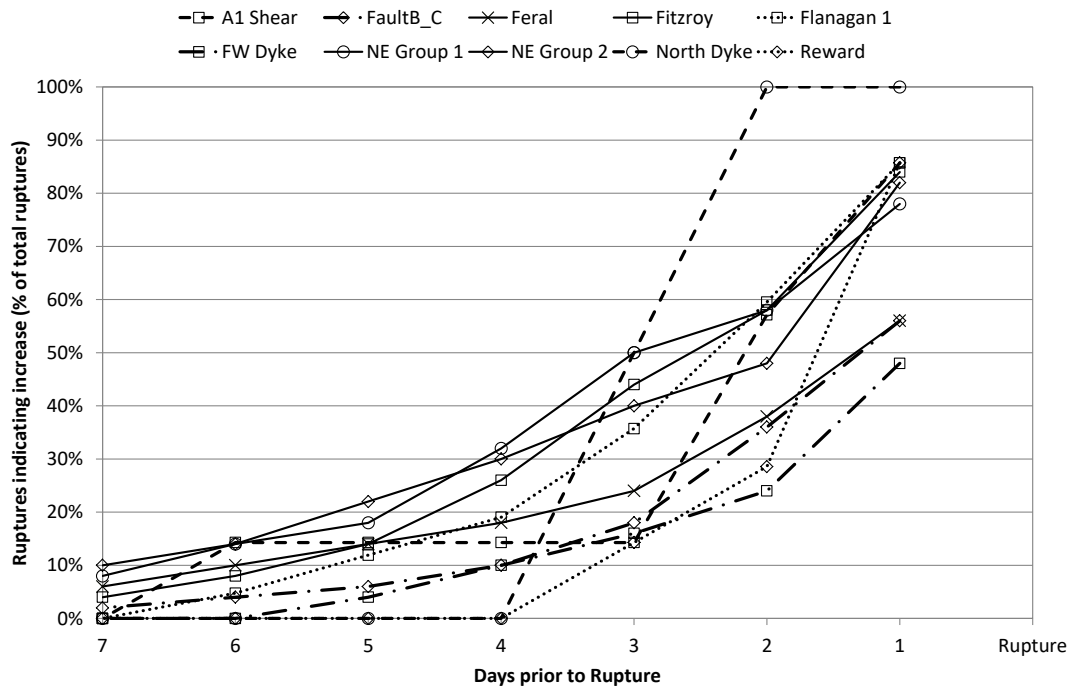


Figure 9.11: Results of 7 day group 5 conditional analyses for accelerating slip failures.

9.6 7 day group 20 results

In order to evaluate the effect of group size on the results it was increased to include more events in the calculation. A group size of 20 events over a week was selected for analysis. This value was selected as it was assumed to be sufficiently larger than the previous analysis to evaluate the effects of the change. Larger values were considered but given the low event rates on the faults they were deemed to be not appropriate. A limited number of faults had a high enough event rate for this analysis to be conducted. Consequently, this analysis was only conducted on faults that had greater than 50 days where 20 events or more occurred. This applied to 6 faults; namely, the Esmerelda faults Fault B_C and the FW Dyke, all the Kanowna Bell Faults (Fitzroy faults and the North East Groups 1 and 2) and the Black Swan Feral Fault.

Despite only selecting faults with adequate data for analysis all faults only had values calculated for 35 – 45% of the monitoring days.

Comparative results for of the conditional analysis are provided in Figure 9.12 and Figure 9.13 (instantaneous failures and accelerating slip failures respectively). They indicate that there is no benefit to using a high number of events in the calculation if it decreases the number of monitoring days where results are generated.

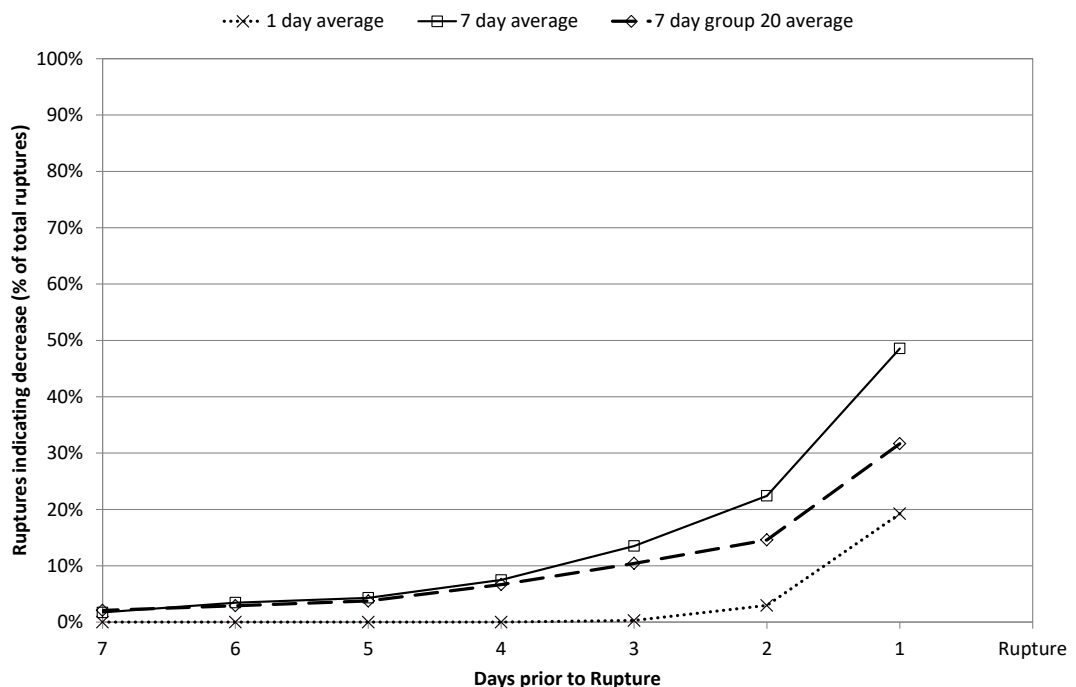


Figure 9.12: Comparison of average results of the conditional assessment of the instantaneous failures from the 7 day group 20 data with the results from the 7 day group 5 and daily group 5 data.

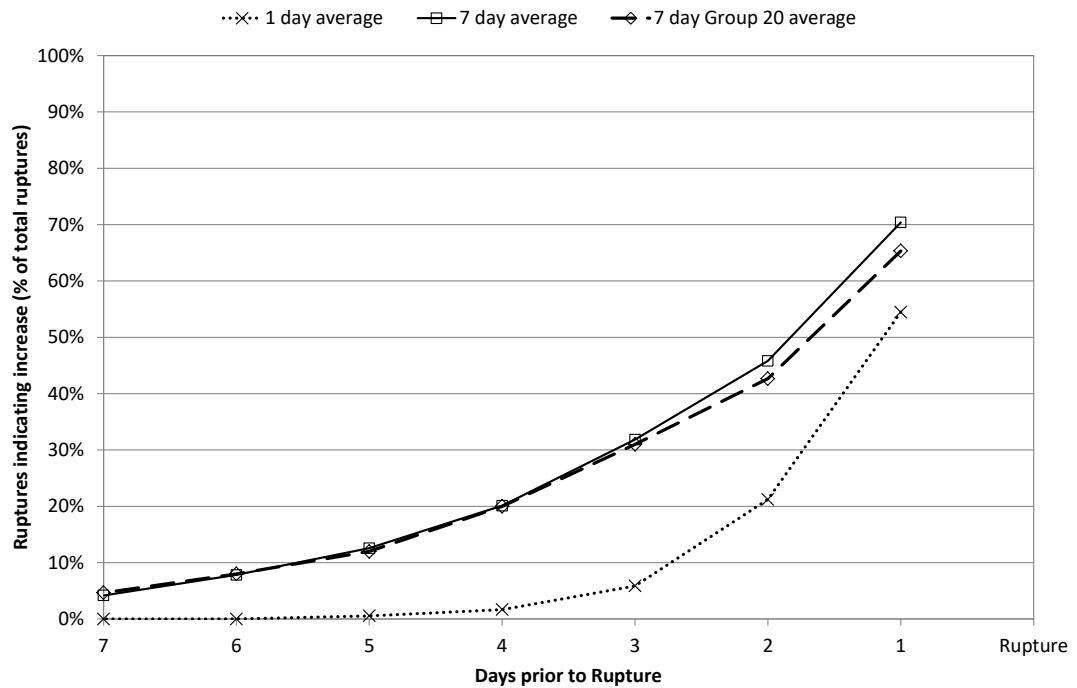


Figure 9.13: Comparison of average results of the conditional assessment of the instantaneous failures from the 7 day group 20 data with the results from the 7 day group 5 and daily group 5 data.

9.7 Discussion

A general drop in the SCL can indicate that failure is occurring at a global level within the mine or along a particular structure. It is suggested that SCL decreases can be used to highlight high risk periods with values less than 10 indicating failure is in progress. Further analysis would be required to determine where fracturing was occurring and the effect of that fracturing.

This analysis has determined that evaluation of the SCL has limited success in highlighting specific ruptures. This is primarily due to the low event rate on the faults. The selection of the minimum number of events can influence the results. A balance must be found between having an adequate number of events for clustering to be identified and the event rate on the structure.

10. Magnitude and b-value

10.1 Introduction

Aside from event rate and location studies, magnitude is one of the most analysed properties of seismic events. Temporal variations in magnitude have been observed prior to earthquakes and rock sample ruptures since the 1960s. The theory suggests that warning earthquakes of small to moderate magnitude occur prior to large damaging earthquakes. The warning earthquakes are called foreshocks and are typically only identified after the main quake (United States Geological Survey, 2016).

Mogi, 1962b undertook various studies on rock samples and found that the magnitude of “*elastic shocks*” fluctuated with time. It was observed that as the event rate increased prior to failure so too did the magnitude. The b-value is calculated as an inverse relationship to the magnitude and hence theoretically the b-value decreases prior to failure. Lei et al., 2003a states that “*low values of b do not correspond simply to the effect of a few large events but rather a shift of all magnitudes*”. The following section reviews the different methods for determining temporal b-value and tests the theory of decreasing b-value against each fault dataset.

10.2 Magnitude and b-value concept

As discussed in Chapter 5.4, Gutenberg and Richter, 1949 observed that there was a relationship between the magnitude of an event and the number of events. This relationship is calculated using Equation 10.1.

$$\text{Log}10N=a-bM$$

Equation 10.1

The “b” in this equation is referred to as the b-value and calculated by determining the slope of the line formed by this relationship (Figure 10.1). As demonstrated in Chapter 5.4 the current method of determining b-value in mining applications is static and does not consider temporal changes.

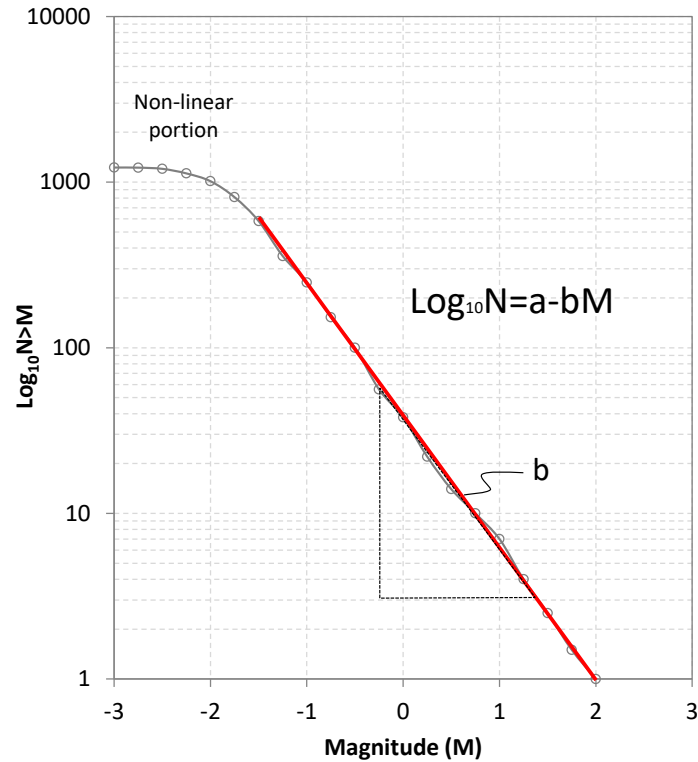


Figure 10.1: b-value is determined by the slope of the Magnitude – Frequency chart.

Utsu, 1965, developed a formula accurately estimating b-value using the statistical maximum likelihood method (Equation 10.2). The symbol m denotes the total number of earthquakes whereas M denotes the magnitude. The constant 0.4343 relates to the value $\log_{10}(e)$, The denominator is determined by calculating the average of the magnitude over a specific time period (M_i) and subtracting the minimum magnitude for the dataset used in the calculations (M_m). Aki, 1965 presented a simplified version of this formula as shown in Equation 10.2.

$$b = \frac{0.4343m}{\sum_{i=1}^m M_i - mM_m} = \frac{0.4343}{\overline{M_i} - M_m}$$

Equation 10.2

Variations of this formula have been used by many authors to assess the temporal change of b-value (Scholz, 1968c, Meredith et al., 1990, Lockner et al., 1991 Lei et al., 2000a etc). These temporal variations in b-value will be evaluated in the following sections.

10.3 Temporal changes in b-value

Earthquake and Acoustic Emission researchers in the 1960s identified temporal variations in b-value prior to failure (Lomnitz, 1966, Scholz, 1968c). The results indicate b-value behaves inversely to the event rate. Scholz, 1968 states that b-value varies in the following way:

“At low stress, where crack closing and sliding are important, high values of b are observed. Above about 50 per cent of the fracture strength, where new fractures are propagating, b is lower, in the range usually found for earthquakes, and decreases with stress”.

Many additional authors have observed these changes (Robinson, 1979, Main et al., 1989, Main and Meredith, 1989, Meredith et al., 1990, Lockner et al., 1991, Lei et al., 2000a, Lei et al., 2003a, Rao and Prasanna Lakshmi, 2005). In summary it is the general consensus that b-value behaves in the following manner: Initially the b-value increases with increasing stress to a maximum value. The maximum indicates the transition from the primary to the secondary stage of failure. During the secondary stage of failure, b-value decreases with increasing stress. During the nucleation phase the b-value reaches its global minimum before fluctuating as failure initiates. This behaviour is indicated in Figure 10.2. As Indicated in the figure the nucleation phase makes up a very short time period of the overall rupture time frame and can be difficult to identify.

Whilst the above described behaviour is generally accepted, variations exist depending on the rock homogeneity (or lack thereof). Lei, 2006 demonstrates that b-value is not only related to the localised stress conditions but also to the heterogeneity of the rock mass.

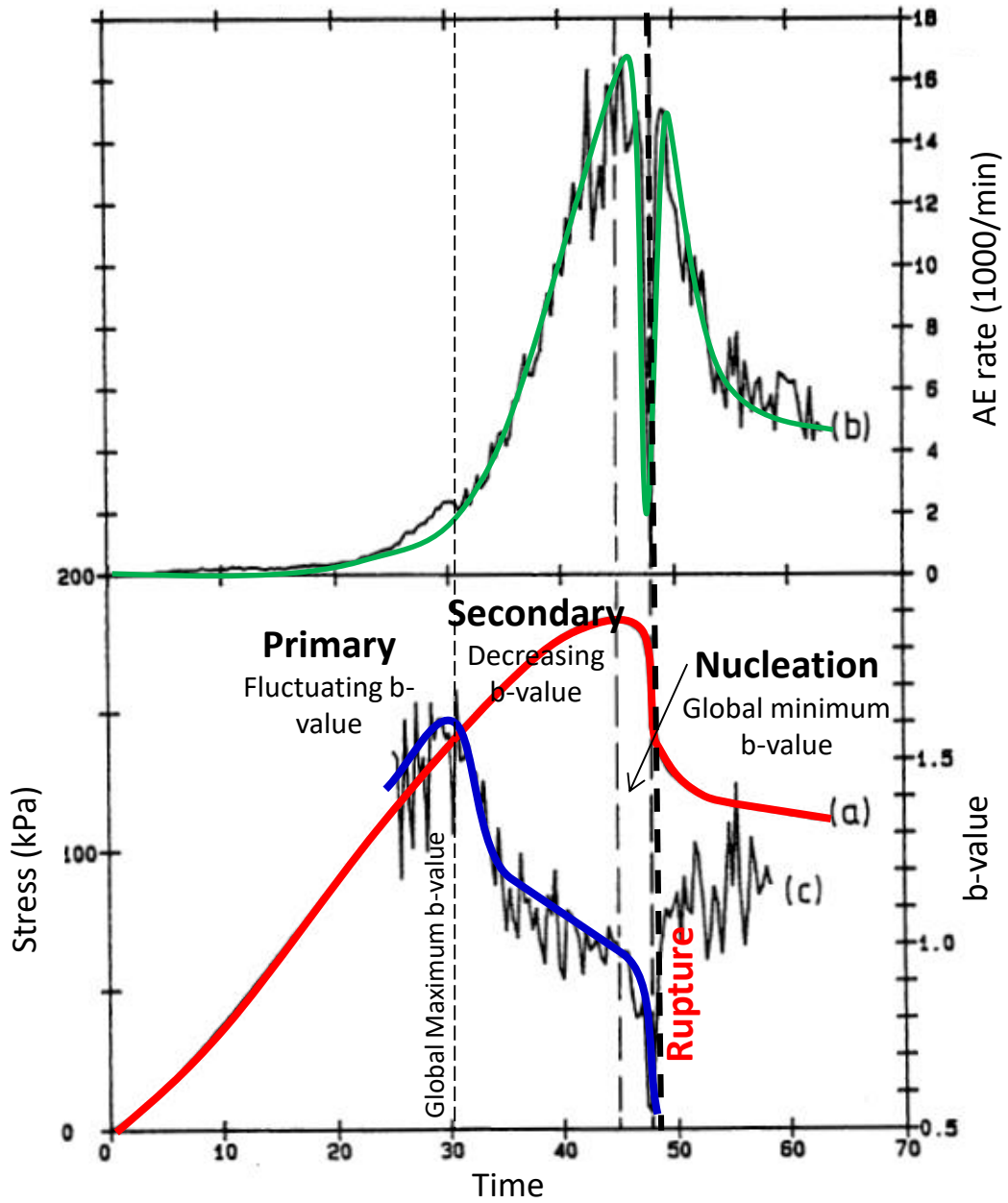


Figure 10.2: Typical change in b-value during testing of a sample (after Main and Meredith, 1989).

As described, the primary phase is characterised by a b-value that increases with increasing stress. This indicates the “*opening or rupturing of pre-existing micro-cracks*” (Lei et al., 2004). Consequently, the primary stage is well defined in coarse grained rocks and rocks with a high density of pre-existing micro-cracks. The b-value in these rocks increases from approximately 1.1 to 1.3. For homogeneous fine-grained materials, the primary stage b-value can be poorly defined and is generally slightly lower than that of the coarse-grained materials. For these materials the b-value increases from approximately 0.8 to 1.1.

The maximum b-value indicates the transition from the primary stage to the secondary stage. During the secondary stage the b-value decreases with increasing stress. This feature indicates sub-critical crack growth whereby fracturing will cease if loading is removed. The minimum b-value occurs just prior to a main shock and is indicative of the nucleation phase. In rock masses with well-defined pre-existing fractures the b-value decreases from 1.3 to a minimum value of 0.5 during the secondary stage. The nucleation phase is characterised by clear foreshock / aftershock sequences that cause the b-value to fluctuate.

Rupture of fine-grained homogeneous rock masses occurs rapidly compared with heterogeneous rock masses. Cyclic failure as described above is not observed and consequently there is less fluctuation in the b-value. During the secondary stage the b-value drops from 1.1 to 0.7 with dynamic fracturing occurring almost immediately after the minimum b-value is reached.

The aim of this evaluation will be to determine whether the b-value consistently decreases prior to rupture.

10.4 b-value calculation

The conditional analysis described in Chapter 7.5 will be applied the b-value to determine if decreasing trends can be identified prior to rupture and if so how far prior to rupture the decrease occurs.

Two methods of calculating b-value were considered; that described by Utsu, 1965 and Aki, 1965 (Equation 10.2) and a modified version used by Lei et al., 2000a (Equation 10.3). In these equations m is the number of data points, M_i is the magnitude of the number of data points selected for analysis. M_m is the minimum magnitude for the dataset being used in the calculations (i.e. the minimum for each day, 7 days or 14 days). Several authors explore the accuracy and application of this formula (i.e. Page, 1968, Weichert, 1980) however this will not be discussed as part of this thesis.

$$b = \frac{0.4343m}{\sum_{i=1}^m M_i - mM_m} = \frac{0.4343}{\overline{M}_i - M_m}$$

Equation 10.2

$$b = \frac{\log_{10} e}{\overline{M}_i - M_c + c}$$

Equation 10.3

Lei et al., 2000a recognised that all seismic record databases are incomplete and that a statistical bias exists. This assumes that event size is a continuous scale. At the lower end of the scale the seismic database is limited by the sensitivity of the monitoring system rather than the lack of existence of events. In order to account for this, the minimum magnitude value was replaced with a cut-off value (M_c) and a constant that accounts for the bias in the determination of the frequency magnitude curve (c). These values are described in more detail below.

10.4.1 Cut-off value (M_c)

The cut-off value (M_c) represents the limit of the accuracy of the monitoring system. As presented in Chapter 3 the magnitude distribution for each site conforms to a normal distribution. This however does not represent reality: the bottom half of the normal curve represents the limit of the systems sensitivity (Figure 10.3). Events of magnitude less than the median value occur but are only recorded if they are within close proximity to enough sensors to enable the event source parameters to be calculated. Consequently, seismic databases are always assumed to be incomplete.

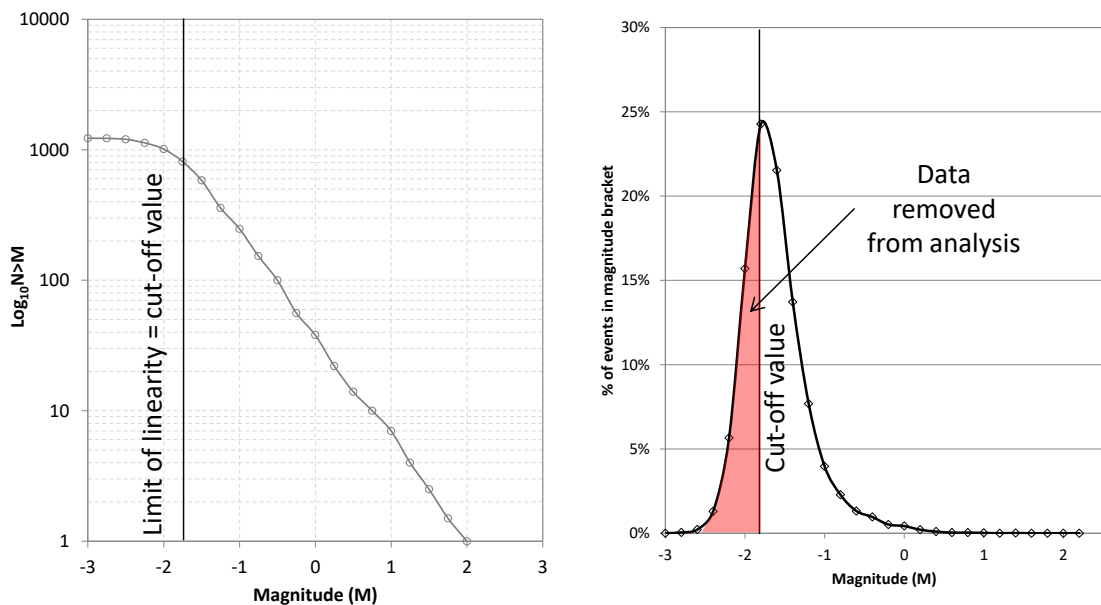


Figure 10.3: Limits of sensitivity for the seismic data records.

To account for this Lei et al., 2000a introduced a cut-off value. This value is determined from the magnitude frequency chart. The cut-off value is determined as the lowest magnitude where the chart deviates from a linear relationship (Figure 10.4).

Table 10.1 provides the cut-off value and the number of data points to be removed from the dataset. Compared with AE datasets the mining data sets have comparatively low numbers of points and hence a high percentage of the fault data subsets are removed using this method. This deems the method impractical and hence only Equation 10.2 (Aki, 1965) will be implemented.

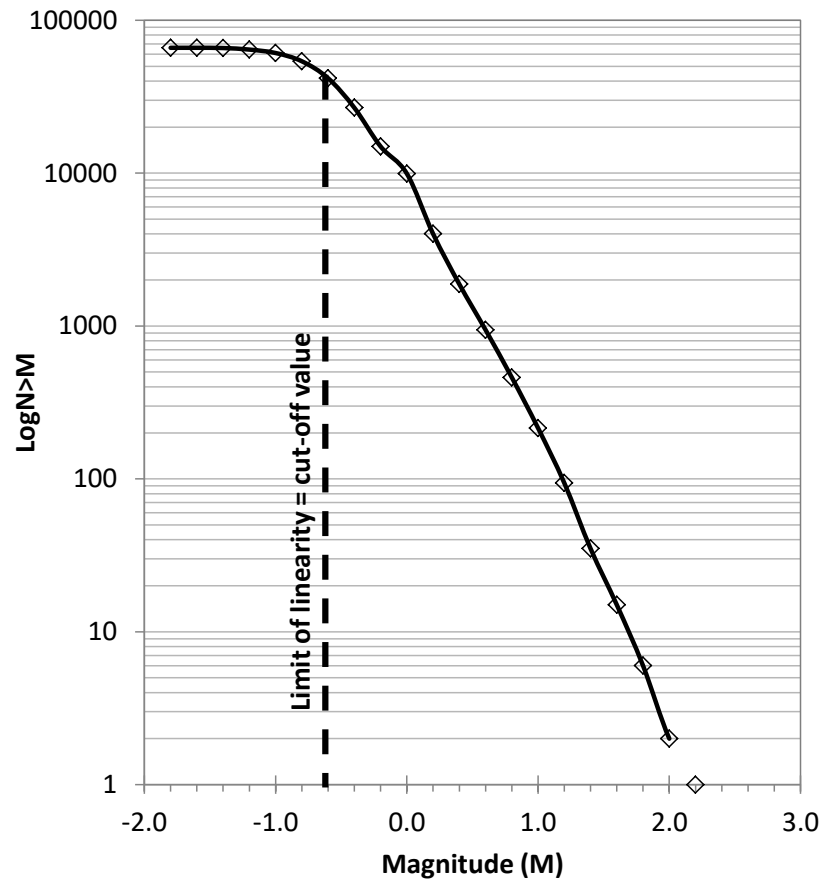


Figure 10.4: Example of cut-off value determination (FW Dyke).

Table 10.1: Cut-off values for each structure.

Structure	Original No of data points	Cut off value	No of events removed	% of events removed	No of events for analysis.
A1 Shear	2120	-2.0	425	20%	1695
Fault B_C	30741	-0.6	10856	35%	19885
FaultP_1	3524	-0.6	216	6%	3308
Feral	4950	-2.4	884	18%	4066
Fitzroy	14475	-3.0	6207	43%	8268
Flanagan 1	4987	-1.6	1888	38%	3099
FW Dyke	66046	-0.6	19747	30%	46299
Great Lyell	247	-2.25	94	38%	153
Maritana	250	-1.6	42	17%	208
Mini Dyke	791	-1.8	236	30%	555
NE Group 1	18070	-2.8	4922	27%	13148
NE Group 2	20038	-3.0	8650	43%	11388
North Dyke	635	-2.0	106	17%	529
Reward	1496	-1.6	577	39%	919

10.4.2 Data steps

Due to the high number of sensors acoustic emission testing produces very large datasets with AE events recorded in the thousands. The application of the b-value equations is typically undertaken using fixed data steps i.e. the calculation is undertaken on x number of points and then a step of y number of points is taken before the next calculation is conducted (e.g. Lei et al., 2000a). Evaluation of the event rate using this method (Chapter 8.3) determined that fixed event steps are impractical in the mining environment due to the lower number of data points in the dataset and irregularity of the events over time. Consequently, the analysis will be undertaken on daily b-values rather than event steps.

10.5 Magnitude variability (b-value estimation) evaluations

10.5.1 Average daily magnitude variations.

As discussed above, the calculation of the b-value estimation was undertaken using Equation 10.2. The average magnitude (sum of magnitudes divided by the number of events) was calculated for each day and the minimum was determined in order to undertake the calculation. As the calculations are averages they are dependent on the number of events occurring per day. The formula will not be resolved where there is 1 event or less per day. In this case a value of 0 is applied. An example of the resultant daily chart is provided in Figure 10.5. Results from all faults are provided in Appendix 7.

The values calculated and represented within the charts do not reflect realistic b-values for the mining data sets. Equation 10.2 standardises magnitude to enable analysis between groups of data in the same dataset, across different time scales or across different datasets. The term b-value applied to this number becomes confusing when applied to mining datasets. Consequently, it will be referred to as the Magnitude variability measure (MVM).

In the example provided in Figure 10.5 instability is evident in 2006 as indicated by the increasing cumulative event rate. Prior to this period the MVM clearly fluctuates. During the instability (increased event rate) the MVM remains low. Once the event rate reduced the MVM again began to fluctuate. This behaviour is symptomatic of the progression of failure. The fluctuating phase characterises the primary stage of failure whilst the decreasing MVM characterises the secondary and nucleation phases. This suggests that MVM may be used to evaluate global instability however it remains to be determined if MVM can indicate more localised instability.

Conditional analysis (as described in Chapter 7.5) was undertaken to determine if the trend of the MVM was decreasing prior to instantaneous failures and accelerating slip failures. The results are provided in Figure 10.6 and Figure 10.7 respectively. The results indicate varying success of decreasing MVM prior to failure. Generally, the results indicate that failure may be identified 2 days prior to rupture for both instantaneous failures and accelerating slip failures. However, overall, all structures indicated that less than 40% of ruptures present a decreasing MVM trend 2 days prior to failure. With such low success rates, it is difficult to apply this analysis in a practical environment. As with the event rate it was deemed necessary to smooth out the fluctuations to determine the overall trend of the dataset. This has the potential to improve the reliability of the analysis.

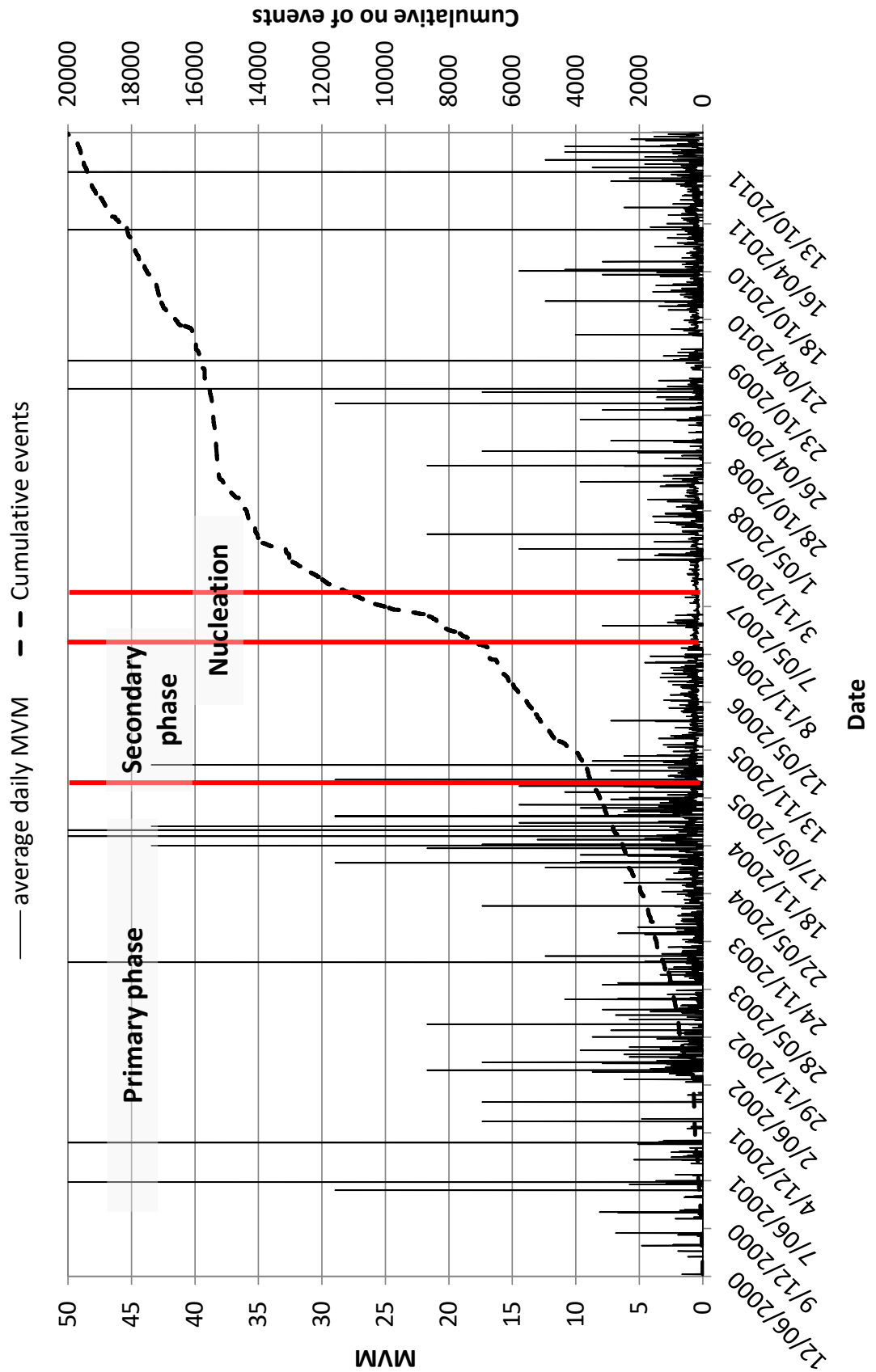


Figure 10.5: Example of the daily MVM (NE Faults G2).

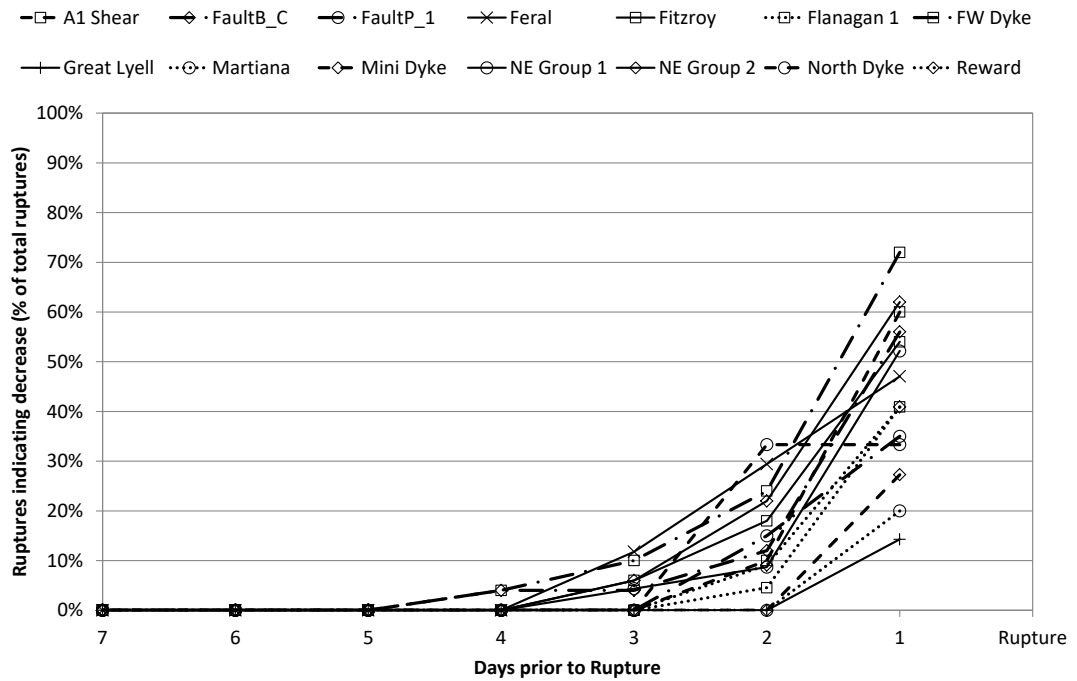


Figure 10.6: Results of daily MVM conditional analysis on instantaneous failures.

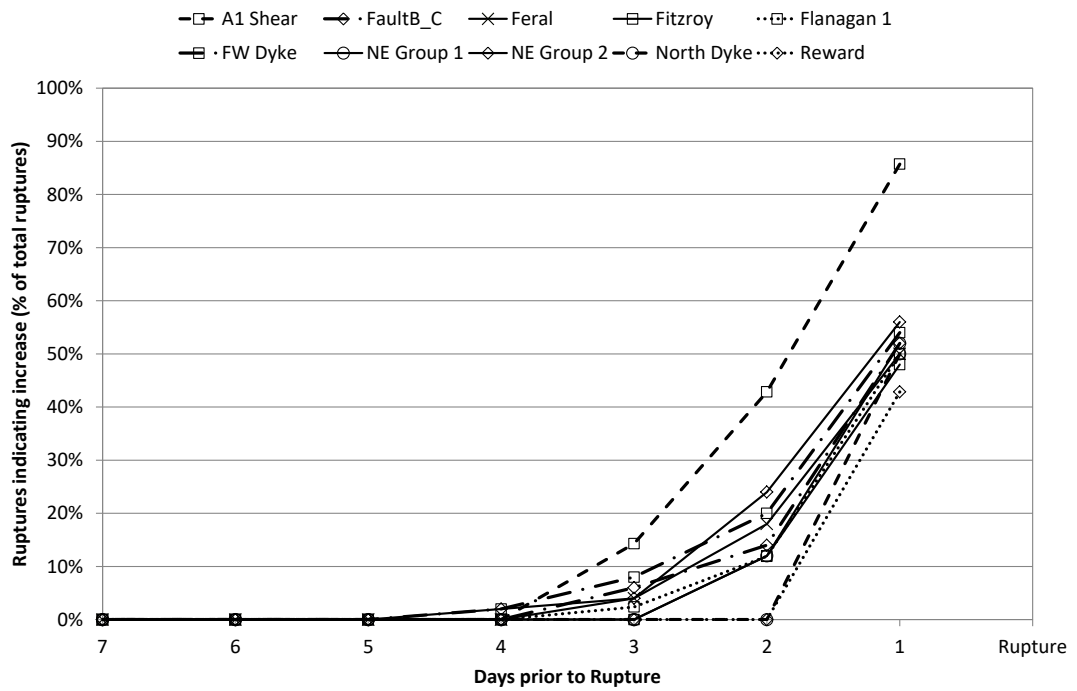


Figure 10.7: Results of daily MVM conditional analysis on accelerating slip failures.

10.5.27 and 14 day rolling averages

Rolling averages were calculated for each dataset to determine if higher success rates could be achieved. The event rate analysis (Chapter 8) determined that 2 and 3 day rolling averages did not significantly alter the results. Consequently, only 7 day and 14 day rolling averages have been calculated. An example of the 7 day MVM results is provided in Figure 10.8. The example represents the major failure provided in Figure 10.5. As can be seen the MVM range has been greatly reduced using the 7 day values. The change from the primary stage to the secondary stage is still evident. However, the change from the secondary phase to the nucleation phase is much harder to determine. As for the previous chapters a quantitative assessment of the trends prior to failure was undertaken.

The average results for the conditional analysis for instantaneous failures and accelerating failures are provided in Figure 10.9 and Figure 10.10 respectively. They indicate that data smoothing marginally improves the long-term forecasting of the ruptures however the improvement is not significant. The transition from the primary to the secondary stage of failure is indicated approximately 3 days prior to failure rather than 2 days without data smoothing. Despite this, less than 20% of all failures indicate the decreasing trend 3 days prior to rupture. The success rate is too low to be applied on mine sites as 80% of failures would not be recognised. Furthermore, minor changes such as those exhibited are unlikely to be identified and less likely to be taken seriously with such low confidence levels. The limited success of the method is understandable for accelerating slip failures but a little unexpected for instantaneous failures. Accelerating slip failures are based on an increased event rate independent of the magnitude. Whilst strain is able to accumulate prior to this type of rupture it is typically released more frequently but with less energy associated with individual events. Consequently, large changes in magnitude are not expected with accelerating slip failures. The results suggest that foreshocks prior to an instantaneous failure are not a common phenomenon in the mining environment.

Although the results are not overly convincing in terms of identifying the change from primary to secondary failure there is still potential merit in evaluating the change in magnitude over time. The formulas above are unnecessarily complex in evaluating magnitude. A much simpler solution is to calculate and evaluate the average daily magnitude.

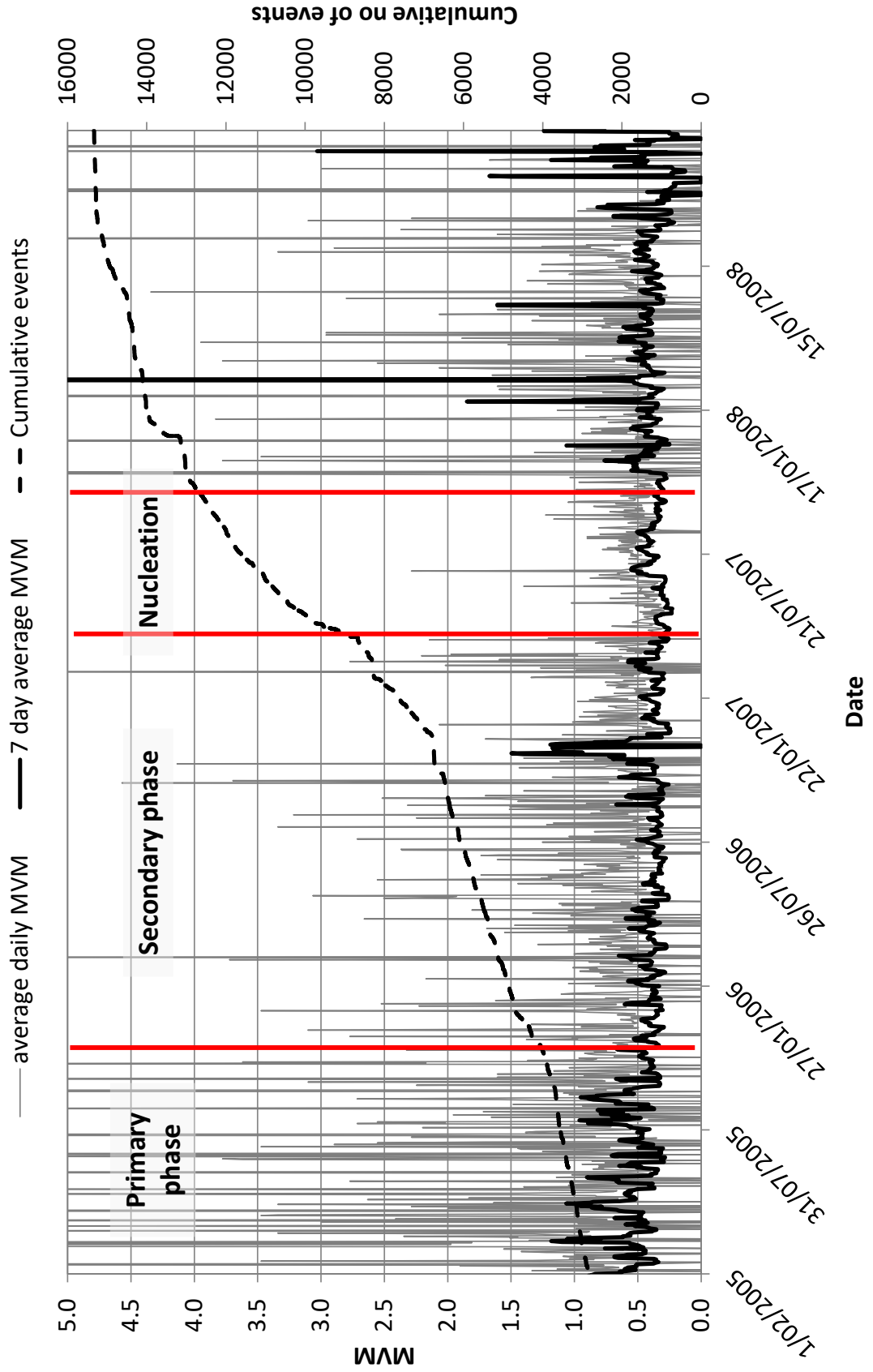


Figure 10.8: Example of 7 day average MVM (NE Faults G2).

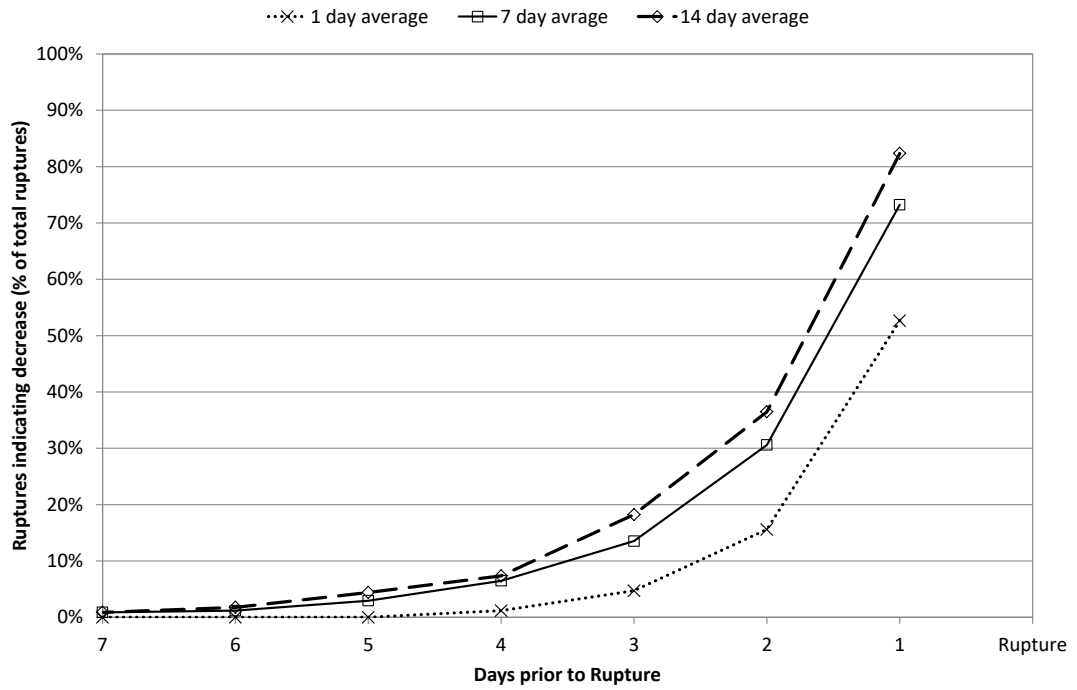


Figure 10.9: Average results of data smoothing for instantaneous failures.

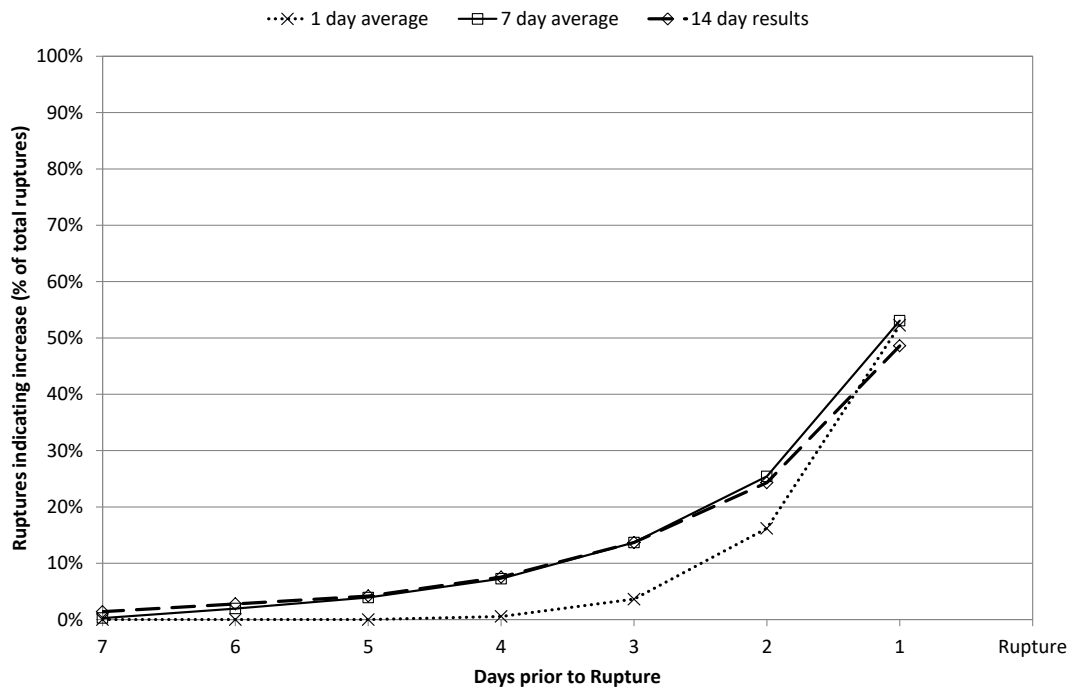


Figure 10.10: Average results of data smoothing for accelerating slip failures.

10.6 Magnitude analysis

As MVM is a measure of the change in magnitude over time the formula was simplified to calculate and evaluate the average daily event magnitude (sum of magnitude divided by the number of events per day). An example of the resultant chart is provided in Figure 10.11. The example indicates that the change in the average magnitude is actually very small and highly influenced by the number of events. A qualitative evaluation of the trends suggests that the stages of failure are apparent; however not in the way that was expected. Initially, the magnitude is observed to fluctuate highly. This is diagnostic of the primary phase of failure. Prior to rupture the background average magnitude decreases and stabilises. The nucleation phase is not discernible from the secondary phase. This is likely to be due to an increase in the number of events rather than a change in the overall trend of the magnitude. Rapid, though very small, increases are seen in the average magnitude just prior to individual ruptures (Figure 10.12). These changes are difficult to identify using qualitative evaluations however they can be identified using the conditional analysis method described previously.

As discussed, accelerating slip failures are not necessarily connected with increasing magnitude and hence have not been evaluated. The results of the conditional analysis of the average daily magnitude for each fault are provided in Figure 10.13. The results indicate a marked improvement in the success of the conditional analysis in comparison to the MVM. On average over 80% of failures display an increase in magnitude in the day prior to rupture. Less than 20% of ruptures show an increase in magnitude in the 3 days prior to rupture. This suggests that the secondary and nucleation phase of rupture is only evident in the magnitude in the day prior to rupture. Data smoothing was undertaken to determine if the reliability of the 2 – 3 day trends could be improved. An example of the smoothing effect of the 7 day average magnitude is provided in Figure 10.14. The average results of the conditional analysis for the average daily magnitude, the 7 day average magnitude and the 14 day average magnitude are provided in Figure 10.15. Overall only minor improvements were achieved using the data smoothing technique. The improvements are not enough to be deemed pertinent.

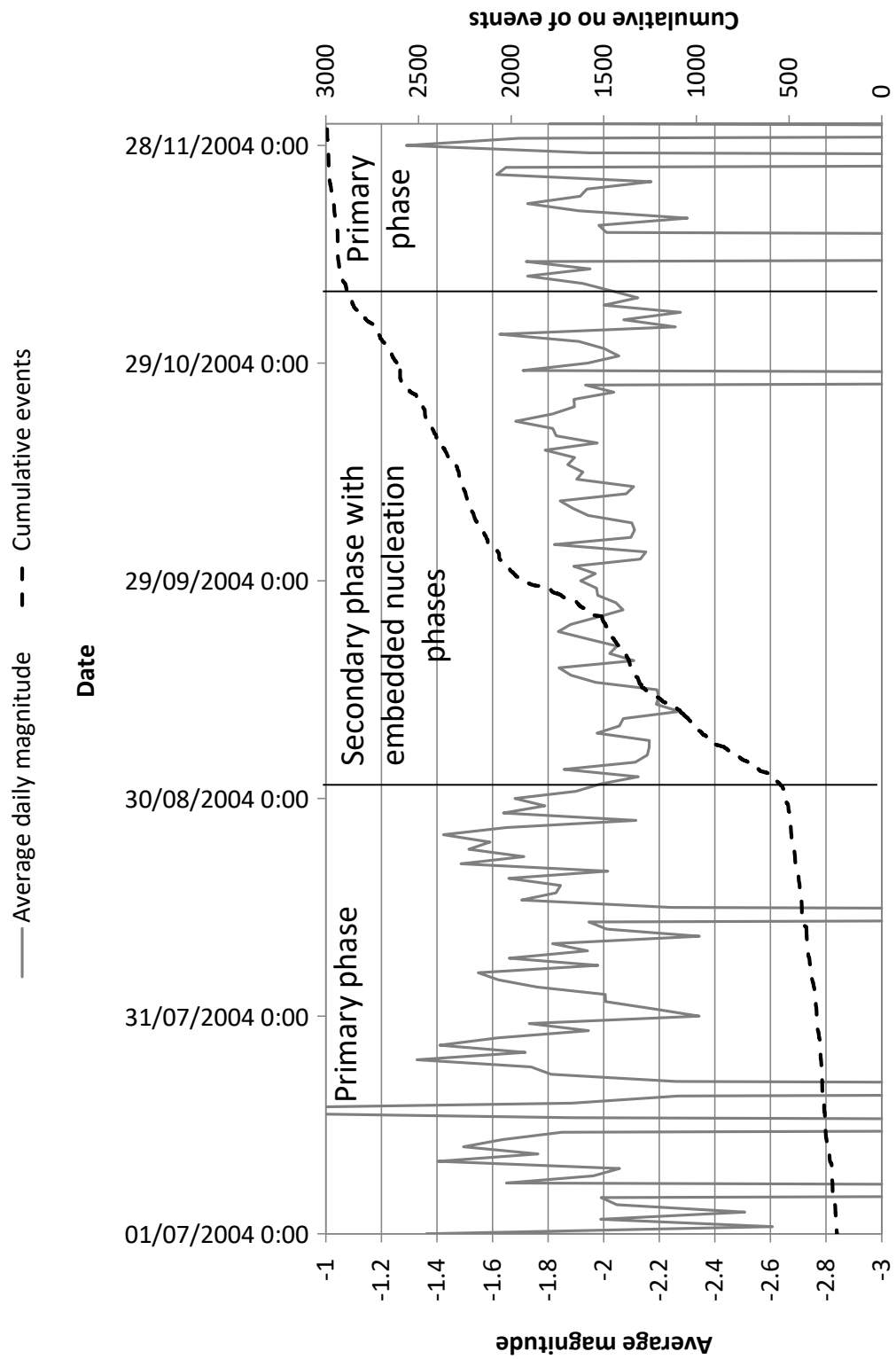


Figure 10.11: Example of the average daily magnitude with the phases of failure characterised (Feral Fault).

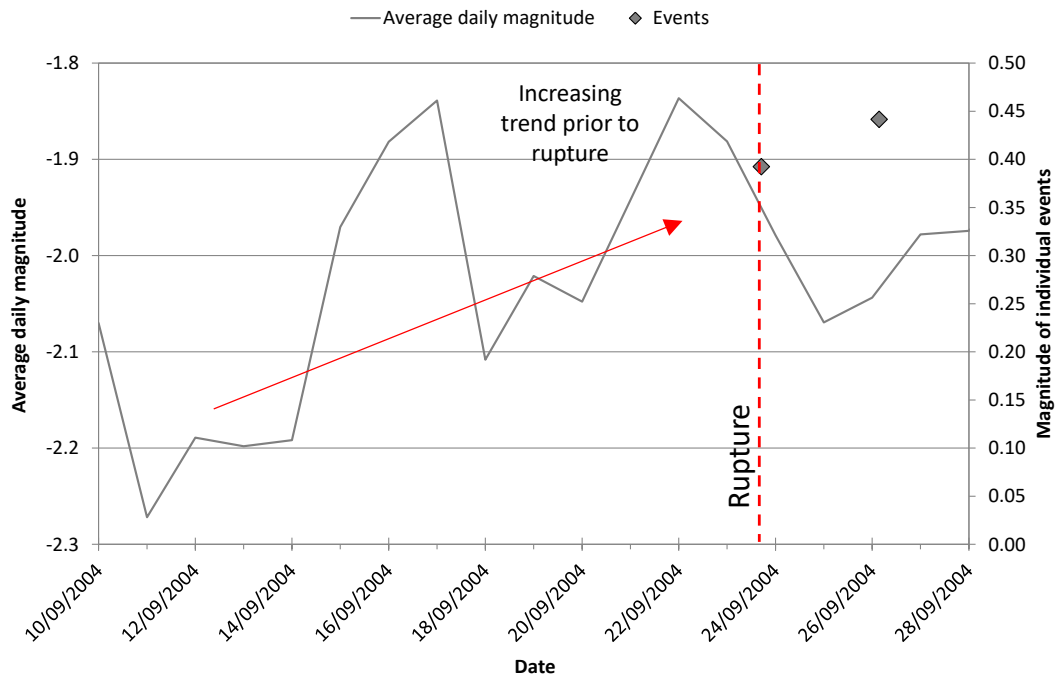


Figure 10.12: Qualitative assessment of the increasing trend prior to rupture (Feral Fault).

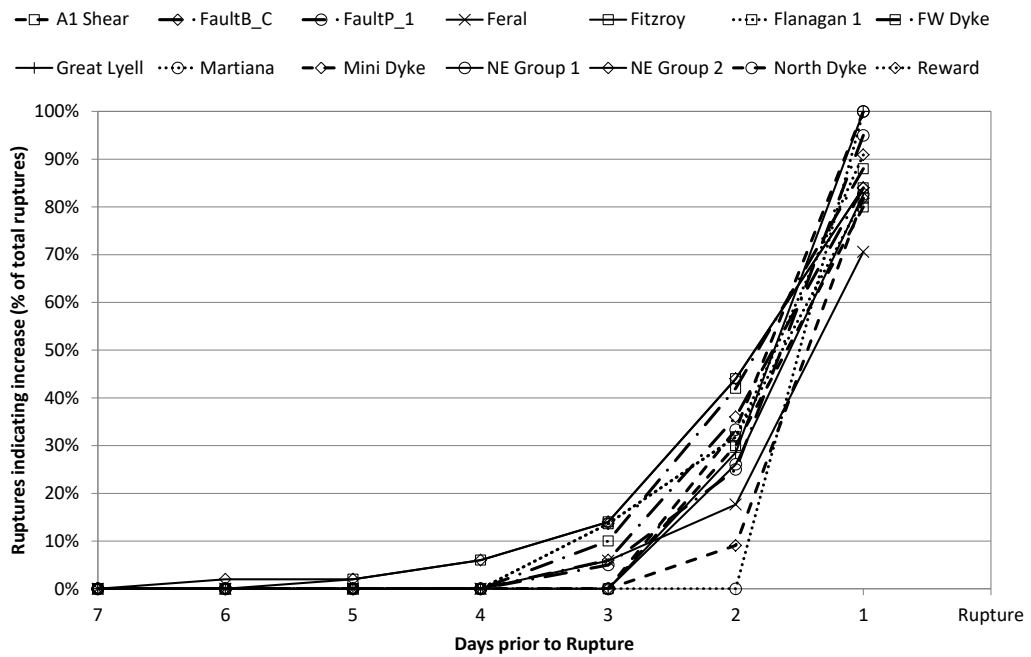


Figure 10.13: Results of average daily magnitude conditional analysis on instantaneous failures.

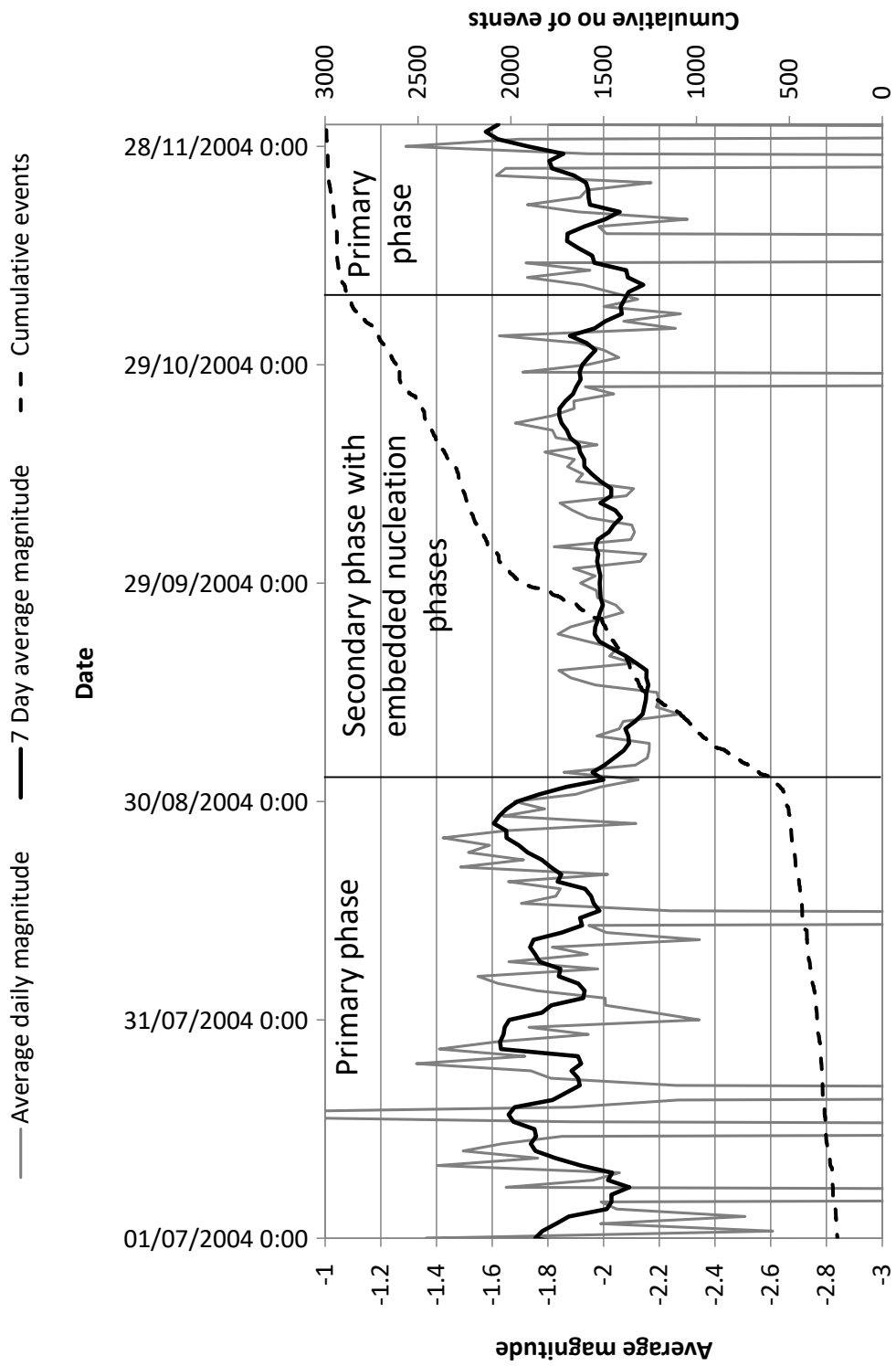


Figure 10.14: Average magnitude trends indicating phases of failure (Feral Fault).

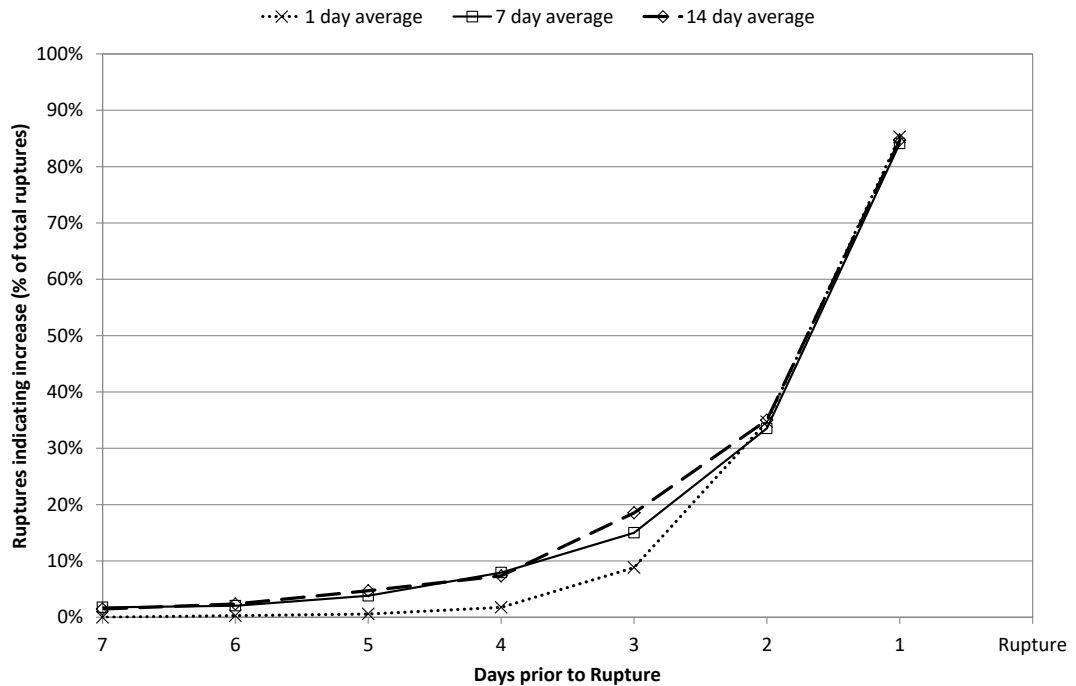


Figure 10.15: Results of data smoothing of average magnitude for instantaneous failures.

10.7 Discussion

Lei, 2006 states that “*b-value (MVM) can be considered a good parameter for measuring the capability of rocks to release accumulated strain energy*”. This analysis has shown that this is not the case when considering mining seismic data trends. The MVM calculation overcomplicates a very basic premise; that magnitude increases just prior to an instantaneous rupture. Analysis of the variations in magnitude has shown that as a stand-alone parameter it is not reliable long-term indicator of pending rupture. The event rate analysis in the previous chapter indicates that the nucleation phase can be determined 3 days prior to rupture. Overall this analysis suggests that the event rate will increase in the secondary and nucleation phases however the magnitude of these events will only increase in the very final stages of failure.

This analysis method does, however, provide an overall indication of the general state of failure. Despite the lack of reliability in the conditional analysis it can be determined that if the MVM remains consistently low, failure is either occurring or impending. If magnitude is increasing it is likely that the final stages of failure are nearing and safety measures for underground operators should be implemented. Analysis of magnitude in conjunction with other parameters or over shorter time-frames may improve the reliability and be of more use in the mining environment.

11. Energy Release Rate

11.1 Introduction

The previous chapter evaluated the precursory changes in magnitude. The most common magnitude formula provided by the sites combines energy and moment in the calculation (Equation 5.1). In this chapter energy will be evaluated as a stand-alone parameter.

Gutenberg and Richter, 1949 evaluated the energy of earthquakes at various depths. They concluded that “*the rate of energy release is extremely irregular*”. Kanamori, 1977 states that “*the energy released in earthquakes is one of the most fundamental subjects in geophysics*”. He examined the energy of large earthquakes between 1904 and 1977 and evaluated them over time. He used a 5 year running average and found variability in the energy released over time. Further earthquake studies have been undertaken by Robinson, 1979, Kanamori, 1977, Jeng et al., 2002, to name but a few. Many of the earthquake research papers are limited by the knowledge of the rock mass and by the completeness of the seismic records. The geological knowledge of faulting systems at depth is limited and also frequently changing at intercontinental boundaries making specific assessments of faults difficult. Lei, 2006 states that “*because large earthquakes are nucleated at depths of between a few km and tens of km, it is impossible to obtain sufficient information from the surface-based seismic monitoring networks*”. This results in incomplete seismic datasets with the lower bounds governed by the density of the sensor network and the positioning of the sensors in relation to the events. Furthermore, it seems not all seismic events are routinely processed and hence are not included in the analysis. Frequently only larger events are included.

Mining seismicity studies of energy are relatively common. As described in Chapter 5.7, Energy index is already used for evaluating energy on mine sites. As the review highlights, the method of evaluation has flaws. Energy release rate (ERR) has been commonly assessed in the South African mining industry since the 1960s. Lachenicht, 2001 describes the ERR as a concept “*based on the fact that if an excavation is made, energy changes*”. ERR is a “*measure of the changes and stress concentrations*”. This definition and application of ERR is centred on energy changes in the mining system. This thesis sets out to examine energy being release during failure, and hence further reviews of the application of mining definition ERR will not be undertaken.

Acoustic emission studies of energy have been relatively recent due to the difficulty in estimating the energy of AE events. Lockner et al., 1991 contoured the ERR on the fine-grained intact rock sample during the final stages of the test. The results clearly show a strength disparity in the sample. The results demonstrate that despite the appearance of homogeneity in the sample, the strength heterogeneity exists.

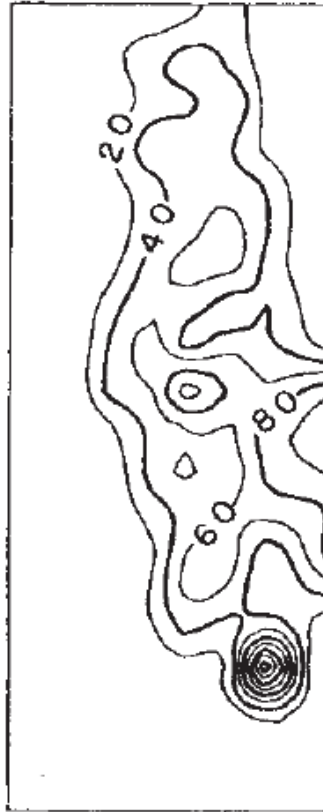


Figure 11.1: Contouring of the energy of the AE events in the latter stages of sample failure clearly indicate strength heterogeneity (Lockner et al., 1991)

Tang and Kaiser, 1998 used modelling to simulate brittle failure of rock samples using acoustic emission outputs. The results demonstrated that “*the largest energy release occurs when the high strength areas fail*”. They also observe that “*after each big event, there is a drop in the energy release before the next big event*”. They suggest that “*a decrease in the energy release might provide a precursor for large rock bursts*”.

Lei, 2006 simply calculated the sum of energy over time steps as the energy release rate. In the experiments, magnitude is calculated from amplitude and energy is estimated from the magnitude. He demonstrated that as with other pre-cursors, the energy release rate changes during the phases of failure. In the primary phase the ERR is minimal. The secondary phase is characterised by an increase in the energy release rate, consistent with models suggesting sub-critical crack growth. In the nucleation phase the energy release rate further increases resulting in rupture. The behaviour in the different phases are provided in Figure 11.2. This behaviour is in contradiction to the findings of Tang and Kaiser, 1998. The following sections outline the analysis method and will aim to test both these theories of behaviour.

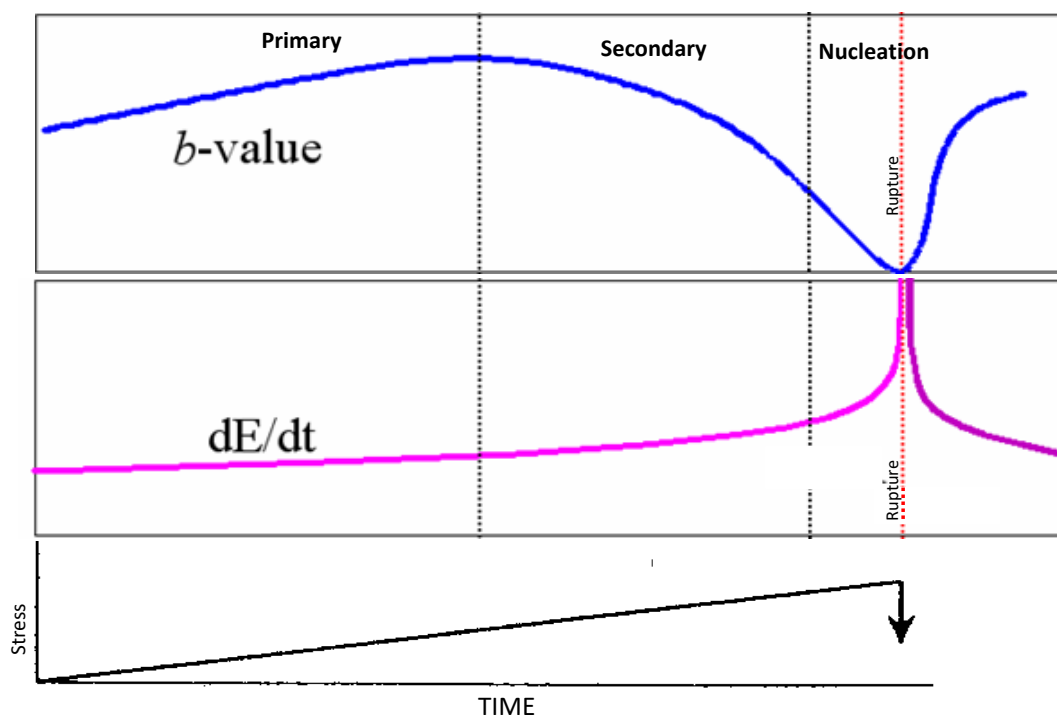


Figure 11.2: Comparative behaviour of cumulative energy over time with b -value and the phases of failure (after Lei, 2006).

11.2 Analysis method

Rather than using logarithmic relationships, the following assessments will be conducted on the base energy values. Frequently, the energy parameter provided from site was specified in logarithmic form (i.e. LogE). Where this occurred, the data was converted back to raw energy using Equation 11.1.

$$Energy = 10^{(logE)}$$

Equation 11.1

The evaluations will be undertaken on the average energy per day. This will be calculated by dividing the sum of the energy for the day by the number of events on the given day.

As described above, theoretically, energy released during fracturing should increase prior to rupture. However, another theory exists that energy in the system must be conserved or “built-up” to enable a significant event to occur. Both theories will be investigated in the following sections.

11.3 Results

11.3.1 Energy per day

An example of the energy per day is provided in Figure 11.3. The results for each structure are provided in Appendix 8. The example provided indicates that up until late 2006 the general behaviour conforms to the conventional theory. Time period A and C indicate periods of low event rate and low energy. Large scale failure occurs in 2003 / 2004 and coincides with an increase in energy. In the latter part of 2006 the trend changes. Low or decreasing energy per day rates accompany periods of high seismic activity. Figure 11.4 provides a closer examination of the 2007 time period. It shows that there is indeed a very low event rate during the period between March and September 2007 and December 2007 and March 2008. This trend is also observed on other structures. The behaviour is likely to be associated with a high number of small events that on average produce little cumulative energy release. Small spikes in the energy rate correlate with large events. Overall, qualitatively, there does not appear to be significant global indications of increasing energy prior to large events. However, quantitative assessments must be undertaken to confirm this.

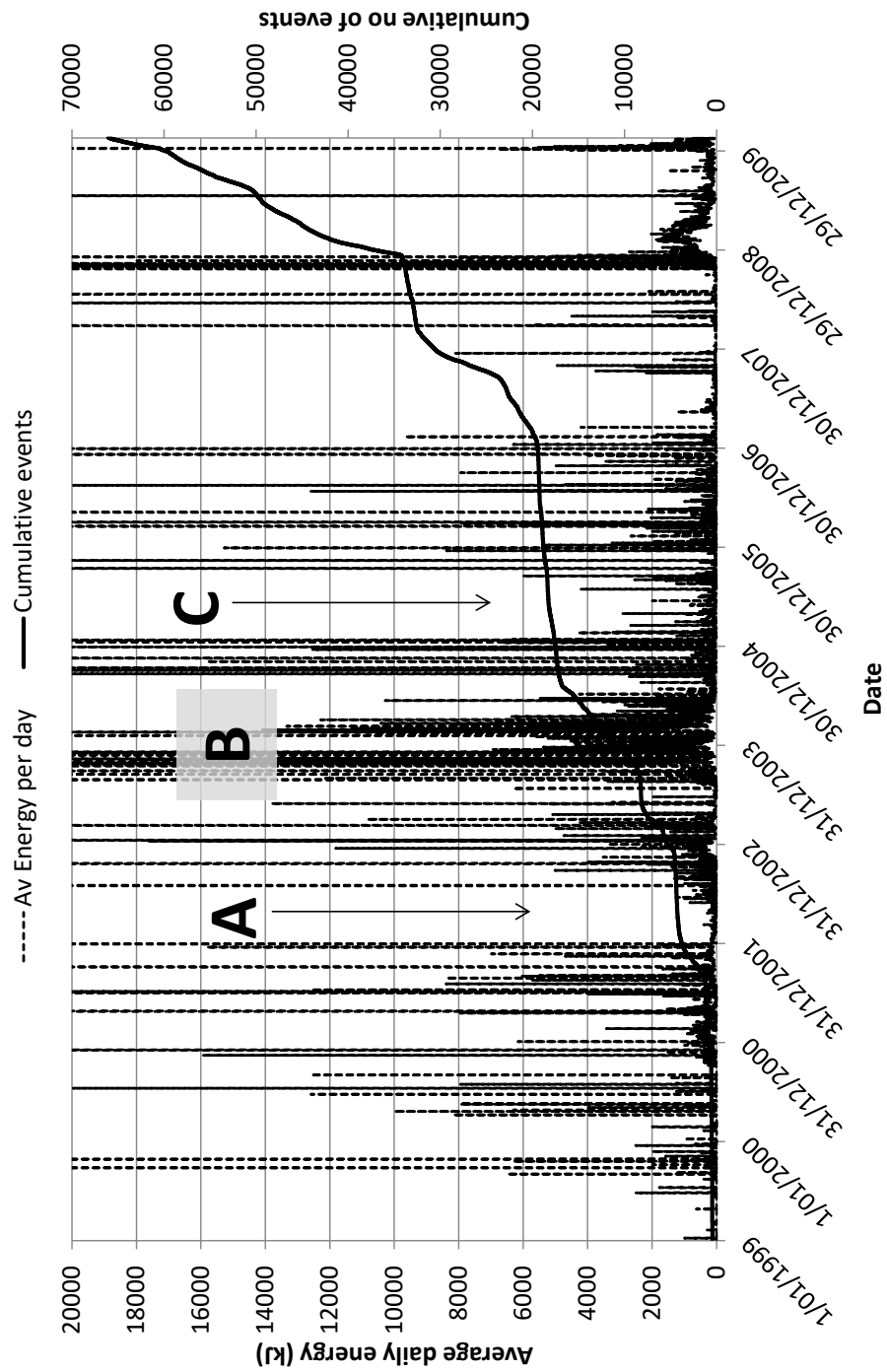


Figure 11.3: Example of average daily energy with the cumulative event rate. Time periods A and C highlight where that the energy is low during periods of low seismic activity. Time period B indicates where high energy confers with failure (FW Dyke).

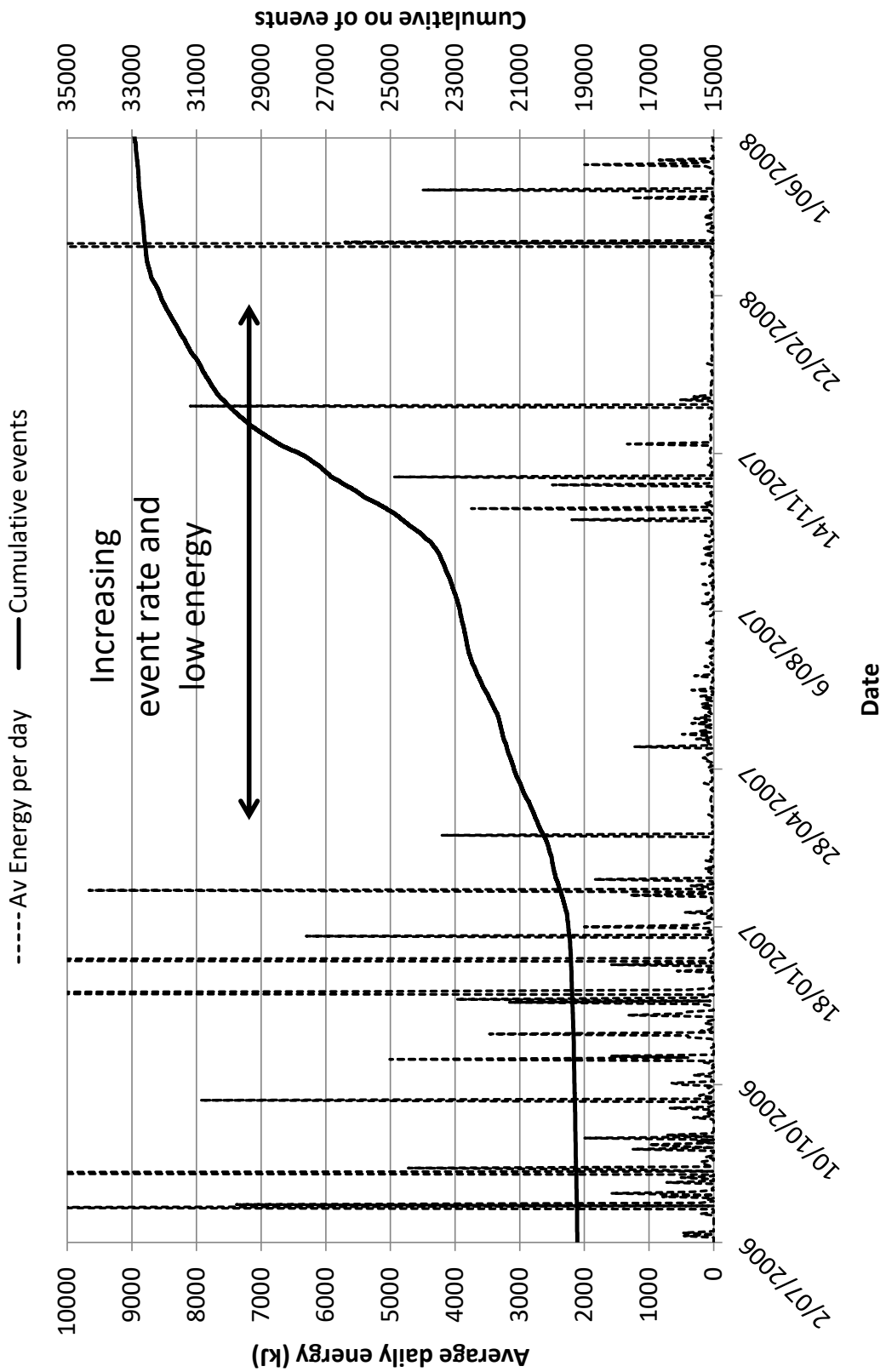


Figure 11.4: Examination of the trend in 2007 that highlights increasing event rate with low values of energy (FW Dyke).

Conditional analysis was undertaken to determine if an increasing trend could be identified in the data. The results are provided in Figure 11.5 and Figure 11.6 for instantaneous failures and accelerating slip failures respectively. The results for instantaneous failures demonstrate that the energy released on the day of rupture will almost always be greater than the previous day. This effect is logical due to the effect of the failure itself. A large brittle failure causes a significant release of energy and hence the energy on that day will be significantly higher than preceding days. The results do however suggest that there is an indication of an increasing trend 2 and 3 days prior to the rupture for some structures. The results show that the success of identifying an increasing trend 2 days prior to rupture is highly variable with a range in success varying from 0% to approximately 70%. On average, 40% of events indicated an increasing trend in the 2 days prior to rupture. The average value dropped to approximately 15% 3 days from rupture. Less than 10% of the ruptures indicated an increasing trend further than 4 days from rupture.

The accelerating slip failures have a much lower rate of identifiable trends than the instantaneous failures. This is likely to be due to the low energy release rates coinciding with large increases in events discussed above. On average just over 20% of accelerating slip failures demonstrate 2 days of consecutive increasing trends. The range of values for the faults was between 0% and 45%. Less than 10% of accelerating slip failures showed consecutive days of increase after 3 days.

It should be noted that the alternative theory of a decreasing trend in energy release prior to rupture is not indicated by the data. Enough failures indicate an increasing trend in the 2 – 3 days prior to rupture to discount the decreasing theory.

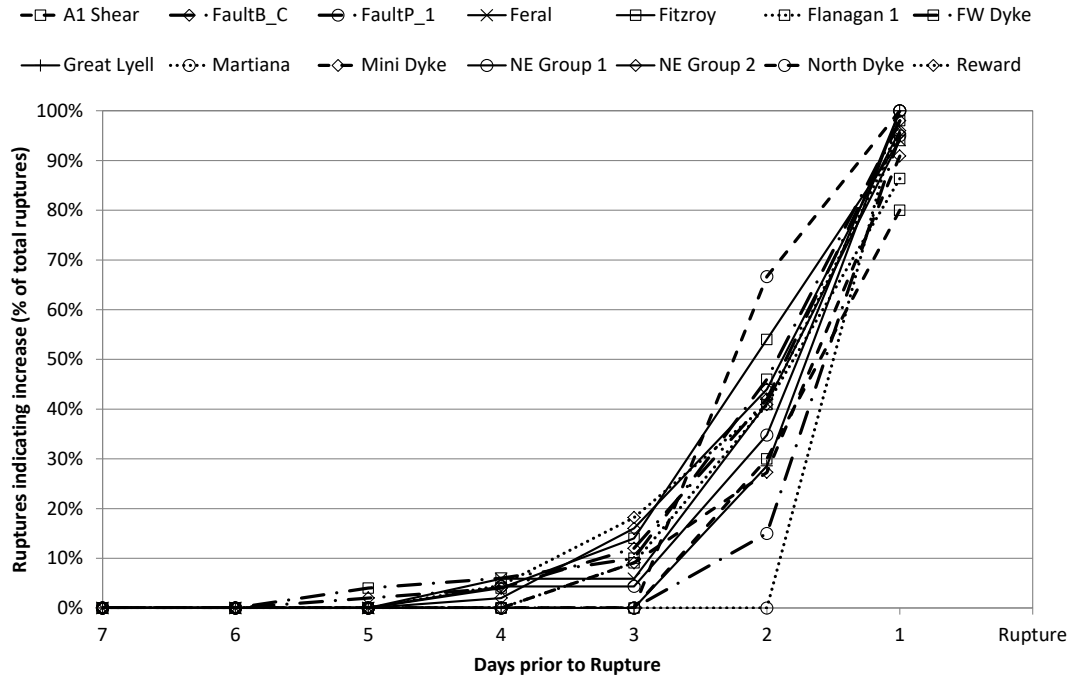


Figure 11.5: Results of conditional analyses of daily energy release for instantaneous failures.

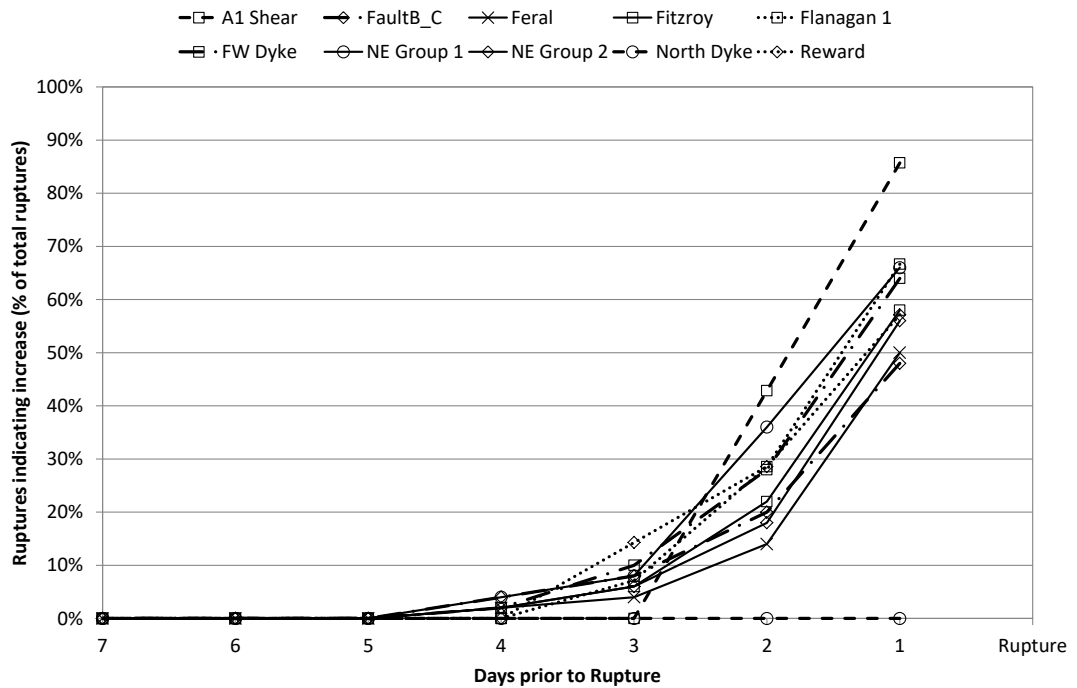


Figure 11.6: Results of conditional analyses of daily energy release for accelerating slip failures.

11.3.27 day average energy

As with the previous analysis, the energy data was averaged over 7 days in an attempt to smooth the daily variations into a more identifiable trend. An example of the results is provided in Figure 11.7. The example demonstrates that smoothing of the data has exaggerated the low energy during high event rate period. The average results of the conditional analysis (Figure 11.8 and Figure 11.9 for instantaneous and accelerating slip failures respectively) shows that the smoothing of the data only marginally improves the long term forecasting of the results.

Longer time frames have been examined but as they did not significantly improve the result they have not been reported.

11.4 Discussion

As with all the previous parameters the energy values fluctuate on a day-to-day basis. Data smoothing does not adequately reduce the level of fluctuations to provide more consequential results. The energy calculation method predisposes the results to having an increase in energy on the day of an instantaneous failure in comparison to the previous day. Despite this, the number of instantaneous failures displaying increases 2 and 3 days prior to failure is significant. Accordingly, the energy values can potentially provide indications of impending instantaneous failures.

However, this method is not appropriate for the analysis of accelerating slip failures. The results are heavily influenced by the number of events occurring on a particular day. High event rates dilute the energy release causing a reduction in the rate.

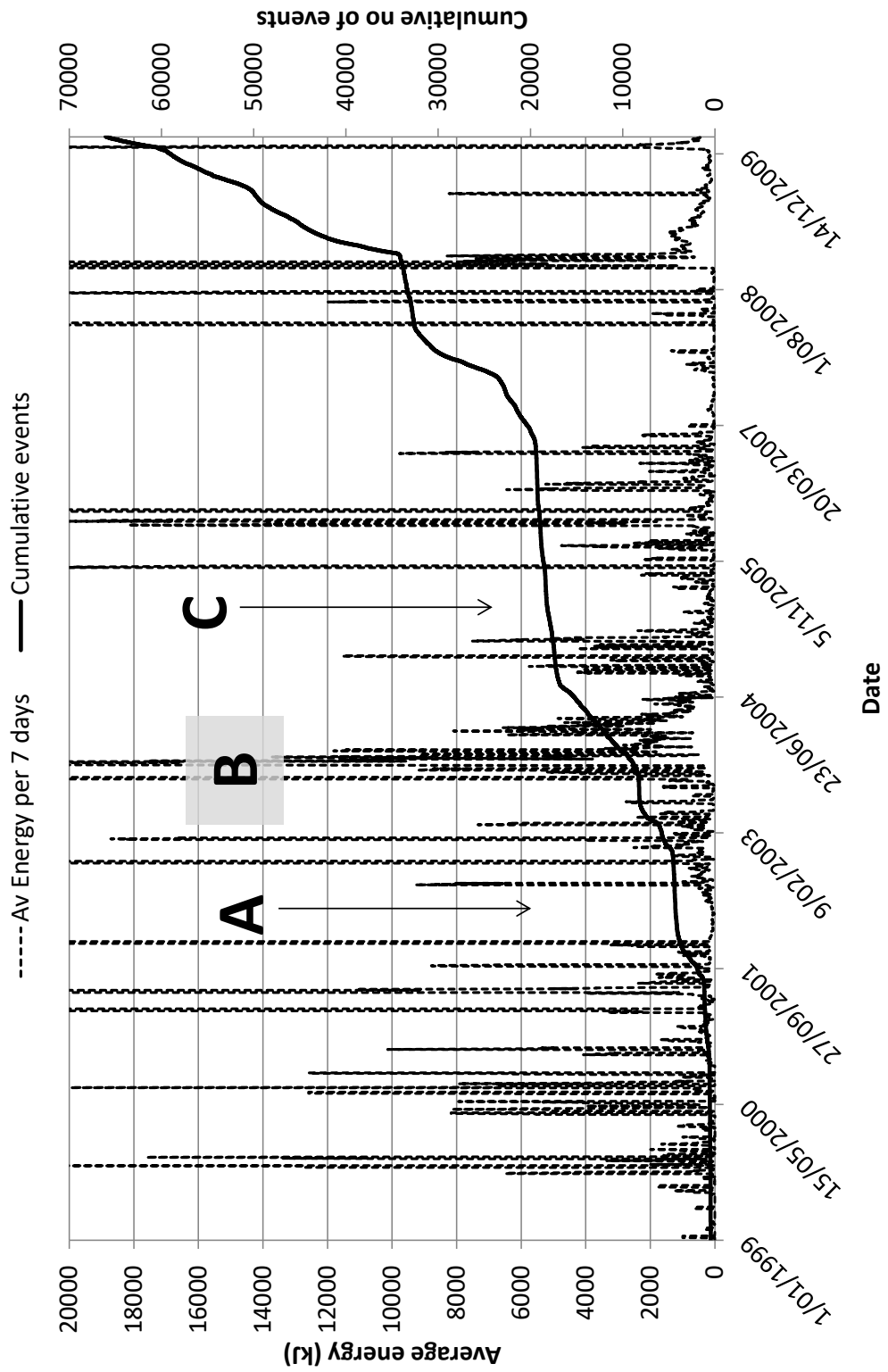


Figure 11.7: Average 7 day energy for FW Dyke.

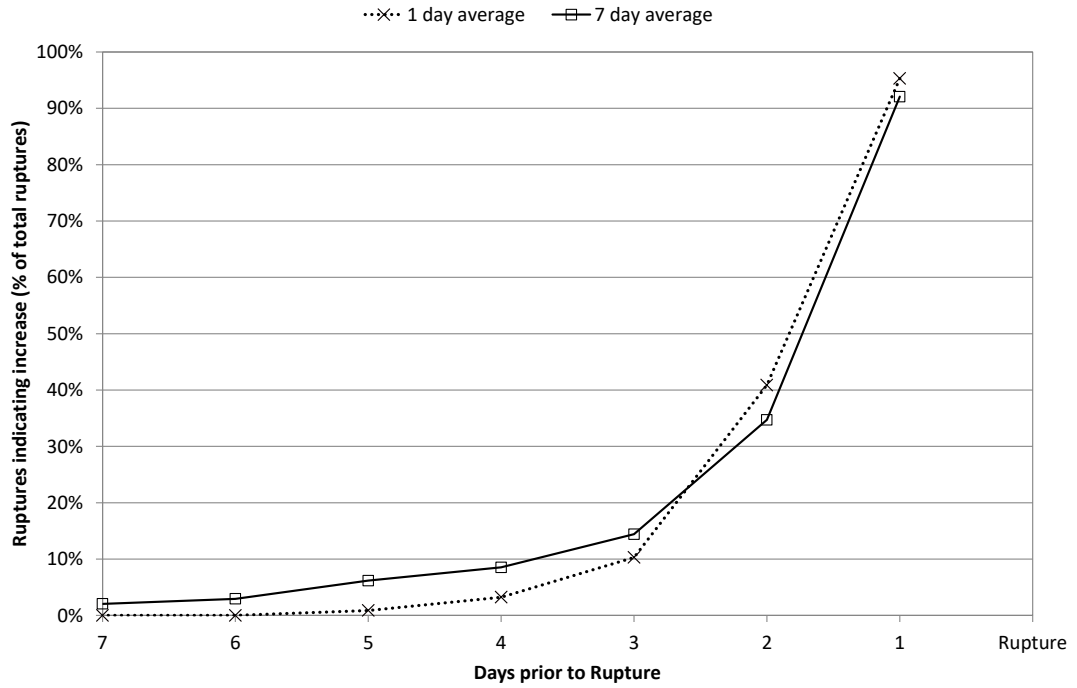


Figure 11.8: Comparison of results of conditional analysis for energy release for instantaneous failures.

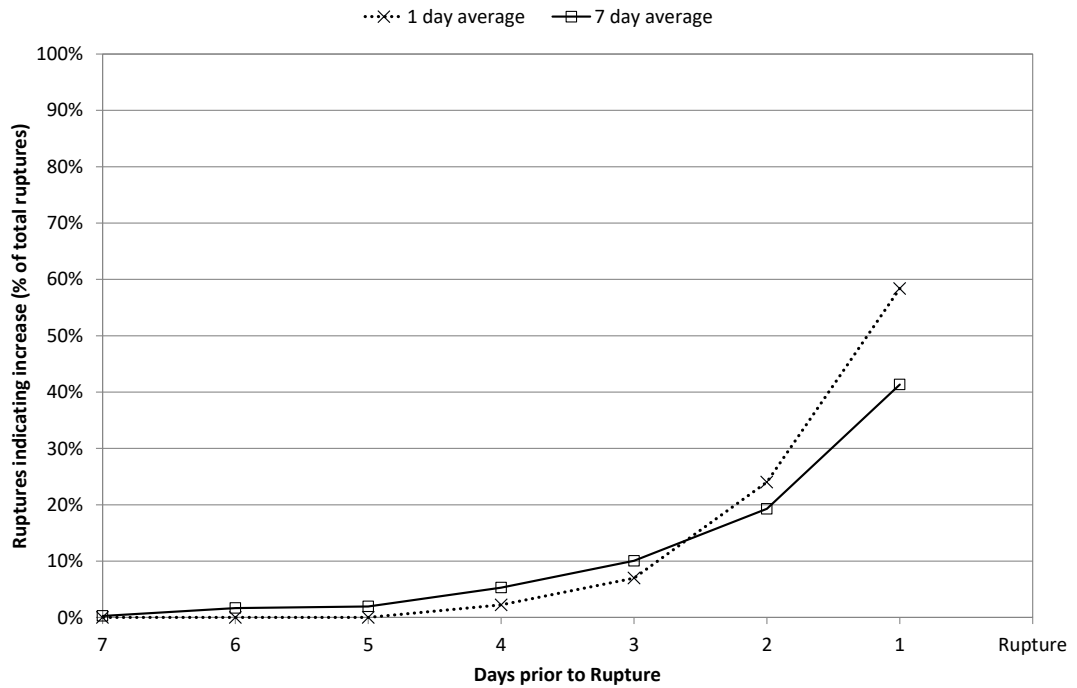


Figure 11.9: Comparison of results of conditional analysis for energy release for accelerating slip failures.

12. Comparison of precursors

The assessments described in the previous chapter were undertaken on 347 instantaneous failures and 360 accelerating slip failures on 14 structures. This section provides a compilation of the results of the conditional analysis to enable a comparison of the all the precursory behaviours. Precursor comparison charts for each structure are provided in Appendix 9 to Appendix 12. The average results are discussed below.

12.1 Precursors calculated using the daily averages

Comparison of the average results of the conditional analysis for each precursor calculated using the daily average is provided in Figure 12.1 and Figure 12.2 (instantaneous failures and accelerating slip failures respectively). There is no significant disparities between the results of the 2 failure modes. Both sets of results show that there is no indication of failure 5 days prior to rupture. Up to 10% of failures show indications of impending rupture between 3 and 5 days. Most instability can only be recognised between 1 and 2 days prior to rupture. Energy and magnitude are related mathematically, and both show high percentages of instantaneous ruptures that have an increasing trend between the day prior to rupture (day 1) and the day of rupture. This is a directly related to the analysis method as the energy and magnitude of the failure itself heavily influences the results. Despite this many of the instantaneous failures (40% of energy and 35% for magnitude) indicate increasing trends 2 days prior to rupture.

SCL is the least reliable parameter for determining trends prior to rupture. Less than 20% of failures indicate strong clustering prior to rupture.

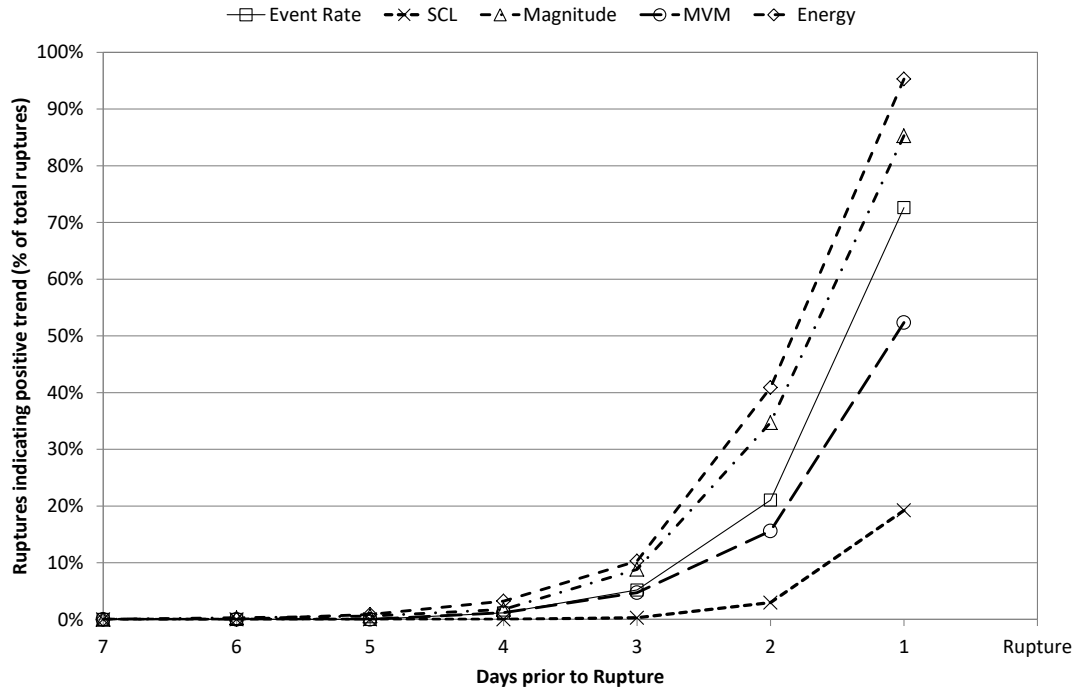


Figure 12.1: Average results of the conditional analysis of instantaneous failures for each precursor.

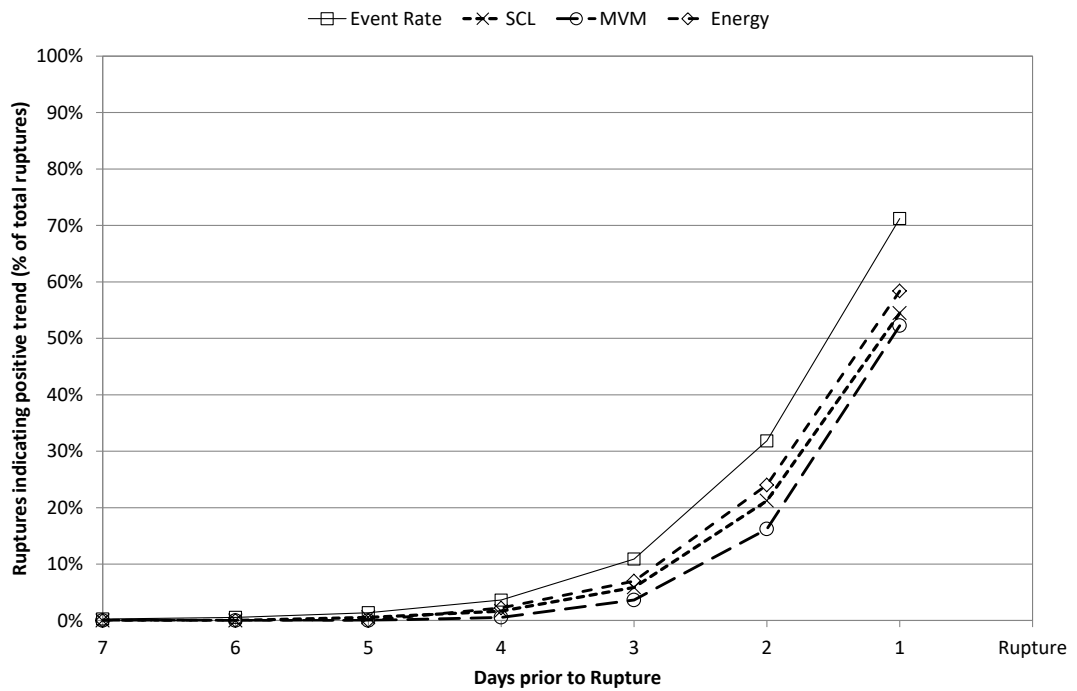


Figure 12.2: Average results of the conditional analysis of accelerating slip failures for each precursor.

12.2 Precursors calculated using the 7 day averages

In the previous chapters the 7 day rolling average calculations were demonstrated to improve the long term indicators of failure for some precursors. Comparison of the average results of the conditional analysis for each precursor calculated using the 7 day average is provided in Figure 12.3 and Figure 12.4 (instantaneous failures and accelerating slip failures respectively). The results show that data smoothing is most successful for the event rate. Using the data smoothing technique between 5 and 10% of ruptures demonstrated an increasing 7 day average event rate for 7 days prior to rupture.

As the previous chapters have discussed data smoothing does not have a significant effect on the overall results of the magnitude and energy results. Less than 6% of failures showed any indication of instability prior to 5 days before rupture for all these parameters.

The SCL remains the poorest indicator with less than half of the instantaneous failures demonstrated convergence of seismic locations prior to rupture.

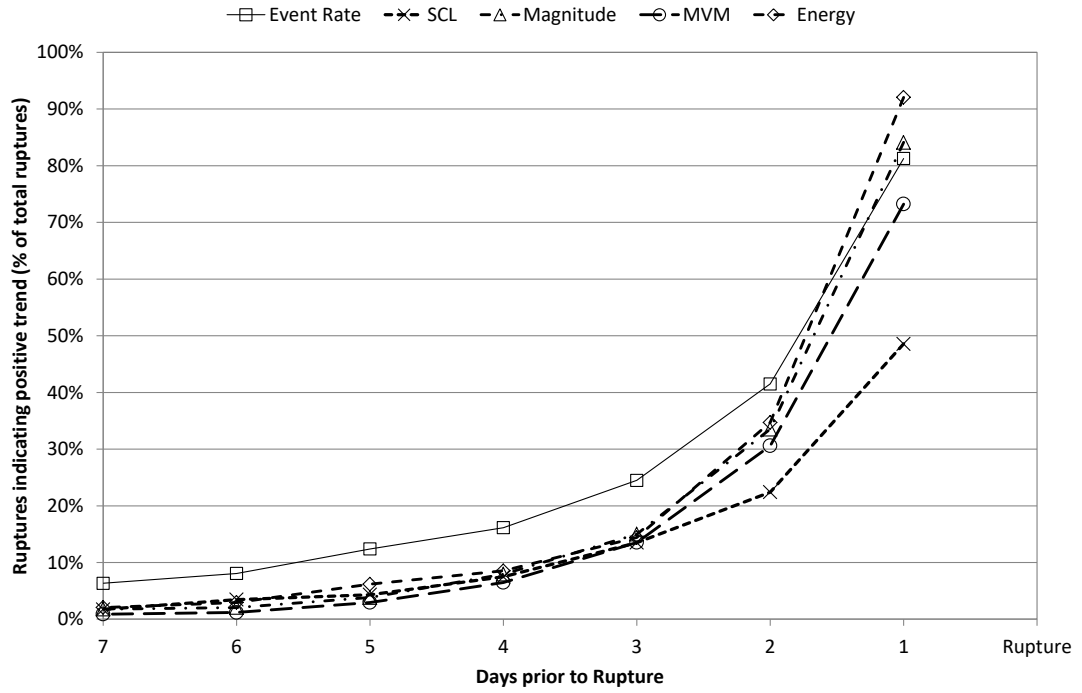


Figure 12.3: Average results of the conditional analysis of instantaneous failures for each precursor.

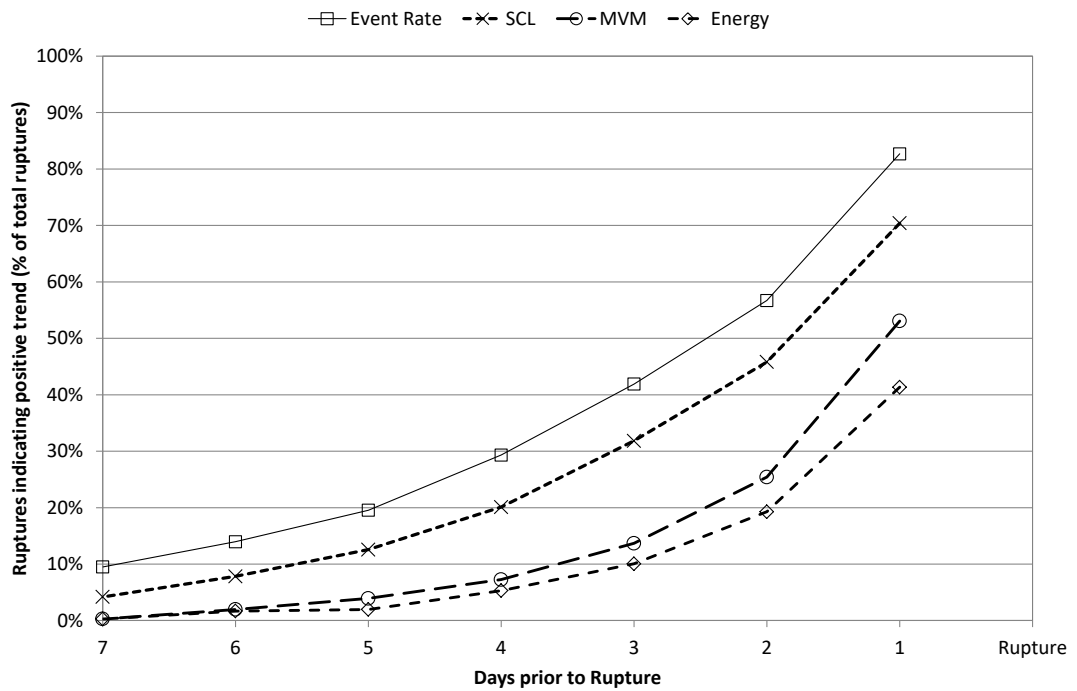


Figure 12.4: Average results of the conditional analysis of instantaneous failures for each precursor.

12.3 Forward Analysis

It is apparent from the analyses in the previous section that the transition from the primary to secondary stage of failure occurs approximately 3 days prior to failure. Trends can be identified up to 7 days prior to failure depending on the failure mode and the level of data smoothing undertaken.

In order for these methods to be effective in determining when failure is occurring, the number of occurrences of any particular parameter needs to be infrequent enough to enable specific analysis.

Given this, the data were re-analysed to determine how many positive trends (decreasing for SCL and increasing for all other parameters) can be identified. To undertake this analysis, the data were assessed to determine how many occurrences of increasing (or decreasing for SCL) trends exist. Simply, the number of days where consecutive increases were measured was counted. The average results for each of the parameters are provided in Figure 12.5.

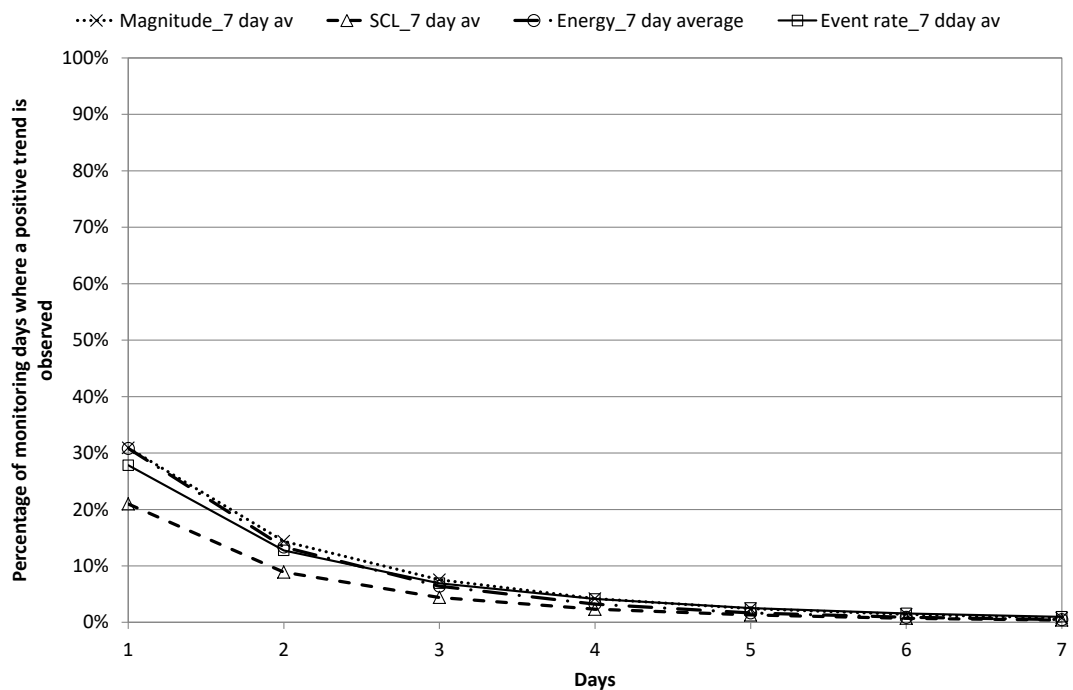


Figure 12.5: Average results for the number of days that show an increasing trend in the overall dataset.

Overall the results demonstrate little difference between the parameters. SCL has the lowest number of occurrences of sequential daily changes. Less than a third of all monitoring days have 2 days where the parameter indicates consistent positive trend (decrease or increase) from 1 day to the next. Approximately 5% of monitoring days have 3 days of consecutive change (i.e. $D1 < D2 < D3$). This equates to signs of rupture occurring less than 20 times annually. From a practical point of view, it is not unreasonable to use these occurrences for further analysis.

It should be noted however, that the transition from primary to secondary failure does not always result in nucleation. The mining environment is one of constant change and many variables contribute to ultimate failure.

12.4 Discussion

Lei and Satoh, 2007 state that *“it is clear that energy release, seismic b-value, fractal dimension and SCL of the hypocentre distribution are all functions of the time-to-failure. Therefore, it might be expected that such parameters could be used as indicators of critical point. However, each parameter exhibits large-amplitude fluctuations superimposed on longer-term variations”*. The results contained in these investigations have confirmed this behaviour. The proposed method of smoothing has gone some way to improving the analysis of mining data. This enables trends to be more clearly identified.

Overall the assessments have shown that simplicity is the key. Parameters in their purest form can provide as much insight as complicated statistical parameters. The best parameter for evaluating any type of failure is the cumulative event rate. Clustering of seismic events was able to provide an insight into the accelerating slip failures. However, clustering was inadequate in providing any insight into instantaneous failures. Conversely, increasing magnitudes and event energy rates can provide an insight into instantaneous failures but not accelerating slip failures.

13. Discussion

The results included in the above assessments demonstrate that no individual parameter can adequately provide quantitative confirmation of all failure modes. Despite this, the patterns of behaviour were recognisable on all structures in spite of the differing structure types, rock mass properties, stress conditions and mining methods. Furthermore, all values provided an overall picture of the global behaviour of the rock mass. Used in conjunction with each other, the parameters can provide an indication of approaching rupture.

The identification of rupture can be limited by many factors including:

- Changes in the mining environment
- The definition of failure
- Geological understanding
- Data collection
- Data quality

Given the forward analysis results it is obvious that not all positive patterns of failure result in final rupture. Mining is a dynamic environment and the extraction of voids inherently changes the stress field. This means that impending failures may be removed during the extraction process preventing such a failure. Alternatively, the creation of the void changes the stress field to an extent that returns the area of impending instability to a state of equilibrium.

A further limitation of this particular analysis also lies in the definition of failure. Whilst failure has been given a rigid definition for the purposes of this analysis, every event can be considered failure. The understanding of the rock mass and consequently failure within the rock mass is extremely limited. Often “failure” around an excavation is determined by visual inspections which are highly subjective and also limited to the surface of the excavation. Given the rarity of 3 consecutive days demonstrating a positive trend towards rupture, it is likely that any occurrence of the positive trend may be indicative that instability is developing. However, to understand the failure of the rock mass first you must understand the rock mass.

13.1 Incorporation of geology into analysis

Currently, the consideration of the geological features on mine sites is, at best, ad hoc and based on the diligence and experience of the Mine Site Engineer. Seismic events are often attributed to fault movement anecdotally rather than scientifically. The association of a seismic event to a large-scale structure is based on the location of the event, the location of the damage cause by such an event and knowledge of the rock mass.

The location of the event is dependent on the seismic system accuracy. Mendecki, 1997 states that the location error depends on the following factors:

- Errors in the arrival time determination
- Inadequate knowledge of the velocity model
- Inaccuracy in the station co-ordinates
- The method of solution
- The spatial distribution of stations with respect to the event.

Most of these parameters cannot be directly quantified and it can be expected that some location inaccuracy occurs within the data.

The location of damage is also relative with many variables including ground support suitability, quality of ground support installation, site specific amplification effects and proximity of the event to the excavation. Knowledge of the rock mass is dependent on the information available. Often geological studies concentrate on the geology of the ore-body and the near-field rock mass at the expense of adequate knowledge of the structural features within the environment. This area has been identified as deficient in many sites and several research projects are currently being undertaken to develop methods of improving structural models using discrete fracture networks.

Using a set domain methodology as described in Chapter 2.2.5 allows for location error inherent in the system but removes the subjectivity within the analysis process. This method needs to be incorporated into the analytical process to remove the subjectivity of the operator from the analysis.

Notwithstanding, the results were limited by the quality of the data. Seismic system management had the greatest influence over the results. The following sections discuss improvements to the way seismic systems are managed that would enable more proactive identification of rock mass failure.

13.2 Sensitivity of seismic systems

Laboratory test work typically uses a very high density of sensors to record acoustic emissions over the duration of the test. Typically, between 2 and 36 sensors are used. This density of monitoring allows for a high volume of events to be recorded over the duration of the test. The density and sensitivity of the instrumentation also allows for very low magnitude events to be recorded.

Conversely, earthquake monitoring has a very low density of sensors given the extent of the geological environment. This is partially due to the density of the sensors over the earth's surface and restrictions in the depth to which sensors can be installed. However, limitations in the sensitivity of earthquake monitoring are offset by the extended time scale over which monitoring has been undertaken. Detailed earthquake monitoring was developed in the mid-1700s and has been evolving ever since. Active seismic zones such as the east coast of Japan have been monitored with various levels of sensitivity for at least 100 years. This extended length of monitoring enables detailed analysis of seismic patterns despite the lack of sensitivity.

Mining seismic monitoring has neither the extended monitoring time of earthquake monitoring nor the sensitivity of laboratory testing. The location of the sensors is critical to the success of a seismic system.

The design of mine seismic systems is limited by the geometry of the mining development. Typically, sensors are installed in short boreholes drilled off a mining access drive. This frequently leads to planar or semi-planar arrays that limit the ability of the systems to accurately locate seismic events and to accurately calculate source parameters. Chapter 3 highlights the deficiencies in the coverage of the mine and of the structures used in this investigation.

When designing a seismic system coverage of current and future mining areas must be considered. Furthermore, a detailed understanding of the geology is required, and the likely failure mechanisms identified. This will enable the seismic system to be designed to ensure critical areas of failure can be recognised.

13.3 Timing of seismic system installation

Typically, historically, the installation of seismic monitoring systems is reactionary. Systems are installed after seismic activity becomes audible to miners or after visible damage occurs. Coulson, 2009 states that the seismic system at Williams gold mine was installed after a magnitude 3.0 event occurred and after the sill pillar was deemed highly stressed indicated by blast hole crushing, failure of in-stope raisebores and the *“triggering of seismic flurries through blast hole drilling activity”*.

By delaying installation data from the primary (and often the secondary) stage of failure is lost and hence changes in the pattern of seismicity are not identified. Whilst there has been some proactive change within the industry it is still critical that seismic systems are designed and installed prior to the onset of seismicity to enable changes to be accurately identified.

13.4 Data processing time frames

Real-time data processing is typically only undertaken as a reaction to failure. Additionally, data evaluation is often undertaken on an as-need basis and may also be conducted by multiple personnel. Consequently, on-going trends in the seismic data may not be identified. This is further exacerbated by the current methods of clustering that create a large number of clusters that are not necessarily associated with anything meaningful to the assessors. The results in the previous chapters highlight that trends in failure are conclusively identifiable less than 3 days prior to failure. The current methods of processing are not adequate to be able to identify trends prior to failure. The management of seismic data should be simplified to enable better real-time evaluation of the data that relates to either stoping areas or geological structures. These should be customisable to the operator to allow for changes in the mining geometry and geological interpretations.

14. Conclusion

The results in Chapter 5 demonstrate that the incorporation of geology into current seismic analysis techniques improves the outcome of the current techniques. Some of the current techniques (such as the magnitude – time history analysis) have been shown to provide insight into impending failures. Nevertheless, many of these techniques are still flawed as they do not consider temporal changes. The mining environment is changeable and consequently the risk of failure is likely to change with extraction.

The evaluation of precursors in mining seismic data has demonstrated that this phenomenon occurs at different scales. This supports the theory that seismicity is self-similar and that studies in earthquakes and laboratory scale experiments can be applied to mining seismic data and vice-versa. Importantly, the patterns of failure in precursor data were recognisable on all structures in spite of the differing structure types, rock mass properties, stress conditions and mining methods.

Additionally, the results demonstrate that indications of instability are not likely to be observed in the daily average data prior to 5 days before rupture. This applies for all parameters. Between 3 and 5 days, some failures may be able to be recognised. However, most instability could only be identified less than 3 days prior to rupture. Weekly rolling averages proved to be the most consistent for use in long term forecasting.

Event rate proved to be the best indicator for determining rupture for both instantaneous and accelerating slip failures. Between 5 and 10% of ruptures demonstrated an increasing 7 day average event rate for 7 days prior to rupture. Magnitude, MVM and energy are related and consequently demonstrated similar trends. Less than 6% of all failures showed any indication of instability prior to 5 days before rupture for all these parameters. Indications of instability in the average 7 day magnitude, MVM and energy could be identified for over 30% of instantaneous failures 2 days prior to rupture. These parameters did not apply to accelerating slip failures.

Global structural failure was associated with a convergence of seismic events. An SCL of less than 10 was observed for all macro-failures. Accelerating slip failures are easily identified using the SCL as a precursor. However, less than half of the instantaneous failures demonstrated convergence of seismic locations prior to rupture.

14.1 Recommended further work

The purpose of this thesis was to evaluate already identified pre-cursors to determine if their theories could be applied to mining seismic data. Further work is required in refining and automating the methods of evaluation included in this thesis to enable simplified on-site, real-time evaluations.

Most importantly, automated unbiased systems of associating seismic events with specific geological structures to enable the evaluation of the risk of failure must be established. Additionally, assessment methods should be established that combine the evaluation of precursors to enable effective on-site, real-time risk management.

To better understand the failure processes occurring in the mining environment this study should be extended to enable comparison of the parameters alongside mining volumes or extraction rates. This may assist in evaluating false-positive results and provide a better understanding of the failure processes in the rock mass.

Additional assessment methods to be considered include the evaluation of other seismic parameters such as moment and evaluating shorter time frames to failure where they can be evaluated effectively.

All evaluations must account for different failure mechanisms that reflect the nature of the host rock mass and associated geological structures.

15. References

Every reasonable effort has been made to acknowledge the owners of copyright material. I would be pleased to hear from any copyright owner who has been omitted or incorrectly acknowledged.

ACG (2005). Seismic hazard mapping with MS-RAP version 3. Technical report for mine seismicity and rockburst risk management project. Phase II - 2003 - 2005., Australian Centre for Geomechanics.

ACG (2009). Mine Seismicity and Rockburst Risk Management 1999 - 2009. Project review 19/8/2009. ACG.

Aki, K. (1965). Maximum likelihood estimate of b in the formula $\log N = a - bM$ and its confidence limits. Bulletin of earthquake research, University Tokyo, 43, pp.237-239.

Aki, K. (1984). Asperities, barriers, characteristics earthquakes and strong motion prediction. Journal of Geophysical Research, 89, pp.5867-5872.

Aki, K. (1987). Magnitude-frequency relation for small earthquakes: A clue to the origin of f_{max} of large earthquakes. Journal of Geophysical Research, 92, pp.1349-1355.

Albrecht, J. (2005). Delineating rockburst damage to underground development subjected to seismic loading. PhD Thesis, University of Western Australia.

Andrews, P. (2006). Implementation of a new mining method at Argo underground mine. Masters Thesis, Curtin university.

Beck, D. (2004). Rough notes on some aspects of geotechnical monitoring and measurements for dynamic mine environments. Notes present at the mine seismicity and rockbursting short course presented by the Australian Centre of Geomechanics. Beck Mining Engineering.

Beck, D., Gllbert, D and Stacey, K. (2010). Mine to tunnel scale discontinuum simulation of repeated dynamic loading of mine excavations. In P. Hagan and S. Saydam (ed.), Second Australasian Ground Control in Mining Conference: Proceedings, University of New South Wales, Sydney, 23-24 November, 2010.

Blake, W. and Hedley, D. (2003). Rockburst Phenomenon. In Rockbursts. Society for mining, metallurgy and exploration, pp1-14.

Boatwright, J. and Fletcher, J. (1984). The partition of radiated energy between P and S waves. Bulletin of the Seismological Society of America, 74, pp.361-376.

Brzovic, A. (2010). Characterisation of primary copper ore for block caving at the El Teniente mine, Chile. PhD Thesis, Curtin University.

CAMIRO (1996). Canadian rockburst research handbook. CD_ROM version. CAMIRO.

Camus, F. (1975). Geology of the El Teniente orebody with emphasis on wall-rock alteration. Economic Geology, 70, pp.1341-1372.

Cepuritis, P. (2011). An integrated approach to span design in open stope mining. PhD Thesis, Curtin University.

Clout, J., Cleghorn, J and Eaton, P. (1990). Geology of the Kalgoorlie Gold Field. In F. Hughes (ed.), Geology of the mineral deposits of Australia and Papua New Guinea, AusIMM, Melbourne, pp.411-431.

Corskie, J. (2013). Stope design in a structurally controlled environment at Mt Charlotte underground Mine. Masters Thesis, Curtin University.

Coulson, A. (2009). Investigation of the pre to post peak strength state and behaviour of confined rock masses using mine induced microseismicity. PhD Thesis, University of Toronto.

de Beer, W. (2000). Seismology for rockburst prediction. GAP report 409. SIMRAC.

Durrheim, R. and Riemer, K. (2010). History of endeavours to mitigate the rock burst risk in South African gold mines. In J. Brune (ed.), Extracting the science: a century of mining research. pp.156-171.

Dusci, M., Trueman, A, Eddie, A, Kalla, J, Fairley, K, Crawford, M and Hamlyn, C. (2003). Argo Mineral Resource Report F2003. Gold Fields internal report.

- Enescu, B. and Kiyoshi, I. (2001). Some premonitory phenomena of the 1995 Hyogo - Ken Nanbu (Kobe) earthquake: seismicity, b-value and fractal dimension. *Tectonophysics*, 338, pp.297-314.
- Engineering Seismology Group Inc. (2013). <https://www.esgsolutions.com/english/view.asp?x=1>. (accessed 2013).
- Esterhuizen, G. (1994). Preliminary study of the effects of fault properties and mining geometry on the stiffness of the loading system in fault slip seismic events as a basis for identifying situations prone to seismic activity. GAP report 003. SIMRAC.
- Esterhuizen, G. (2000). Study of loading system stiffness in fault slip seismic events. GAP 114. SIMRAC.
- Falmagne, V. (2002). Quantification of rock mass degradation using microseismic monitoring and applications for mine design. PhD Thesis, Queens University.
- Frohlich, C. and Davis, S. (1986). Single-link cluster analysis as a potential tool for evaluating spatial and temporal properties of earthquake catalogs. *EOS*, 67, pp.1119.
- Geller, R. (1997). Earthquake prediction: a critical review. *Geophysics Journal International*, 131, pp.425-450.
- Gibowicz, S. and Kijko, A. (1994). An introduction to mining seismology. Academic Press.
- Gibowicz, S., Young, R, Talebi, S and Rawlence, D. (1991). Source parameters of seismic events at the underground research laboratory in Manitoba Canada: scaling relations for events with magnitude smaller than -2. *Bulletin of the Seismological Society of America*, 81, pp.1157-1182.
- Gressier, J. and Kolkert, R. (2002). Structural controls on gold mineralisation of the Argo deposit, Western Australia. In S. Vearncombe (ed.), *Applied structural geology for mineral exploration and mining. International symposium Kalgoorlie Western Australia*, pp.72-74.
- Grincer, M. (2002). Structural and spatial controls to seismicity at the Big Bell gold mine. Undergraduate thesis. Undergraduate thesis. University of Western Australia.
- Gutenberg, B. and Richter, C. (1949). *Seismicity of the earth and related phenomena*. Princeton University press.
- Hardy, H.J. (1972). Application of acoustic emission techniques to rock mechanics research. In (ed.), *Acoustic Emission. American society for testing and materials*, pp41-83.
- Hasegawa, H., Wetmiller, R and Gendzwill, D. (1989). Induced seismicity in mines in Canada - An Overview. *Pure and Applied Geophysics*, 129, pp.423-453.
- Heal, D. (2010). Observations and analysis of incidences of rockburst damage in underground mines. PhD Thesis, University of Western Australia.
- Hedley, D. and Udd, J. (1989). The Canada - Ontario - Industry rockburst project. *Pure and Applied Geophysics*, 129, pp.661-672.
- Hirata, T. (1989). Fractal dimension of the fault systems in Japan: Fractal structure in rock fracture geometry at various scales. *PAGEOPH*, 131, pp.157-164.
- Hirata, T., Satoh, T and Ito, K. (1987). Fractal structure of spatial distribution of microfracturing in rock. *Geophysical Journal of the Royal Astronomical Society*, 90, pp.369-374.
- Hudyma, M. (2005). Mine seismicity and rockburst risk management - Phase I. REPORT NO. 237. MERIWA.
- Hudyma, M. (2008). Analysis and interpretation of clusters of seismic events in mines. PhD Thesis, University of Western Australia.
- Hudyma, M. and Mikula, P. (2001). Quantifying seismic hazard using neural networks. In G. van Aswegen, R. Durrheim and W. Ortlepp (ed.), *Proceedings of Fifth International Conference on Rockburst and Seismicity in Mines*, pp.551-555.
- Hudyma, M. and Potvin, Y. (2009). An engineering approach to seismic risk management in hard rock mines. *Rock Mechanics and Rock Engineering*.
- Hudyma, M., Heal, D and Mikula, P. (2003). Seismic monitoring of mine - old technology, new applications. *Proceedings 1st Australasian Ground Control in Mining Conference*, Sydney. pp.209-226.
- Institute of Mine Seismology. (2013). <http://www.imseismology.org/products/software/index.html>. (accessed 2013).
- Jeng, F., Lin, M, Lu, C and Huang, K. (2002). Characteristics of seismic energy release of subduction zones - examples from Taiwan. *Engineering geology*, 67, pp.17-38
- Kagan, Y. (1997). Are earthquake predictable? *Geophysics journal International*, 131, pp.505-525

- Kanamori, H. (1977). The energy release in great earthquakes. *Journal of geophysical research*, 82, pp.2981-2987
- Kgarume, T. (2010). Mine aftershocks and implications for seismic hazard. Masters Thesis, University of the Witwatersrand.
- Kijko, A. and Funk, C. (1996). Space-time interaction amongst clusters of mining induced seismicity. *Pure and Applied Geophysics*, 147, pp.277-288
- Kusui, A. and Villaescusa, E. (2016). Seismic response prior to spalling failure in highly stressed underground tunnels. In *Seventh international conference and exhibition on mass mining*. Sydney, NSW, 9-11 May.
- Lachenicht, R. (2001). Relationship between ERR, system stiffness parameters and seismic energy release for different geotechnical areas. Final report GAP612a. SAIMM.
- Lei, X. (2003b). How do asperities fracture? An experimental study of unbroken asperities. *Earth and planetary science letters*, 213, pp.347-359
- Lei, X. (2006). Typical phases of pre-failure damage in granitic rocks imder differential compression. 261, pp.11-29.
- Lei, X. and Satoh, T. (2007). Indicators of critical point behaviour prior to rock failure inferred from pre-failure damage. *Tectonophysics*, 431, pp.97-111.
- Lei, X., Guozheng, Y, Ma, S, Wen, X and Wang, Q. (2008). Earthquakes induced by water injection at ~3km depth within the Rongchang gas field, Chongqing, China. *Journal of Geophysical Research*, 113, pp.1-12.
- Lei, X., Kusunose, K, Rao, M, Nishizawa, O and Satoh, T. (2000a). Quasi-static growth and cracking in homogeneous brittle rock under triaxial compression using acoustic emissions monitoring. *Journal of Geophysical Research*, 105, pp.6127-6139.
- Lei, X., Kusunose, K, Satoh, T and Nishizawa, O. (2003a). The hierarchical rupture process of a fault: an experimental study. *Physics of the earth and planetary interiors*, 137, pp.213-228.
- Lei, X., Masuda, K, Nishizawa, O, Jouniaux, L, Liu, L, Ma, W, Satoh, T and Kusunose, K. (2004). Detailed analysis of acoustic emission activity during catastrophic fracture of faults. *Journal of Structural Geology*, 26, pp.247-258.
- Lei, X., Nishizawa, O, Kusunose, K and Satoh, T. (1992). Fractal structure of the hypocentre distributions and focal mechanism solutions of acoustic emission in two granites of different grain sizes. *Journal of Physics of the Earth*, 40, pp.617-634.
- Lei, X., Nishizawa, O, Kusunose, K, Cho, A, Satoh, T and Nishizawa, O. (2000b). Compressive failure of mudstone samples containing quartz veins using rapid AE monitoring: the role of asperities. *Tectonophysics*, 328, pp.329-340.
- Lockner, D., Byerlee, J, Kuksenko, V, Ponomarev, A and Sidorin, A. (1991). Quasi-static fault growth and shear fracture energy in granite. *Nature*, 350, pp.39-42.
- Lockner, D., Byerlee, J, Kuksenko, V, Ponomarev, A and Sidorin, A. (1992). Observations of quasistatic fault growth from acoustic emissions. In B. Evans and T. Wong (ed.), *Fault mechanics and transport of rocks*, Academic press, pp.3-32.
- Lomnitz, C. (1966). Magnitude stability in earthquake sequences. *Bulletin of the seismological society of America*, 56, pp.247-249.
- Main, I. and Meredith, P. (1989a). Classification of earthquake precursors from a fracture mechanics model. *Tectonophysics*, 167, pp.273-283.
- Main, I., Meredith, P and Jones, C. (1989). A reinterpretation of the precursory seismic b-value anomaly from fracture mechanics. *Geophysical Journal*, 96, pp.131-138.
- Mendecki, A. (1997). Seismic monitoring in mines.
- Mendecki, A., Brink, A, Green, R, Mountfort, P, Dzhafarov, A, Niewiadomski, J, Kijko, A, Sciocatti, M, Radu, S, Van Aswegen, G, Hewlett, P, de Kock, E and Stankiewicz, T. (1996). Seismology for rockbursts prevention, control and prediction. GAP report 017. SIMRAC.
- Mendecki, A., Lynch, R and Malovichko, D. (2010). Routine micro-seismic monitoring in mines. *Proceedings of the Australian earthquake engineering society conference*, Perth, Western Australia.
- Meredith, P., Main, I and Jones, C. (1990). Temporal variations in seismicity during quasi-static and dynamic rock failure. *Tectonophysics*, 175, pp.249-268.

- Mikula, P. and Poplawski, R. (1995). The seismic monitoring decision at Mt Charlotte gold mine. In T. Golosinski (ed.), 6th Underground operators conference, pp. 79-85.
- Mikula, P., Heal, D and Hudyma, M. (2008). Generic seismic risk management plan for underground hardrock mines. Technical report for mine seismicity and rockburst risk management project. Phase III - 2006 - 2008., Australian Centre for Geomechanics.
- Mogi, K. (1962). Magnitude-frequency relation for elastic shocks accompanying fractures of various materials and some related problems in earthquakes (2nd paper). Bulletin of earthquake research institute, 40, pp.831-853.
- Mogi, K. (1962). Study of elastic shocks caused by the fracture of heterogeneous materials and its relations to earthquake phenomena. Bulletin of earthquake research institute, 40, pp.125-173.
- Mogi, K. (1968). Source locations of elastic shocks in the fracturing process in rocks (1). Bulletin of the Earthquake Institute, 46, pp.1103-1125.
- Moriya, H., Naoi, M, Nakatani, M, Aswegen, G, Murakami, O, Kgarume, T, Ward, A, Durrheim, R, Phillip, J, Yabe, Y, Hironri, H and Ogaswara, H. (2015). Delineation of large localised damage structures forming ahead of an active mining front by using advanced acoustic emission mapping techniques. International journal of rock mechanics and mining sciences, 79, pp.157 – 165.
- Morton, E. and Sweby, G. (2005). Draft ground control management plan. Black Swan Nickel.
- Naoi, M., Nakatani, M, Kgarume, T, Khambule, S, Masakale, T, Ribeiro, L, Philip, J, Horiuchi, S, Otsuki, K, Miyakawa, K, Watanabe, A, Moriya, H, Murakami, O, Yabe, Y, Kawakata, H, Yoshimitsu, N, Ward, A, Durrheim, R and Ogaswara, H. (2015). Quasi-static slip patch growth to 20m on a geological fault inferred from acoustic emissions in a South African gold mine. Journal of geophysical research, 120, pp.1692-1707
- Ogasawara, H., Durrheim, R, Nakatani, M, Yabe, Y, Milev, A, Cichowicz, A, Kawakata, H and Moriya, H. (2009). A Japanese - South African collaboration to mitigate seismic risks in deep gold mines. The South African Institute of mining and metallurgy hard rock safety conference, pp.115-134.
- Omori, F. (1894). On the aftershocks of earthquakes. Journal of the college of science, Imperial University of Tokyo, 7, pp.111-200
- Owen, M. (2004). Exposure model – Detailed profiling and quantification of the exposure of personnel to geotechnical hazards in underground mines. PhD Thesis, University of Western Australia.
- Owen, M. (2006). Black Swan Nickel Mine - Analysis of seismic data and seismic hazard assessment. Mine Seismicity and Rockburst Risk Management Project Phase III – 2006-2008. ACG
- Page, R. (1968). Aftershocks and microshocks of the great Alaska earthquake of 1964. Bulletin of seismological society of America, 58, pp.1131-1168.
- Pardo, C. and Villaescusa, E. (2012). Methodology for back analysis of intensive rock mass damage at the el Teniente Mine. MassMin 2012: 6th International Conference and Exhibition on Mass Mining. Sudbury, Ontario, Canada, CIM.
- Pardo Mella, C. (2015). Back analysis of intensive rock mass damage at the El Teniente Mine. PhD Thesis, Curtin University.
- Phillips, G. (1986). Geology and alteration in the golden mine, Kalgoorlie. Economic geology, 81, pp.779-808.
- Phillips, G. and Nooy, D. (1988). High-grade metamorphic processes which influence Archaean gold deposits, with particular reference to Big Bell, Australia. Journal of metamorphic geology, 6, pp.95-114
- Player, J. (2004). Rock mass damage and excavation response - Big Bell longitudinal sub level caving operation. Masters Thesis, Curtin University.
- Player, J. (2004). Strain energy for the Big Bell longitudinal sublevel cave. Massmin Santiago Chile Aug 22, 2004.
- Poplawski, R. (1997). Seismic parameters and rockburst hazard at Mt Charlotte mine. International Journal of Rock Mechanics and Mining Sciences, 34, pp.1213-1228.
- Potvin, Y., Jarufe, J and Wesseloo, J. (2010). Interpretation of seismic data and numerical modelling of fault reactivation at El Teniente, Reservas Norte sector (RENO). In Y. Potvin (ed.), Proceedings of the second international symposium on block and sublevel caving, pp.483-494.
- Rao, M. and Prasanna Lakshmi, K. (2005). Analysis of b-value and improved b-value of acoustic emissions accompanying rock fracture. Current science, 89, pp.1577-1582.

- Raymond, O. (1995). Pyrite composition and ore genesis in the Prince Lyell deposit, Mt Lyell mineral field, western Tasmania, Australia. *Ore geology reviews*, 10, pp.231-250.
- Reimer, K. and Durrheim, R. (2011). Mining seismicity in the Witwatersrand Basin: Monitoring mechanisms and mitigation strategies in perspective. *Journal of rock mechanics and geotechnical engineering*, 3, pp.250-259.
- Reimnitz, M. (2004). Shear-slip induced seismic activity in underground mines: A case study in Western Australia. Masters Thesis, University of Western Australia.
- Ridley, J. and Mengler, F. (2000). Lithological and structural controls on the form and setting of vein stockwork orebodies at the Mount Charlotte gold deposit, Kalgoorlie. *Economic Geology*, 95, pp.85-98.
- Robinson, R. (1979). Variations of energy release, rate of occurrence and b-value of earthquakes in the main seismic region, New Zealand. *Physics of the earth and planetary interiors*, 18, pp.209-220.
- Rojas, E., Cavieres, P, Dunlop, R and Gaete, S. (2000). control of induced seismicity at El Teniente mine, Codelco - Chile. In G. Chitombo and T. Brown (ed.), *Massmin 2000 29 October - 2 November Brisbane, Queensland, AusIMM*, pp.775-781.
- Ross, A., Barley, M, Brown, S, McNaughton, N, Ridley, J and Fletcher, I. (2004). Young porphyries, old zircons: new constraints on the timing of deformation and gold mineralisation in the Eastern Goldfields from SHRIMP U–Pb zircon dating at the Kanowna Belle Gold Mine, Western Australia. *Precambrian research*, 128, pp.105-142.
- Rundle, J. (1989). Derivation of the Complete Gutenberg-Richter Magnitude-Frequency Relation Using the Principle of Scale Invariance. *Journal of Geophysical Research*, 94, pp.12337-12342.
- Scholz, C. (1968a). Experimental study of the fracturing process in brittle rock. *Journal of geophysical research*, 73, pp.1447-1454.
- Scholz, C. (1968b). Microfracturing and inelastic deformation of rock in compression. *Journal of Geophysical Research*, 73, pp.1417-1432.
- Scholz, C. (1968c). The frequency magnitude relation of microfracturing in rock and its relation to earthquakes. *Bulletin of the Seismological Society of America*, 58, pp.399-415.
- Scholz, C., Sykes, L and Aggarwal, Y. (1973). Earthquake prediction: A physical basis. *Science*, 181, pp.803-810.
- Slade, J. (2004). Seismic characteristics of faults at the Kundana Gold Mine Eastern Goldfields Western Australia. Masters Thesis, Curtin University.
- Spottiswoode, S., Napier, J, Milev, A and Vieira, F. (2000). The relationship between ERR and seismic energy release for different geotechnical areas. GAP 612C. SIMRAC, Cape Town.
- Stern, C., Skewes, M and Arevalo, A. (2011). Magmatic evolution of the giant El Teniente Cu-Mo deposit, central Chile. *Journal of Petrology*, 52, pp.1591-1617.
- Tang, C. and Kaiser, P. (1998). Numerical simulation of cumulative damage and seismic energy release during brittle rock failure - Part I: Fundamentals. *International journal of Rock Mechanics and mineral science*, 35, pp.113-121.
- Turner, M. and Player, J. (2000). Seismicity at Big Bell Mine. *Massmin 2000 Brisbane QLD*, pp. 791-798.
- United States Geological Survey. (2016). <http://earthquake.usgs.gov/learn/glossary/>. (accessed 2016).
- Urbancic, T., Trifu, C, Long, J and Young, R. (1992). Space-time correlations of b values with stress release. *Pure and Applied Geophysics*, 139, pp.449-462.
- Utsu, T. (1965). A method for determining the value of b in the formula $\log N = a - bM$ showing the magnitude-frequency relation for earthquakes. *Geophysics bulletin of the Hokkaido University*.
- Varden, R. and Esterhuizen, H. (2012). Kanowna Belle—evolution of seismicity with increasing depth in an ageing mine. In Y. Potvin (ed.), *Deep Mining 2012*.
- Varden, R., Lachenicht, R, Player, J, Thompson, A and Villaescusa, E. (2008). Development and Implementation of the Garford Dynamic Bolt at the Kanowna Belle Mine. 10th AusIMM Underground Operators conference Launceston Tasmania.
- Villaescusa, E. (2013). Mt Lyell internal report.
- Weichert, D. (1980). Estimation of the earthquake recurrence parameters for unequal observation periods for different magnitudes. *Bulletin of seismological society of America*, 70, pp.1337-1346.
- Wesseloo, J. and Potvin, Y. (2012). Advancing the strategic use of seismic data in mines. *Meriwa Reoprt No 269. MERIWA*.

Wiles, T. (2002). Loading system stiffness - a parameter to evaluate rockburst potential. In Australian Centre for Geomechanics (ed.), Deep and High stress mining: Section 8, pp.1-11.

Wiles, T. (2005). Rockburst prediction using numerical modelling - Realistic limits for failure prediction accuracy. In Y. Potvin and M. Huydma (ed.), Sixth international symposium on rockburst and seismicity in mines, pp. 57-63.

Wright, C., Kijko, A, Linzer, L and Smith, M. (2003). Recent research in earth structure, earthquake and mine seismology, and seismic hazard evaluation in South Africa. South African Journal of Science, 99, pp.389-393.

Wyss, M. (2001). Why is earthquake research not progressing faster. Tectonophysics, 338, pp.217-223.

Appendix 1 – Calculation of seismic parameters.

Appendix 1

A1: 1. Seismic source parameter formulae

Seismic source parameters are calculated differently for each branch of seismology. All data used in this thesis is generated from IMS seismic systems and consequently it is these parameters that will be outlined in this appendix.

Seismic source parameters are typically calculated by the seismic monitoring system automatically. The main reference for these calculations is Mendecki, 1997 and Webber, 2008. Mendecki, 1997 has been updated through various papers written by Mendecki and others (Mendecki et al., 1999, Mendecki, 2005, Mendecki et al., 2010) and the IMS monitoring system manuals provide a brief but updated list of these parameters.

A1: 1.1 Location

The location of the event can be calculated using a number of different methods. Lenhardt, 2013 lists them as:

- Geiger method
- Bayesian approach
- Velocity model approximation
- Relative location technique
- Simultaneous hypocentre and velocity determination

The IMS system uses the Geiger method (Mendecki, 1997). This method uses an iterative process that combines the velocity of the seismic wave and the arrival time at each sensor. Traditionally, the main assumption is that the ray path is in a straight line. This, however, appears to have been updated and modified over the years with more complex ray tracing now being utilised.

Mendecki, 1997 states that *“the location error depends on the following factors:*

- *Errors in the arrival time determination*
- *Inadequate knowledge of the velocity model*
- *Inaccuracy in the station co-ordinates*
- *The method of solution*
- *The spatial distribution of stations with respect to the event.”*

The design of mine seismic systems is limited by the geometry of the mining development. Typically sensors are installed in short boreholes drilled off a mining access drive. This frequently leads to planar or semi-planar arrays that limit the ability of the systems to accurately locate seismic events and to accurately calculate source parameters.

A1: 1.2 Energy

Essentially the Energy is calculated by determining the area under the velocity time curve. P and S wave energy is calculated separately and added together to determine the total energy. Typically, only the total energy is used in analysis. The most quoted energy formula is the following:

$$E_{p,s} = 4\pi\rho CR^2 \int_0^{t_s} v^2 dt$$

Equation 1.1

where ρ is rock density, C is wave velocity p and s represent p and s waves, R is the distance from the source and t represents time. The integral represents the corrected far field velocity pulse for P and S waves.

This formula has been updated to the form presented in Equation 1.2 by Mendecki et al., 2010. The constants have been slightly modified and rationalised. The integral is presented in a different form but is essentially the same.

$$E_{p,s} = \frac{8}{5}\pi\rho v_{p,s}R^2 \int_0^{t_s} \dot{u}_{corr}^2(t)dt$$

Equation 1.2

where ρ is rock density, v is wave velocity p and s represent p and s waves, R is the distance from the source and t represents time. The integral $\int_0^{t_s} \dot{u}_{corr}^2(t)dt$ represents the corrected far field velocity pulse for P and S waves.

A1: 1.3 Moment

In the past moment has been a key source parameter for calculating secondary parameters such as apparent stress, apparent volume and energy index. More recently the IMS system has used potency in exchange for moment in many of these calculations. Moment is related to the shear modulus of the rock (μ) and fault displacement through the following formula:

$$M_o = \mu AD$$

Equation 1.3

where A is the area of fault slip and D is the average slip of the area. D can only be directly measured and so typically the following formula is used to calculate moment from corner frequency:

$$M_{o(p,s)} = \frac{4\pi\rho v_{(p,s)}^3 R \Omega_0}{a}$$

Equation 1.4

Where v is P or S wave velocity, ρ is the rock density, R is distance between the event and the sensor and Ω_0 is the corner frequency. “ a ” is a constant accounting for the radiation pattern of the seismic wave. It is 0.39 and 0.57 for the P and S wave respectively.

A1: 1.4 Corner frequency

The corner frequency is conceptualised in the Brune Model (Brune, 1968, Brune, 1970). To determine the corner frequency the velocity time chart is converted into an amplitude frequency chart using Fast Fourier Transforms (FFT). An example of this chart is provided in Figure 1.1.

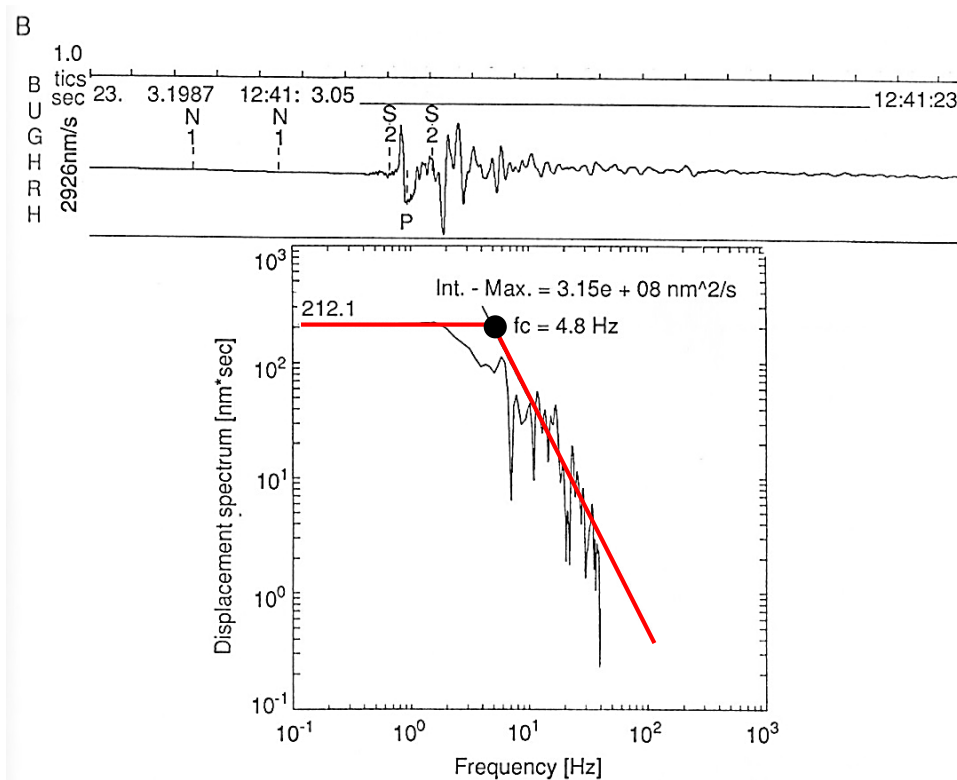


Figure 1.1: Example of corner frequency concept (Gibowicz and Kijko, 1994)

The corner frequency is the point at which the frequency changes from constant to decreasing amplitude. The shape of the displacement spectra is expressed mathematically using the following formula:

$$\Omega(f) = \frac{\Omega_0}{1 + \left(\frac{f}{f_0}\right)^2}$$

Equation 1.5

where Ω_0 is the constant portion of the chart, f is the frequency, f_0 is the corner frequency.

A1: 1.5 Apparent Stress

Apparent stress is described by Boatwright and Fletcher, 1984 as the “*ratio of the radiated energy to the moment multiplied by the rigidity*” (Equation 1.6). They suggest the apparent stress is an estimate of stress release. Lachenicht, 2001 states that apparent stress is a “*model independent measure of the stress change at the source*”.

$$\sigma_A = \frac{\mu E}{M_o}$$

Equation 1.6

Where μ is the rigidity of the rock mass, E is energy and M_o is moment.

A1: 1.6 Apparent Volume

Lachenicht, 2001 defines apparent volume (Equation 1.7) as the “*volume of rock with coseismic inelastic strain*”.

$$V_A = \frac{M_o}{2\sigma_A} = \frac{M_o^2}{2\mu E}$$

Equation 1.7

where M_o is seismic moment, σ_A is apparent stress μ is rigidity and E is seismic energy.

A1: 1.7 Radius

Radius (or source radius) is a parameter that estimates the dimension of the fault slip. It is based on a circular fault model and is calculated using the following formula:

$$r_o = \frac{K v_s}{2\pi f_o}$$

Equation 1.8

where K is a constant based on the source model, v_s is the S wave velocity and f_o is the corner frequency.

The main assumption is that a uniform stress release occurs over the entire source area. The Canadian Rockburst Handbook (CAMIRO, 1996) suggests that some “*estimates of source radius have been found to be too large relative to the observed geological evidence*”.

A1: 1.8 Potency

Mendecki, 1997 defines potency as the source strength. The calculation is dependent on the model. Utilising the volumetric model potency is calculated by dividing the seismic moment by the rigidity of the rock mass (Equation 1.9). For planar models it is calculated by multiplying the average displacement by the area of slip (Equation 1.10).

$$P = \frac{M_o}{\mu}$$

Equation 1.9

$$P = \bar{u}A$$

Equation 1.10

A1: 1.9 Stress drop

Gibowicz and Kijko, 1994 state that there are four estimates of stress release in seismology. The most accurate is the static stress drop defined as “*the difference between the initial and final stresses on a plane*”. It is estimated from the seismic moment and the seismic radius using the following formula:

$$\Delta\sigma = \frac{7 M_o}{16 r_o^3}$$

Equation 1.11

where M_0 and r_0 is the moment and radius of the event respectively. Mendecki et al., 1996 describes dynamic stress drop (Equation 1.12) as “*the difference between the initial stress and the kinetic friction level on the fault area.*”

$$\Delta\sigma = \frac{7}{17} \frac{M_0}{r_0}$$

Equation 1.12

Whilst the stress drop parameter is commonly used it is widely known that this parameter is dependent on models used to determine the moment and the source radius. It also assumes that the initial stress have been determined, however it is difficult to accurately determine the stress profile of mining excavations at any point in time without specific instrumentation or testing. McGarr, 1984 states that stress drop “*conveys little or no information regarding the state of the rock and the observed variation does not appear to relate systematically to any other essential aspect of seismic event*”. Despite this, the parameter is commonly used in mining seismic analysis.

A1: 1.10 Magnitude

Magnitude is a relative scale typically used to describe the size of the event. There are many different scales. One of the first magnitude scales was the Mercalli scale (Table 1.1) developed in the late 1800s - early 1900s. This scale is based on how the event is felt on surface and the area over which it is felt. At the lower end of the scale events are only felt by people with no damage detected. As the scale increases damage becomes increasingly significant. This scale depends on the presence and perceptions of nearby habitation and is unreliable where habitation is not present.

Table 1.1: Mercalli scale

Mercalli Scale	Definition
I. Instrumental	Generally not felt by people.
II. Weak	Felt only by a couple people that are sensitive, especially on the upper floors of buildings.
III. Slight	Felt quite noticeably by people indoors, especially on the upper floors of buildings. Many do not recognize it as an earthquake. Vibration similar to the passing of a truck.
IV. Moderate	Felt indoors by many people, and outdoors by few people. Some awakened. Dishes, windows, and doors disturbed, and walls make cracking sounds. The sensation is more like a heavy truck striking building. Damage none.
V. Rather Strong	Felt inside by most or all, and outside. Dishes and windows may break and bells will ring. Vibrations are more like a large train passing close to a house. Possible slight damage to buildings. Liquids may spill out of glasses or open containers.
VI. Strong	Felt by everyone, outside or inside. Windows, dishes, glassware broken; books fall off shelves; some heavy furniture moved or overturned; a few instances of fallen plaster. Damage slight to moderate in poorly designed buildings, all others receive none to slight damage.
VII. Very Strong	Difficult to stand. Furniture broken. Damage light in building of good design and construction; slight to moderate in ordinarily built structures; considerable damage in poorly built or badly designed structures.
VIII. Destructive	Damage slight in structures of good design, considerable in normal buildings with a possible partial collapse. Damage great in poorly built structures. Brick buildings easily receive moderate to extremely heavy damage.
IX. Violent	General panic. Damage slight to moderate (possibly heavy) in well-designed structures. Well-designed structures thrown out of alignment. Damage moderate to great in substantial buildings, with a possible partial collapse. Some buildings may be shifted off foundations. Walls can fall down or collapse.
X. Intense	Many well-built structures destroyed, collapsed, or moderately to severely damaged. Most other structures destroyed, possibly shifted off foundation. Large landslides.
XI. Extreme	Few, if any structures remain standing. Numerous landslides, cracks and deformation of the ground.
XII. Catastrophic	Total destruction – everything is destroyed. Objects thrown into the air. The ground moves in waves or ripples. Landscape altered, or levelled by several meters.

The Richter scale was first published in 1935 (Richter, 1935) and modified over the next 20 years. The development of the scale coincided with the development of the seismograph. It is defined as the *“logarithm of the maximum trace amplitude... with which the standard short-period torsion seismometer... would register that earthquake at an epicentral distance of 100 kilometers”* (Gutenberg and Richter, 1942).

In the late 1970s it was found that the Richter scale was limited in its application particular at the upper end of the scale. Furthermore the scale was purely empirical and did not relate to the size of the event. Hanks and Kanamori, 1979 proposed a new scale based on moment (Equation 1.13). Kanamori, 1983 states that seismic moment can be related to the amount of slip on a fault and can be easily calculated from seismograms. The constants in the magnitude formula have been modified since the late 1970s. Current earthquake and mining applications use Equation 1.14 to calculate the moment magnitude. The moment magnitude is currently the most utilised scale in earthquake applications. Some mine sites also prefer this scale.

$$m = \frac{2}{3} \text{Log}M - 10.7$$

Equation 1.13

$$m = \frac{2}{3} \text{Log}M - 6.01$$

Equation 1.14

Mining seismologists have developed their own magnitude scales. Australian mining seismologic is heavily influenced by South African practices. The IMS local scale was developed for the IMS seismic system and is the default magnitude scale used by many Australian mines sites. It is calculated using Equation 1.15.

$$M_L = \alpha \log E + \beta \log M + \gamma$$

Equation 1.15

Energy (E) and Moment (M) are calculated by the monitoring system and α , β and γ are constants. These constants are set typically set at the default system values of 0.272, 0.392 and -4.62 respectively.

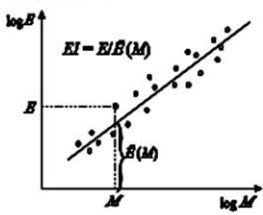
A1: 1.11 References

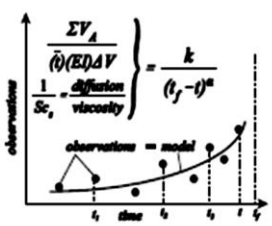
- Boatwright, J. and Fletcher, J. (1984). The partition of radiated energy between P and S waves. *Bulletin of the Seismological Society of America*, 74, pp.361-376.
- Brune, J. (1968). Seismic moment, seismicity and rate of slip along major fault zones. *Journal of Geophysical Research*, 73, pp.777-784.
- Brune, J. (1970). Tectonic stress and the spectra of seismic shear waves from earthquakes. *Journal of Geophysical Research*, 75, pp.4997-5009.
- CAMIRO (1996). Canadian rockburst research handbook. CD_ROM version. CAMIRO.
- De Beer, W. (2000). Seismology for rockburst prediction. GAP report 409. SIMRAC.
- Gibowicz, S. and Kijko, A. (1994). *An introduction to mining seismology*. Academic Press.
- Gutenberg, B. and Richter, C. (1942). Earthquake magnitude, intensity, energy and acceleration. *Bulletin of the Seismological Society of America*, 32, pp.163-191.
- Hanks, T. and Kanamori, H. (1979). A moment magnitude scale. *Journal of Geophysical Research*, 84, pp.2348-2350.
- Kanamori, H. (1983). Magnitude scale and quantification of earthquakes. *Tectonophysics*, 93, pp.185-199.
- Lachenicht, R. (2001). Relationship between ERR, system stiffness parameters and seismic energy release for different geotechnical areas. Final report GAP612a. SAIMM.
- Lenhardt. (2013). http://www.oge.or.at/Lecture_Interpretation.pdf. (accessed 2013).
- McGarr, A. (1984). Some applications of seismic source mechanism studies to assessing underground hazard. In N. Gay and E. Wainwright (ed.), *Proceedings of the 1st international congress on rockburst and seismicity in mines*, SAIMM, Johannesburg.
- Mendecki, A. (1997). *Seismic monitoring in mines*.
- Mendecki, A. (2005). Persistence of seismic rockmass response to mining. In Y. Potvin and M. Hudyma (ed.), *Controlling seismic risk: Proceedings of the 6th International symposium on rockbursts and seismicity in mines*, ACG, Perth, pp. 97-105.
- Mendecki, A., Brink, A, Green, R, Mountfort, P, Dzhafarov, A, Niewiadomski, J, Kijko, A, Sciocatti, M, Radu, S, Van Aswegen, G, Hewlett, P, de Kock, E and Stankiewicz, T. (1996). *Seismology for rockbursts prevention, control and prediction*. GAP report 017. SIMRAC.
- Mendecki, A., Lynch, R and Malovichko, D. (2010). Routine micro-seismic monitoring in mines. *Proceedings of the Australian earthquake engineering society conference*, Perth, Western Australia.
- Mendecki, A., Van Aswegen, G and Mountford, P. (1999). A guide to routine seismic monitoring in mines. In Jager A and Ryder J (ed.), *A handbook on rock engineering practice for tabular hard rock mines*, Creda Communications, Cape town.
- Richter, C. (1935). An instrumental earthquake magnitude scale. Technical report. *Bulletin of the Seismological Society of America*.
- Webber, S. (2008). Mine Seismicity 603. Mining Geomechanics Masters course. Curtin University.

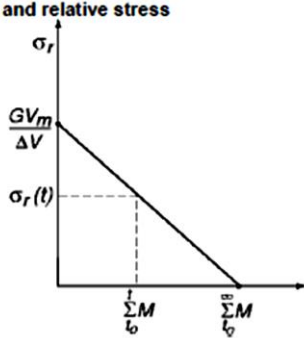
A1: 2. Description of terms used by De Beer, 2000 for seismic prediction.

Parameter, relevant formula	Description
Magnitude, m $m = \log(A/T) + C$ A/T - the maximum displacement over associated period in the P- or S-wave group C - corrections for path effects, site response and source region	Magnitude is a relative measure of the strength of a seismic event based on measurements of maximum ground displacement at a given frequency at multiple seismic sites. A unit increase in magnitude corresponds to a 10-fold increase in amplitude of ground displacement. Gutenberg and Richter related seismic energy and magnitude derived from P-waves recorded at large distances from the source at 1sec period as $\log E(\text{ergs}) = 2.4m + 5.8$
Seismic moment, M, [Nm] and Moment-magnitude, m $m = 2/3 \log M - 6.1$	A scalar that measures the coseismic inelastic deformation at the source. Since seismic moment is proportional to the integral of the far field displacement pulse it can easily be derived from recorded waveforms. A relation that scales seismic moment into magnitude of a seismic event is called moment-magnitude.
Seismic moment tensor $M_{ij} = \int_V c_{ijkl} \Delta \varepsilon_{kl} dV = \int_V \Delta \sigma_{ij} dV$ where c_{ijkl} - elastic constants $\Delta \varepsilon_{kl}$ - strain change at the source $\Delta \sigma_{ij}$ - stress change or change in moment per unit volume $\Delta \theta = \text{tr}(M_{ij}) / (3\lambda + 2G)$, where λ - the second Lamé constant G - rigidity	The most general description of the processes at the seismic source V is by the distribution of forces or moments equivalent to the inelastic deformation. One can describe the inelastic processes at the source as the stress-free change of size and shape of an elastic body without alteration of the elastic properties of the region. If change in size and shape can be expressed as a change in strain $\Delta \varepsilon_{kl}$, then the equivalent stress change, or change in moment per unit volume is proportional to the strain change. The total moment integrated over the source volume is the seismic moment tensor, M_{ij} . For long waves compared to the source size, the whole source volume V can be considered to be a system of couples located at, say, the centre of V , and the moment tensor components can be defined by the equation at left. The moment tensor measures the inelastic deformation at the source during the seismic event and its value at the end of the source process measures the permanent inelastic strain produced by the event. The seismic moment tensor can be decomposed into isotropic (or volume change) and deviatoric components providing an additional insight into the nature of the coseismic strain drop. For a homogeneous body, the coseismic volumetric change, $\Delta \theta$, can be calculated from the second equation at left. The eigenvalues and corresponding eigenvectors of the deviatoric component of the seismic moment tensor describe the magnitude and orientation, respectively, of the principal moment axes (neglecting gravity) acting at the source. These principal moment axes are uniquely determined by moment tensor inversion. Principal moment orientation data can

Parameter, relevant formula	Description
	provide sufficient information to find the best stress tensor.
Radiated seismic energy, E , [J]	The portion of the energy released or work done at the source that is radiated as seismic waves. Seismic energy is proportional to the integral of the squared velocity spectrum in the far field and can be derived from recorded waveforms. Radiated seismic energy increases with stress drop, seismic moment and with the traction rate i.e., stress oscillations at the source.
Corner frequency, f_c [Hz] and Source size, l , [m] $l = c_1 / f_c$ $c_1 = 2500$ for S-wave in hard rock	The frequency at which a source radiates the most seismic energy observed as the maximum on the source velocity spectrum or as the point at which a constant low frequency trend and a high frequency asymptote on the recorded source displacement spectrum intersect. The corner frequency is inversely proportional to the characteristic size of the source.
Stress drop, $\Delta\sigma$, [Pa] $\Delta\sigma = c_2 M_0^2$ $c_2 = 1.8 \times 10^{-10}$ for S-waves in hard rock $\Delta\sigma = G\Delta\varepsilon$, and $\Delta\varepsilon$ - strain drop	Stress drop estimates the stress release at the seismic source. Although it is model dependent it provides reasonable estimates and a fair comparison amongst different sources from the same region recorded by the same seismic system.
Source area, [m ²] $A = M / (Gu)$ u - average displacement at the source.	The area of coseismic inelastic deformation over the planar source.
Source volume, [m ³] $V = M / \Delta\sigma$	The volume of coseismic inelastic deformation of the order of $\Delta\sigma/G$.
Apparent stress, [Pa] $\sigma_A = GE / M = E / (\Delta\varepsilon V)$ or $\sigma_A = E / (uA)$.	Apparent stress is recognised as a model independent measure of the stress change at the seismic source.
Apparent volume, [m ³] $V_A = M / (c_3 \sigma_A) = M^2 / (c_3 GE)$ c_3 - scaling factor - 2.	The apparent volume scales the volume of rock with coseismic inelastic strain of an order of apparent stress over rigidity. The apparent volume V_A is less model dependent than the source volume V .

Parameter, relevant formula	Description
Energy index, EI 	The notion of comparing the radiated energies of seismic events of similar moments can be translated into a practical tool called Energy Index (EI) – the ratio of the radiated energy of a given event (E) to the energy $\bar{E}(M)$ derived from the regional $\log E$ vs $\log M$ relation for a given moment M . Since $\log \bar{E}(M) = c + d \log M$, then $\bar{E}(M) = 10^{c+d \log M}$ where c and d are constant for a given ΔV and Δt . In general d -value increases with the system's stiffness and c , for a given d , increases with stress. A small or moderate event with $EI > 1$ suggests a higher than average shear stress at its location. The opposite applies to the $EI < 1$ case.
Seismic strain, $\varepsilon_s(\Delta V, \Delta t) = \sum M / (2G\Delta V)$ and Seismic strain rate, [s ⁻¹] $\dot{\varepsilon}_s(\Delta V, \Delta t) = \varepsilon_s / \Delta t$	Seismic strain measures strain due to cumulative coseismic deformations within the volume ΔV over the period Δt . Its rate is measured by $\dot{\varepsilon}_s$.
Seismic stress, [Pa] $\sigma_s(\Delta V, \Delta t) = 2G \sum E / \sum M$	Seismic stress measures stress changes due to seismicity.
Seismic stiffness modulus, K_s [Pa] $K_s(\Delta V, \Delta t) = \sigma_s / \varepsilon_s$ $\varepsilon_s = 4G^2 \Delta V \sum E / (\sum M)^2$	Seismic stiffness measures the ability of the system to resist seismic deformation with increasing stress. The stiffer systems limit both the frequency and the magnitude of intermediate and large events but have time-of-day distribution with larger statistical dispersion, thus are less time predictable.
Seismic viscosity, [Pa s] $\eta_s(\Delta V, \Delta t) = \sigma_s / \dot{\varepsilon}_s$	Seismic viscosity characterises the statistical properties of the seismic deformation process. Lower seismic viscosity implies easier flow of seismic inelastic deformation or greater stress transfer due to seismicity.
Seismic relaxation time, [s] $\tau_s(\Delta V, \Delta t) = \eta_s / G$	Seismic relaxation time quantifies the rate of change of seismic stress during seismic deformation processes and it separates the low frequency response from the high frequency response of the system under consideration. It also defines the usefulness of past data and the predictability of the flow of rock. The lower the relaxation time, the shorter the time span of useful past data and the less predictable the process of seismic deformation.

Parameter, relevant formula	Description
Seismic Deborah number $De_s(\Delta V, \Delta t) = \tau_s / \text{flowtime}$ where <i>flowtime</i> is a design parameter not necessarily equal to Δt .	Seismic Deborah number measures the ratio of elastic to viscous forces in the process of seismic deformation and has successfully been used as a criterion to delineate volumes of rockmass softened by seismic activity (soft clusters). The lower the Deborah number the less stable is the process or the structure over the design <i>flowtime</i> - what may be stable over a short period of time (large De_s) may not be stable over a longer time (lower De_s).
Seismic diffusivity, [m²/s] $D_s(\Delta V, \Delta t) = (\Delta V)^{2/3} / \tau_s$, or in a statistical sense $d_s = (\dot{X})^2 / \bar{t}$.	Seismic diffusivity can be used to quantify the magnitude, direction, velocity and acceleration of the migration of seismic activity and associated transfer of stresses in space and time. There is an inverse relationship between the diffusivity D_s and the friction parameters.
Seismic Schmidt number $Sc_{sd}(\Delta V, \Delta t) = \eta_s / (\rho D_s)$ or $Sc_{sd} = \eta_s / (\rho d_s)$ where ρ is rock density.	Seismic Schmidt number measures the degree of complexity in space and time (the degree of turbulence) of the seismic flow of rock. Note that seismic Schmidt number Sc_{sd} encompasses all four independent parameters describing seismicity: $\bar{t}, \bar{X}, \Sigma M, \Sigma E$.
Time to failure, ($t_f - t$) $d\Omega / dt = k(t_f - t)^m$ Ω - measurable quantity t - current time t_f - time of failure k, m - constants 	This concept describes the behaviour of materials in the terminal stages of failure. It views instability as a critical point, then precursors should follow characteristic power laws in which the rate of strain or other observable, measurable, quantity Ω is proportional to the inverse power of remaining time to failure. Observed oscillations in Ω of an increasing frequency as the failure approaches are part of the solution to time-to-failure equation with a complex exponent, where the imaginary part relates to discrete scale transformation and introduces log-periodic oscillations decorating the asymptotic power law. The observations Ω can be a combination of different seismic parameters that would exhibit power law type increase before failure. For well behaved data sets the time at failure t_f can be estimated from the times of three successive maxima (t_1, t_2, t_3) of the observed process $t_f = (t_2^2 - t_1 t_3) / (2t_2 - t_1 - t_3)$ Note that, in theory, $t_3 - t_2 < t_2 - t_1$

Parameter, relevant formula	Description
Seismic moments, volume mined and relative stress 	If a volume of rock, V_m , is mined out at time t_0 and if the altered stress and strain field can readjust to an equilibrium state through seismic movements only, the sum of seismic moments released within a given period of time would be proportional to the excavation closure and in the long term at $t = t_f$, $\sum_{t_0}^{\infty} M = GV_m$ where M is the scalar seismic moment. The relative stress level at the time, t , in a given volume of rock ΔV surrounding the excavation, can be calculated from the difference between GV_m and the cumulative moments released to date: $\sigma_r(t) = (GV_m - \sum_{t_0}^t M) / \Delta V$
Seismic moments and volume of elastic convergence $\Sigma M = \gamma GV_e$	The amount of strain energy stored when mining in elastic rock is directly proportional to the volume of elastic convergence, V_e . It has been found that the total amount of seismic moment resulting from mining within a large area and time period is related to the change in elastic convergence V_e . The proportional constant gamma, γ , has been found to vary between about 0.03 and 1.0. There is some evidence that γ is a function of the geotechnical area being mined.

Appendix 2 – Cumulative event rate charts

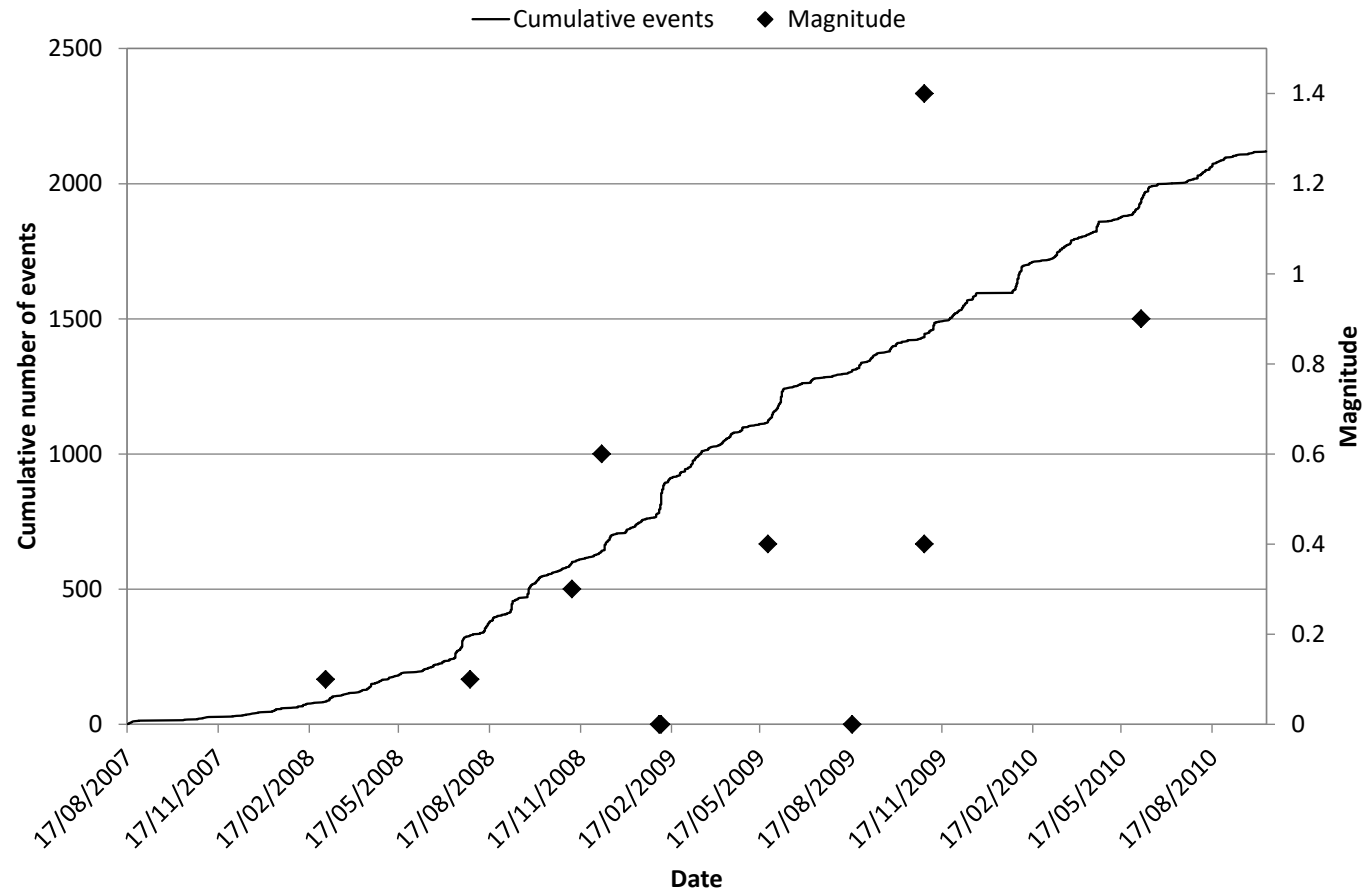


Figure A2 1: Cumulative event chart for the A1 Shear.

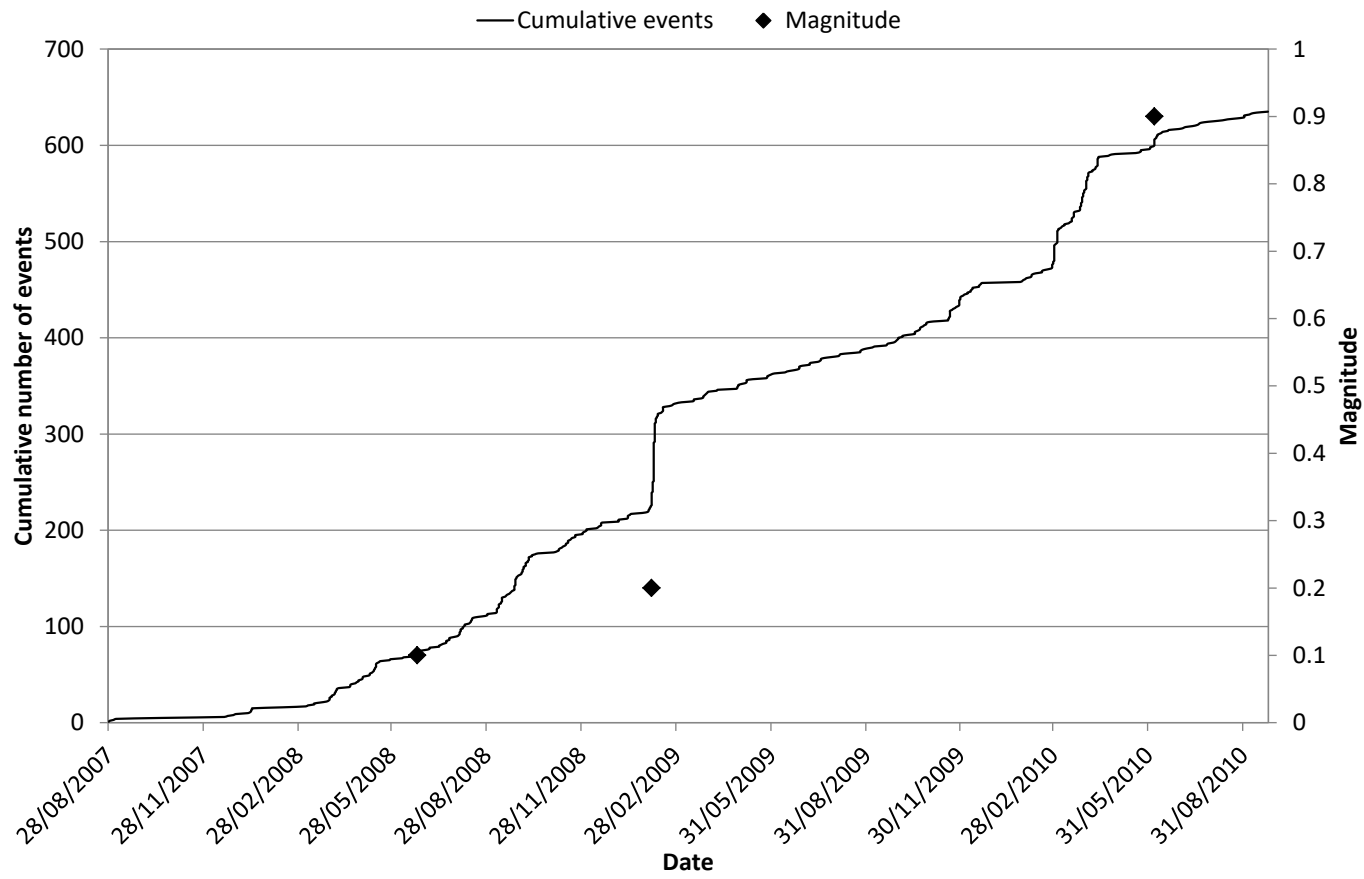


Figure A2 2: Cumulative event chart for the North Dyke.

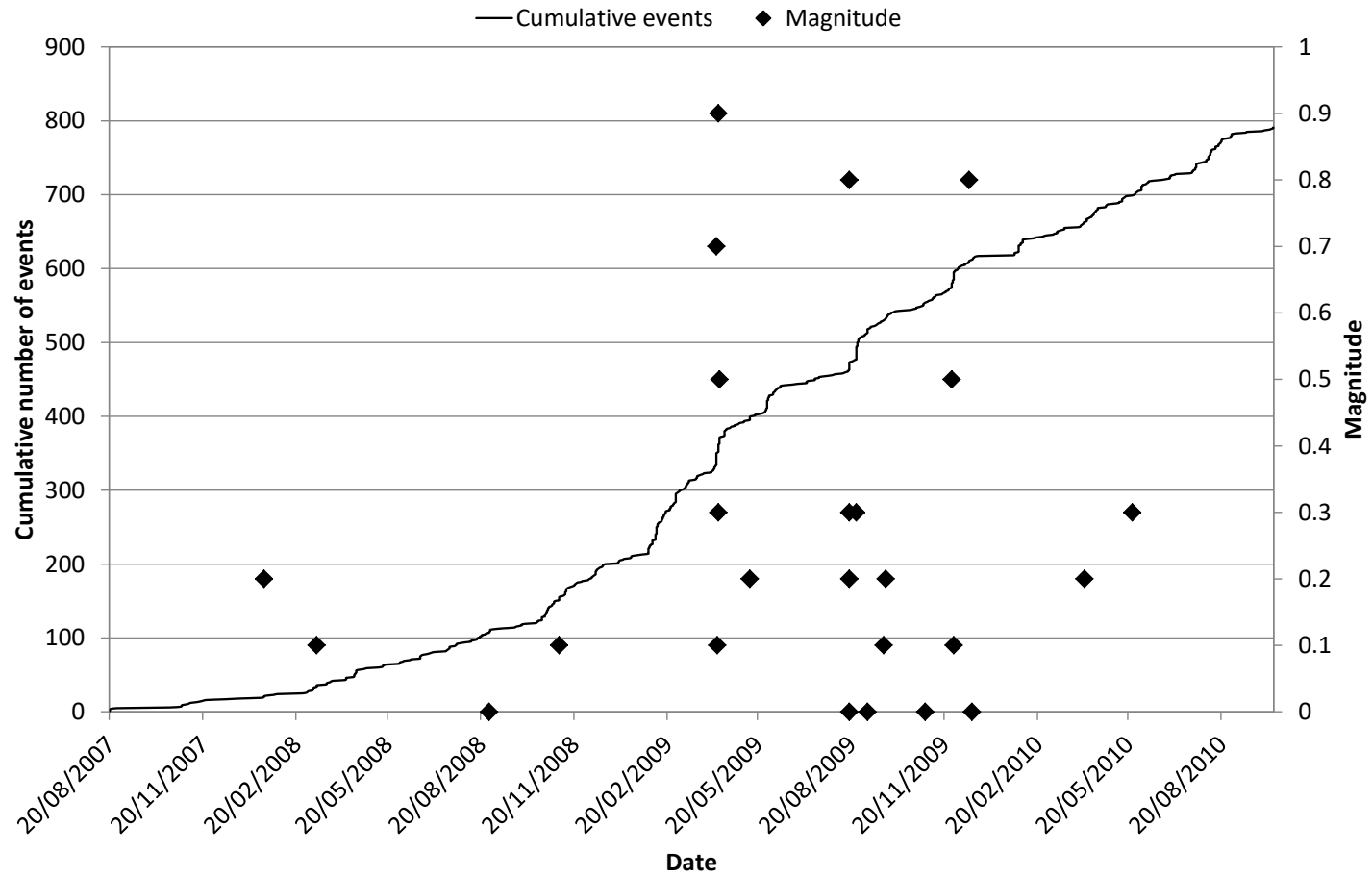


Figure A2 3: Cumulative event chart for the Mini Dyke.

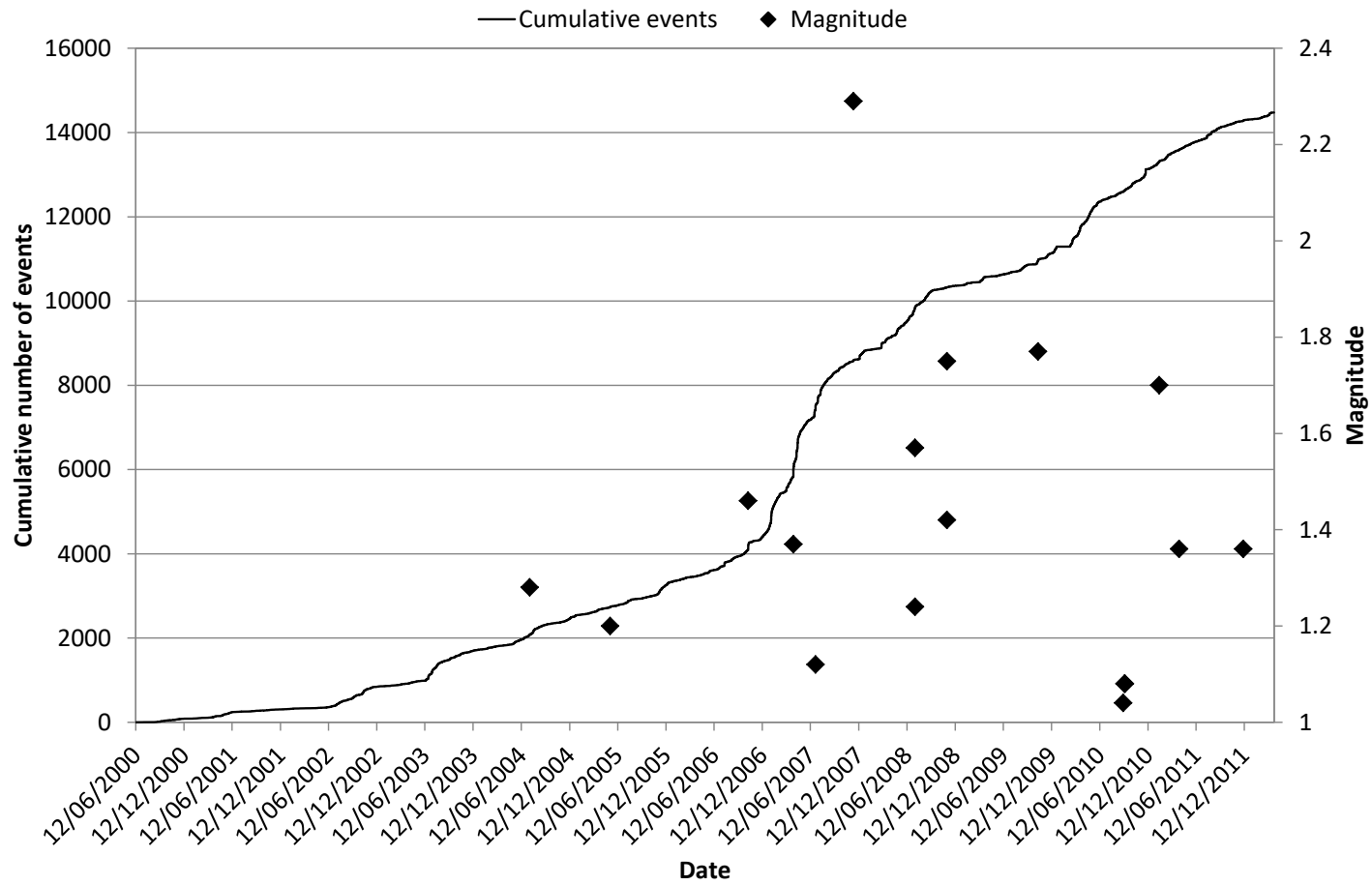


Figure A2 4: Cumulative event chart for Fitzroy Fault.

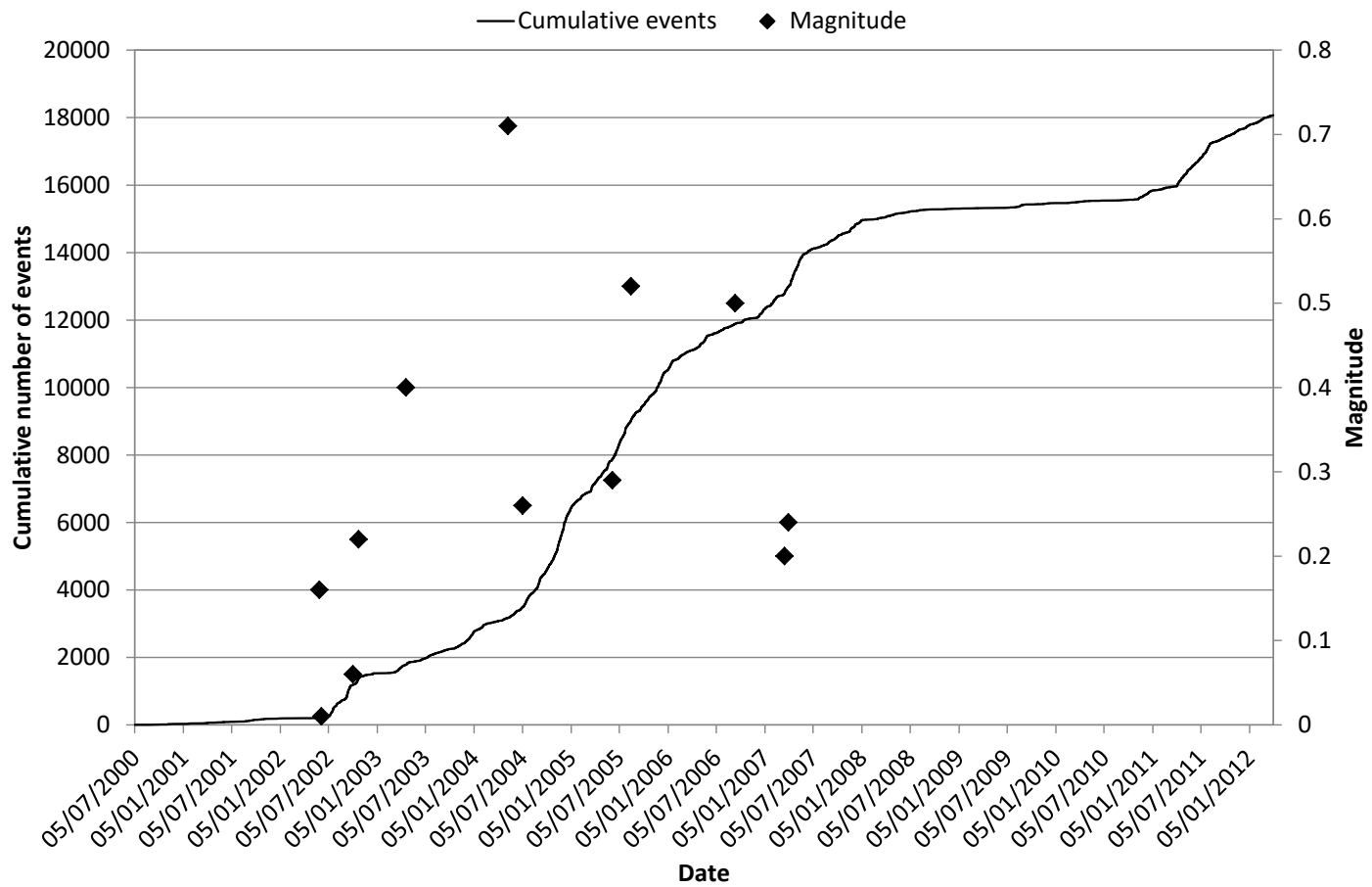


Figure A2 5: Cumulative event chart for North East Faults Group 1.

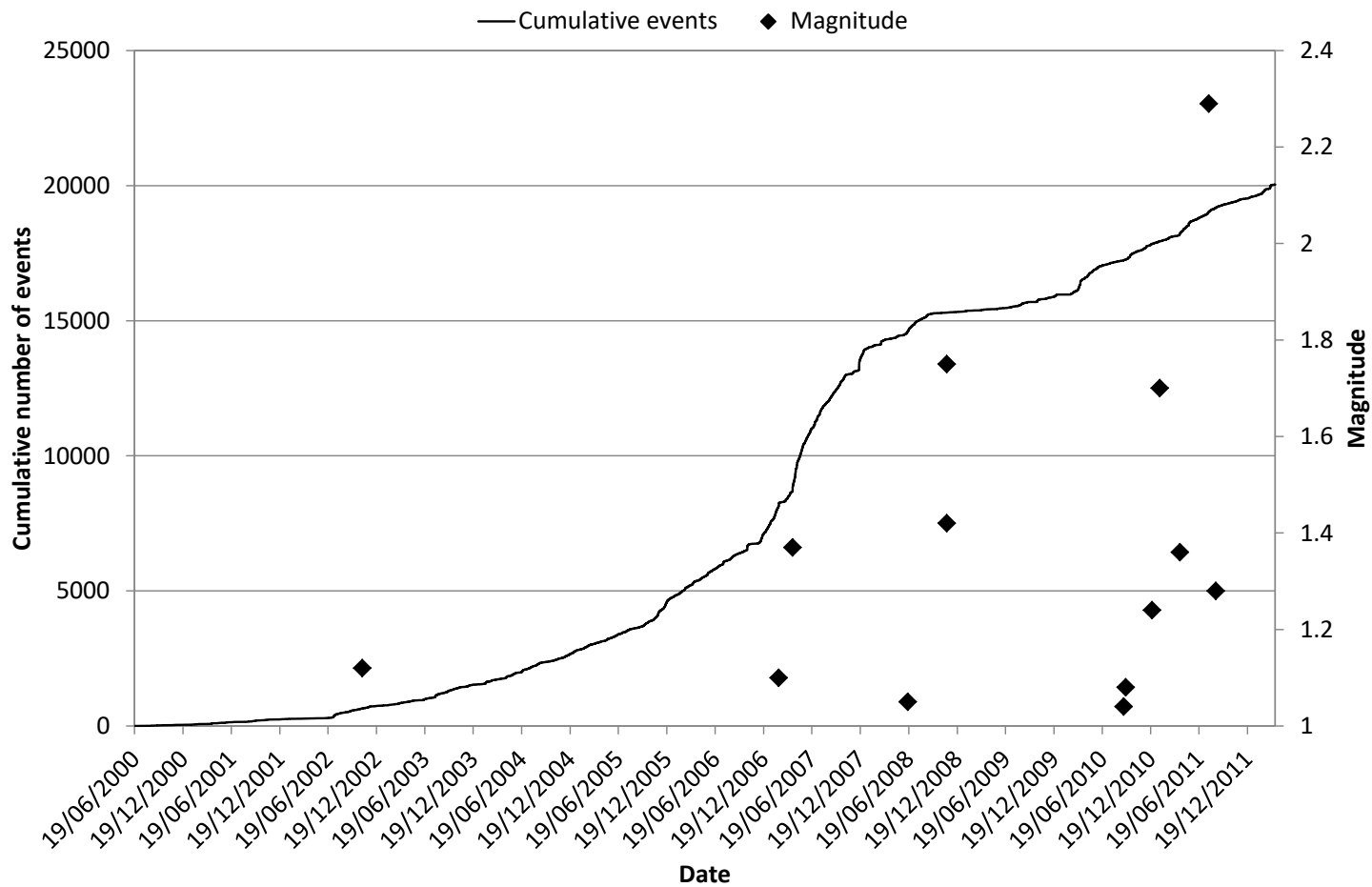


Figure A2 6: Cumulative event chart for North East Faults Group 2.

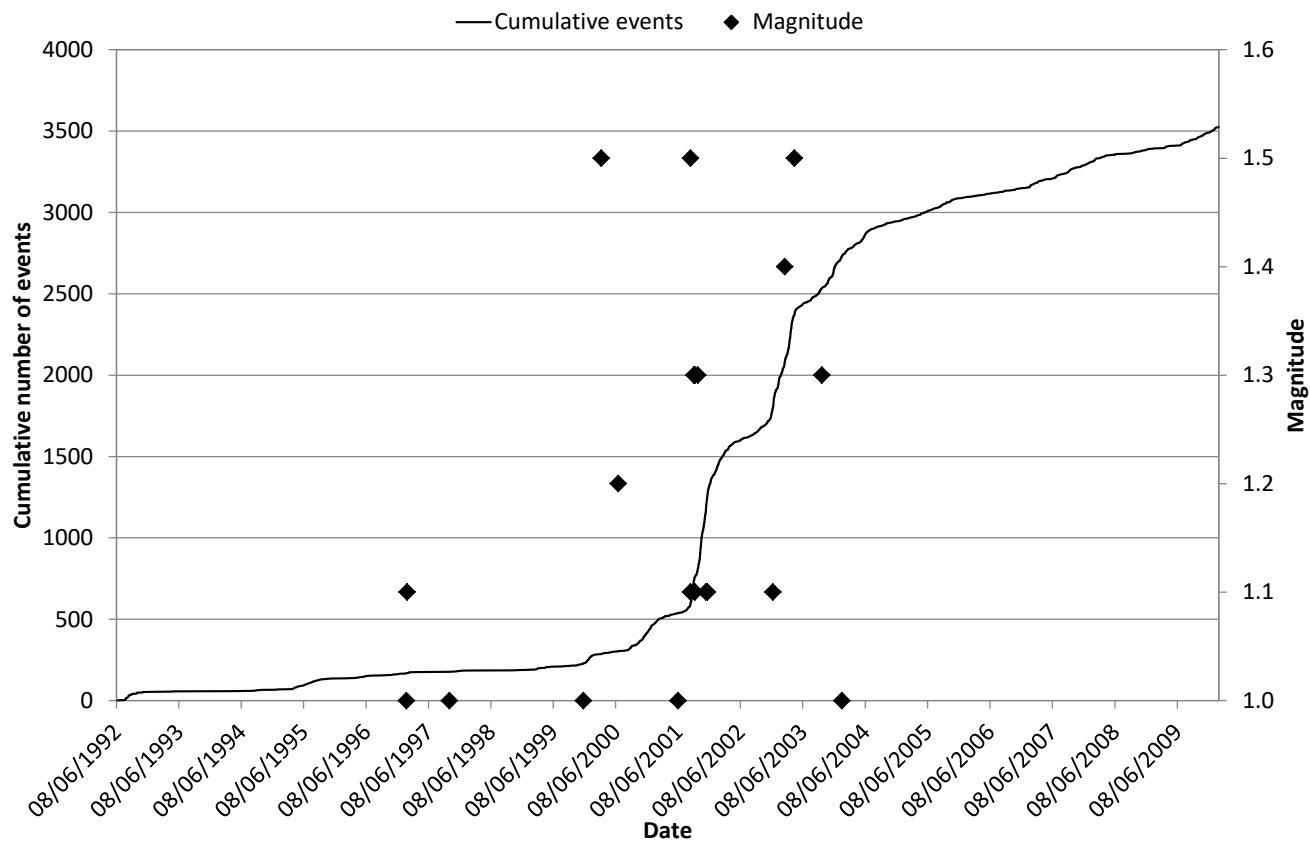


Figure A2 7: Cumulative event chart for FaultP_1

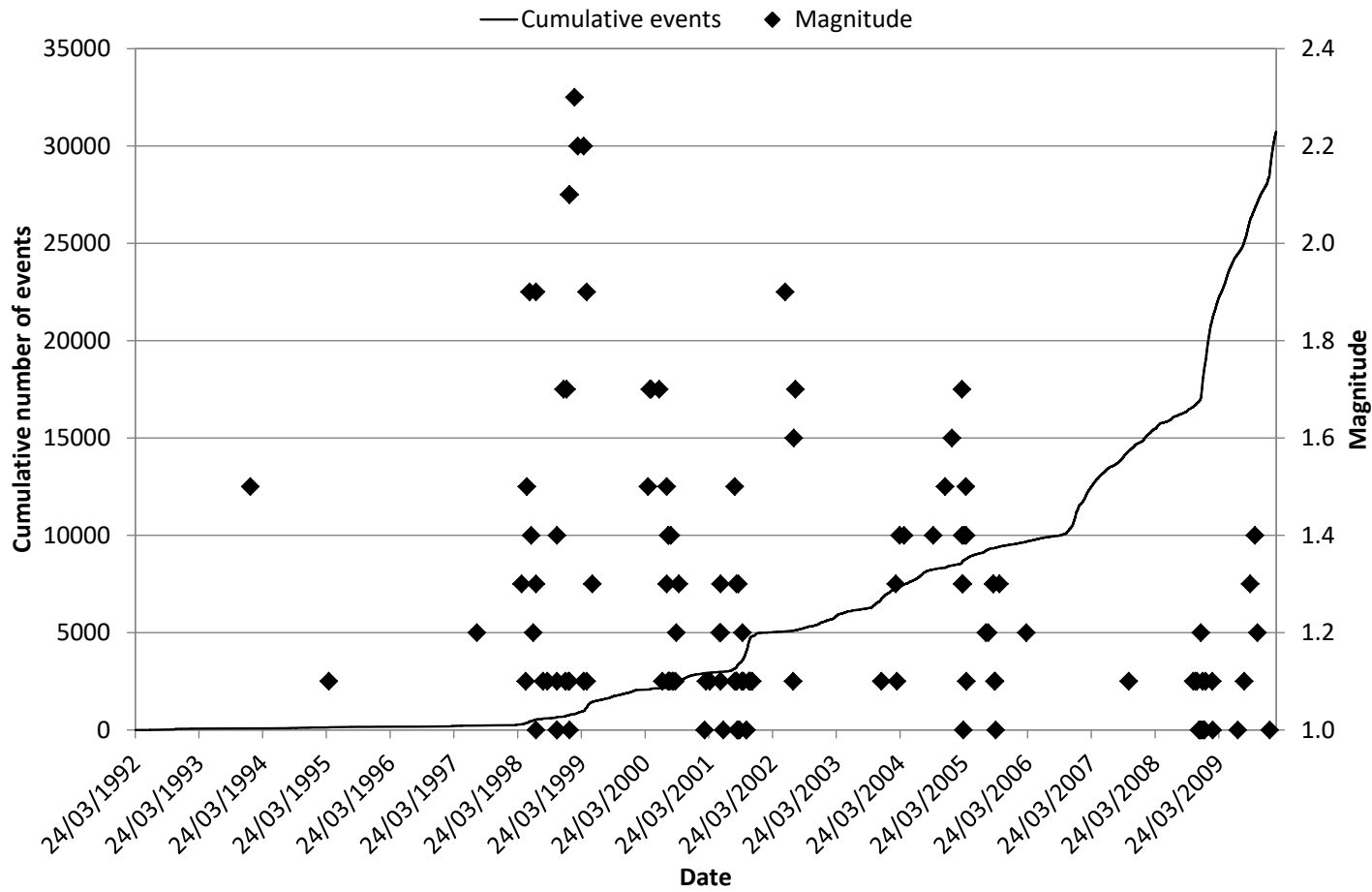


Figure A2 8: Cumulative event chart for Fault B_C.

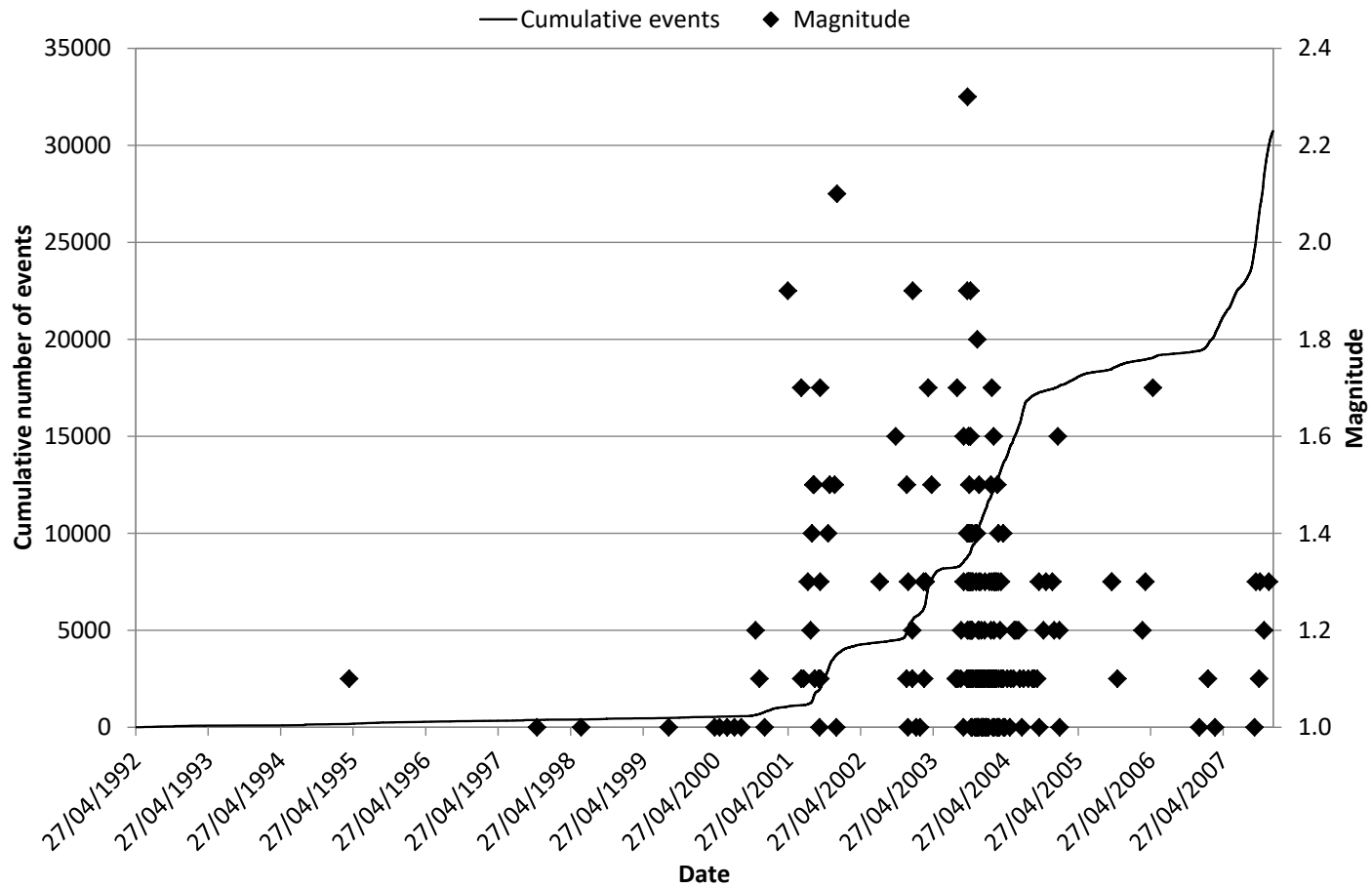


Figure A2 9: Cumulative event chart for the FW Dyke.

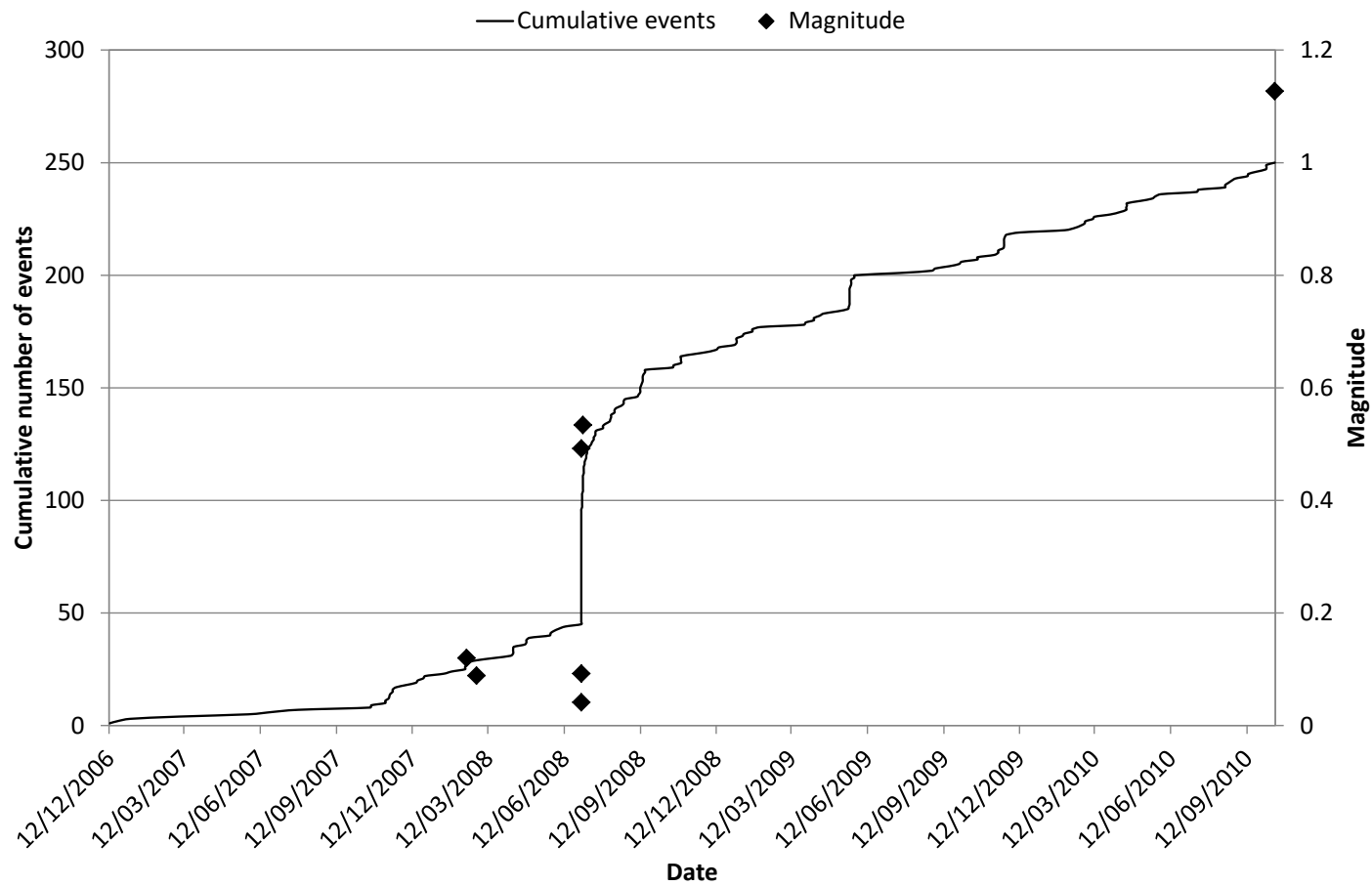


Figure A2 10: Cumulative event chart for Maritana Fault.

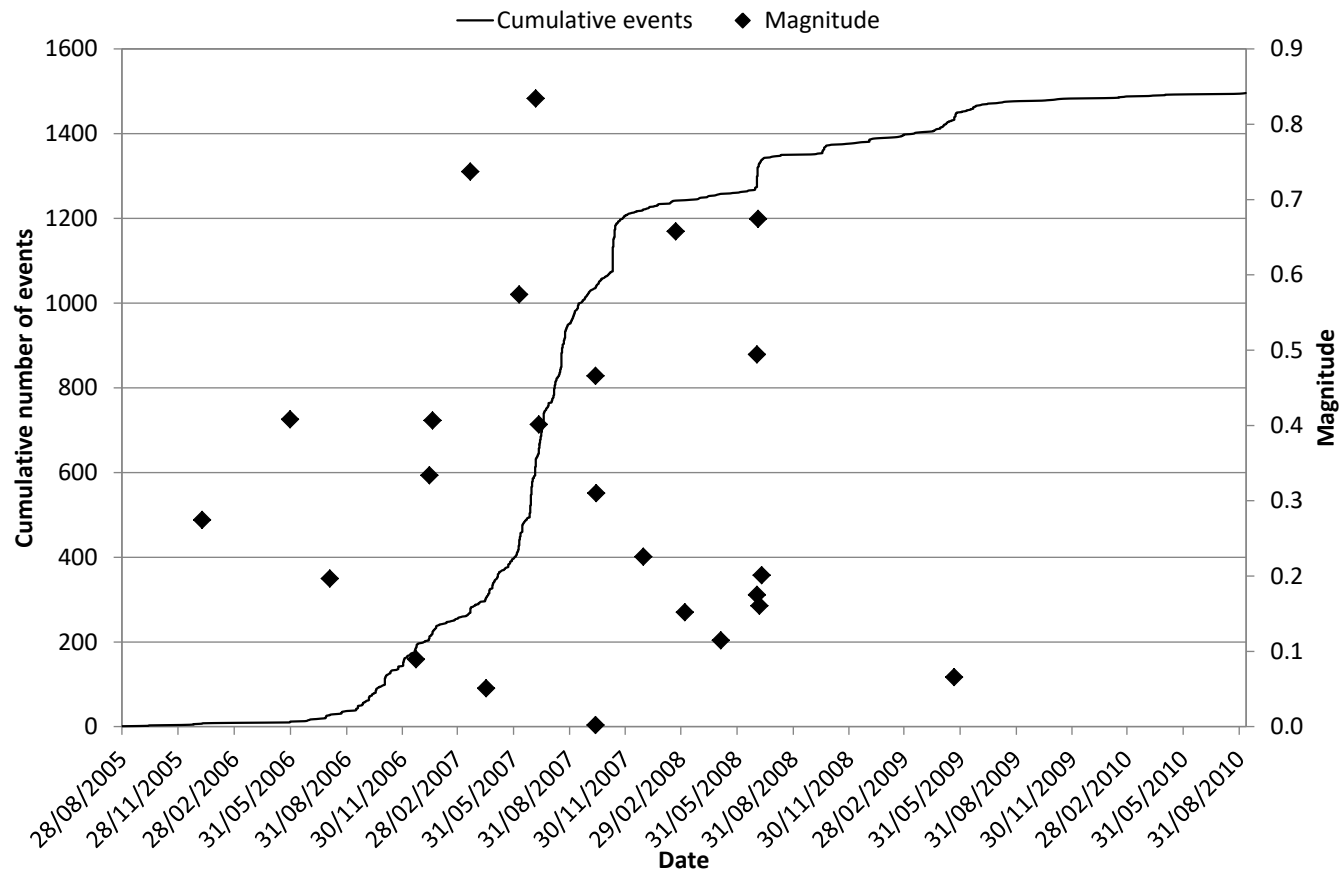


Figure A2 11: Cumulative event chart for Reward Fault.

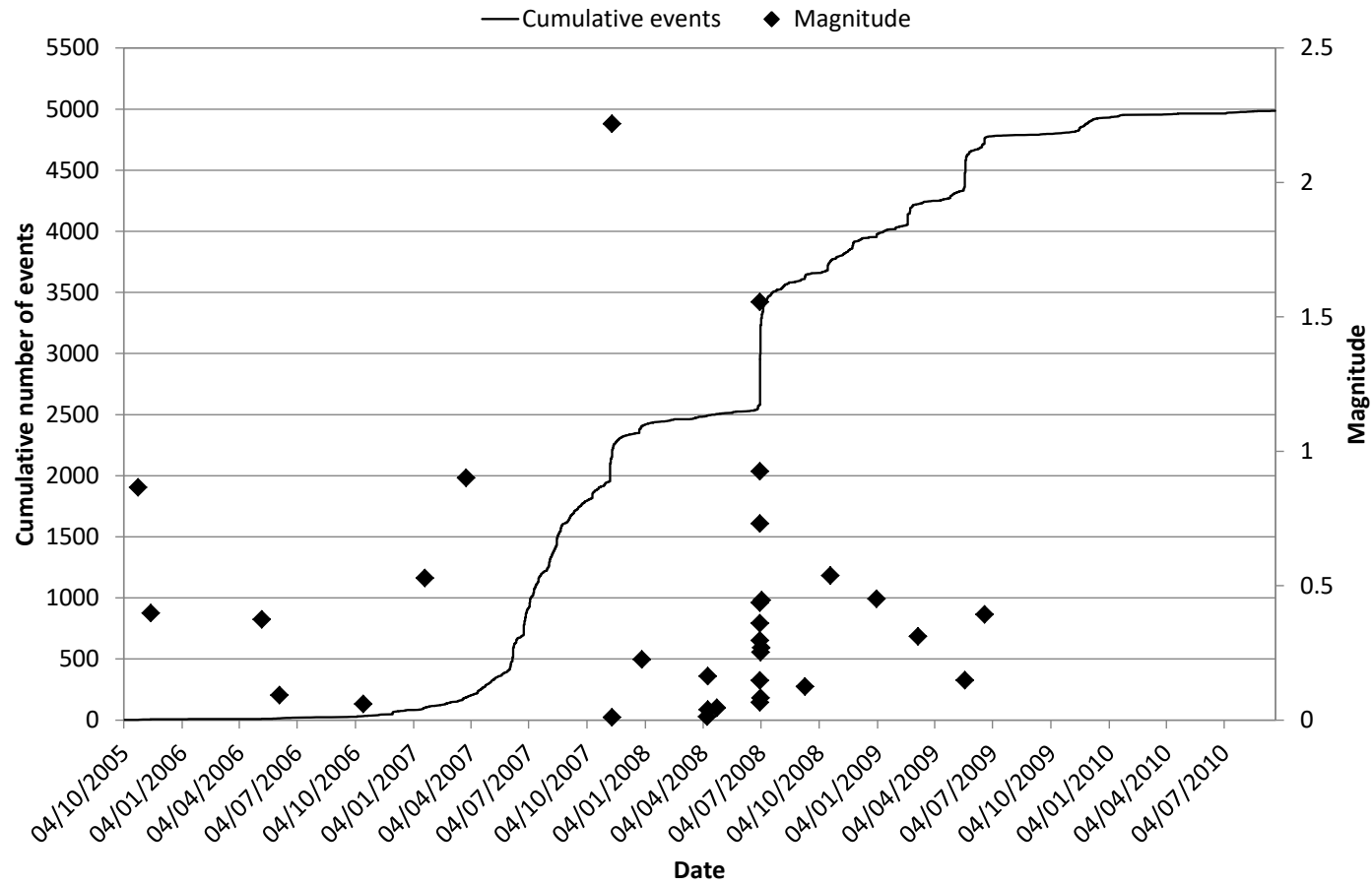


Figure A2 12: Cumulative event chart for Flanagan Fault.

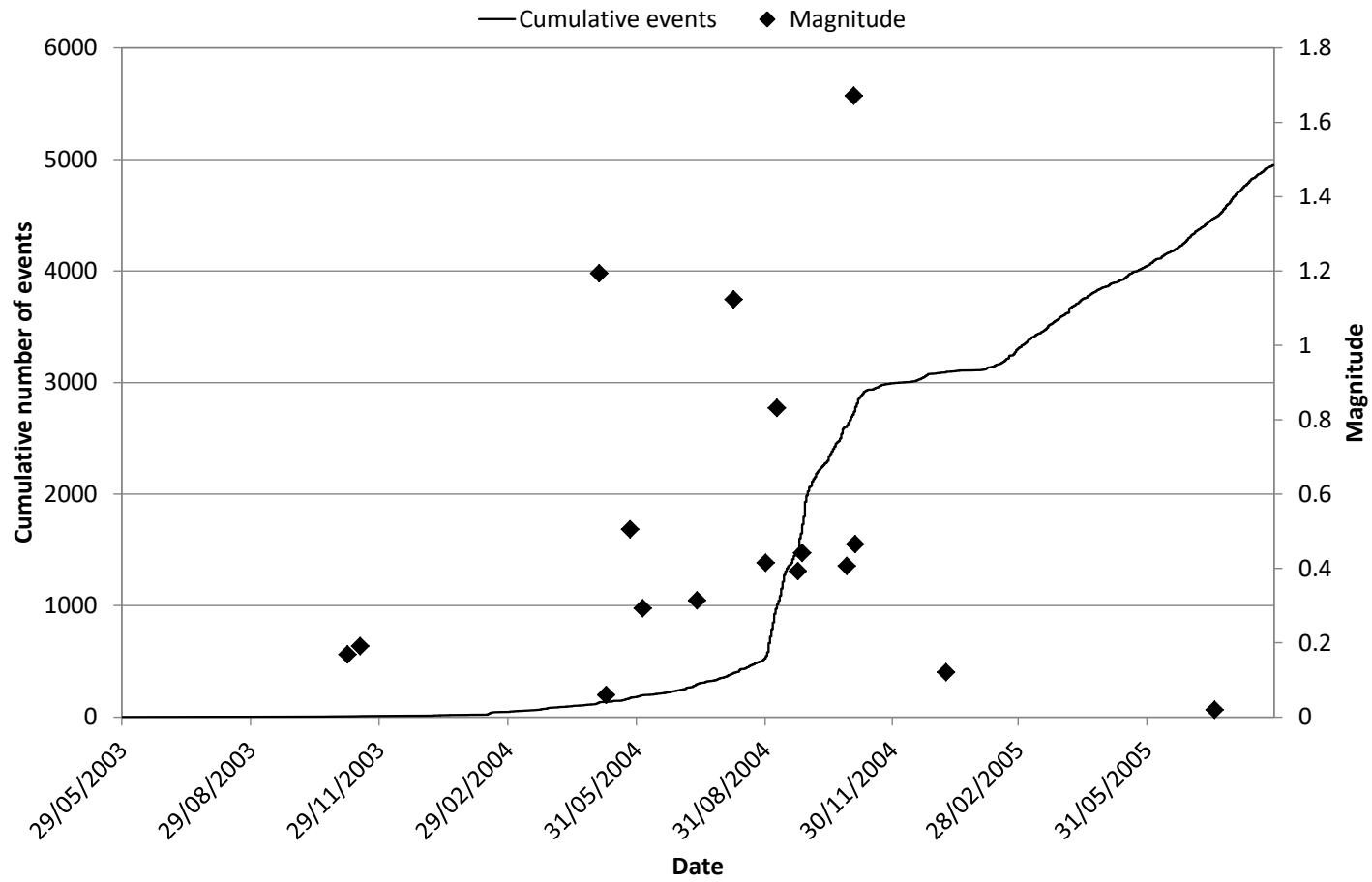


Figure A2 13: Cumulative event chart for Feral Fault.

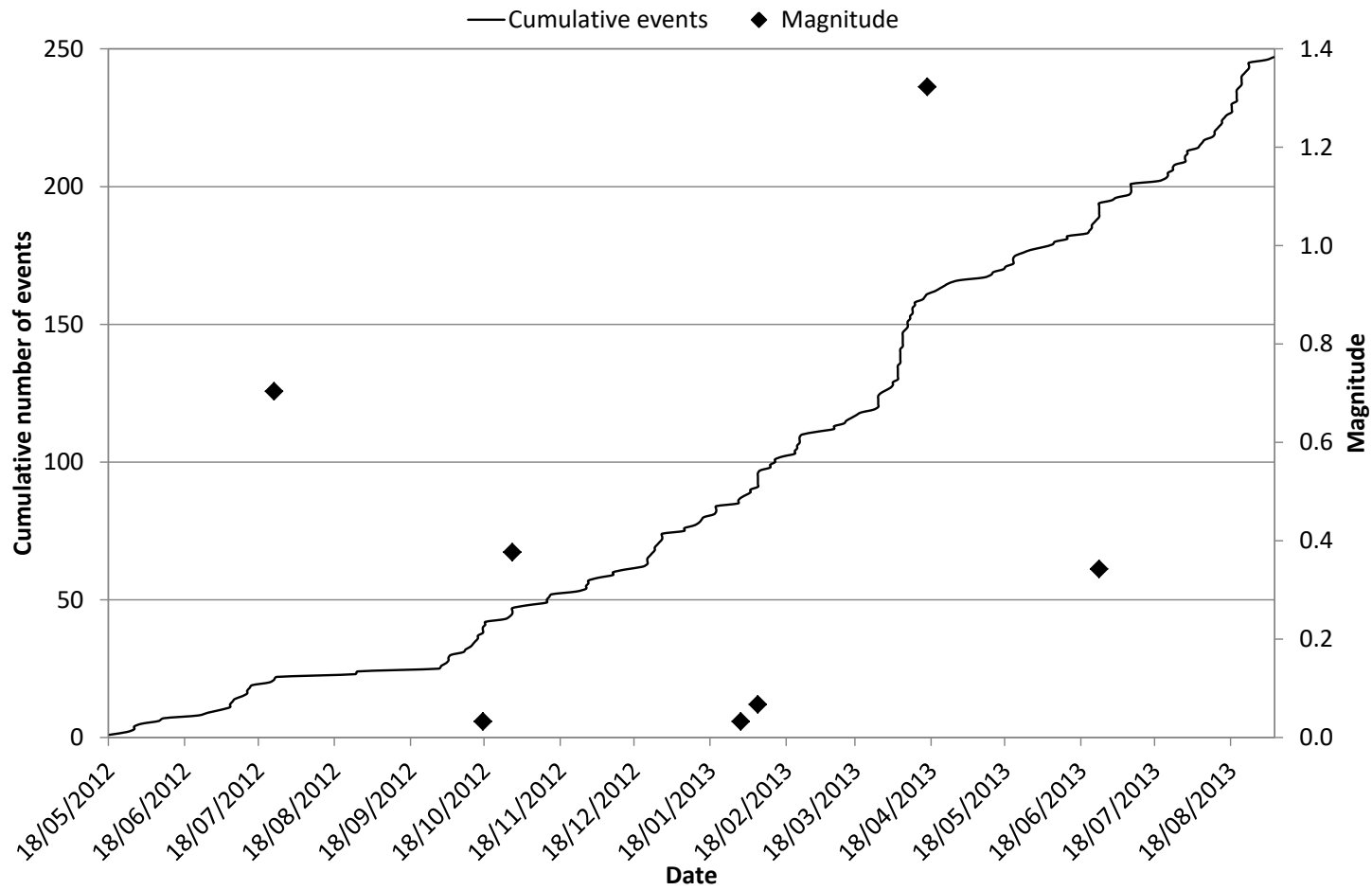


Figure A2 14: Cumulative event chart for Great Lyell Fault.

Appendix 3 – Time difference charts

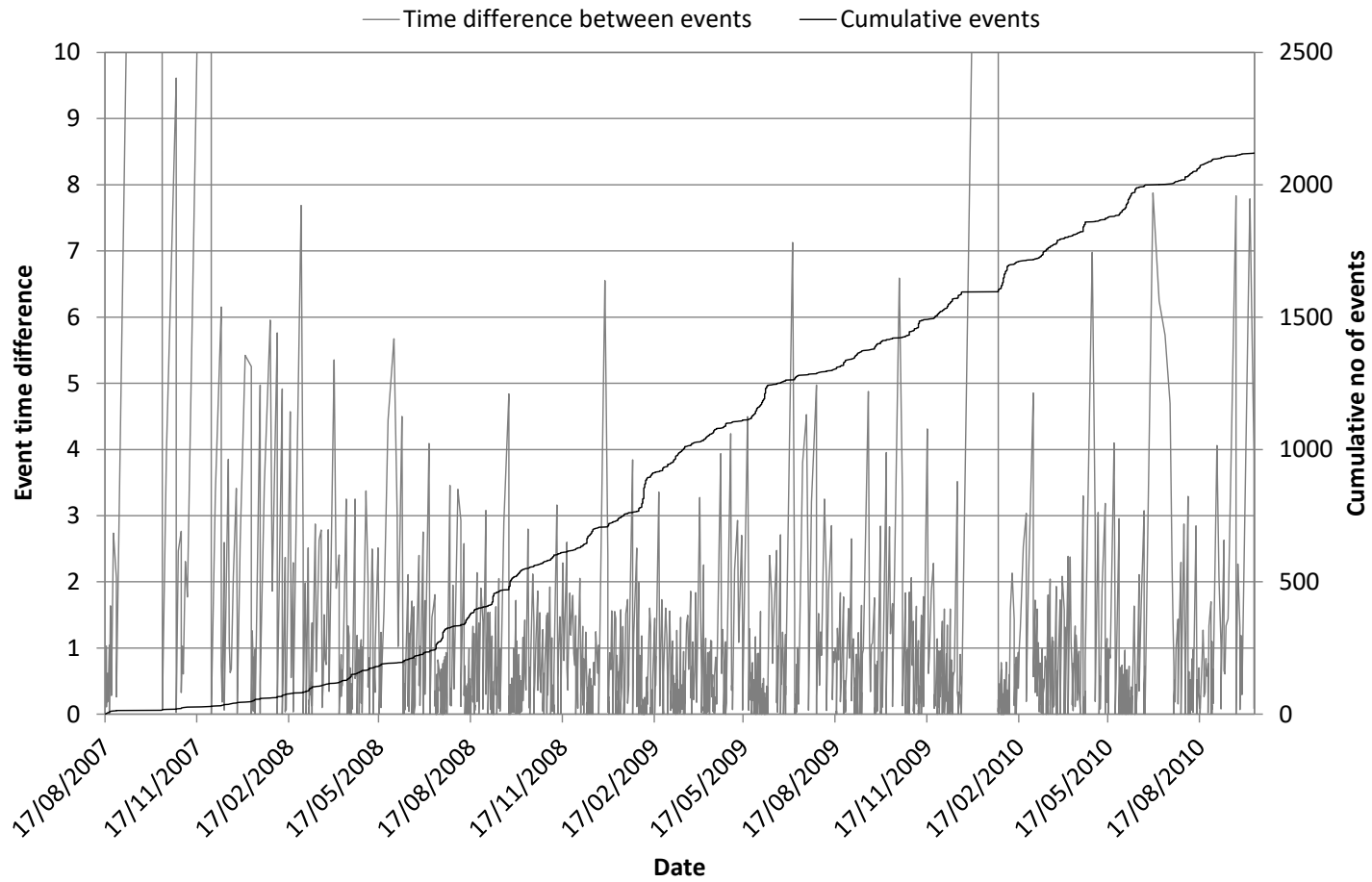


Figure A3 1: Time difference chart for the A1 Shear.

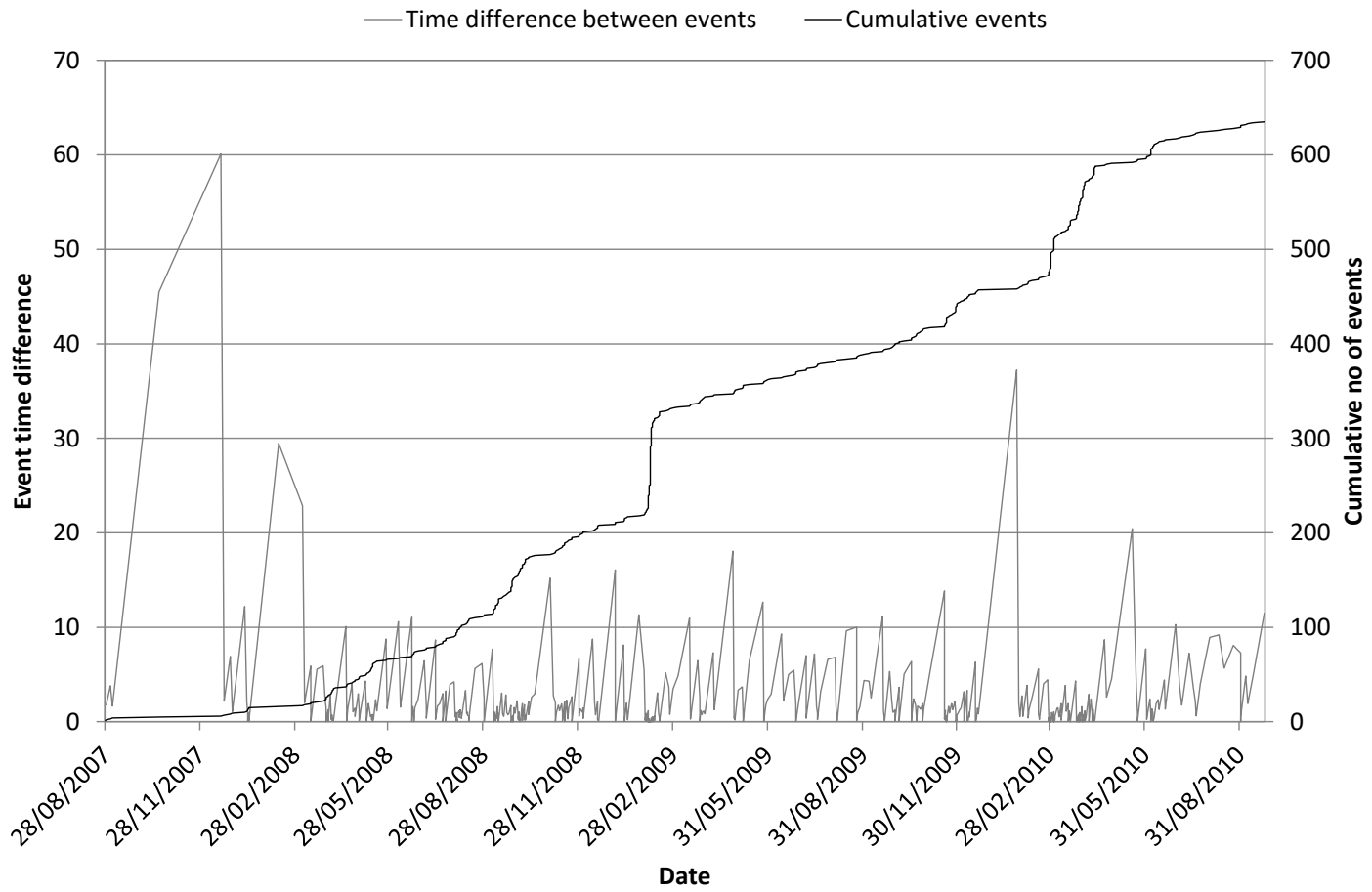


Figure A3 2: Time difference chart for the North Dyke.

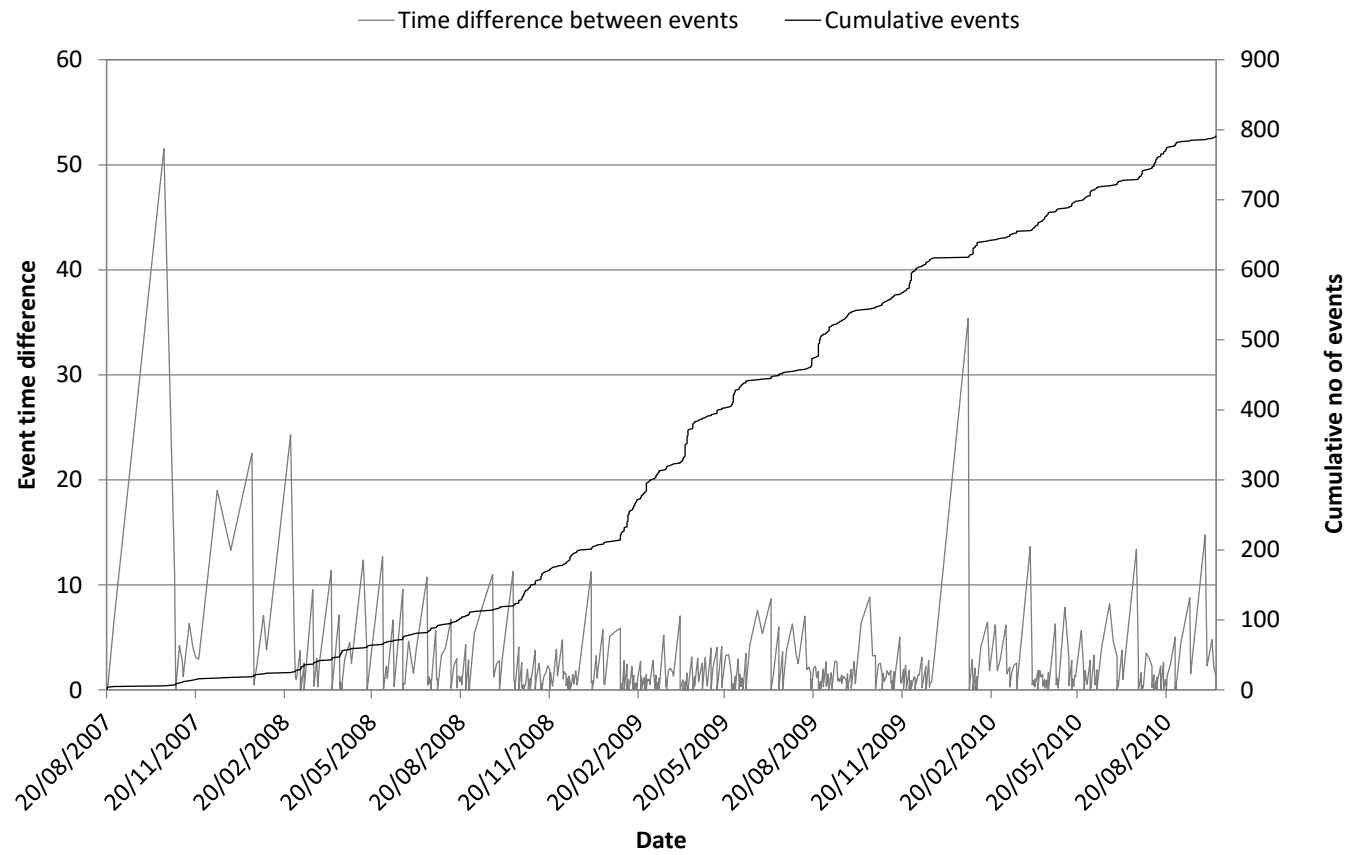


Figure A3 3: Time difference chart for the Mini Dyke.

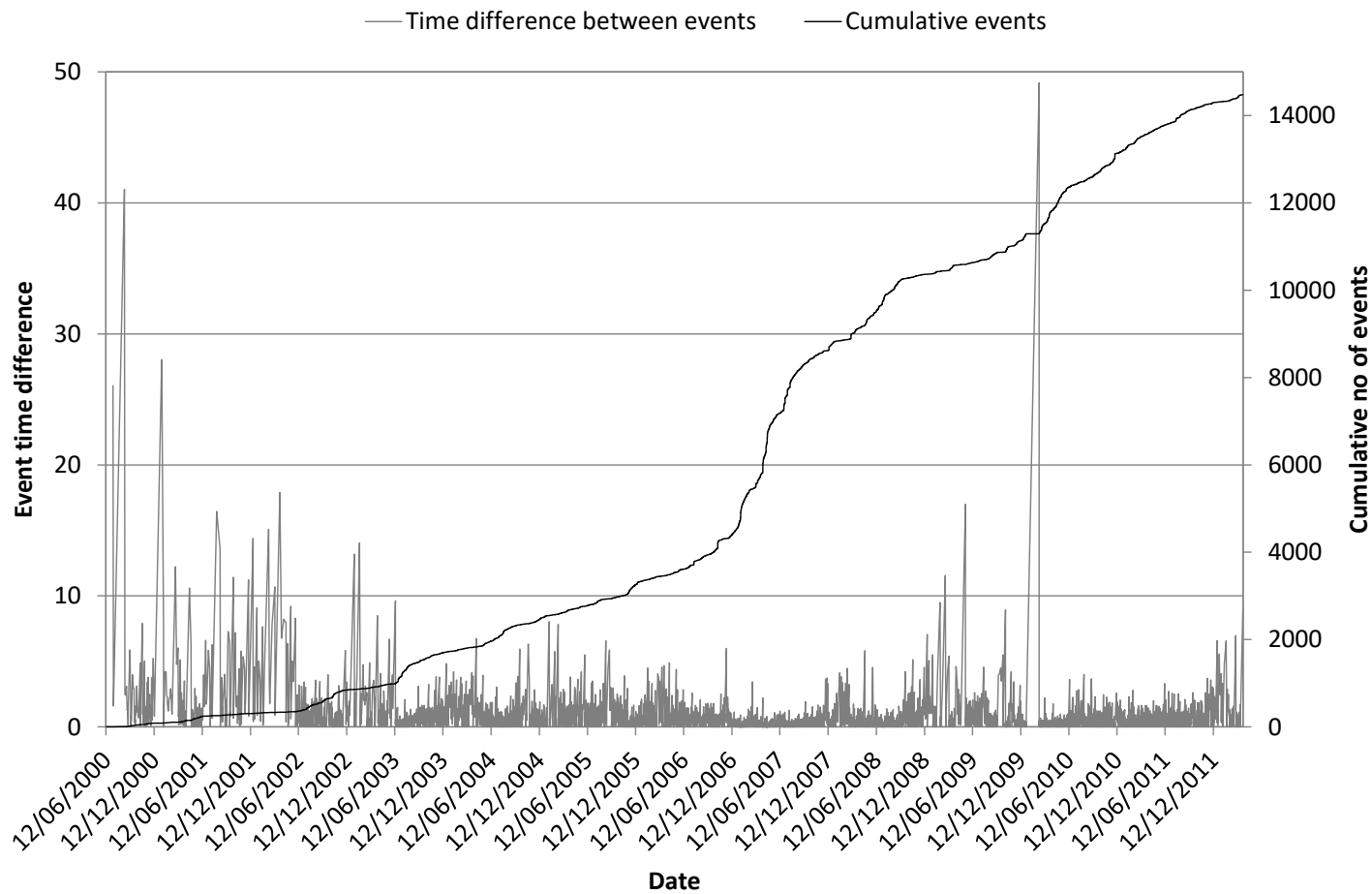


Figure A3 4: Time difference chart for Fitzroy Fault.

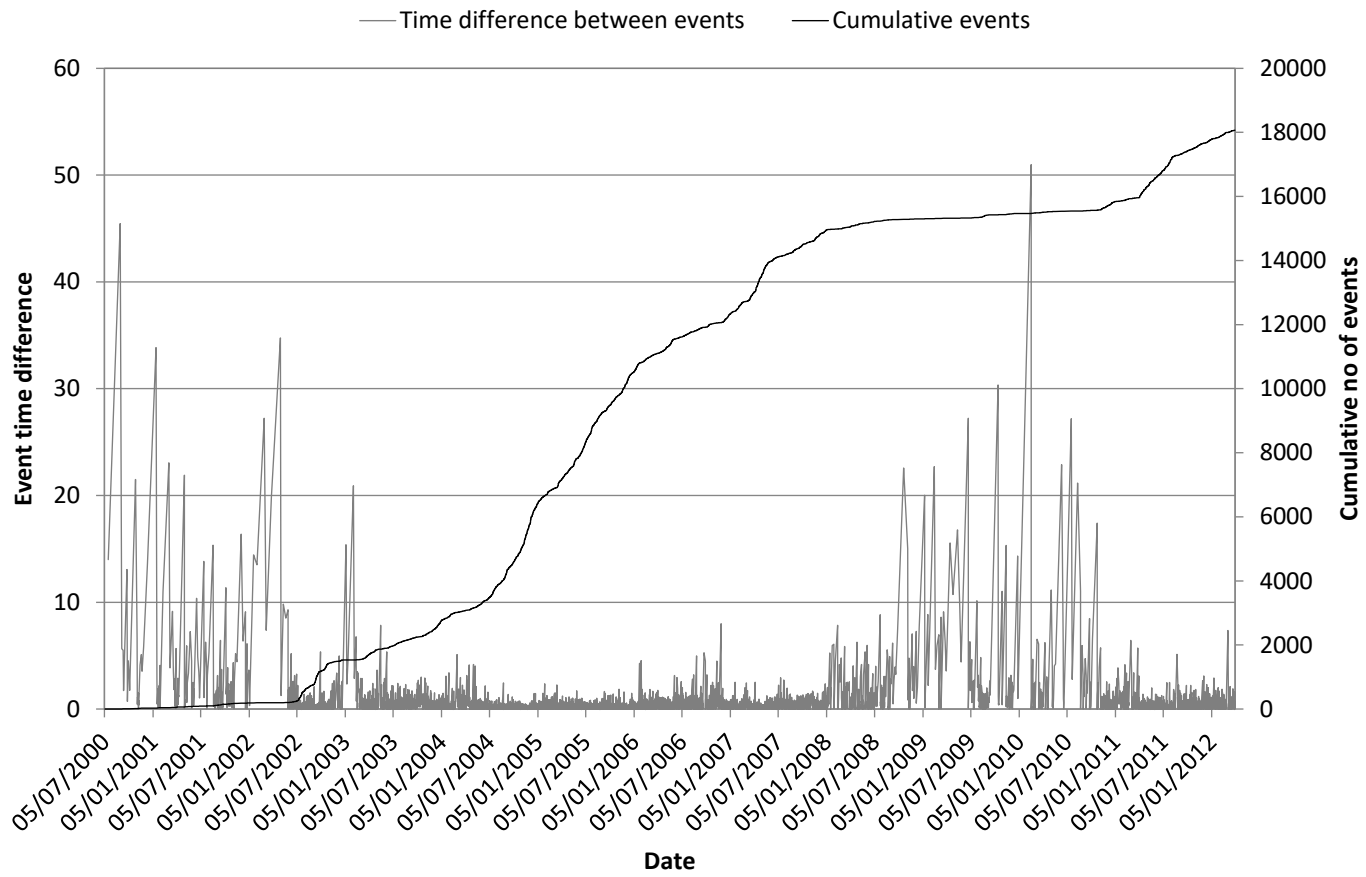


Figure A3 5: Time difference chart for North East Faults Group 1.

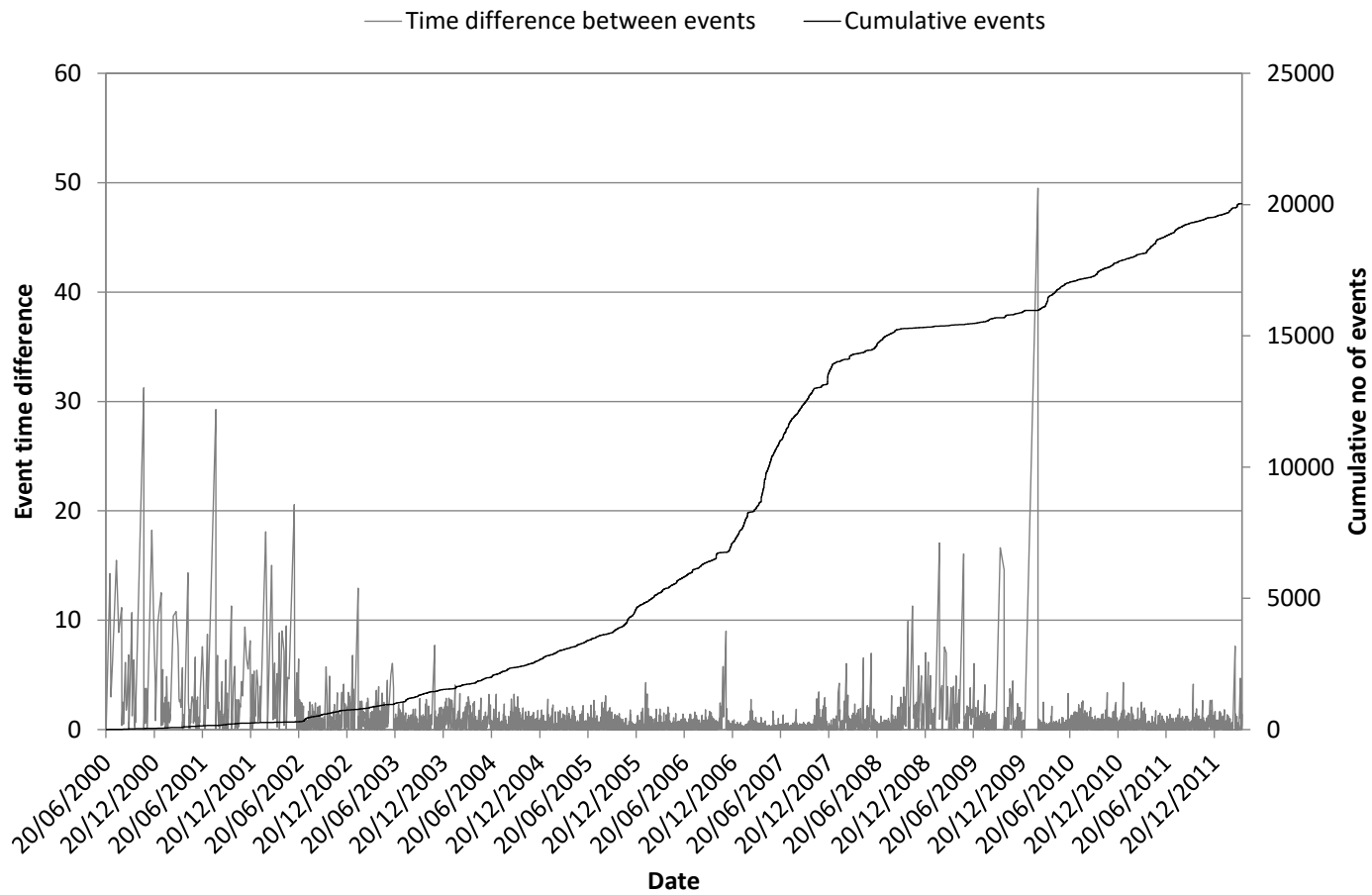


Figure A3 6: Time difference chart for North East Faults Group 2.

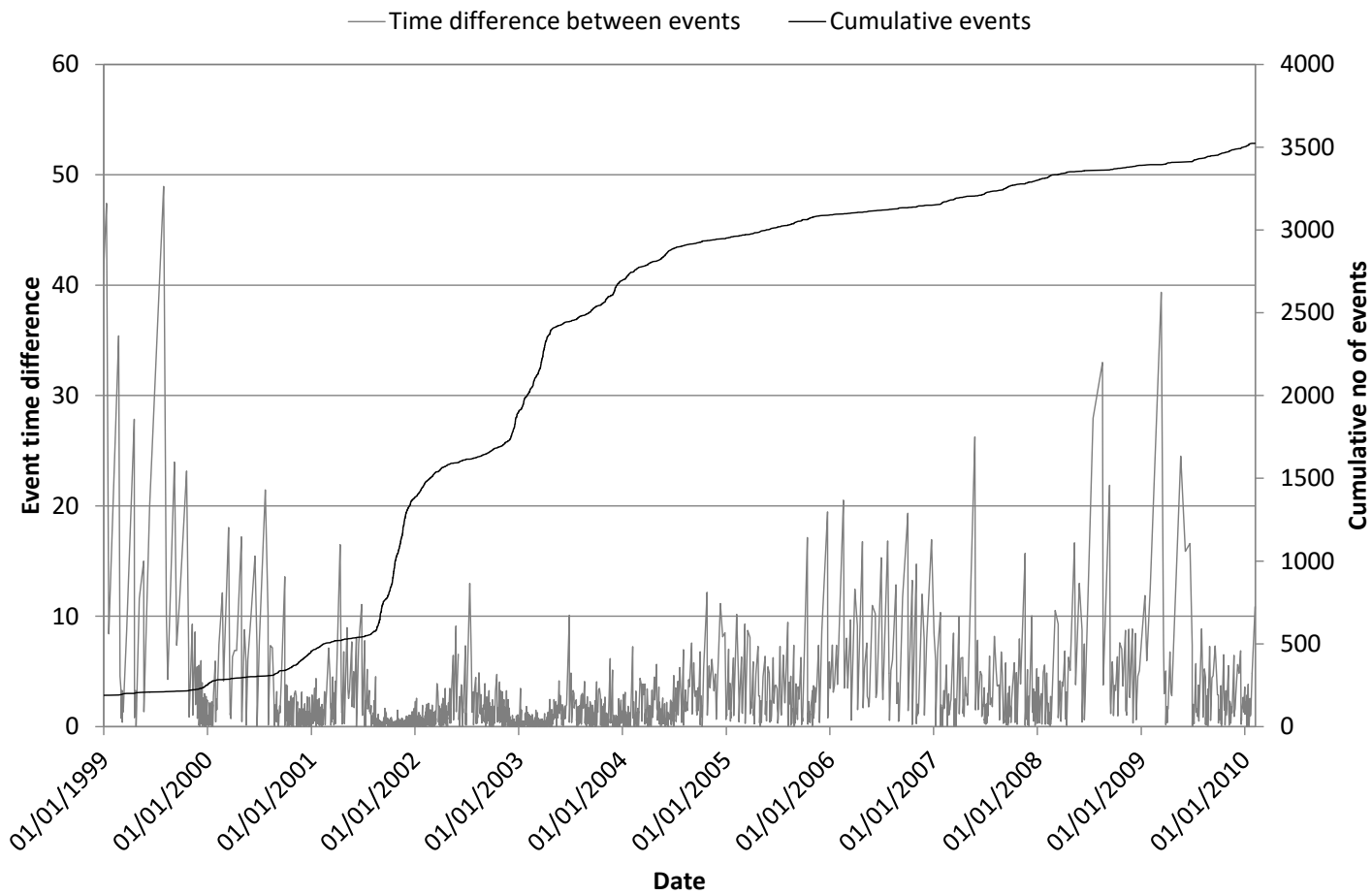


Figure A3 7: Time difference chart for FaultP_1

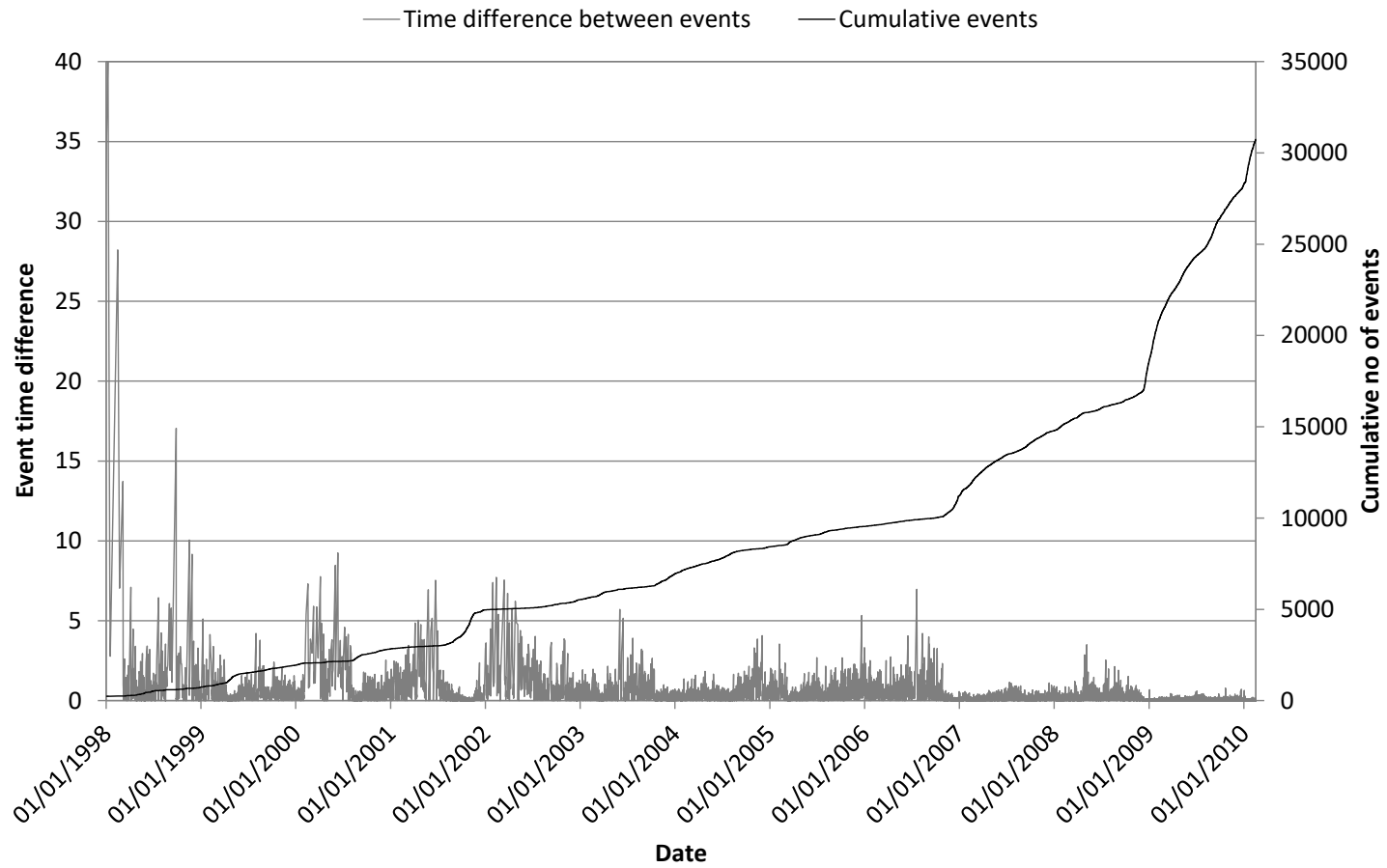


Figure A3 8: Time difference chart for Fault B_C.

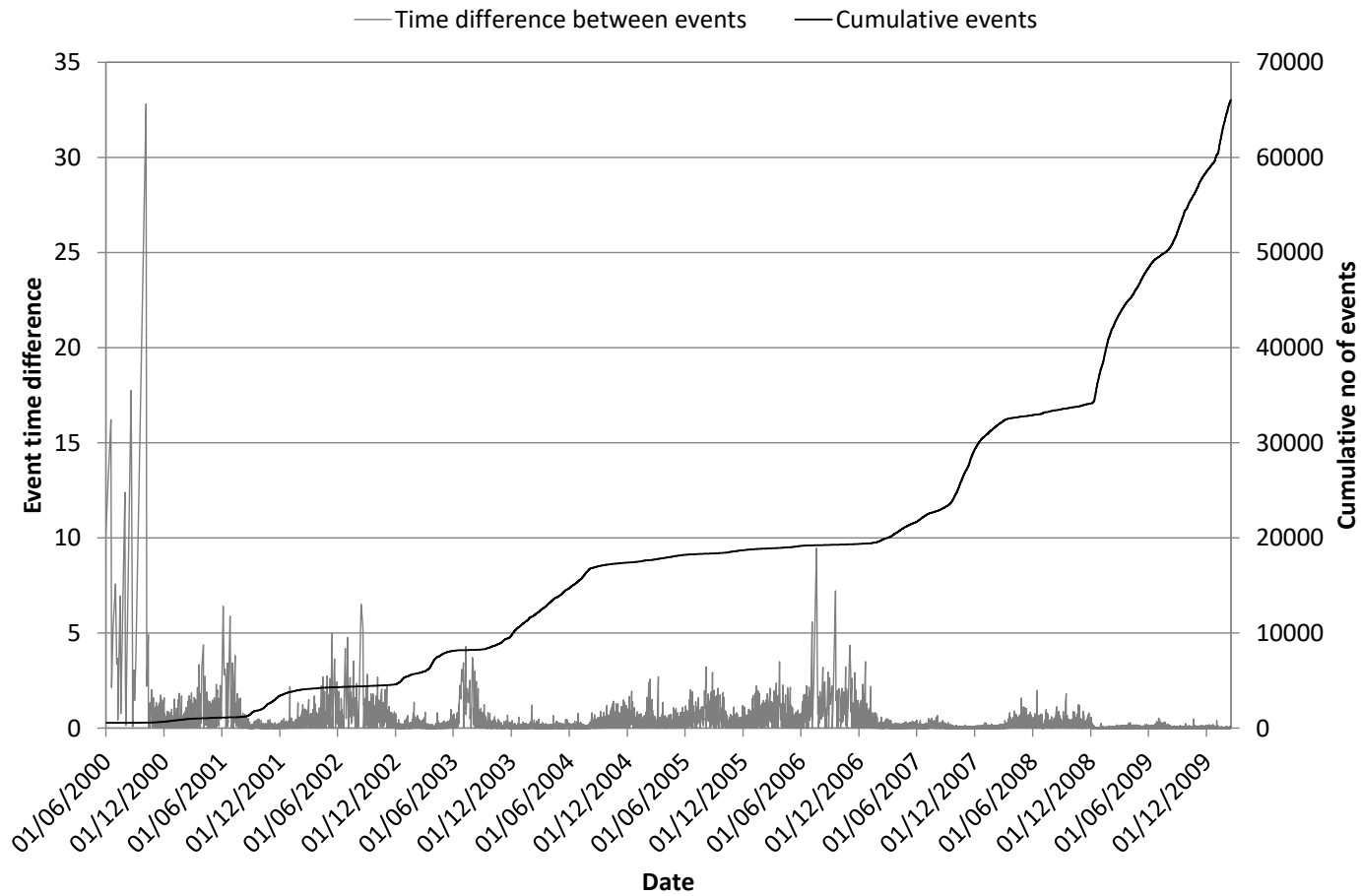


Figure A3 9: Time difference chart for the FW Dyke.

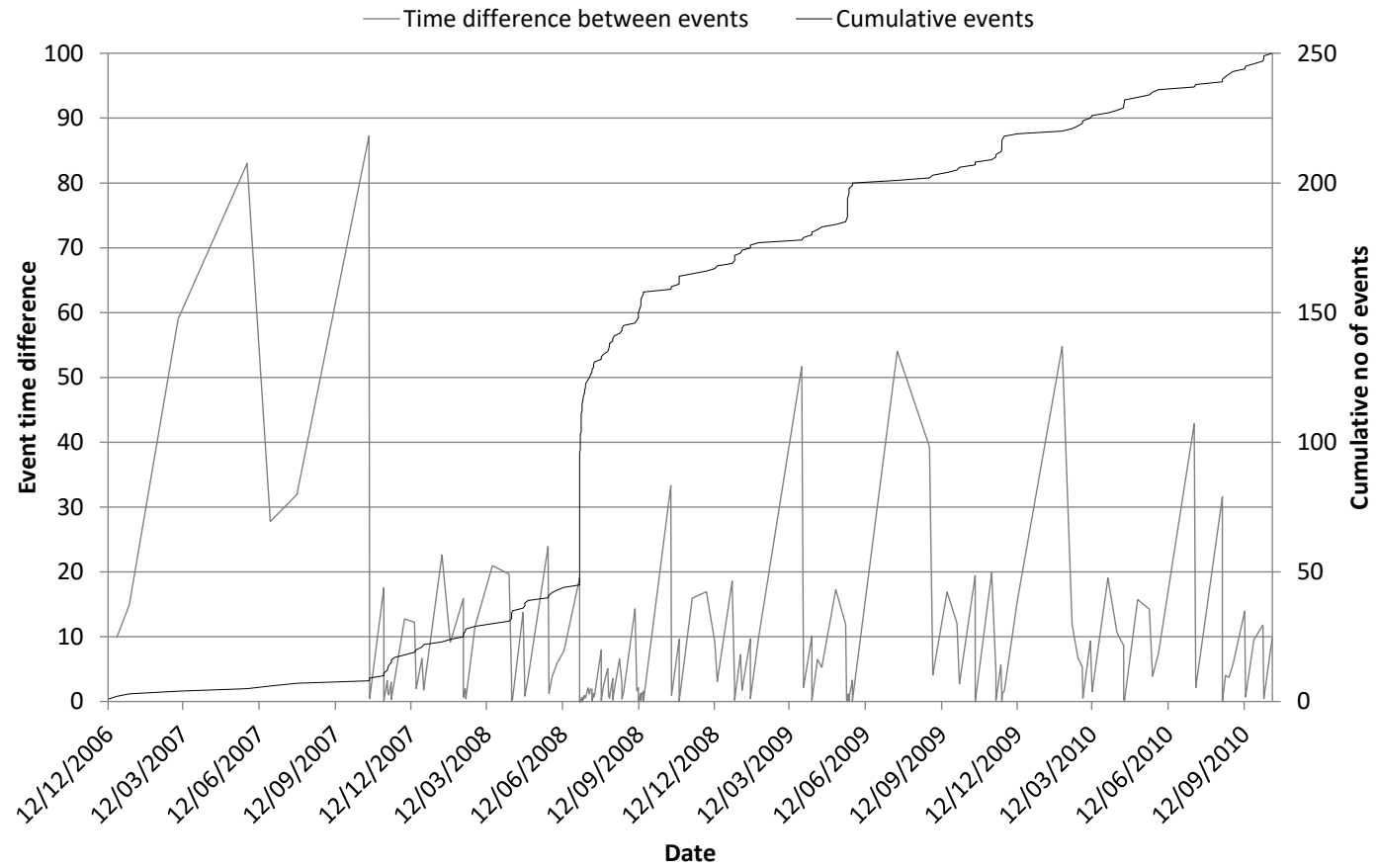


Figure A3 10: Time difference chart for Maritana Fault.

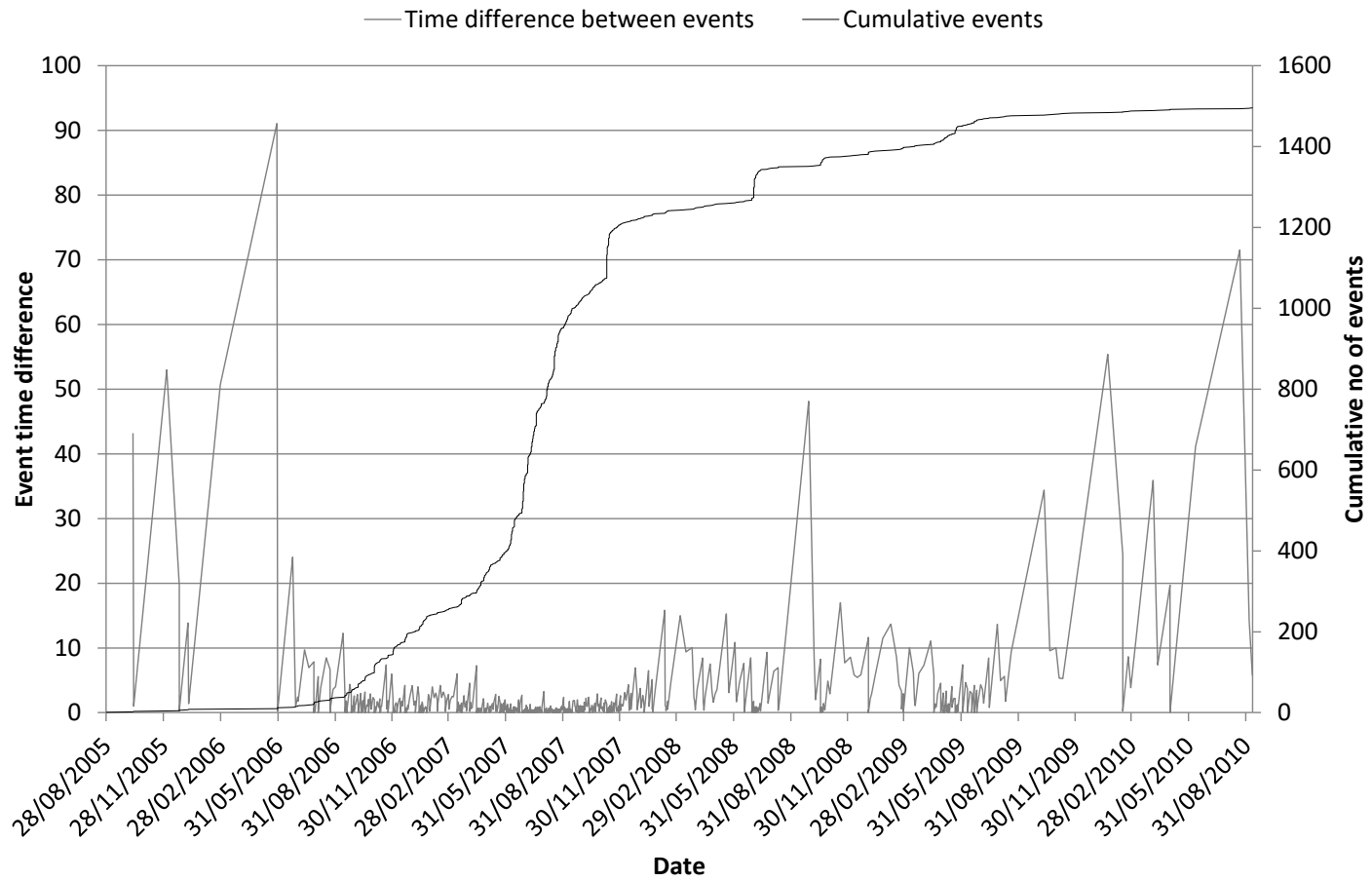


Figure A3 11: Time difference chart for Reward Fault.

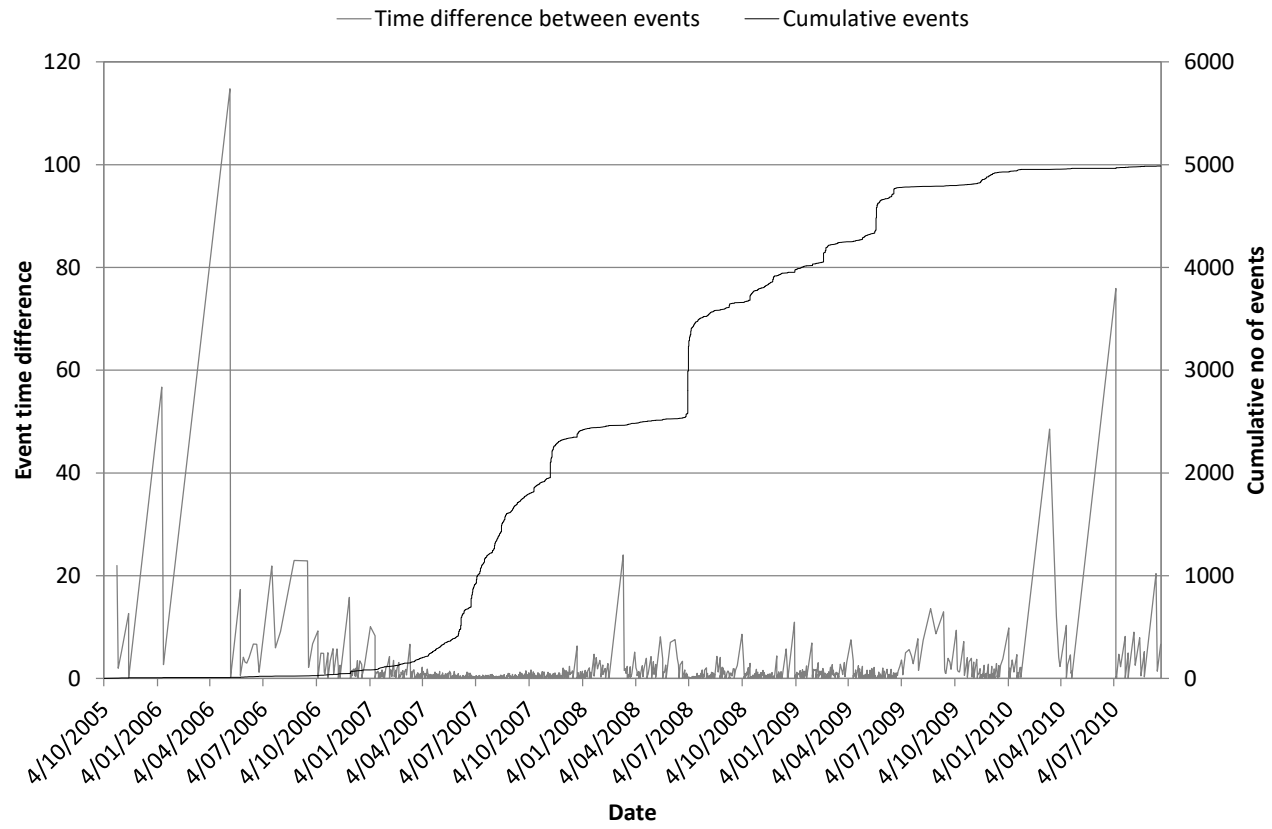


Figure A3 12: Time difference chart for Flanagan Fault.

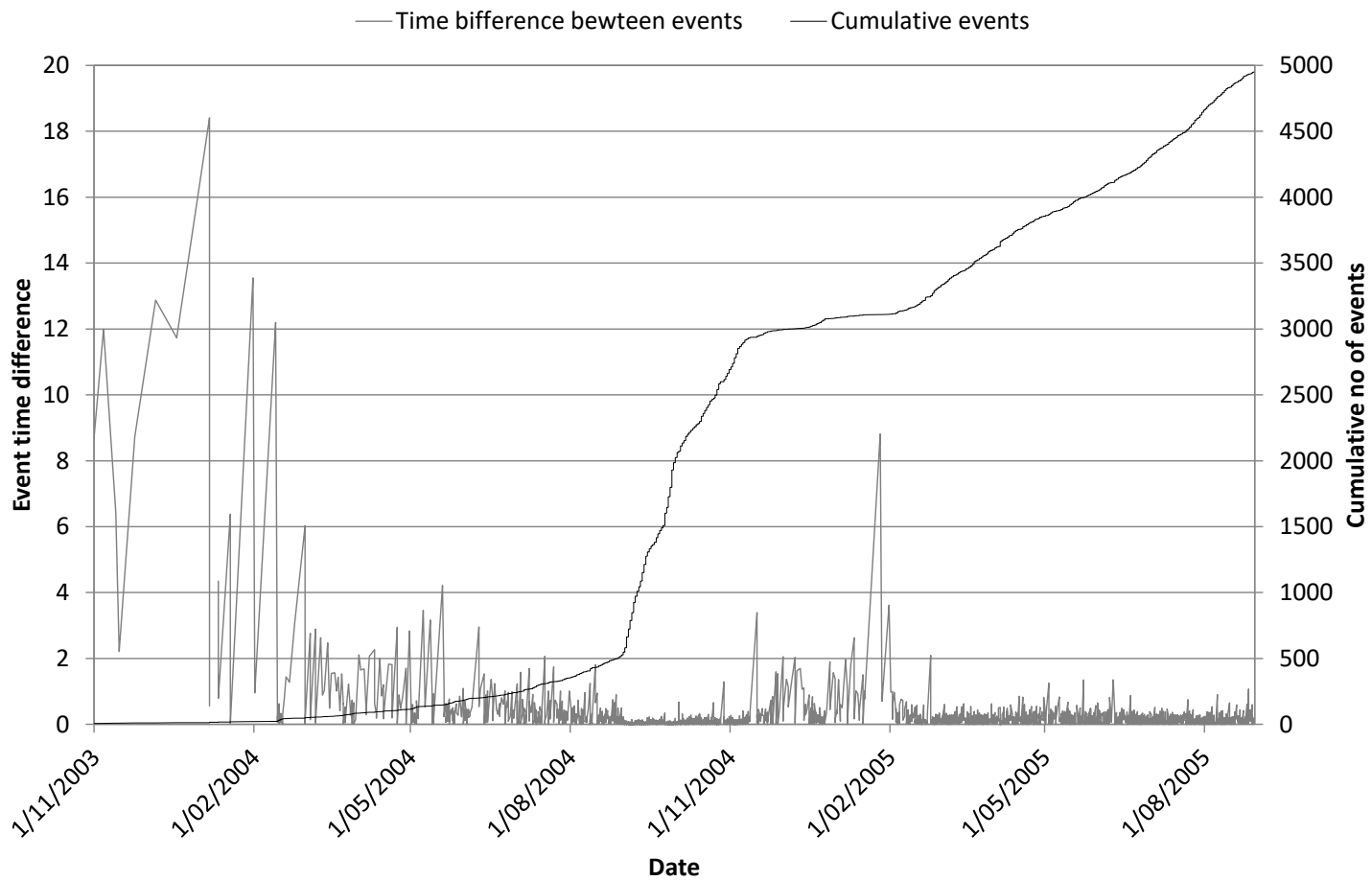


Figure A3 13: Time difference chart for Feral Fault.

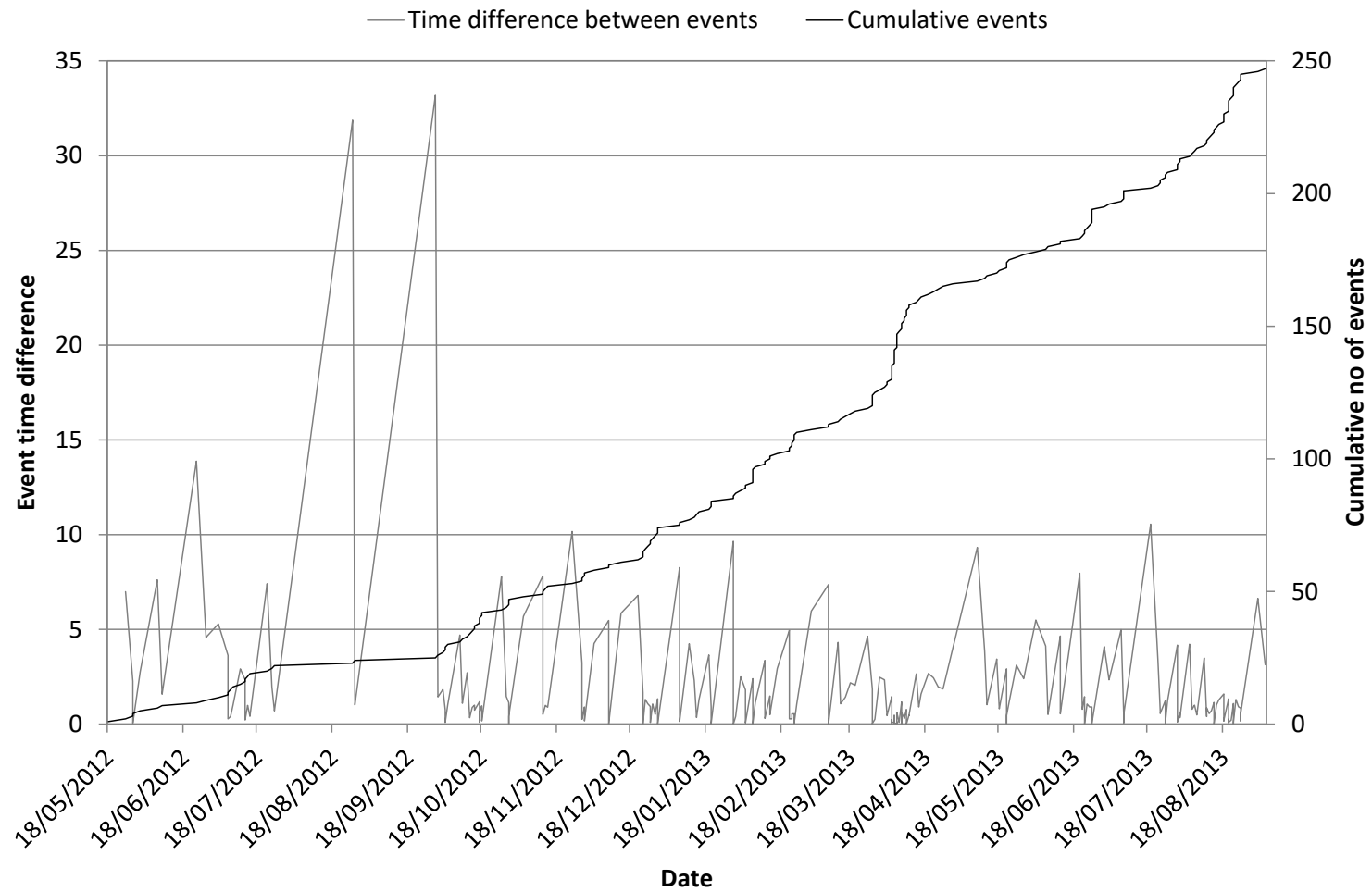


Figure A3 14: Time difference chart for Great Lyell Fault.

Appendix 4 – Daily event rates

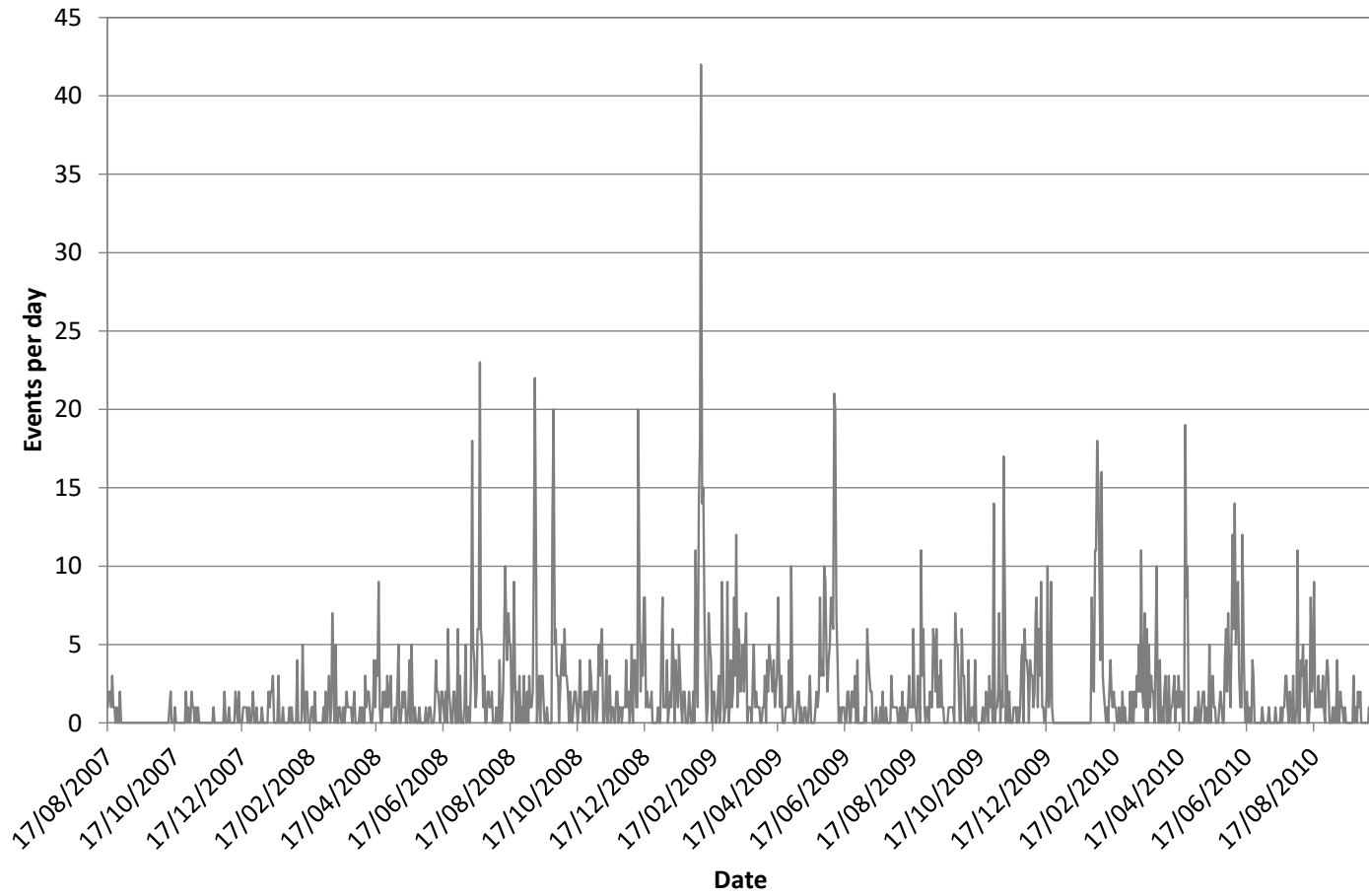


Figure A4 1: Events per day chart for the A1 Shear.

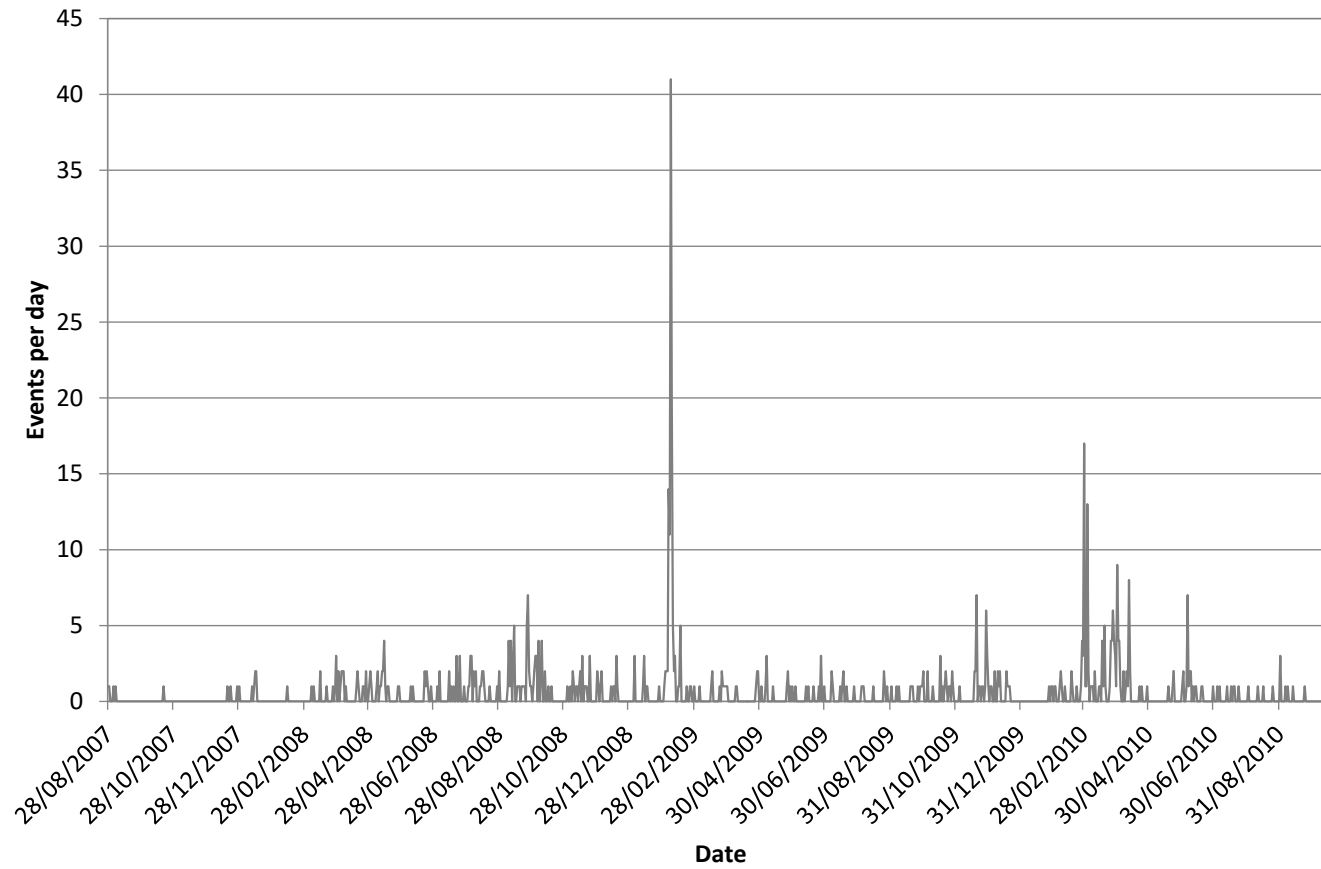


Figure A4 2: Events per day chart for the North Dyke.

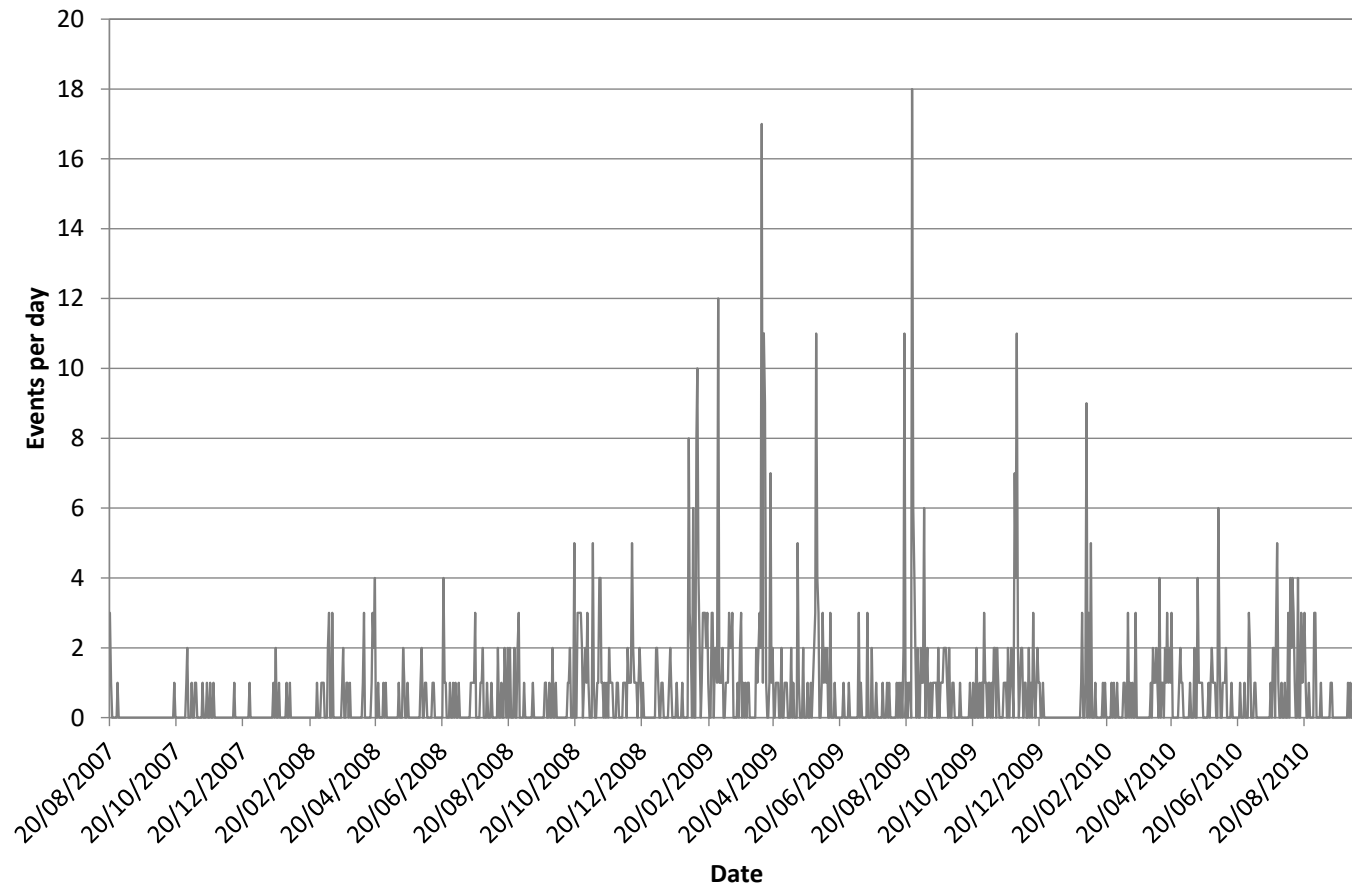


Figure A4 3: Events per day chart for the Mini Dyke.

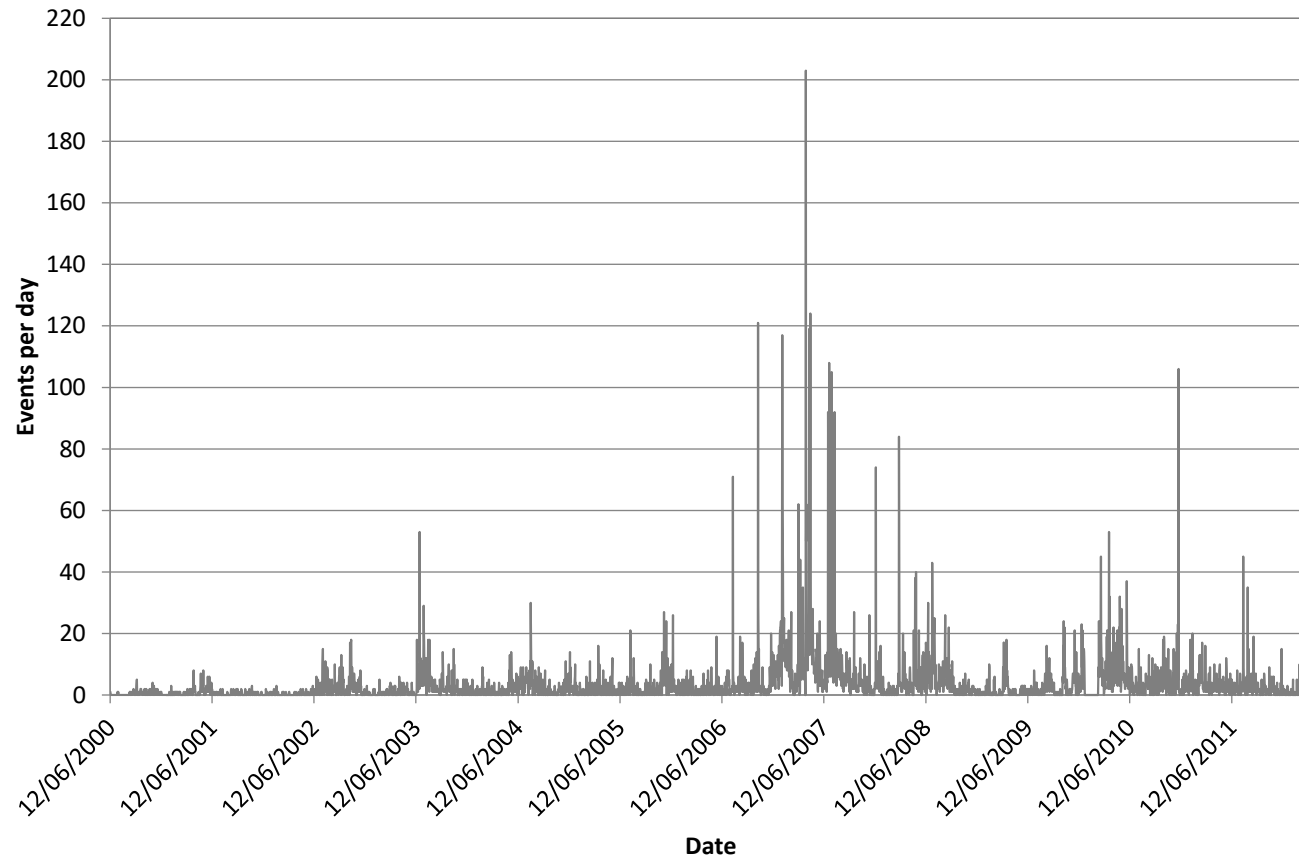


Figure A4 4: Events per day chart for Fitzroy Fault.

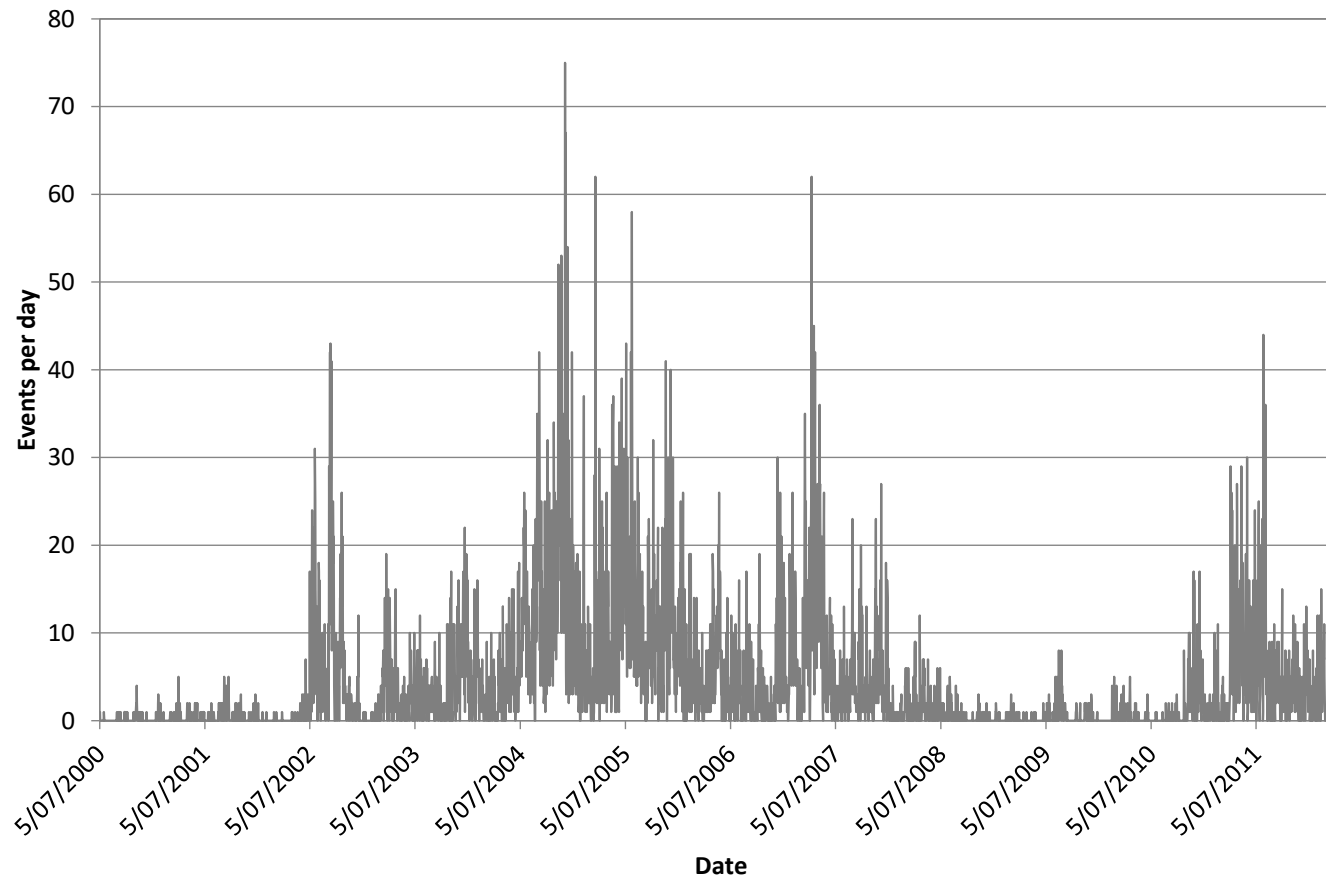


Figure A4 5: Events per day chart for North East Faults Group 1.

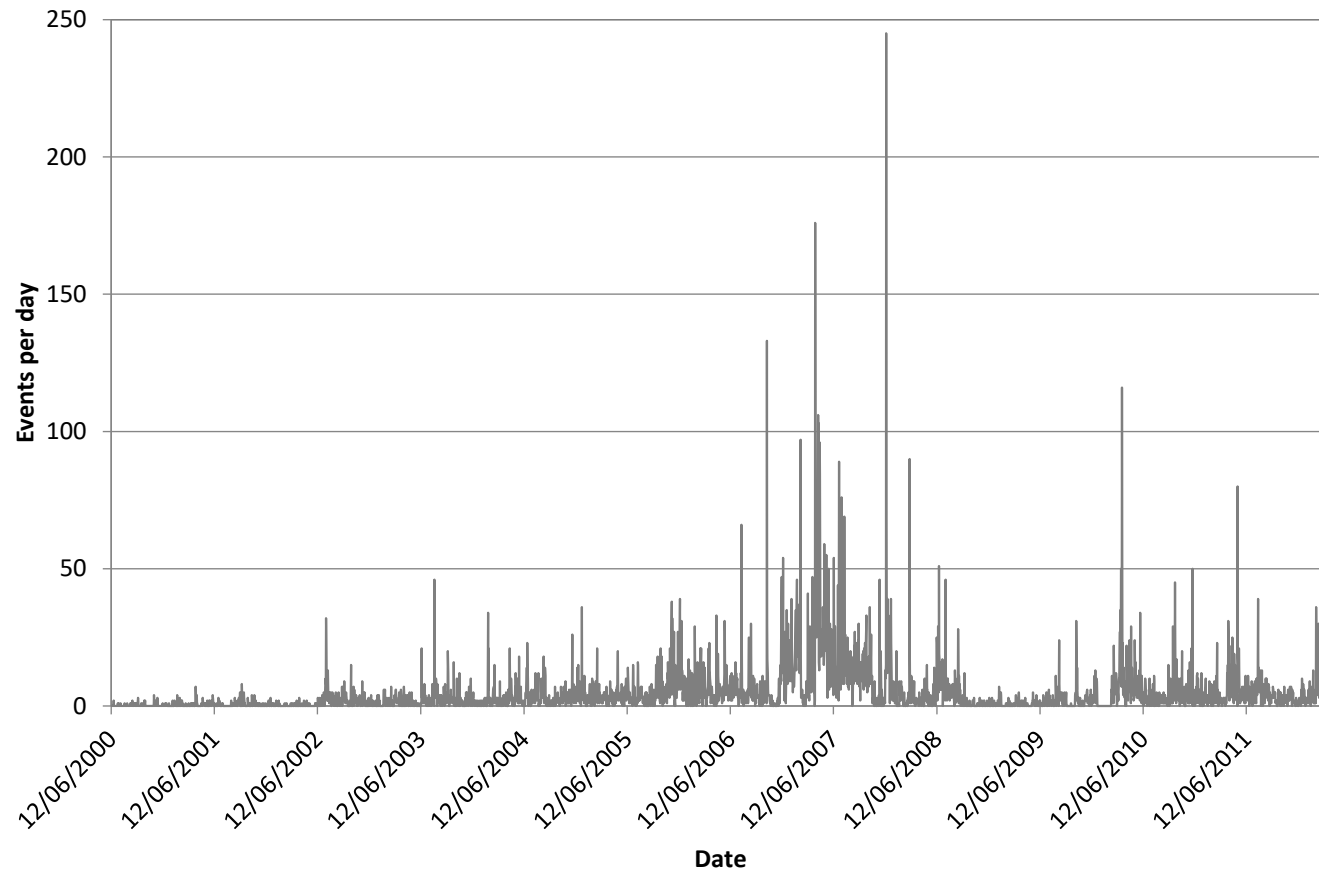


Figure A4 6: Events per day chart for North East Faults Group 2.

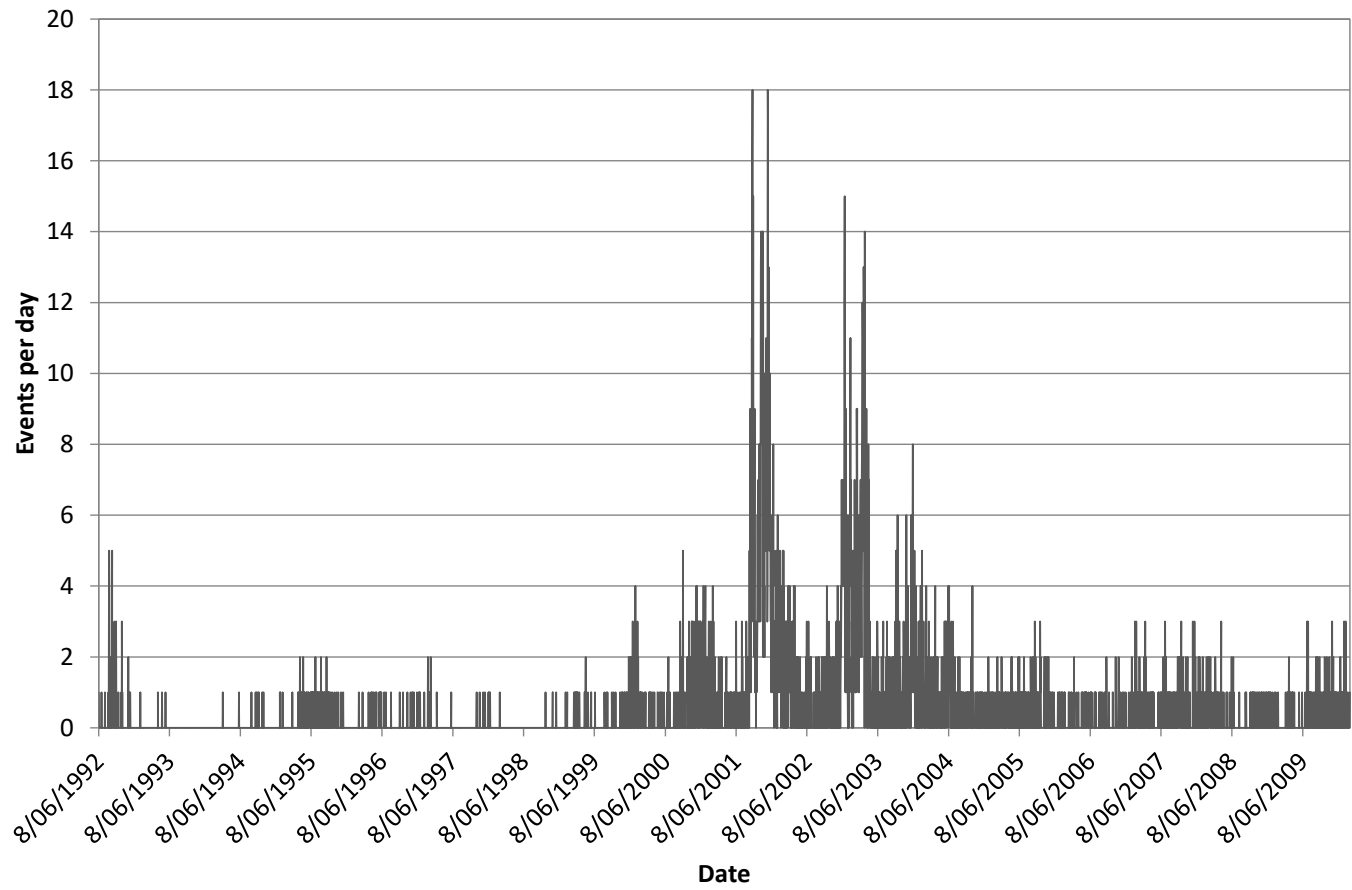


Figure A4 7: Events per day chart for FaultP_1

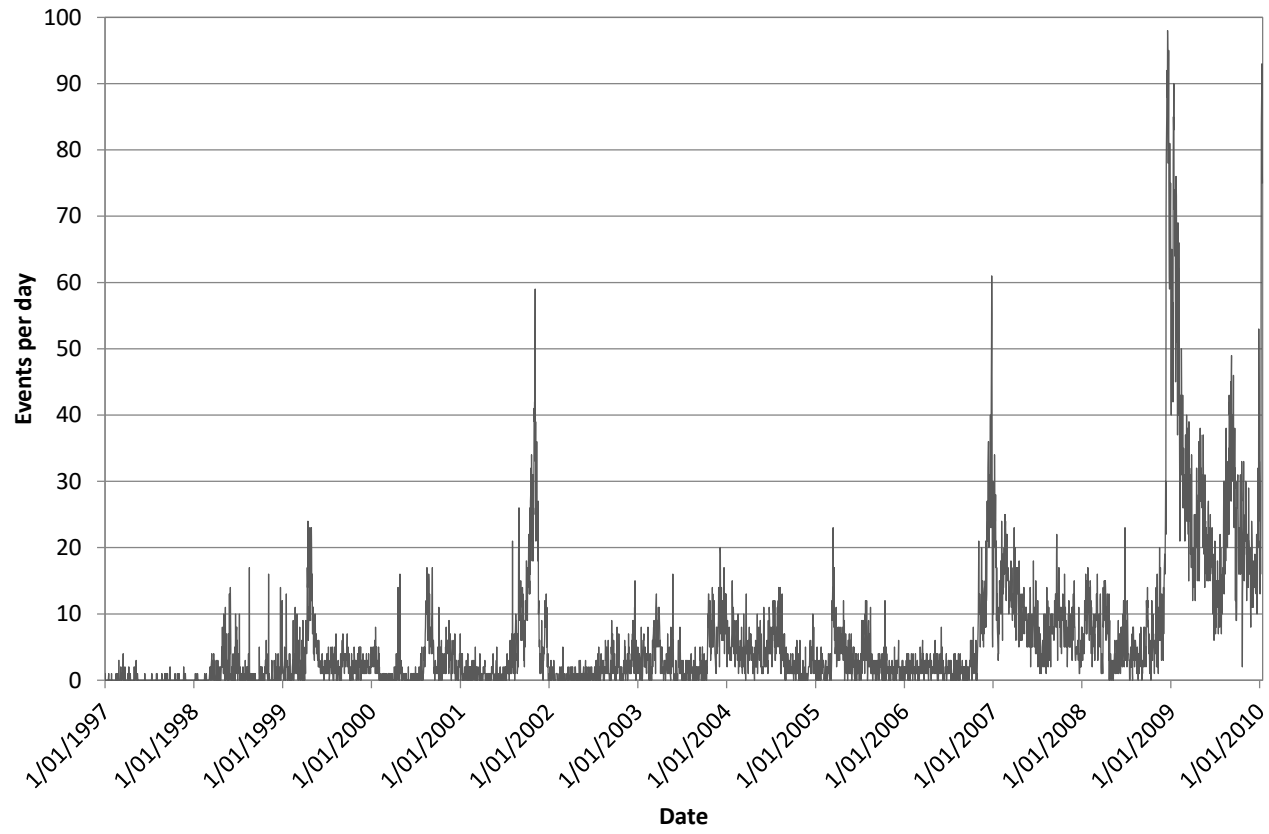


Figure A4 8: Events per day chart for Fault B_C.

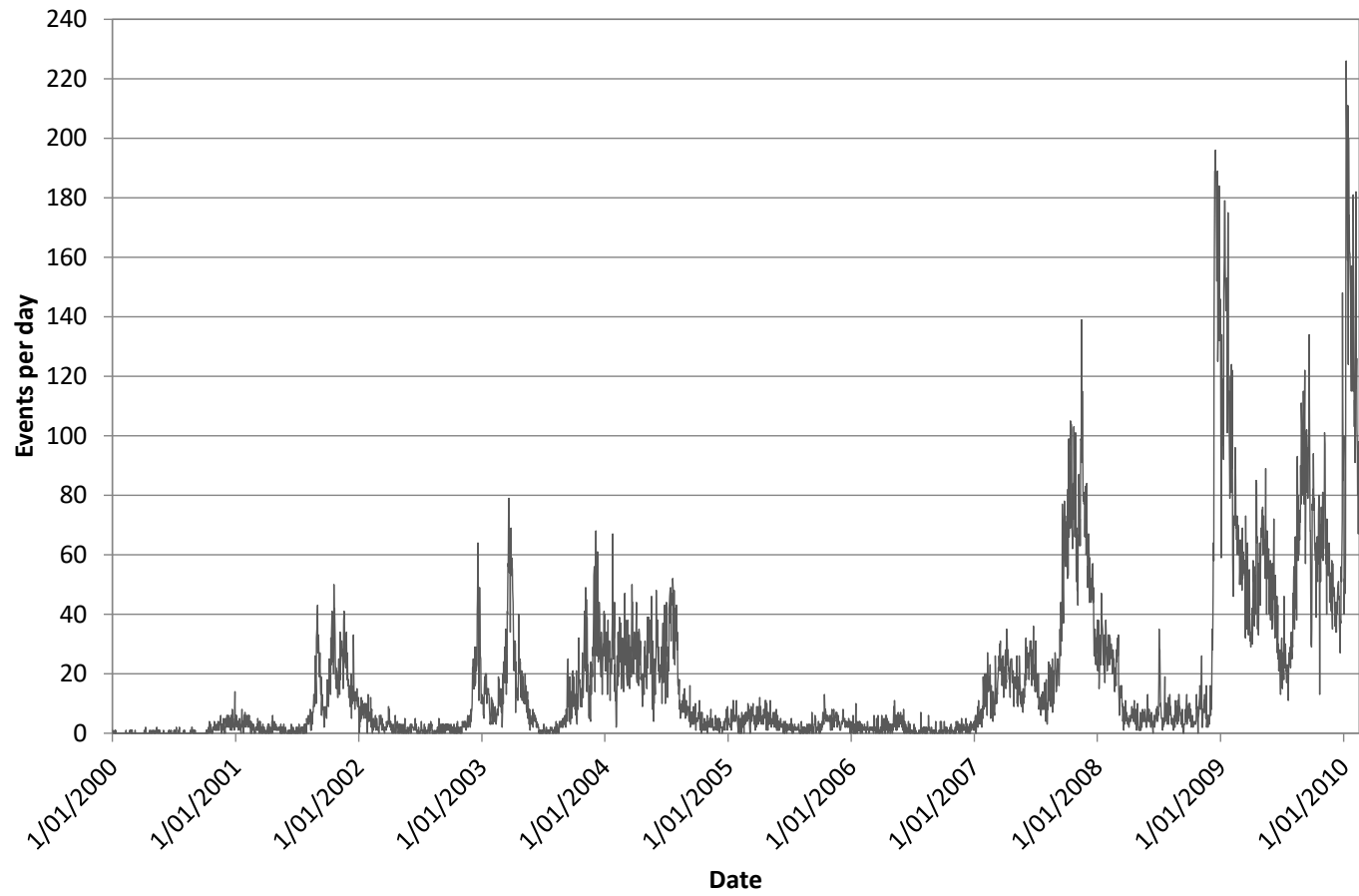


Figure A4 9: Events per day chart for the FW Dyke.

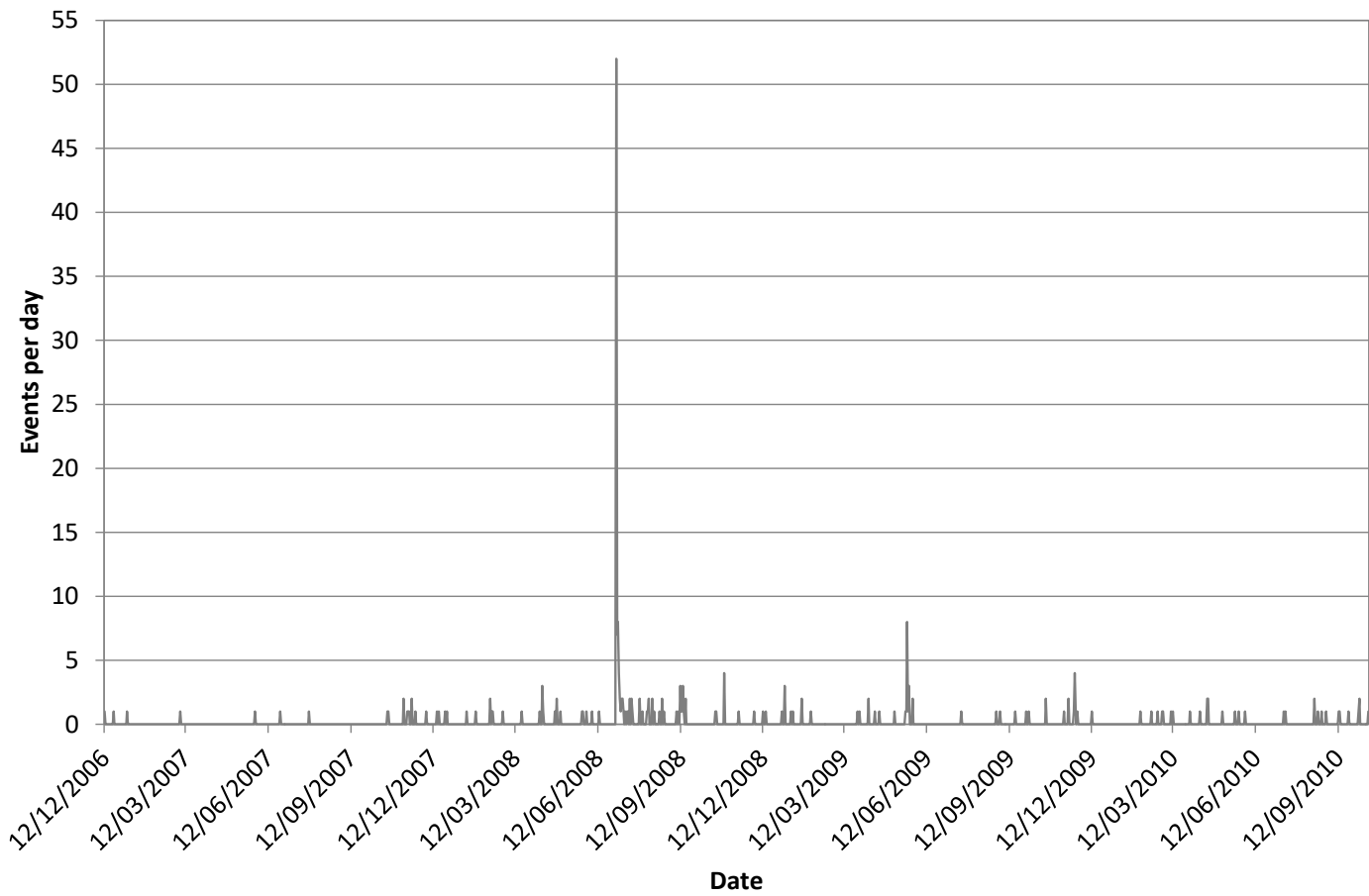


Figure A4 10: Events per day chart for Maritana Fault.

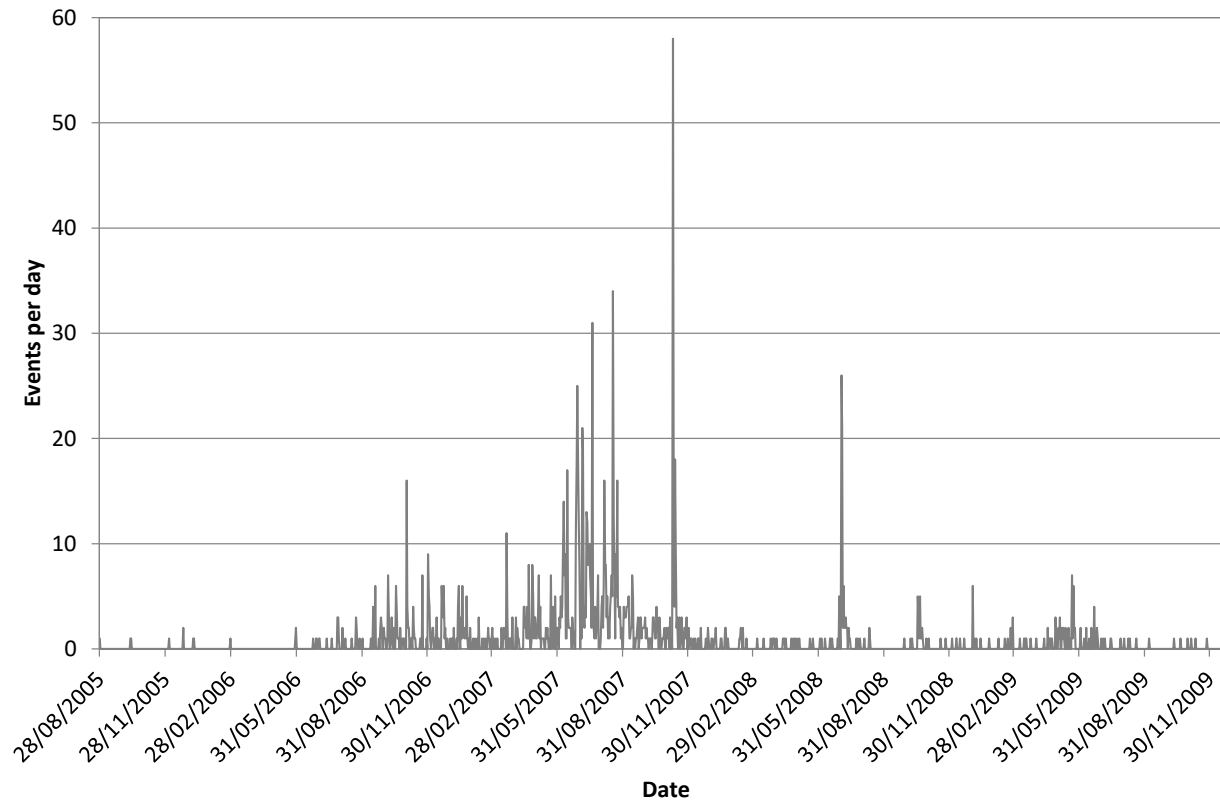


Figure A4 11: Events per day chart for Reward Fault.

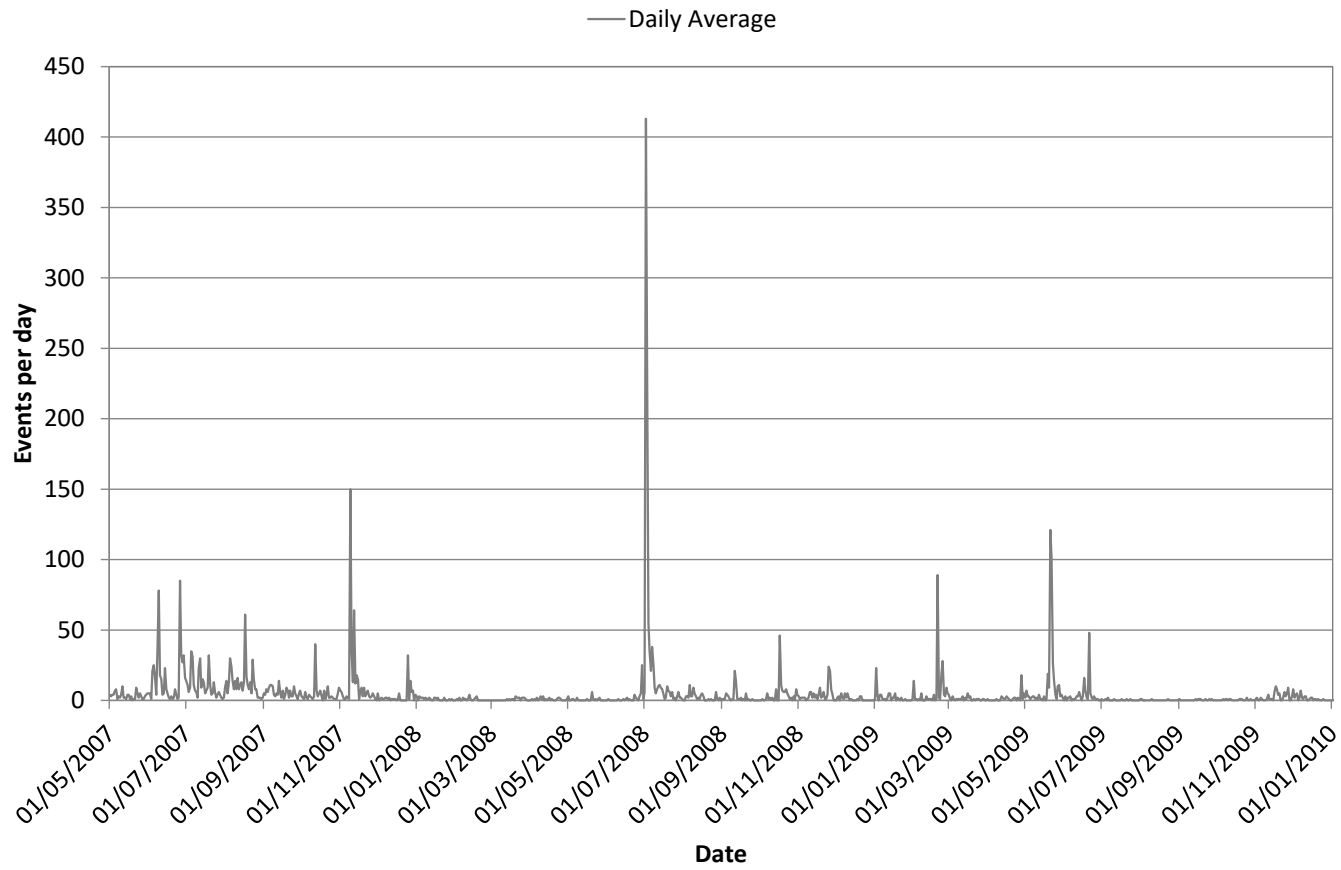


Figure A4 12: Events per day chart for Flanagan Fault.

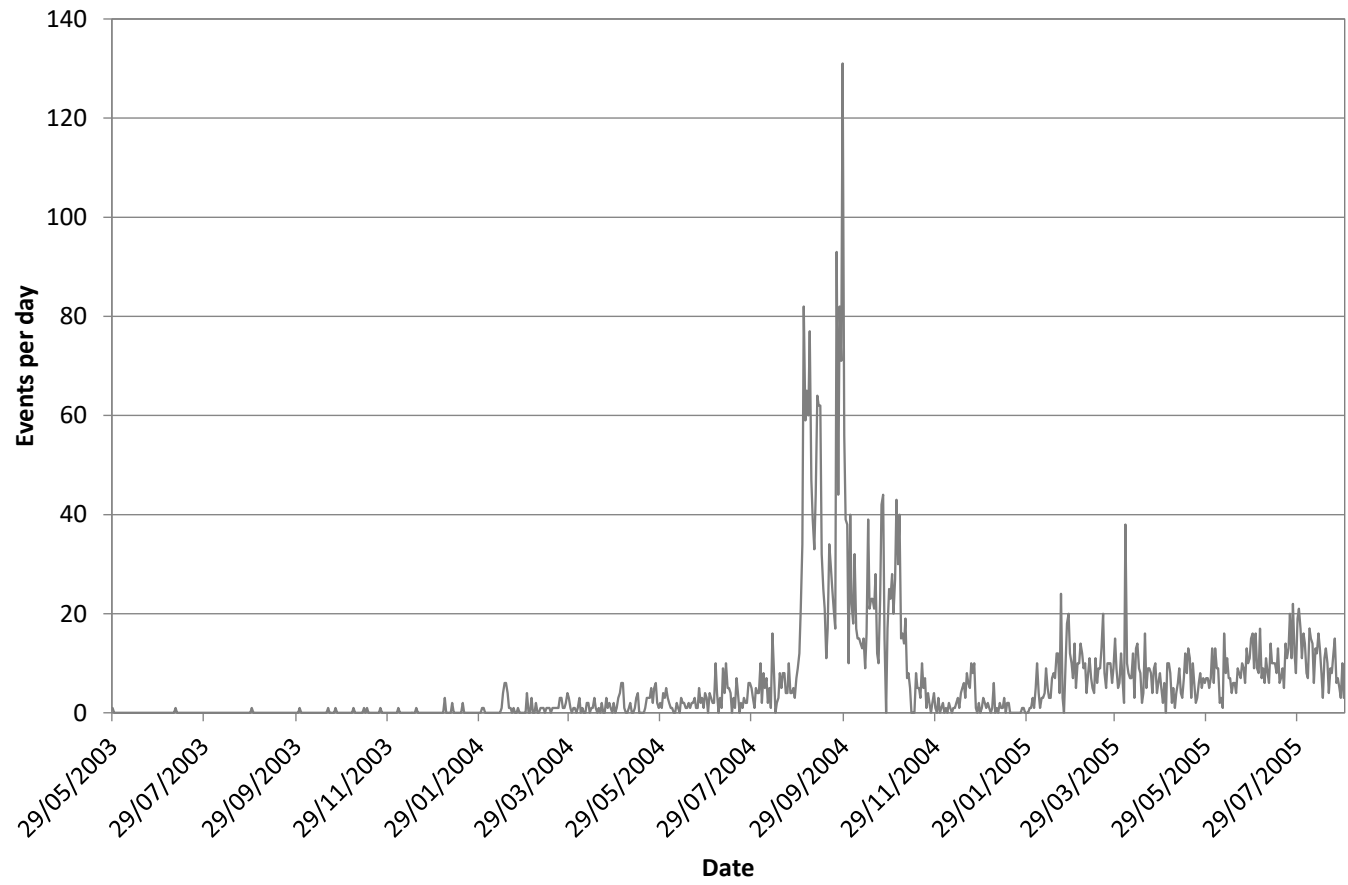


Figure A4 13: Events per day chart for Feral Fault.

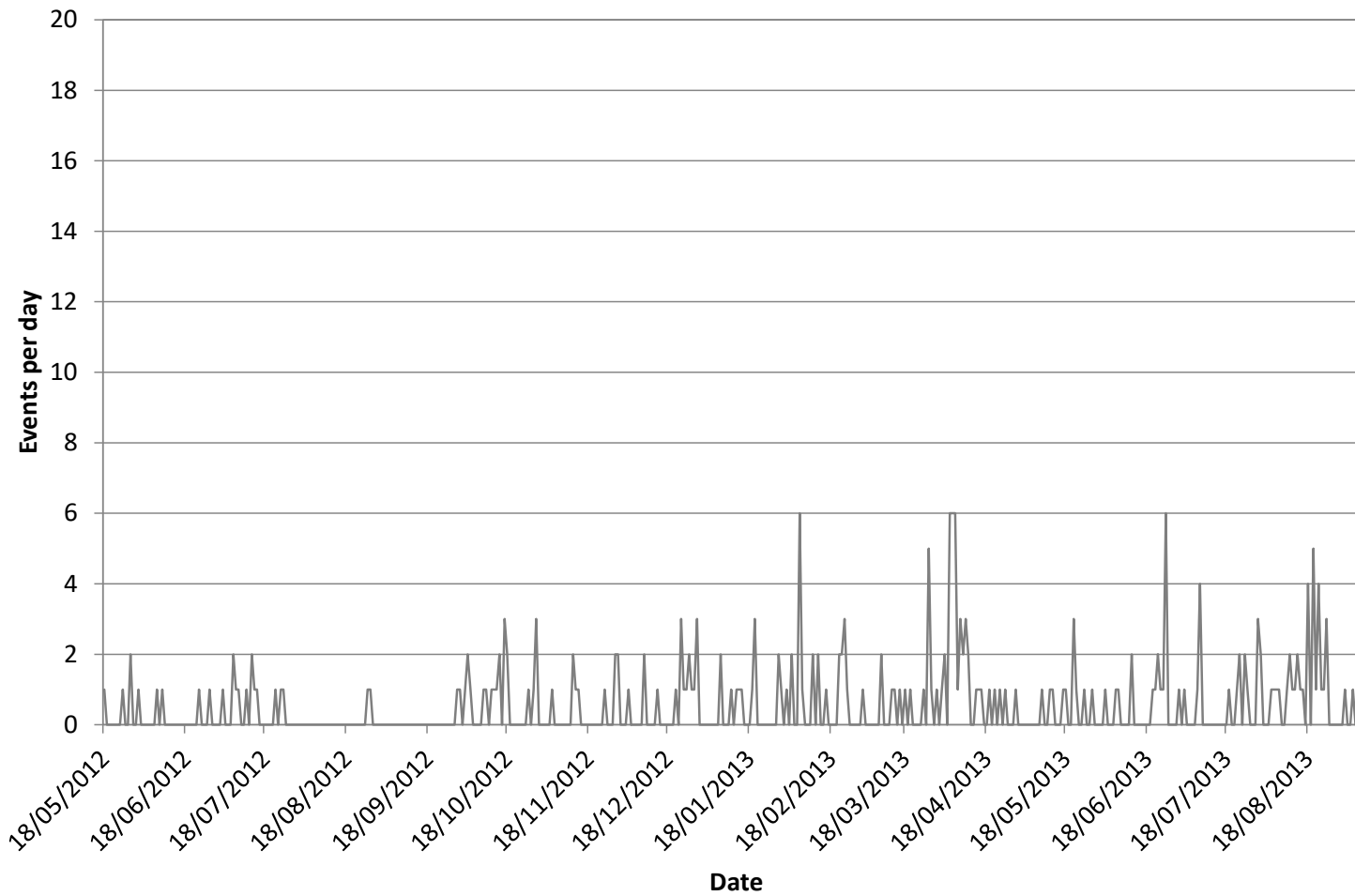


Figure A4 14: Events per day chart for Great Lyell Fault.

Appendix 5 – Daily and 7 day event rate charts

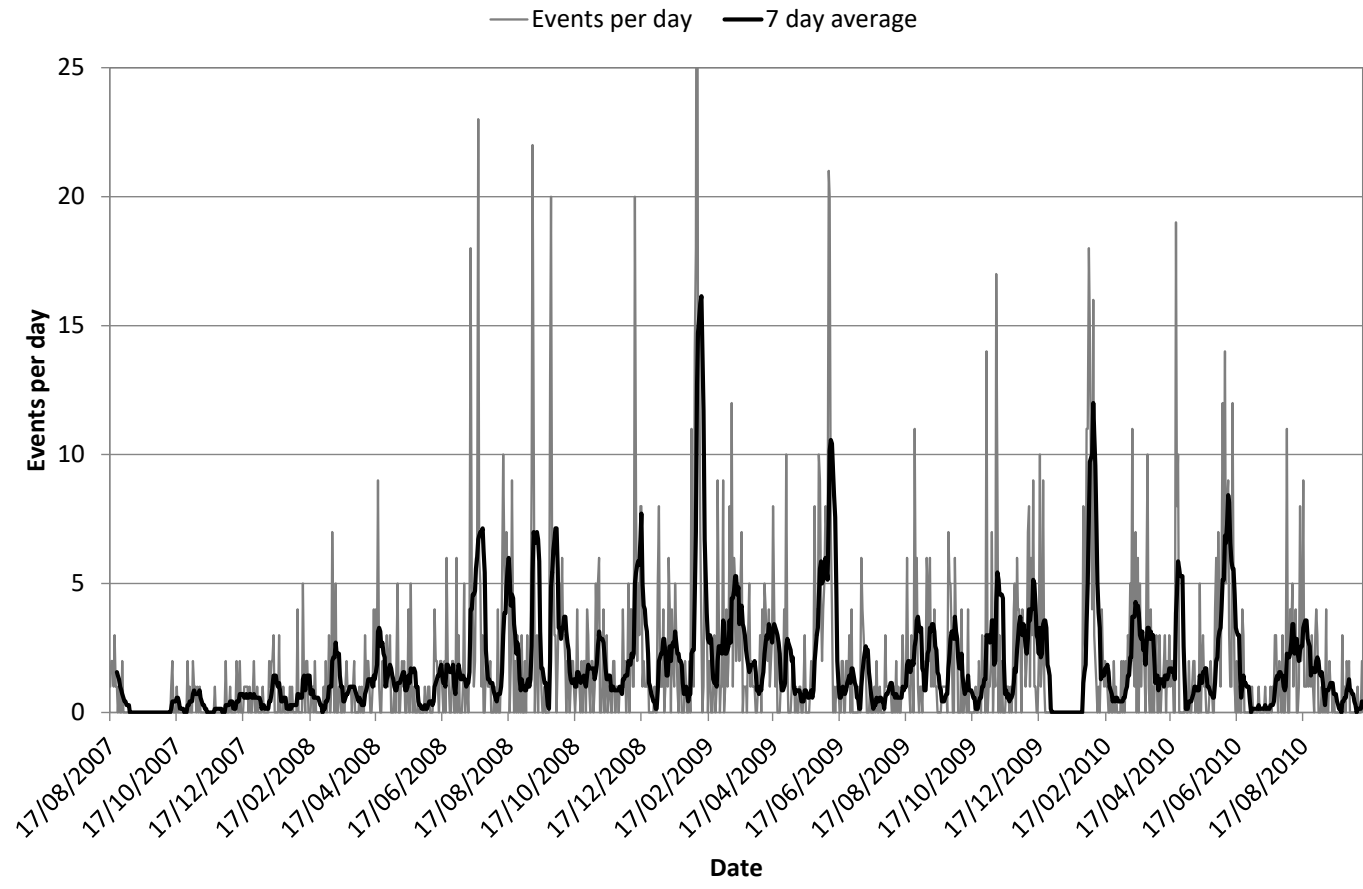


Figure A5 1: 7 day average events per day chart for the A1 Shear.

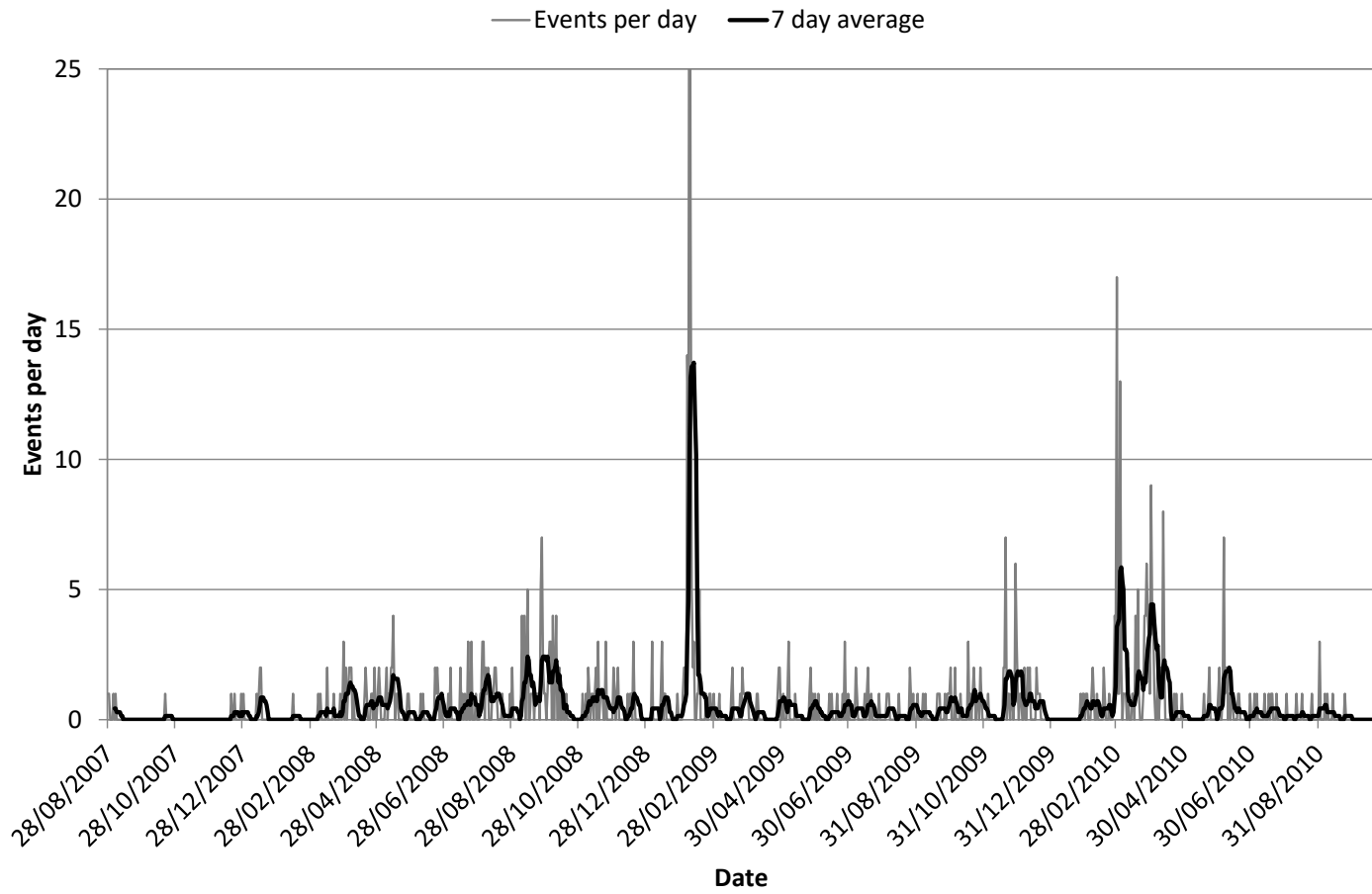


Figure A5 2: 7 day average events per day chart for the North Dyke.

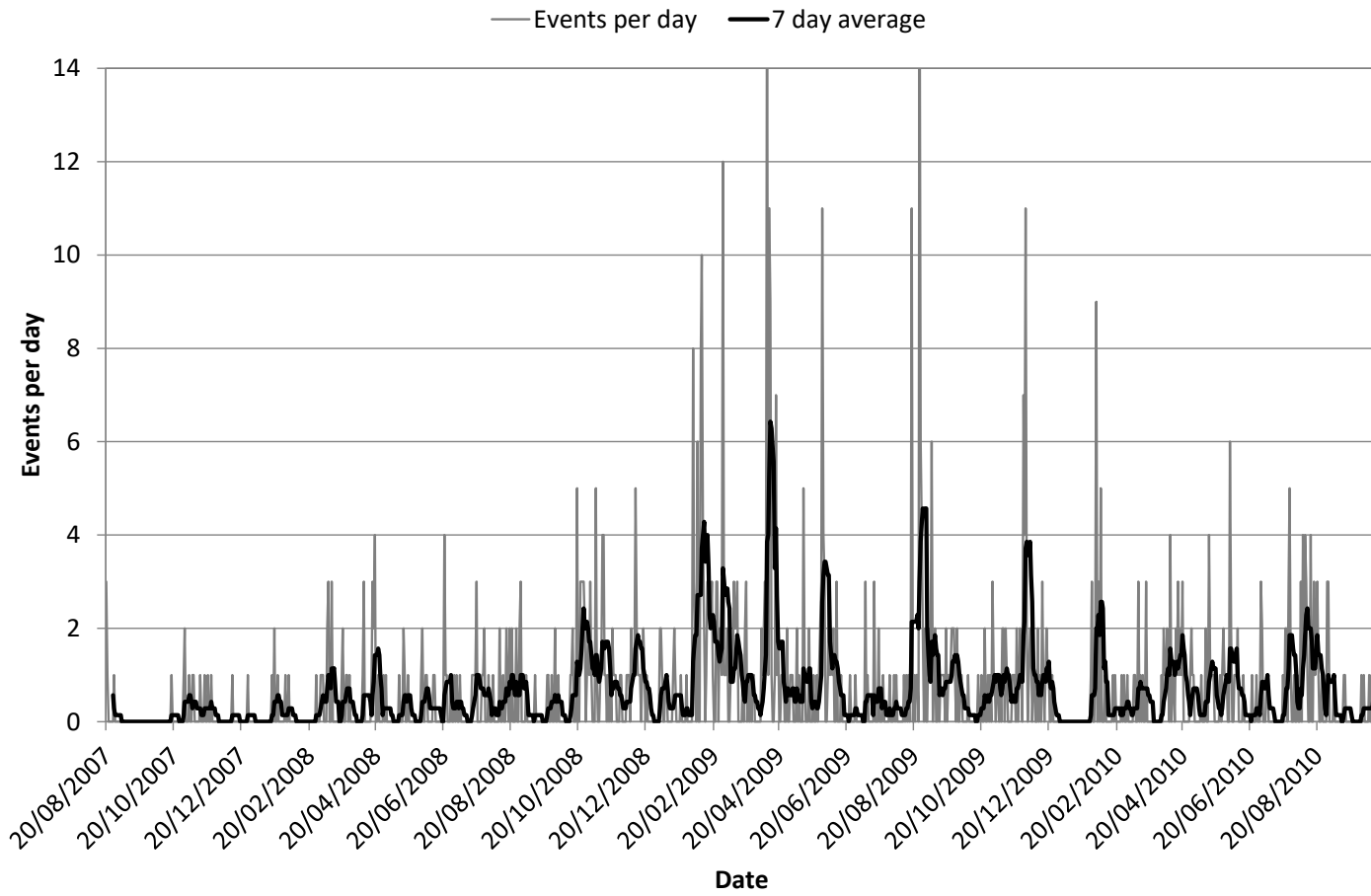


Figure A5 3: 7 day average events per day chart for the Mini Dyke.

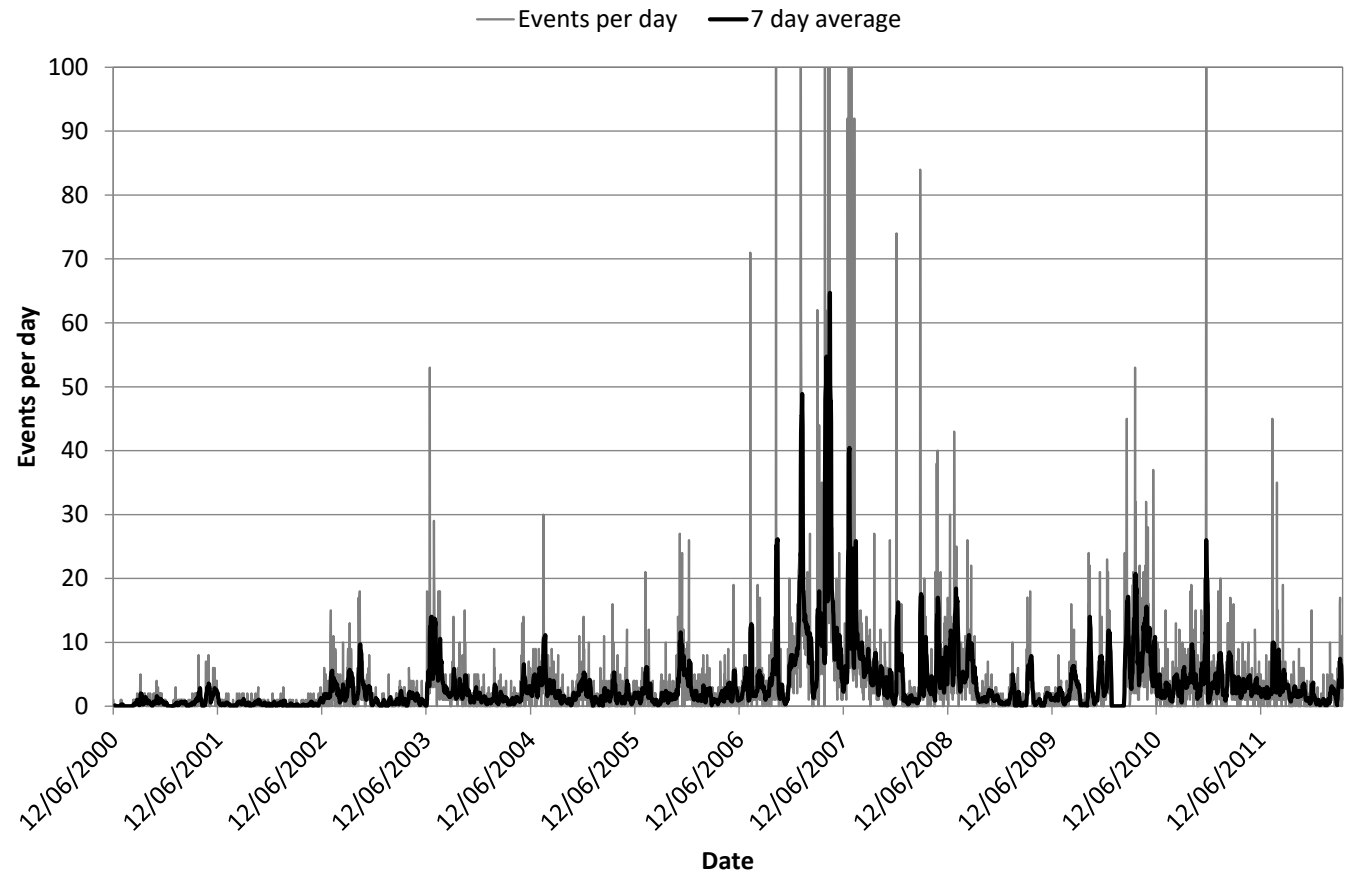


Figure A5 4: 7 day average events per day chart for Fitzroy Fault.

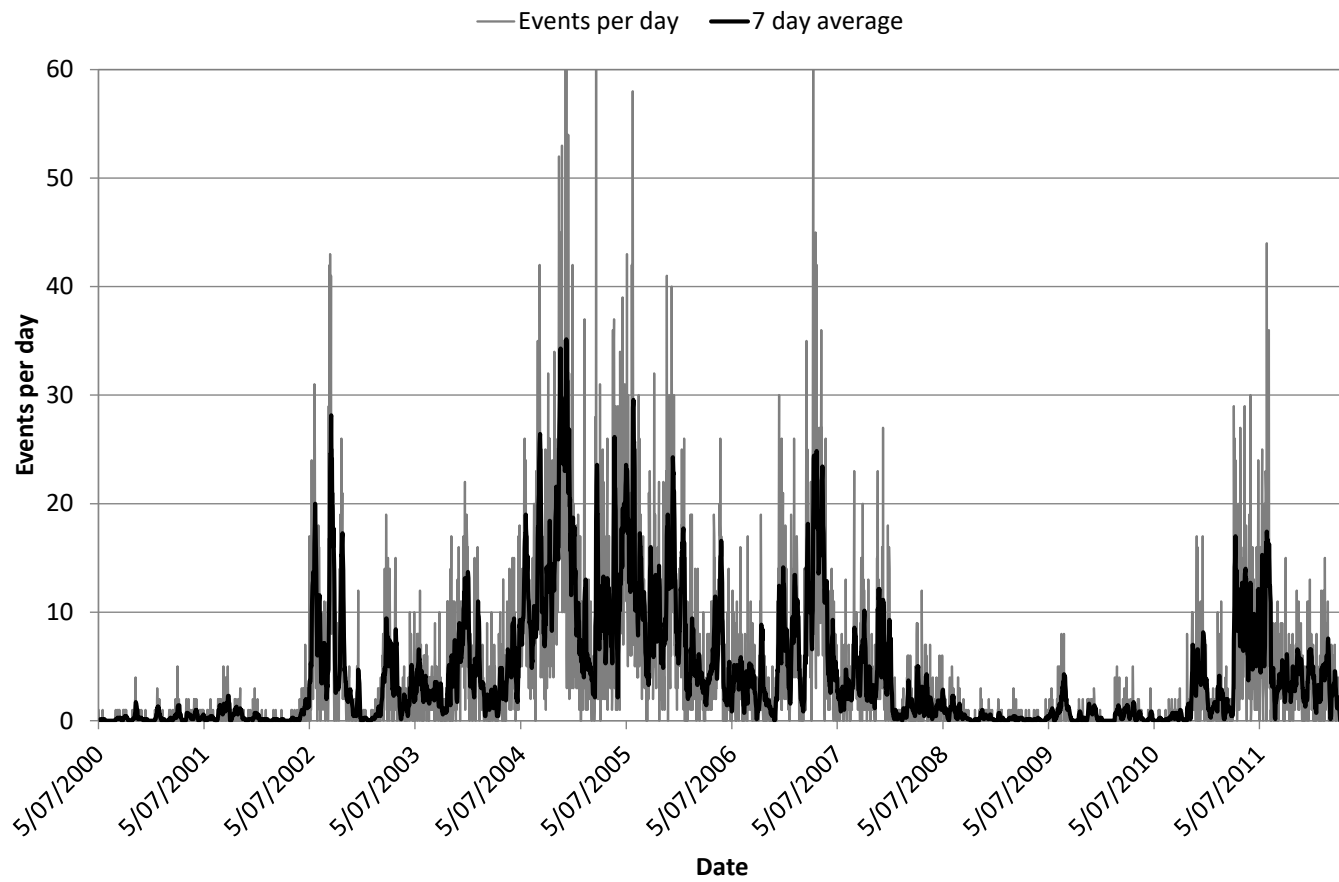


Figure A5 5: 7 day average events per day chart for North East Faults Group 1.

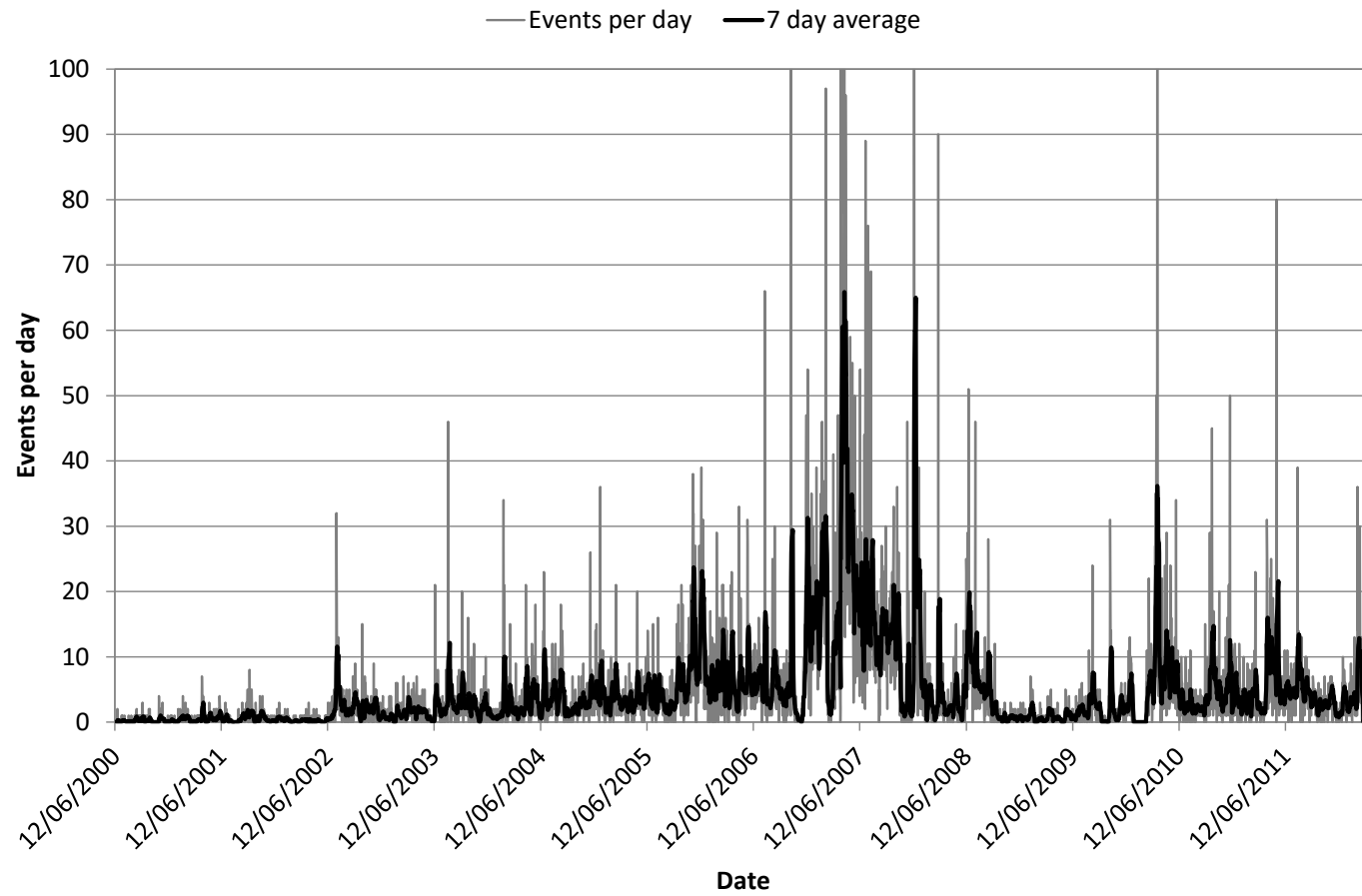


Figure A5 6: 7 day average events per day chart for North East Faults Group 2.

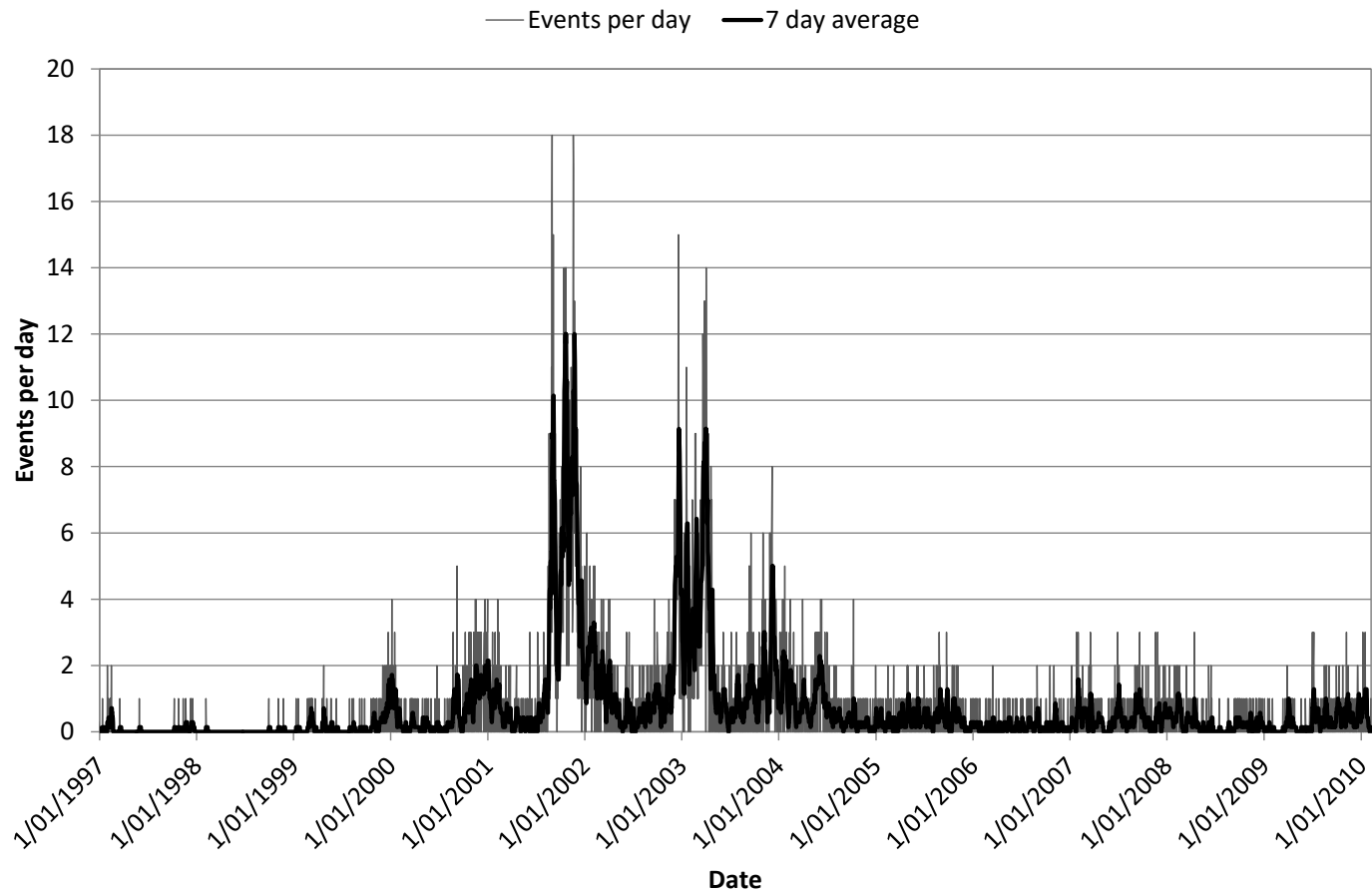


Figure A5 7: 7 day average events per day chart for FaultP_1

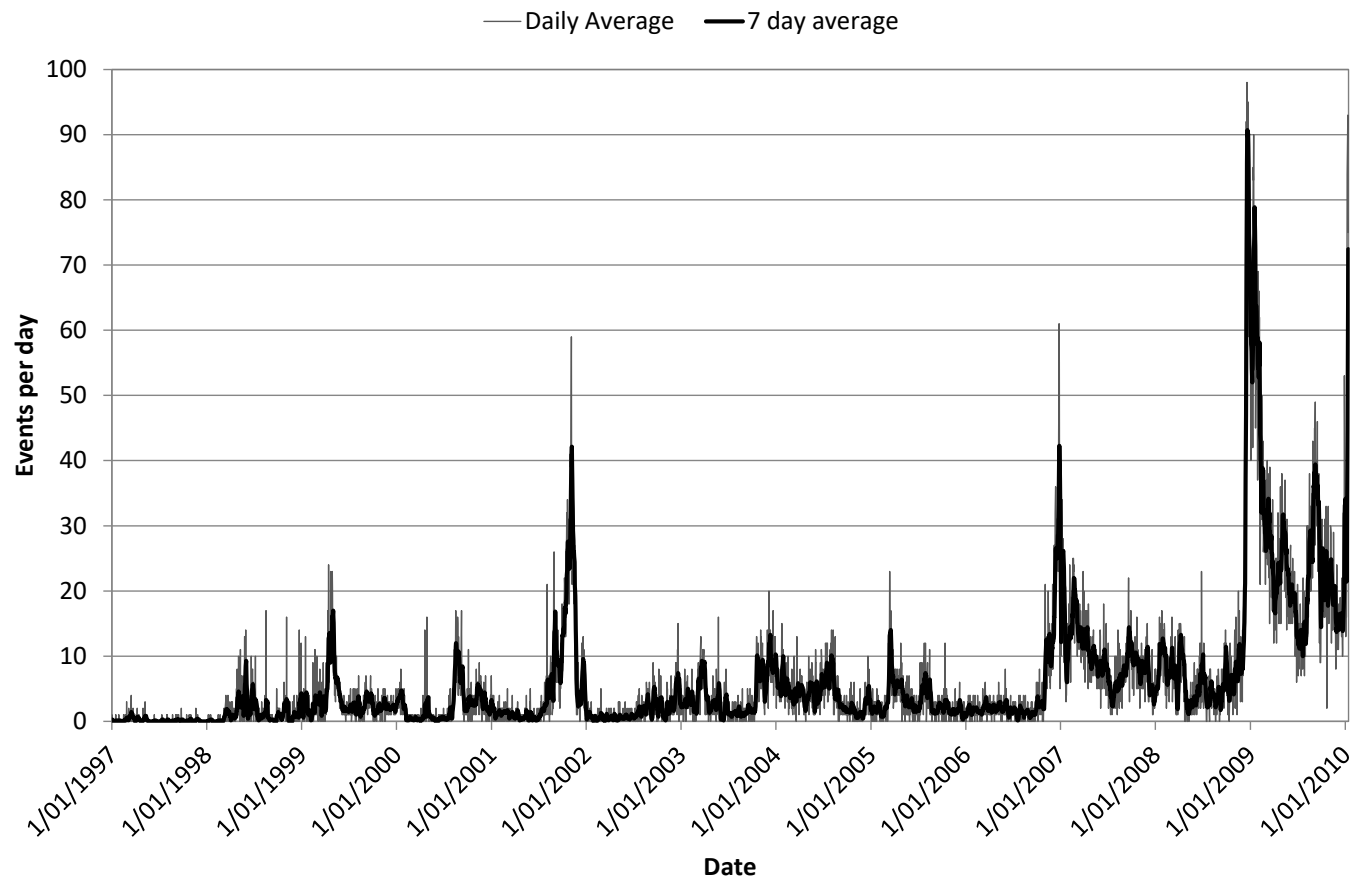


Figure A5 8: 7 day average events per day chart for Fault B_C.

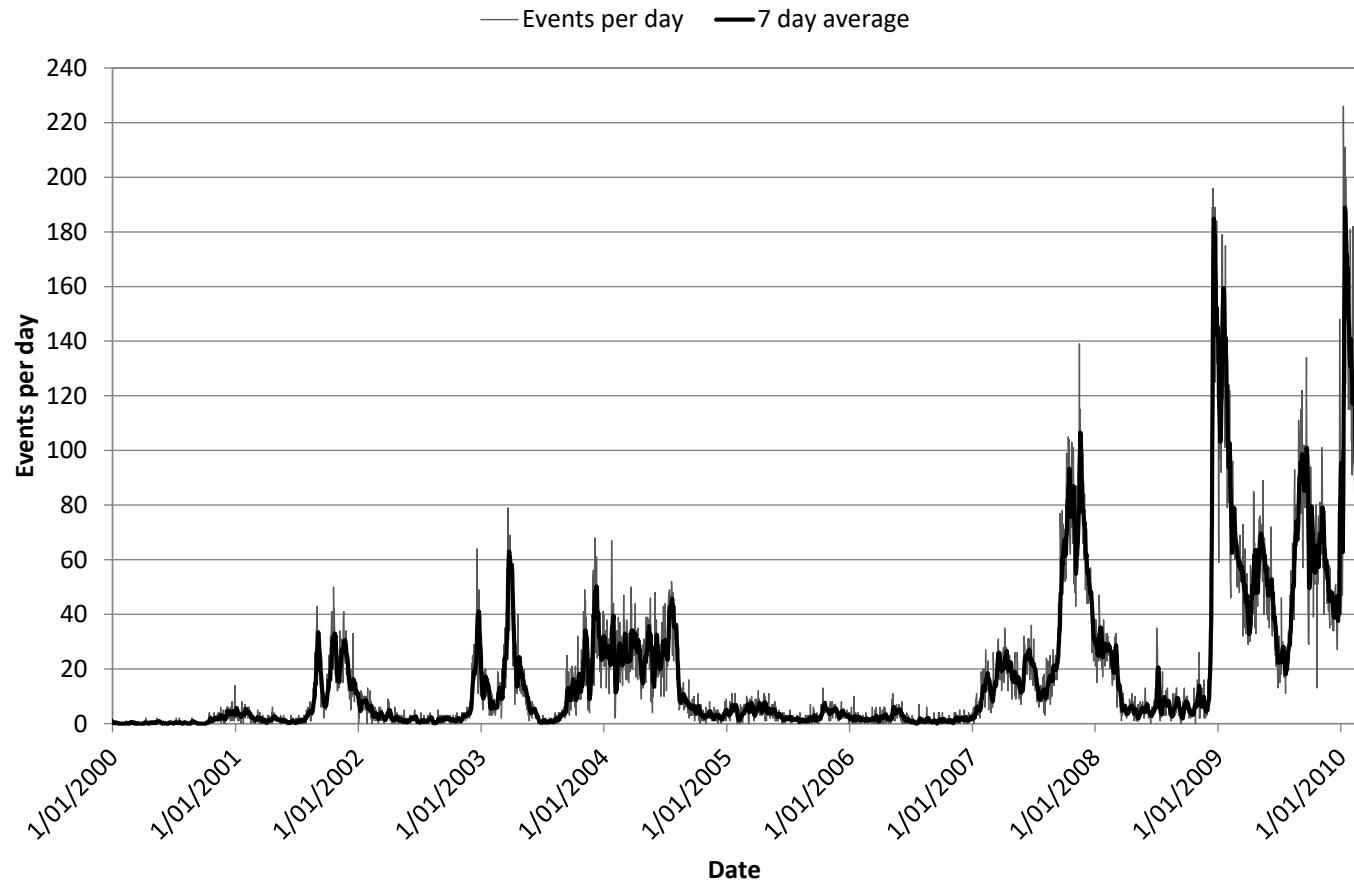


Figure A5 9: 7 day average events per day chart for the FW Dyke.

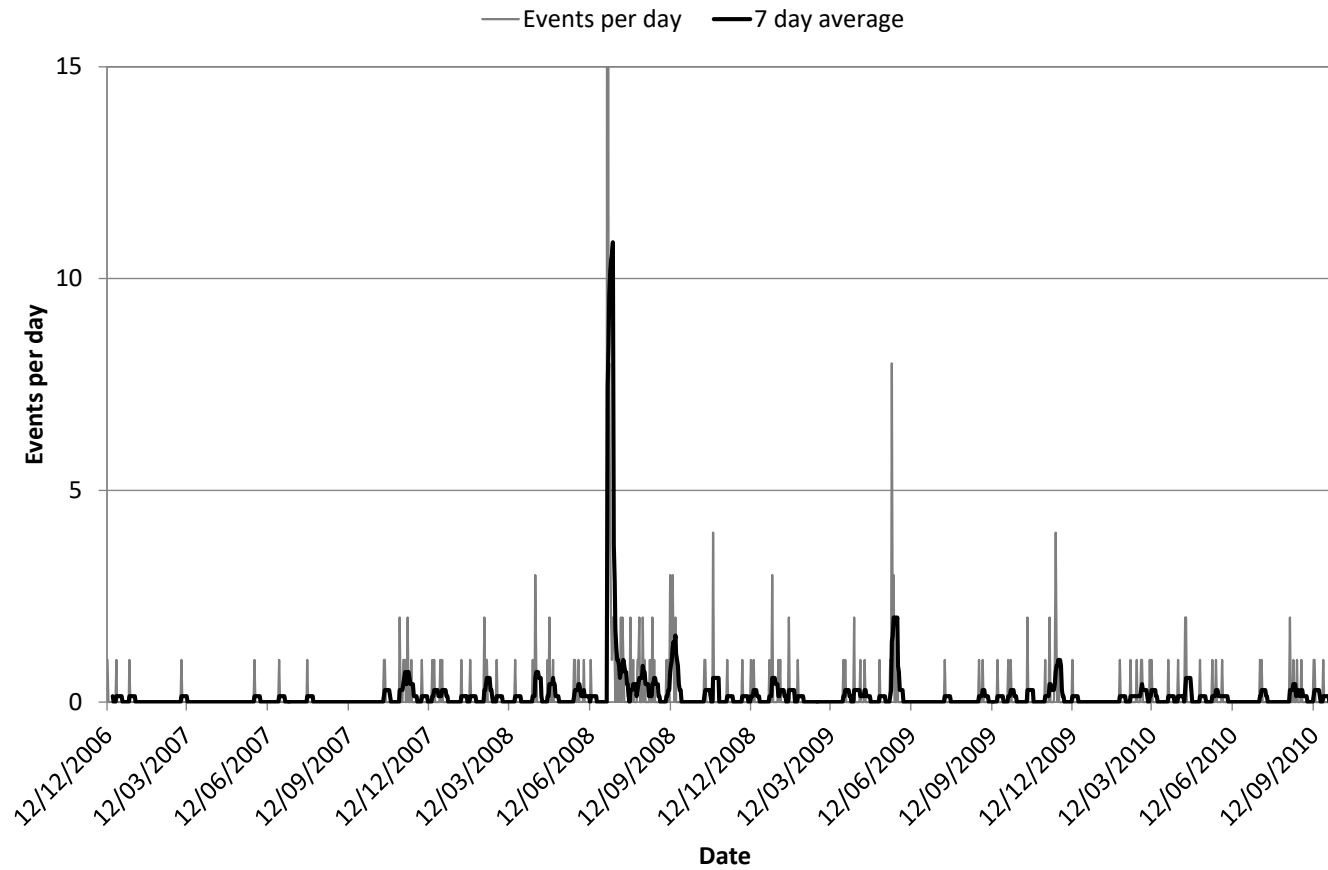


Figure A5 10: 7 day average events per day chart for Maritana Fault.

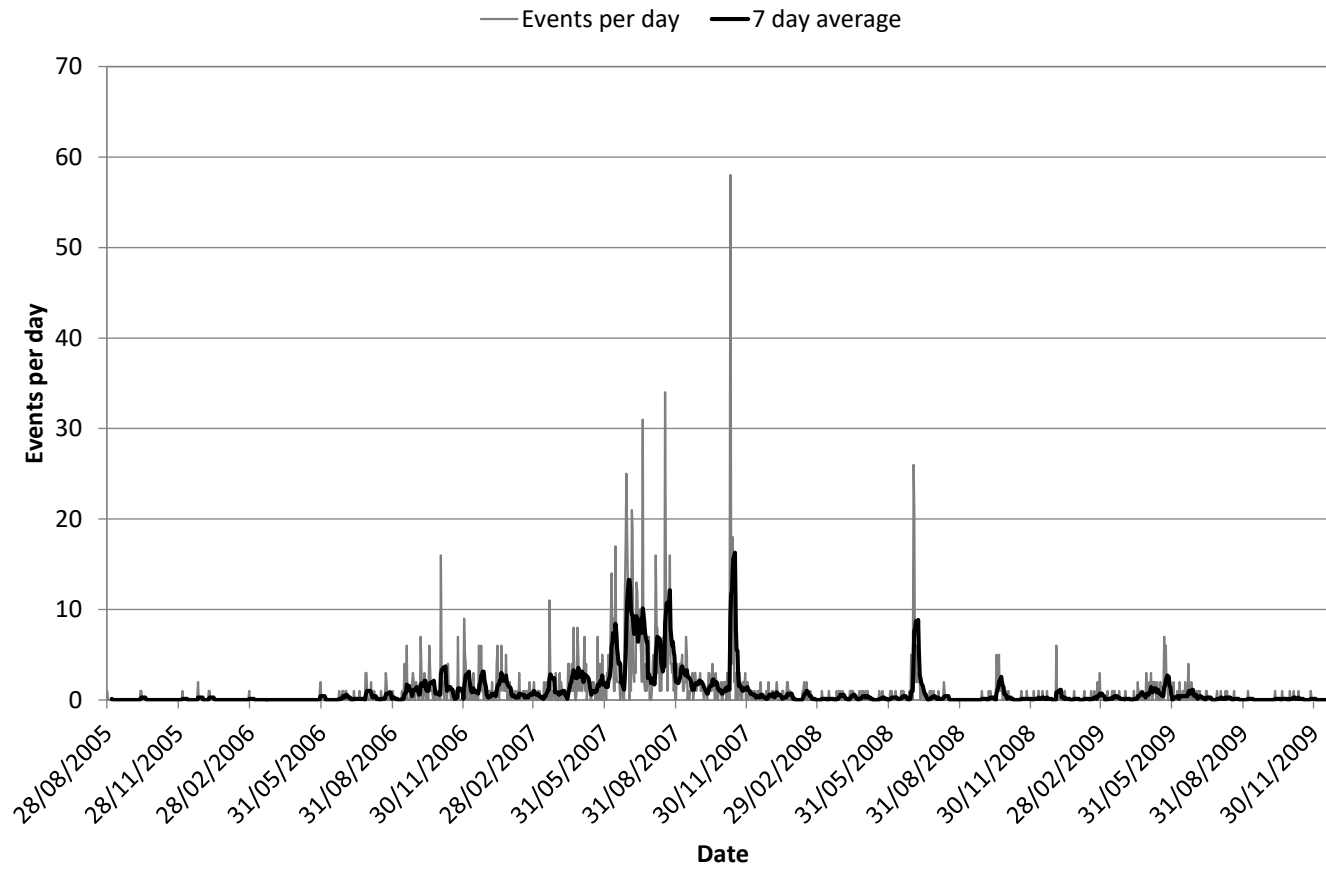


Figure A5 11: 7 day average events per day chart for Reward Fault.

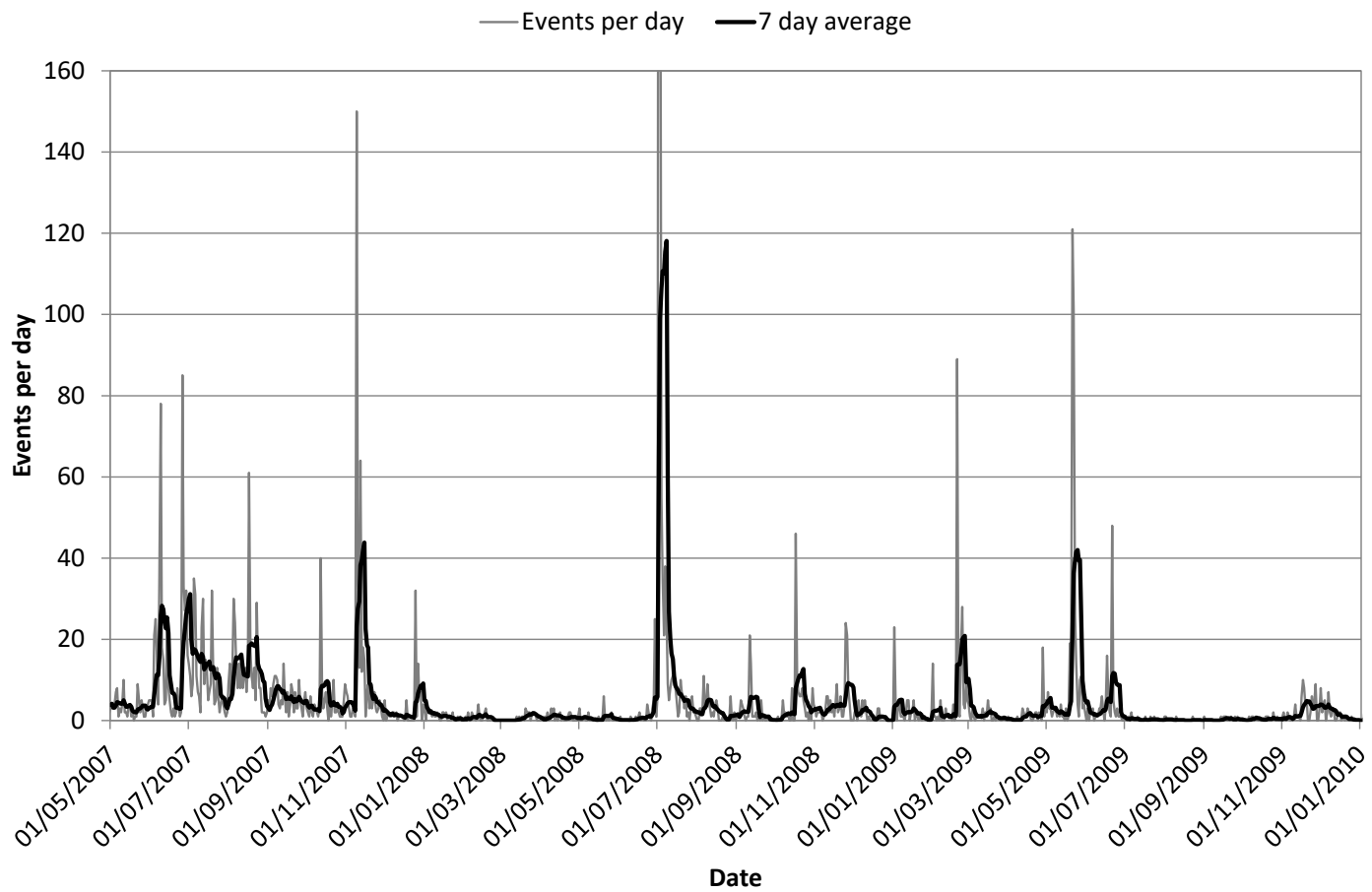


Figure A5 12: 7 day average events per day chart for Flanagan Fault.

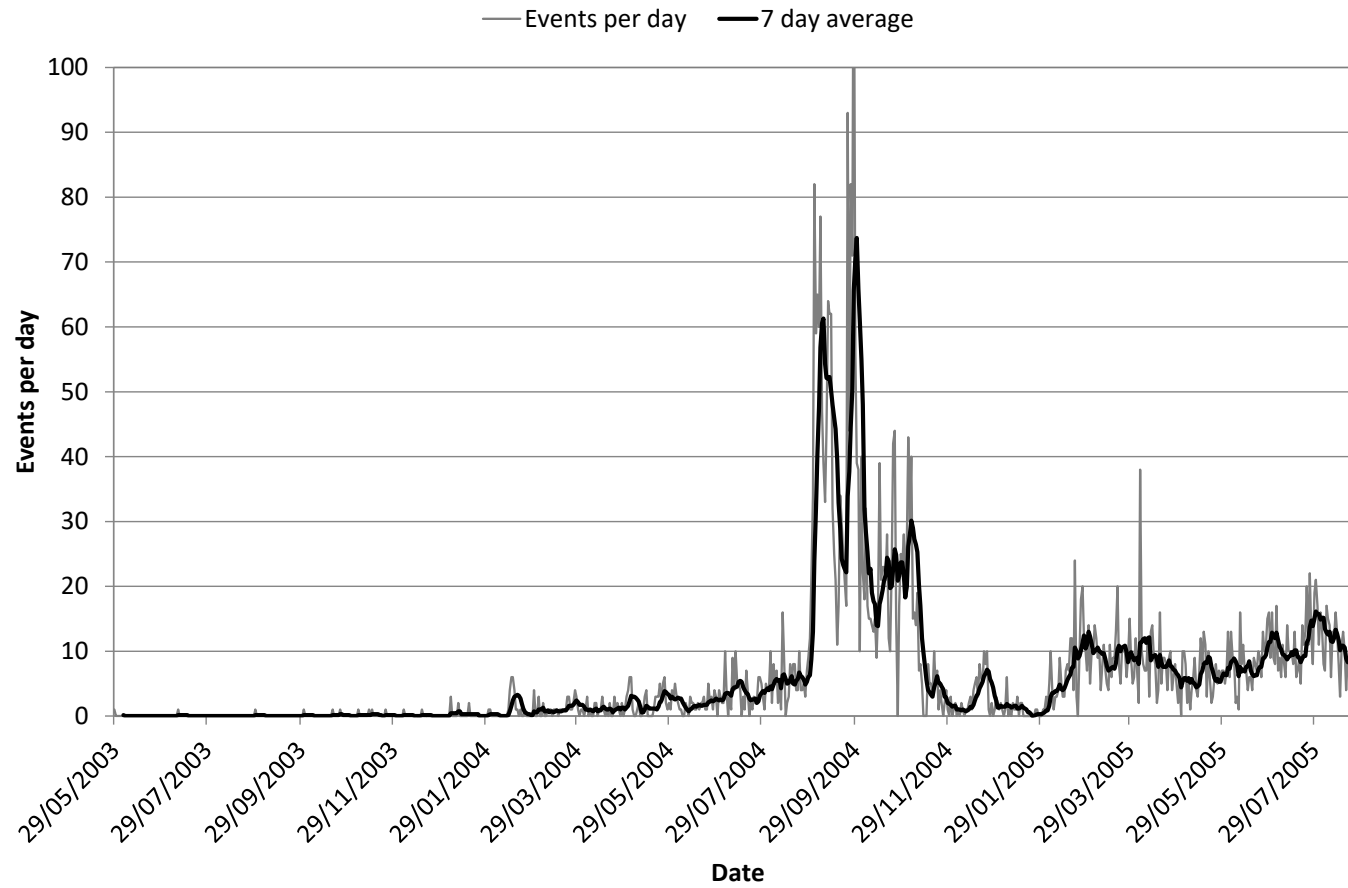


Figure A5 13: 7 day average events per day chart for Feral Fault.

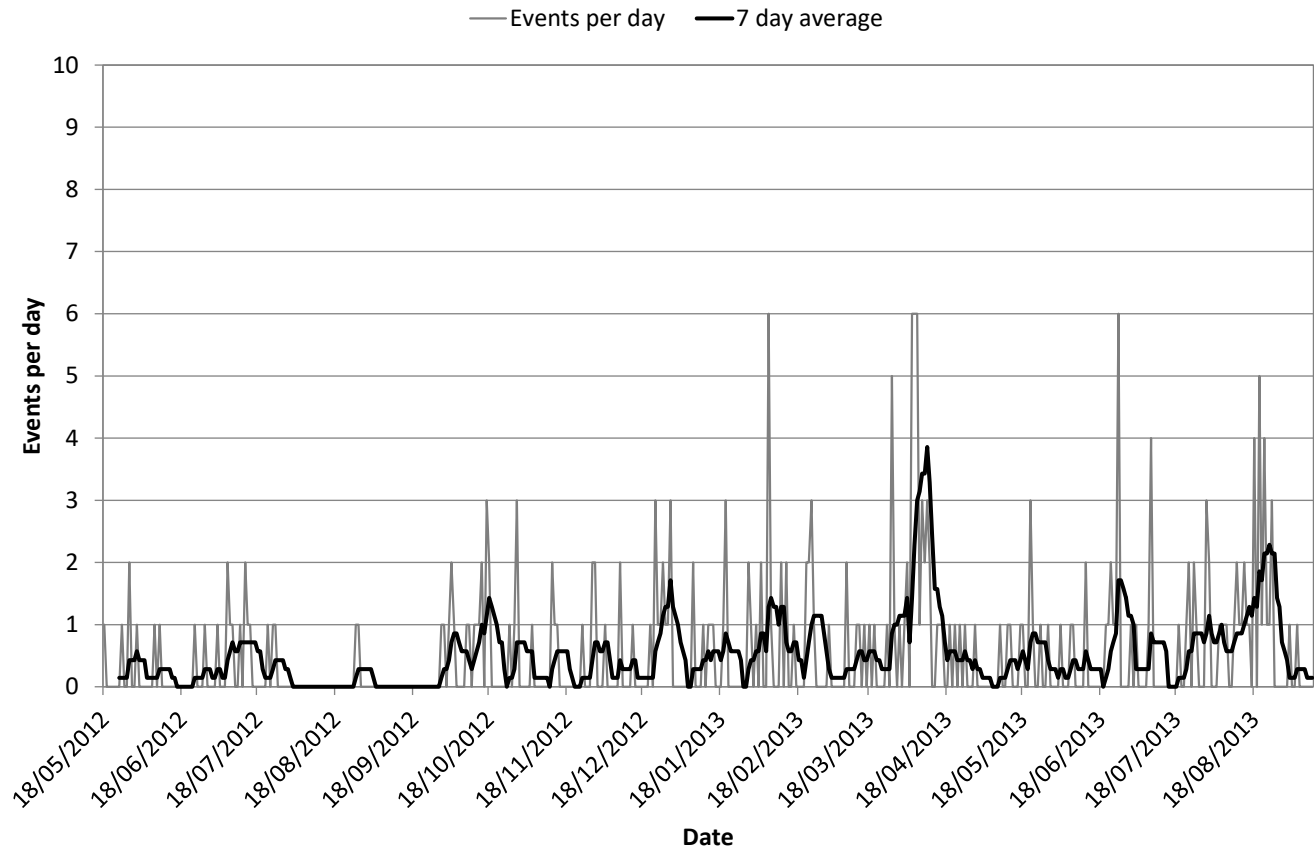


Figure A5 14: 7 day average events per day chart for Great Lyell Fault.

Appendix 6 – SCL 7 day group 5 charts

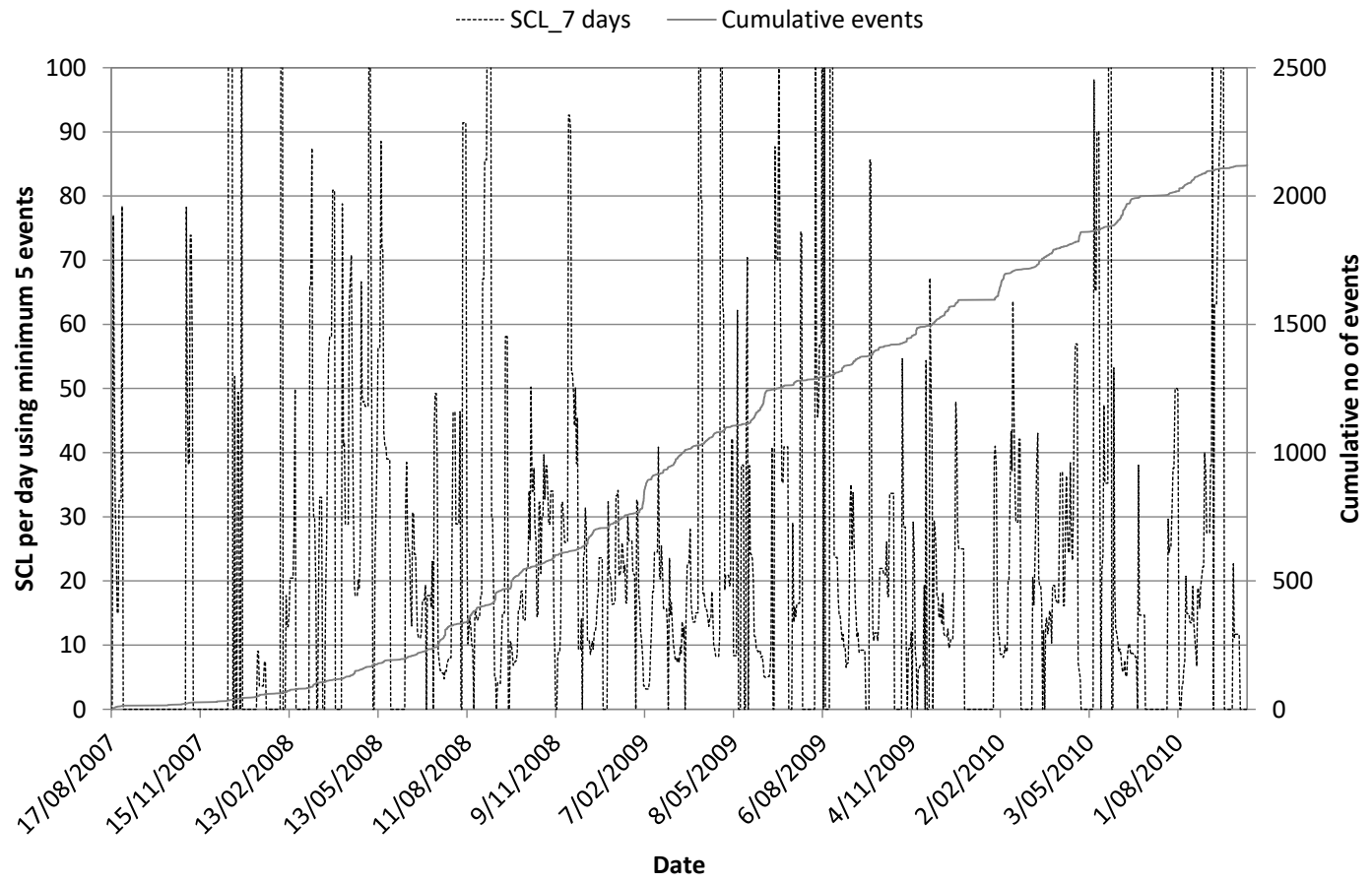


Figure A6 1: 7 day SCL chart for the A1 Shear.

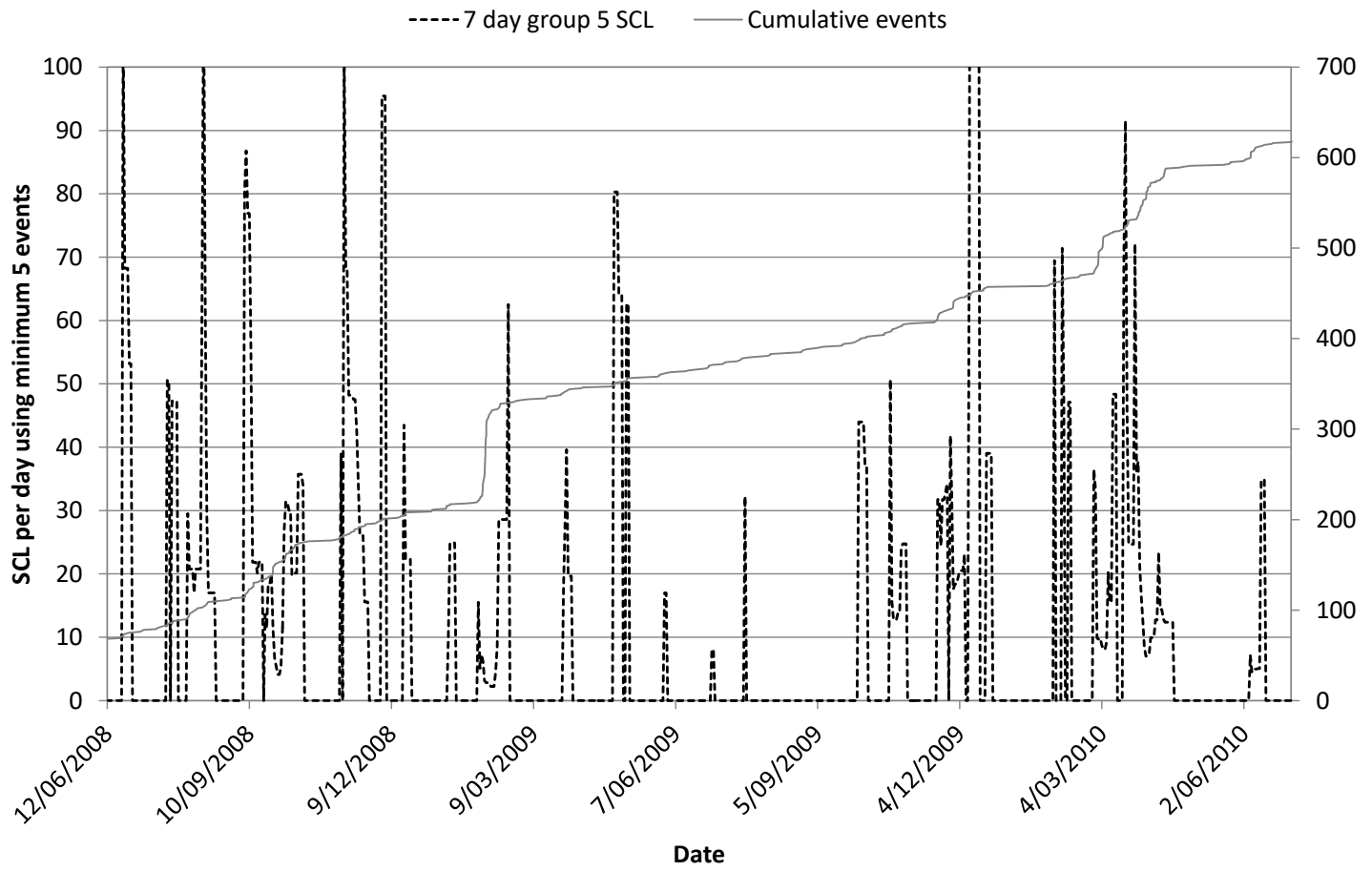


Figure A6 2: 7 day SCL chart for the North Dyke.

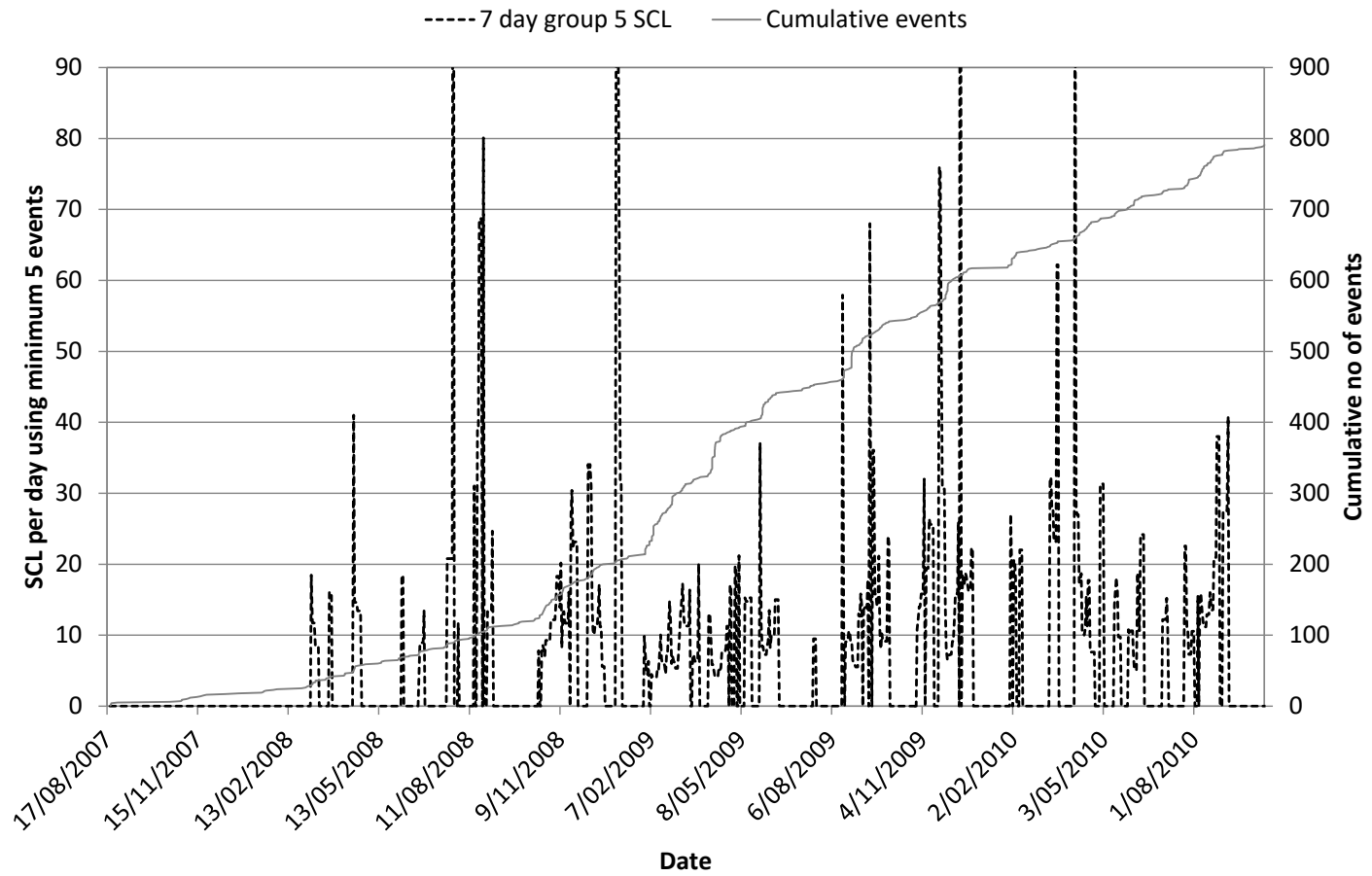


Figure A6 3: 7 day SCL chart for the Mini Dyke.

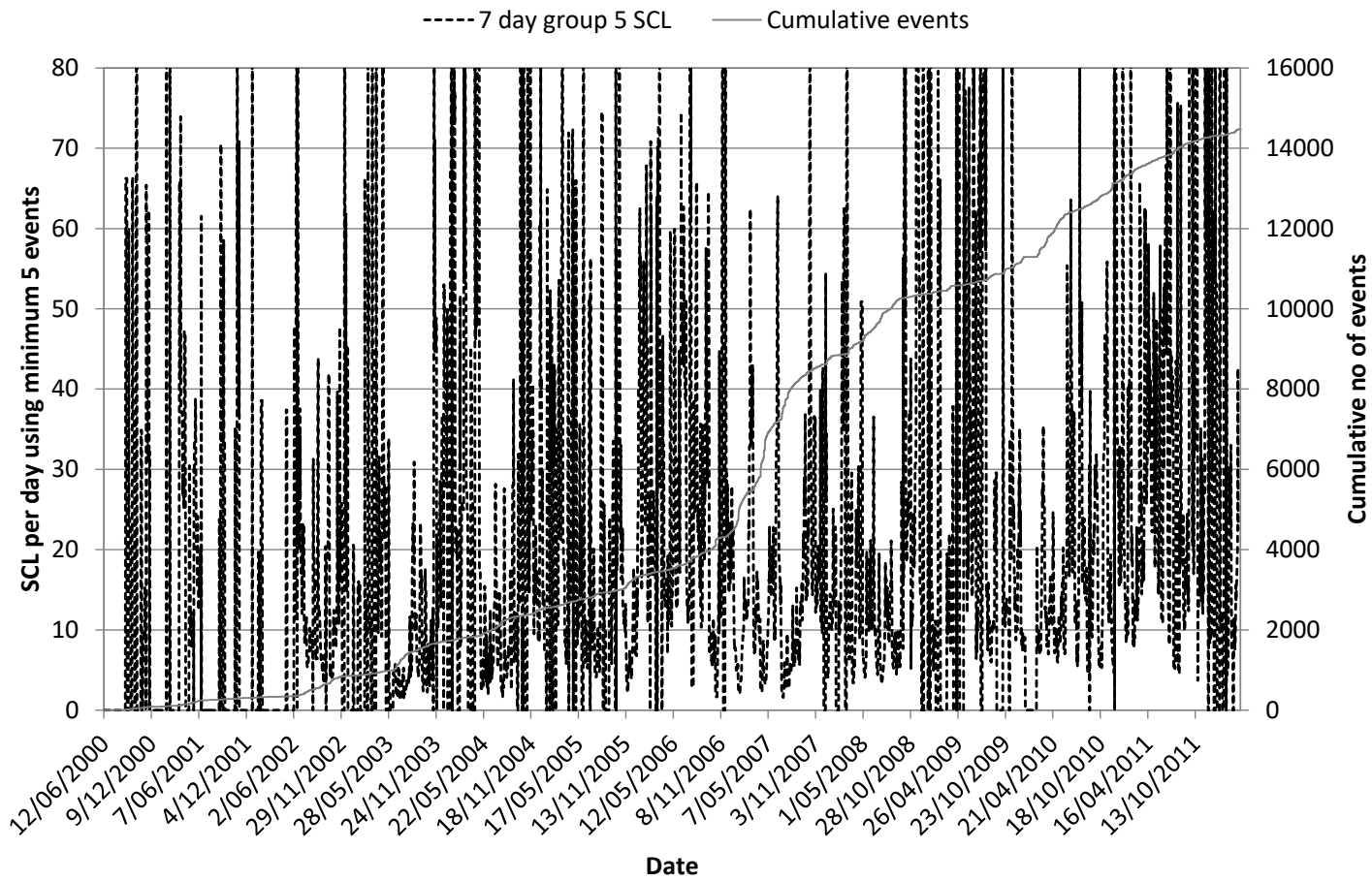


Figure A6 4: 7 day SCL chart for Fitzroy Fault.

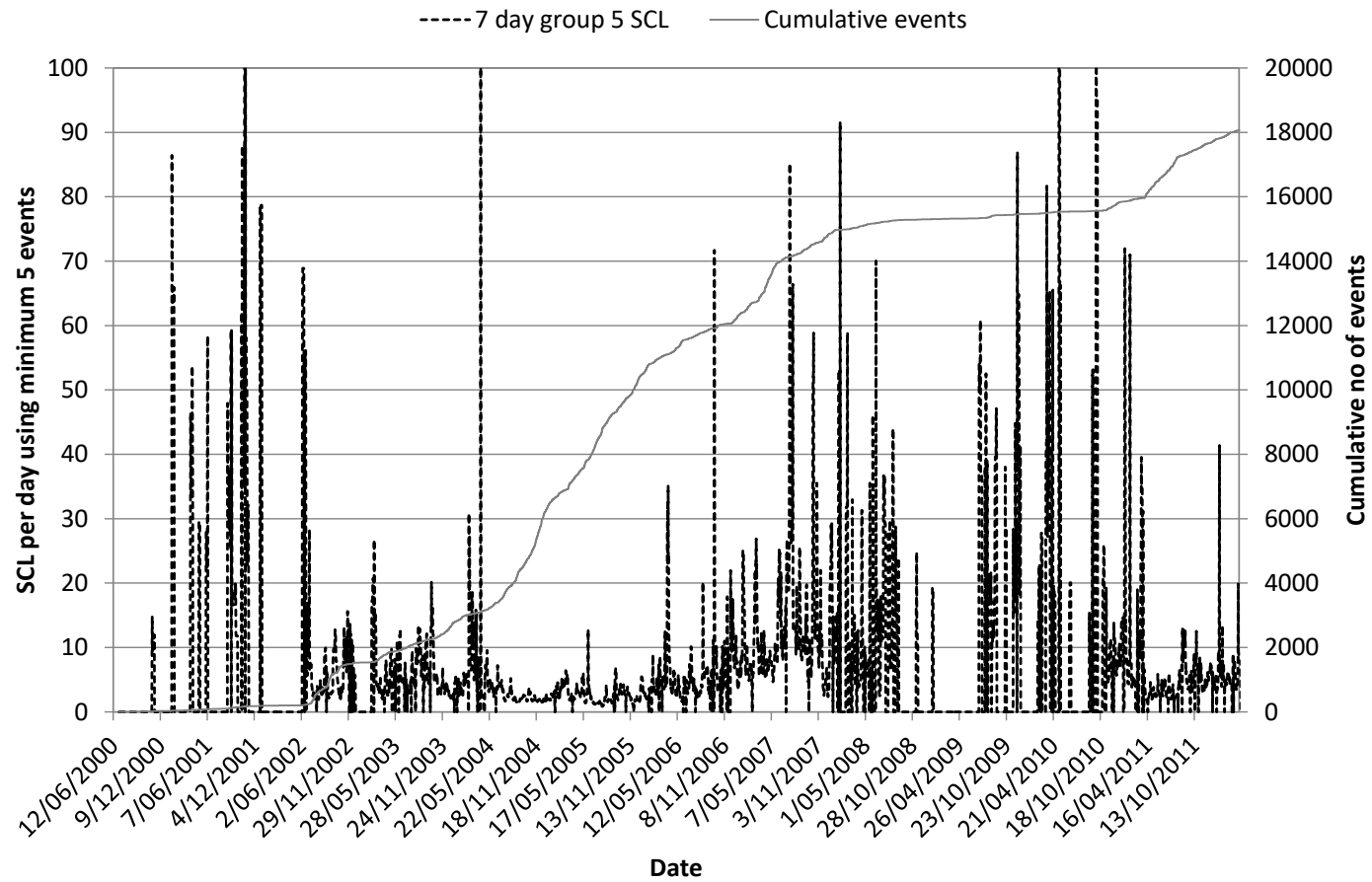


Figure A6 5: 7 day SCL chart for North East Faults Group 1.

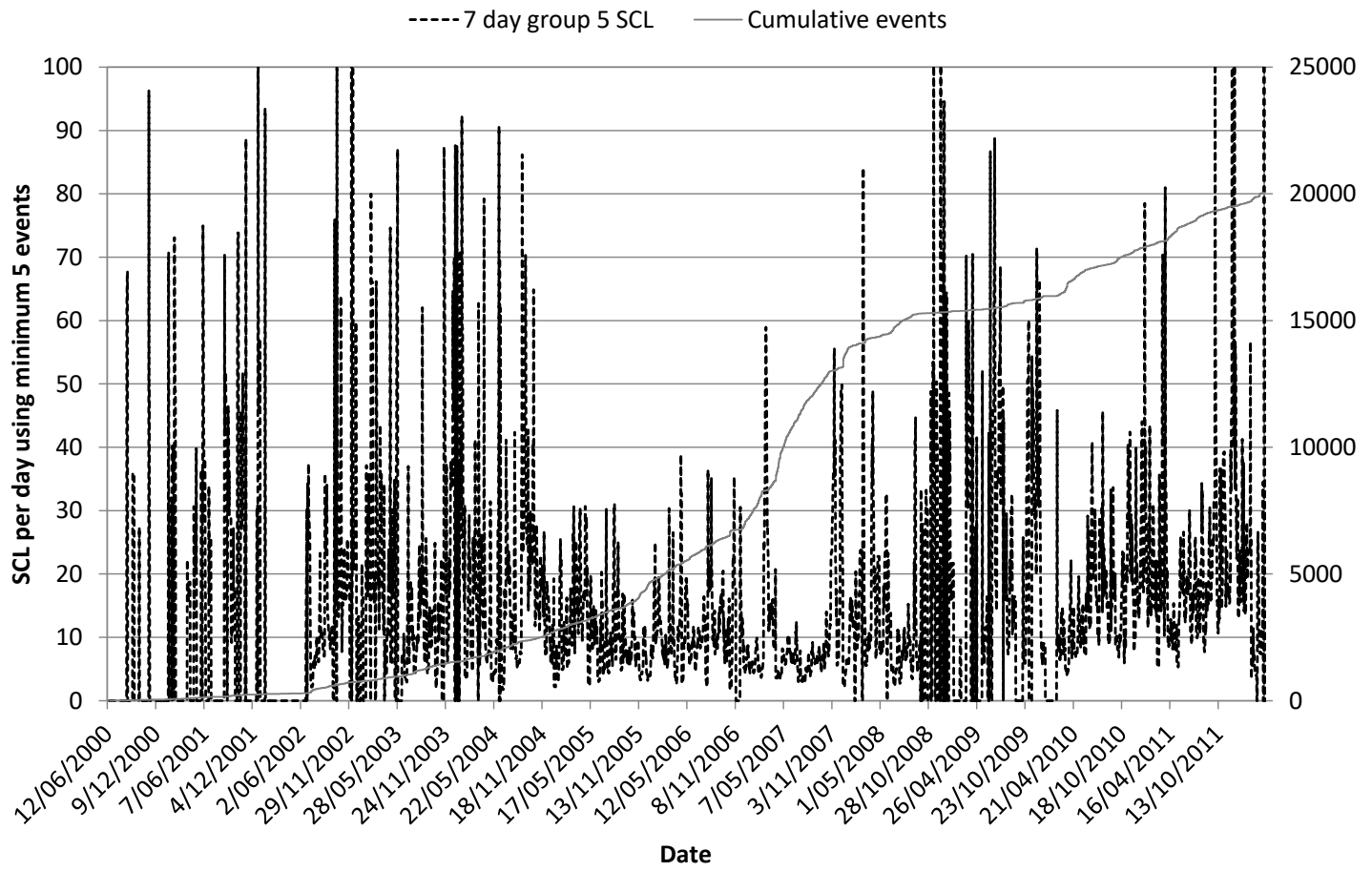


Figure A6 6: 7 day SCL chart for North East Faults Group 2.

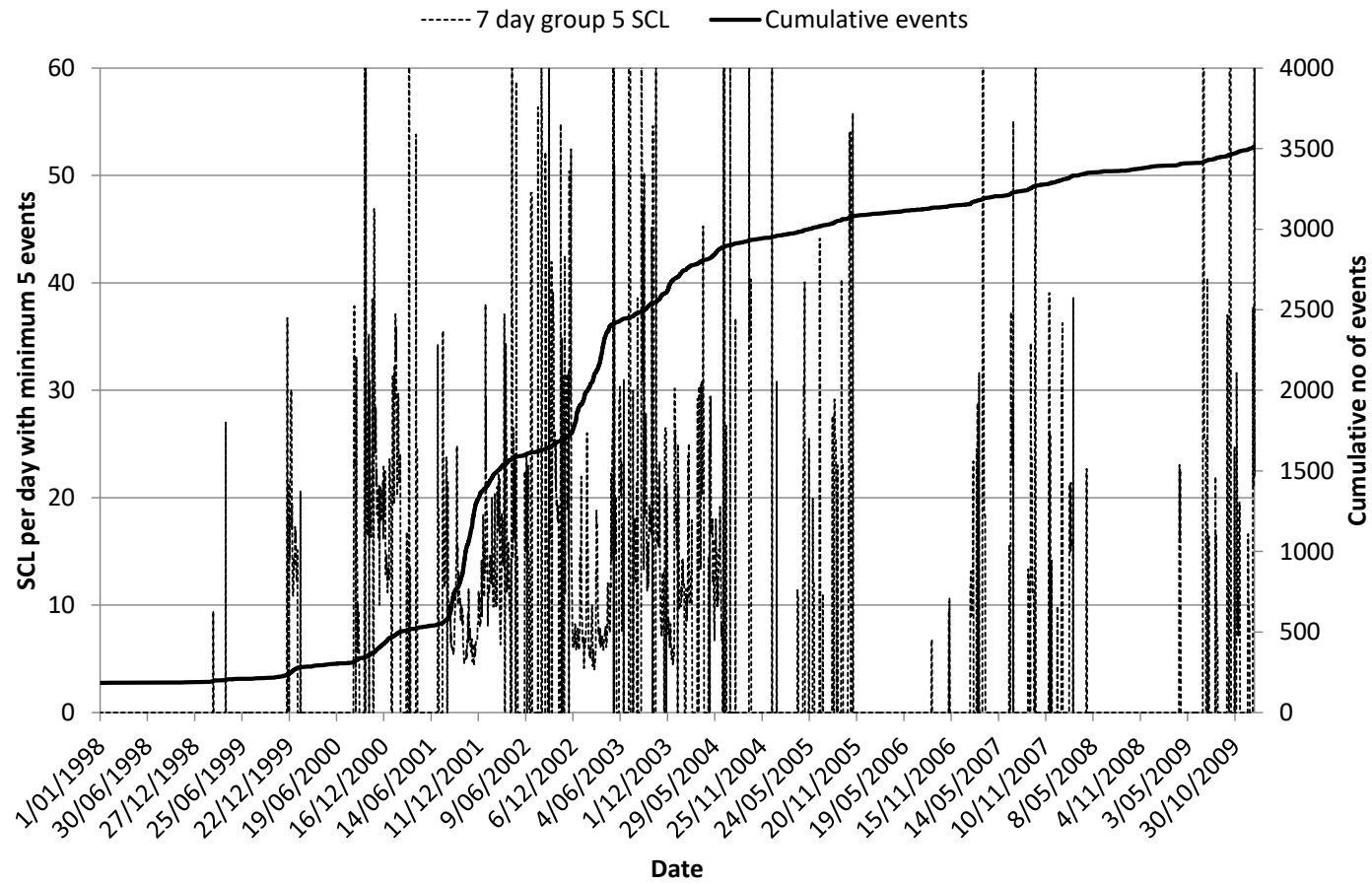


Figure A6 7: 7 day SCL chart for FaultP_1

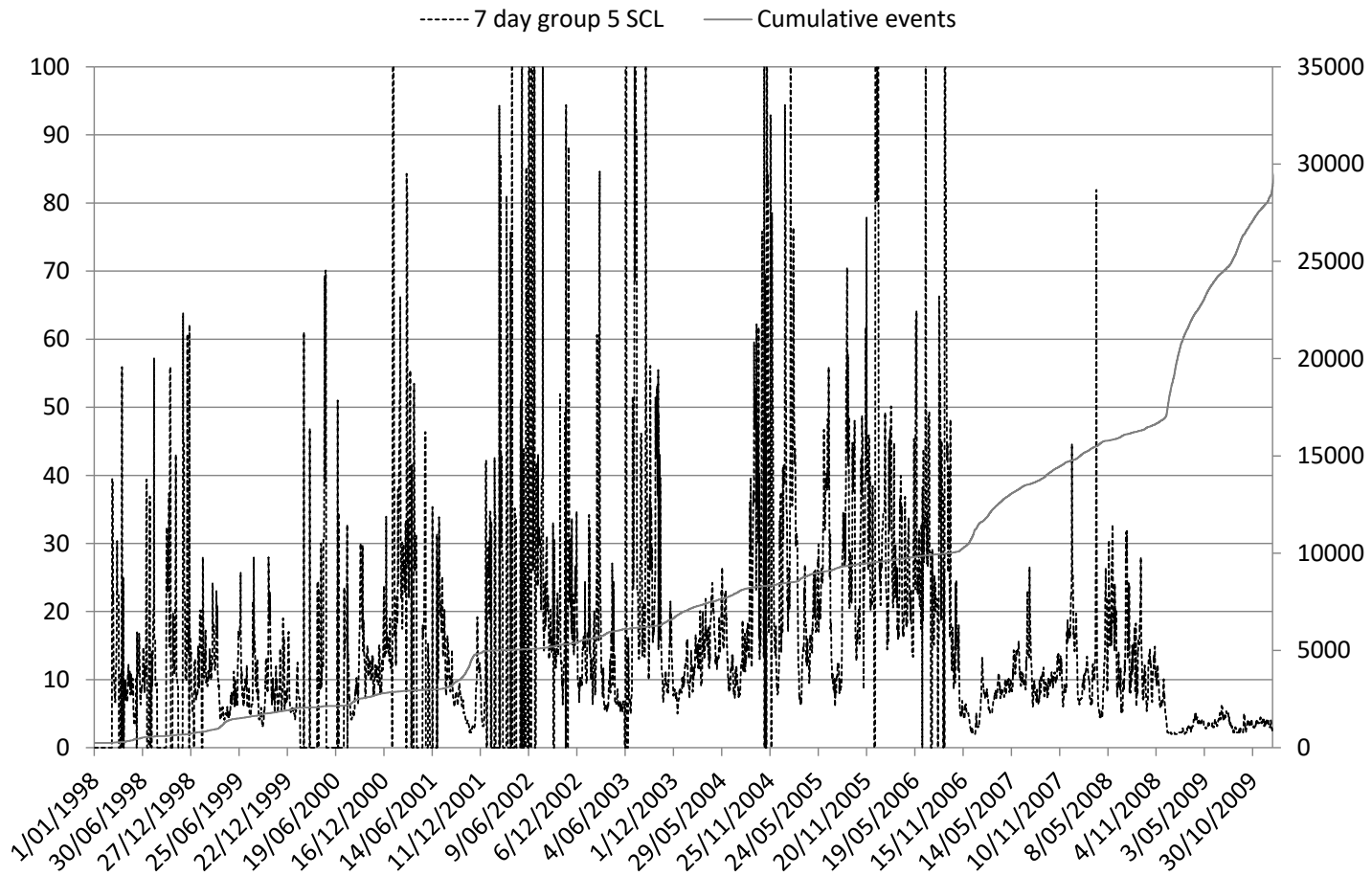


Figure A6 8: 7 day SCL chart for Fault B_C.

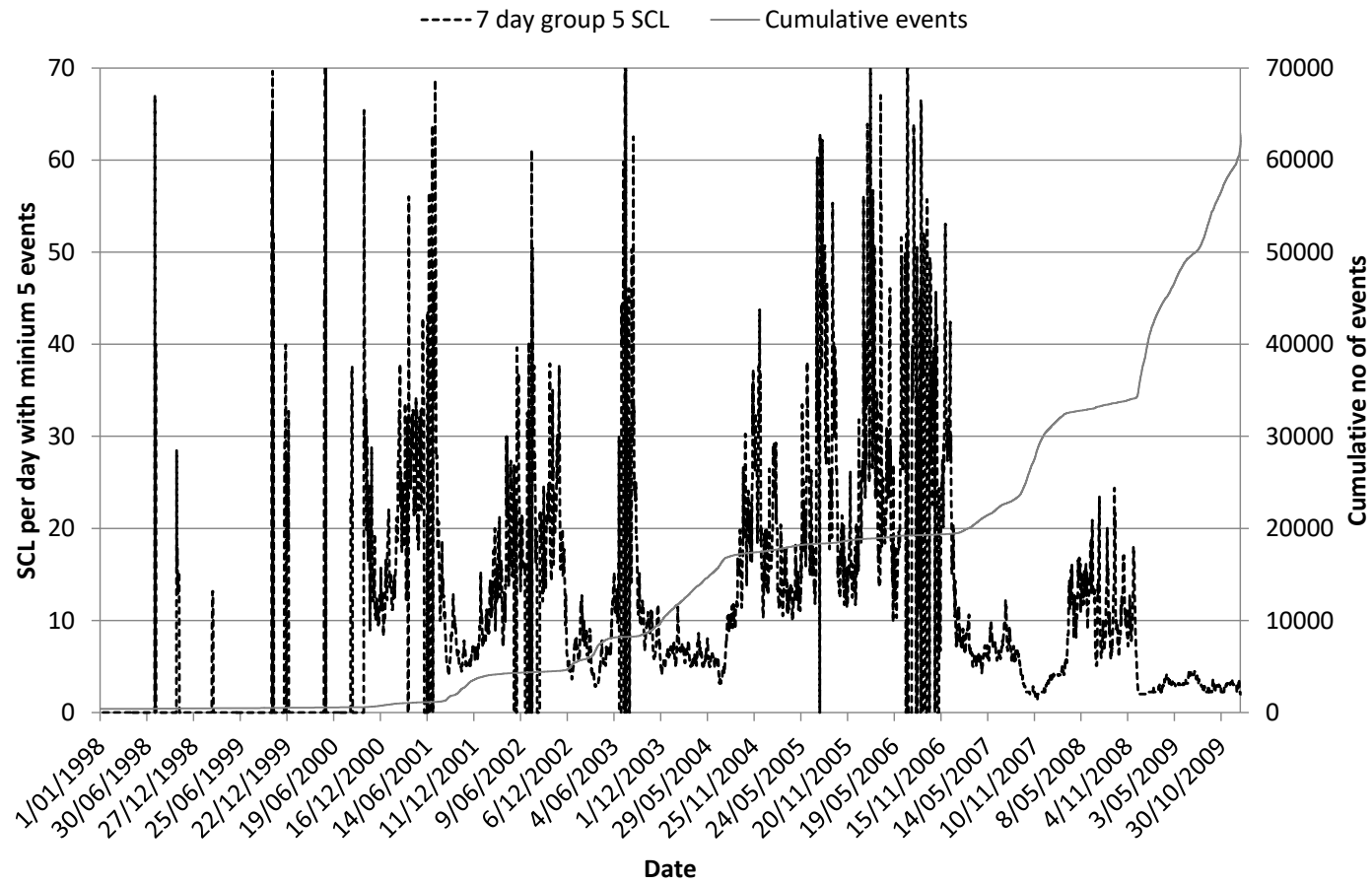


Figure A6 9: 7 day SCL chart for the FW Dyke.

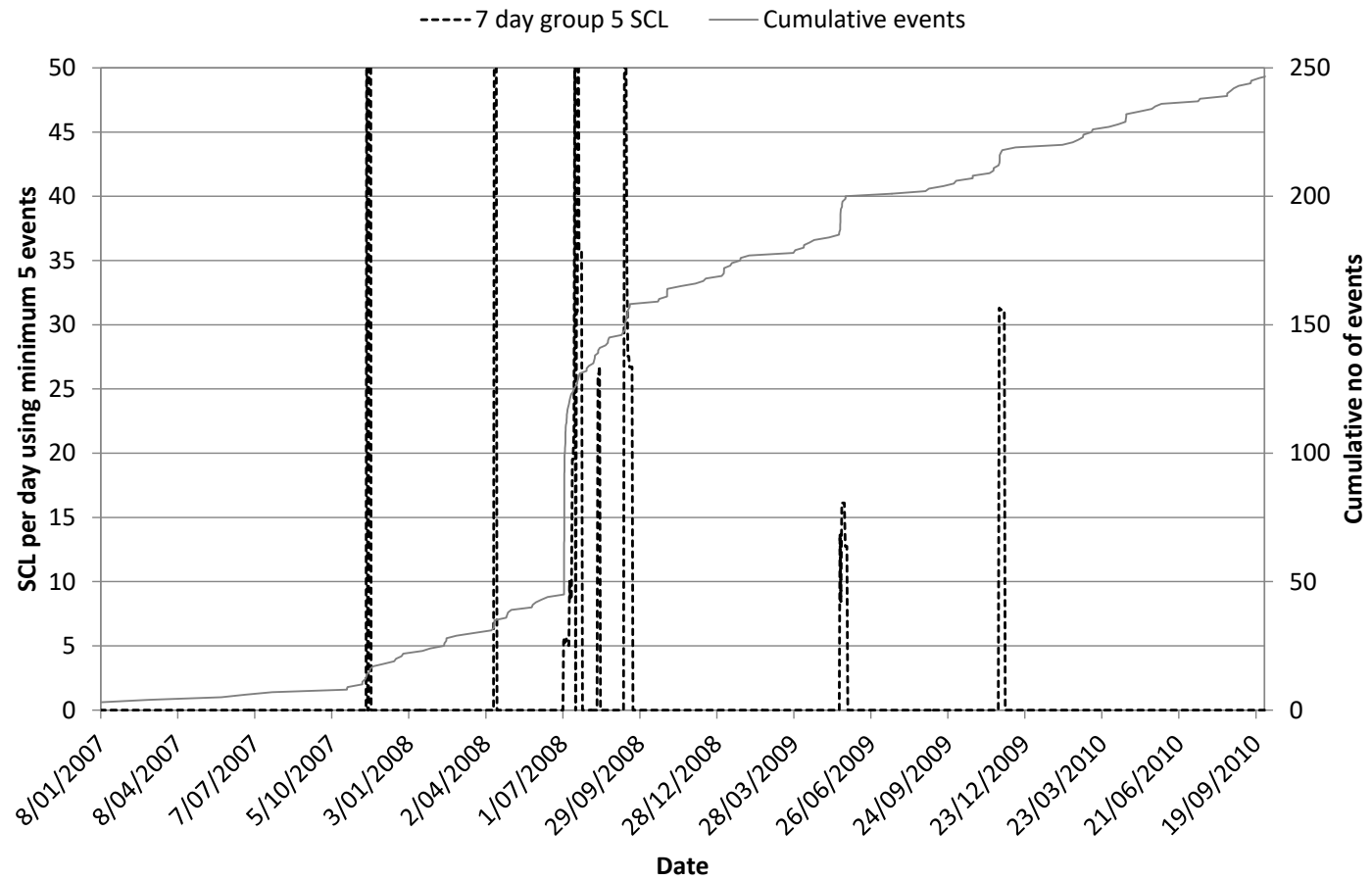


Figure A6 10: 7 day SCL chart for Maritana Fault.

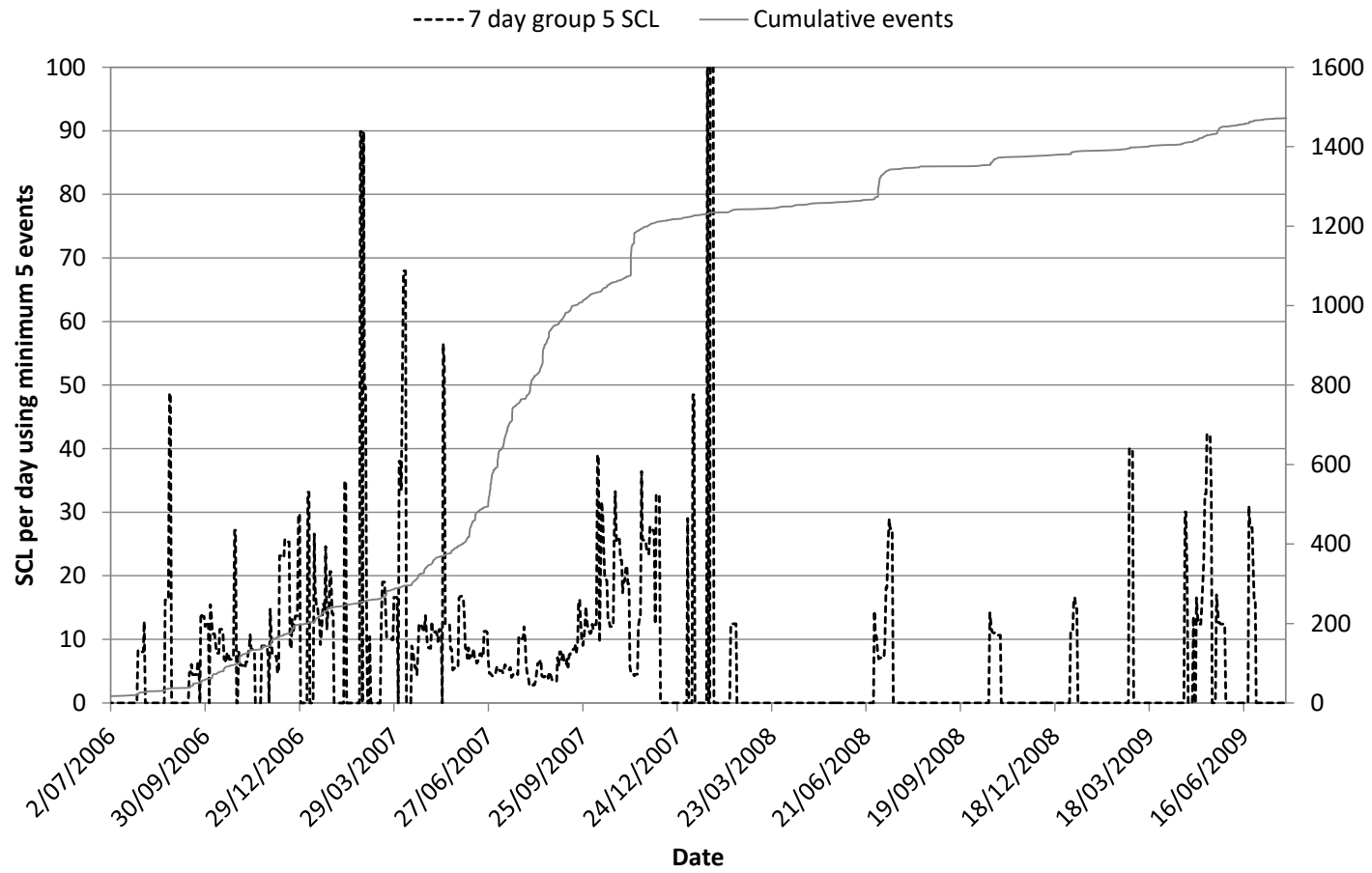


Figure A6 11: 7 day SCL chart for Reward Fault.

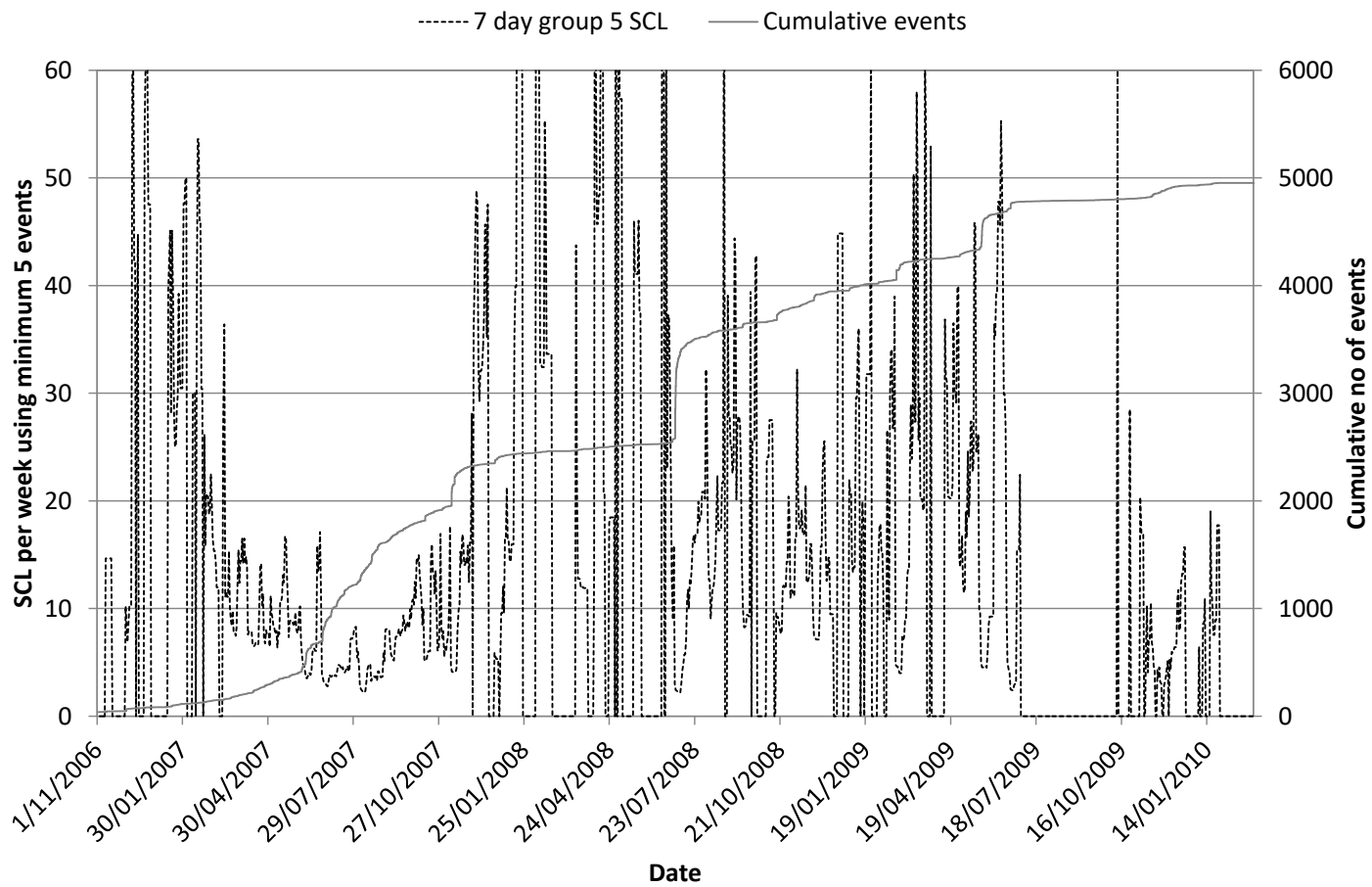


Figure A6 12: 7 day SCL chart for Flanagan Fault.

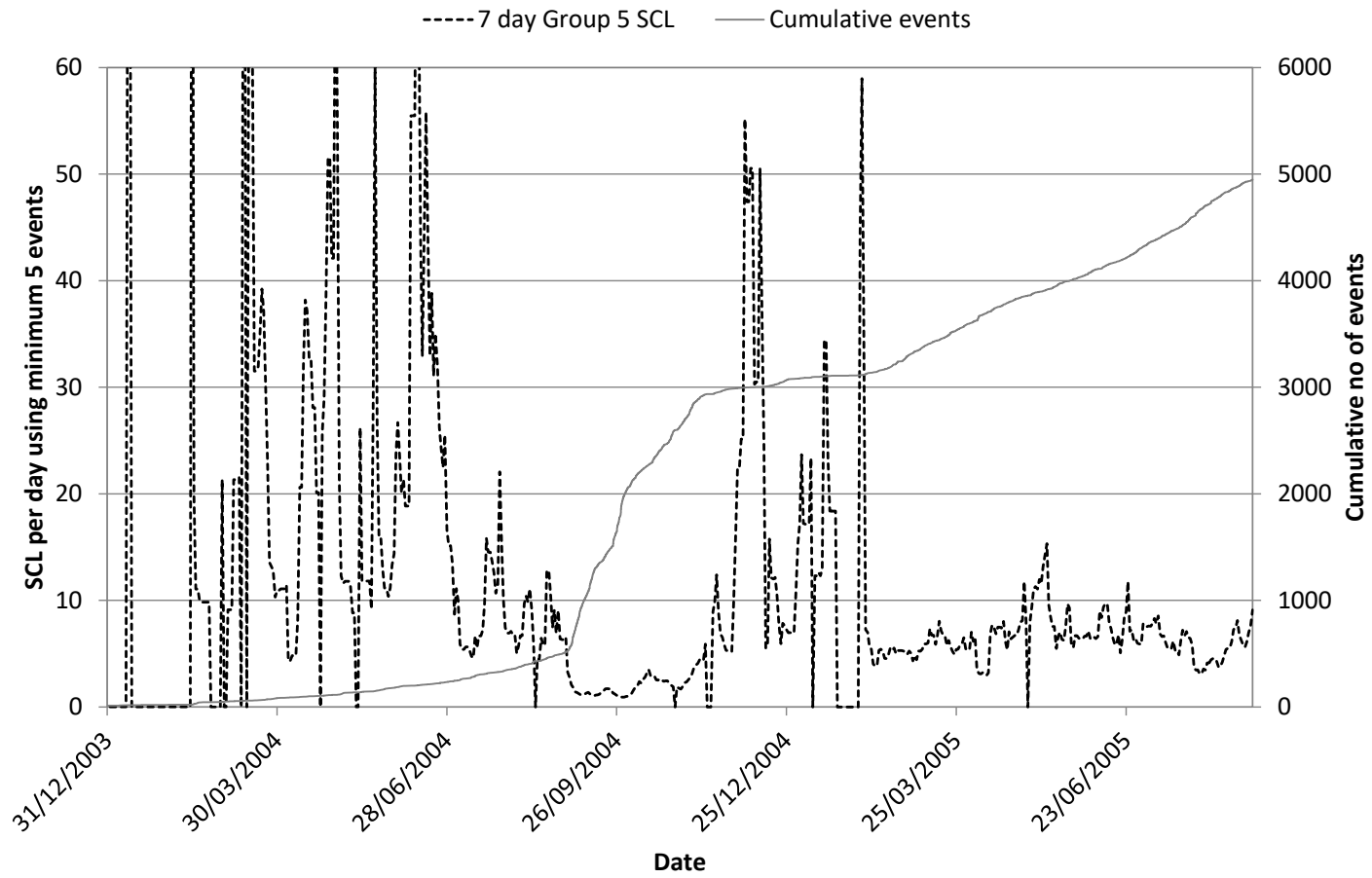


Figure A6 13: 7 day SCL chart for Feral Fault.

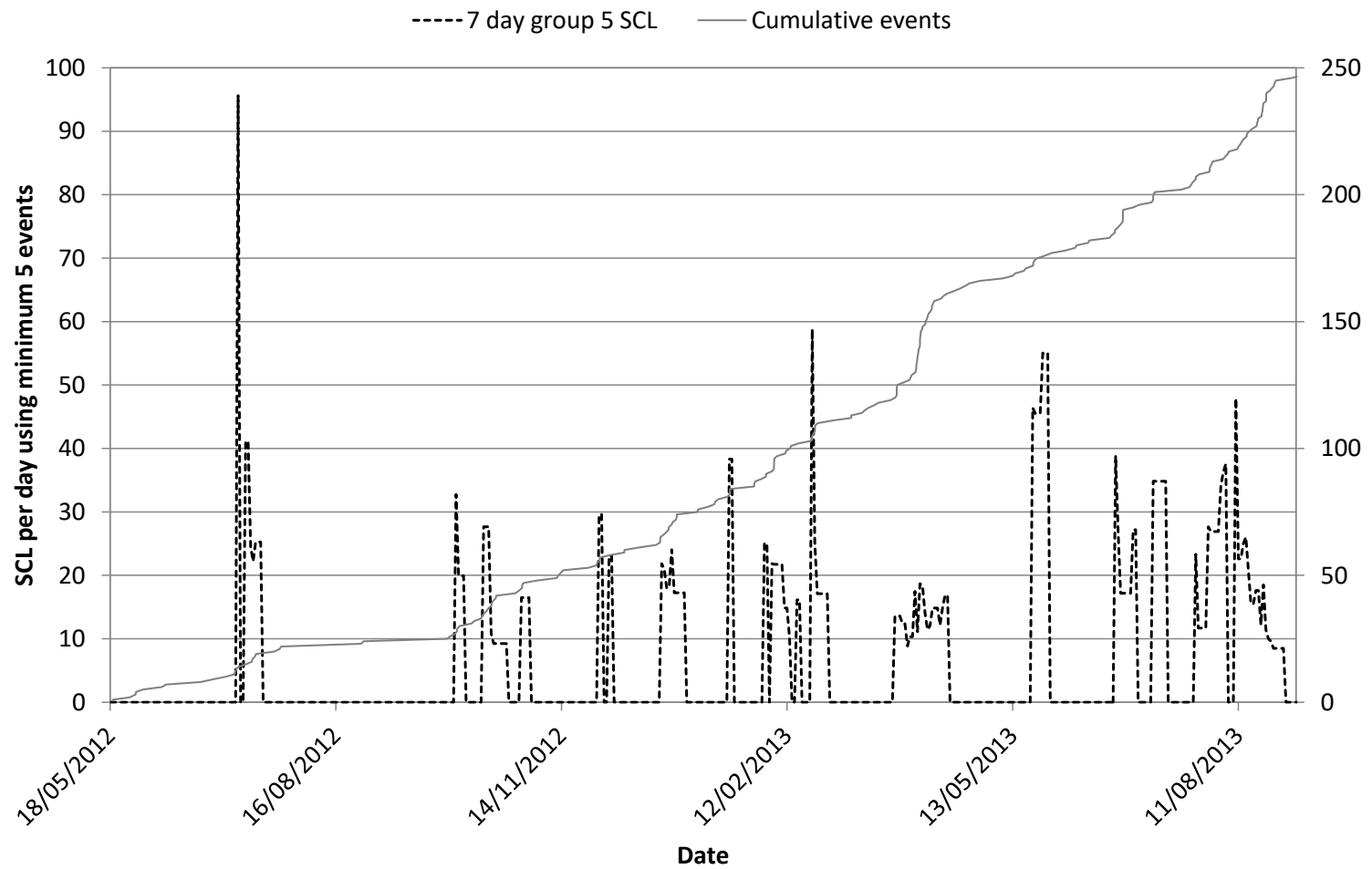


Figure A6 14: 7 day SCL chart for Great Lyell Fault.

Appendix 7 – MVM daily and 7 day charts

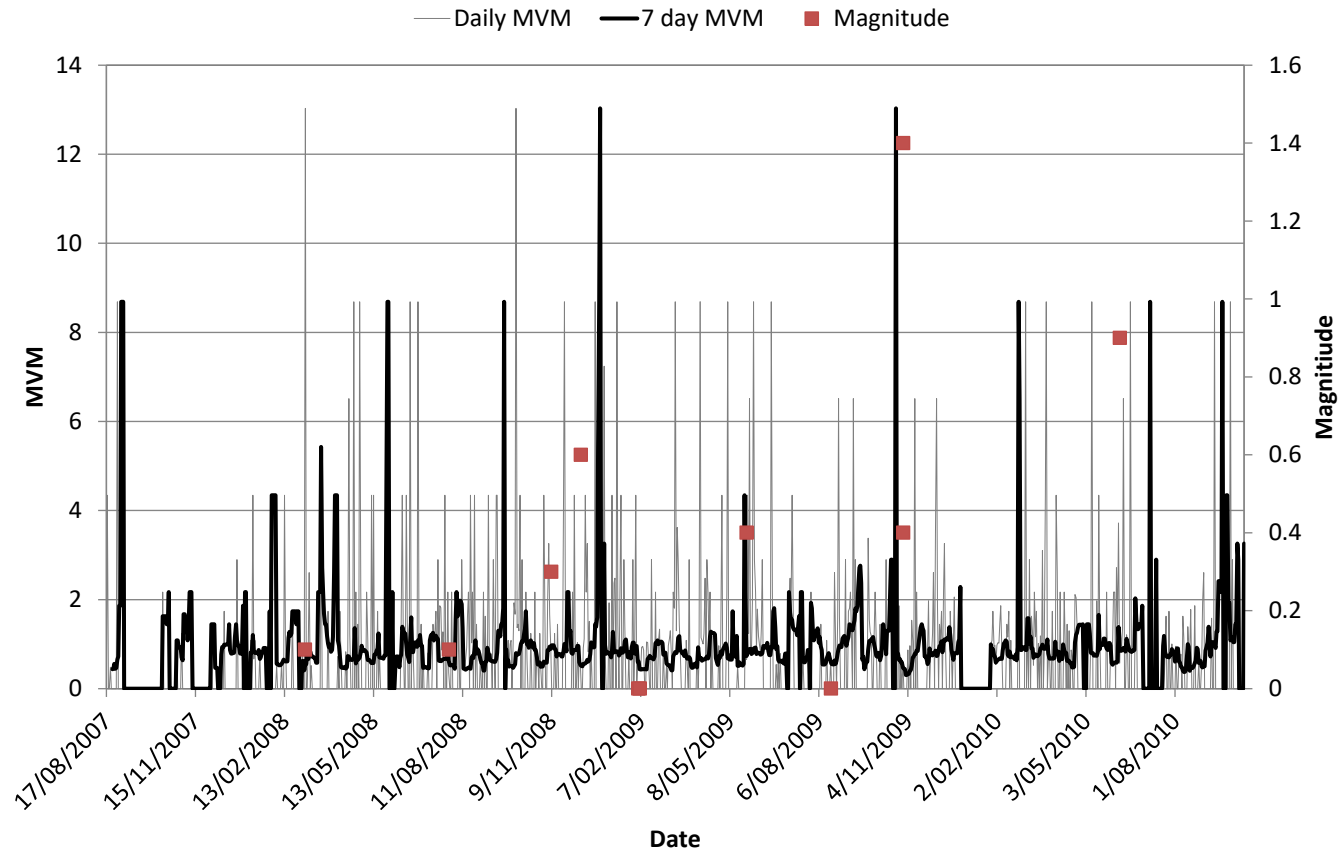


Figure A7 1: Daily MVM chart for the A1 Shear.

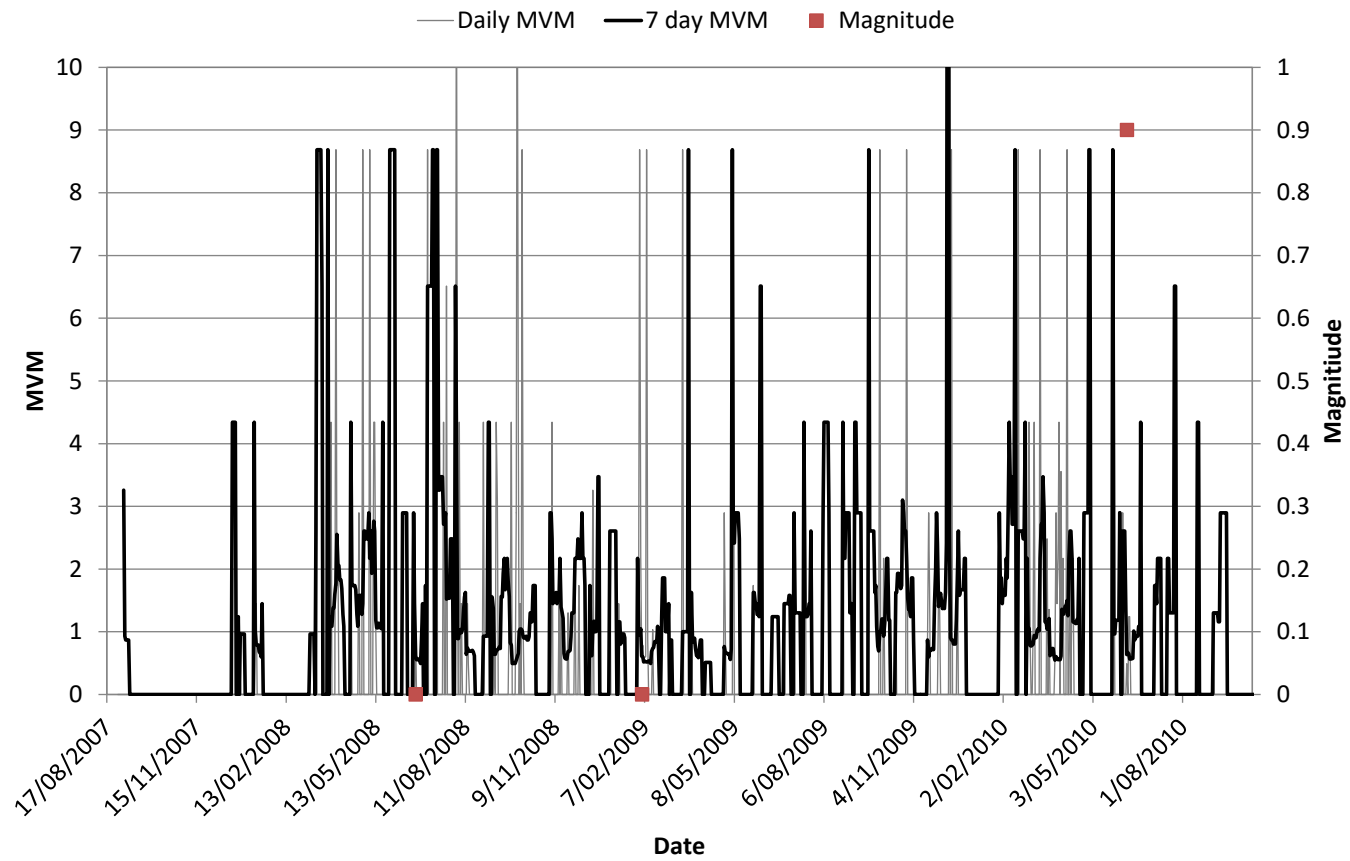


Figure A7 2: Daily MVM chart for the North Dyke.

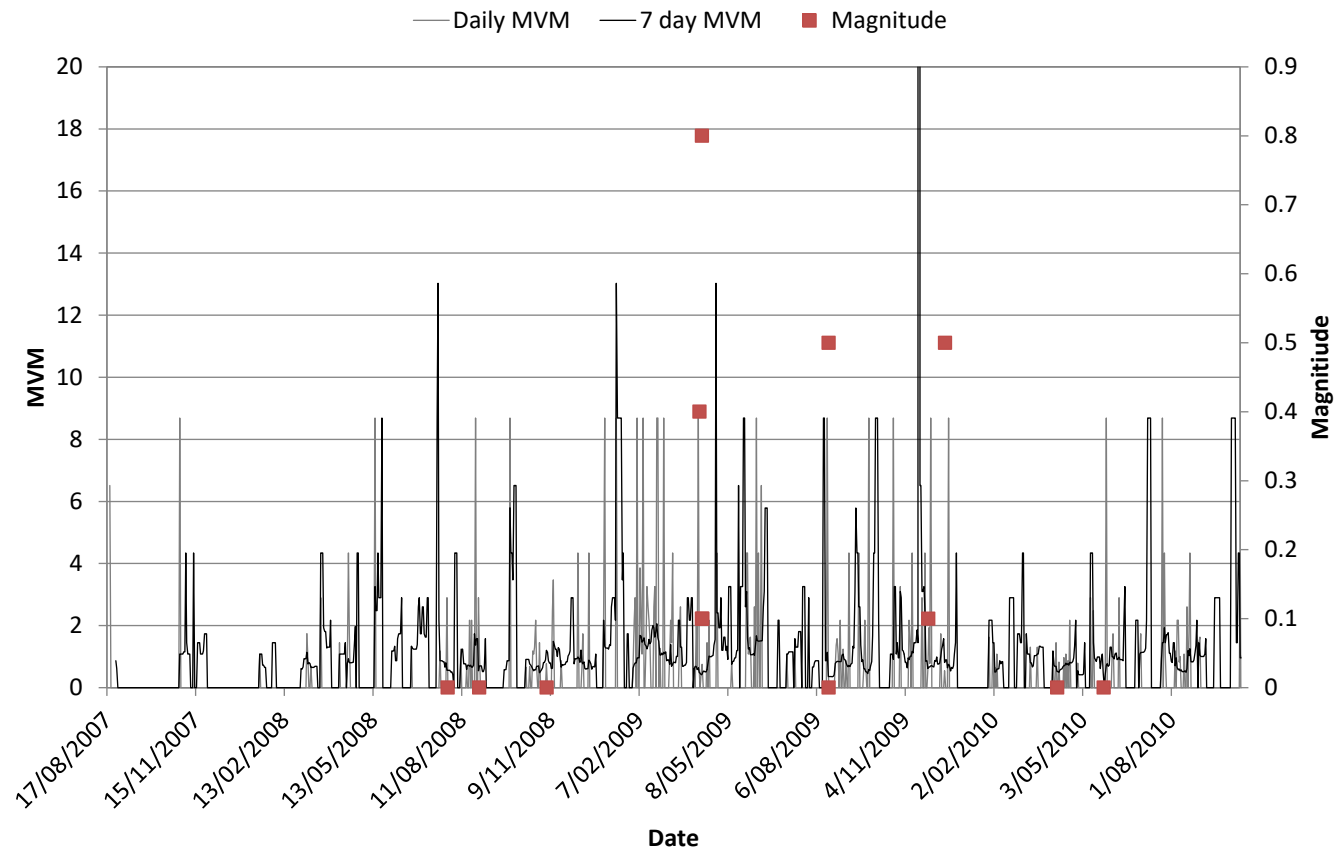


Figure A7 3: Daily MVM chart for the Mini Dyke.

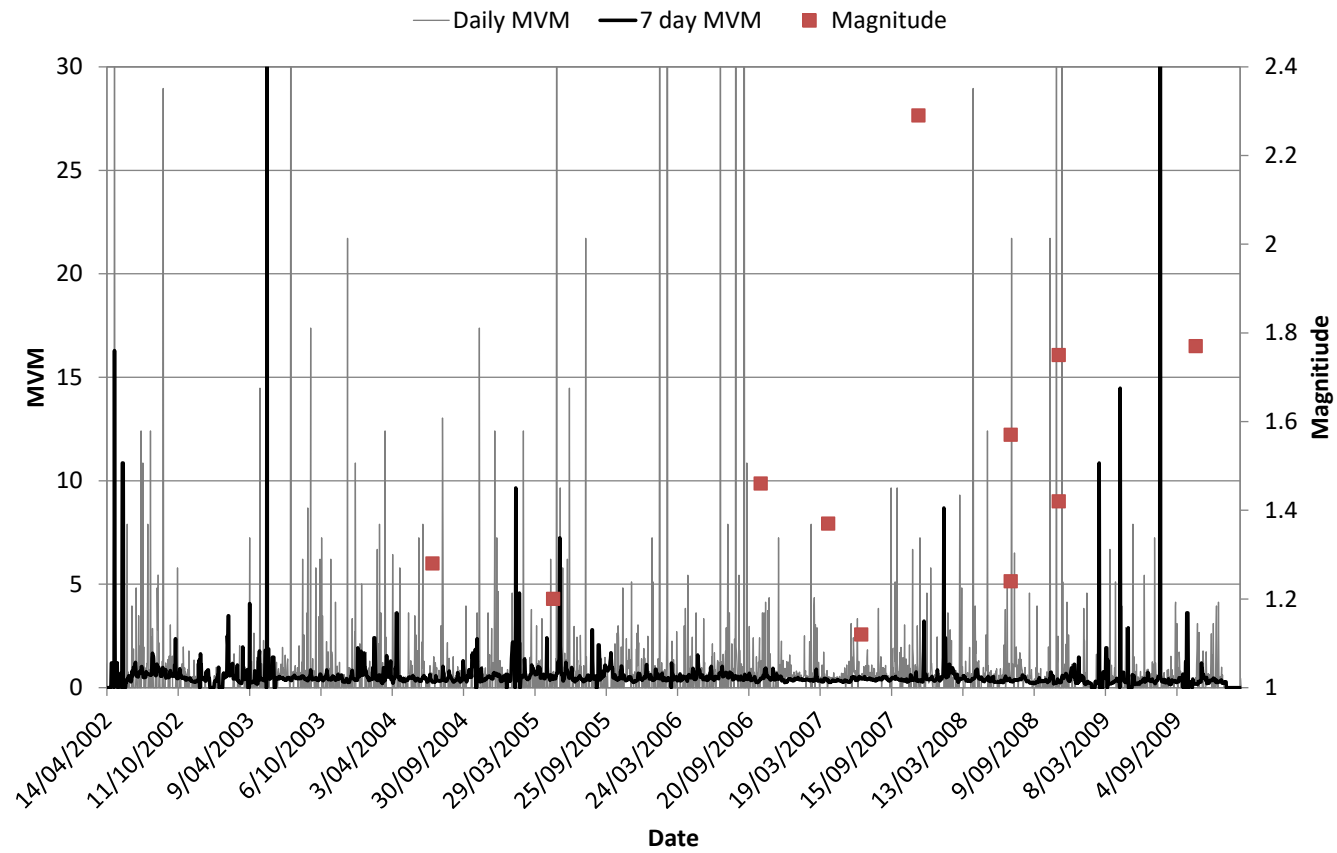


Figure A7 4: Daily MVM chart for Fitzroy Fault.

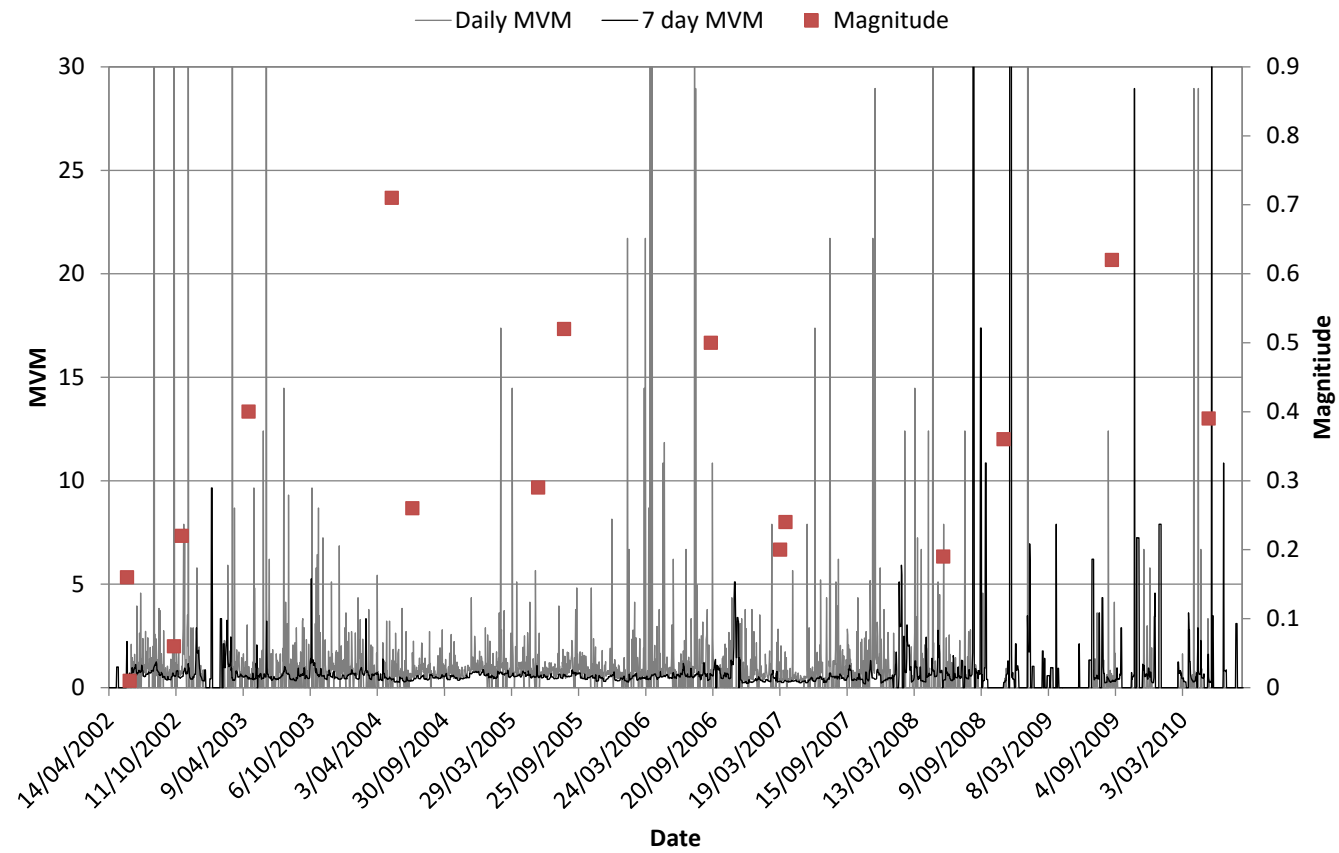


Figure A7 5: Daily MVM chart for North East Faults Group 1.

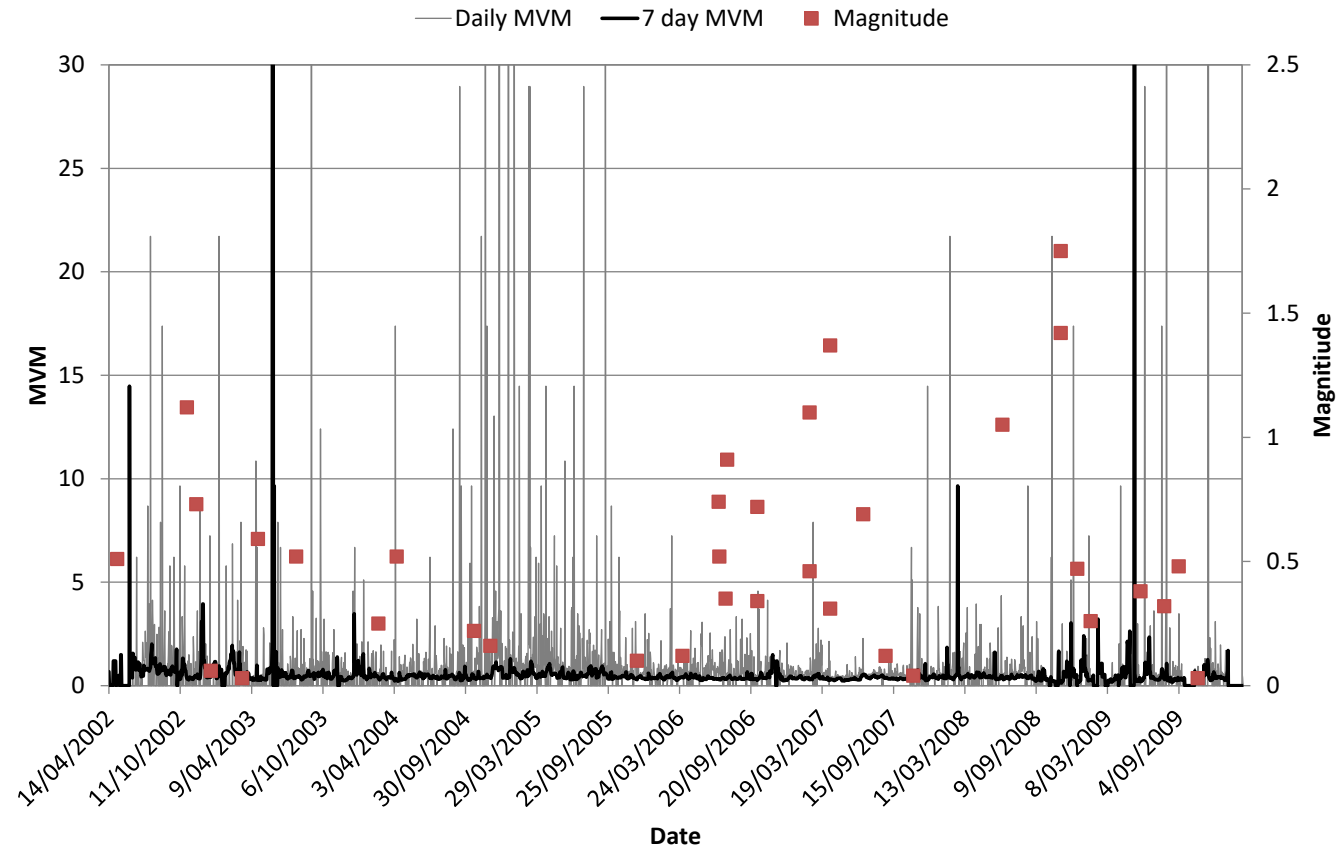


Figure A7 6: Daily MVM chart for North East Faults Group 2.

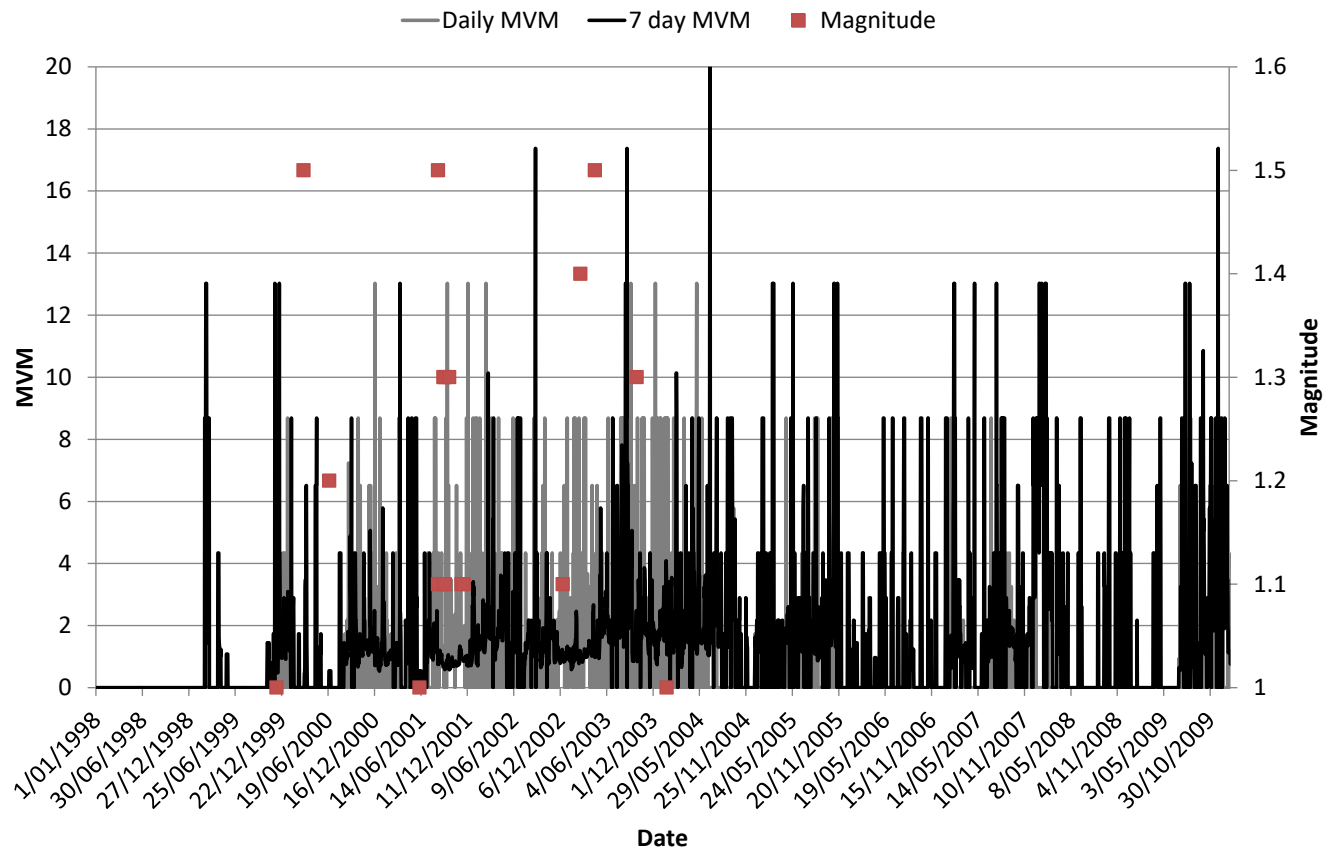


Figure A7 7: Daily MVM chart for FaultP_1

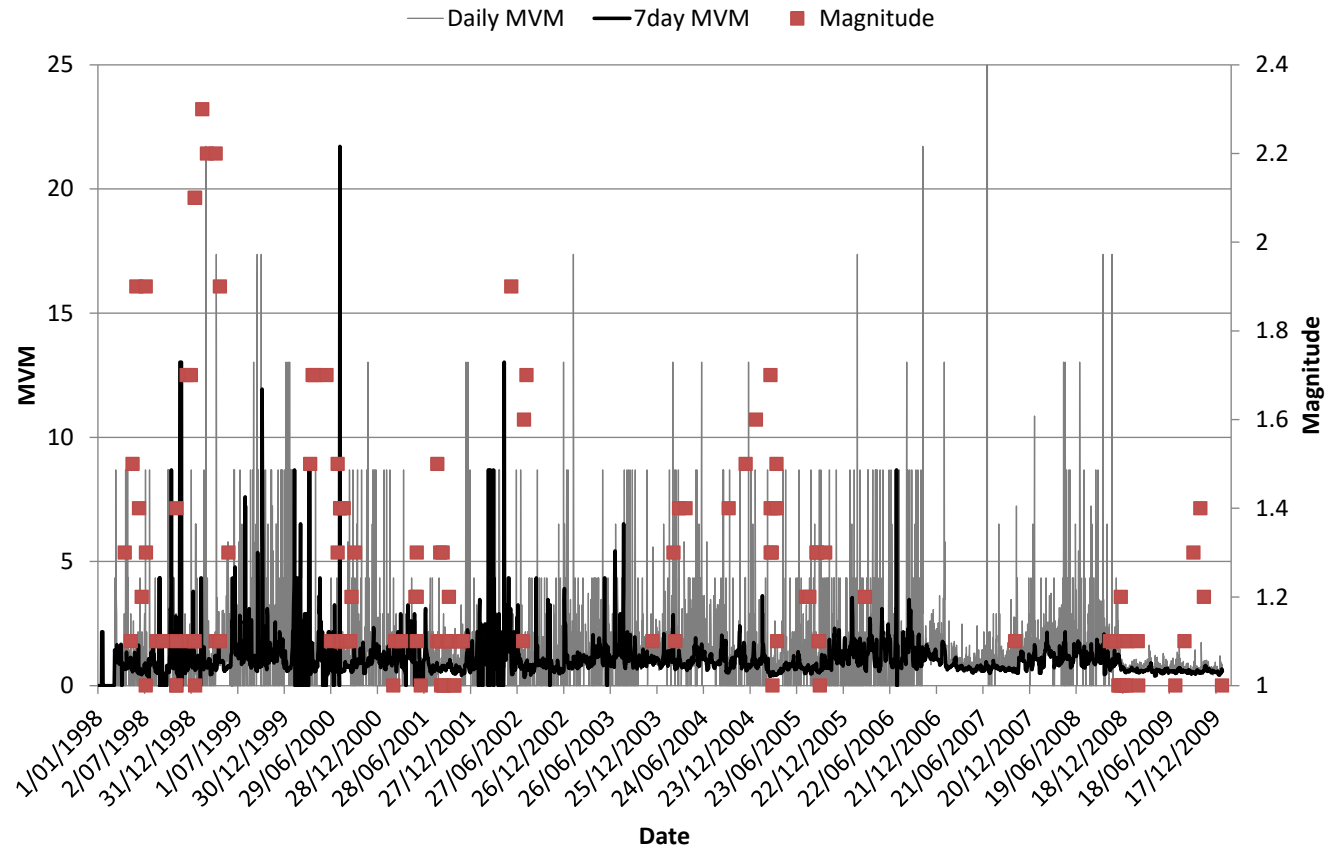


Figure A7 8: Daily MVM chart for Fault B_C.

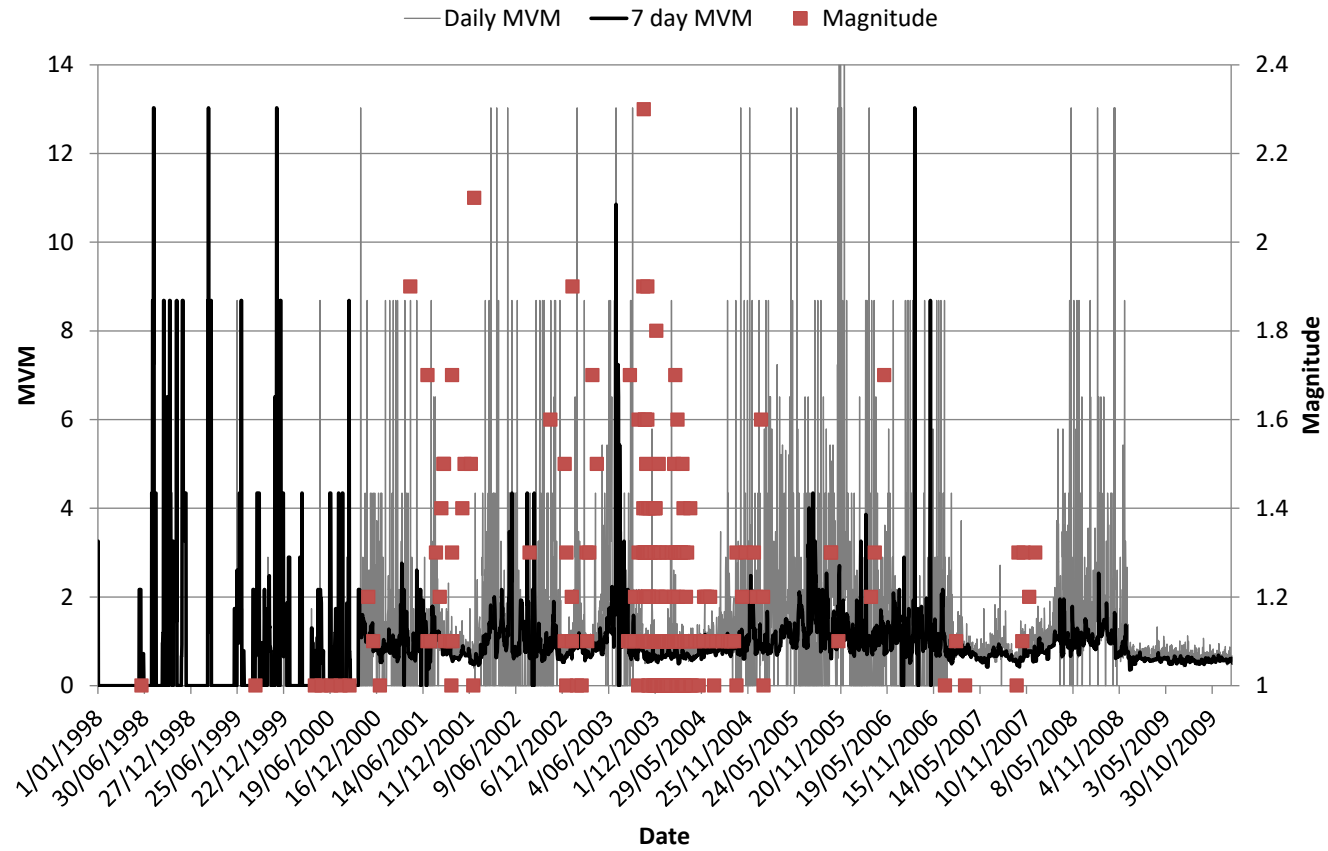


Figure A7 9: Daily MVM chart for the FW Dyke.

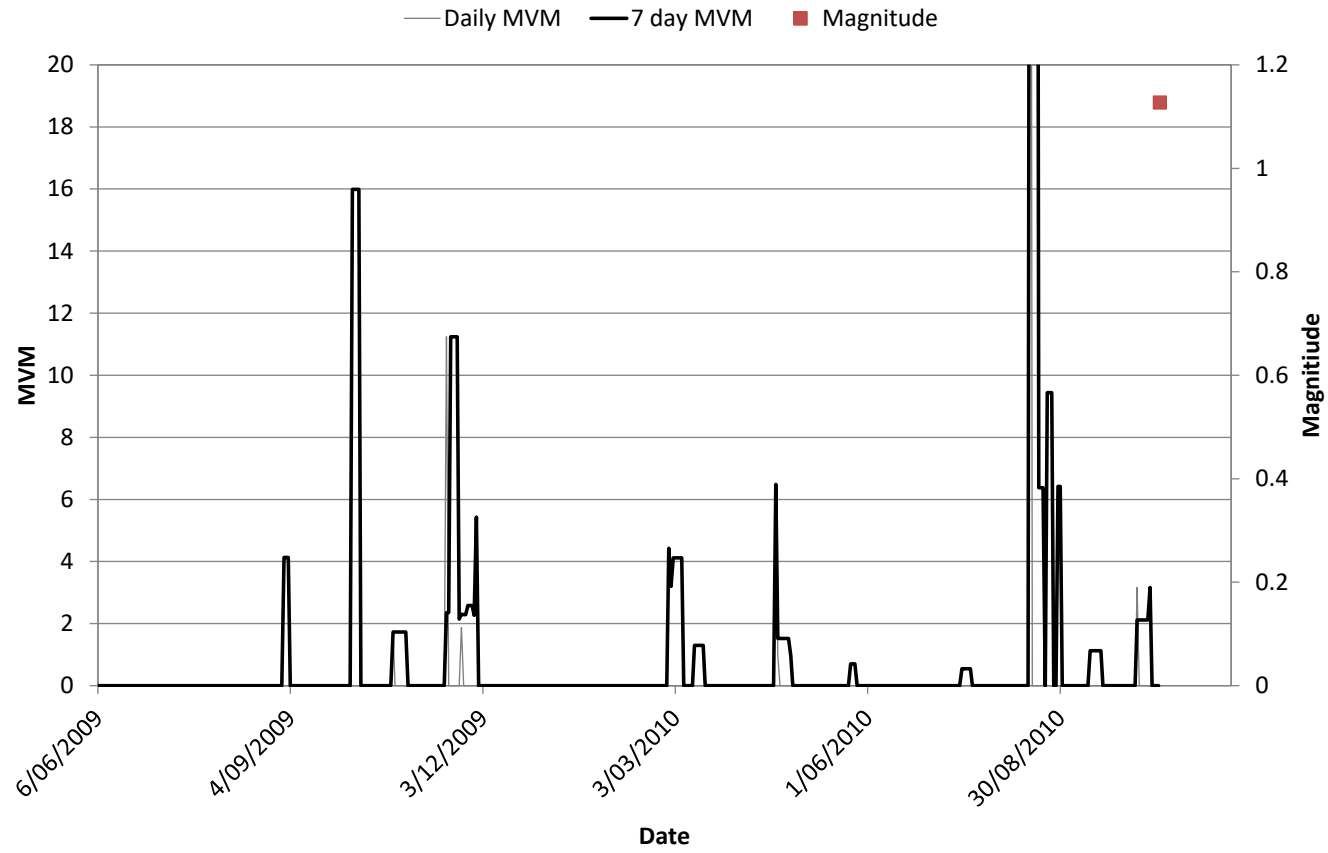


Figure A7 10: Daily MVM chart for Maritana Fault.

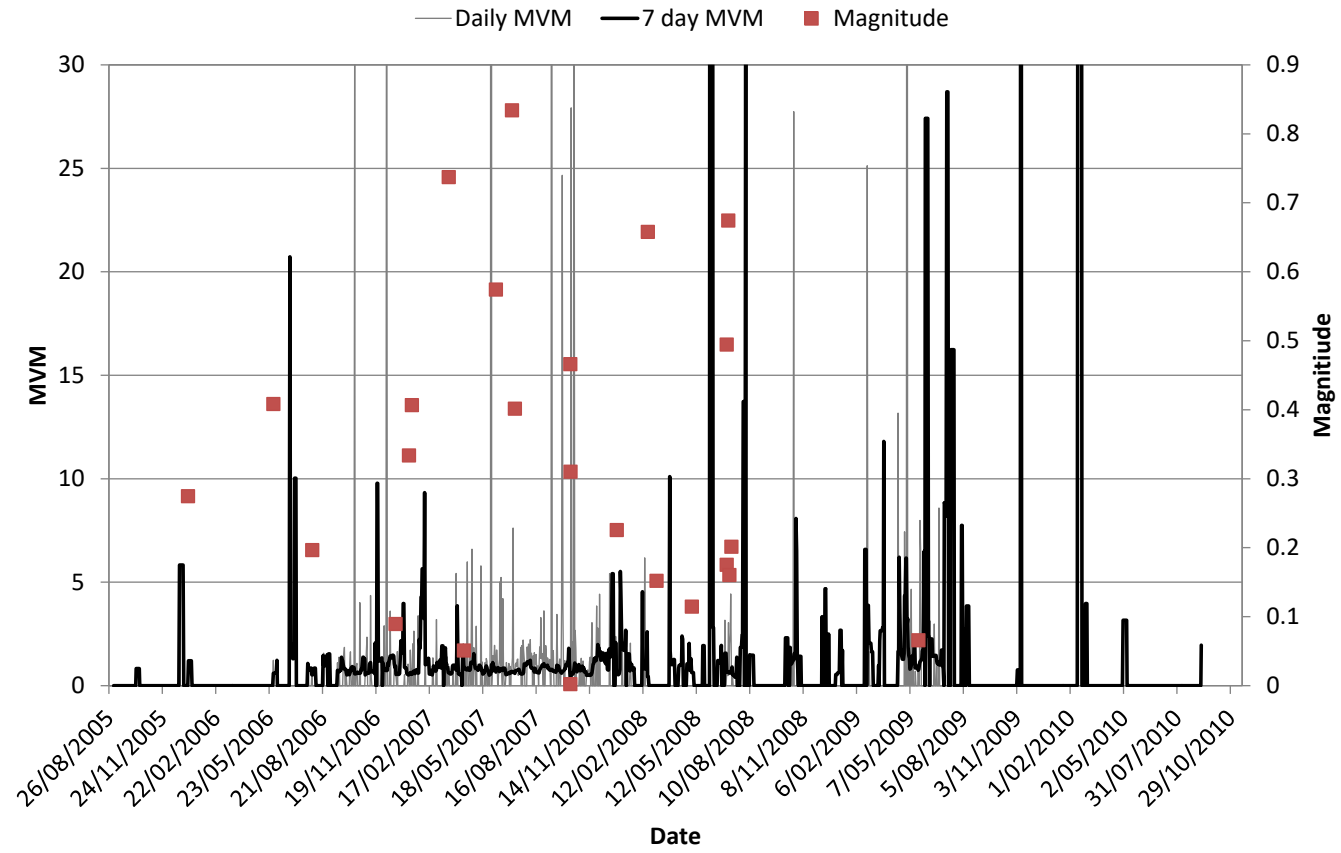


Figure A7 11: Daily MVM chart for Reward Fault.

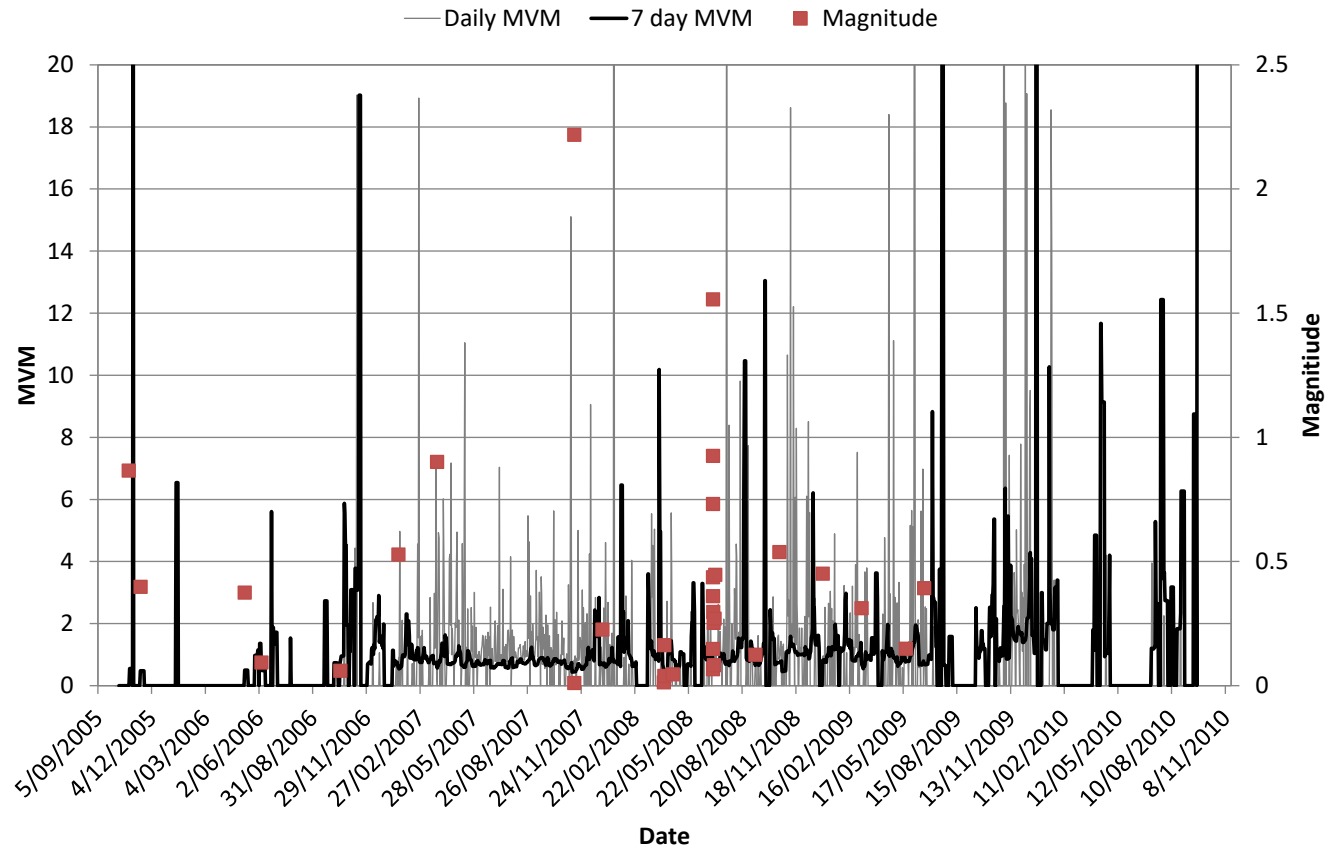


Figure A7 12: Daily MVM chart for Flanagan Fault.

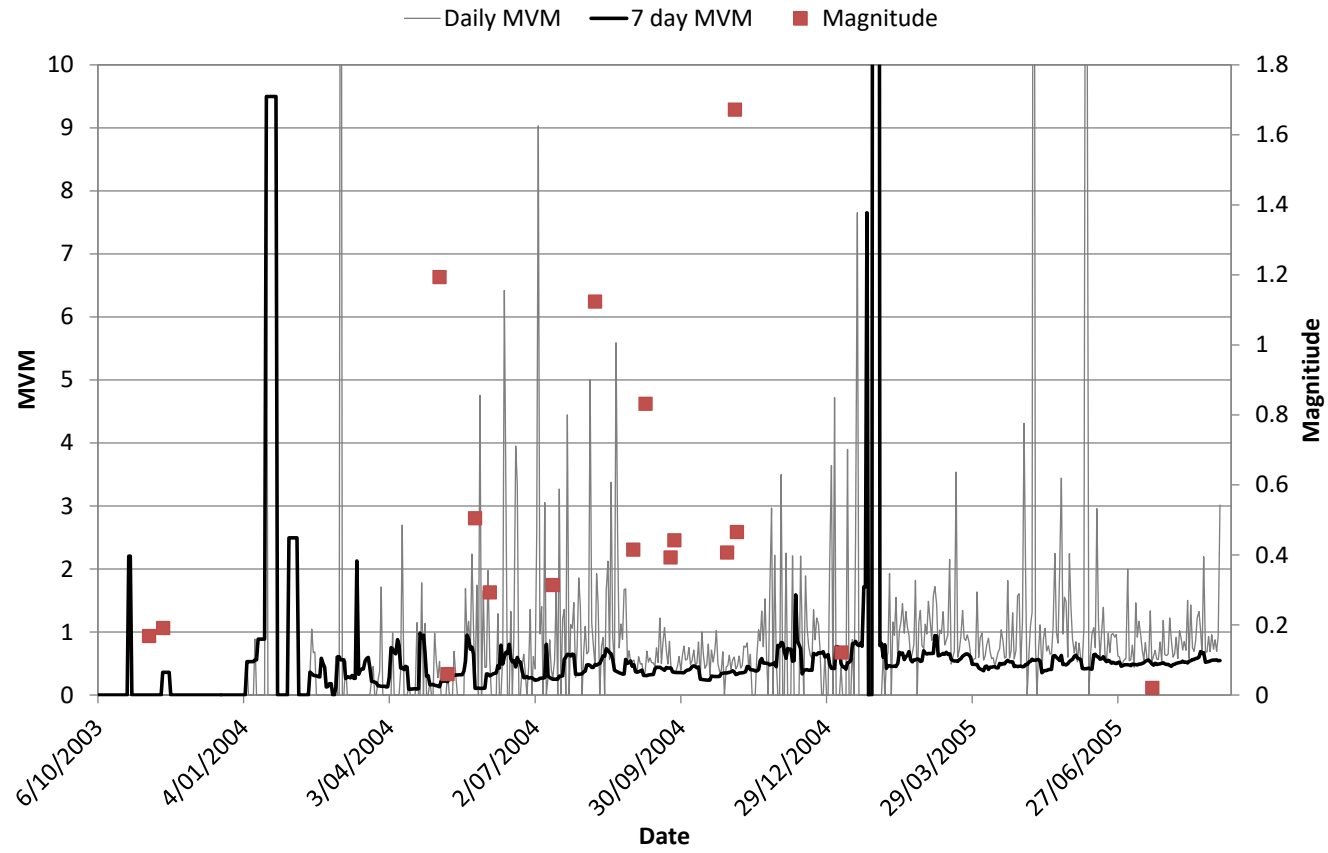


Figure A7 13: Daily MVM chart for Feral Fault.

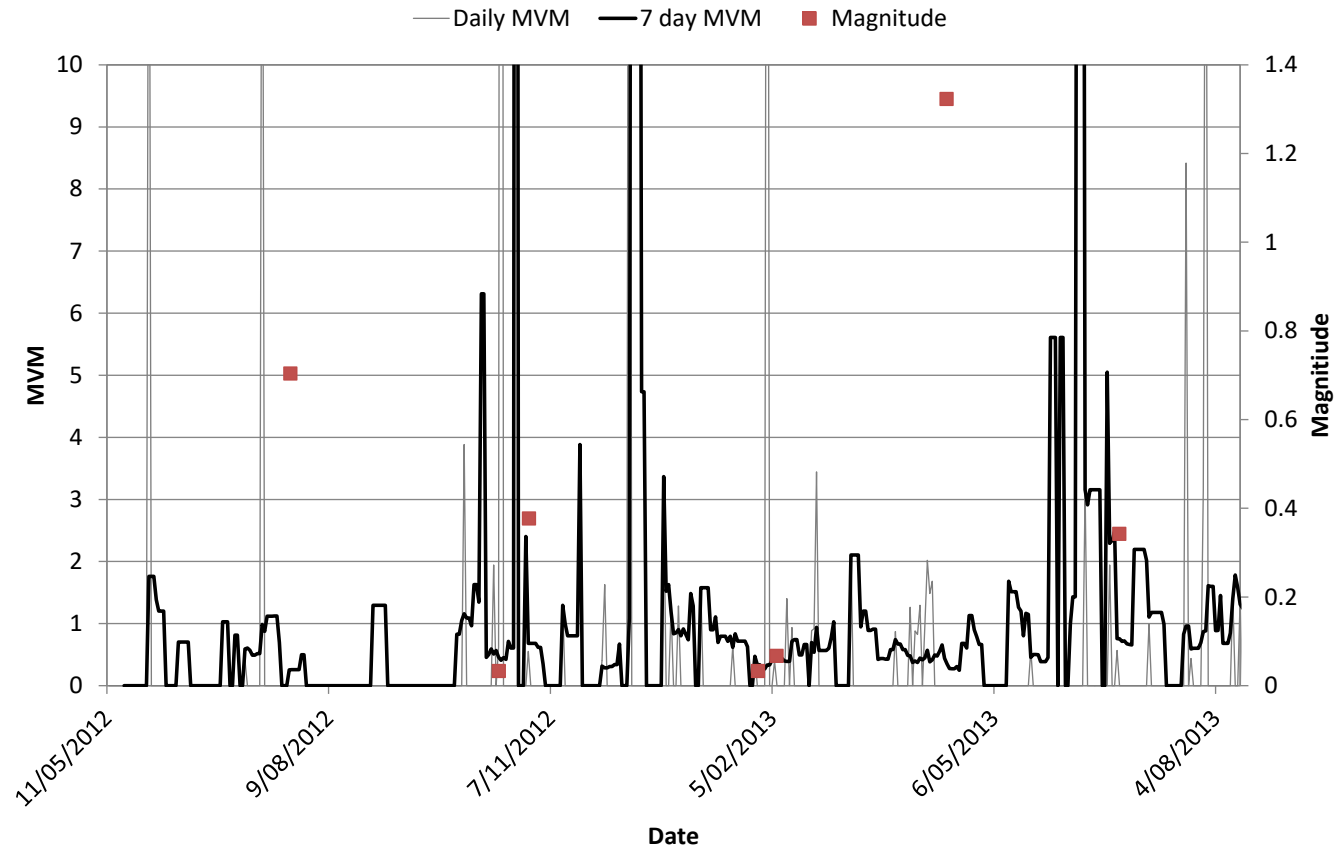


Figure A7 14: Daily MVM chart for Great Lyell Fault.

Appendix 8 – Energy daily charts

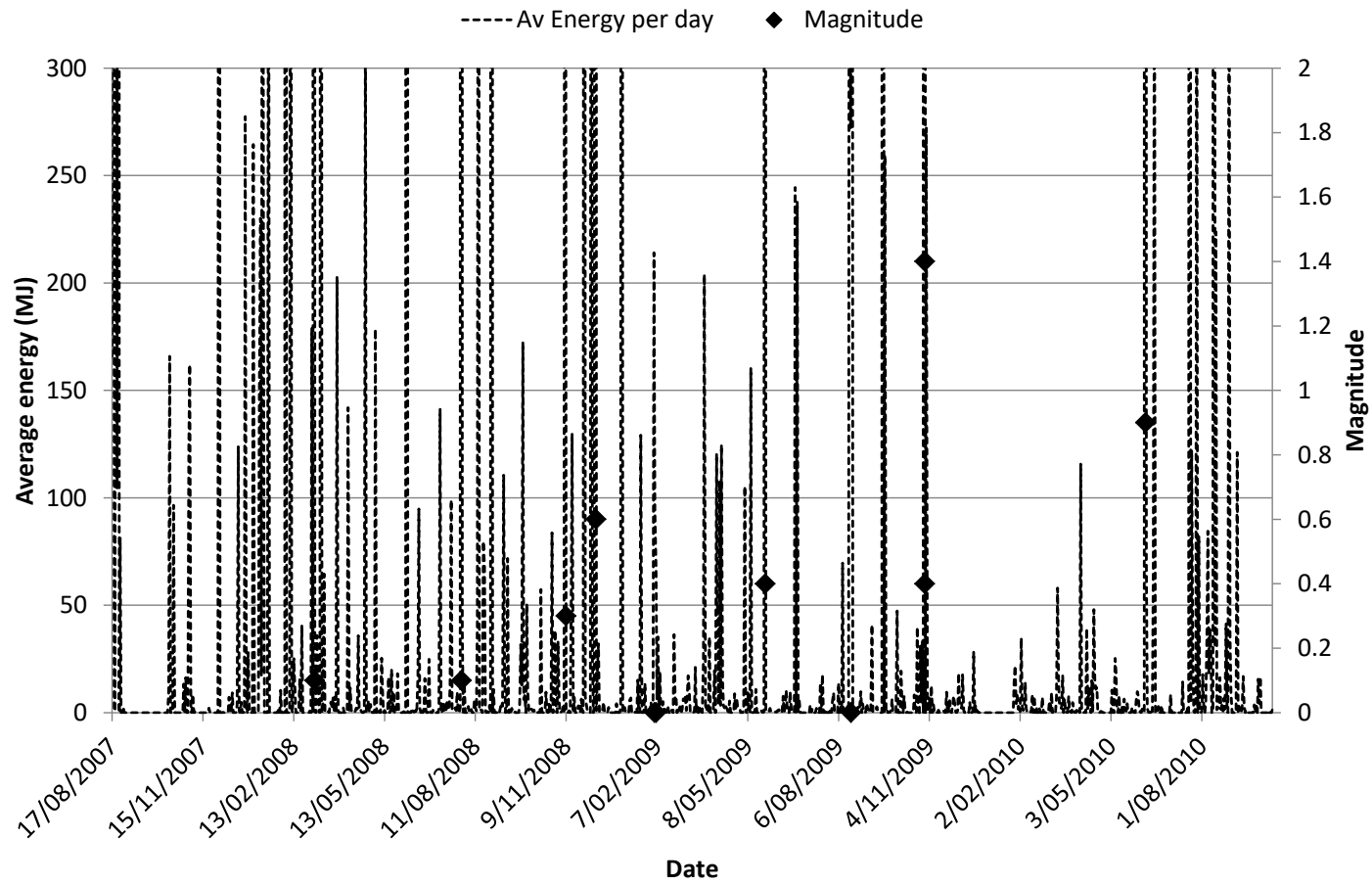


Figure A8 1: Daily ERR chart for the A1 Shear.

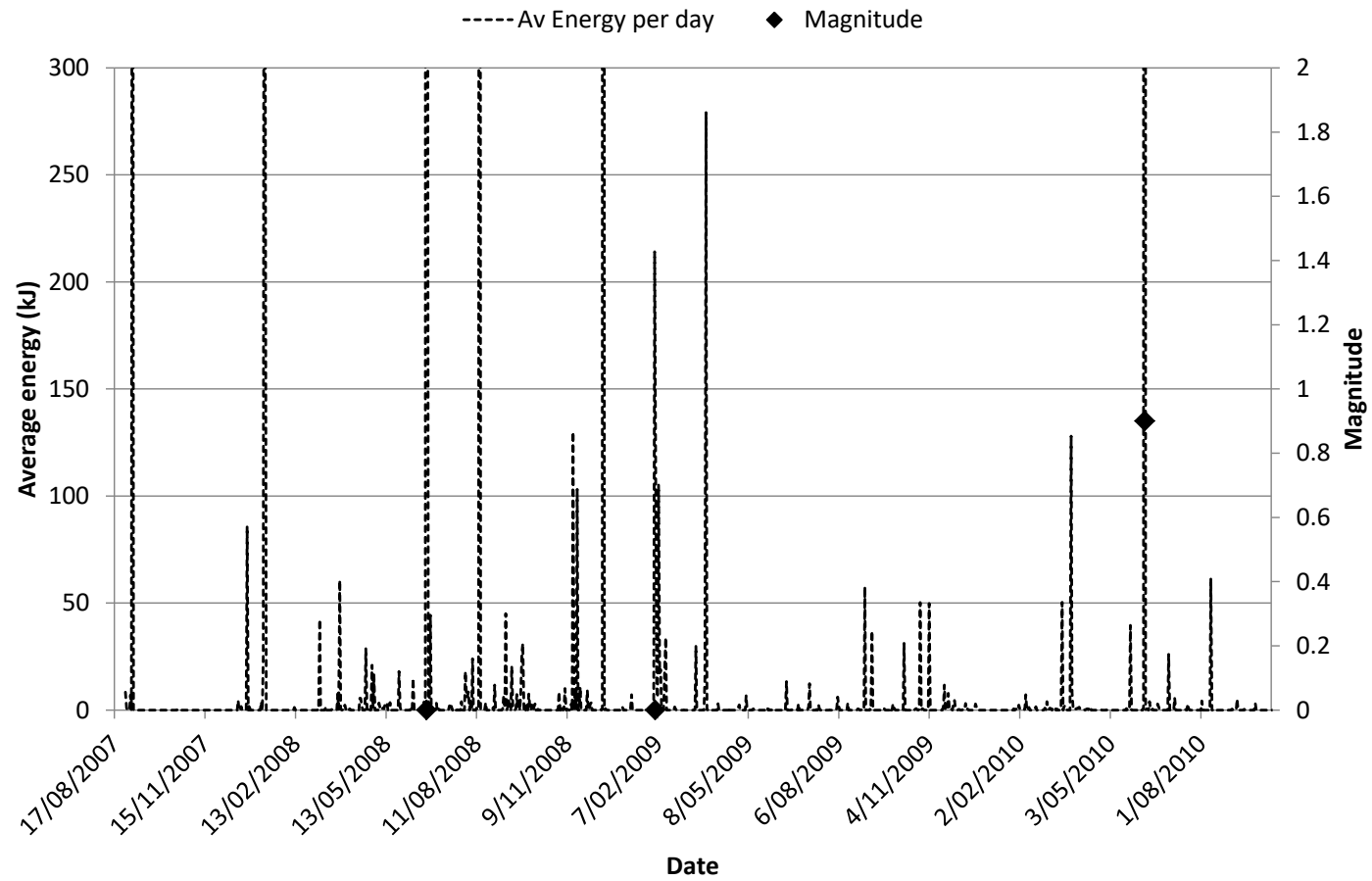


Figure A8 2: Daily ERR chart for the North Dyke.

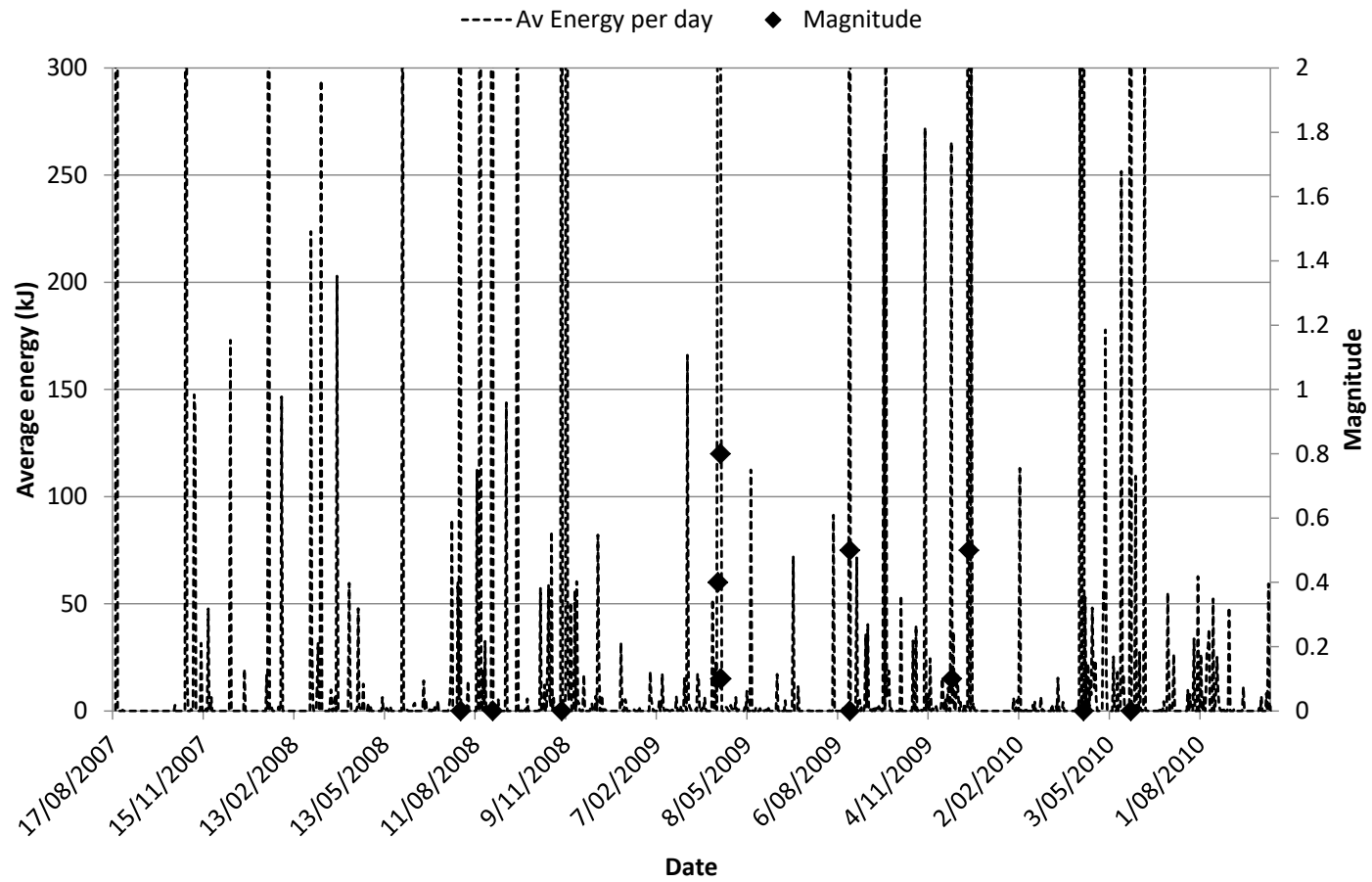


Figure A8 3: Daily ERR chart for the Mini Dyke.

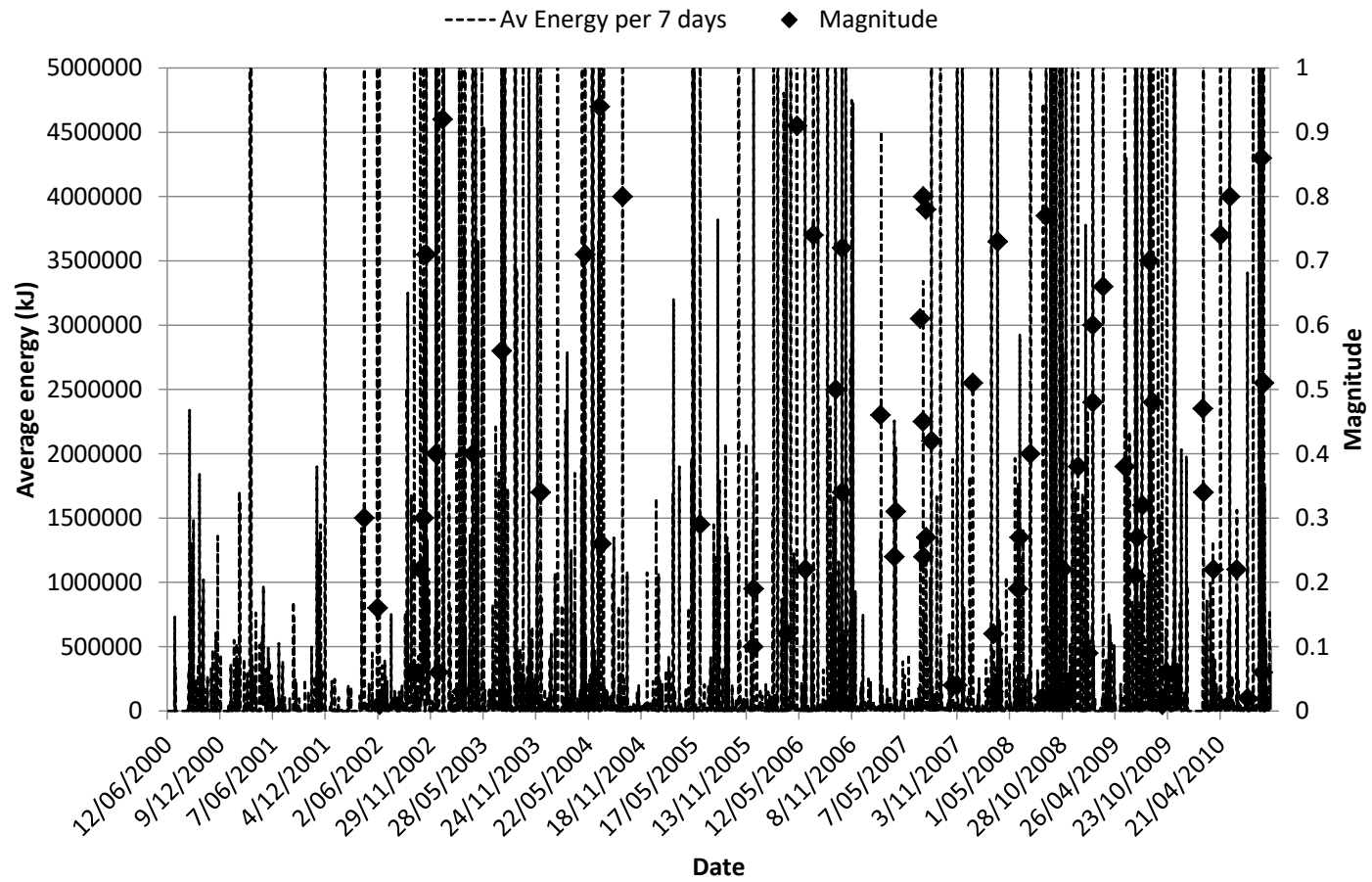


Figure A8 4: Daily ERR chart for Fitzroy Fault.

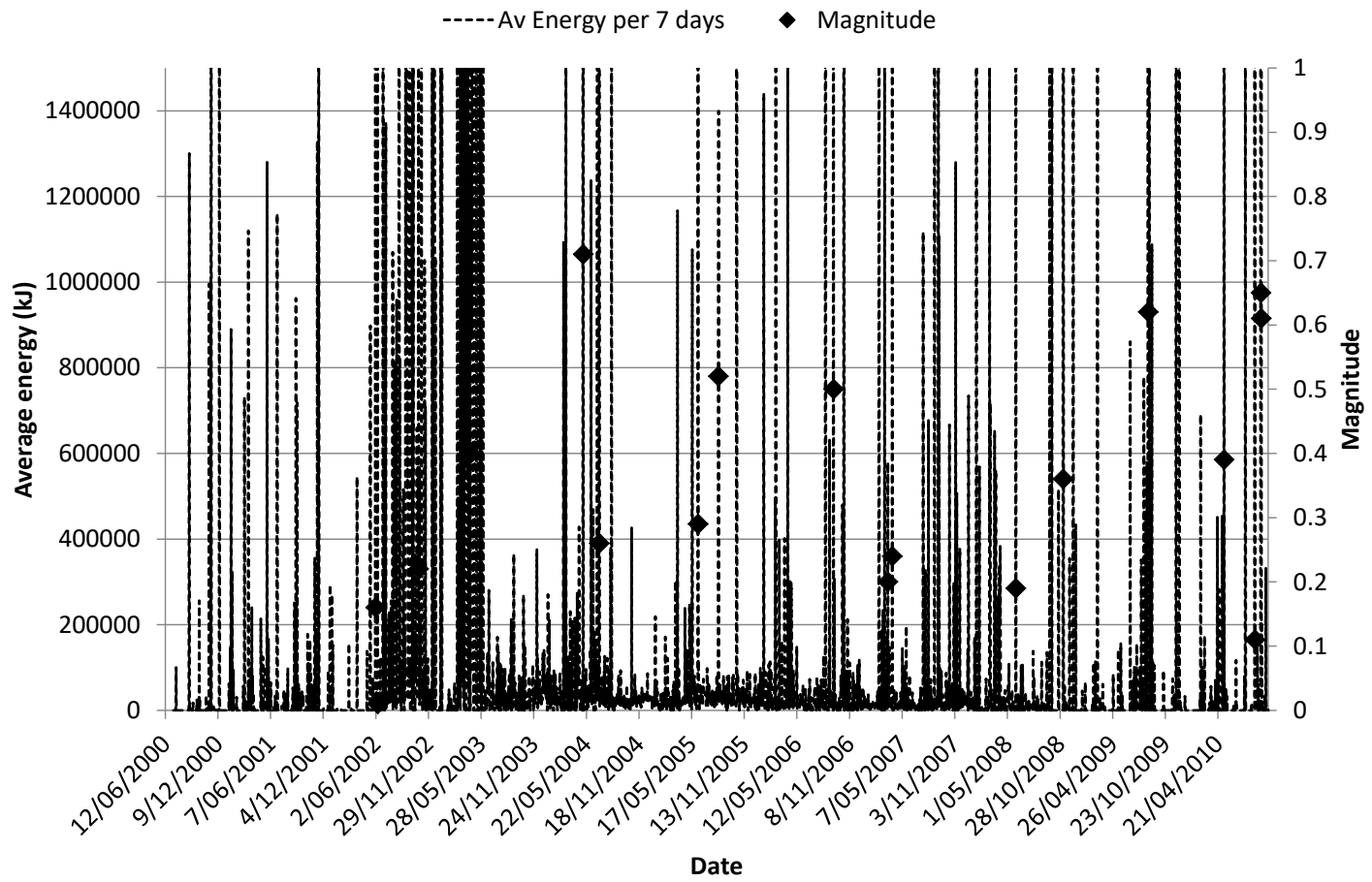


Figure A8 5: Daily ERR chart for North East Faults Group 1.

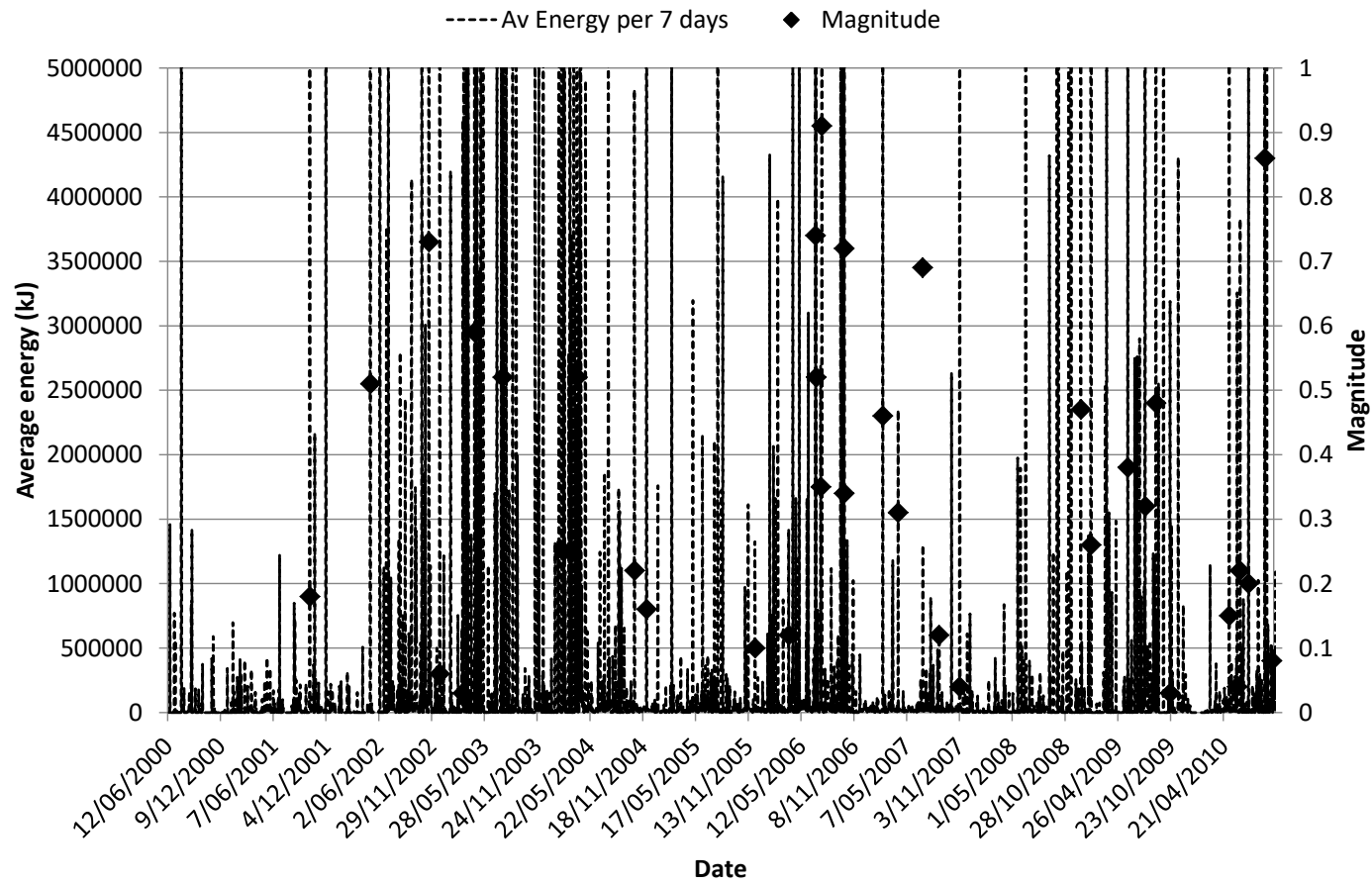


Figure A8 6: Daily ERR chart for North East Faults Group 2.

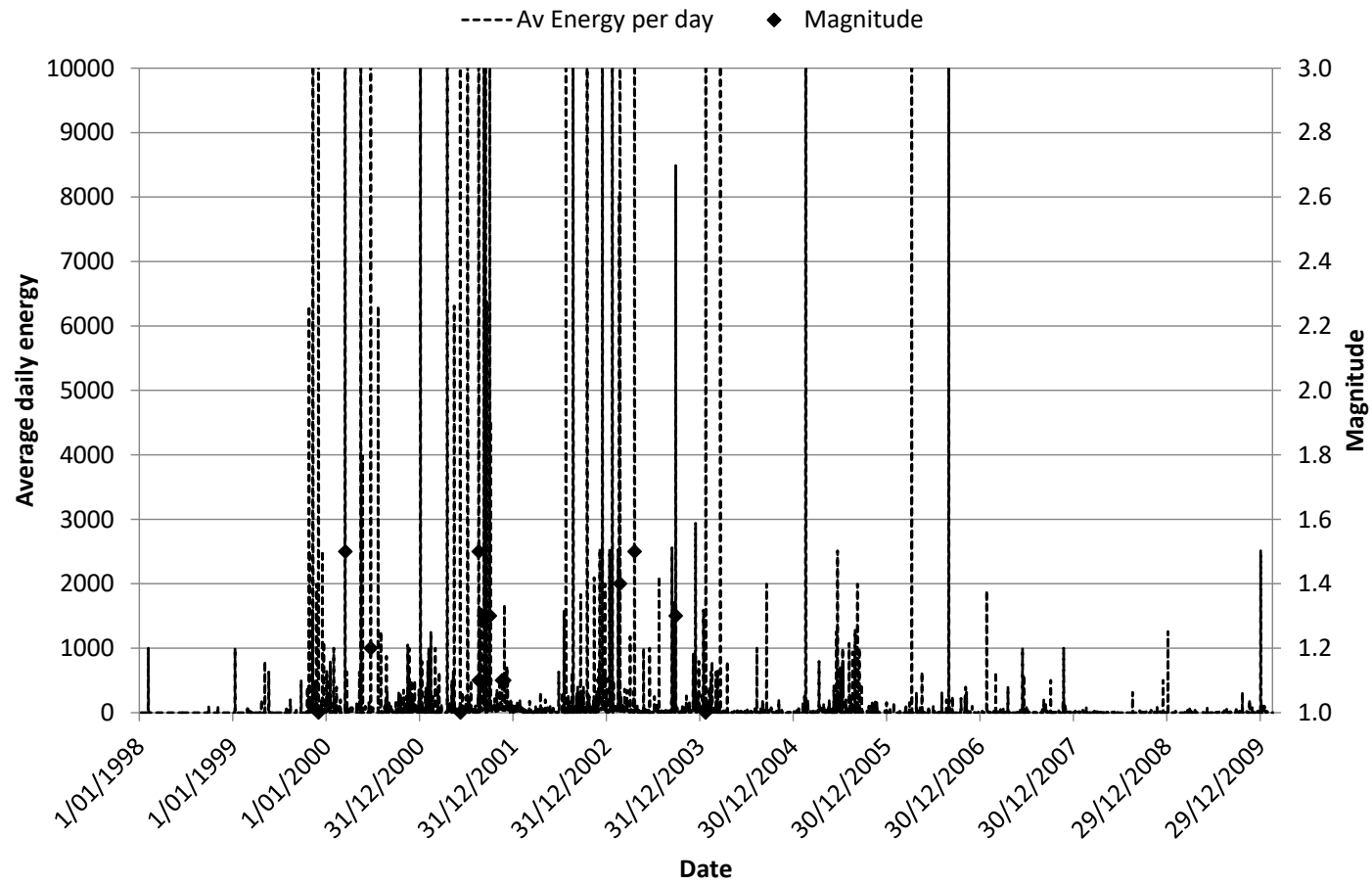


Figure A8 7: Daily ERR chart for FaultP_1

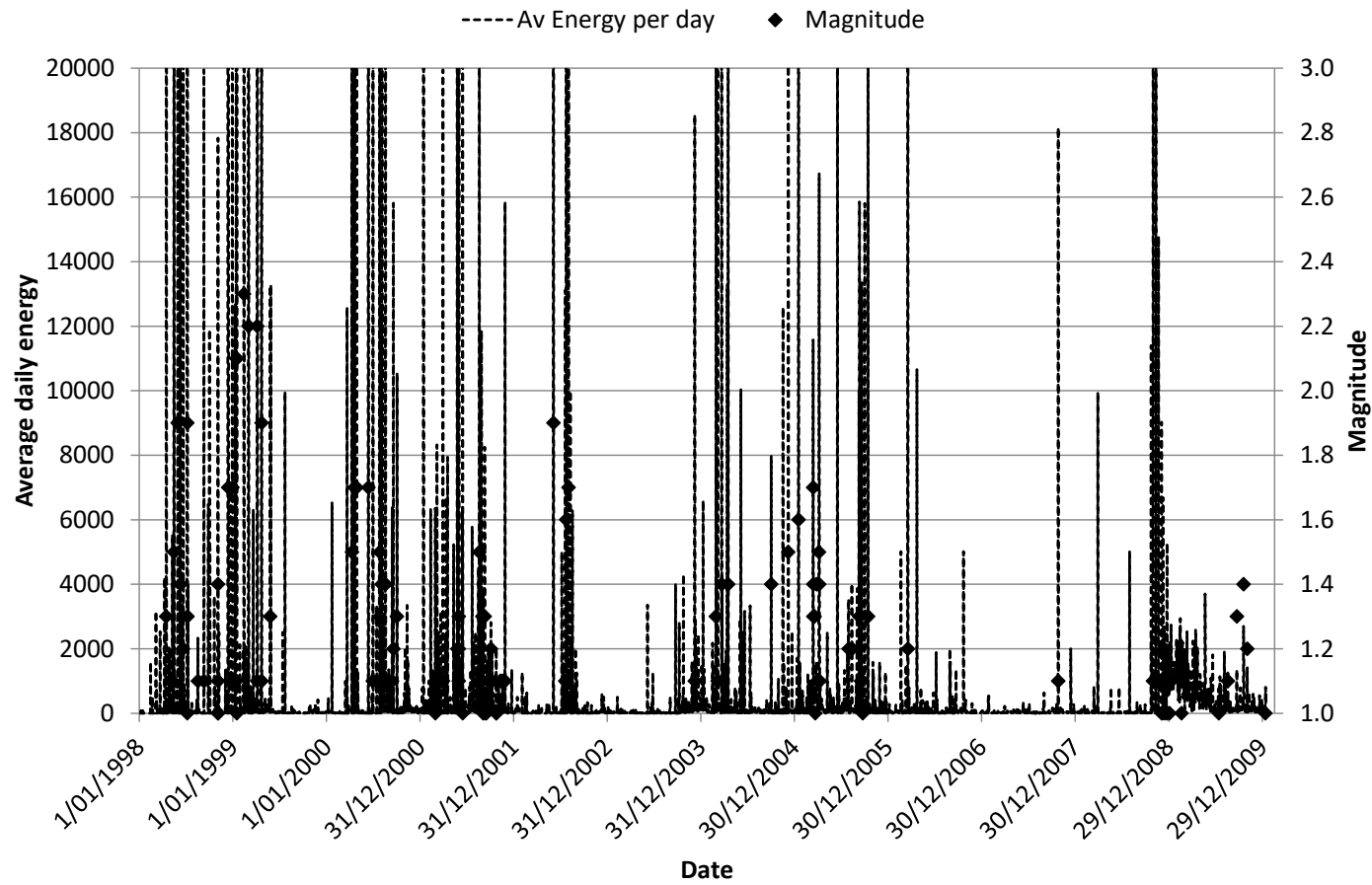


Figure A8 8: Daily ERR chart for Fault B_C.

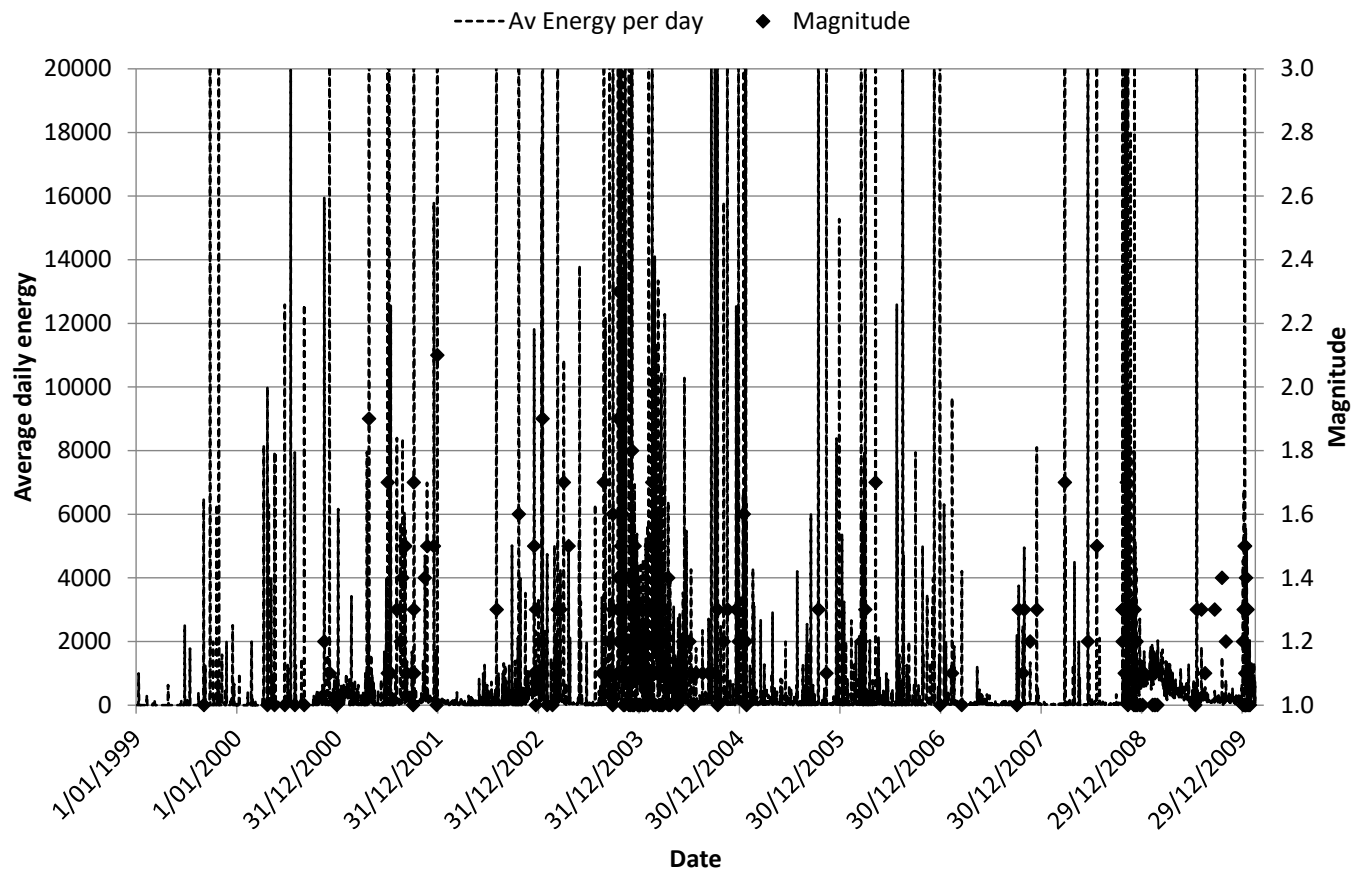


Figure A8 9: Daily ERR chart for the FW Dyke.

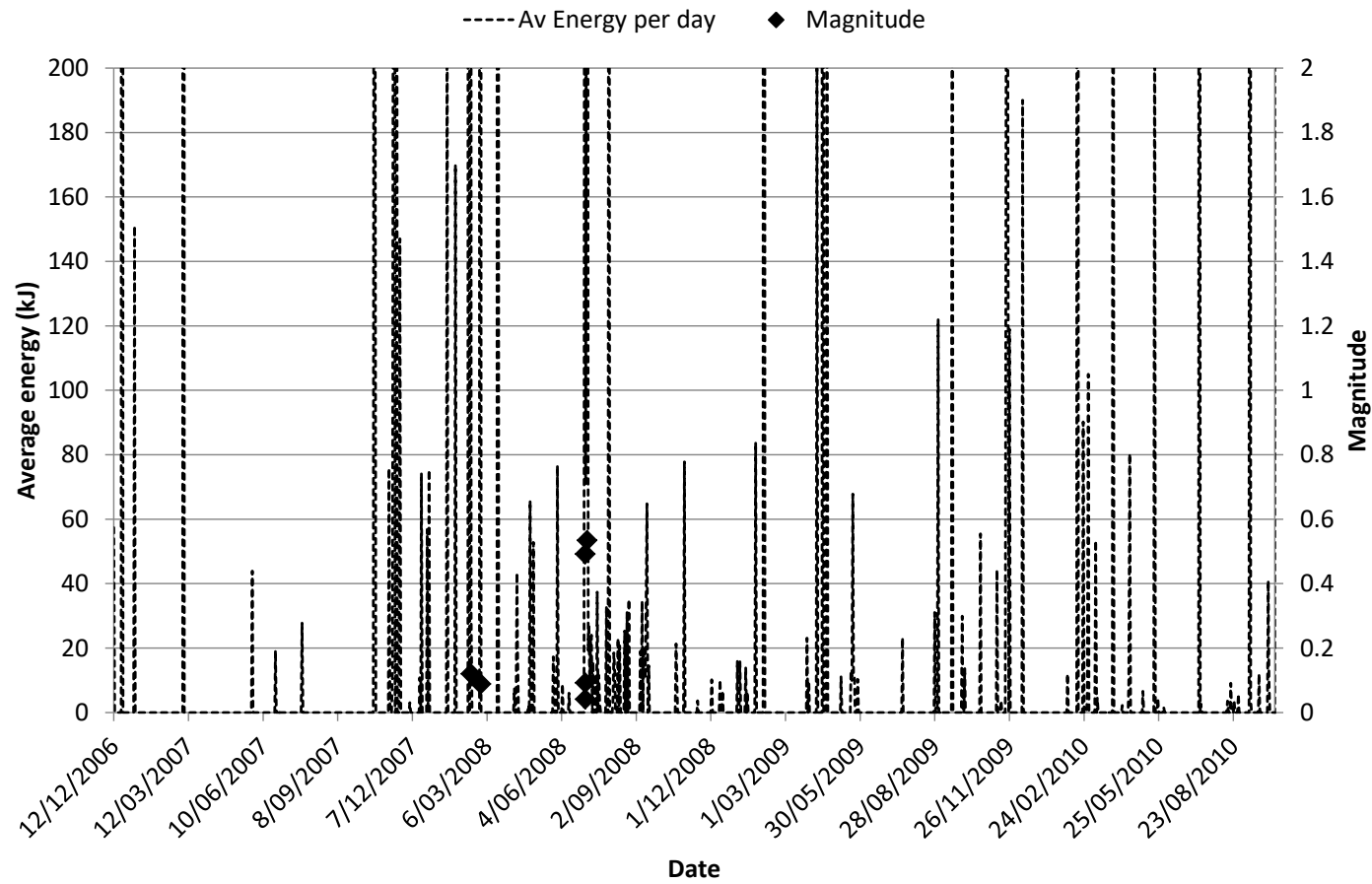


Figure A8 10: Daily ERR chart for Maritana Fault.

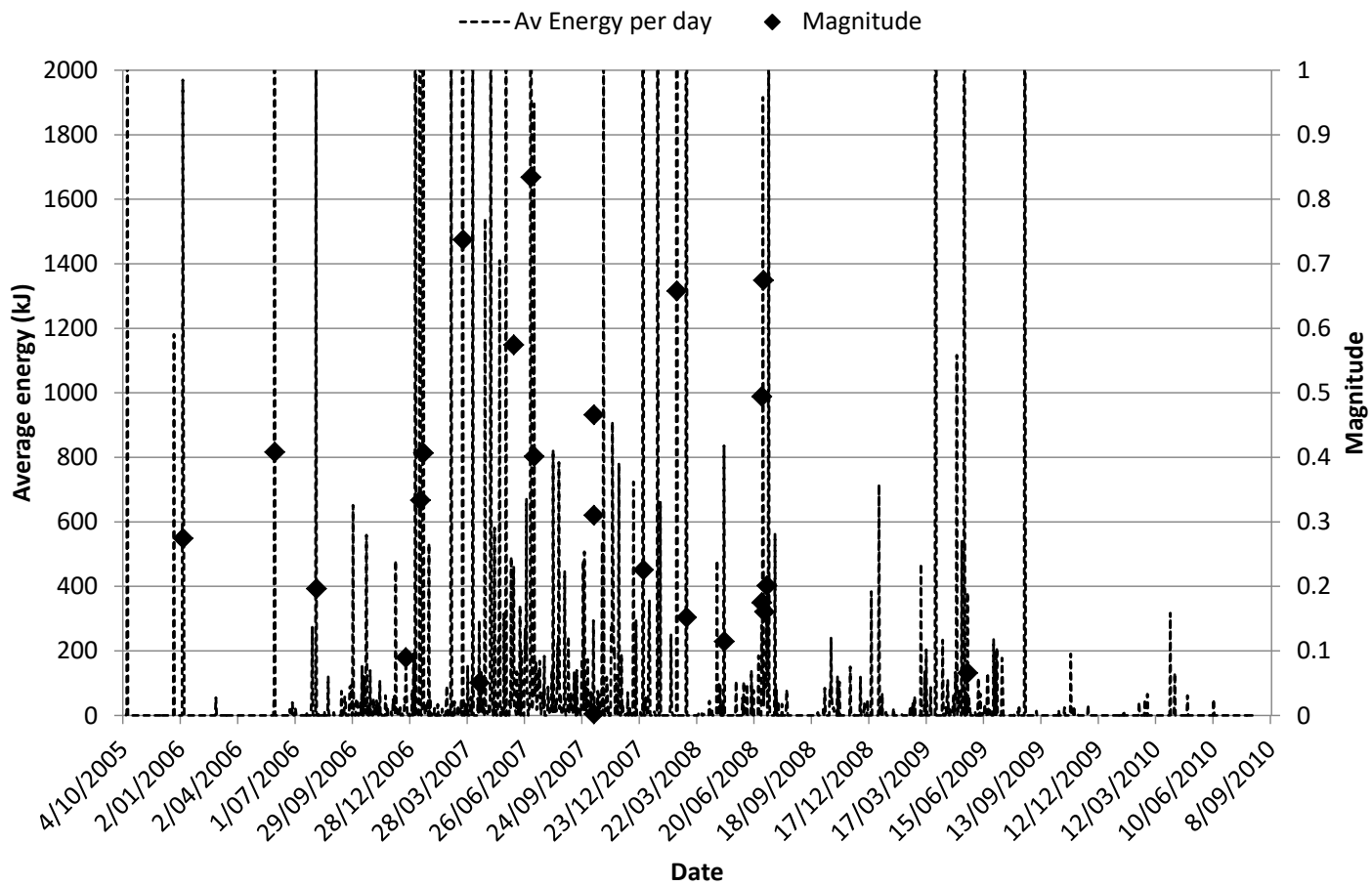


Figure A8 11: Daily ERR chart for Reward Fault.

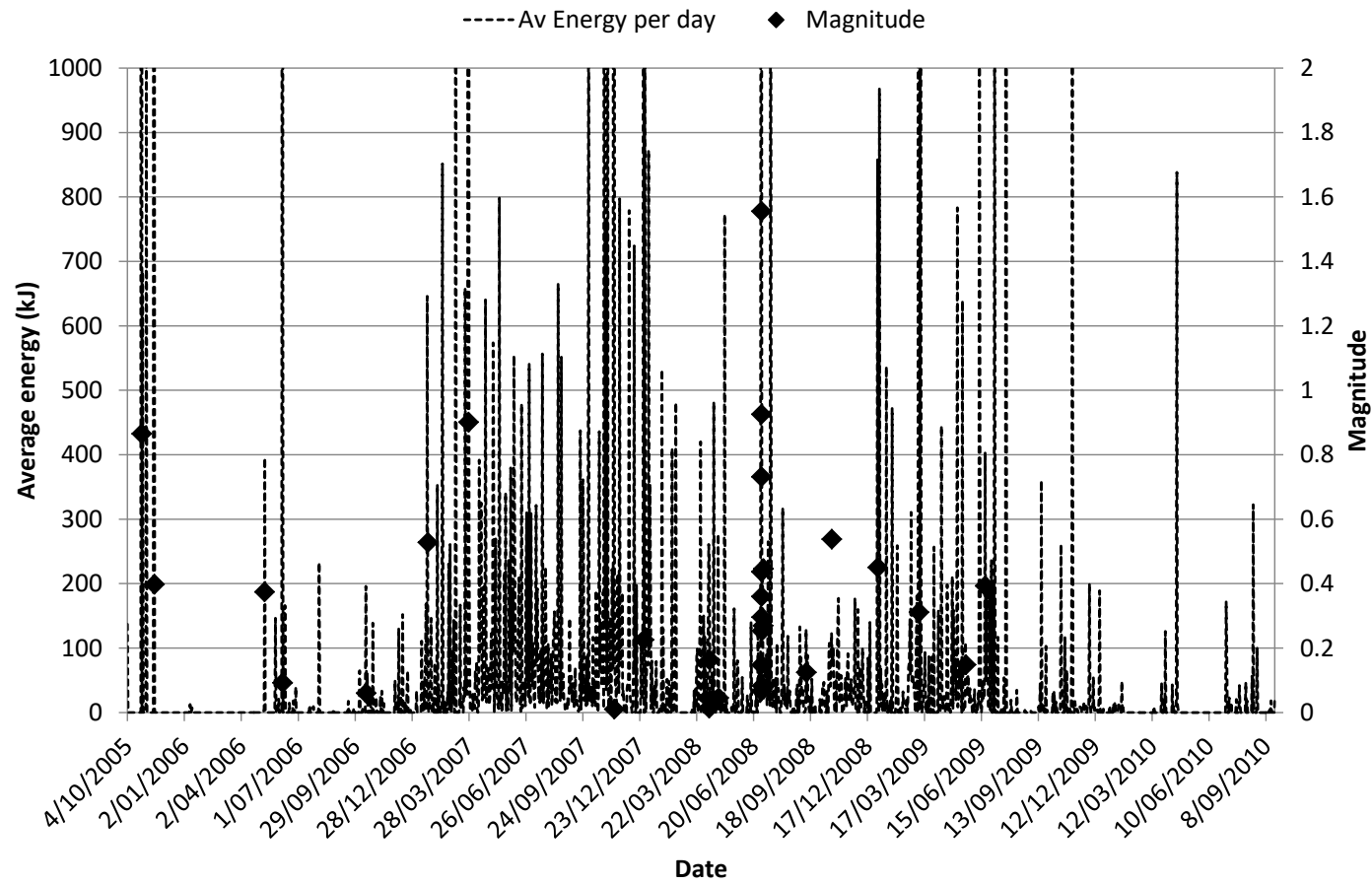


Figure A8 12: Daily ERR chart for Flanagan Fault.

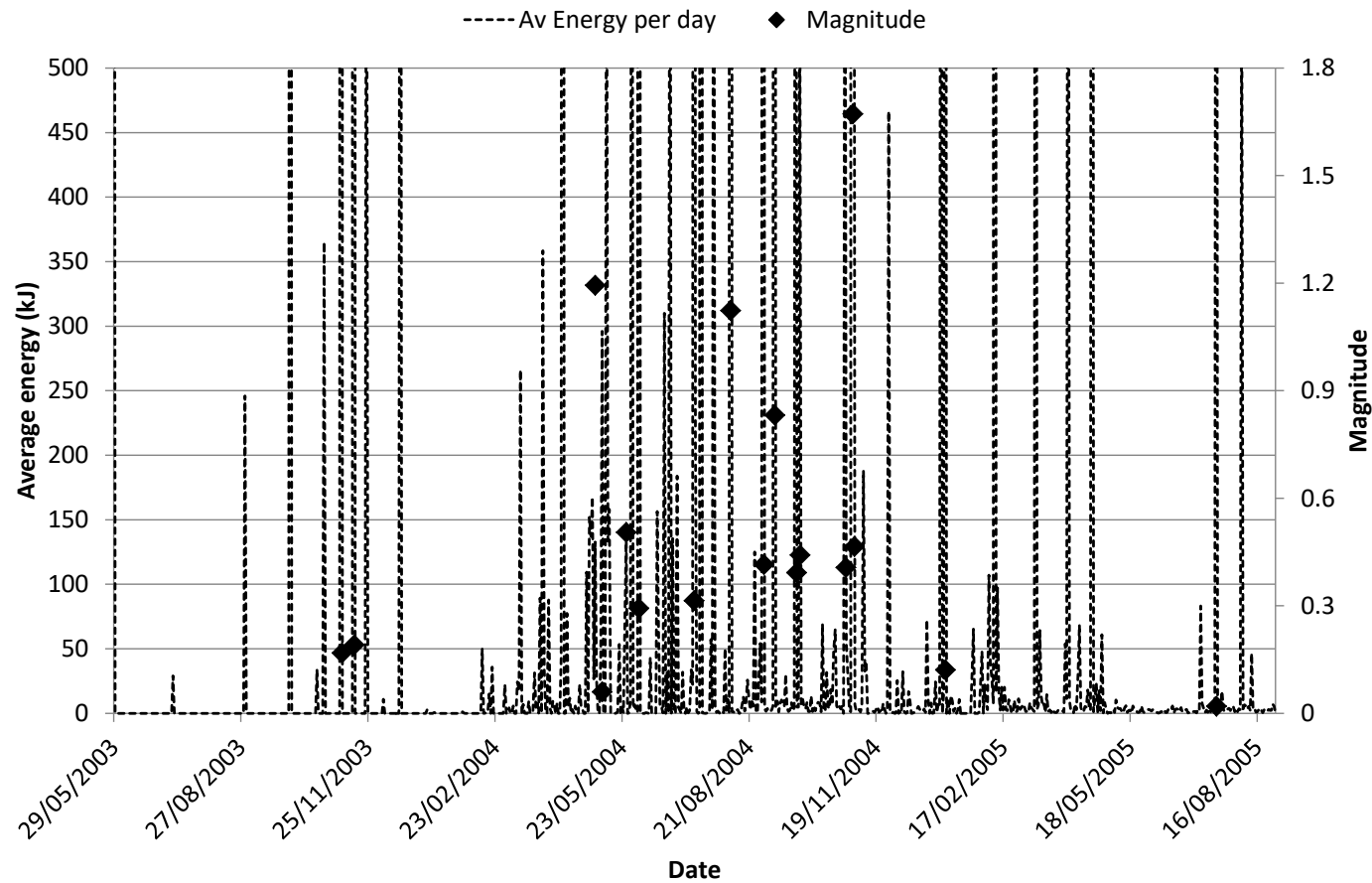


Figure A8 13: Daily ERR chart for Feral Fault.

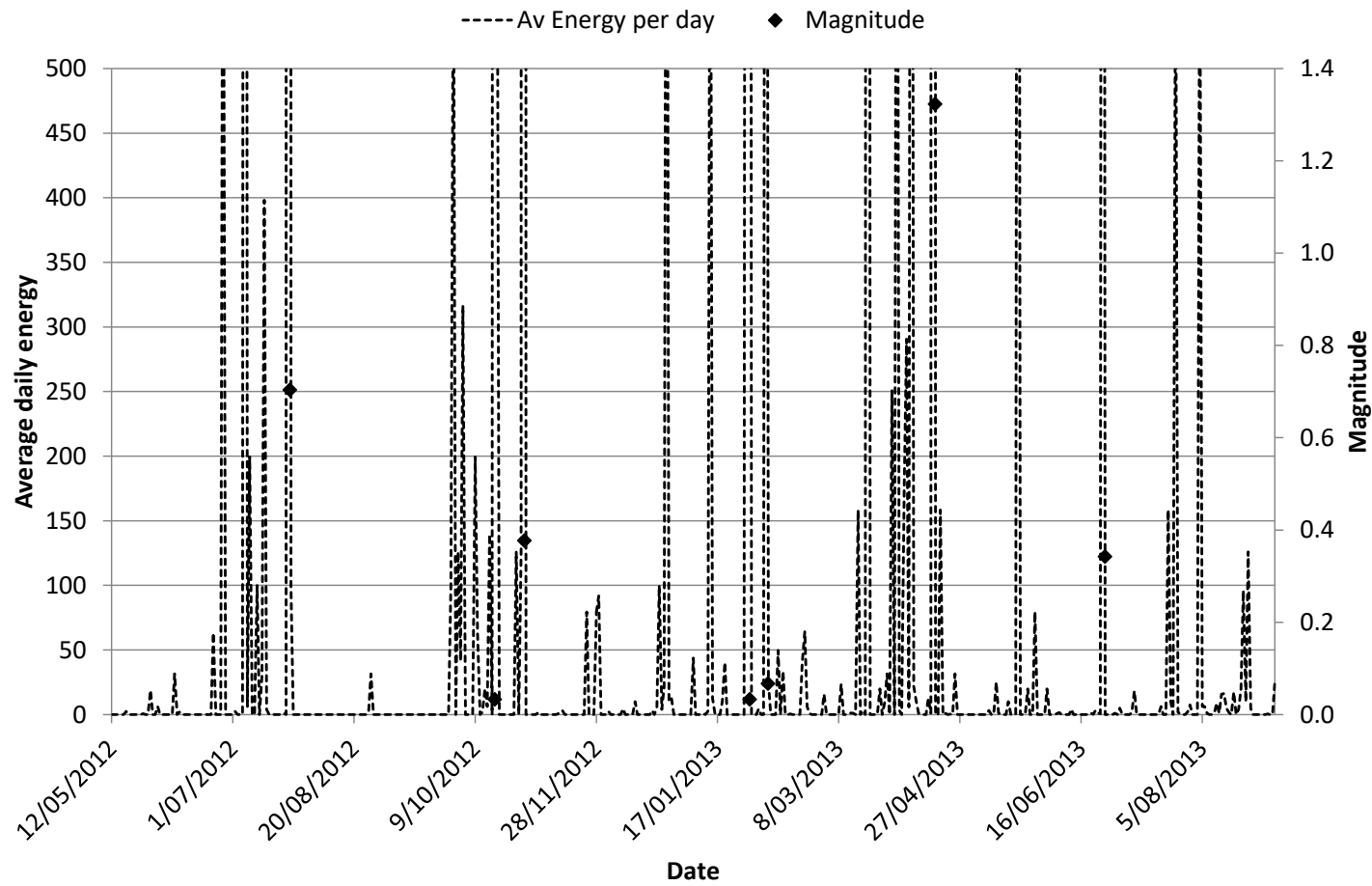


Figure A8 14: Daily ERR chart for Great Lyell Fault.

**Appendix 9 – Precursor comparison charts - daily averages,
instantaneous failures results**

Comparison of parameters on each structure

Daily Instantaneous Results

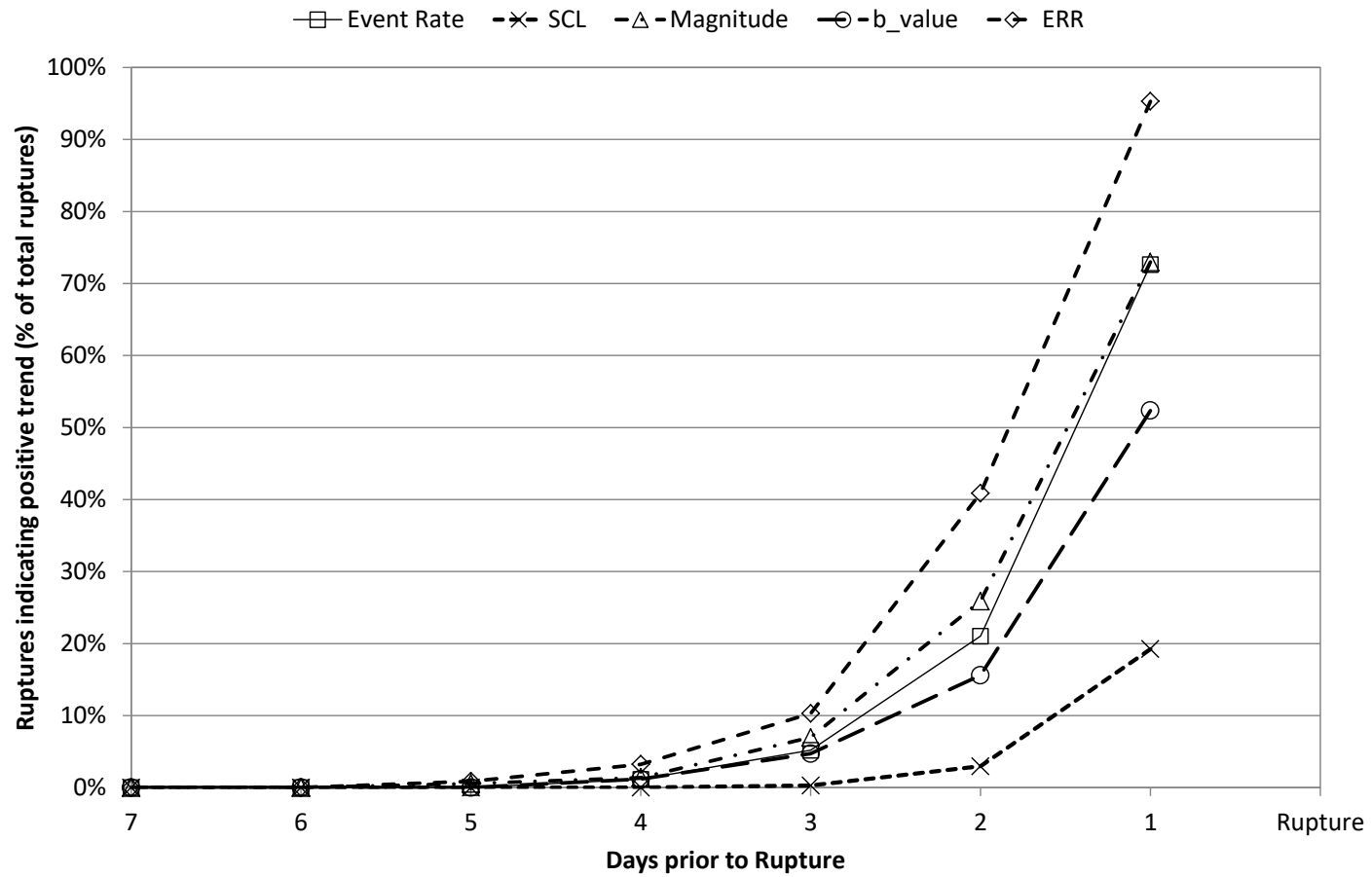


Figure A9 1: Comparison of average daily parameters for instantaneous failures on all structures.

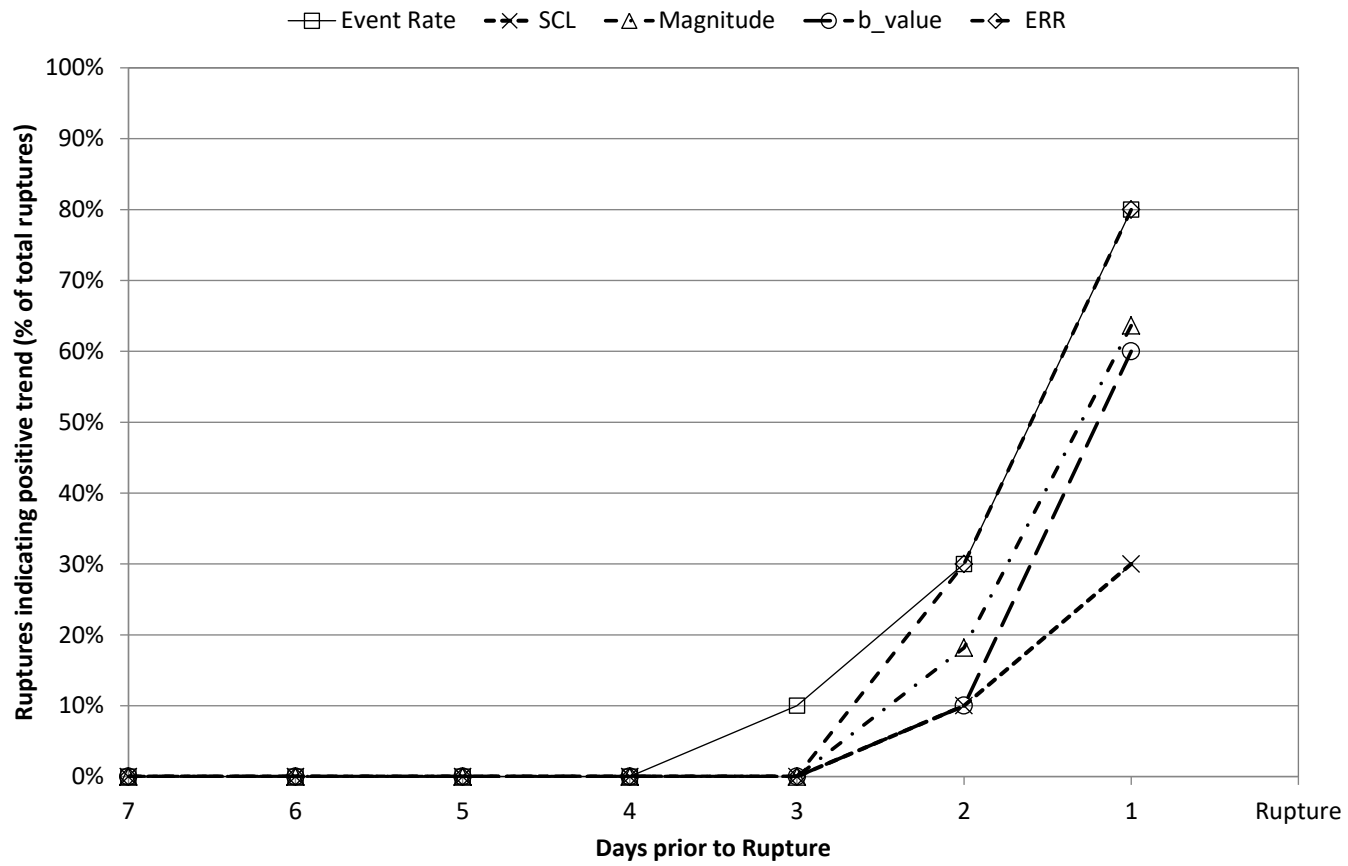


Figure A9 2: Comparison of daily parameters for instantaneous failures on the A1 Shear (10 failures).

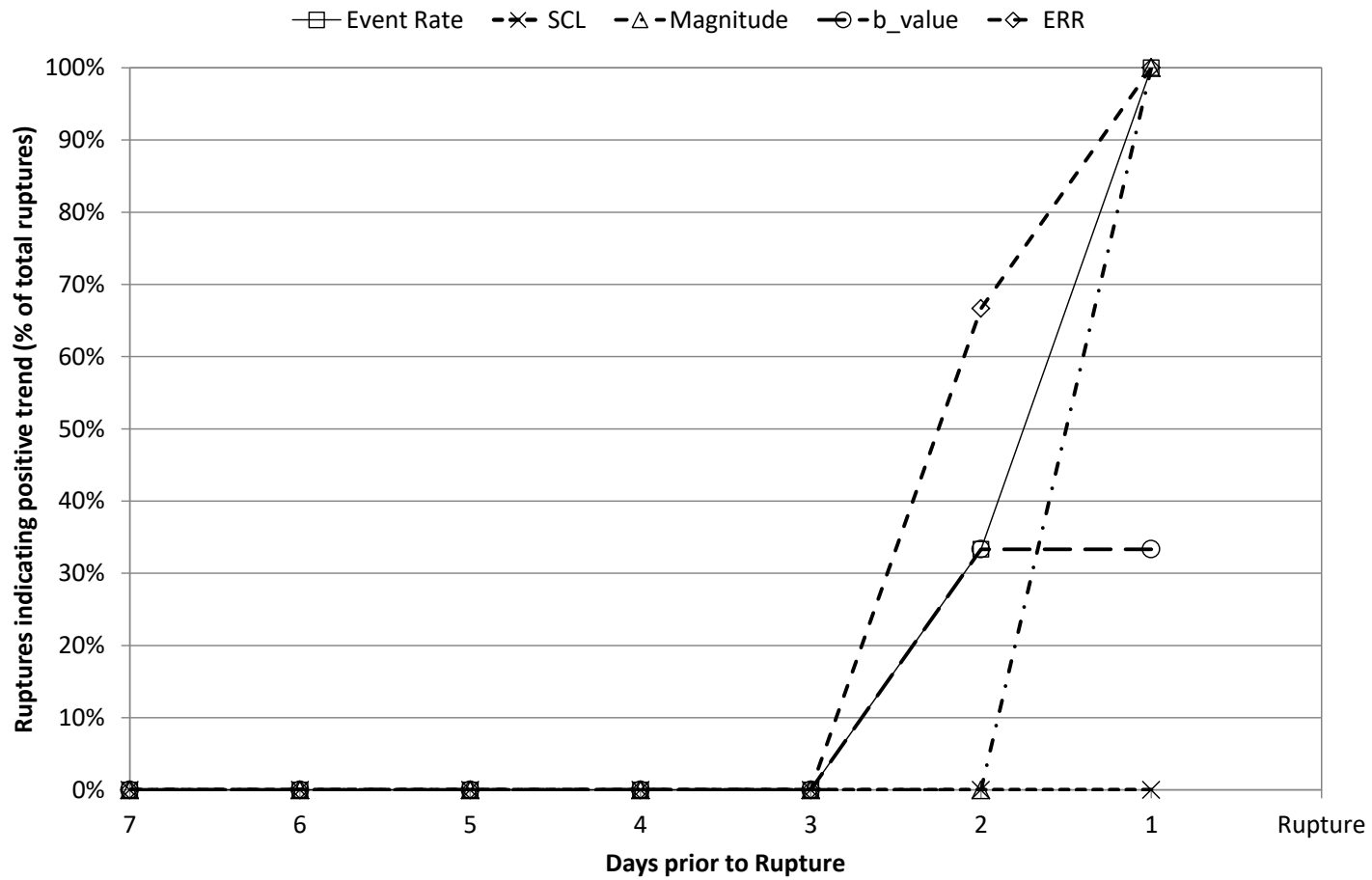


Figure A9 3: Comparison of daily parameters for instantaneous failures for the North Dyke (3 failures).

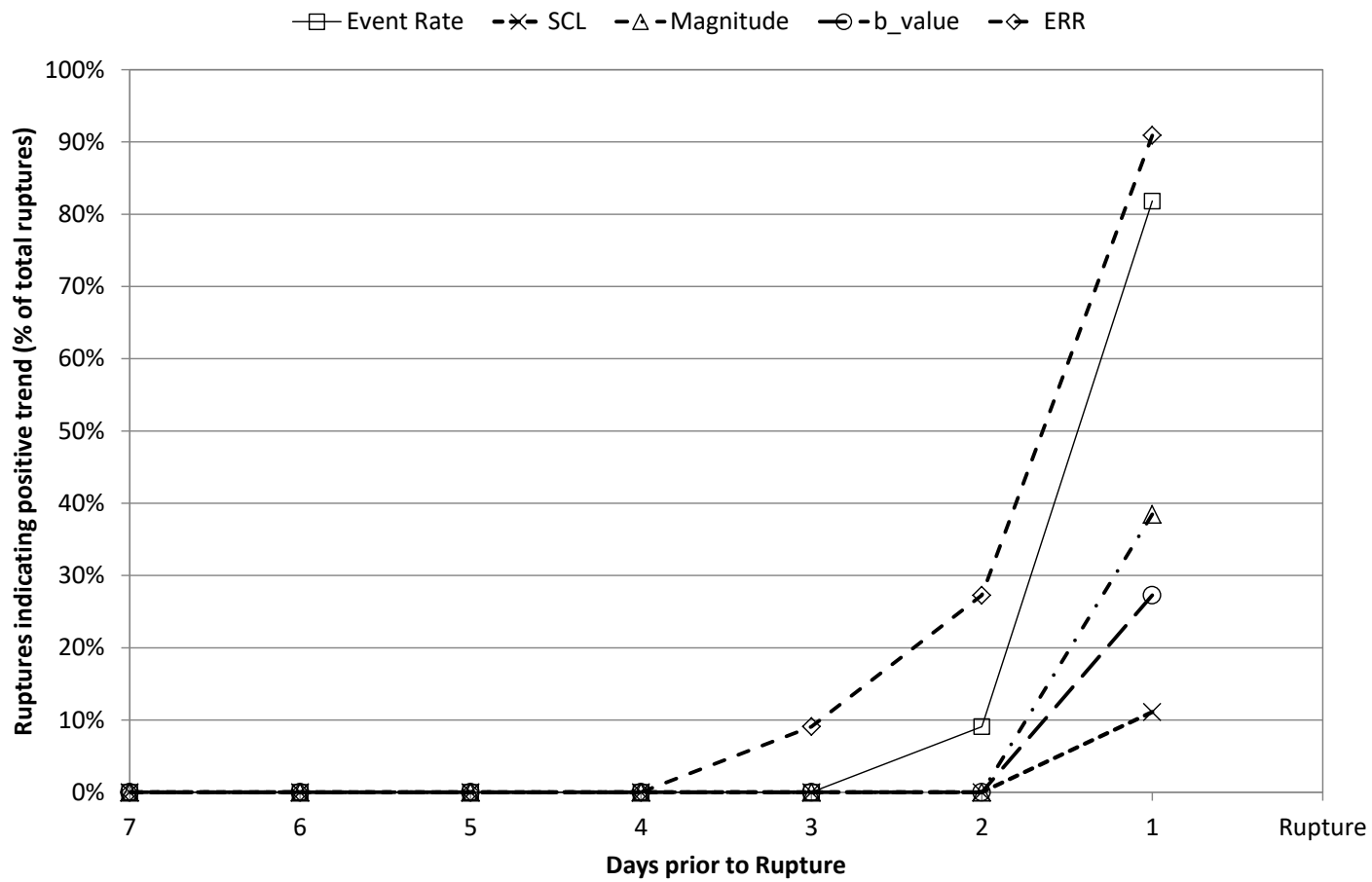


Figure A9 4: Comparison of daily parameters for instantaneous failures for the Mini Dyke (11 failures).

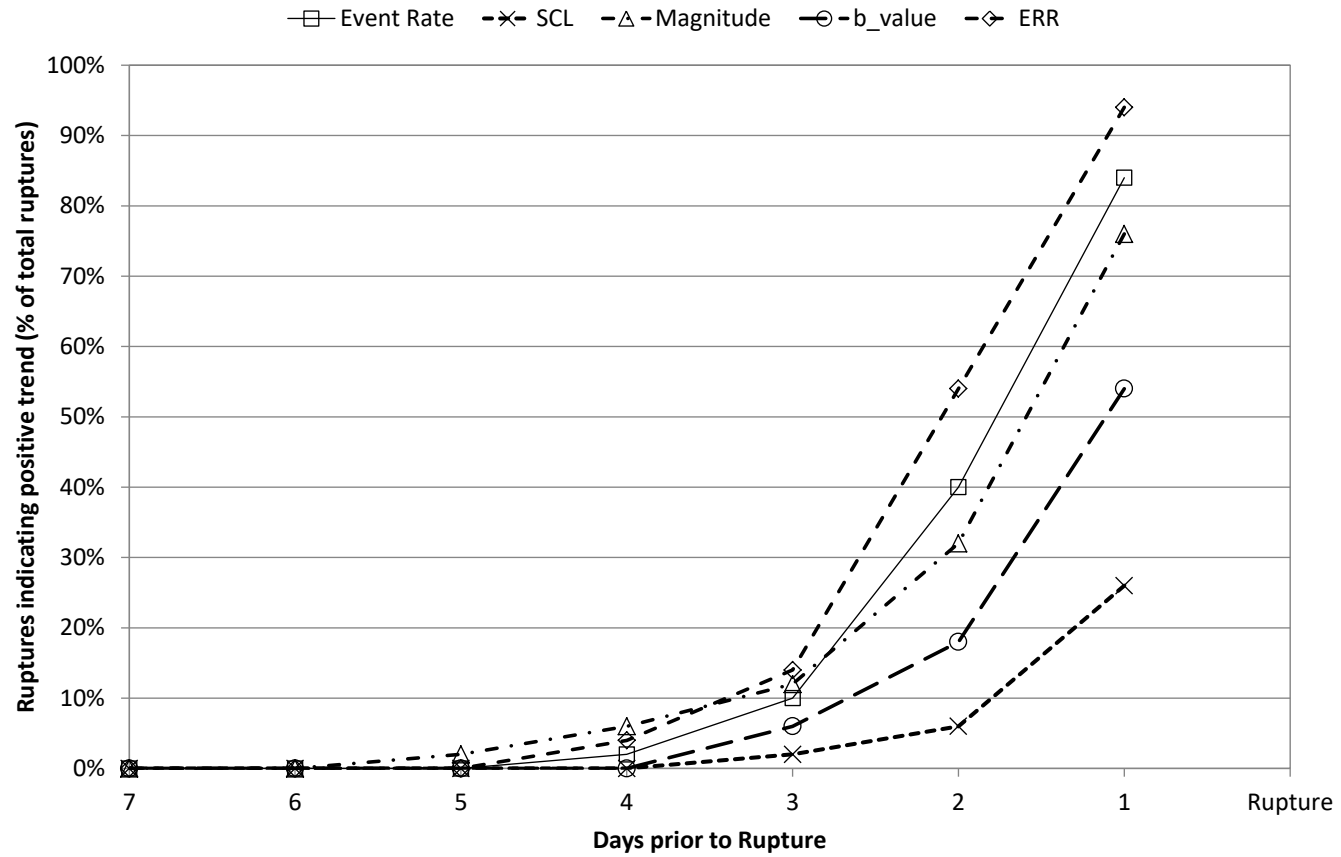


Figure A9 5: Comparison of daily parameters for instantaneous failures for the Fitzroy Fault (50 failures).

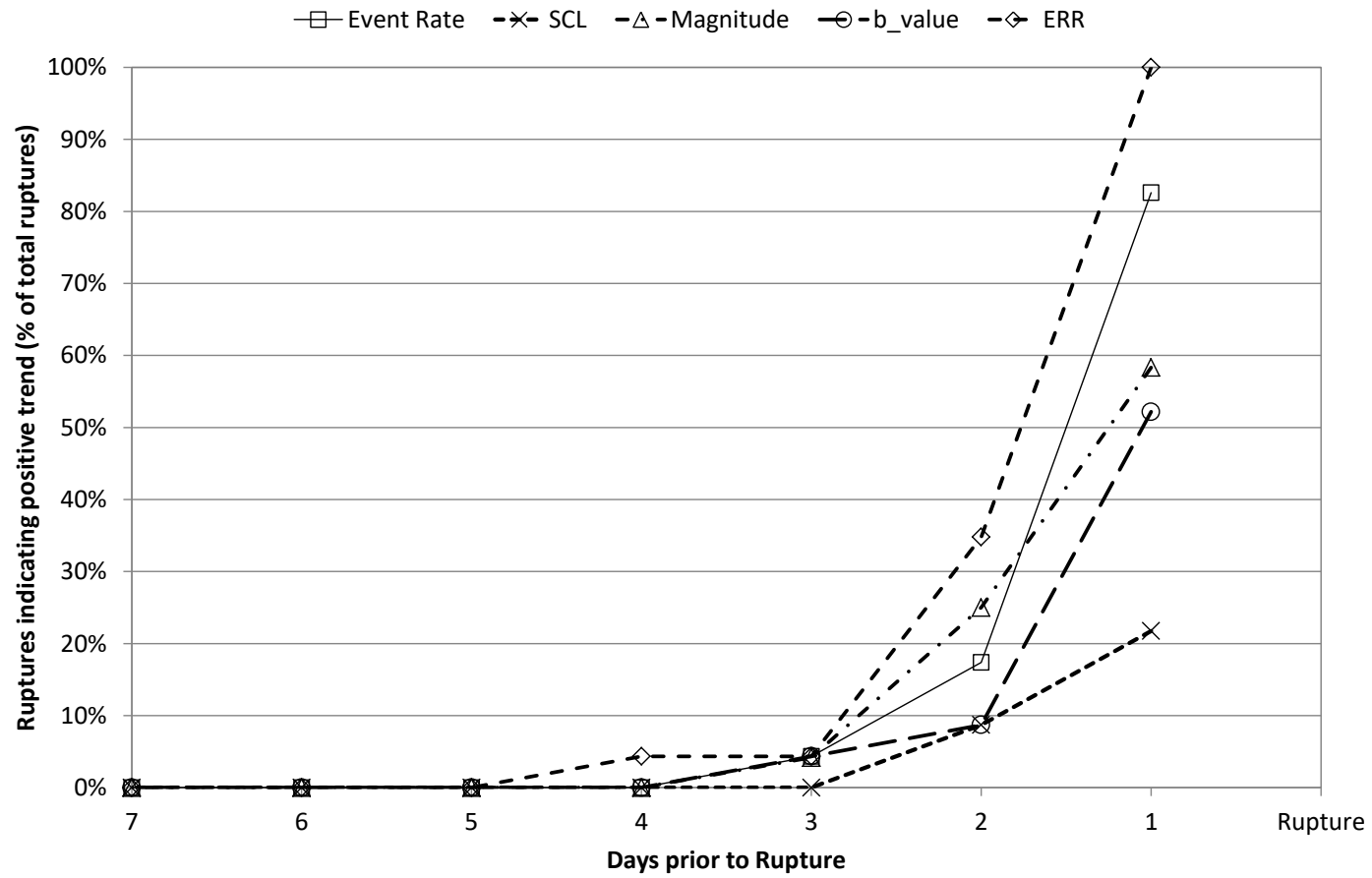


Figure A9 6: Comparison of daily parameters for instantaneous failures for the North East Faults Group 1 (23 failures).

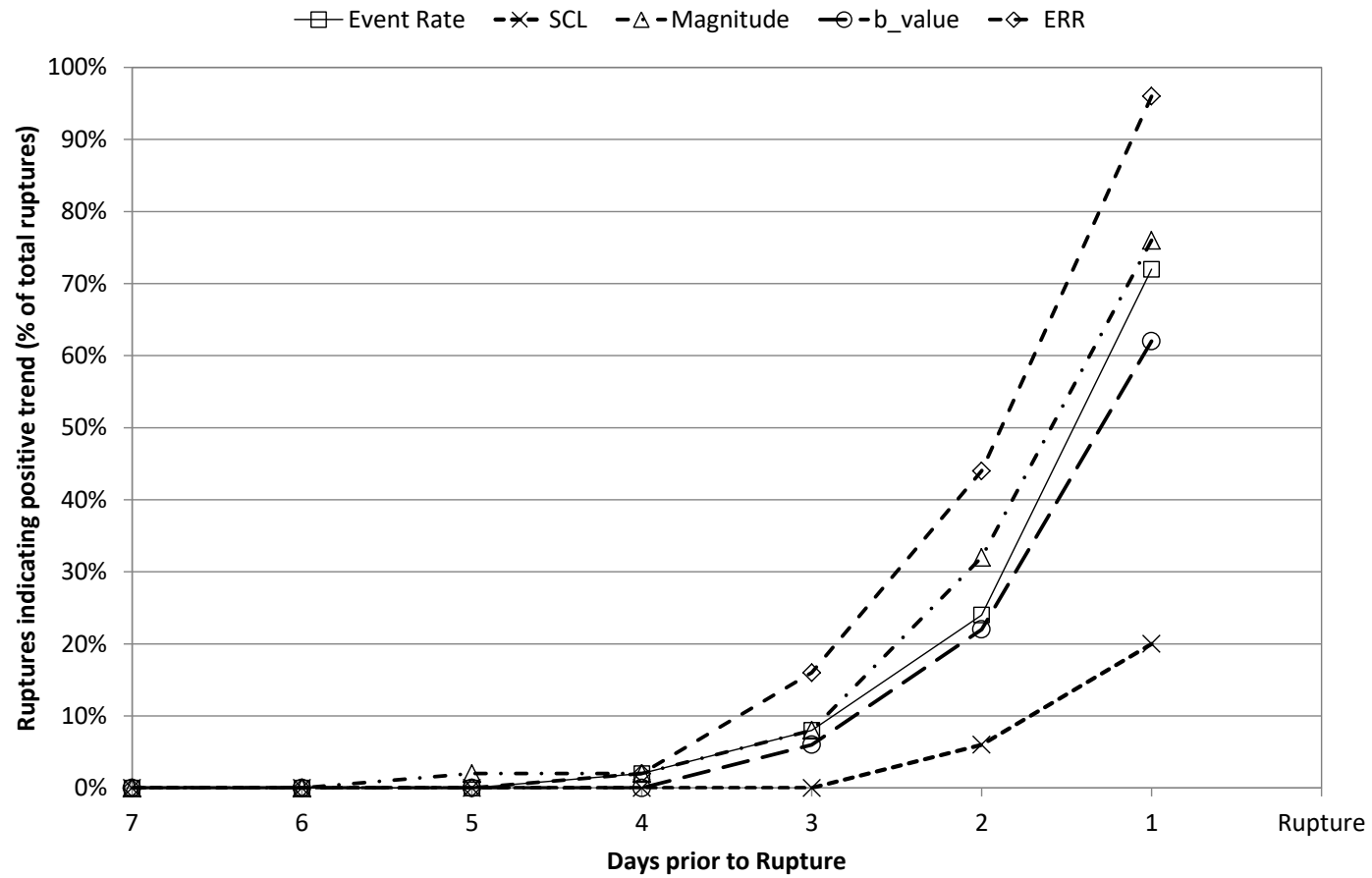


Figure A9 7: Comparison of daily parameters for instantaneous failures for the North East Faults Group 2 (50 failures).

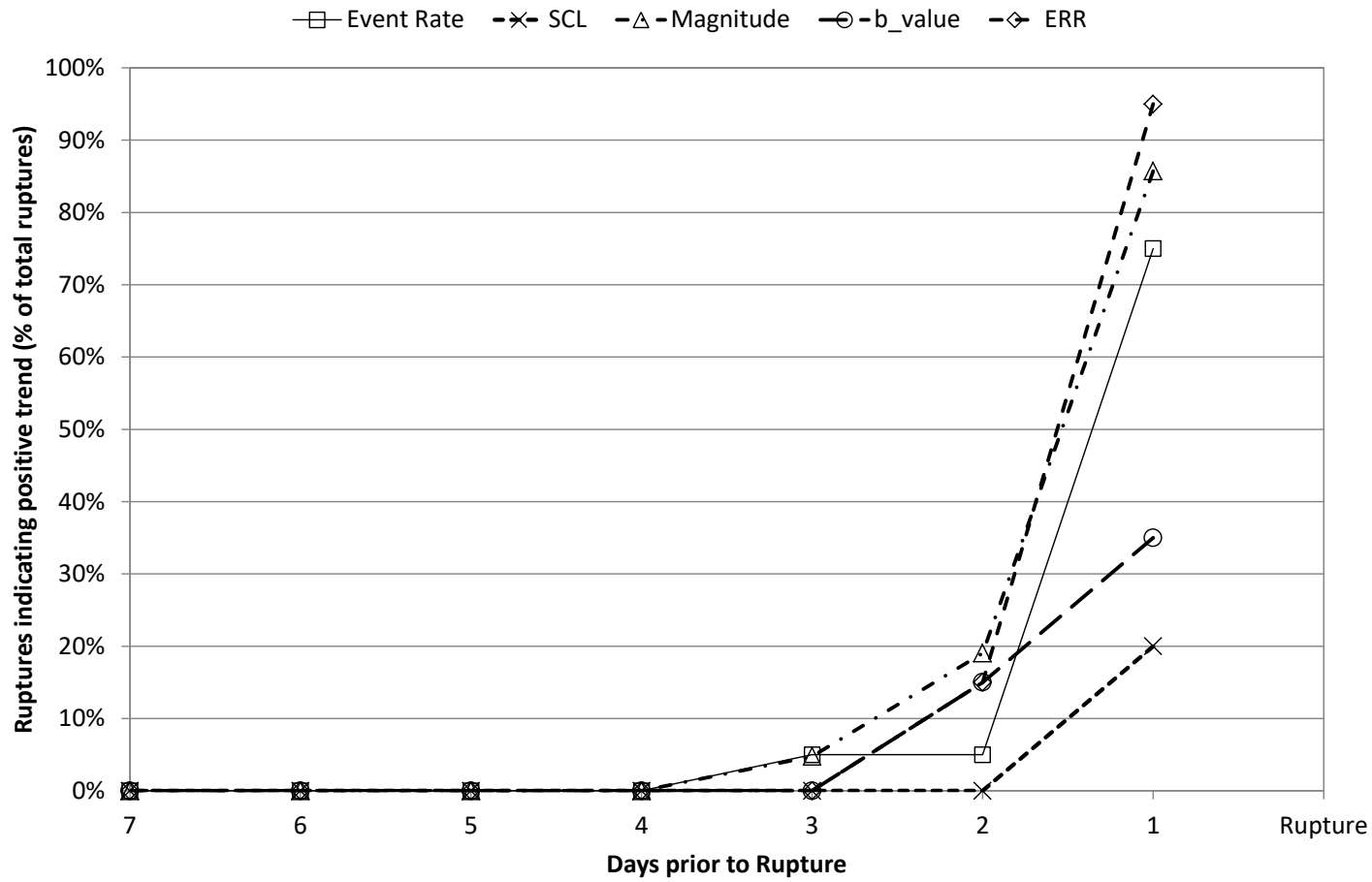


Figure A9 8: Comparison of daily parameters for instantaneous failures for the FaultP_1 (20 events).

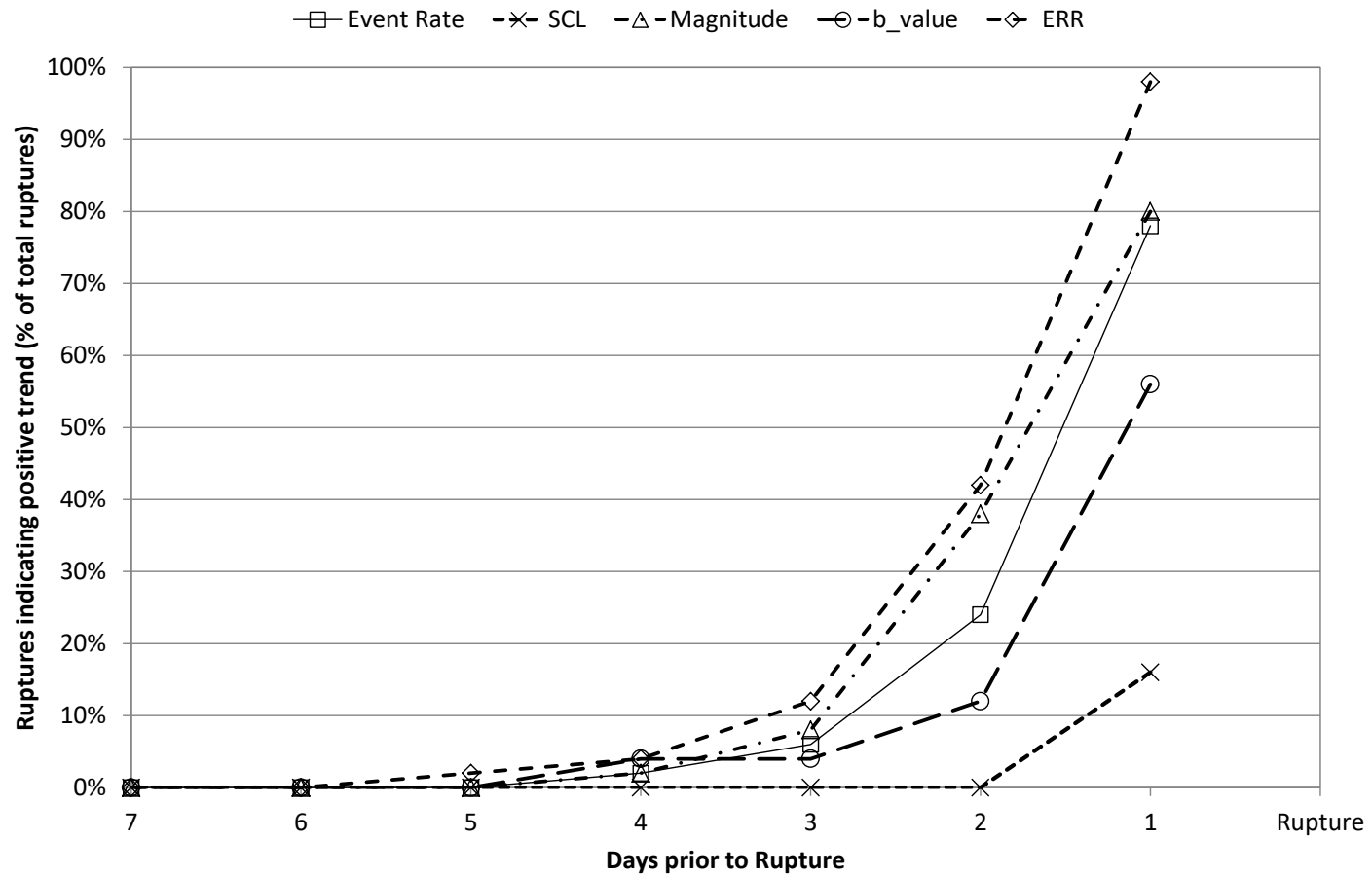


Figure A9 9: Comparison of daily parameters for instantaneous failures for the Fault B_C (50 failures).

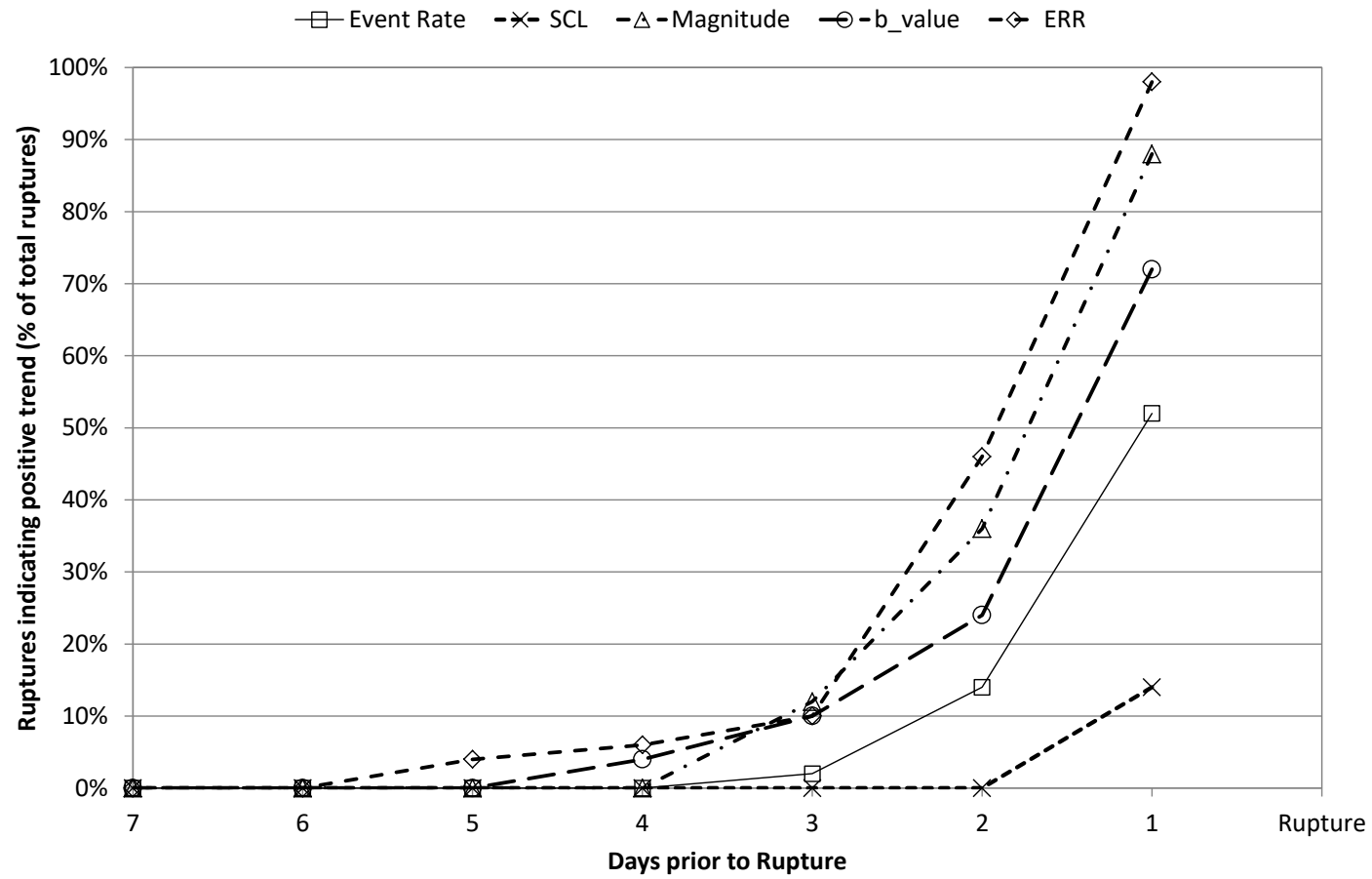


Figure A9 10: Comparison of daily parameters for instantaneous failures for the FW Dyke (50 failures).

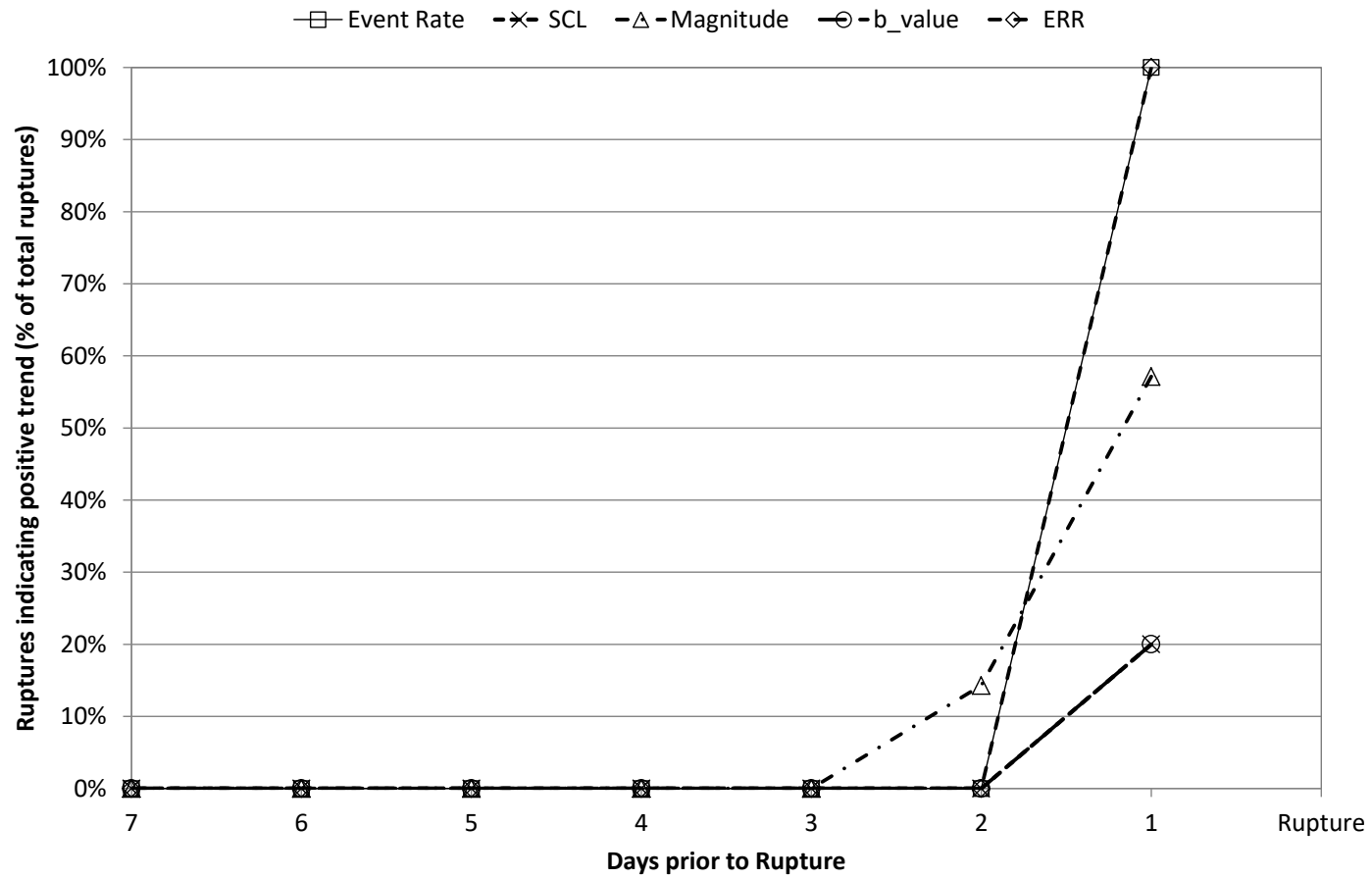


Figure A9 11: Comparison of daily parameters for instantaneous failures for the Maritana Fault (5 failures).

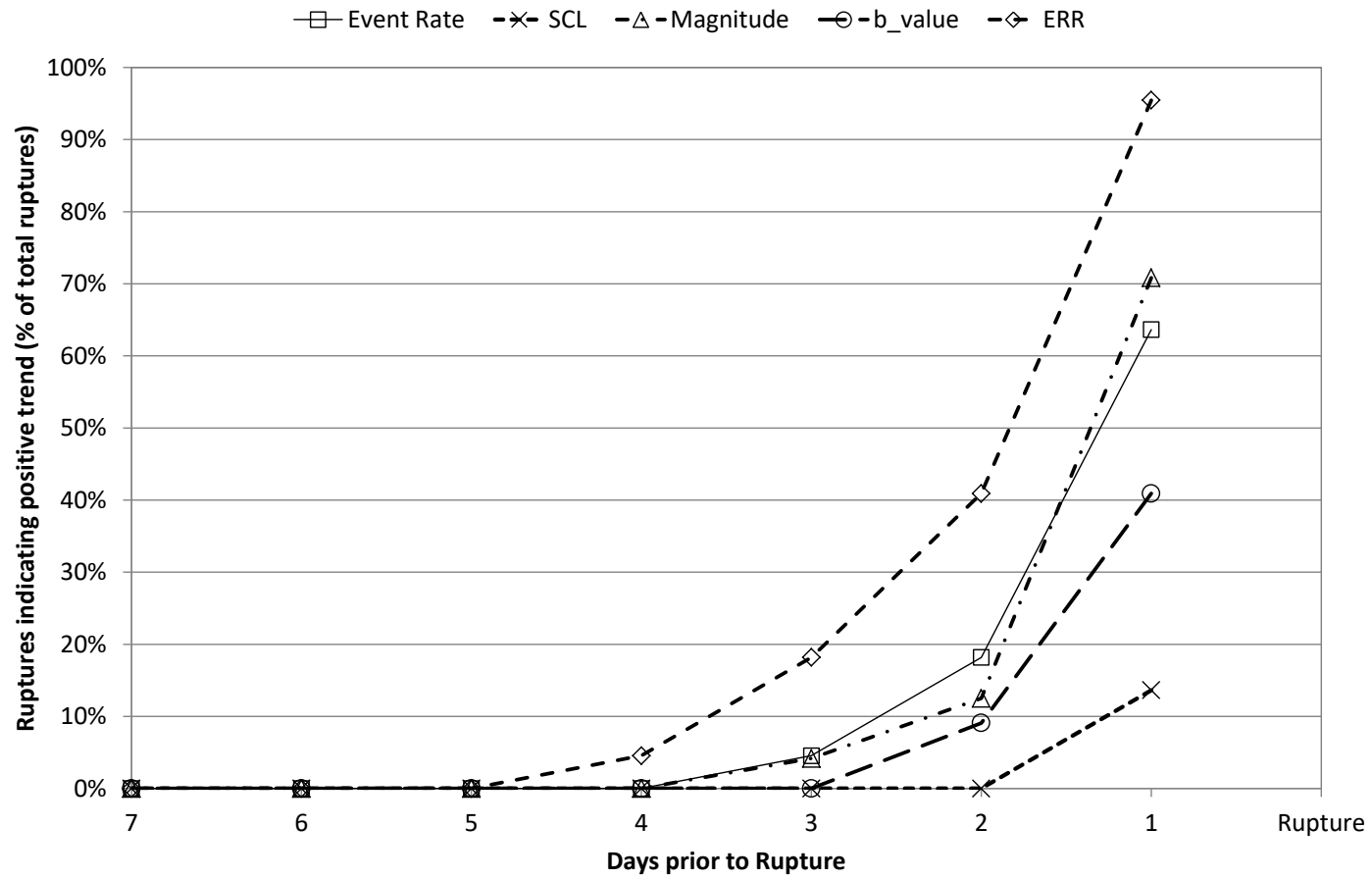


Figure A9 12: Comparison of daily parameters for instantaneous failures for the Reward Fault (22 failures).

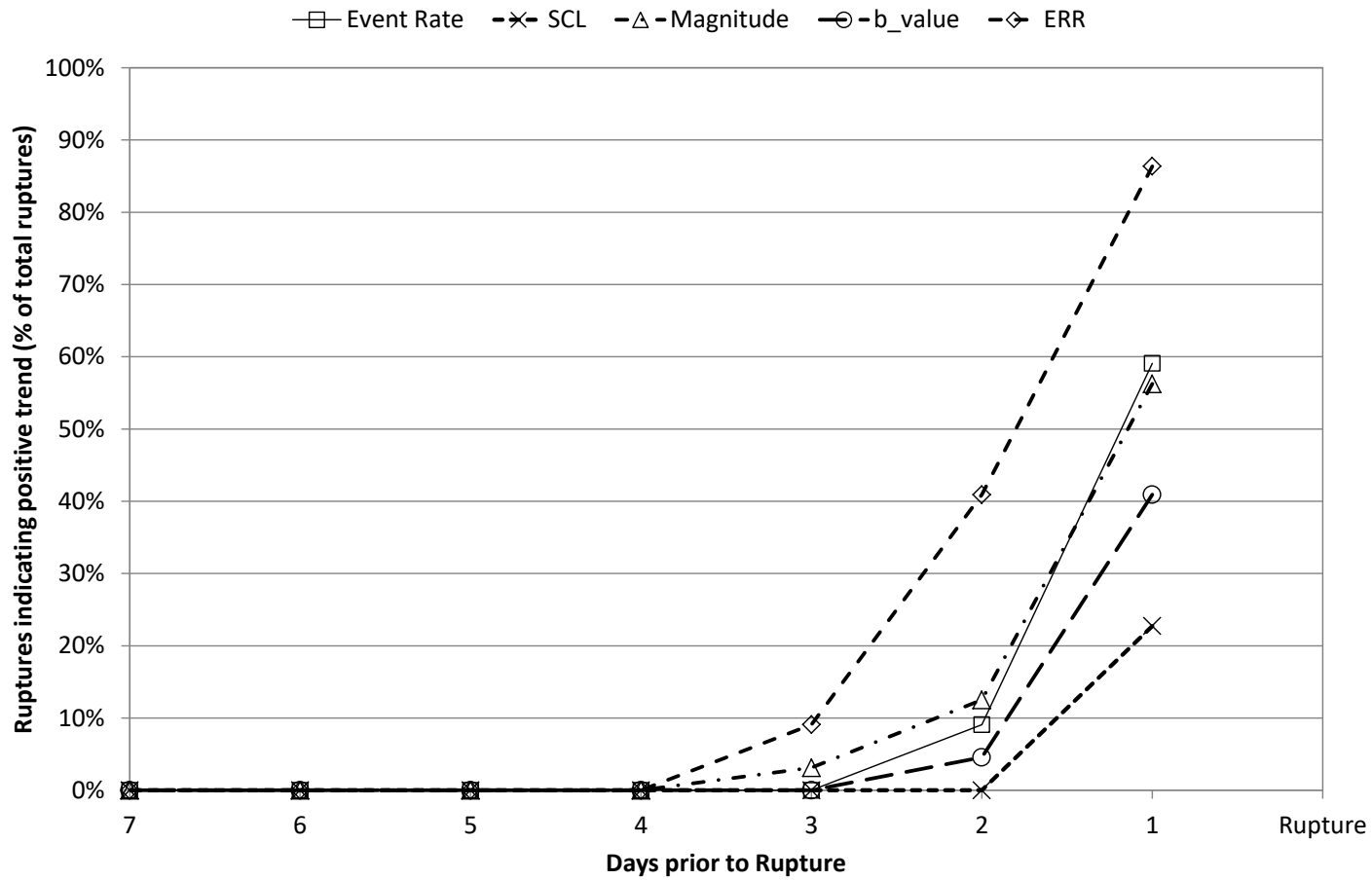


Figure A9 13: Comparison of daily parameters for instantaneous failures for the Flanagan Fault (22 failures).

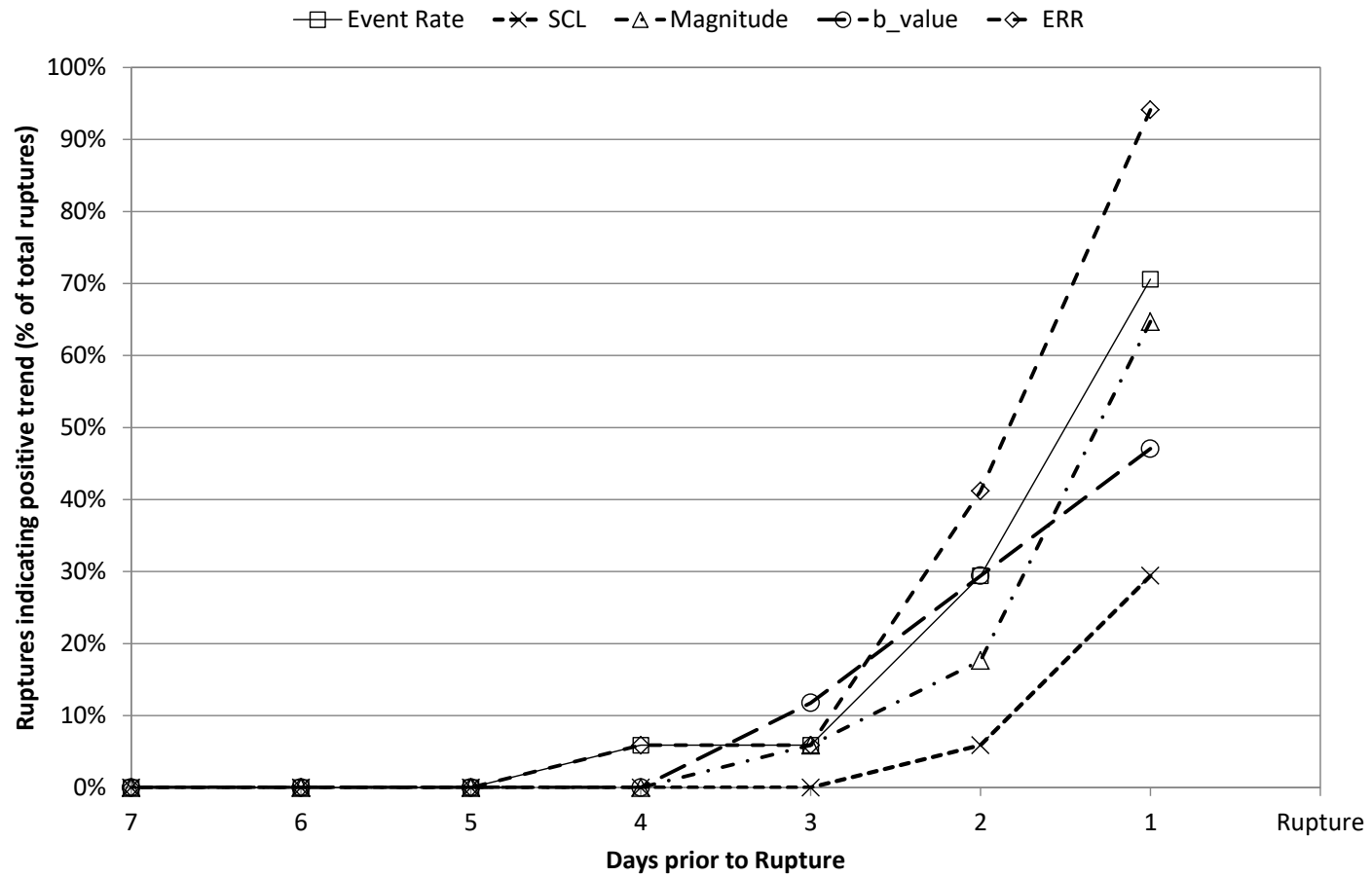


Figure A9 14: Comparison of daily parameters for instantaneous failures for the Feral Fault (17 failures).

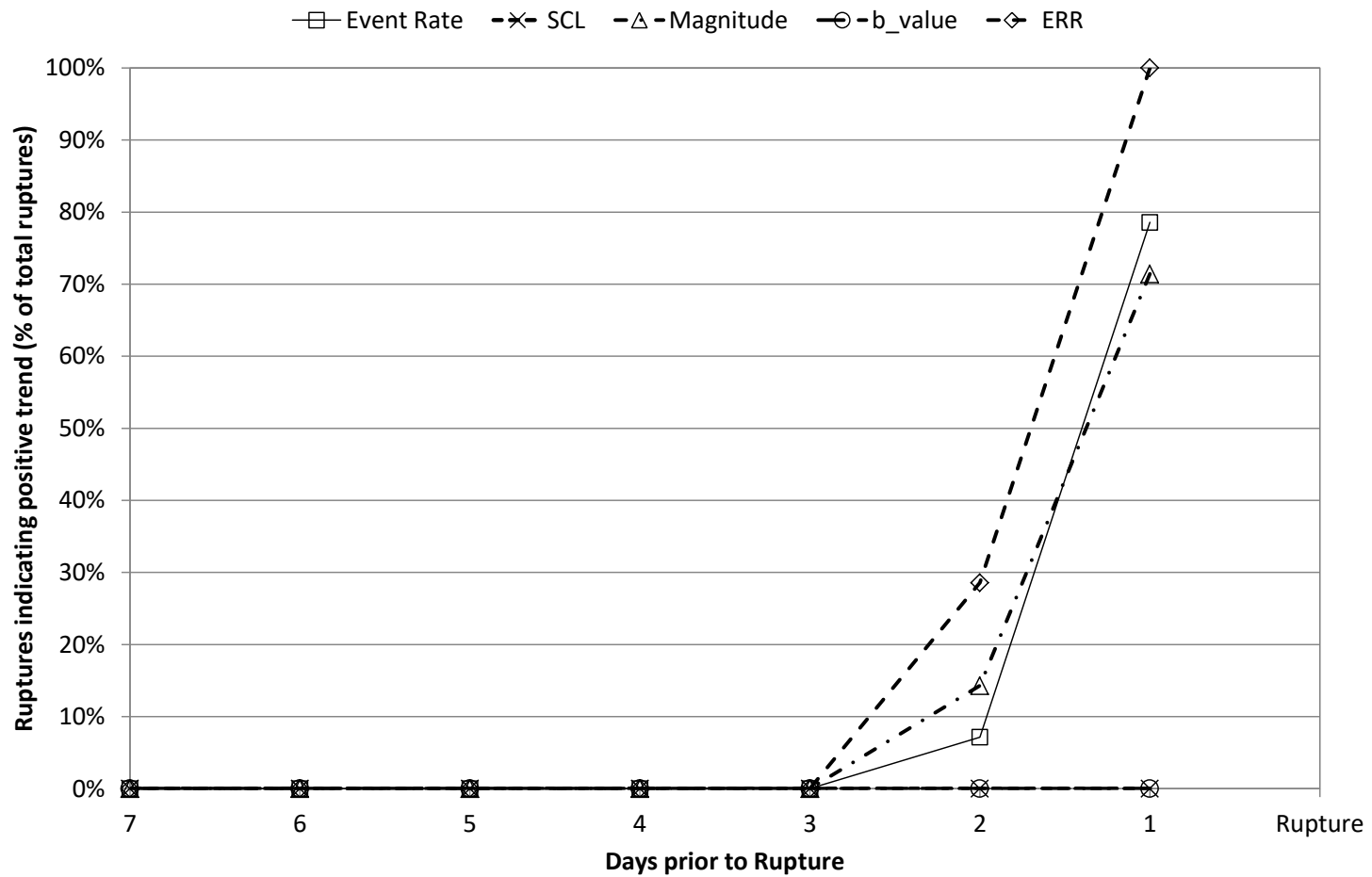


Figure A9 15: Comparison of daily parameters for instantaneous failures for the Great Lyell Fault (14 failures).

**Appendix 10 – Precursor comparison charts - daily averages,
accelerating slip failures results**

Comparison of parameters on each structure

Daily Accelerating Slip Results

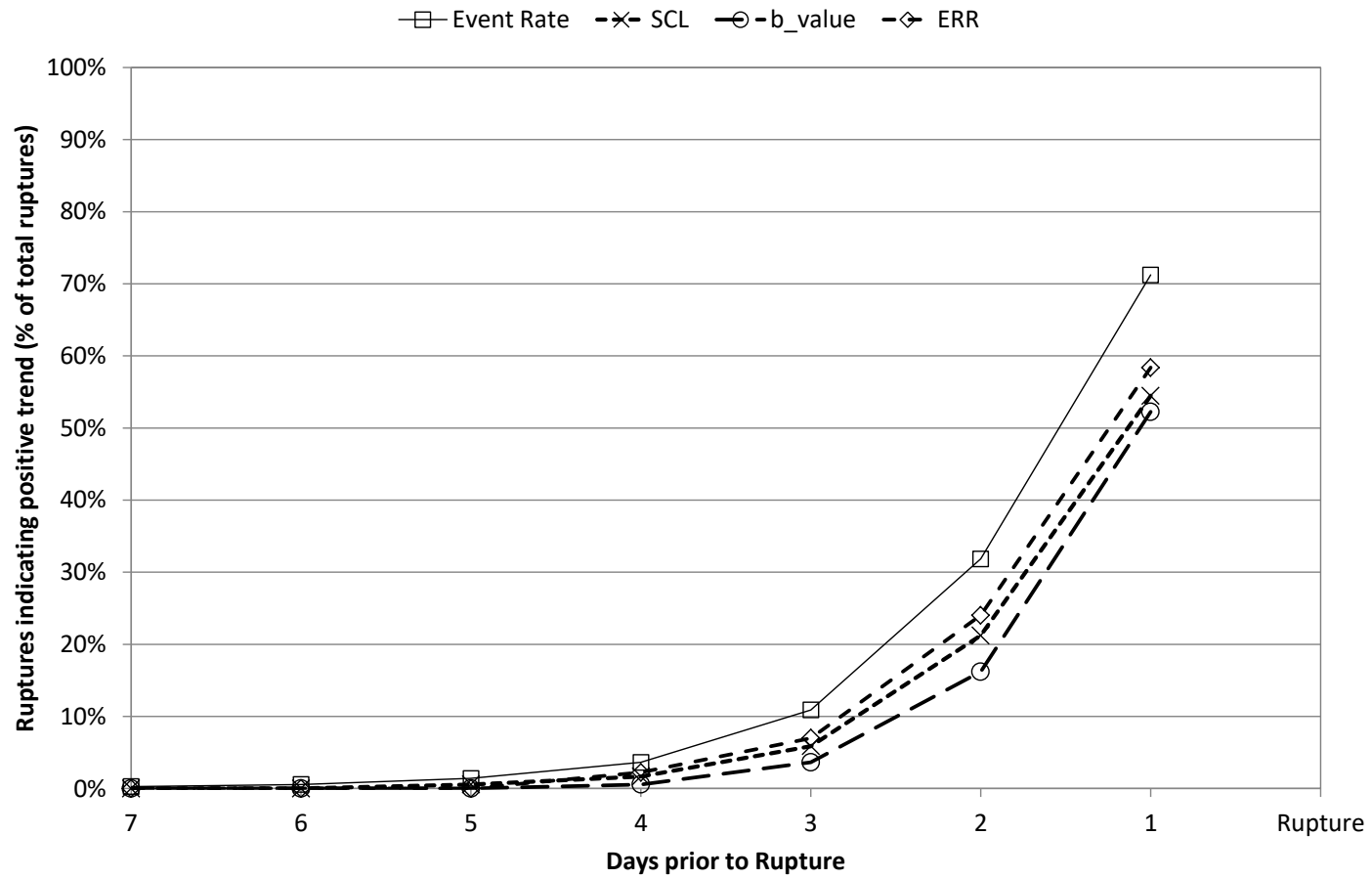


Figure A10 1: Comparison of average daily parameters for accelerating slip failures on all structures.

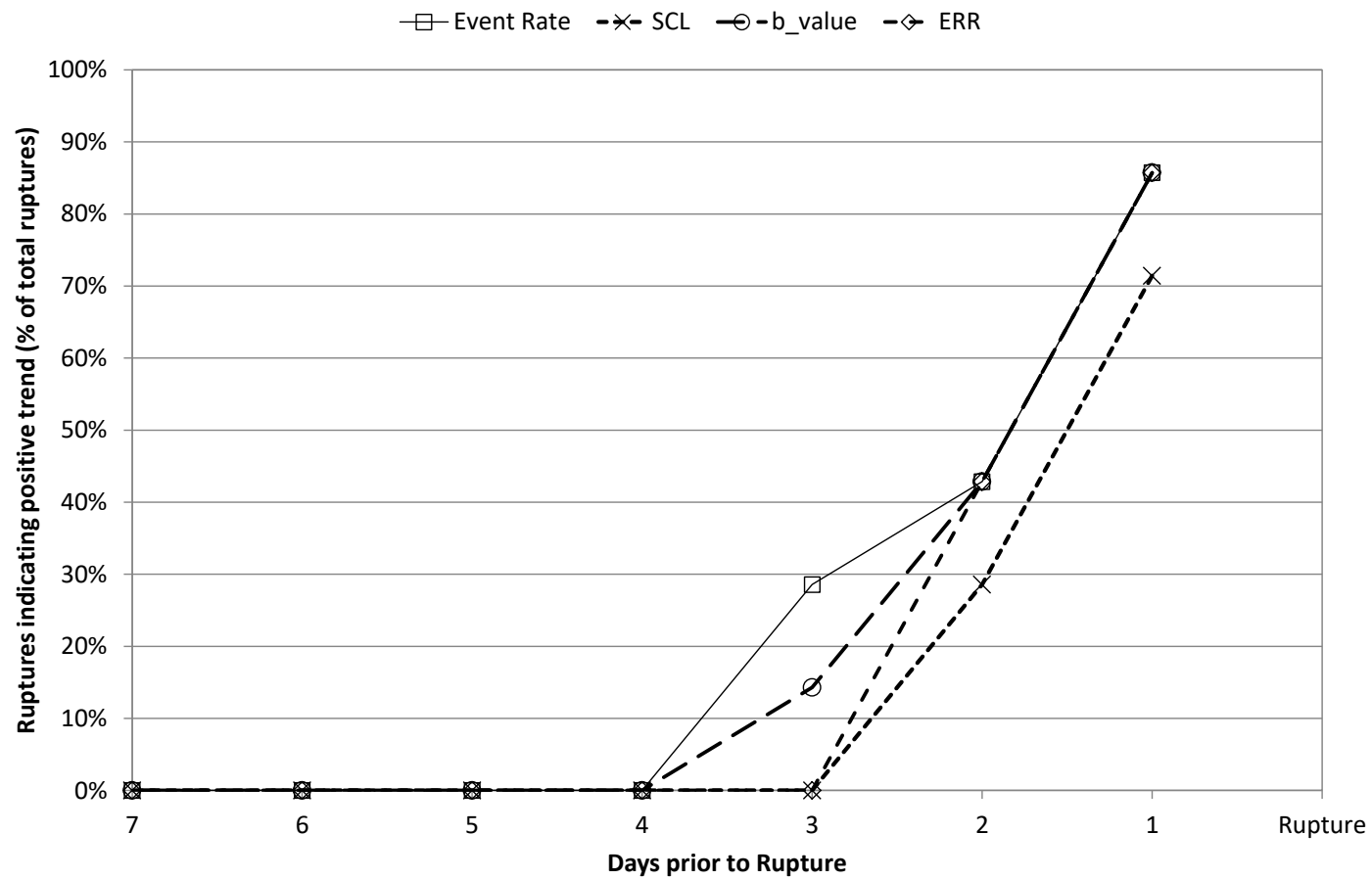


Figure A10 2: Comparison of daily parameters for accelerating slip failures on the A1 Shear (7 failures).

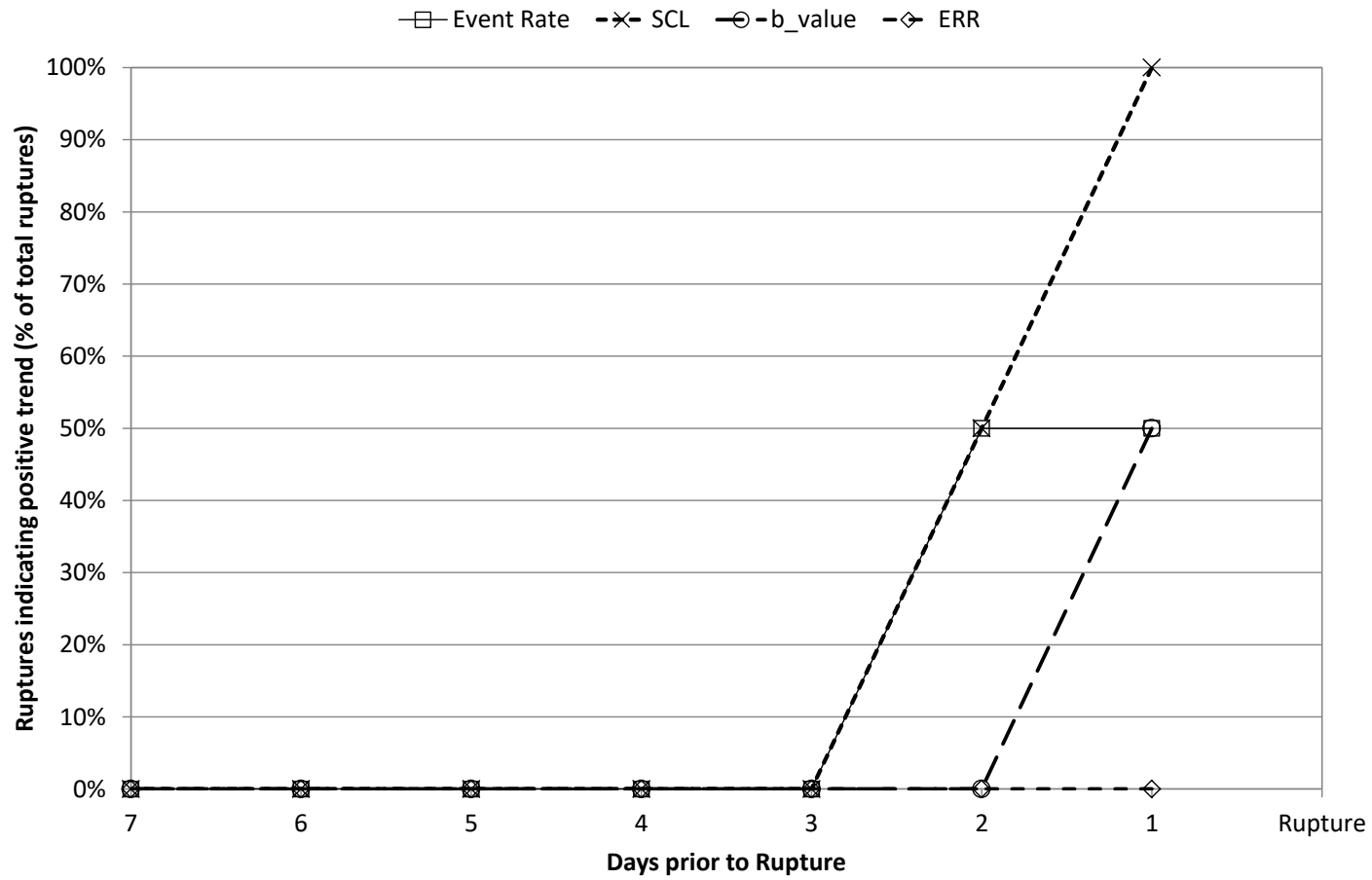


Figure A10 3: Comparison of daily parameters for accelerating slip failures for the North Dyke (2 failures).

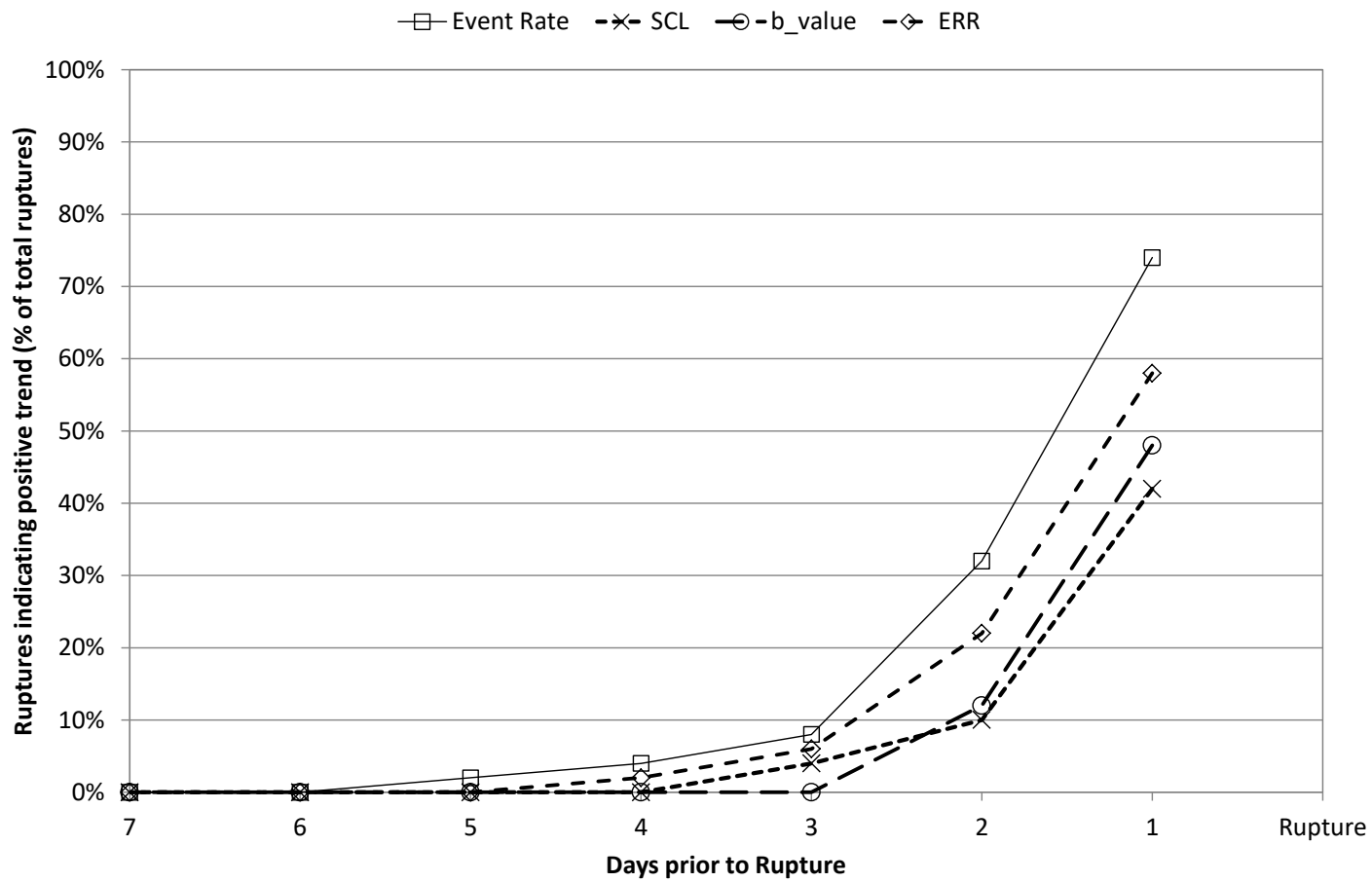


Figure A10 4: Comparison of daily parameters for accelerating slip failures for the Fitzroy Fault (50 failures).

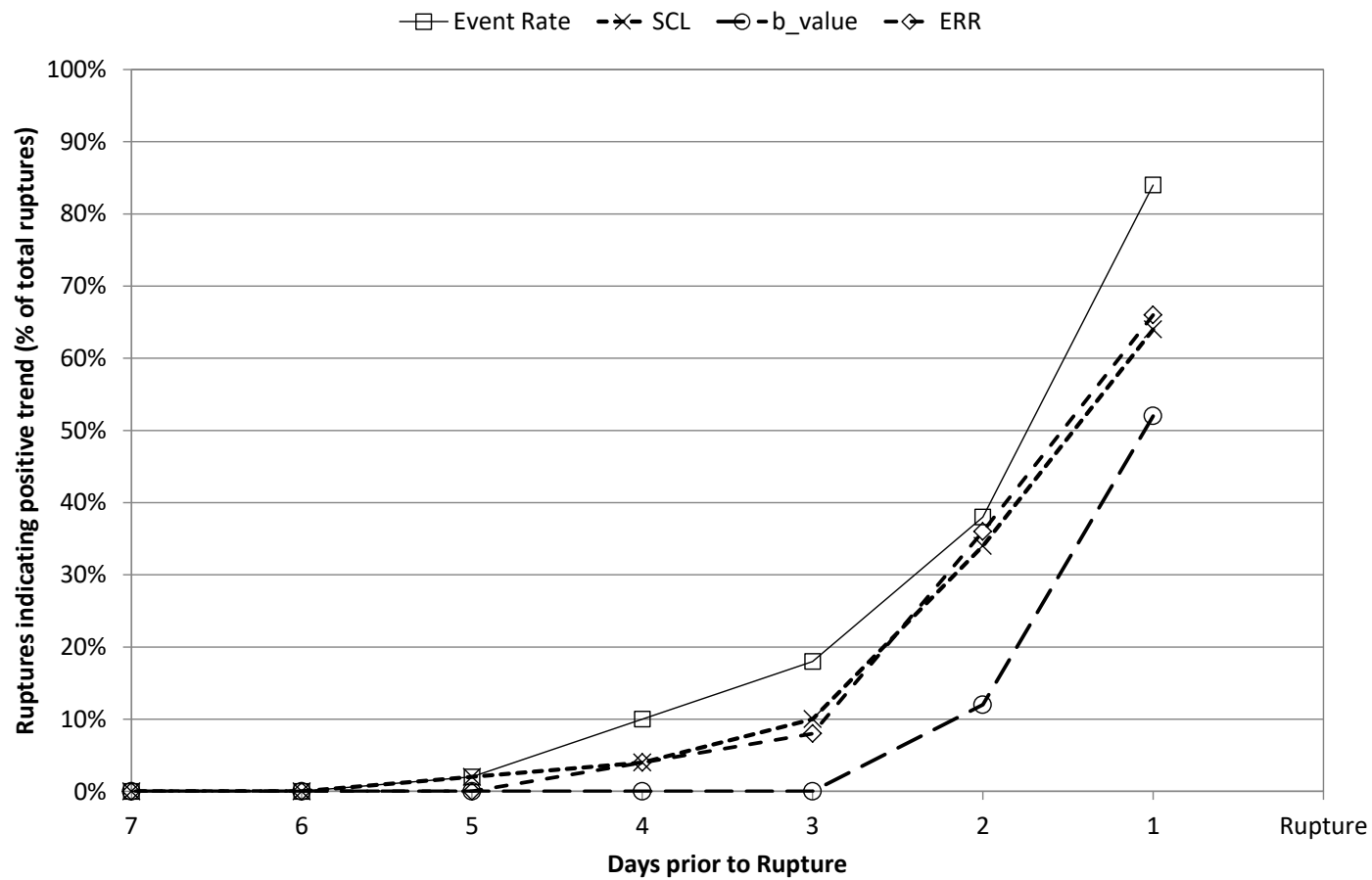


Figure A10 5: Comparison of daily parameters for accelerating slip failures for the North East Faults Group 1 (50 failures).

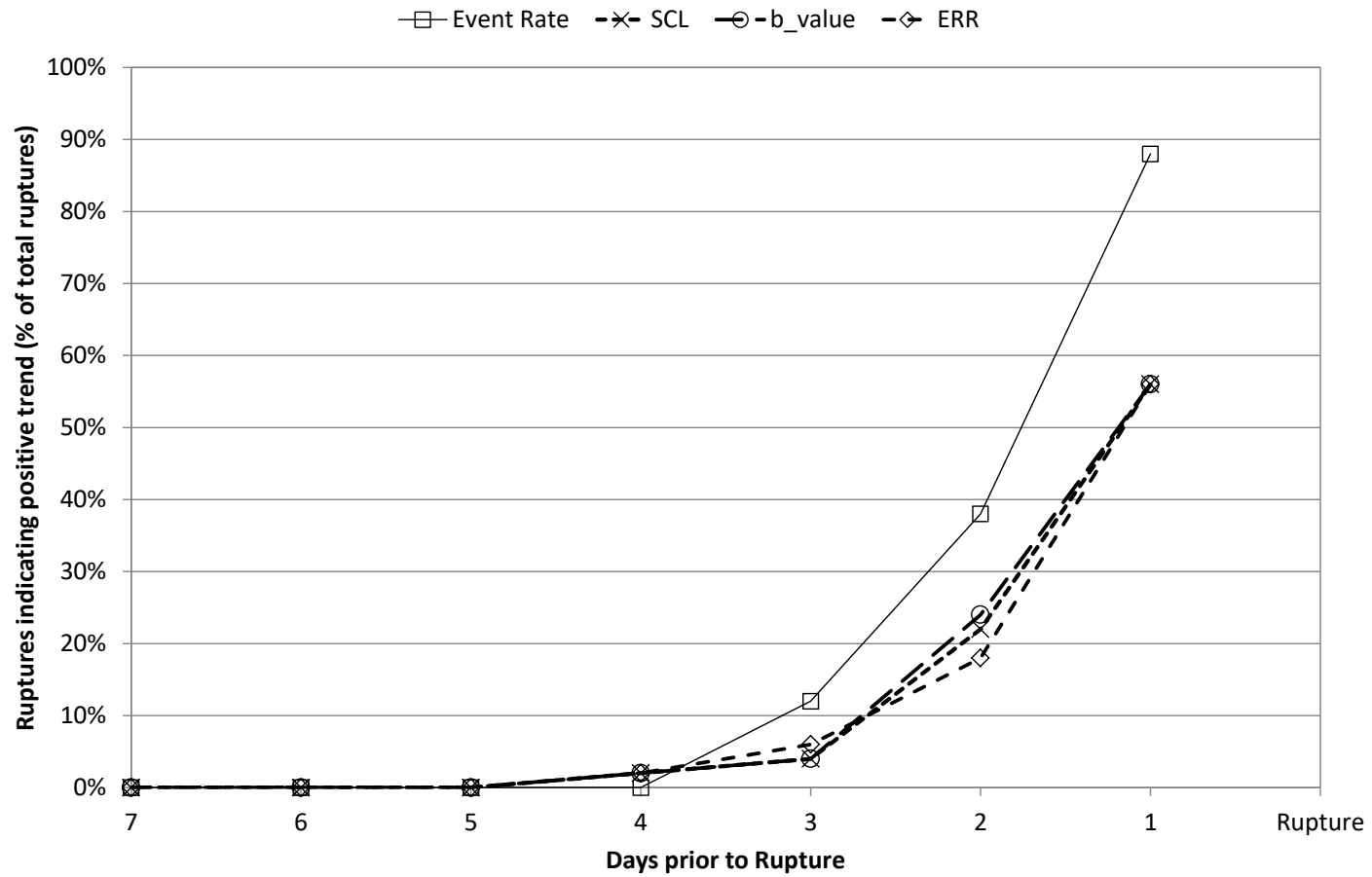


Figure A10 6: Comparison of daily parameters for accelerating slip failures for the North East Faults Group 2 (50 failures).

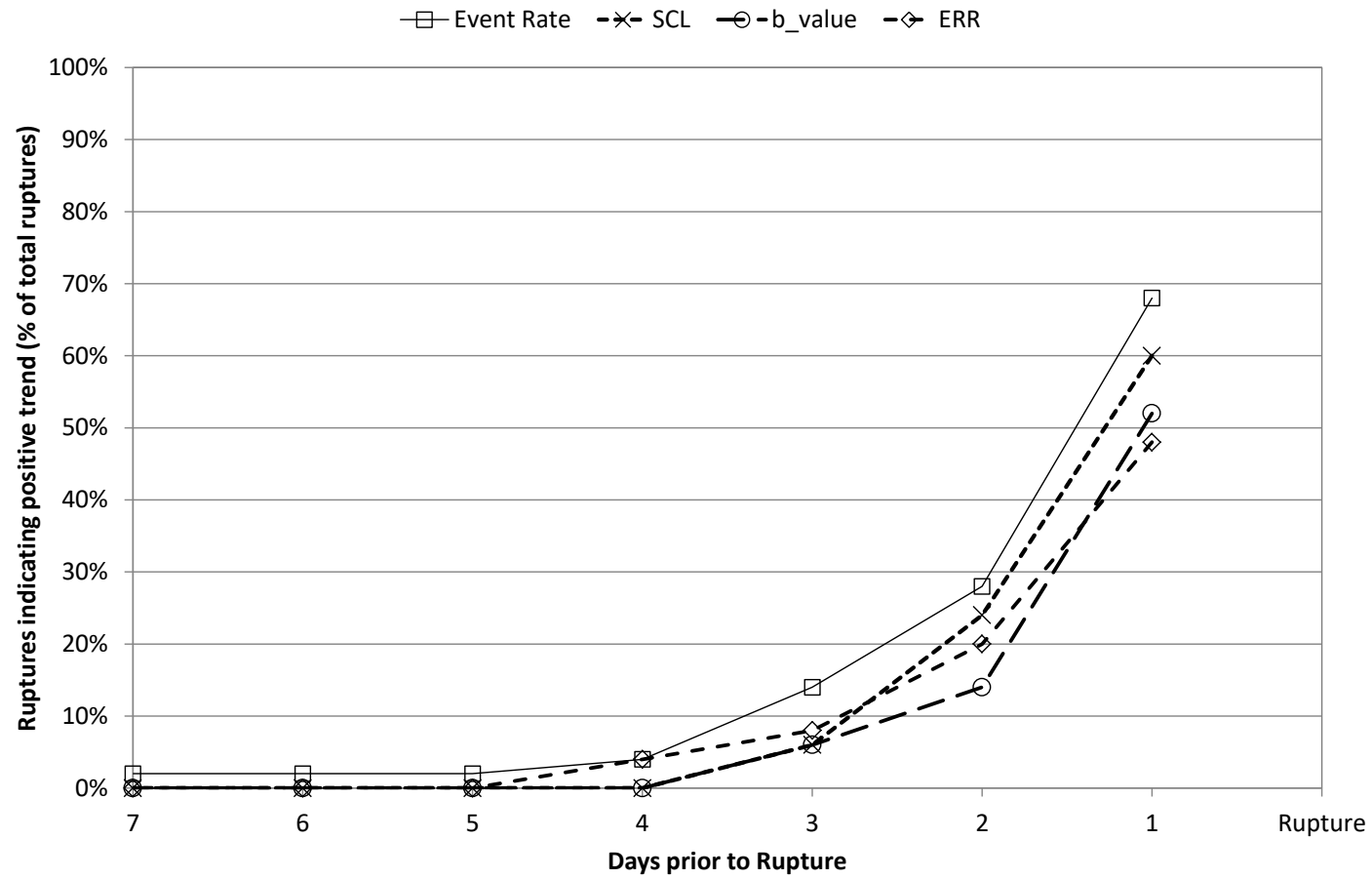


Figure A10 7: Comparison of daily parameters for accelerating slip failures for the Fault B_C (50 failures).

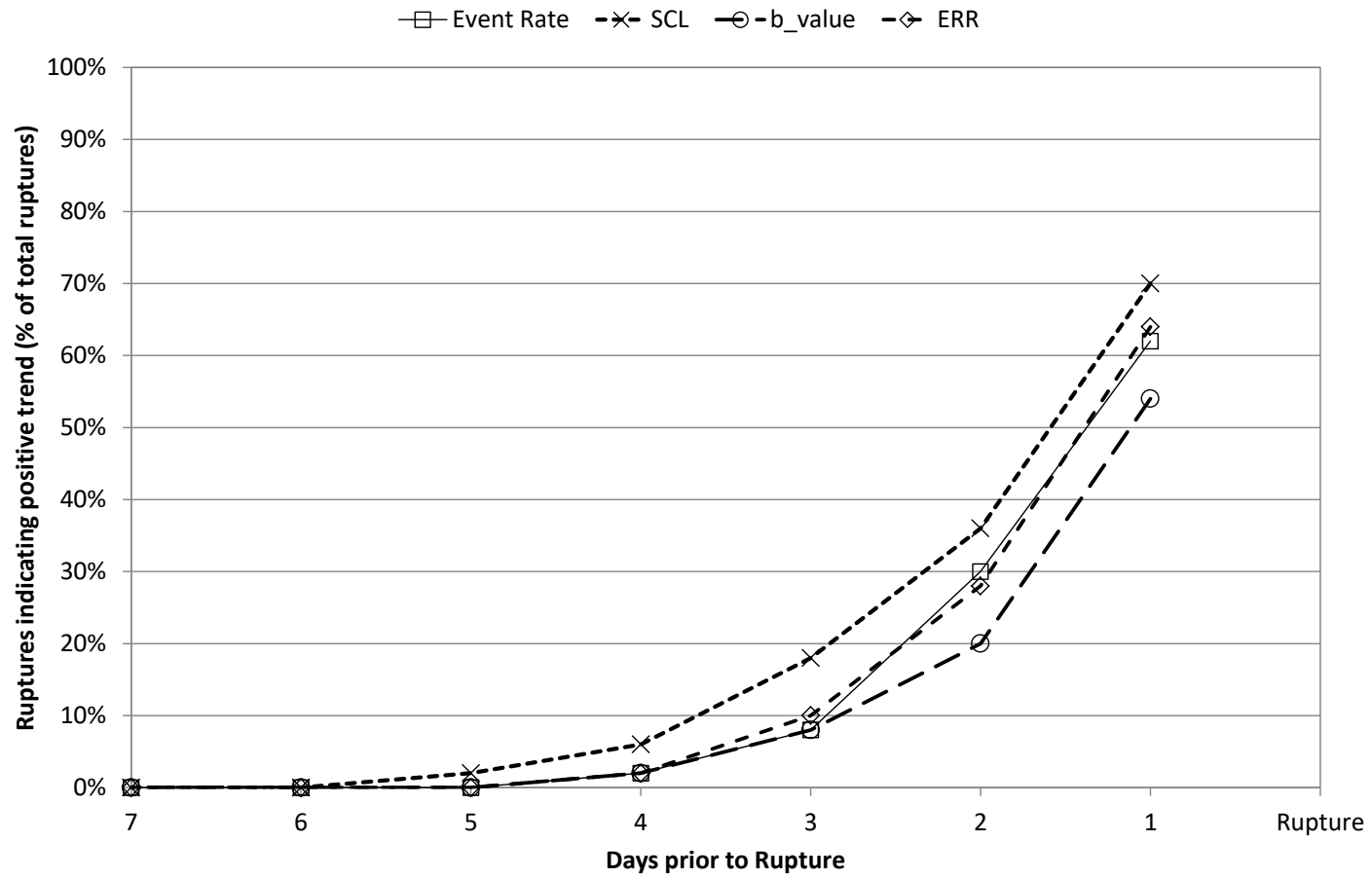


Figure A10 8: Comparison of daily parameters for accelerating slip failures for the FW Dyke (50 failures).

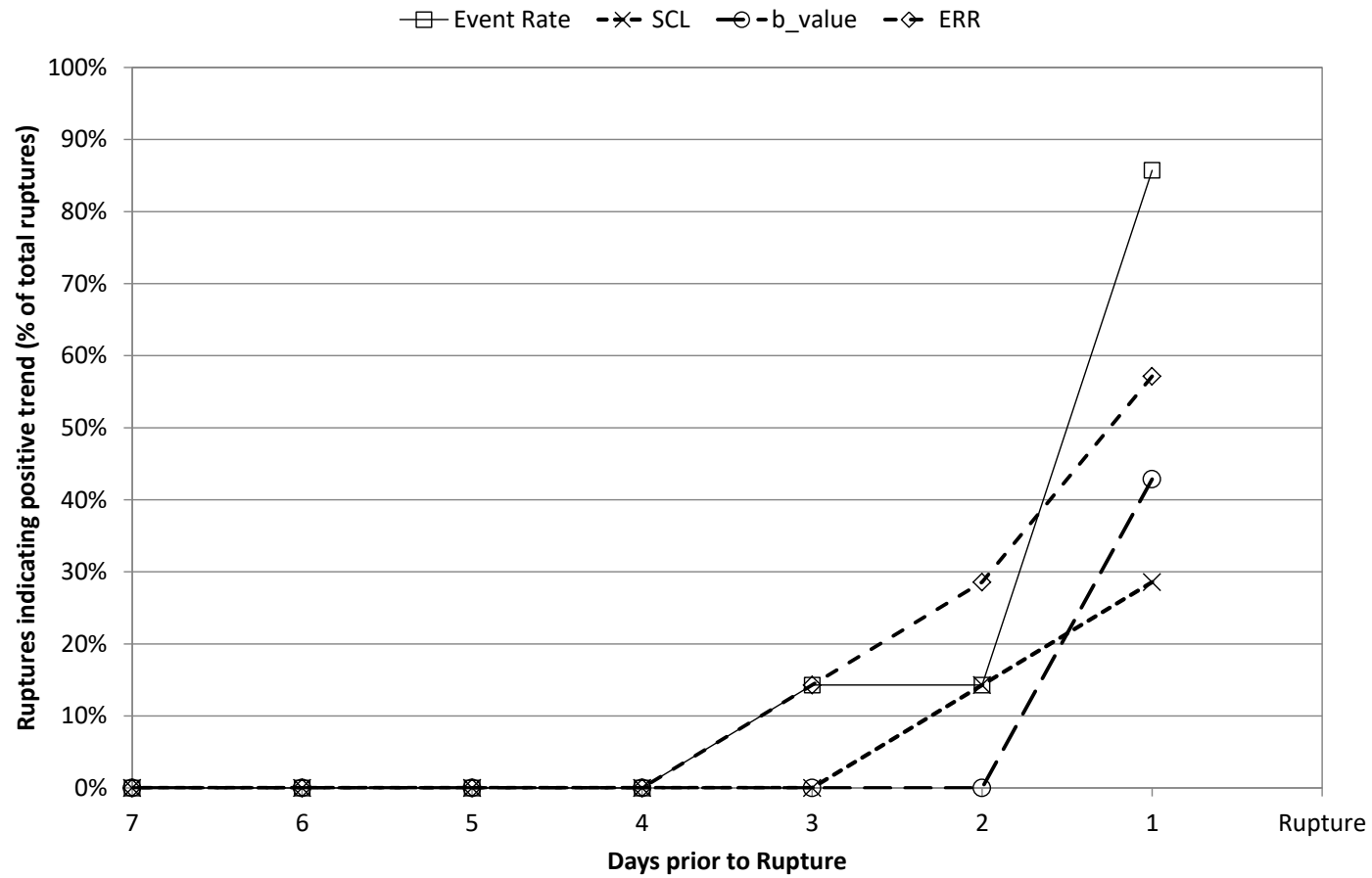


Figure A10 9: Comparison of daily parameters for accelerating slip failures for the Reward Fault (7 failures).

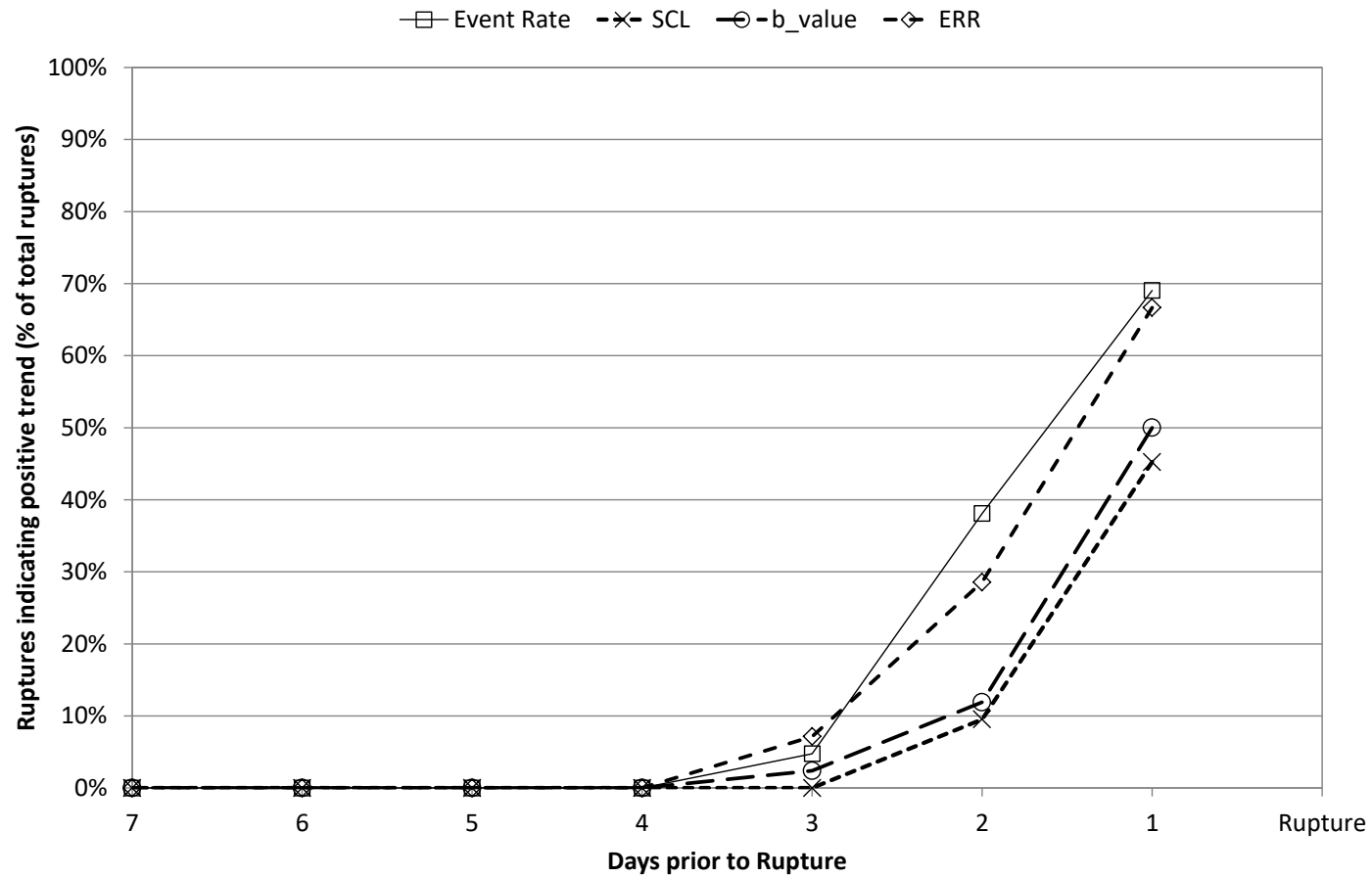


Figure A10 10: Comparison of daily parameters for accelerating slip failures for the Flanagan Fault (42 failures).

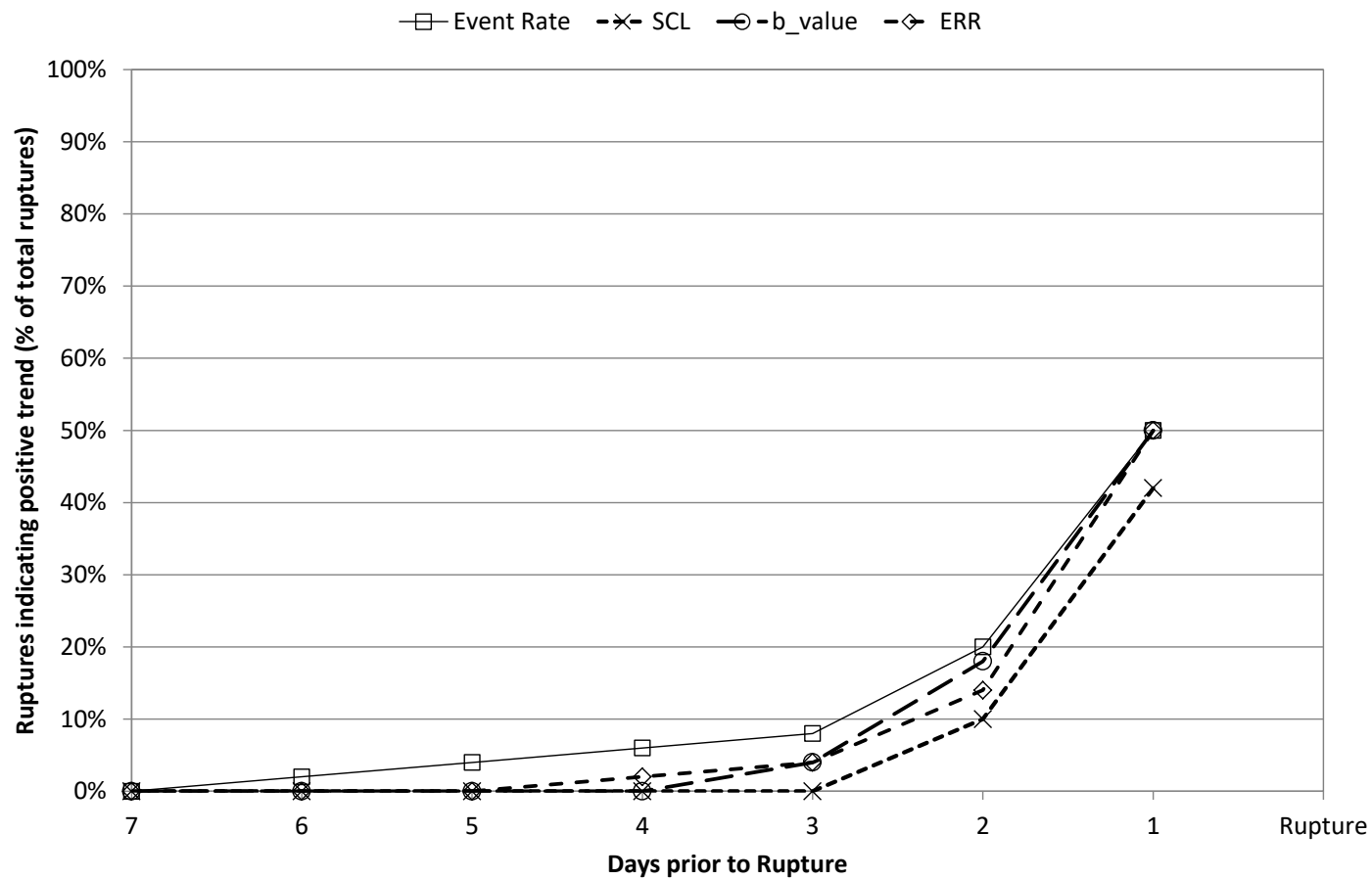


Figure A10 11: Comparison of daily parameters for accelerating slip failures for the Feral Fault (50 failures).

**Appendix 11 – Precursor comparison charts - 7 day averages,
instantaneous failures results**

Comparison of parameters on each structure

7 day Instantaneous Results

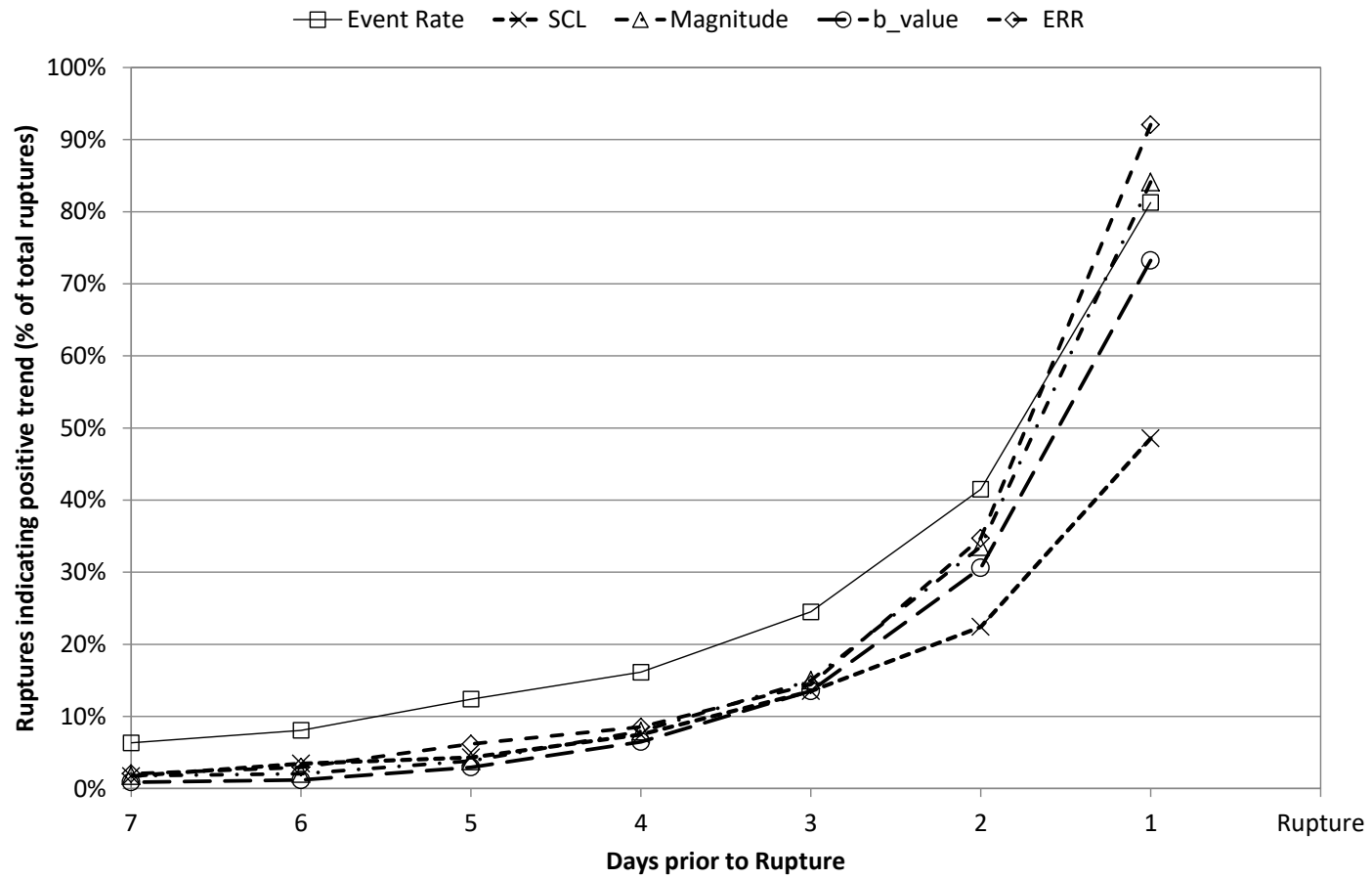


Figure A11 1: Comparison of average 7 day parameters for instantaneous failures on all structures.

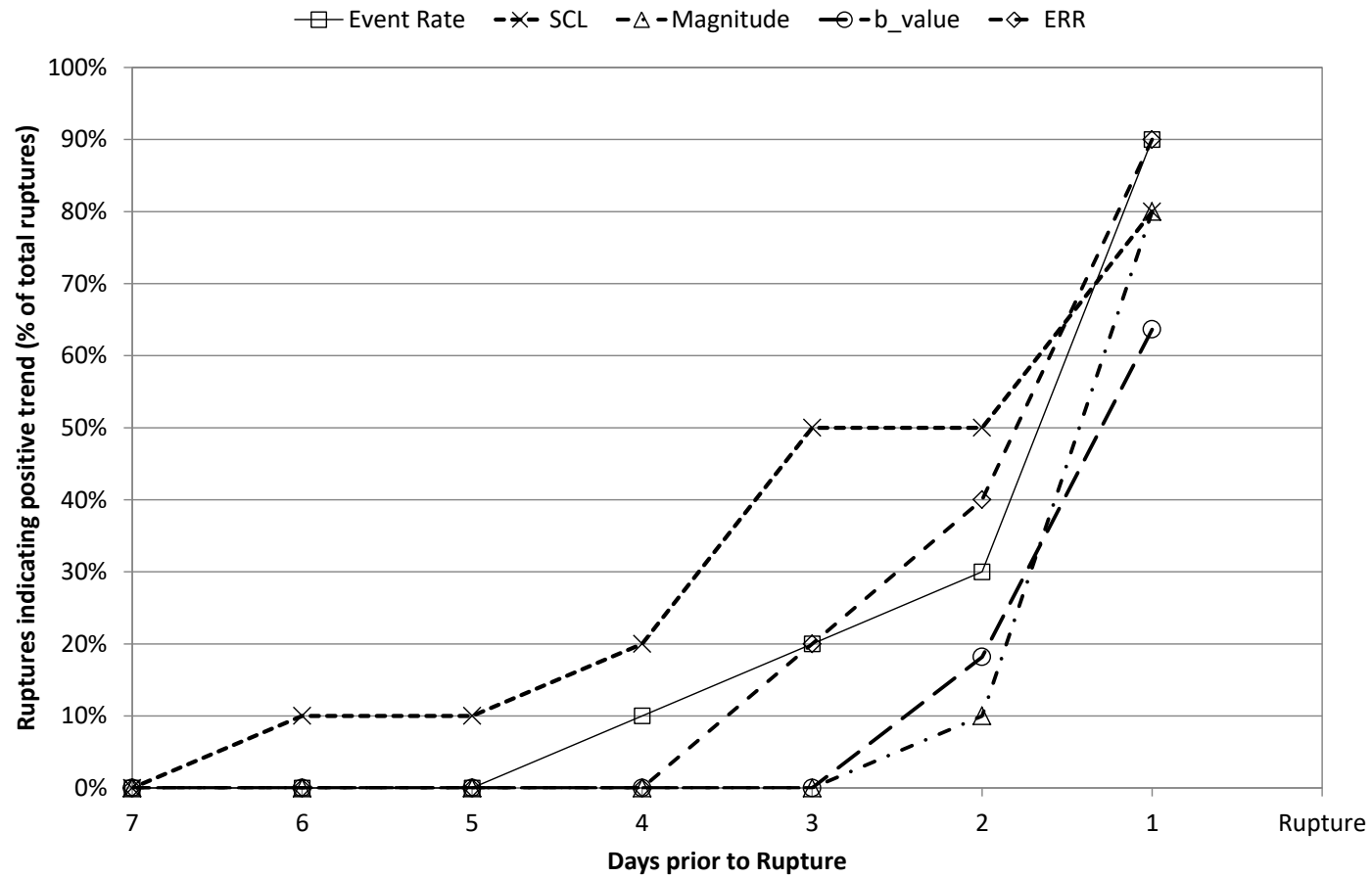


Figure A11 2: Comparison of 7 day parameters for instantaneous failures on the A1 Shear (10 failures).

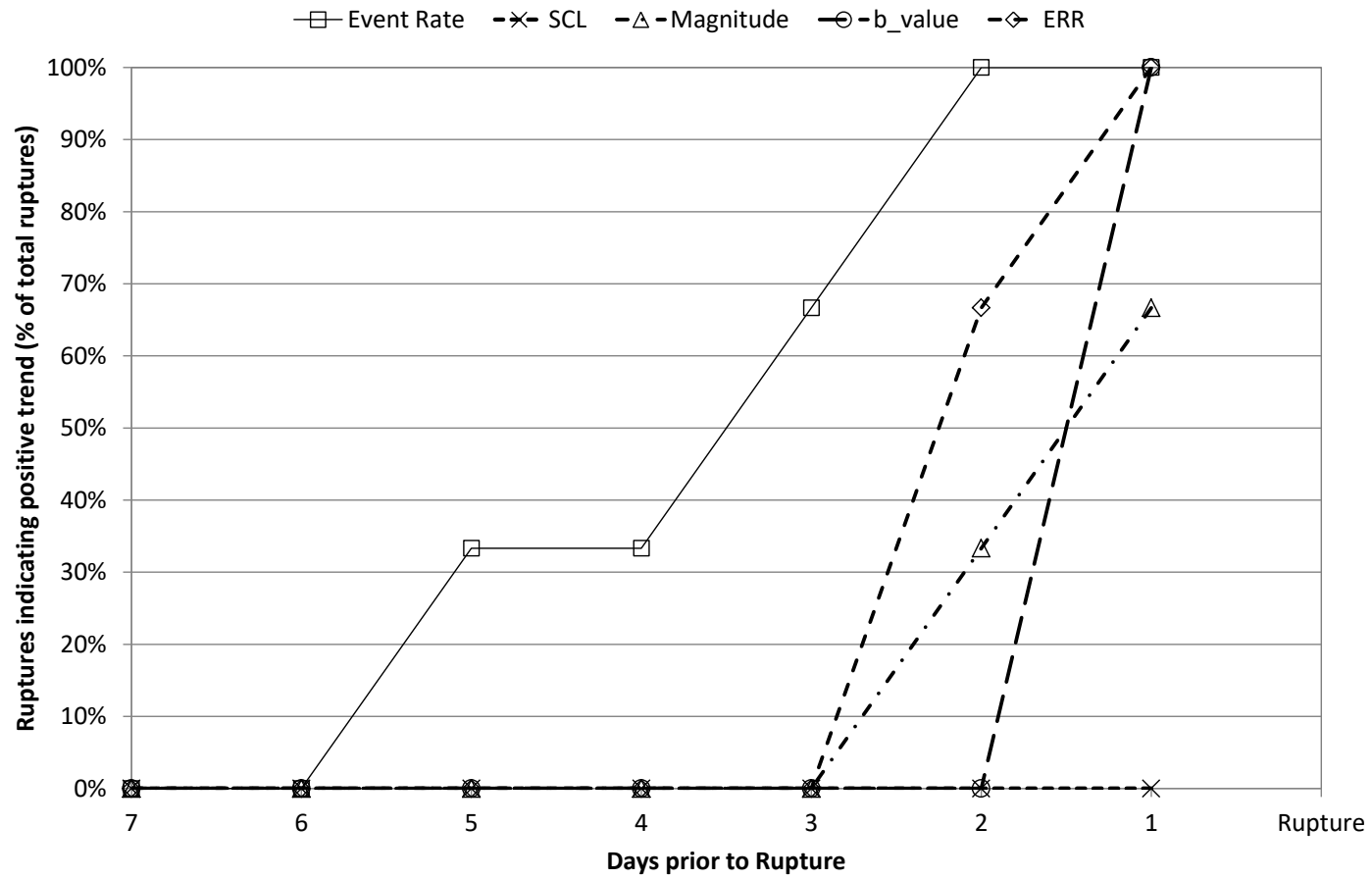


Figure A11 3: Comparison of 7 day parameters for instantaneous failures for the North Dyke (3 failures).

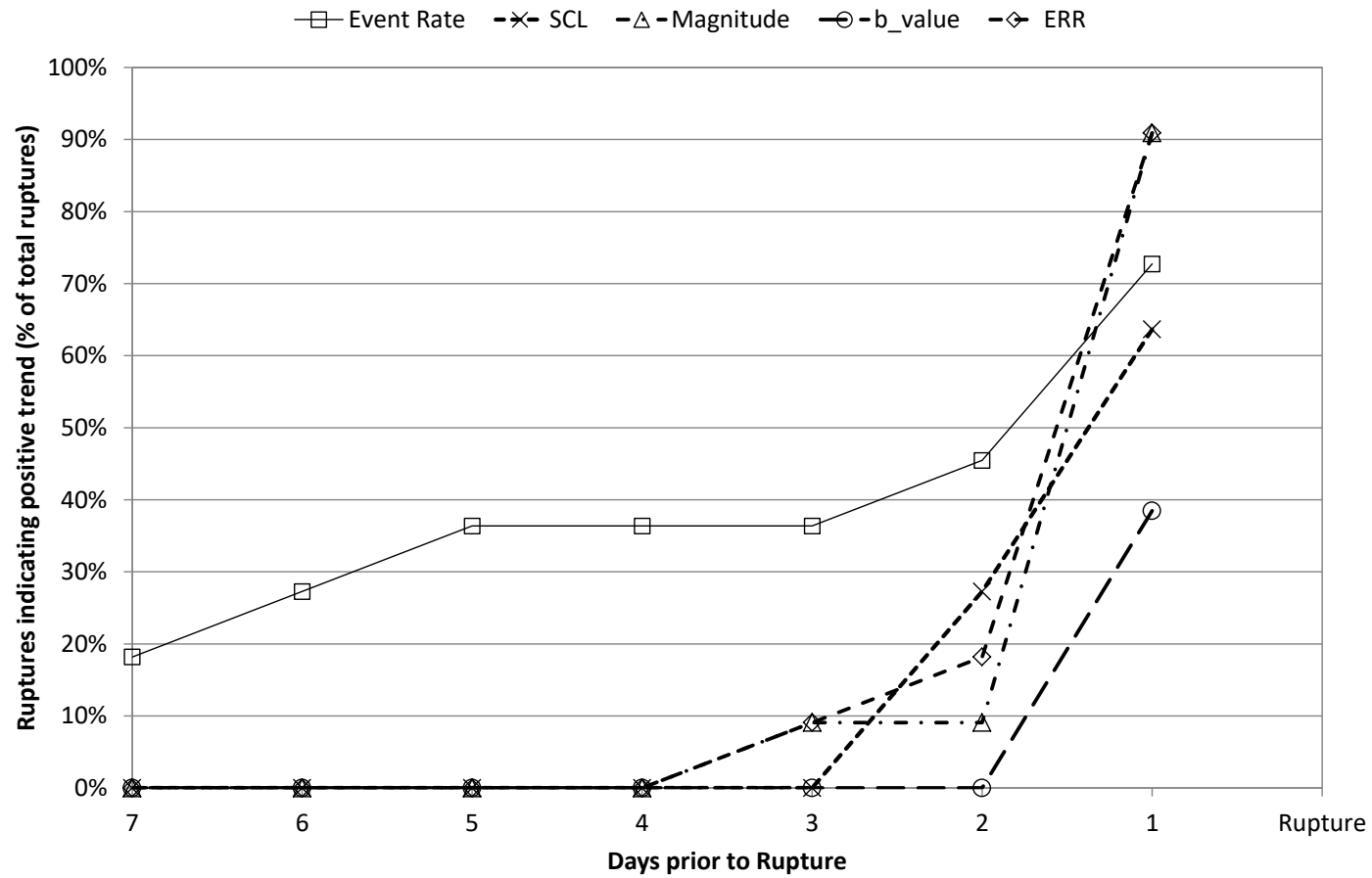


Figure A11 4: Comparison of 7 day parameters for instantaneous failures for the Mini Dyke (11 failures).

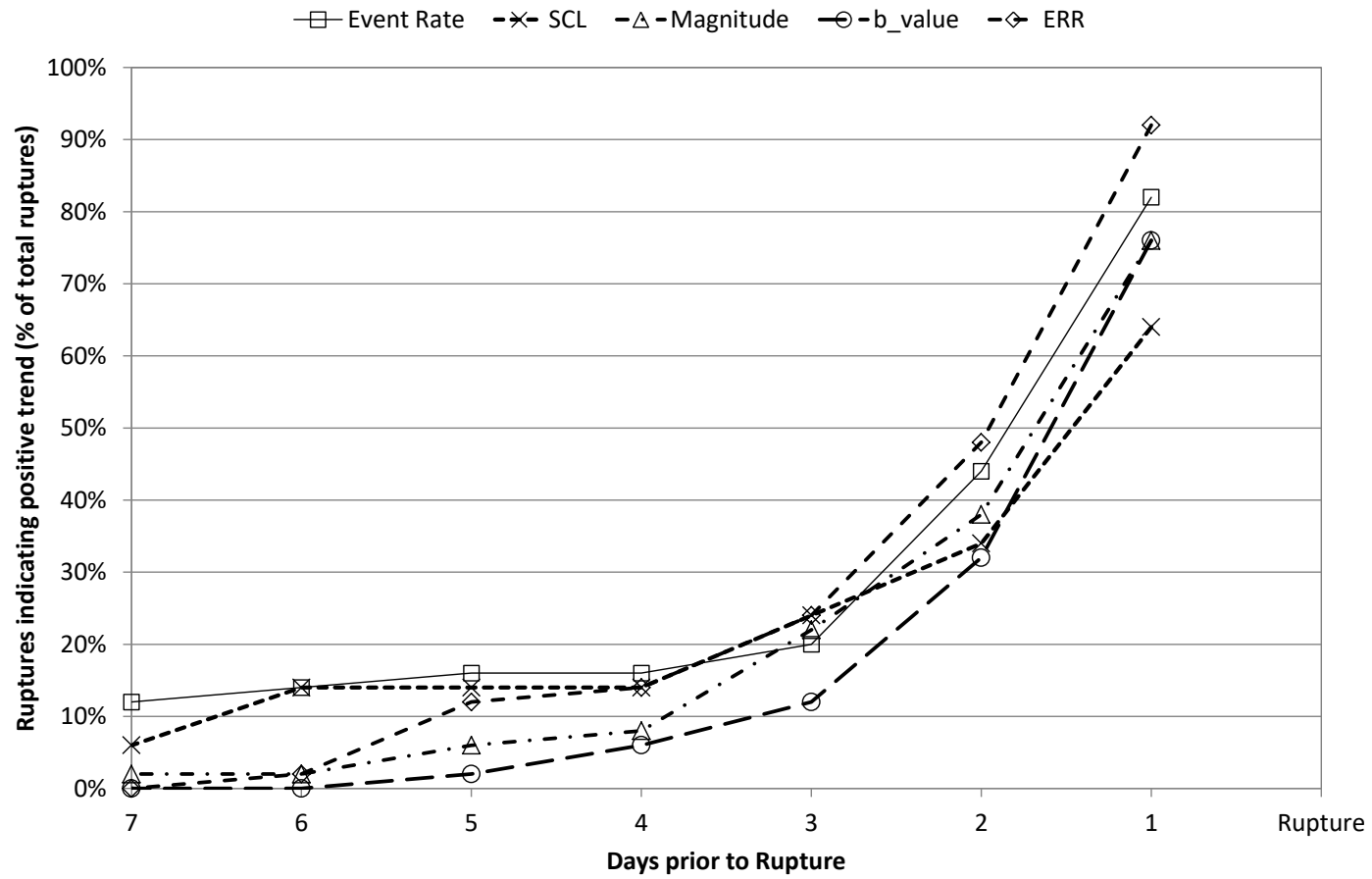


Figure A11 5: Comparison of 7 day parameters for instantaneous failures for the Fitzroy Fault (50 failures).

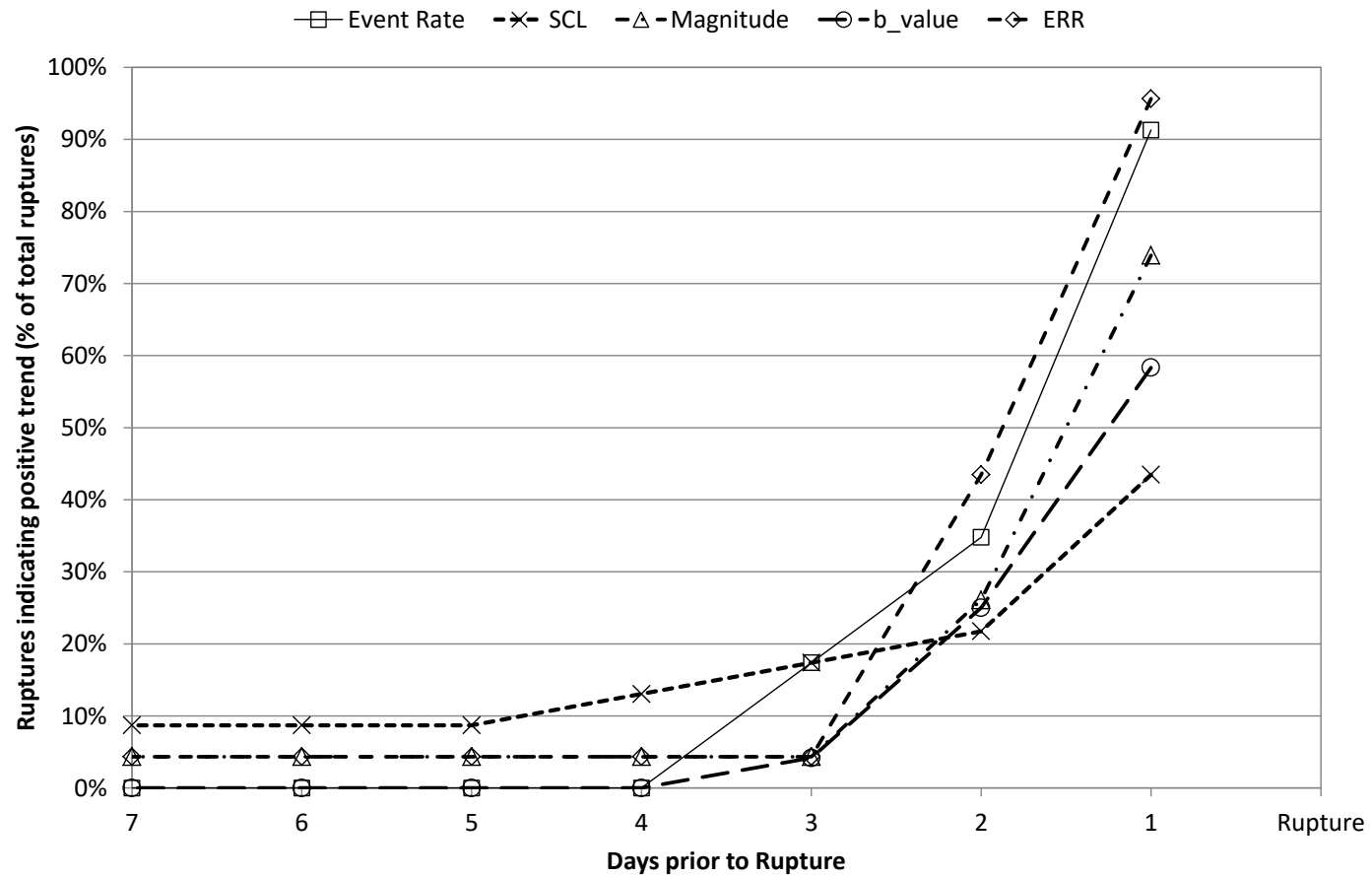


Figure A11 6: Comparison of 7 day parameters for instantaneous failures for the North East Faults Group 1 (23 failures).

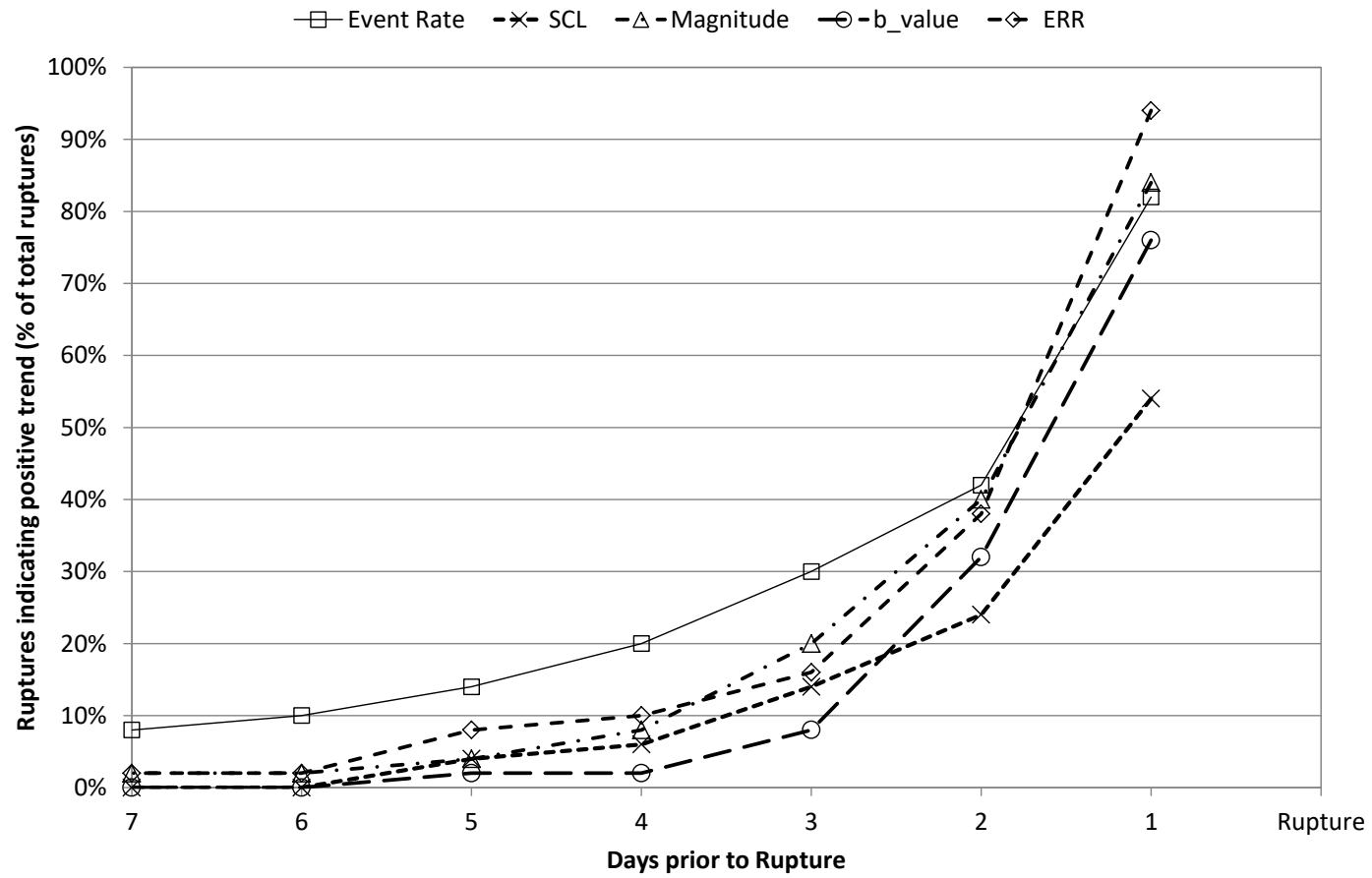


Figure A11 7: Comparison of 7 day parameters for instantaneous failures for the North East Faults Group 2 (50 failures).

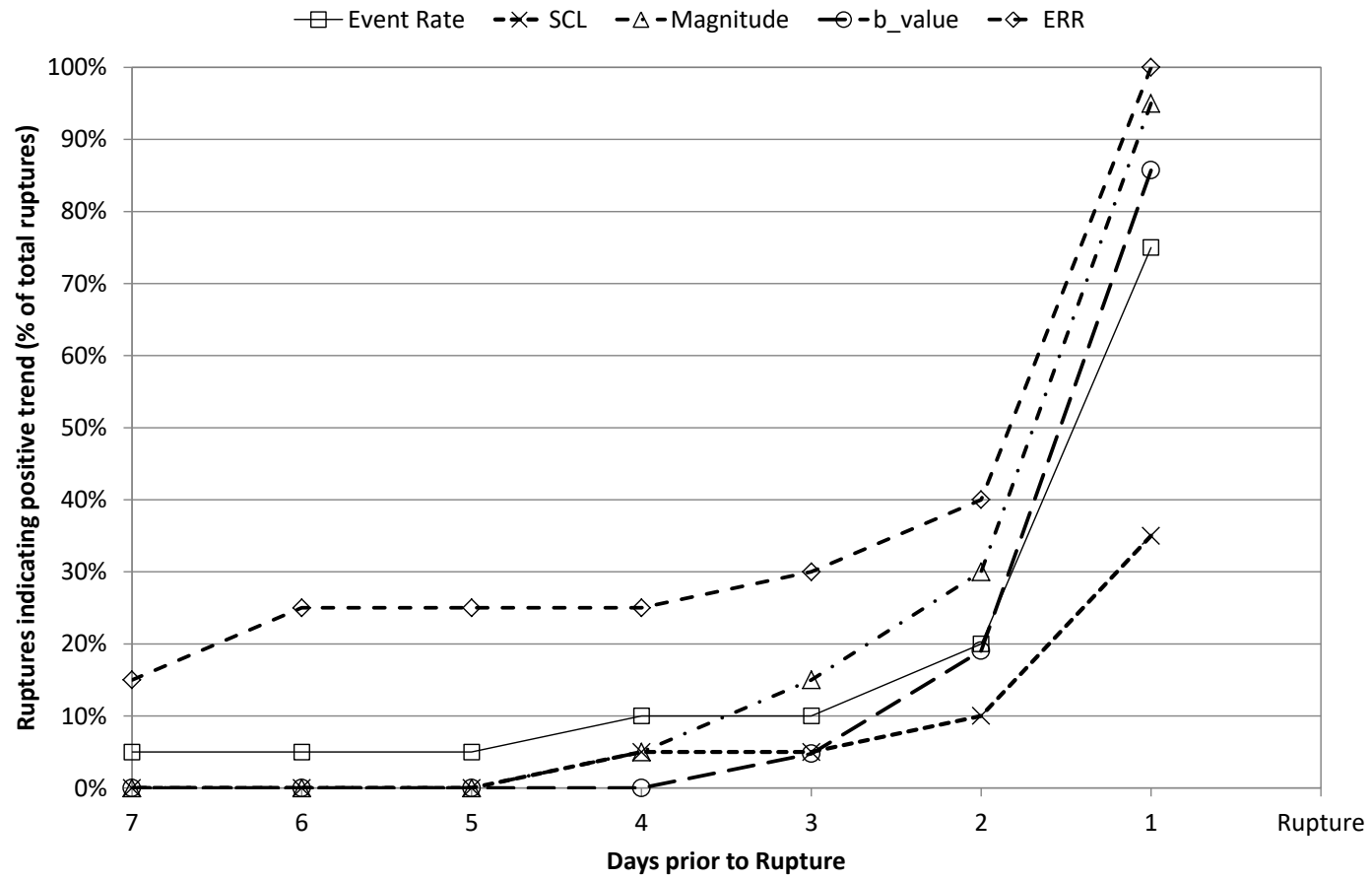


Figure A11 8: Comparison of 7 day parameters for instantaneous failures for the FaultP_1 (20 events).

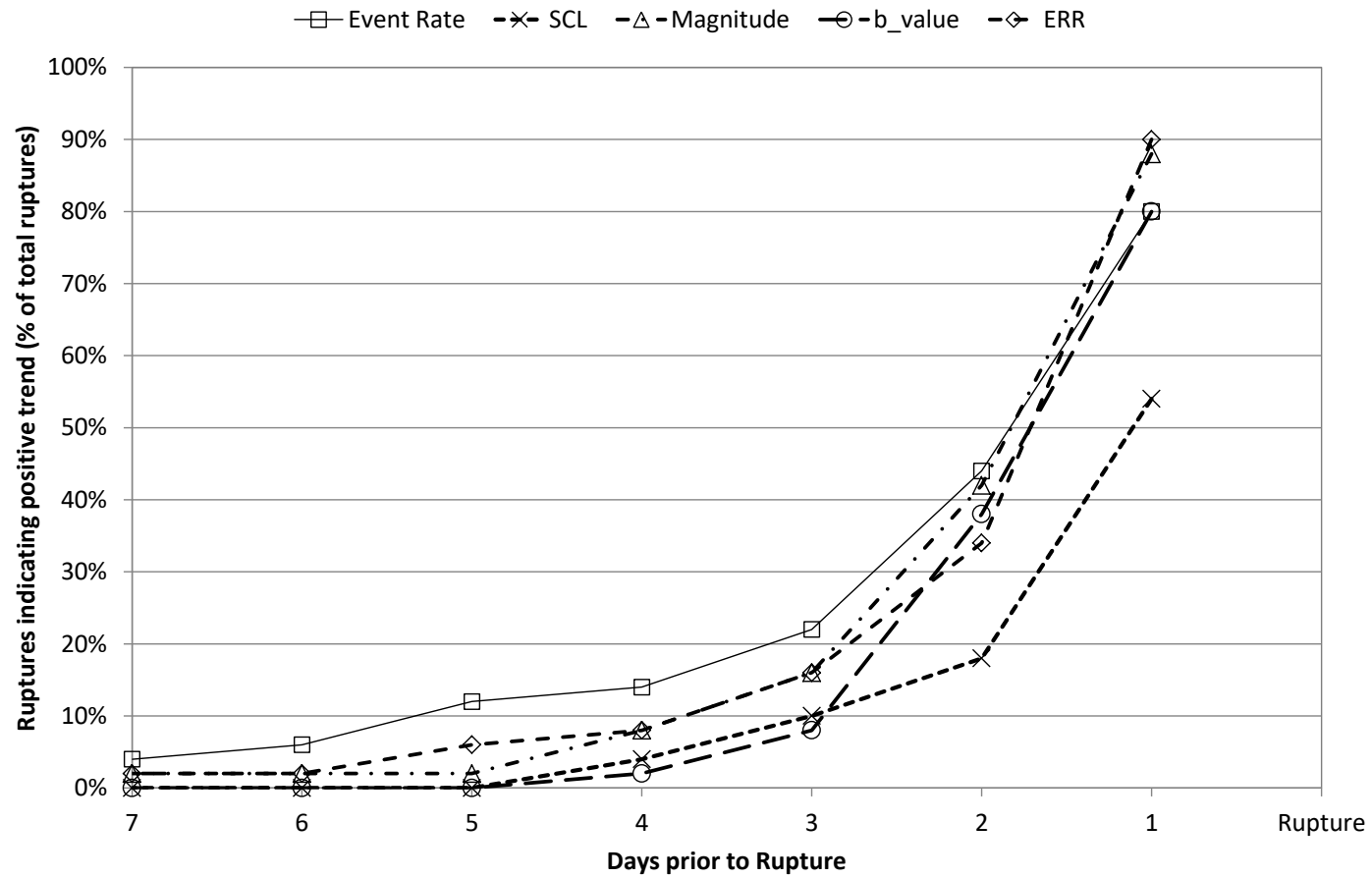


Figure A11 9: Comparison of 7 day parameters for instantaneous failures for the Fault B_C (50 failures).

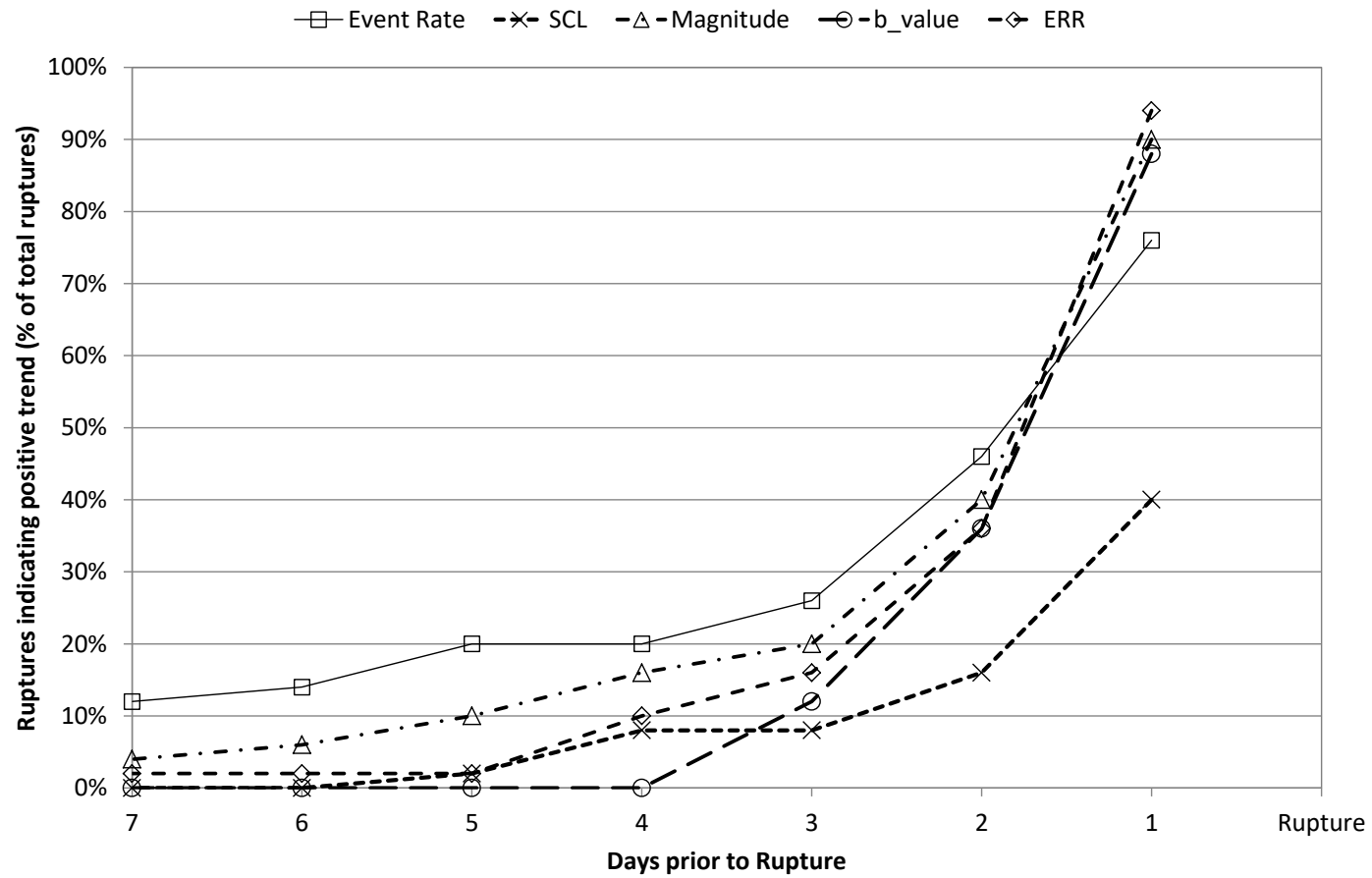


Figure A11 10: Comparison of 7 day parameters for instantaneous failures for the FW Dyke (50 failures).

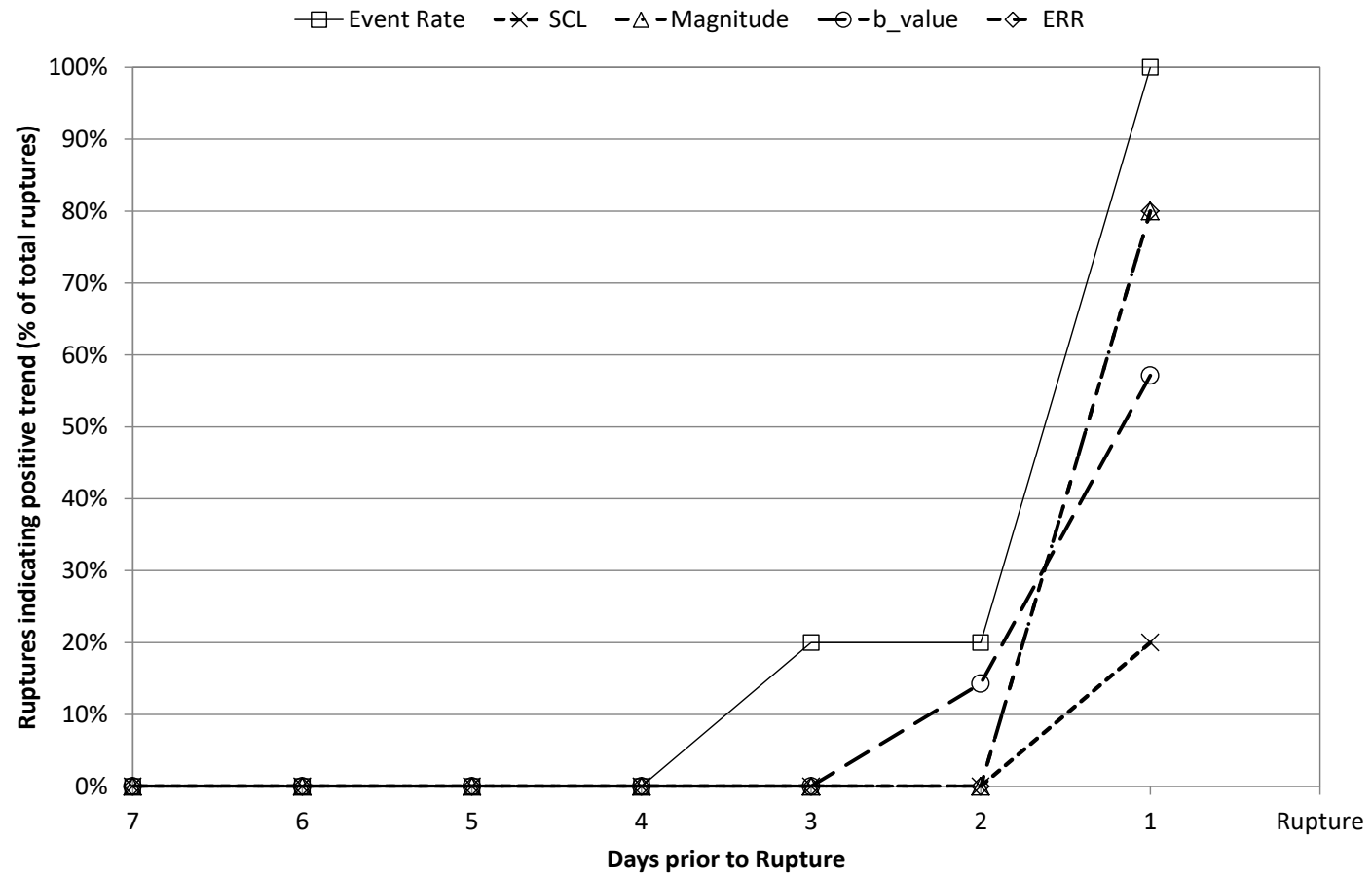


Figure A11 11: Comparison of 7 day parameters for instantaneous failures for the Maritana Fault (5 failures).

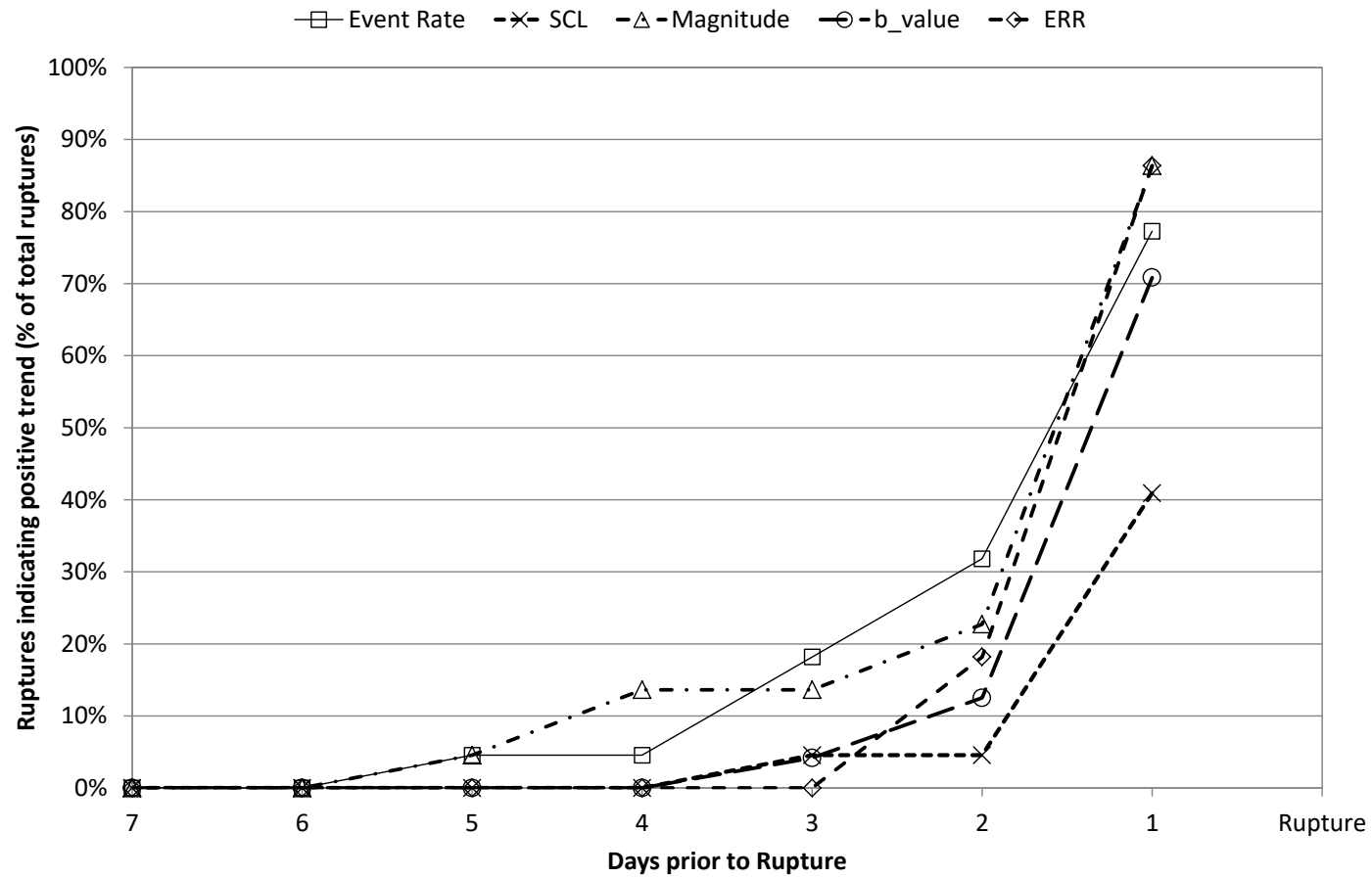


Figure A11 12: Comparison of 7 day parameters for instantaneous failures for the Reward Fault (22 failures).

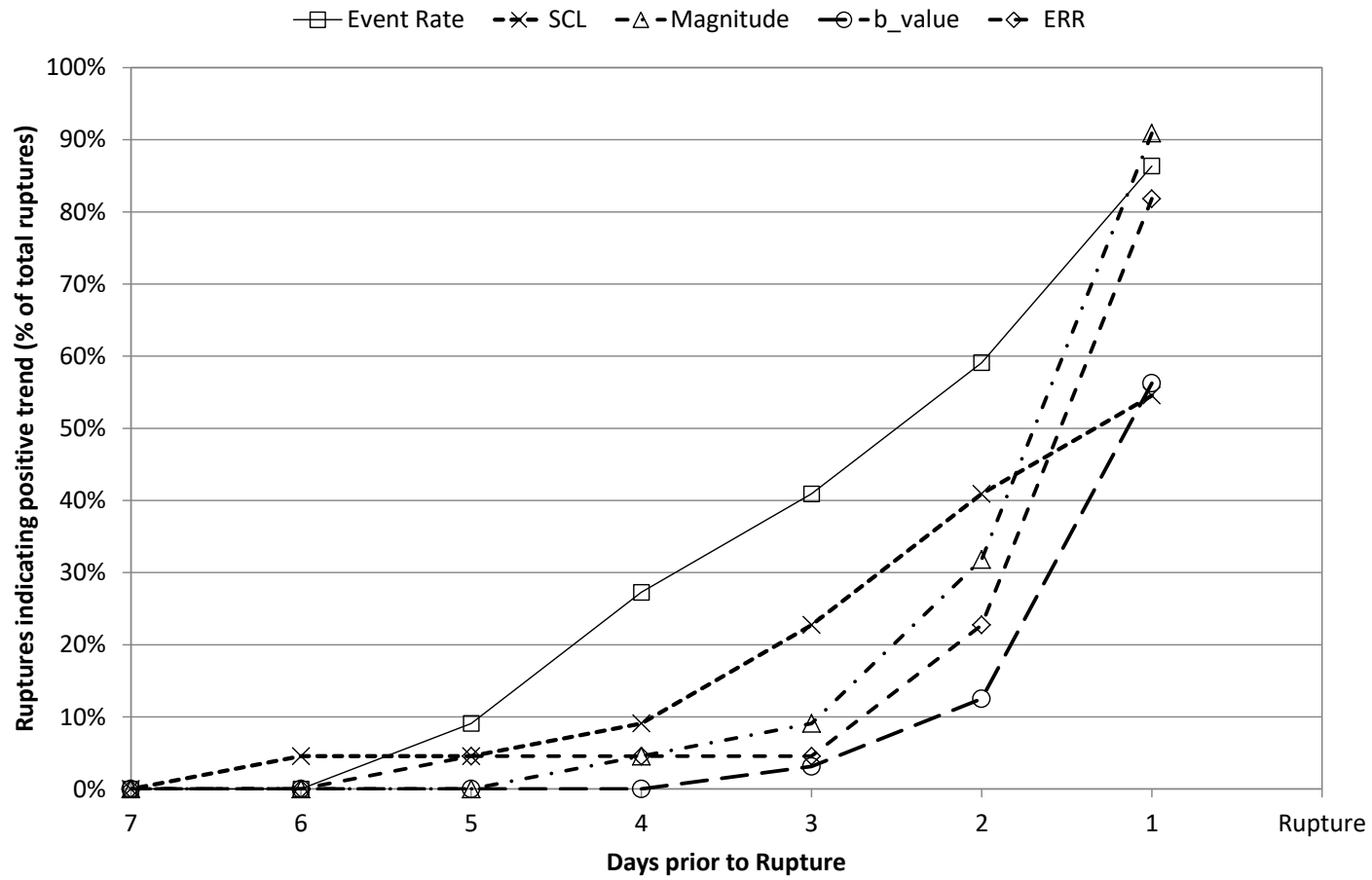


Figure A11 13: Comparison of 7 day parameters for instantaneous failures for the Flanagan Fault (22 failures).

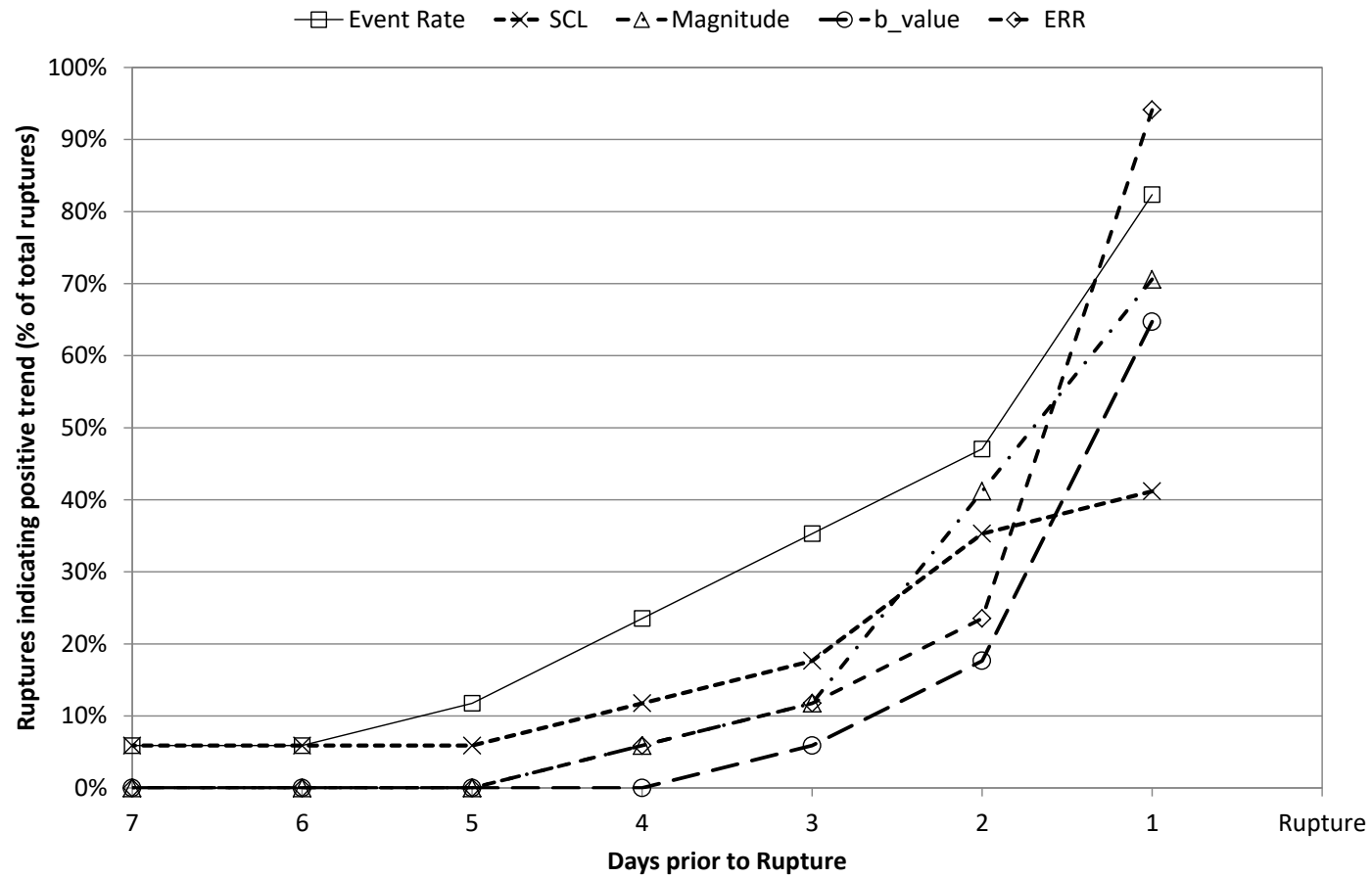


Figure A11 14: Comparison of 7 day parameters for instantaneous failures for the Feral Fault (17 failures).

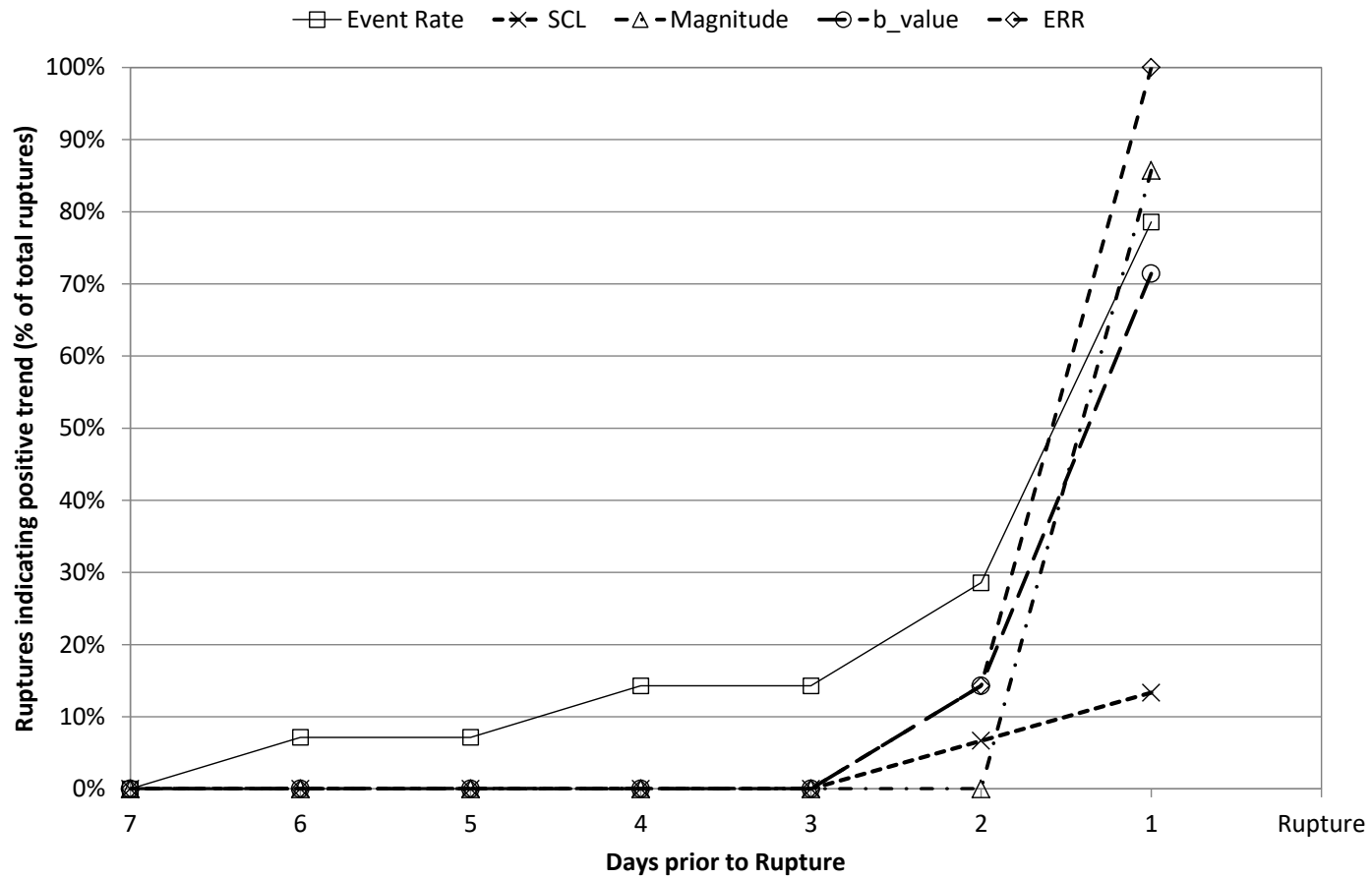


Figure A11 15: Comparison of 7 day parameters for instantaneous failures for the Great Lyell Fault (14 failures).

**Appendix 12 – Precursor comparison charts - 7 day averages,
accelerating slip failure results**

Comparison of parameters on each structure

7 Day Accelerating Slip Results

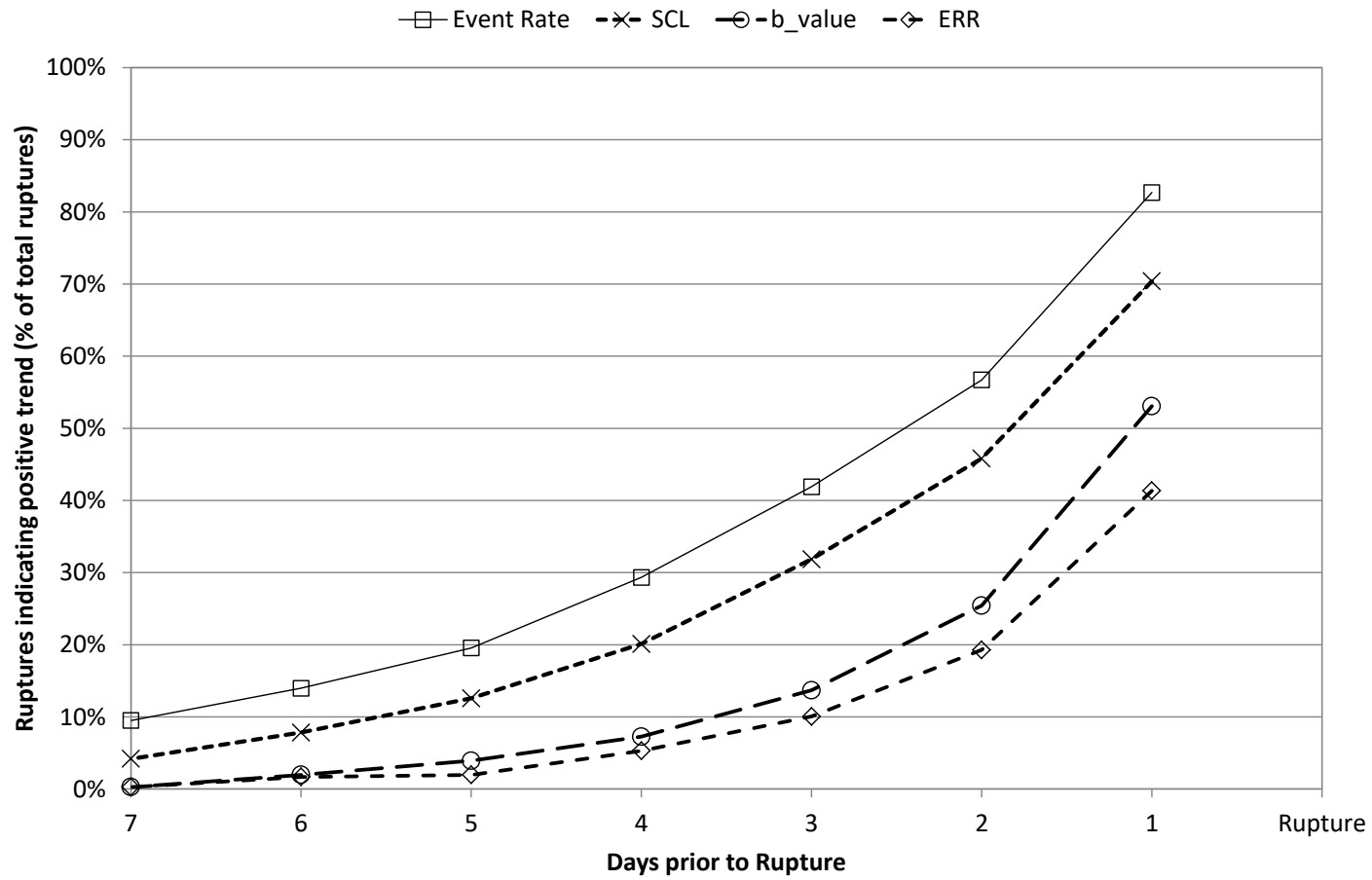


Figure A12 1: Comparison of average 7 Day parameters for accelerating slip failures on all structures.

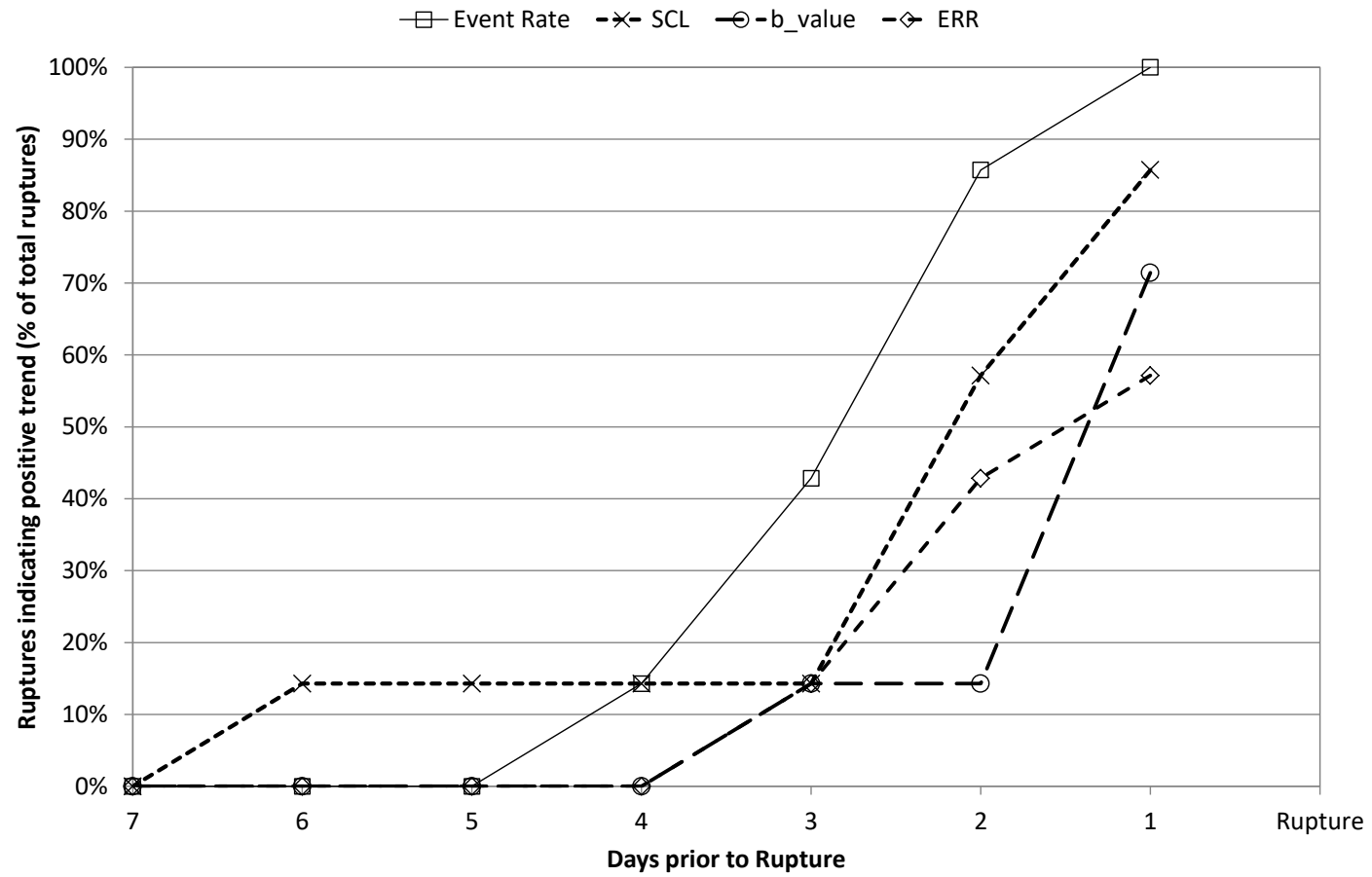


Figure A12 2: Comparison of 7 Day parameters for accelerating slip failures on the A1 Shear (7 failures).

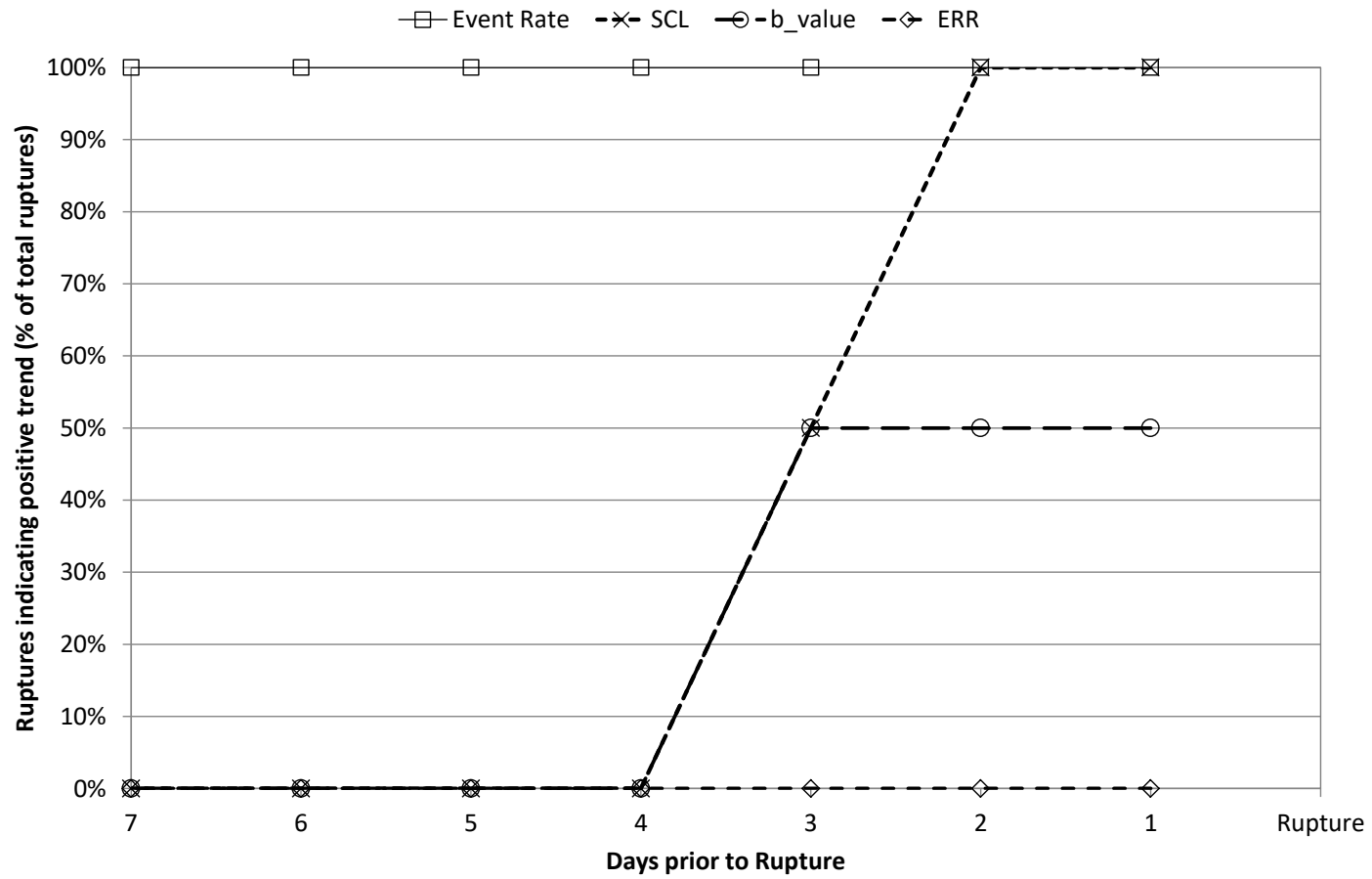


Figure A12 3: Comparison of 7 Day parameters for accelerating slip failures for the North Dyke (2 failures).

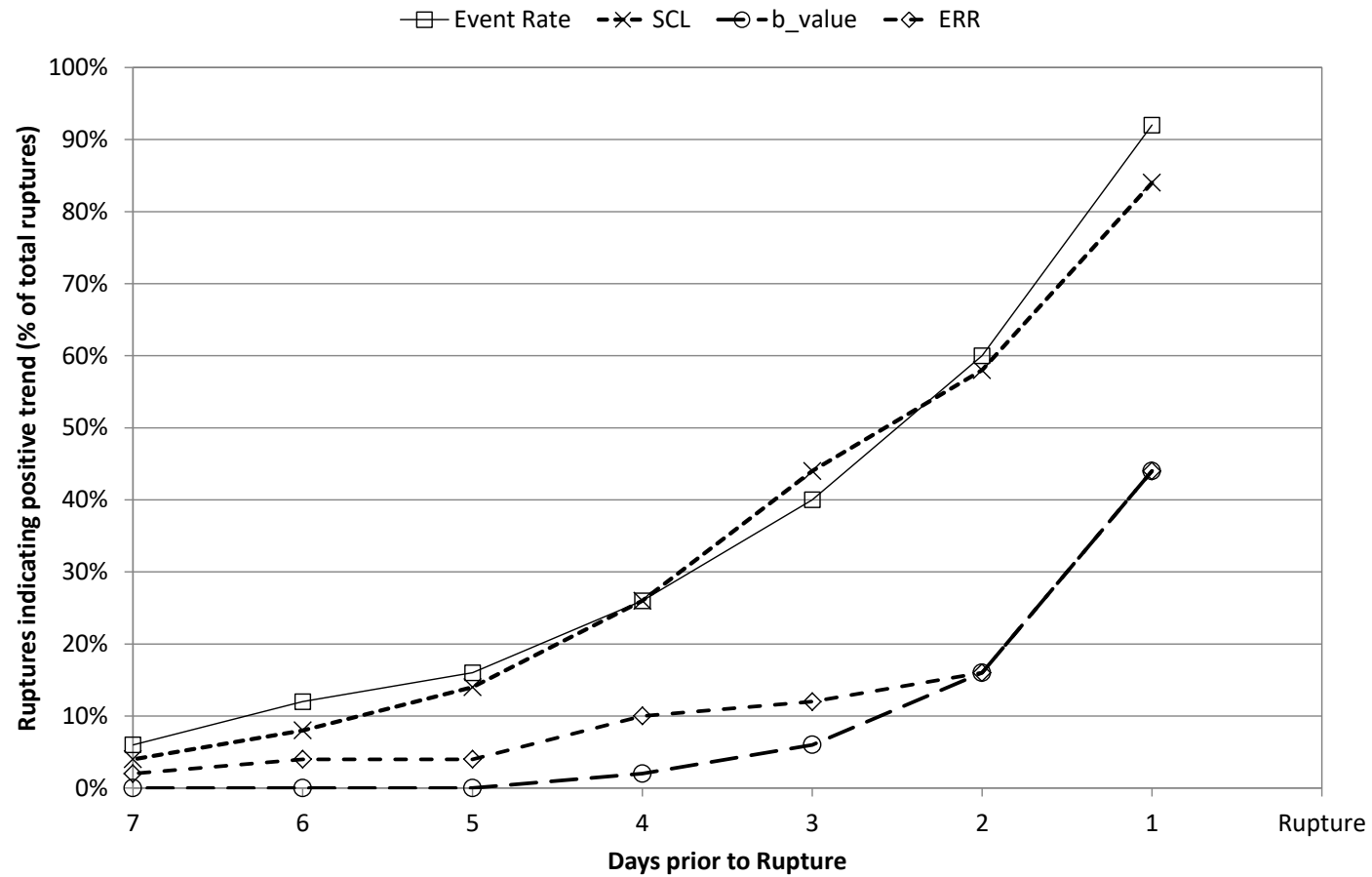


Figure A12 4: Comparison of 7 Day parameters for accelerating slip failures for the Fitzroy Fault (50 failures).

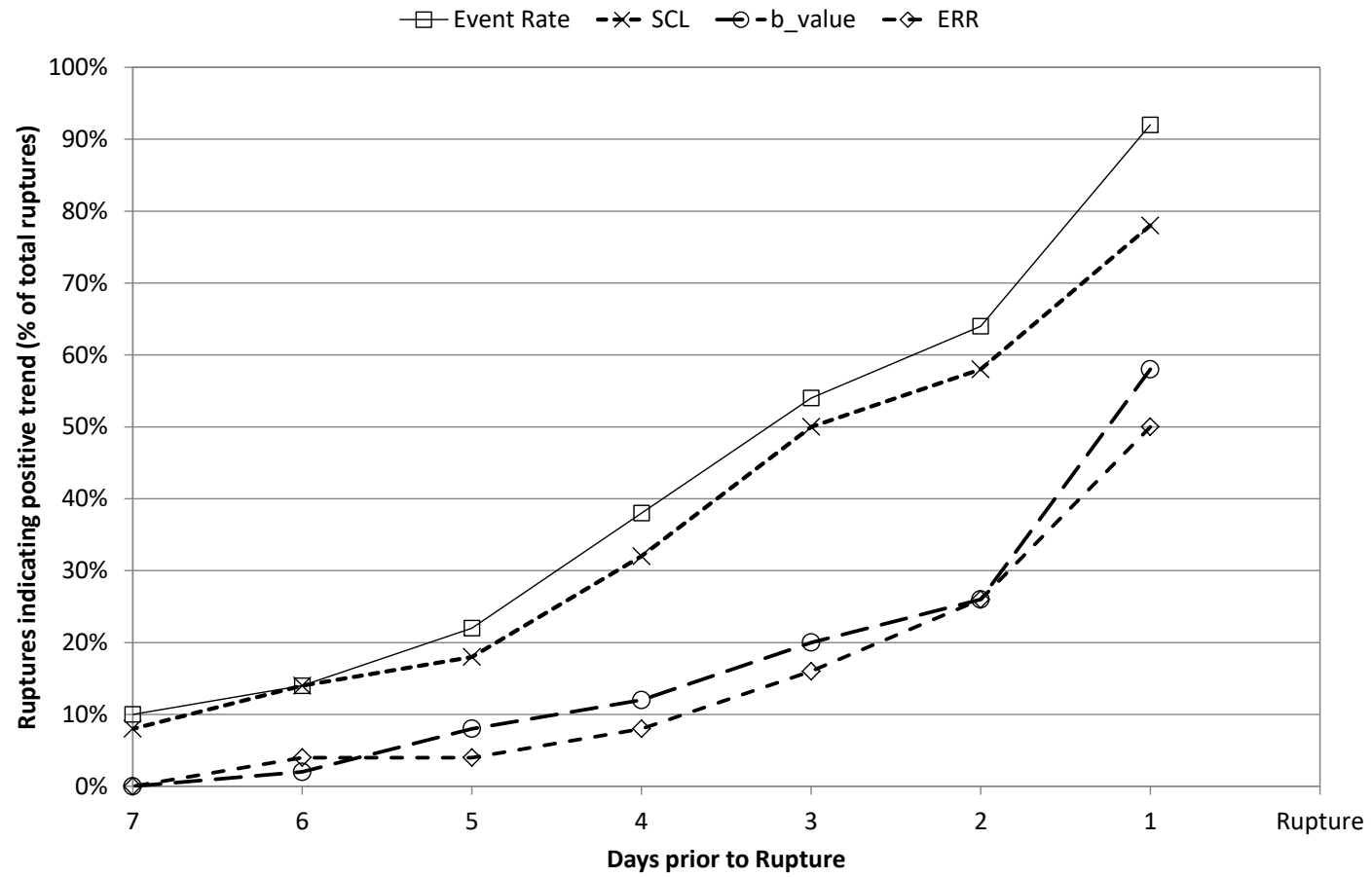


Figure A12 5: Comparison of 7 Day parameters for accelerating slip failures for the North East Faults Group 1 (50 failures).

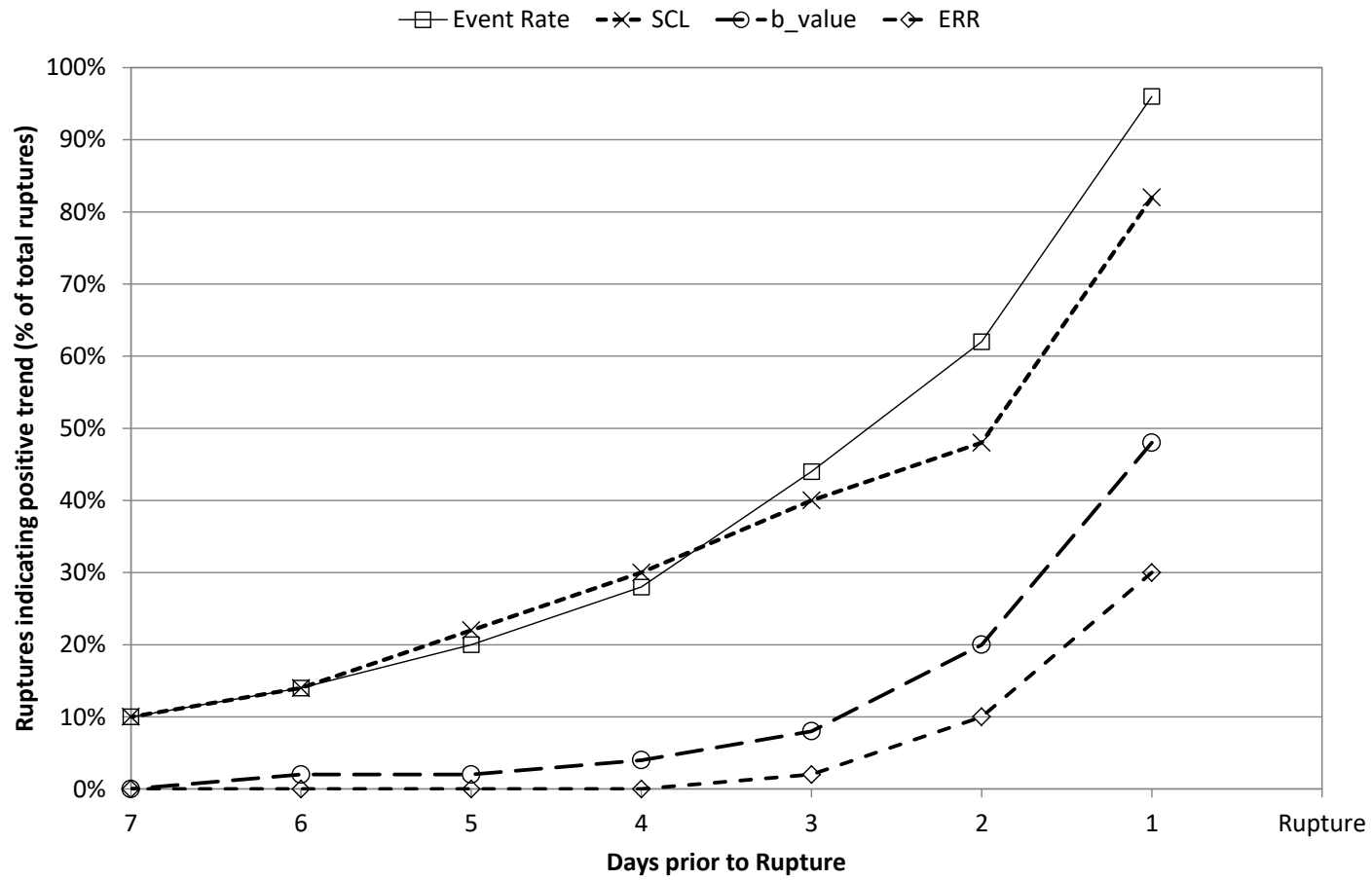


Figure A12 6: Comparison of 7 Day parameters for accelerating slip failures for the North East Faults Group 2 (50 failures).

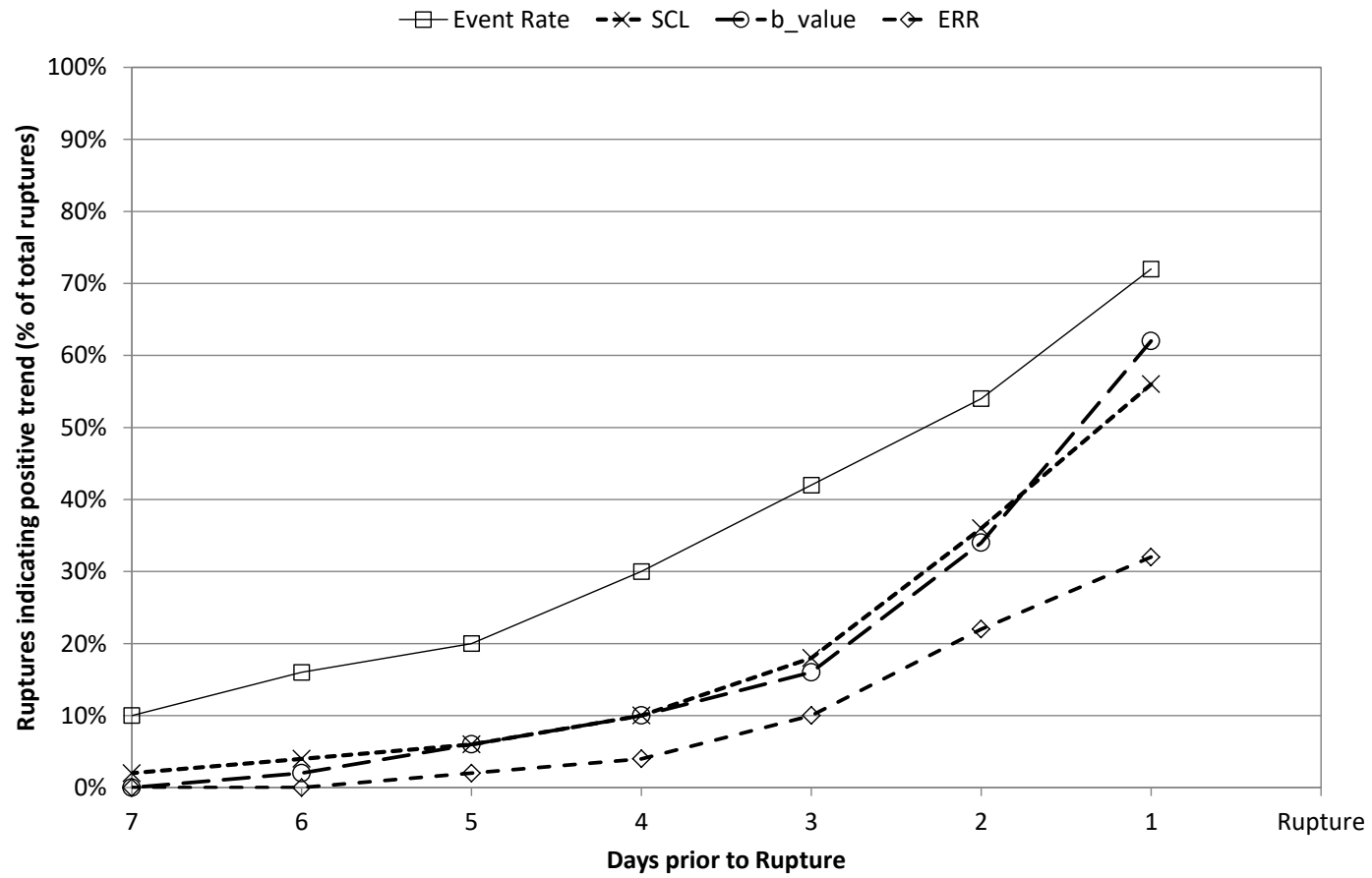


Figure A12 7: Comparison of 7 Day parameters for accelerating slip failures for the Fault B_C (50 failures).

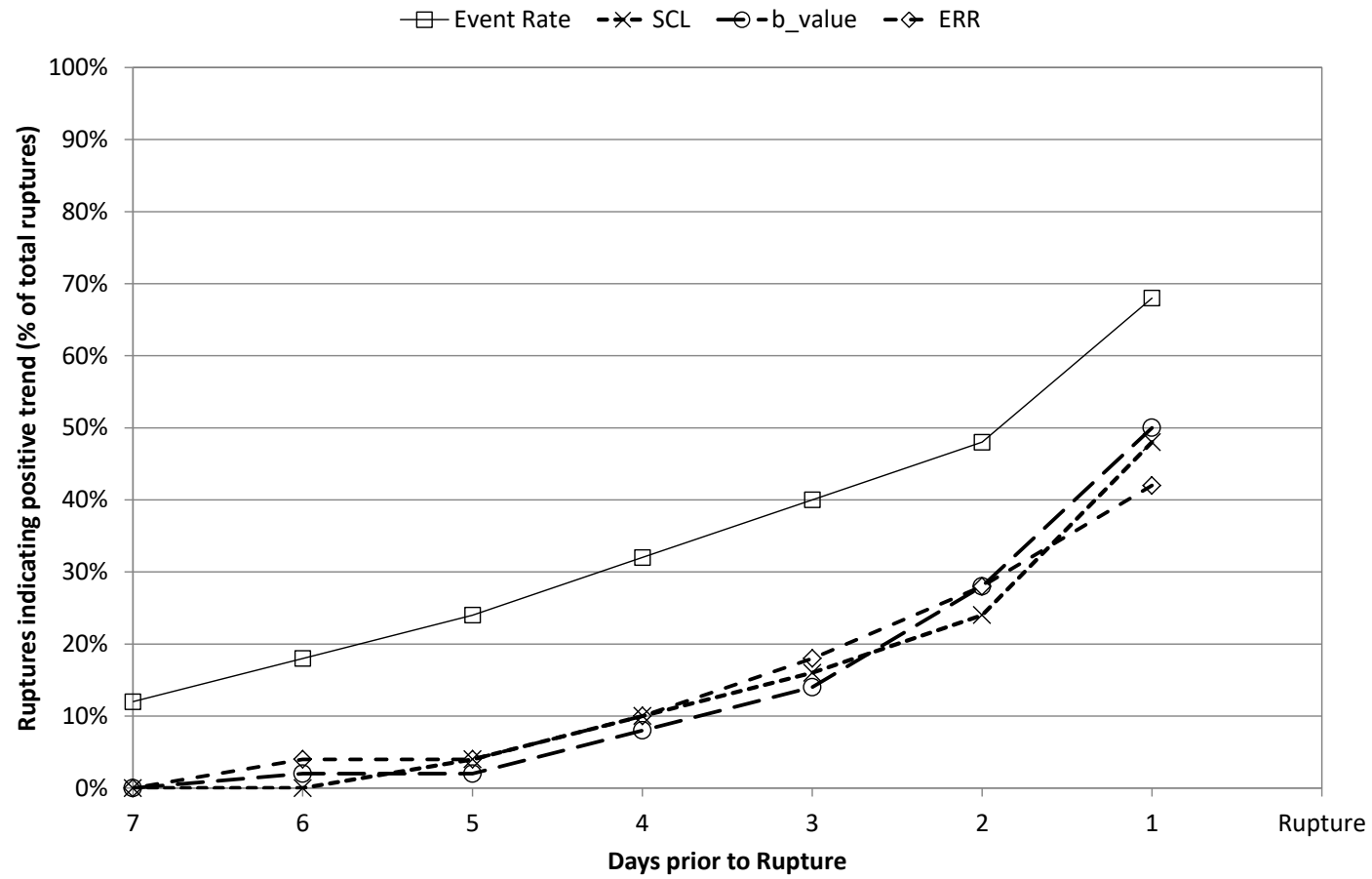


Figure A12 8: Comparison of 7 Day parameters for accelerating slip failures for the FW Dyke (50 failures).

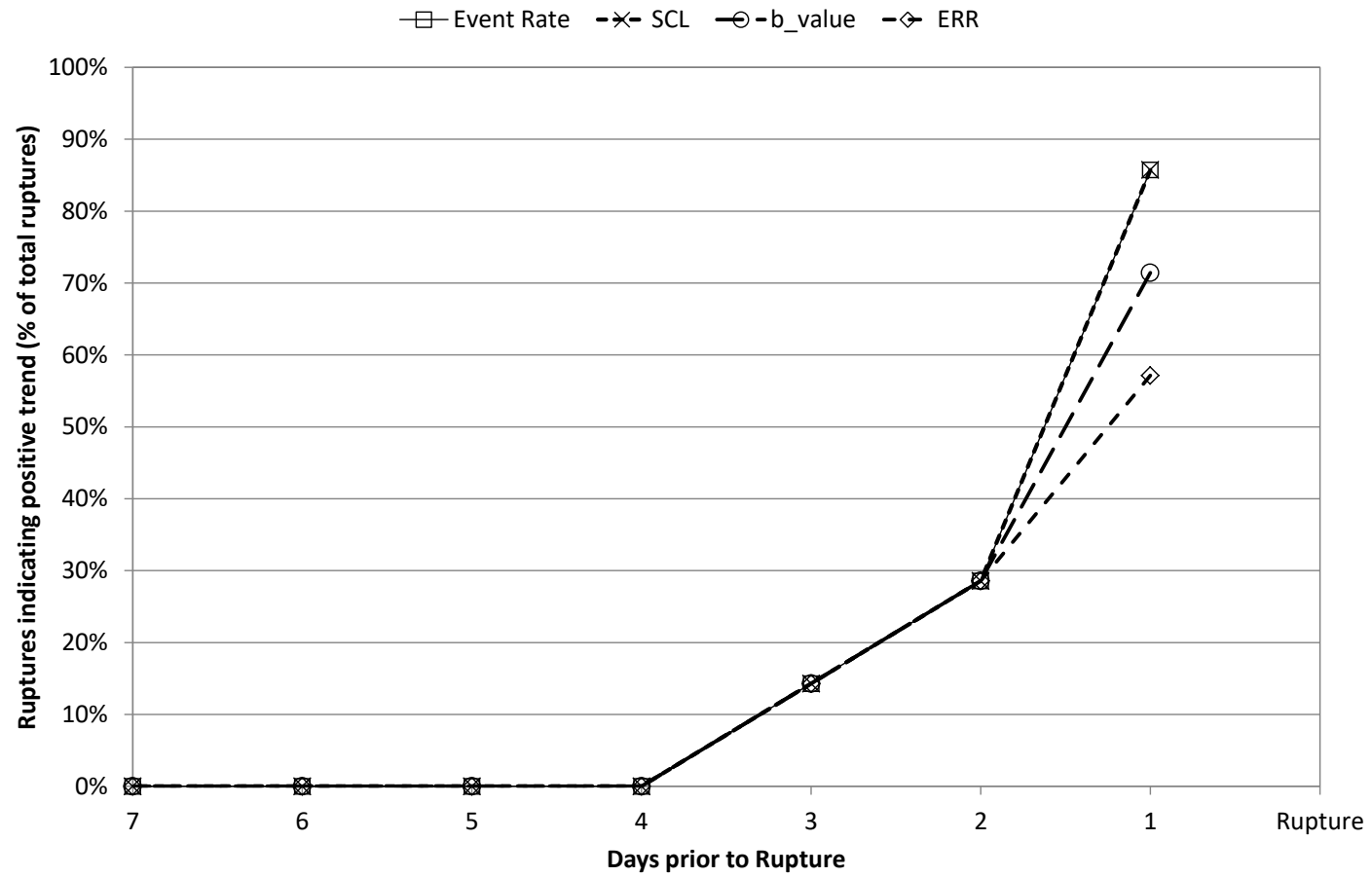


Figure A12 9: Comparison of 7 Day parameters for accelerating slip failures for the Reward Fault (7 failures).

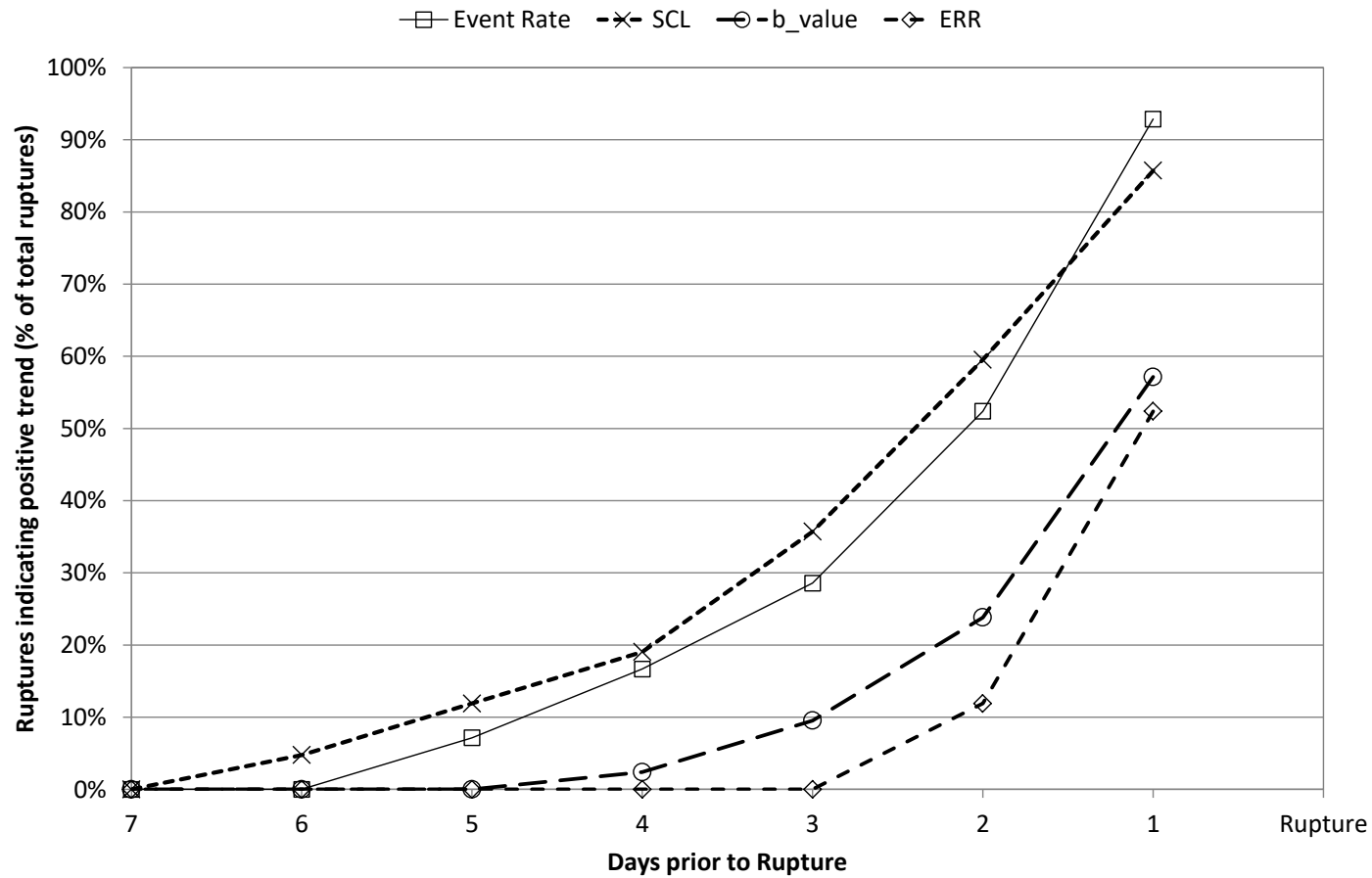


Figure A12 10: Comparison of 7 Day parameters for accelerating slip failures for the Flanagan Fault (42 failures).

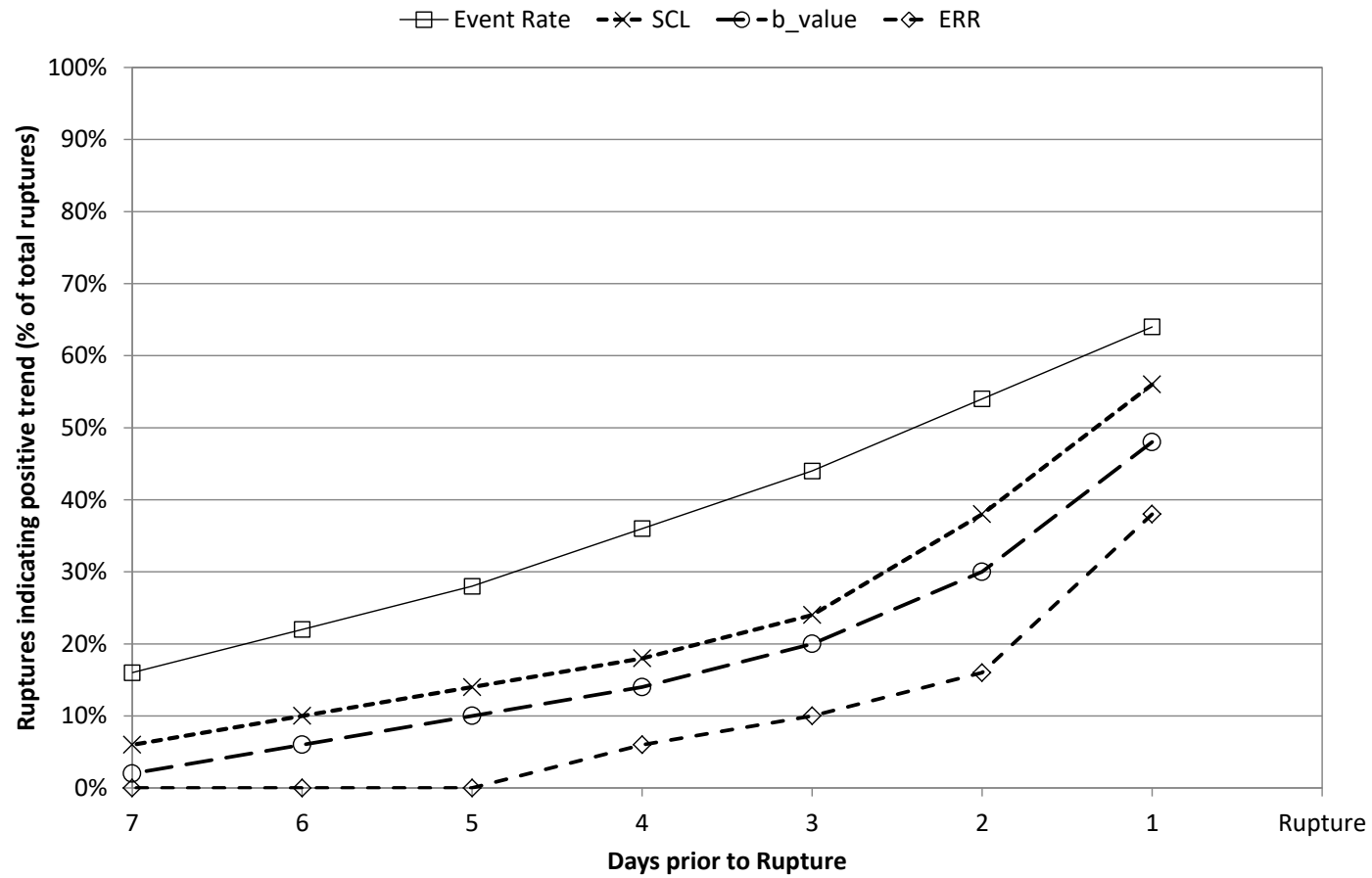


Figure A12 11: Comparison of 7 Day parameters for accelerating slip failures for the Feral Fault (50 failures).

